

**Edited by: A. Roósz, Zs. Veres, M. Svéda, G. Karacs**

# **Solidification and Gravity VII**

Edited by:  
A. Roósz  
Zs. Veres  
M. Svéda  
G. Karacs



# Solidification and Gravity VII



Selected, peer reviewed papers from the  
SEVENTH INTERNATIONAL CONFERENCE  
ON  
SOLIDIFICATION AND GRAVITY  
Miskolc-Lillafüred, Hungary  
September 3-6, 2018

*Edited by:*  
**A. Roósz, Zs. Veres, M. Svéda, G. Karacs**



Sponsored by

Nemak, Győr Hungary

Fux, Miskolc Hungary

Cover page: Dendrites

Painted by Karin Exner, 2014

ISBN: 978-963-508-889-8

Publisher

Hungarian Academy of Sciences – University of Miskolc, Materials Science Research Group  
Miskolc Committee of Hungarian Academy of Sciences,  
A. Roósz

# Preface

The “Solidification and Gravity International Conference”-series started in 1991. The first conference was held in Miskolc-Tapolca. The reason for organizing this conference was that the construction of Hungarian space furnace developed in co-operation with the Soviet partners became impossible.

Based on the theories worked out by Prof. Erik Fuchs, the development of a new type solidification equipment started at the Faculty of Material Science of University of Miskolc in 1984 (Faculty of Metallurgical Engineering in 1980) in co-operation with the Soviet partners on the basis of the experiences of BEALUCA space-experiment realized during the Hungarian-Soviet common space flight in 1980. Till now, this space materials science research work has been the first planned and prepared by the Hungarian researchers. The novelty of equipment is that neither the sample nor the furnace move; the required temperature distribution is developed by changing the temperatures of the 24 heating units that can be controlled separately during the melting and solidification process. The equipment would have been put to a platform flying individually; by this all of the possible disturbing acceleration (owing to the moving mechanisms and to the operation of life-sustaining devices in the space station) could have been excluded. However this process was interrupted by the political changes taken place in 1990; the co-operation with the Soviet partner ceased. At this time we decided with Prof. Pál Bárczy the manager of furnace building project to organize an international solidification conference in 1991 in which a version of the developed solidification equipment would be shown. The representatives of NASA (MFSC, Dr. Lehoczky) were also invited to the conference hoping by this that the construction of the equipment could be continued in co-operation with NASA in the future. It proved to be an excellent idea – the construction of equipment could be continued by the support of NASA (at that time the equipment was called Universal Multizone Crystallizator – UMC). Finally the equipment was delivered to the laboratory of NASA in Huntsville where it was tested for three years then three units were purchased. Unfortunately, the equipment was not sent to ISS in spite of the fact that it was suitable for this purpose. About 40 research workers coming mainly from the different countries of Europe took part in the first conference. The most famous participants were Prof. Martin Glicksman (Lenselear University, USA) and Prof. Wilfried Kurz (University of Lausanne, Switzerland).

Owing to the successes obtained by constructing the equipment and the results obtained during the investigation of solidification processes (a lot of papers were published in leading scientific journals and PhD dissertations were written both in Hungary and in Germany) as well as due to the close scientific relationships developing with the Max Planck Institute in Stuttgart and later with the Darmstadt University, the Conference entitled “Solidification and Gravity International Conference” could be organized in this case in Hotel Palota in Miskolc-Lillafüred several times (in 1995, 1999, 2004, 2008, 2013). High level papers were read by a lot of research workers from many countries on these conferences. In 2013, 70 research workers from 25 countries took part in the conference from different countries of Europe as well as from USA, China, Japan and Australia.

80 research workers from 17 countries were at the present conference (SG’18). The leading research workers of ESA and NASA reported about the situation of researches of space-material technology financed by the two organizations. 80 oral presentations were held in the 10 sessions; among them 7 summarizing plenary papers concerning the projects financed by ESA as well as 12 invited lectures dealing with the different fields of solidification were held.

In the papers published in the Conference Proceedings, the fast development of solidification theories as well as the shift of simulation of processes towards the numeric methods (Phase Field, Monte Carlo, Finite Difference) can be followed. The investigation technology has developed in a great extent since the first SG conference as well. The X-ray in situ investigations have been developed and applied and the solidified samples are investigated by using X-ray tomography and EBSD

method. This new knowledge contributes to the development of practical solidification technology (e.g. continuous and semicontinuous casting as well as pressure die-casting).

In the course of the conferences, we placed emphasis on showing Miskolc and its surroundings to the participants. Eger, Sárospatak and Tokaj were visited by the participants of conference. The research workers could take part in a marriage folk dance moreover in violin- organ- and jazz concerts. They tasted Tokaj Aszu which is called the vine of kings and the king of vines and they could swim in the famous cave bath in Miskolc-Tapolca during a night bathing.

Comprehensive information about Hungary and about the vicinity of Miskolc can always be found in the bag decorated by the emblem of Conference. The present bag contains a very nice photo album showing Hungary (I. Kolozsváry, J. Hajnal: Hungary) and a book describing the history of Hungary (Ignác Romsics: Short History of Hungary).

In the name of the Organizing Committee, I wish Good Luck to the participants by hoping that these almost four days spent in Miskolc-Lillafüred proved to be useful for them and they will keep the good impressions in their memory after returning home where they will develop the solidification theories or investigate the solidified microstructures in the future.

Miskolc, September, 2018

András Roósz  
Conference Chairman

**Organised by**  
Hungarian Academy of Sciences – University of Miskolc  
Materials Science Research Group  
Miskolc Committee of Hungarian Academy of Sciences



**Miskolc-Lillafüred, Palace Hotel**



## **International scientific committee**

S. Akamatsu, French National Centre for Scientific Research, Paris, France  
J.B. Andrews, University of Alabama, USA  
L. Arnberg, NTNU, Trondheim, Norway  
L. Battezzati, NIS, University of Torino, Italy  
C. Beckerman, University of Iowa, Iowa City, USA  
A. Diószegi, Jönköping University, Jönköping, Sweden  
S. Dost, University Of Victoria, Canada  
R. G. Erdmann University of Arizona, Tucson, Arizona, USA  
Y. Fautrelle, SIMAP/EPM/CNRS, Grenoble, France  
H. Fredriksson, Royal Institute of Technology, Stockholm, Sweden  
M. E. Glicksman, Florida Institute of Technology, USA  
L. Granasy, Wigner Research Centre for Physics, Budapest, Hungary  
L. Greer, Cambridge University, Cambridge, UK  
W. Kapturkiewicz, University of Mining and Metallurgy, Krakow, Poland  
A. Karma, Northeastern University, Boston, USA  
L. Katgerman, TU Delft, Nederland  
W. Kurz, Ecole Polytechnique Federale, Lausanne, Switzerland  
J. Lacaze, CIRIMAT ENSIACET, Toulouse, France  
P. Lee, Imperial College, London, UK  
A. Ludwig, University of Leoben, Leoben, Austria  
Y. Miyata, Nagaoka University of Technology, Nagaoka, Japan  
B.S. Murty, Indian Institute of Technology, Madras, Chennai, India  
A. Phillon, University of British Columbia, Canada,  
M. Rettenmayr, Friedrich Schiller University, Jena, Germany  
M. Rappaz, Ecole Polytechnique Federale, Lausanne, Switzerland  
I. Ratke, DLR, Cologne, Germany  
P. Schumacher, University of Leoben, Austria  
D. Stefanescu, Ohio State University, USA  
S. Steinbach, DLR, Cologne, Germany  
M. Wu, University of Leoben, Leoben, Austria  
H. Yasuda, Osaka University, Japan  
G. Zimmerman, ACCESS e.V., Aachen, Germany

### **Local Organised Committee**

A. Roósz (chairman)  
Z. Fan (co-chairmen)  
K. Voith, (secretary)  
Zs. Veres, G. Karacs, M. Svéda T. Mende

Contact

A. Roósz

Conference Chairman

Letters: University of Miskolc Institute of Materials Science

H-3515 Miskolc, Egyetemváros

Phone/Fax: +36 46 565 201

E-mail: femroosz@uni-miskolc.hu

<http://www.matsci.uni-miskolc.hu>

## Table of content

CHAPTER 1: Microgravity.....	15
Columnar and equiaxed solidification within the framework of the ESA MAP project CETSOL... <i>G. ZIMMERMANN, L. STURZ, Y.Z. Li, H. Nguyen-Thi, N. Mangelinck-Noël, R. Fleurisson, G. Guillemot, Ch.-A. Gandin, S. McFadden, R.P. Mooney, P. Voorhees, A. Roosz, C. Beckermann, A. Karma, N. Warnken, E. Perchat, G.-U. Grün, M. Grohn, I. Poittrault, D. Toth, W. Sillekens.....</i>	17
The ESA-MAP project “GRADE CET” - An overview of the joint research on solidification of TiAl-based alloys under hypergravity and microgravity conditions ..... <i>Ulrike Hecht, Can Huang, Julien Zollinger, Dominique Daloz, Miha Založnik, Martín Cisternas, Alexandre Viardin, Shaun McFadden, Laszlo Gránásy, Juraj Lapin, Nicolas Leriche, Florian Kargl.....</i>	27
Thermophysical Properties of Electrical Steels under Microgravity conditions ..... <i>Antonia Betzou, Michael Auinger, Sridhar Seetharaman, Begona Santillana, Prakash Srirangam.....</i>	37
Space for science: ESA’s microgravity research programme on materials science ..... <i>Wim Sillekens.....</i>	38
Microgravity Materials Science Solidification Studies – An American Perspective ..... <i>Richard Grugel.....</i>	38
The effect of magnetically controlled fluid flow on microstructure evolution in cast technical Al-alloys: The MICAST project ..... <i>Sonja Steinbach, Lorenz Ratke, Gerhard Zimmermann, Laszlo Sturz, Andras Roosz, Jeno Kovács, Yves Fautrelle, Olga Budenkova, Jacques Lacaze, Sadik Dost, Gerd-Ulrich Grün, Nils Warnken, Menghuai Wu, Wim Sillekens.....</i>	39
Overview of the µg-Foam ESA MAP project ..... <i>F. Garcia-Moreno, T. Neu, P. Kamm, F. Bülk, S. Hutzler and J. Banhart.....</i>	40
Melting in Microgravity: How crystalline shape changes led to new insights about interface dynamics..... <i>Martin Eden Glicksman.....</i>	41
Gravity Dependent Columnar-to-Equiaxed Transition in TiAl alloys: Solidification of Ti-46Al-8Nb in hyper gravity and Multi-physics modelling ..... <i>Can Huang, Ulrike Hecht, Julien Zollinger, Miha Založnik, Alexandre Viardin, Martín Cisternas.....</i>	42
Solidification of Al-Ni melts under terrestrial and microgravity conditions ..... <i>Marcus Reinartz, Stefan Burggraf, Matthias Kolbe, Phillip Paul, Peter Galenko, Dieter M. Herlach, Markus Rettenmayr.....</i>	43
CHAPTER 2: Phase field modelling ..... 45	
Free Energy vs. Grand Potential Energy formulations in phase field modelling of alloy solidification ..... <i>P.C. BOLLADA, A.M. MULLIS P.K. Jimack.....</i>	47
Meshless Phase Field Modeling of Dendritic Growth <i>TADEJ Dobravec, BOŠTJAN Mavrič, and BOŽIDAR Šarler.....</i>	52
Phase-field modeling of complex polycrystalline structures..... <i>László Gránásy, Tamás Pusztai.....</i>	59
Equiaxed growth of Al-Cu dendrites : 3D phase-field simulations ..... <i>Ahmed Kaci BOUKELLAL, Jean-Marc DEBIERRE.....</i>	59
Grain coarsening in two-dimensional orientation-field-based phase-field models ..... <i>Tamás Pusztai, Bálint Korbuly, Hervé Henry, Mathis Plapp, Markus Apel, László Gránásy</i>	60
CHAPTER 3: In situ observation ..... 61	
In-situ observation of the effects of gravity direction on directional solidification of the transparent alloy NPG-35wt%-DC <i>Turlough HUGHES, Shaun MCFADDEN, Anthony Robinson.....</i>	63

Real-time and full-field quantification of buoyant convection during multi-component solidification .....	
<i>Virkeshwar KUMAR, Atul SRIVASTAVA, Shyamprasad Karagadde</i> .....	69
Observation of dendrite evolution in Fe-C system by using time-resolved X-ray tomography.....	
<i>Hideyuki Yasuda, Yuta Tomiyori, Takuya Kawarazaki, Yuichi Kato, Kohei Morishita</i> .....	75
Analysis by in situ X-radiography of the impact of growth velocity on the grain structure during solidification of a refined Al-20wt.%Cu alloy .....	
<i>Hadjer Soltani, Guillaume Reinhart, Mohamed Chérif Benoudia, Moussa Zahzouh, Henri Nguyen-Thi</i> .....	82
Real-time dynamics of rod-like eutectic growth patterns on board the ISS : first results from TRANSPARENT ALLOYS .....	
<i>Silvère Akamatsu, Sabine Bottin-Rousseau</i> .....	88
Interface dynamics and microstructure selection during directional solidification of transparent bulk alloy conducted on DECLIC-DSI .....	
<i>Fatima Mota, Jorge Pereda, Younggil Song, Damien Turret, Rohit Trivedi, Alain Karma, Nathalie Bergeon</i> .....	89
In-situ observation of growth and interaction of equiaxed dendrites in microgravity .....	
<i>Laszlo Sturz, Martin Hamacher, Janin Eiken, Gerhard Zimmermann</i> .....	90
Equiaxed dendrite growth in non-refined Al-base alloys in real-time .....	
<i>Florian Kargl, Maike Becker, Joerg Drescher, Mareike Wegener, Christoph Dreissigacker</i> .....	91
Comparison of x-ray radiography of equiaxed alloy solidification in grain-refined Al-3.5wt.-%Ni with dendrite needle network modeling. ....	
<i>Laszlo Sturz, Angelos Theofilatos</i> .....	91
High resolution synchrotron imaging of dendritic coarsening in Ga – In alloys.....	
<i>Natalia Shevchenko, Joerg Grenzer, Olga Keplinger, Hieram Neumann-Heyme, Alexander Rack, Kerstin Eckert, Sven Eckert</i> .....	92
CHAPTER 4: Grain refinement.....	93
Roles of Mn in refining the grains of magnesium alloys with SiC inoculations .....	
<i>Jian GU, Yuanding HUANG, Karl Ulrich Kainer, Norbert Hort</i> .....	95
The Nucleation Progenitor Function (NPF) approach: An alternative approach to modelling equiaxed solidification .....	
<i>Robin P. MOONEY and Shaun MCFADDEN</i> .....	101
A first-principles study of the formation of atomically rough { 111 } MgO surface and its effect on prenucleation of Mg .....	
<i>C. M. FANG and Z. FAN</i> .....	107
Effect of grain refinement and the solid/liquid interface velocity on the microstructure of Al-20wt% Cu alloy.....	
<i>Arnold RÓNAFÓLDI, András ROÓSZ</i> .....	112
An Overview on Recent Advances in Understanding Early Stages of Solidification .....	
<i>Fan, Zhongyun</i> .....	118
Heterogeneous Nucleation by Structural Templating .....	
<i>H. Men, Z. Fan</i> .....	118
Heterogeneous nucleation on oxide in Al alloys .....	
<i>Feng Wang, Zhongyun Fan</i> .....	119
A novel grain refiner for effective grain refinement Al-alloys.....	
<i>Z.P. Que, Y. Wang, Z. Fan</i> .....	119
Segregation of Ca at the Mg/MgO interface and its effect on grain refinement .....	
<i>Shihao Wang, Yun Wang, Quentin Ramasse, Zhongyun Fan</i> .....	120
Effect of agglomeration of potent nucleant particles on grain size in the as-cast microstructure .....	
<i>F. Gao, Z Fan</i> .....	120
Effect of surface roughness on prenucleation.....	
<i>B. Jiang, H. Men, Z. Fan</i> .....	121

Removal of oxide skin from molten aluminum surface .....	
<i>Zoltán Kéri, György Kaptay</i> .....	121
CHAPTER 5: Casting .....	123
An alternative approach for the experimental verification of microsegregation models using an in-situ hot tensile test during solidification of steel .....	125
<i>Michael BERNHARD, Christian BERNHARD, Peter Presoly and Dali You</i> .....	125
Effect of Pulling Rate on the Structural Zones Localization in the Continuously Cast Brass Ingot <i>Waldemar WOŁCZYŃSKI, Anna A. IVANOVA, Piotr Kwapisiński, and Krzysztof Sztwiertnia</i> .....	131
High concentrations at the final solidification of advanced steels: Thermodynamic evaluation of replicated “segregation-samples” by means of DTA/DSC-measurements .....	
<i>Peter PRESOLY, Michael BERNHARD, Dali You, Christian Bernhard</i> .....	138
Discussion on possible solidification during SEN clogging in steel continuous casting .....	
<i>Hadi BARATI, Menghuai WU, Abdellah Kharicha, Andreas Ludwig</i> .....	144
The Melt Cleaning Efficiency of Fluxes with Different Physical and Chemical Properties .....	
<i>Gábor GYARMATI, György FEGYVERNEKI, Tamás MENDE and Monika TOKÁR</i> .....	150
Pressure driven undercooling at solidification of hypoeutectic cast iron.....	
<i>Attila Diószegi and Péter Svidró</i> .....	157
Fabrication and properties of magnesium matrix composite obtain using thixomolding technology <i>Łukasz Rogal, Bogusław Baran, Lidia Litynska-Dobrzanska</i> .....	157
CHAPTER 6: Modelling, simulation.....	159
3D Modelling of the impact of inlet flow on macrosegregation formation in DC casting of Aluminium alloys accounting for grain morphology and transport.....	161
<i>Akash PAKANATI, Mohammed M'HAMDI, Hervé Combeau and Miha Založnik</i> .....	161
Numerical modelling of the effect of electromagnetic stirring direction in continuous casting of steel billets <i>MRAMOR Katarina, VERTNIK Robert and ŠARLER Božidar</i> .....	167
Numerical simulation series for the investigation and validation of the Lorenz force field in bidirectional travelling magnetic field via thermal gradient shift effect .....	
<i>Csaba Nagy, Olga Budenkova Y. du Terrail A. Rónaföldi A. Roósz</i> .....	173
A 3-phase equiaxed solidification numerical model for binary alloy coupling macroscopic transport and grain growth <i>Tao WANG, Olga BUDENKOVA, Yves Delannoy, Yves Fautrelle and Engang Wang</i> .....	179
Numerical Simulation of Heat Transfer and Fluid Flow in Electroslag Remelting Process <i>Hao SHI, Houfa SHEN</i> .....	185
The Simulation of Special Gravity Filling Conditions <i>Daniel MOLNAR, David HALAPI, Marianna Bubenko</i> .....	191
Investigation of the effect of asymmetric thermal conditions on stresses during continuous casting of steel with the use of meshless travelling-slice model <i>BOŠTJAN Mavrič, TADEJ Dobravec, ROBERT Vertnik and BOŽIDAR Šarler</i> .....	197
Macroscopic modeling of solidification of TiAl alloys in hypergravity .....	
<i>Martín Cisternas, Miha Založnik and Hervé Combeau</i> .....	204
Simulation of mechanical deformation during dendritic solidification .....	
<i>Bogdan Nenchev, Dr. Simon Gill</i> .....	205
Phase-field modeling of mobile dendrites in melt flow .....	
<i>László Rátkai, Tamás Pusztai, László Gránásy</i> .....	205
A quantitative benchmark of multiscale models for dendritic growth.....	
<i>Sabrina Ziri, Laszlo Sturz, Alexandre Viardin, Miha Založnik, Damien Turrett</i> .....	206
Numerical simulation of chill cooling and solidification of a levitated steel droplet in microgravity.....	
<i>Ayoub Aalilija, Elie Hachem, Charles-André Gandin</i> .....	207



3D mesoscopic modeling of isothermal equiaxed dendritic solidification of Al-20 wt% Cu .....	
<i>Antonio Olmedilla, Miha Založnik, Hervé Combeau.....</i>	208
Monte Carlo Simulations of Chemical Segregation at the Liquid/Substrate Interface .....	
<i>H. Tetlow, Z. Fan.....</i>	209
Multiscale modelling of dendritic growth by a combination of three methodologies .....	
<i>Romain Fleurisson, Gildas Guillemot, Charles-André Gandin.....</i>	210
CHAPTER 7: Solidification of dendrite .....	211
A Large-Scale 3D Computer Tomography analysis of Primary Dendrite Arm Spacing Response to Withdrawal Velocity Change Using Dendrite Centre Tracking .....	
<i>J. E. MILLER, L. STURZ, S. Steinbach, G. Zimmermann, and N. Warnken.....</i>	213
Tunable concentration gradients generated by controlled changes in the solidification conditions .....	
<i>Hannes ENGELHARDT, Dorothea MEY and Markus Rettenmayr.....</i>	220
Influence of nucleation and dendrite fragmentation on as-cast structure of Sn- 10wt.%Pb benchmark .....	
<i>Yongjian ZHENG, Menghuai WU, Abdellah Kharicha, Andreas Ludwig.....</i>	226
Effect of temperature and heating rate on dissolution of a 3003 core by a 4004 clad during vacuum brazing .....	
<i>JACQUES Bruno, LACAZE Jacques, MAZET Thierry, VYNNYCKY Michael and DEZELLUS Olivier.....</i>	232
On the Primary Solidification of Fe-C Alloys: Morphological Evolution of Primary Austenite During Coarsening .....	
<i>Juan Carlos HERNANDO, Isabel María MEDINA AGUDO and Attila DIÓSZEGI.....</i>	238
Directional Solidification of the Al-0.25 wt%Zr Overhead Line Conductor .....	
<i>Elif YILMAZ, Emine Acer EROL, Harun Erol and Mehmet Gündüz.....</i>	244
Undercooling studies and growth velocity measurements on multi- component FeCuNi{X} alloys .....	
<i>Rahul M R, Sumanta Samal and Gandham Phanikumar.....</i>	250
Phase selection in solidification of undercooled Co-B alloys .....	
<i>Xiuxun Wei, Wanqiang Xu, Jilong Kang, Michael Ferry, Jinfu Li.....</i>	255
Solidification behavior and microstructure analysis of ternary Zr-Cu-(Al/Ni) alloys.....	
<i>Stefanie Koch, Peter Galenko, Olga Shuleshova, Raphael Kobold, Markus Rettenmayr.....</i>	255
CHAPTER 8: Forced convection .....	257
Effect of forced convection on dendritic growth: theoretical modeling and analysis of recent experimental results .....	
<i>P.K. GALENKO, D.V. ALEXANDROV, L.V. Toropova, M. Rettenmayr and D.M. Herlach.....</i>	259
Numerical simulation of fluid flow in the mushy zone under rotation magnetic field: influence of permeability .....	
<i>Haijie Zhang, Menghuai WU, Yongjian Zheng, Andreas Ludwig, Abdellah Kharicha.....</i>	265
The effect of electromagnetic stirring during solidification of Co-Cr alloys .....	
<i>Inês OLIVEIRA, Rui SOARES, Ricardo Paiva João Ferreira<sup>2</sup>, Ana Reis, Rui Neto.....</i>	271
Influence of Al-alloy composition on the potential of forced convection to reduce grain size and prevent macrosegregation .....	
<i>Räbiger DIRK, Willers BERND, Eckert Sven.....</i>	278
The effect of magnetically controlled fluid flow on microstructure evolution in cast technical Al-alloys: The MICAST project .....	
<i>Sonja Steinbach, Lorenz Ratke, Gerhard Zimmermann, Laszlo Sturz, Andras Roos, Jeno Kovács, Yves Fautrelle, Olga Budenkova, Jacques Lacaze, Sadik Dost, Gerd-Ulrich Grün, Nils Warnken, Menghuai Wu, Wim Sillekens.....</i>	284
Investigations of forced flow effects on dendritic solidification .....	
<i>Natalia Shevchenko, Olga Keplinger, Sven Eckert.....</i>	285
Phase-field modeling of melt flow and directional solidification in Ti48Al alloy .....	
<i>Alexandre Viardin, Julien Zollinger, Markus Apel, Janin Eiken, Ralf Berger, Laszlo Sturz, Dominique Daloz, Ulrike Hecht.....</i>	286

In-situ analysis of thermoelectric magnetic effect by synchrotron X-radiography during directional solidification under static magnetic field .....	
<i>Henri Nguyen-Thi, Lara Abou-Khalil, Georges Salloum-Abou-Jaoude, Jiang Wang, Mariano Garrido, Guillaume Reinhart, Xi Li, Zhong-Min Ren and Yves Fautrelle</i> .....	286
FEM Magneto-thermo-electric modeling around a solid grain during alloy solidification under uniform AC/DC magnetic field .....	
<i>Yves Du Terrail Couvat, Olga Budenkova, Thiago Takamura Yanaguissava, Annie Gagnoud</i> .....	287
The effect of strong melt flow induced by the rotating magnetic field on the structure of Al <sub>6</sub> Si <sub>4</sub> Cu alloy.....	
<i>Jenő Kovács, Arnold Rónaföldi, Árpád Kovács, András Roósz</i> .....	288
Effect of Travelling Magnetic Field on the Solidified Structure of Peritectic Sn–Cd Alloy .....	
<i>Maria Sveda, Anna Sycheva, Arnold Ronafoldi, Andras Roosz</i> .....	288
CHAPTER 9: Compound solidification.....	289
Microstructure Characterisation of Drop Tube Processed SiGe Semiconductor alloy	
<i>Naveed HUSSAINI and Andrew M MULLIS</i> .....	291
Applying directional solidification to Cu doped Bi <sub>2</sub> Te <sub>3</sub> thermoelectric materials	
<i>Dongmei LIU, Xinzhong LI and Markus Rettenmayr</i> .....	297
Morphology of bismuth precipitates in Zn-Bi single crystals for bactericidal applications .....	
<i>Grzegorz Boczkal, Paweł Palka, Wojciech Spisak, Andrzej Chlebicki</i> .....	303
A Novel Directional Solidification of TiAl-based Alloy Using Y <sub>2</sub> O <sub>3</sub> Mould Coupled with Electromagnetic Cold Crucible Zone Melting Technology .....	
<i>Hongsheng Ding, Hailong Zhang, Haitao Huang, Ruirun Chen, Jingjie Guo, Hengzhi Fu</i> .	304
CHAPTER 10: Eutectic, peritectic. monotectic, foam .....	305
Reduced Gravity Processing of Cu-Co Metastable Monotectic Alloy via Drop-Tube Processing	
<i>Andrew M MULLIS, Oluwatoyin JEGEDE and Robert F Cochrane</i> .....	307
Microstructure evolution and mechanical properties of Co-Fe-Ni-Ti-V eutectic high entropy alloy	
<i>Rahul M R, Reliance Jain, Sumanta Samal, Gandham Phanikumar</i> .....	313
Investigation on the Liquid Flow ahead of the Solidification Front During the Formation of Peritectic Layered Solidification Structures .....	
<i>J.P. MOGERITSCH, T.PEIFER, M. Stefan-Kharicha, A. Ludwig</i> .....	319
Liquid phase separation and rapid solidification of Ti <sub>60</sub> Y <sub>40</sub> alloys	
<i>Dandan ZHAO, Jianrong GAO, Dirk Holland-Moritz and Matthias Kolbe</i> .....	325
Investigation on the Binary Organic Components TRIS-NPG as Suitable Model Substances for Metal-Like Solidification .....	
<i>J.P. Mogeritsch, A. Ludwig</i> .....	330
Overview of the µg-Foam ESA MAP project .....	
<i>F. Garcia-Moreno, T. Neu, P. Kamm, F. Bülk, S. Hutzler and J. Banhart</i> .....	336
The effect of forced melt flow induced by rotating magnetic field on the structure of Al-Si eutectic.....	
<i>Zsolt Veres, Arnold Rónaföldi, Kassab Al-Omari, András Roósz</i> .....	337



# CHAPTER 1: MICROGRAVITY





# Columnar and equiaxed solidification within the framework of the ESA MAP project CETSOL

G. ZIMMERMANN<sup>1,a</sup>, L. STURZ<sup>1</sup>, Y.Z. Li<sup>2</sup>, H. Nguyen-Thi<sup>2</sup>, N. Mangelinck-Noël<sup>2</sup>, R. Fleurisson<sup>3</sup>, G. Guillemot<sup>3</sup>, Ch.-A. Gandin<sup>3</sup>, S. McFadden<sup>4,5</sup>, R.P. Mooney<sup>4</sup>, P. Voorhees<sup>6</sup>, A. Roos<sup>7</sup>, C. Beckermann<sup>8</sup>, A. Karma<sup>9</sup>, N. Warnken<sup>10</sup>, E. Perchat<sup>11</sup>, G.-U. Grün<sup>12</sup>, M. Grohn<sup>13</sup>, I. Poitroult<sup>14</sup>, D. Toth<sup>15</sup>, W. Sillekens<sup>16</sup>

<sup>1</sup> ACCESS e.V., Intzestrass 5, D-52072 Aachen, Germany

<sup>2</sup> Aix-Marseille Université, CNRS, IM2NP UMR CNRS 7334, Campus Saint Jérôme, case 142, 13397 Marseille Cedex 20, France

<sup>3</sup> MINES Paris Tech CEMEF, 1 Rue Claude Daunesse, F-06904 Sophia Antipolis, France

<sup>4</sup> Trinity College Dublin, Dept. of Mechanical and Manufacturing Engineering, Dublin 2, Ireland

<sup>5</sup> Ulster University, Magee Campus, Londonderry, BT48 7JL Northern Ireland, United Kingdom

<sup>6</sup> Northwestern University Evanston, 2220 Campus Drive, US-Evanston, IL 60208, USA

<sup>7</sup> University of Miskolc, Dept. of Physical Metallurgy, H-3515 Miskolc-Egyetemváros, Hungary

<sup>8</sup> University of Iowa, Department of Mechanical Engineering, IA 52242 Iowa City, USA

<sup>9</sup> Northeastern University, Physics Department, 360 Huntington Ave, MA 02115 Boston, USA

<sup>10</sup> University of Birmingham, School of Metallurgy and Materials, Birmingham B15 2TT, UK

<sup>11</sup> TRANSVALOR, 694, av. du Dr. Maurice Donat, F-06255 Mougins Cedex, France

<sup>12</sup> HYDRO Aluminium Rolled Products GmbH, Georg-von-Boeselager-Str. 21, D-53117 Bonn, D

<sup>13</sup> Incaal GmbH, Beethovenweg 8, 52388 Nörvenich, Germany

<sup>14</sup> ArcelorMittal Industeel, 56 Rue Clémenceau, F-71201 Le Creusot Cedex, France

<sup>15</sup> NEMAK Győr Kft., Ipari Park, Nyírfasor, H-9027 Győr, Hungary

<sup>16</sup> ESTEC, Keplerlaan 1, 2201 AZ Noordwijk, Nederlande

<sup>a</sup> [g.zimmermann@access-technology.de](mailto:g.zimmermann@access-technology.de)

**Keywords:** Solidification, columnar-to-equiaxed transition, microgravity, Aluminum-Silicon alloy

**Abstract.** To improve our understanding of the physical phenomena that govern the columnar-to-equiaxed transition (CET) in alloy solidification and its consequences for casting processes, experiments under microgravity condition were performed within the framework of the ESA MAP project CETSOL (Columnar-to-Equiaxed Transition in SOLidification processing). This environment allows suppression of buoyancy convection in the melt and diffusive growth of equiaxed grains without sedimentation. Refined and non-refined Al-7wt%Si alloys were solidified in the Materials Science Lab on board the International Space Station. From extensive sample analysis, critical values for CET were determined. Depending on the process parameters, sharp or progressive CET was detected in refined alloys. These results were used to improve and validate different numerical models describing grain and microstructure formation as well as CET. Additionally, during the MASER-13 sounding rocket mission, the diffusive growth of equiaxed dendrites was investigated in the transparent model alloy Neopentylglycol-dCamphor. The nucleation rate and the growth of individual dendrites was observed directly with CCD cameras. The interdependence between nucleation and growth during equiaxed solidification could be described successfully by a new method called the Nucleation Progenitor Function approach.

## Introduction

Microstructures and grain structures strongly determine the materials properties of cast components. Dendritic microstructure is formed during solidification and - as a result of competition between the growth of several arrays of dendrites - columnar or equiaxed grain structures, or a transition from columnar to equiaxed growth is observed. The precise investigation on grain formation is hindered by buoyancy-driven flow and by movement of crystals growing in the melt. To suppress these effects and allow for pure diffusive solidification conditions experiments in

microgravity environment were performed within the research project Columnar-to-Equiaxed Transition in SOLidification Processing (CETSOL) in the framework of the Microgravity Application Promotion (MAP) programme of the European Space Agency (ESA). These experiments provided unique data for testing of fundamental theories of grain and microstructure formation and for validation and development of numerical models describing especially the columnar-to equiaxed transition (CET).

This contribution contains the following main topics:

- An overview of different types of columnar-to-equiaxed transition (CET) observed in solidification experiments onboard the International Space Station ISS using refined Al-7wt%Si alloys is given. In addition, the effect of gravity (1g on earth and  $\mu$ g in microgravity environment) on solidification behaviour is investigated. Moreover, different numerical models are applied to predict CET in microgravity experiments. Some examples of numerical results are given showing an excellent agreement with the experimental findings.
- During a sounding rocket mission in the MEDI-experiment the diffusive growth of equiaxed dendrites was investigated in the transparent model alloy Neopentylglycol-dCamphor. The interdependence between nucleation and growth during equiaxed solidification is described successfully by a new method called the Nucleation Progenitor Function approach, which is briefly outlined.

## **CET in microgravity experiments with Al-7wt%Si alloys**

### **Experimental set-up and process parameters**

To investigate the columnar-to-equiaxed transition under diffusive conditions for heat and mass transport, several experiments in microgravity were carried out successfully. Rod-like samples with diameter 7.8 mm and length 245 mm made of Al-7wt%Si alloy, with (gr) and without grain refiner particles, were integrated in a special sample cartridge assembly (SCA). Twelve thermocouples were positioned along each sample to measure the axial temperature profiles. The samples were processed in the Materials Science Laboratory (MSL) on-board the International Space Station (ISS) in two different furnace inserts, i.e. within a Batch1 (B1), six solidification experiments (B1F1 - B1F6) in the Low Gradient Furnace (LGF) module and within a Batch2a (B2), seven solidification experiments (B2F1 - B2F7) in the Solidification and Quenching Furnace (SQF) module [1, 2]. The main difference in process parameters is the initial axial temperature gradient of about 1 K/mm and 4 K/mm in the LGF and SQF furnaces, respectively. In a stage I, with furnace velocities of  $v_1 = 0.01$  mm/s (in the LGF) or  $v_1 = 0.02$  mm/s (in the SQF) columnar dendritic growth is established. A transition to equiaxed growth can be triggered in the solidification stage II, either by increasing the furnace movement to  $v_2 = 0.20$  mm/s or by mainly decreasing the temperature gradient by applying a cooling rate of  $dT/dt = -4K/min$  (in the LGF) or  $dT/dt = -8K/min$  (in the SQF) at the heaters of the hot zone. For the non-refined samples a moderate rotating magnetic field (RMF) with frequency  $f = 57$  Hz and magnetic flux density  $B = 0.5$  mT was applied to promote fragmentation. An overview of the process parameters is given in [2].

### **CET modes in microgravity experiments**

From the temperature measurements along the sample axis, cooling curves, average liquidus isotherm velocities and the temperature gradients ahead of the liquidus isotherm were deduced as a function of time for all samples. It was found that the RMF has almost negligible influence on the heat flow.

The microstructures and the grain structures were identified from axial and longitudinal cross-sections of the samples. Quantitative characterization of the microstructure showed the evolution of eutectic percentage along the sample axis. From electrolytically etched cross-sections observed in a polarizing microscope the different grain structures were identified. Additionally from quantitative EBSD measurements the size, the crystallographic orientation and the elongation factor of each grain

were determined. Several results for the Batch1 and Batch2a benchmark experiments are published [1 - 7] and are summarized here briefly:

- In non-refined alloys, no CET was observed in stage II, but columnar dendritic growth with some fragmentation of the dendritic structures. The fragments have a size comparable to the dendrite side-branch spacing and cannot promote CET during solidification in microgravity environment because the fragments are not transferred by melt convection or buoyancy to the undercooled melt ahead of the columnar front [1, 8].
- CET was obtained only for refined alloys. Depending on the cooling conditions different types of CET were observed: a sharp CET with a change from a columnar to an equiaxed grain structure within a few millimetre distance, or a progressive CET characterized by a mixed structure of columnar and elongated equiaxed grains in a transition region up to tenths of millimetres.

To determine the position of the CET the grain orientation in longitudinal cross-sections is characterized quantitatively using electron backscattered diffraction (EBSD). Based on the EBSD data, the grain contours were reconstructed by separating neighbouring grains with a misorientation being larger than  $5^\circ$ . The grain equivalent diameter and the elongation factor are calculated from the EBSD measurements. The highest position of the columnar grains issued from the initial dendrites zone defines the CET inception [9], and is noted  $CET_{min}$ . In our previous work [1], it has been shown that  $CET_{min}$  is not sufficient to define CET, especially when very elongated equiaxed grains are observed above this position. A second limit for complete CET,  $CET_{max}$ , is then defined by a grain elongation factor value below 2, in agreement with Hunt's criterion. To estimate critical values for CET the local cooling conditions were analysed. Therefore, from the temperature measurements along the sample axis, the liquidus isotherm velocities  $v_c$  and the temperature gradient ahead of the liquidus isotherm  $G_c$  were determined.

Table 1 shows the process parameters of selected CETSOL microgravity experiments with refined Al-7wt%Si alloy. In B1F2 and B2F3, the CET is triggered by a sudden increase of the solidification velocity; in B1F5, B2F5 and B2F7, the CET is mainly the result of a decrease of the temperature gradient and of a continuous increase of the solidification velocity.

**Table 1.** Process parameters of selected CETSOL microgravity experiments with refined Al-7wt%Si alloy showing CET.

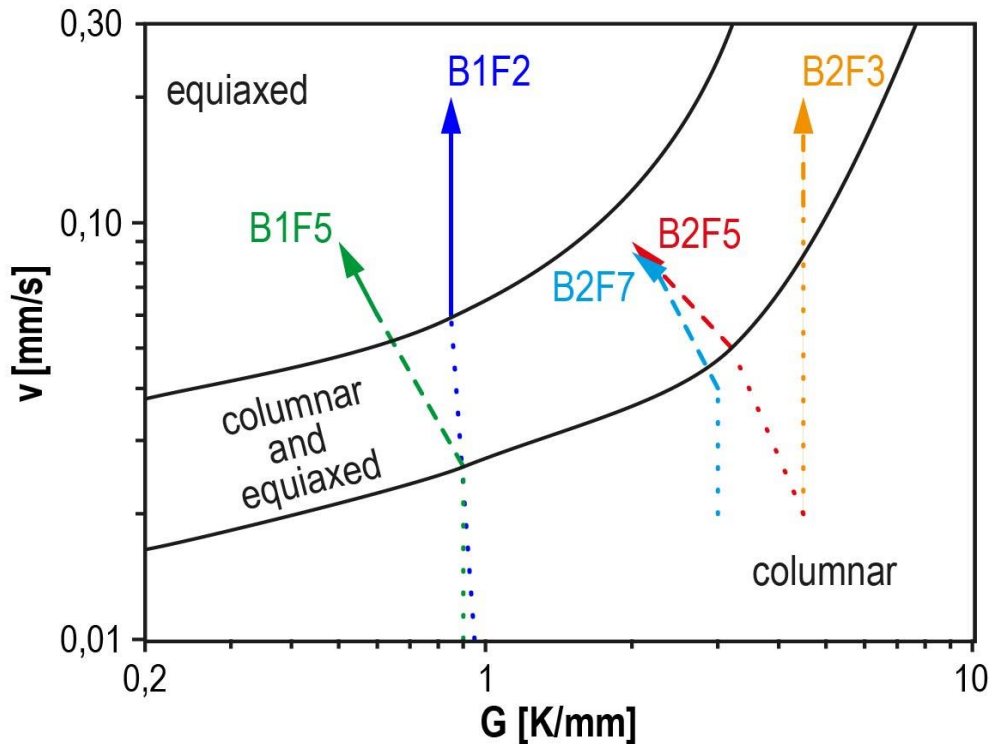
CETSOL Sample	Homogenization time $t_H$ (min)	Initial temperature gradient $G$ (K/mm)	Solidification stage I		Solidification stage II		
			$v_1$ (mm/s)	$z_1$ (mm)	$v_2$ (mm/s)	$z_2$ (mm)	$dT/dt$ (K/min)
B1F2	300	0.95	0.01	20	0.20	50	-4
B1F5	10	0.90	0.01	20	0.01	20	-4
B2F3	60	4.5	0.02	30	0.20	50	-8
B2F5	60	4.5	0.02	30	0.02	50	-8
B2F7	60	3.0	0.02	30	0.02	50	-8



Fig. 1 shows the solidification paths of these 5 CETSOL microgravity experiments (see Table 1). Regions with columnar grain structures are indicated by dotted lines, those with mixed columnar and equiaxed grains by dashed lines, and regions with fully equiaxed grains by solid lines. All experiments started with low solidification velocities of  $v_1 = 0.01$  mm/s (in B1) or  $v_1 = 0.02$  mm/s (in B2) resulting in a columnar dendritic grain structure at the beginning of each experiment.

In samples B1F2 and B2F3, the CET should be triggered by a sudden increase of the furnace velocity to  $v_2 = 0.20$  mm/s. In the case of the lower temperature gradient of 0.9 K/mm (B1F2) a sharp CET at position 128 mm  $\pm$  1 mm is found [1]. At the higher temperature gradient of about 4.5 K/mm (B2F3), mostly elongated and axially oriented equiaxed grains exist in stage II. Here, the rather high temperature gradient results in less continuous nucleation of grains ahead of the solidification front, leading to an elongated equiaxed grain zone and postponing the complete CET. Therefore, CET<sub>min</sub> is evaluated at position 143 mm, but CET<sub>max</sub> is never reached within the sample. Fully equiaxed growth at the given temperature gradient would be expected for higher solidification velocities, which cannot be realized in the MSL-furnace on ISS.

In samples B1F5, B2F5 and B2F7, the CET should be triggered by decreasing the temperature gradient while the low furnace velocities of  $v_1 = 0.01$  mm/s (in B1) or  $v_1 = 0.02$  mm/s (in B2) are maintained. Such a decreasing temperature gradient results in an acceleration of the solidification front. Consequently a progressive CET is found (Fig. 1). In the case of the lower initial temperature gradient of 0.9 K/mm (B1F5), the CET takes place between positions 130 mm and 156 mm [1]. In the case of the higher initial temperature gradients of about 3 K/mm (B2F7) and 4.5 K/mm (B2F5), CET<sub>min</sub> is determined at positions 152 mm and 130 mm, respectively. CET<sub>max</sub> is not reached in these samples. The mixed columnar and equiaxed grain structure in both samples is rather similar, except that the average grain size is larger in case of the lower temperature gradient.

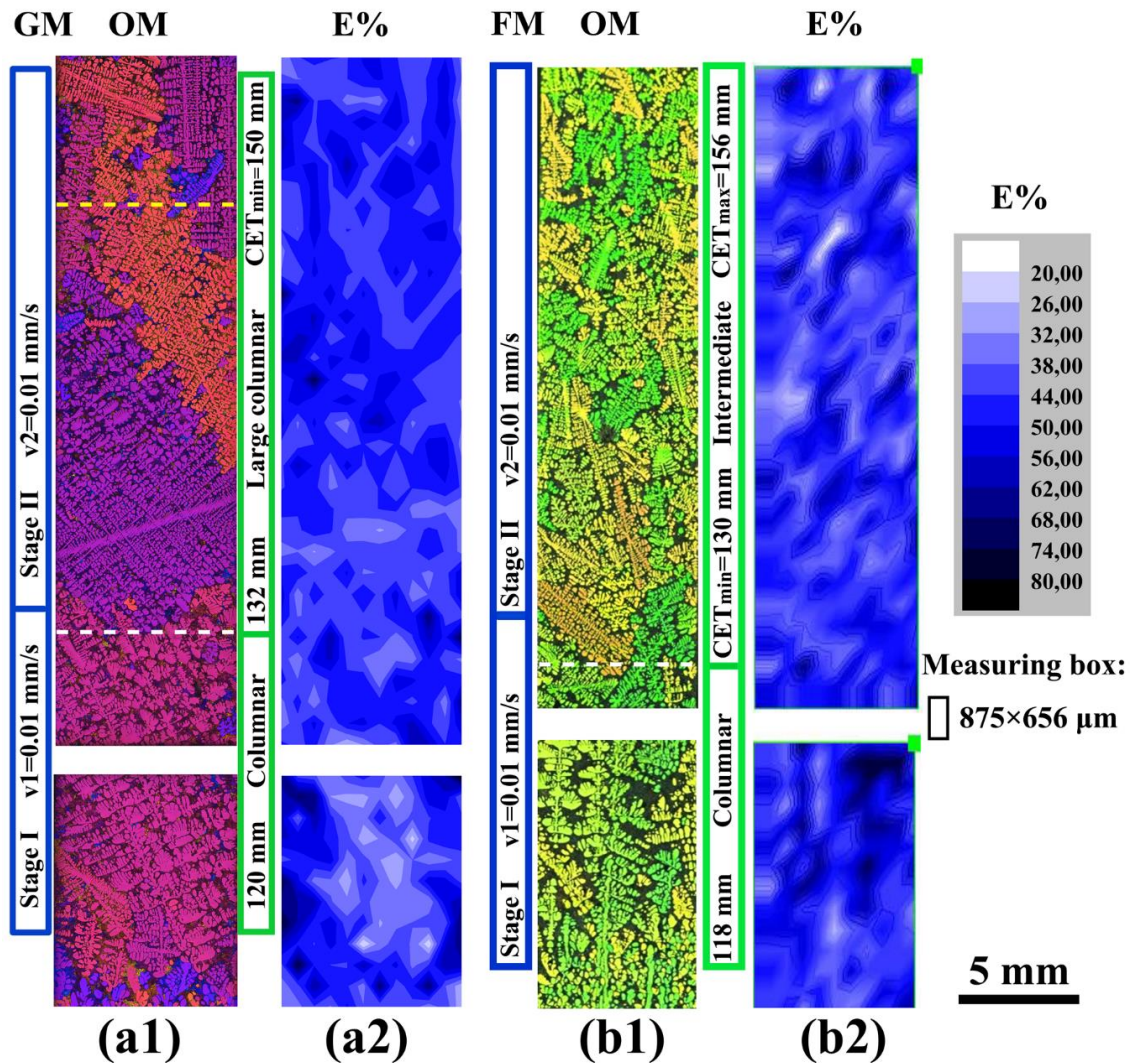


**Figure 1.** Solidification paths of different CETSOL Batch1 and Batch2a microgravity experiment with grain refined Al-7wt%Si alloy, showing regions with columnar (dotted lines), mixed columnar and equiaxed (dashed lines) and fully equiaxed (solid lines) grain structures. The lines separating the different regimes are indicative.

## Effect of gravity on CET

To investigate the impact of the gravity on the solidification microstructure and on the CET a ground reference experiment GM on Earth was performed with the same solidification parameters as for the B1F5 flight sample. Fig. 2 shows the microstructure and the corresponding eutectic percentage distribution maps along longitudinal sections in the region of the transition from stage I to stage II for both the GM and the FM samples.

As a result, the CET is obtained in both samples in a progressive mode. This is directly linked to the applied processing conditions, no velocity jump and an initial temperature gradient of 0.9 K/mm, resulting in low undercooling ahead of the columnar dendrite tips and in a short undercooled region. The gravity significantly influences the microstructure and CET due to the convective liquid flow. Indeed, in the GM experiment, the liquid flow ahead of the solidification front carries both the new grains and the solute away from dendrite tip zone, alleviating or diminishing the blocking effect and promoting the continuous growth of the columnar dendrites. Therefore, the CET is more progressive in the GM sample. Additionally, the E% is lower and the DAS is higher in the GM sample than in the FM sample.

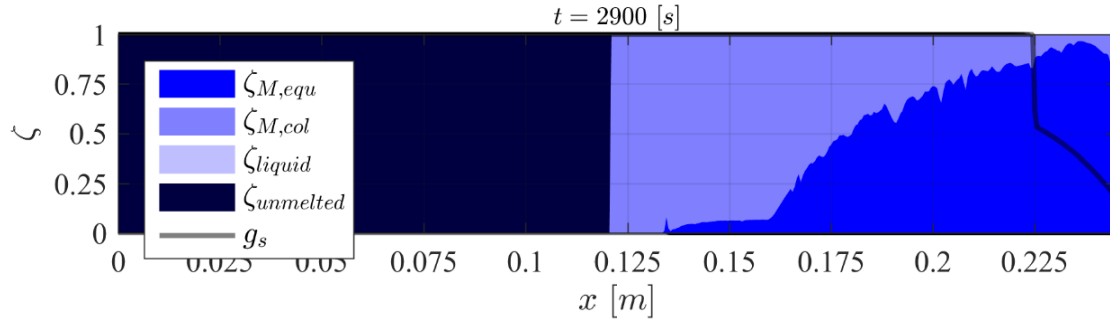


**Figure 2.** Microstructure along longitudinal sections in the region of the transition from stage I to stage II for: (a1) the GM sample and (b1) the FM sample (B1F5). Corresponding eutectic percentage distribution maps (a2 and b2) for both samples. The white dashed lines represent the highest position of the columnar grains issued from the initial dendritic zone. The yellow dashed line represents the position of CET<sub>min</sub> in the GM sample (source: ACCESS e.V. & IM2NP).

## Numerical modelling of CET

The CETSOL flight experiments provide unique data for columnar-to-equiaxed transition in Al-7wt%Si alloy for pure diffusive solidification conditions, i.e. without melt flow and sedimentation and floatation effects. For this reason, they are used to improve several approaches for numerical modelling of CET, as follows:

- An approach that combines Front Tracking (FT) of columnar growth and an equiaxed volume averaging method was employed to model CET. In this approach, the development of the two growth morphologies (columnar and equiaxed) are allowed to proceed simultaneously, thereby allowing the model to predict both sharp and progressive CET. This approach is known as the Concurrent Columnar-to-Equiaxed Transition (CCET) model. The transition from columnar to equiaxed in this model proceeds from fully columnar, to mixed columnar and equiaxed, to fully equiaxed. The resulting total transformed fraction is separated into columnar and equiaxed fractions using an appropriate mathematical treatment. A typical result showing the predicted volume fraction of equiaxed and columnar grains for the B2F7 experiment, as a function of axial position in the sample, is shown in the Fig. 3. Note that the transition from columnar to equiaxed is progressive over the length of the sample from about 0.127 m to 0.23 m.



**Figure 3.** Predicted volume fraction of equiaxed mush ( $\zeta_{M, equ}$ ) and columnar mush ( $\zeta_{M, col}$ ), and internal solid fraction of mush,  $g_s$ , as a function of the axial position,  $x$ , in the B2F7 sample at the end of stage II of the experiment ( $t = 2900$  s) using the concurrent columnar-to-equiaxed transition (CCET) model. The equiaxed nucleation settings for this simulation were as follows:  $N_0 = 5 \times 10^{10}$  seeds/m<sup>3</sup>,  $\Delta T_0 = 4.0$  K,  $\Delta T_\sigma = 1.0$  K (source: Trinity College Dublin).

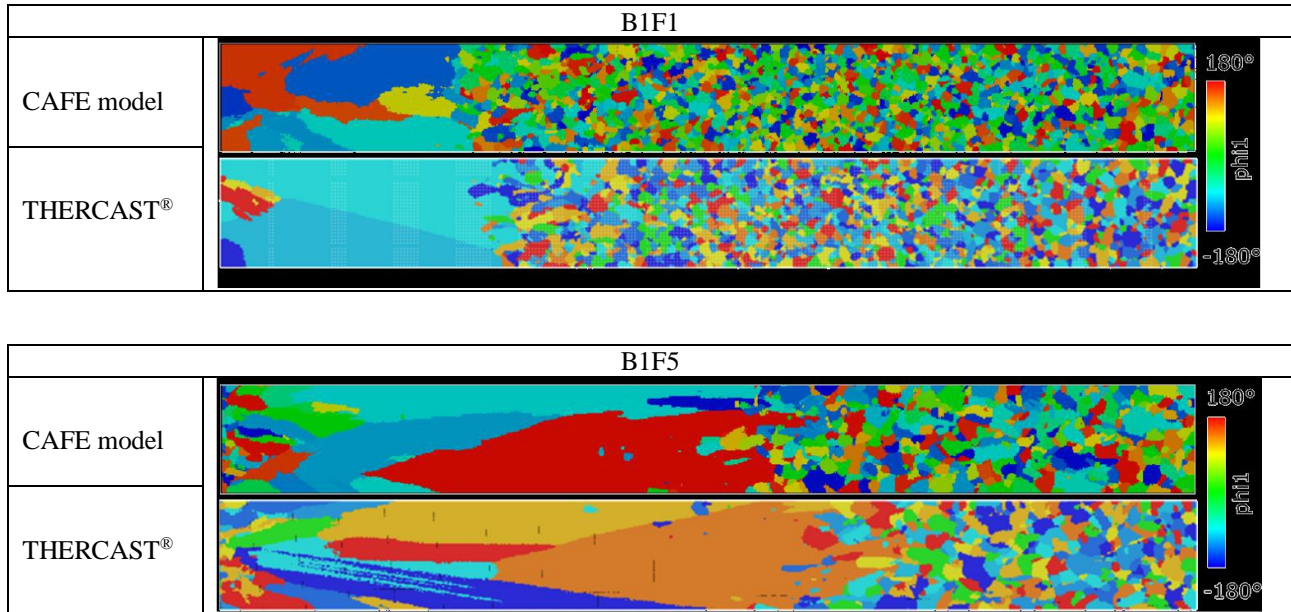
- The CAFE method was proposed to model complex phenomena occurring during solidification processes through the integration of microscopic laws. Results of 2D CAFE modelling of the grain structure evolution and the occurrence of the CET for some of the CETSOL Batch1 experiments demonstrated qualitative agreement for the position of CET and the CET transition mode. Meanwhile, both segregation and grain structures, as well as CET, were numerically modelled in 3D. The CET transition mode, be it sharp or progressive, is retrieved. Distributions of grain elongation factor and equivalent diameter are fairly reproduced and the CET positions are predicted accurately and precisely [2].

As a next step a Dendritic Needle Network (DNN) description has been implemented to predict the growth of dendritic arrays while taking into account the solutal interactions without considering a steady regime for dendritic growth, i.e. the Ivantsov solution for the diffusion field. This is done by approximating each dendrite tip by a single Parabolic Thick Needle (PTN). The goal is now to simulate the columnar-to-equiaxed transition with an improved computation of the growth kinetics as well as the branching mechanisms.

- Within the CETSOL project, the CAFE approach was integrated in the commercial software package THERCAST<sup>®</sup> of TRANSVALOR. Therefore, this modelling technique was added as a new feature to the software after it had been tested, validated and numerically optimized, allowing users to reproduce results of CET simulations. Fig. 4 shows examples of 2D CAFE modelling of the grain structures in samples B1F1 and B1F5, simulated with the academic code of the partner ARMINES-

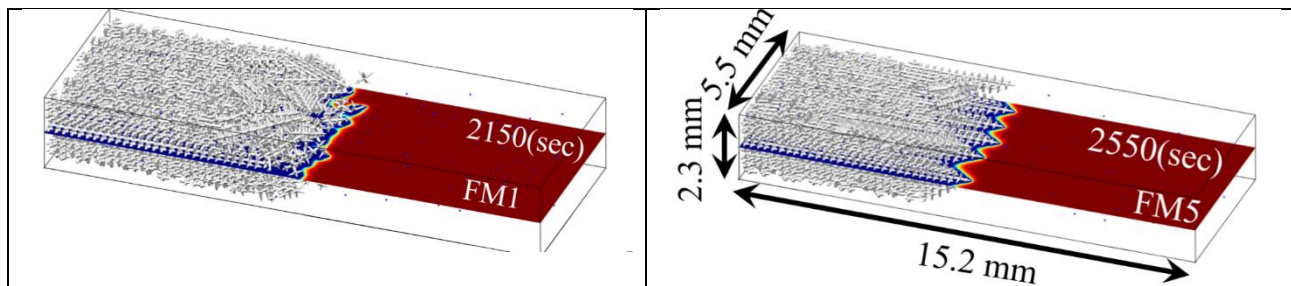


CEMEF and with the commercial code THERCAST<sup>®</sup> of TRANSVALOR [10]. The agreement concerning the positions of CET and the equiaxed grain structure is evident.



**Figure 4.** Comparison of the grain structures with crystallographic orientations (phi1-value) for flight samples B1F1 and B1F5, predicted by the CAFE model approach of partner ARMINES-CEMEF and using THERCAST<sup>®</sup> of partner TRANSVALOR.

- Moreover, to model the CET in the microgravity experiments, also a three-dimensional (3D) multi-scale Dendritic Needle Network (DNN) method was used that tracks the diffusion-controlled dynamics of branches of the hierarchically structured dendritic network [11]. The growth of randomly oriented grains ahead of the columnar front is modelled by incorporating nucleation on foreign inoculant particles randomly located in the melt. Moreover, it is assumed that the grains ahead of the columnar front can grow in any random orientation in space. Fig. 5 shows modelling results with dimensions of the 3D simulation box of 15.2 mm x 5.5 mm x 2.3 mm for samples B1F1 (left) and B1F5 (right). The special extend and position of the transition, especially sharp and progressive CET, are in a good agreement with the experimental measurements in both cases.

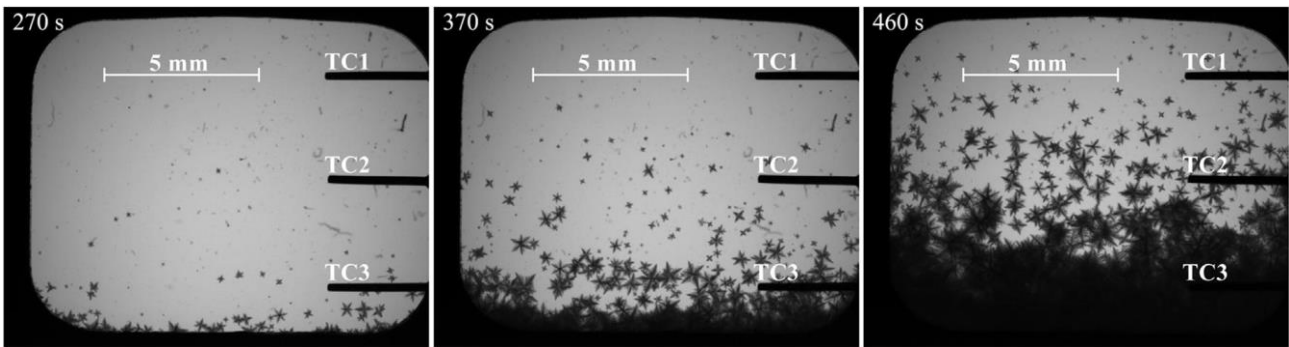


**Figure 5.** DNN modeling of CET with dimension of the 3D simulation box of 15.2 mm × 5.5 mm × 2.3 mm for samples B1F1 (left) and B1F5 (right), showing sharp and progressive CET, respectively (source: Northeastern University Boston).

## Equiaxed growth with NPG-DC alloy in microgravity environment

### Microgravity experiment on MASER-13

In December 2015, polycrystalline equiaxed solidification was investigated under microgravity conditions in the framework of the MEDI experiment on-board the MASER-13 sounding rocket. The sample contained the transparent material Neopentylglycol-30wt%(d)Camphor. In-situ observation of polycrystalline equiaxed nucleation and growth under high-quality microgravity conditions was realized by a fixed cooling rate of  $-0.75$  K/min and a temperature gradient of  $0.3$  K/mm. Fig. 6 shows three overall images recorded at different times during the microgravity phase of the experimental flight. Equiaxed nucleation and growth were observed, starting at the cold end and progressing towards the hot end of the sample. The thermal and image analysis provided macroscopic information like liquid and solid fractions, as well as microscopic information, such as dendrite morphology, crystallographic orientation, nucleation characteristics and dendrite tip kinetics. Additionally, a microscopic optics allows for a 3D reproduction of growing isolated dendrites. Detailed experimental results of MEDI are published in [12, 13] and will be used as a unique data-basis for the improvement of mesoscopic and macroscopic solidification models.

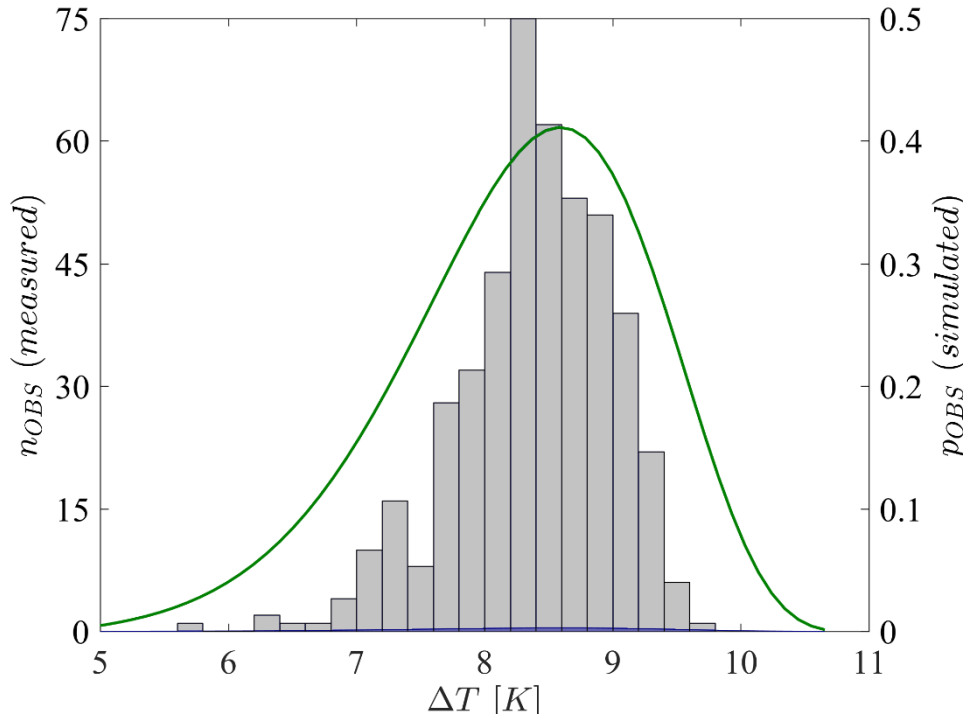


**Figure 6.** Polycrystalline equiaxed nucleation in Neopentylglycol-30wt%(d)Camphor alloy observed in microgravity at 270 s, 370 s and 460 s after lift-off, from left-to-right, respectively. The solid black items to the right of each image are the thermocouples (source: ACCESS e.V.).

### Numerical modelling of equiaxed growth using the NPF approach

To model the solidification physics of the MEDI experiment a novel Nucleation Progenitor Function (NPF) approach was proposed that accounts for the interdependence between nucleation and growth during equiaxed solidification [14-16]. The purpose of this approach was to highlight new functional progenitor-progeny relationships between all available nucleation sites and sites that get the opportunity to nucleate. A nucleation density distribution, based on undercooling, can be identified as a progenitor function. A Kolmogorov statistical approach can be applied to derive progeny functions of actual/observed nucleation events. The approach offers the significant advantage of generating progeny functions for volumetric (3D) data and projected image (2D) data; thereby, providing a stereological correction for over-projection in transparent materials. Progeny functions can be analyzed to obtain statistical output information, e.g., nucleation counts, average nucleation undercooling and standard deviation. The NPF kinetics have been incorporated into a transient thermal model of equiaxed solidification. The model has been applied to characterise the microgravity experiment MEDI with the transparent alloy system Neopentylglycol-30wt%(d)Camphor. Another advantage of the NPF approach was that the effect of temperature gradient on the nucleation rates can be dealt with by combining progeny functions from different locations. This was achieved by using principles of convolution theory.

Fig. 7 shows the overall frequency distribution for the MEDI experiment of the observed nucleation events against undercooling and the probability density function of nucleation undercooling for the entire domain calculated through the NPF approach [16]. Therefore, the model predicted thermal and observed nucleation and growth data with a good level of agreement.



**Figure 7.** Overall distribution of the observed nucleation events as a function of the undercooling, and the probability density function of nucleation undercooling for the entire domain, both for the MEDI experiment and the NPF modelling approach (source: Trinity College Dublin).

## Summary

The microgravity experiments realized in the framework of the CETSOL project are of particular importance because this boundary condition is the only one to allow the suppression of thermosolutal convection in the melt and diffusive growth of equiaxed grains without sedimentation. The experiments provided a unique data basis for development and validation of simulation tools to predict CET using different modelling approaches.

In the next years further experiments will be realized on board the International Space Station ISS to broaden the data basis on CET phenomenon. This holds for Batch3a experiments using metallic Al-Cu alloys with three different compositions, as well as for in-situ experiments with transparent model alloy NPG-DC in the ‘Transparent Alloys’ hardware in the Materials Science Glovebox on ISS. In parallel, numerical simulations of CET, especially using advanced three-dimensional grain structure models, will be achieved and compared to 3D experimental characterisation by serial sectioning to obtain an even more precise understanding of the grain structure formation.

## Acknowledgement

This work has been carried out as part of the CETSOL European Space Agency microgravity application program (ESTEC contract 14313/01/NL/SH). The authors would like to acknowledge funding by the German Space Agency BMWi/DLR (FKZ 50WM1743) and the French National Space Agency (CNES), by Enterprise Ireland via ESA PRODEX Programme (contract number 4000107132), and NASA (NNX14AD69G) supporting the work of C. Beckermann.

## References

- [1] D.R. Liu, N. Mangelinck-Noel, Ch.-A. Gandin, G. Zimmermann, L. Sturz, H. Nguyen Thi, B. Billia, *Acta Materialia* 64 (2014) 253-265.
- [2] G. Zimmermann, L. Sturz, H. Nguyen-Thi, N. Mangelinck-Noel, Y.Z. Li, C.-A. Gandin, R. Fleurisson, G. Guillemot, S. McFadden, R.P. Mooney, P. Voorhees, A. Roosz, A. Ronafoldi, C. Beckermann, A. Karma, C.-H. Chen, N. Warnken, A. Saad, G.-U. Grün, M. Grohn, I. Poitrault, T. Pehl, I. Nagy, D. Todt, O. Minster, W. Sillekens, *JOM* 69 (2017), 1269-1279, doi:10.1007/s11837-017-2397-4.
- [3] G. Zimmermann, L. Sturz, B. Billia, N. Mangelinck-Noël, H. Nguyen Thi, Ch.-A. Gandin, D.J. Browne, W.U. Mirihanage, *Journal of Physics: Conference Series* 327 (2011) 012003.
- [4] G. Zimmermann, L. Sturz, B. Billia, N. Mangelinck-Noël, D.R. Liu., H. Nguyen-Thi, N. Bergeon, C.-A. Gandin, D.J. Browne, C. Beckermann, D. Tournet, A. Karma, *Materials Science Forum* 790-791 (2014) 12-21.
- [5] W.U. Mirihanage, D.J. Browne, G. Zimmermann, L. Sturz, *Acta Materialia* 60(18) (2012) 6362-6371.
- [6] Y.Z. Li, N. Mangelinck-Noël, H. Nguyen-Thi, G. Zimmermann, L. Sturz, T. Cool, E.B. Gulsoy, P.W. Voorhees, *Proc. 6th Decennial International Conference on Solidification Processing SP17* (2017) 317-321.
- [7] G. Zimmermann, L. Sturz, H. Nguyen-Thi, N. Mangelinck-Noel, Y.Z. Li, D.-R. Liu, C.-A. Gandin, R. Fleurisson, G. Guillemot, S. McFadden, R.P. Mooney, P. Voorhees, A. Roosz, A. Ronaföldi, C. Beckermann, A. Karma, N. Warnken, A. Saad, G.-U. Grün, M. Grohn, I. Poitrault, T. Pehl, I. Nagy, D. Todt, O. Minster, W. Sillekens, *Proc. of the 6th Decennial International Conference on Solidification Processes* (2017) 288-291.
- [8] Y.Z. Li, N. Mangelinck-Noël, G. Zimmermann, L. Sturz, H. Nguyen-Thi, *Journal of Alloys and Compounds* 749 (2018) 344-354.
- [9] C.A. Gandin, *Acta Materialia* 48 (2000) 2483-2501.
- [10] A. Saad, P. Lasne, R. Miranda, G. Zhanli, J.-P. Shcillé, *The 12th International Conference on Numerical Methods in Industrial Forming Processes*, vol. 80 (2016).
- [11] D. Tournet, A. Karma, *Acta Materialia* 120, (2016) 240-254.
- [12] L. Sturz, M. Hamacher, J. Eiken, G. Zimmermann, *Proc. of the 23rd ESA Symposium on European Rocket and Balloon Programmes and Related Research*, 11-15 June 2017, A-029.
- [13] L. Sturz, M. Hamacher, G. Zimmermann, *Proc. 6th Decennial International Conference on Solidification Processing SP17* (2017) 300-303.
- [14] R.P. Mooney, S. McFadden, *J. Cryst. Growth* 480 (2017) 43–50.
- [15] R.P. Mooney, L. Sturz, G. Zimmermann, S. McFadden, *Int. J. Thermal Sciences* 125 (2018) 283-292.
- [16] S. McFadden, R.P. Mooney, L. Sturz, G. Zimmermann, *Acta Materialia* 148 (2018) 289-299.

# The ESA-MAP project “GRADE CET” - An overview of the joint research on solidification of TiAl-based alloys under hypergravity and microgravity conditions

Ulrike Hecht<sup>a</sup>, Can Huang<sup>a</sup>, Julien Zollinger<sup>b</sup>, Dominique Daloz<sup>b</sup>, Miha Založnik<sup>b</sup>, Martín Cisternas<sup>b</sup>, Alexandre Viardin<sup>a</sup>, Shaun McFadden<sup>c</sup>, Laszlo Gránásy<sup>d</sup>, Juraj Lapin<sup>e</sup>, Nicolas Leriche<sup>f</sup>, Florian Kargl<sup>g</sup>

<sup>a</sup>Access e.V, Intzestr. 5, 52072 Aachen, Germany

<sup>b</sup>Institut Jean Lamour, Campus Artem, 2 allée André Guinier, 54011 Nancy, Frankreich

<sup>c</sup>Trinity College Dublin, College Green, Dublin 2, Irland

<sup>d</sup>Wigner Research Center for Physics, Konkoly-Thege Miklós út 29-33, Budapest, Hungary

<sup>e</sup>Institute for Machine Mechanics, Slovak Academy of Sciences, Dúbravská cesta 9/6319, Bratislava, Slovak Republic

<sup>f</sup>SAFRAN Aircraft Engines, F-92702 Colombes Cedex, France

<sup>g</sup>Deutsches Zentrum für Luft- und Raumfahrt (DLR), Institut für Materialphysik im Weltraum, Linder Höhe, 51147 Köln, Germany

u.hecht@access-technolgy.de

**Keywords:** solidification, microgravity, hyper-gravity, dendritic growth, titanium aluminides

## Abstract

Titanium aluminides are light-weight structural materials for use at elevated temperatures, e.g. up to 800°C, with applications in the aero-engine and automotive markets. Different manufacturing routes have been developed to produce near-net shape components including casting, and more specifically *centrifugal casting*. On this background, the European MAP-project GRADECET proposed to investigate the solidification of two TiAl-based alloys under hyper-gravity and microgravity conditions: Hyper-g experiments were performed in EAS's Large Diameter Centrifuge (LDC) and reference micro-g experiments onboard the sounding rocket MAXUS 9. The project team investigated the columnar growth and the columnar-to-equiaxed transition of the primary bcc-phase  $\beta(\text{Ti})$  as to comprehend the segregation behavior and grain formation as function of the gravity level. In this overview talk we will present the experimental set-up and give an account of the experimental results. We will briefly outline the modelling work that has been done so far at distinct scales, spanning from CFD at the macro-scale to PF-modelling at the micro-/ meso-scale. The observed effects of acceleration forces on the solidification structure will be summarized and discussed.

## 1. Introduction and research objectives

Titanium aluminides are light-weight structural materials for use at elevated temperatures, i.e. up to 800°C. Just recently, the alloy *GE4822* with the nominal composition Ti-48Al-2Cr-2Nb, (all at. %), has been successfully implemented into commercial aircraft engine applications. The GEnx™ engines are the first to use TiAl (alloy *GE4822*) for their low pressure turbine blades [1]. Extensive research and engineering efforts have enabled this commercial implementation [2]. In terms of processing developments, conventional gravity casting and centrifugal casting have been established but also newer and non-conventional forging as well as additive manufacturing routes are emerging. Research efforts thus continue in several directions, among other aiming at a better and quantitative knowledge about the solidification morphology and texture evolution as function of alloy composition and processing conditions. For casting and specifically *centrifugal casting* the effects of

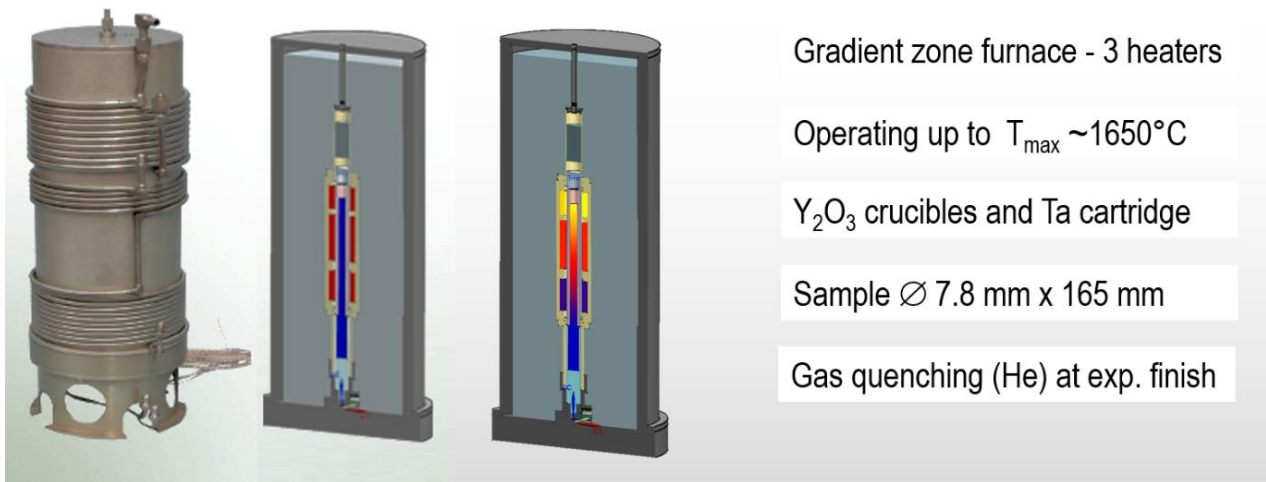


acceleration forces, which may reach 20g, are of special interest: they will alter the segregation, the extent of the mushy zone, the solidification morphology and last but not least the final grain size and texture in the cast sample or component. Among other, the transition from columnar to equiaxed solidification of the primary phase can contribute to texture mitigation and grain refinement [3] thus being of particular interest.

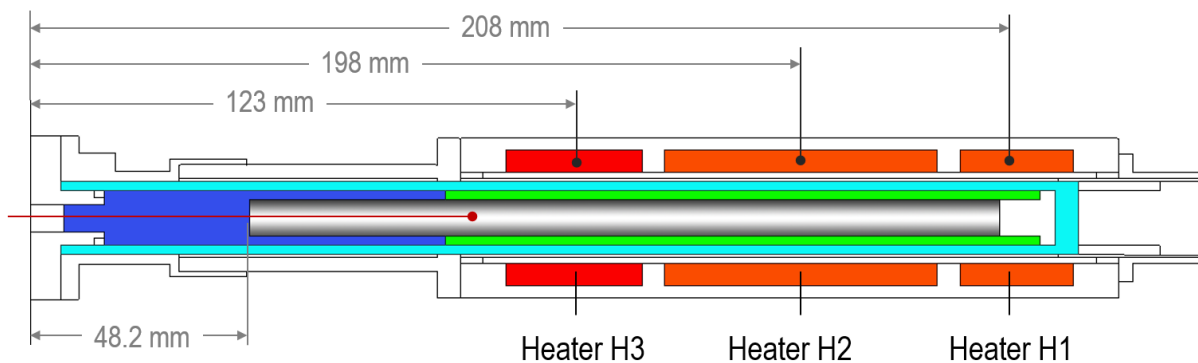
The joint European Project “GRADE CET” proposed to investigate the columnar solidification and the columnar-to-equiaxed transition in two TiAl-based alloys using hyper-g experiments in EAS’s Large Diameter Centrifuge (LDC) and reference micro-g experiments on-board the sounding rocket mission MAXUS 9. In this contribution we describe the experiment design and implementation and present the analysis methods applied for sample characterization. We briefly outline the experimental observations and the modelling efforts undertaken to substantiate them, while referring to the work of the European project partners.

## 2. Experiment design and implementation

The experiment configuration employed for the research purposes of “GRADE CET” was based on the hardware developed by Airbus Defense & Space for a previous flight experiment [4]. The core facility is a gradient zone furnace for operation in hyper-g and micro-g conditions, which is capable of achieving directional melting and solidification of TiAl-based alloys. The core facility is displayed in fig. 1 along with a schematic drawing of the main components, specifically the three resistance heaters H1, H2 and H3 used to impose the desired temperature profiles inside a long cylindrical sample (diam. 7.8 mm, length 165 mm). The samples were machined by spark erosion from cast ingot material.



**Fig. 1(a):** Overview of the gradient zone furnace developed by Airbus Defense & Space



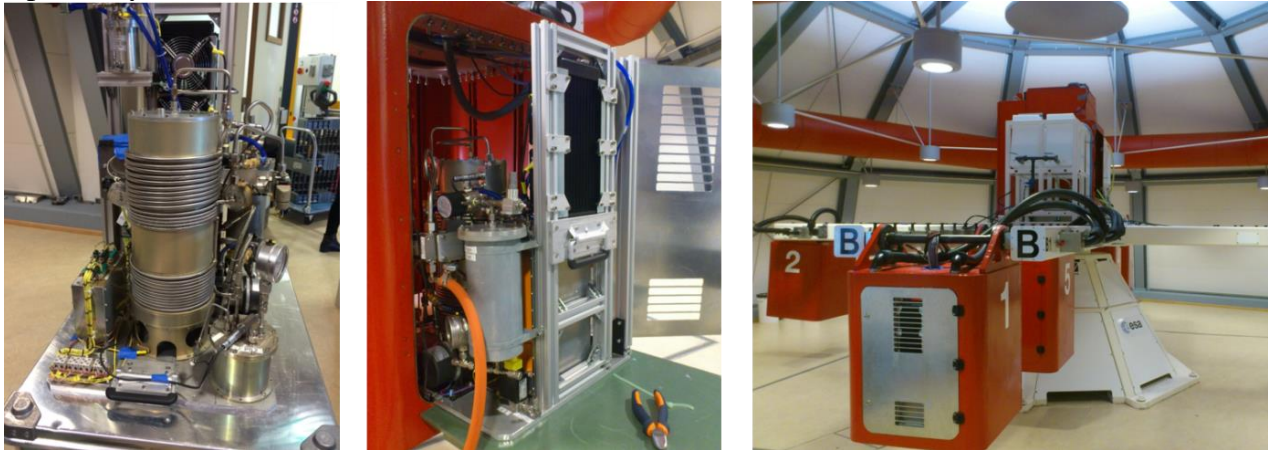
**Fig. 1(b):** Schematic drawing of the main furnace components

The furnace is equipped with three control thermocouples, one at each heater, and with one thermocouple implemented in a blind hole at the cold (and unmolten) end of the sample. The exact locations of the thermocouples are measured and documented in the control sheet for each experiment. This is due to the fact, that it turned out to be more efficient to operate with several furnaces, rather than disintegrating and replacing the sample for the follow-up run. One furnace unit and the electronic devices for process control, gas supply and other fit well into one gondola of ESA's Large Diameter Centrifuge (LDC) [5], while four furnace units fit together into one experiment module of the MAXUS sounding rocket. The gradient zone furnace was used to perform two experimental campaigns at ESA's LDC as well as one experimental campaign on the Sounding rocket MAXUS 9. An overview of the experiments is given in table 1.

**Table 1:** Overview of experimental campaigns in hyper-g, 1-g and micro-g conditions

Campaign	Alloy, at.%	Experiments	Date
LDC-Campaign I	Ti-46Al-8Nb	5 experiments + 1g reference	September 2014
LDC-Campaign II	Ti-48Al-2Cr-2Nb	5 experiments + 1g reference	March 2016
MAXUS-9	Ti-48Al-2Cr-2Nb	4 experiments	April 2017

The 1-g reference experiments were carried out with the furnace in vertical position and the direction of solidification against earth's gravity. The hyper-g experiments in the LDC were carried out such that the direction of solidification was opposite to the resultant from the centrifugal force and earth's gravity. The resultant force reached equivalent g-levels of 5g, 10g, 15g and 20g, respectively at some mid-sample height position. The 20g experiment was performed twice. This implementation corresponds to a liquid density profile which is thermally stable, but solutally unstable, the partition coefficient for Aluminium being  $k_{Al} \sim 0.9$  and for Niobium  $k_{Nb} \sim 1.1$ . The density inversion thus comes from the mushy zone, where lighter liquid is created in interdendritic regions. Fig. 2 displays the assembly of the furnace on the base-plate of the experiment gondola and also gives an impression of ESA's LDC at Estec. All experiments were operated by Airbus Defence & Space and supported by the Centrifuge team at ESA / Estec and the team at the Swedish Space Corporation in Kiruna, respectively.



**Fig. 2:** Overview of experiment implementation in one gondola of the LDC at ESA / Estec. The set-up and images refer to the LDC-Campaign II. The operating parameters are tabulated below.

Experiment name	Angular velocity		Set acceleration	Resultant acceleration @ sample position $z=80$ mm	Swinging angle, $\alpha$
	rpm	rad/s	$*9.81 \text{ m/s}^2$	$*9.81 \text{ m/s}^2$	$^\circ$
LDC-II-5g	35.2	3.69	5.5	4.9	11.3
LDC-II-10g	50.1	5.25	11.0	10.0	5.7
LDC-II-15g	61.4	6.43	16.5	15.1	3.8
LDC-II-20g	67.5	7.07	20.0	18.3	3.1

The operating parameters of the LDC are listed in the table associated with Fig.2 for the LDC-II campaign, but were similar in the LDC-I campaign. The main difference was the position of the furnace inside the gondola: in the LDC-II experiments the furnace was mounted in the center of gravity of the base-plate inside the gondola, while in LDC-I it was mounted at off-set coordinates. Consequently, the resultant force in the LDC-I experiments was not neatly aligned along the samples longitudinal axis giving rise to an additional small force component in tangential direction (about 2% of the axial force component). The effects of this off-set will be discussed elsewhere.

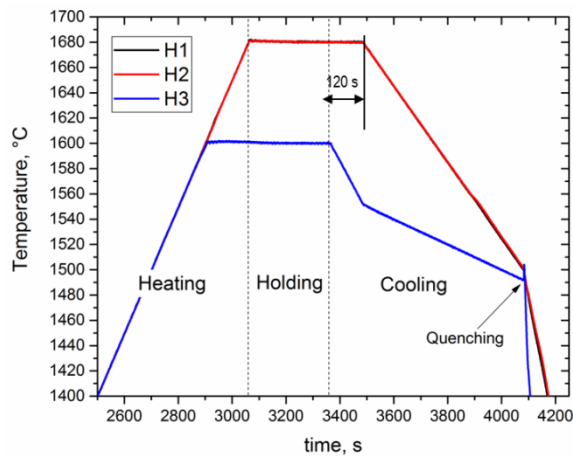
The solidification parameters of the experiments were prescribed temperature-time profiles at the three heaters of the gradient zone furnace. The profiles were optimized in a series of preparatory experiments as to fit into the time span of the sounding rocket flight. Fig. 3 displays the T-t profiles defined for the two alloys, i.e. Ti-46Al-8Nb and Ti-48Al-2Cr-2Nb, respectively. The profiles account for the different liquidus and solidus temperatures of the two alloys with quenching being initiated just below solidus temperature. Liquidus and solidus were measured a priori by differential scanning calorimetry (DSC) during melting with a rate of 20 K/min in a DSC Type NETZSCH DSC 404F3.

(a) LDC-I campaign: Alloy Ti-46Al-8Nb

$T_{\text{liq}}=1570^{\circ}\text{C}$ ,  $T_{\text{sol}}=1504^{\circ}\text{C}$ ,  $\Delta T=66\text{K}$

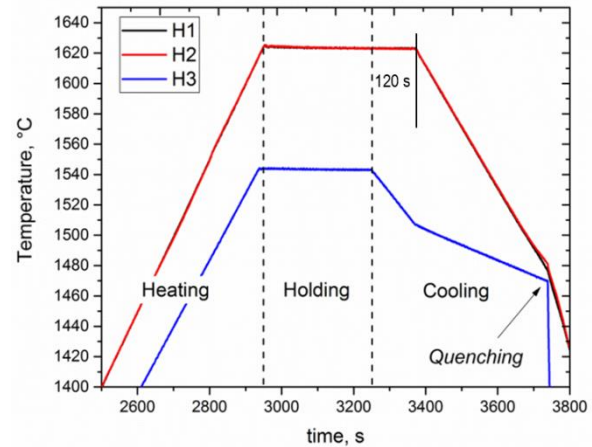
(b) LDC-II campaign: Alloy Ti-48Al-2Cr-2Nb

$T_{\text{liq}}=1505^{\circ}\text{C}$ ,  $T_{\text{sol}}=1463^{\circ}\text{C}$ ,  $\Delta T=42\text{K}$



(a) Alloy Ti-46Al-8Nb

	$T_{\text{ini}}, ^{\circ}\text{C}$	Cooling rates, K/s	
H1	1680	0.0 ( $t < 120\text{s}$ )	0.3 ( $t > 120\text{s}$ )
H2	1680	0.0 ( $t < 120\text{s}$ )	0.3 ( $t > 120\text{s}$ )
H3	1600	0.4 ( $t < 120\text{s}$ )	0.1 ( $t > 120\text{s}$ )



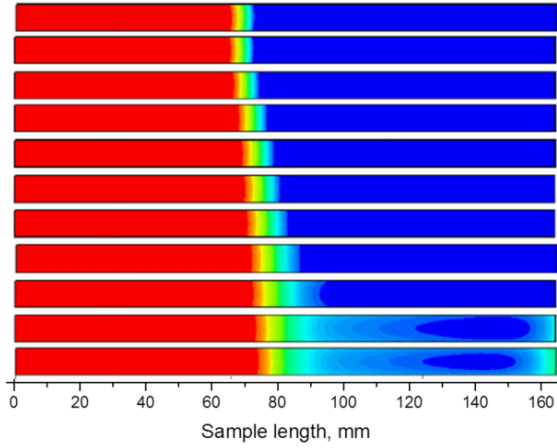
(b) Alloy Ti-48Al-2Cr-2Nb

	$T_{\text{ini}}, ^{\circ}\text{C}$	Cooling rate, K/s	
H1	1620	0.0 ( $t < 120\text{s}$ )	0.3 ( $t > 120\text{s}$ )
H2	1620	0.0 ( $t < 120\text{s}$ )	0.3 ( $t > 120\text{s}$ )
H3	1540	0.4 ( $t < 120\text{s}$ )	0.1 ( $t > 120\text{s}$ )

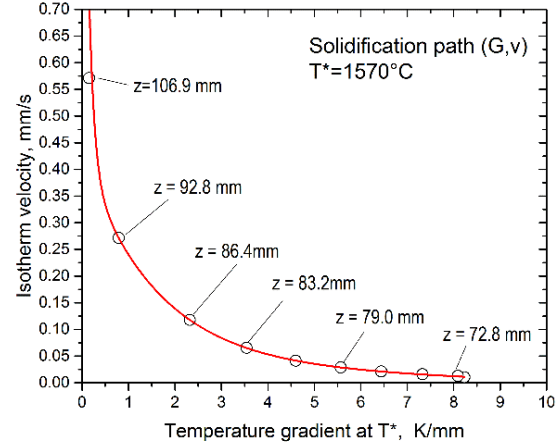
**Fig. 3:** Time-temperature profiles imposed at the heaters for the LDC experiments, the 1g reference experiments and for two  $\mu\text{g}$ -experiments on the sounding rocket MAXUS9 (b).

The experimental configuration with only one independent thermocouple inserted in the sample's cold end does not allow to directly measuring the temperature distribution along the sample. For this reason solidification modelling was carried out with and without coupling to fluid flow, encompassing on the macro-scale the entire furnace, e.g. sample, crucible, cartridge, heaters etc. The materials thermophysical properties were read from database entries, while heat transfer coefficients were iterated such that experimental measurements could be recovered within reasonable error margins. The available measurements were the temperatures recorded by the thermocouple and, more importantly, the position of the fusion front visible in metallographic sections of 1g test samples and assigned to liquidus and solidus temperatures, respectively. Two independent simulation codes were used to this end, one being the commercial CFD-code STAR-CCM+ (Siemens PLM) and the second one being developed in OpenFoam by one of the authors, Can Huang. STAR-CCM+ was employed for thermal modelling only, since its solidification model currently does not provide for element

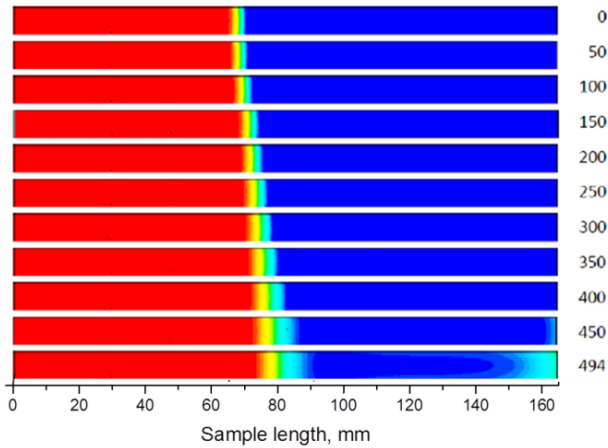
partitioning between the solid and liquid phase. None the less, the thermal computations give a fairly good estimate of the temperature distribution in the sample and capture main features of the transient solidification process. The main results from STAR-CCM+ simulations are summarized in fig.4 based on snapshots of the fraction solid evolution and computed (G,v) conditions which were evaluated at the isotherm  $T^*=T_{\text{liquidus}}$  in the sample axis.



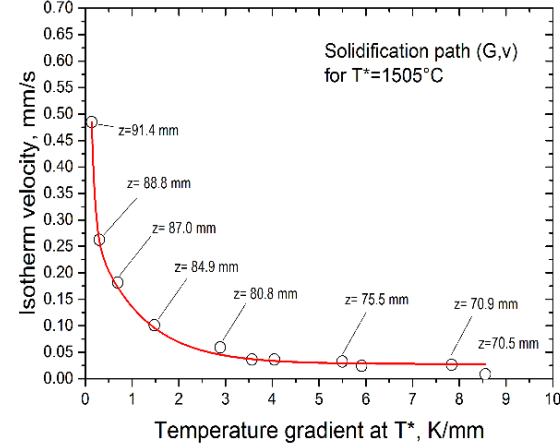
(a) Ti-46Al-8Nb: Fraction solid



(b) Ti-46Al-8Nb: (G,v) at  $T^*=1570^\circ\text{C}$



(c) Ti-48Al-2Cr-2Nb: Fraction solid



(d) Ti-48Al-2Cr-2Nb: (G,v) at  $T^*=1505^\circ\text{C}$

**Fig. 4:** Solidification of the two alloys (a,b) and (c,d) from STAR-CCM+ simulations of the temperature evolution in the entire furnace. Input data are the temperature-time profiles at the heaters and thermophysical materials properties from database entries. Solidification is modelled by coupling to pre-defined fraction solid vs. temperature curves, such that the release of latent heat is accounted for.

The STAR-CCM+ simulations show that the transient experiments lead to significantly different solidification length of the two alloys, basically due to the different solidification intervals at case and to minor differences in the thermophysical materials properties. One can also observe from the snapshots in fig. 4(a) that the solidification front develops a pronounced curvature as solidification proceeds, because radial temperature gradients gradually dominate over the axial gradient. This behavior is inherent to the furnace design and to the desired decrease of the axial temperature gradient. Obviously alloy Ti-46Al-8Nb with a large solidification interval ( $\Delta T=66$  K) and a comparatively large mushy zone is more prone to experience radial growth, once the solidification front advances above the position  $z \sim 100$  mm measured from the cold end of the sample. In fact from the experimental series in 1g we observed that the columnar-to-equiaxed transition (CET) and the columnar-to-radial transition (CRT) compete with one another.

From 10 preparatory 1g-experiments performed with slightly different parameters only 1 experiment resulted in CET while 9 resulted in CRT. Likewise, as reported in [4], the MAXUS-8 flight experiments with Ti-46Al-8Nb also displayed CRT. A systematic meso-scale modelling of the

distinct and competing dendrite morphologies at curved solidification fronts is still missing, specifically also including the role of interfacial anisotropy and dendrite growth directions. While some aspects of the competitive growth have been tackled [4], the topic remains interesting and demanding for future simulation work. It is all the more interesting to note, that the hyper-g experiments from the LDC-I and LDC-II campaign lead to clear CET events, as shall be outlined in the following sections. At contrary, CET was not observed in the 1g reference and  $\mu\text{g}$  experiments.

## 2. Experiment analysis: goals, methodology and highlights

The analysis focused on two distinct aspects, (i) the characterization of the CET-events as function of the acceleration forces in the LDC-experiments and (ii) the analysis of columnar growth, specifically the dendrite spacing evolution and its dependency on the gravity level. The second subject was included after observing that the residual microsegregation in the samples from alloy Ti-48Al-2Cr-2Nb revealed good image contrast in back-scatter diffraction and also in X-ray tomography. The rich results and experimental observations will be presented and discussed in dedicated publications by the responsible partners of the GRADECET project team. Here we only describe the experimental analysis procedures and selected highlight results. The overarching goal is to understand and model the gravity dependency of CET and spacing evolution.

### 2.1 Sample preparation and microstructure observations at CET

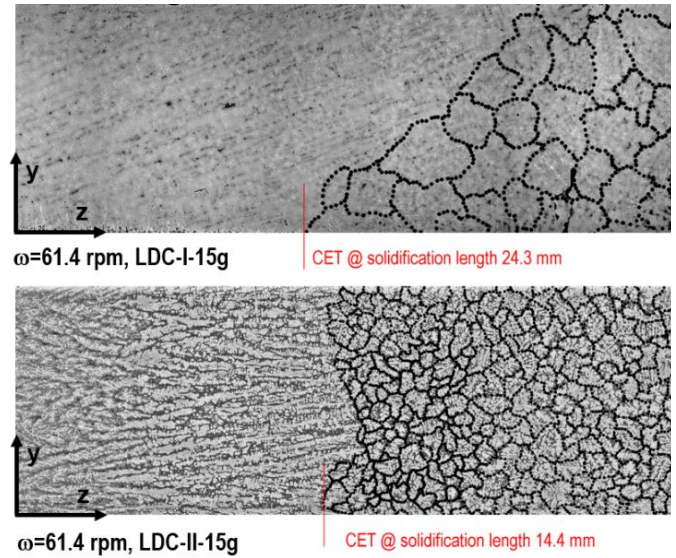
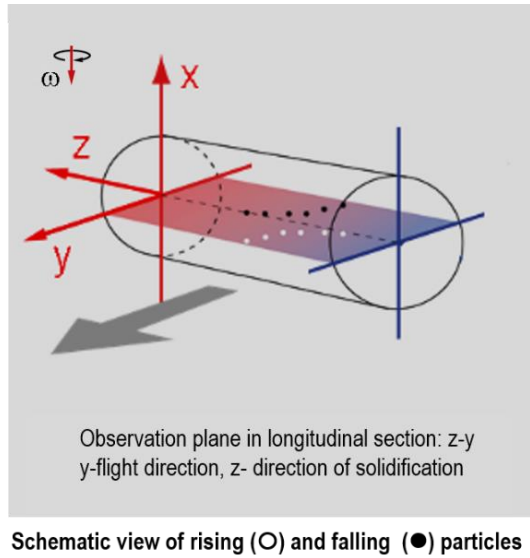
LDC-samples were cut by water-jet along a longitudinal plane which corresponds to the orthogonal plane in the rotating coordinate system, containing the growth direction  $z$  and the flight direction  $y$  as depicted in fig. 5a. The plane has been marked on the sample surface before integration into the furnace. Overview images in the section planes were taken in the back-scatter electron imaging mode, which is sensitive to the atomic number  $Z$  and thus to chemical composition. The location of CET-events was readily observed on the overview images. The analysis of the equiaxed grain structure above CET was however rather tedious and not automated, because the phase transformations in TiAl-alloys preclude a direct access to the primary bcc- $\beta(\text{Ti})$ . Crystallographic determination of the  $\beta(\text{Ti})$  grains by electron backscatter diffraction EBSD is not practicable.

Grain reconstruction was therefore done manually by outlining the grain boundaries following the microsegregation pattern in Ti-48Al-2Cr-2Nb and the grain boundary allotriomorphic films in Ti-46Al-8Nb, respectively. The full characterization work is still to be completed, but some results can be highlighted, as shown in fig. 5b. The present observations show that the two alloys behave quite differently with respect to the CET:

- In alloy Ti-46Al-8Nb the equiaxed grain size is independent of the angular velocity and the corresponding acceleration forces, the volumetric grain density ranging at  $N \cong 0.7 \times 10^8 \text{ m}^{-3}$  as an average from the LDC-I experiments.
- In alloy Ti-48Al-2Cr-2Nb the equiaxed grain size depends on the angular velocity and the corresponding acceleration forces, the volumetric grain density increasing from  $N \cong 8 \times 10^8 \text{ m}^{-3}$  in the experiment LDC-II-5g to  $N \cong 2.4 \times 10^{11} \text{ m}^{-3}$  in the experiment LDC-II-20g [6]

Further microstructure details suggest that this difference relates in fact to a different CET mechanism, being related to fragmentation of the columnar mush in Ti-48Al-2Cr-2Nb, but to heterogeneous nucleation on unknown seed crystals (impurities) in Ti-46Al-8Nb. According to this hypothesis the equiaxed grains are rising particles in the first case [6], but falling particles in the second case. This observation is presently being checked with great care, among other by analyzing and simulating the accumulation of grains in the distinct locations expected from fluid flow and the Coriolis force. The simulation efforts are challenging because several scales need to be tackled and bridged, work is still ongoing.





**Fig. 5:** Microstructure at the CET-event from the LDC-experiments performed at 15g. Shown is the transition region with outlined equiaxed grains in the z-y plane. The micrographs encompass the full sample width of about 7.9 mm in y-direction.

## 2.2 Sample preparation and characterization of columnar dendrite growth

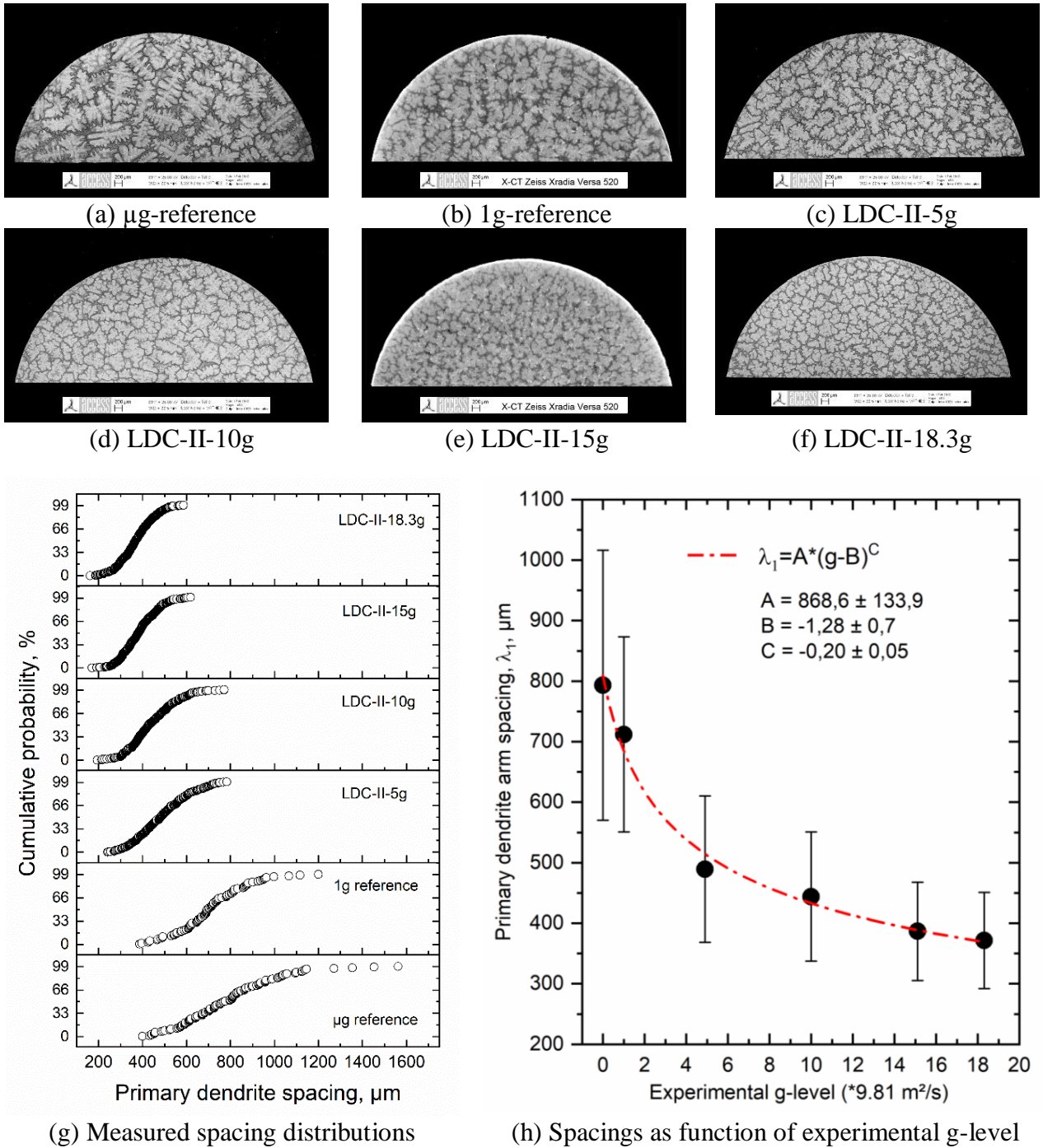
For the Ti-48Al-2Cr-2Nb samples processed under  $\mu g$ , 5g, 15g and 18.3g the primary dendrite arm spacing (PDAS) in the columnar region was evaluated on transverse section planes imaged by SEM in the backscatter electron mode. For the samples processed under 1g and 15g conditions the PDAS was evaluated on transverse section planes from X-ray tomography data. X-ray tomography was accomplished using the Zeiss Xradia Versa 520 with kind support from Carl Zeiss Microscopy GmbH. The volume scanned at 140 kV and 10 W encompassed two sample halves mounted together to give a cylinder with a diameter of about 7.9  $\mu m$ . The scanned height was equally 7.9 mm extending from  $z \approx 77$  to  $z \approx 85$  from the samples cold ends, respectively. The scan resolution was 4  $\mu m$  /pixel.

The primary  $\beta(Ti)$  dendrites in the transverse sections as well as their centers were outlined manually and further analyzed by the ImageJ software [7] using the Delaunay triangulation method. The determined mean values and the standard deviations of the PDAS are listed in table 2. The values correspond to a solidified length of 9 to 10 mm in each case.

The experimentally observed dependency of the primary dendrite arm spacing on the experimental g-level is very similar to the one reported by [8] for Pb-50 wt.%Sn samples which were processed on a centrifuge using directional solidification with constant withdrawal velocity. However this is for the first time that experimental data include not only 1g-reference but also  $\mu g$ -reference data. This is essential and will allow discriminating between the models proposed so far in literature: in an upcoming publication we will discuss the scaling laws proposed by [9, 10, 11, 12] and propose an amended model which well describes the overall behavior. The model operates for both steady state and transient solidification conditions.

**Table 2.** Primary dendrite arm spacing as function of the resultant g-level

Ti-48Al-2Cr-2Nb	MAXUS-9, 1g reference and LDC-II experiments					
	$\mu g$	1g	5g	10g	15g	18.3g
PDAS, mean value, $\mu m$	793	712	489	444	385	372
PDAS, std. deviation, $\mu m$	223	162	121	107	84	79



**Fig. 6:** Columnar  $\beta(\text{Ti})$  dendrites in alloy Ti-48Al-2Cr-2Nb from transverse section planes corresponding to about 10 mm growth length (a through f) along with the measured spacing distributions (g) and the experimentally observed scaling behavior (h) for the mean spacing.

### 3. Modelling strategy at the micro-, meso- and macro-scale

The GRADECET partners put significant efforts on modelling the solidification coupled to fluid flow at the relevant length- and time-scales, spanning from phase-field simulations of dendrite growth and motion in response to body forces, to meso-scale modelling of columnar growth in transient solidification conditions and last but not least to macro-scale modeling of solidification and fluid flow in a rotating frame of reference. Dedicated aspects of model development and preliminary simulation results have published, while consolidated and scale bridging simulations of the GRADECET experiments are still pending.

We briefly outline the current state of modelling with reference to the work of the involved partners. Details will be presented at the S&G2018 conference by the partners directly.

(i) The group of Lazlo Gránásy at the Wigner Research Center is further developing and testing a computer code that couples a binary quantitative phase-field model to quasi-incompressible lattice-Boltzmann hydrodynamics in the presence of gravitational forces, while assuming a repulsive interaction between crystalline grains [13]. The final goal is to capture some key aspects of the equiaxed grain motion under the given acceleration forces and flow conditions (input from macro-scale) for falling particles (LDC-I-campaign) and rising particles (LDC-II-campaign), respectively. Phase-field simulations at Access e.V. using the Micress code focus on columnar growth of  $\beta(\text{Ti})$  dendrites while systematically varying the direction and magnitude of the gravity vector [14].

(ii) Meso-scale modelling of columnar dendrites under the transient growth conditions of the MAXUS-9 experiments will be taken up by Miha Založnik at the Institut Jean Lamour, based on a recently developed envelope model [15]. The computational cost of the mesoscopic model is several orders of magnitude lower than phase field modelling and can bridge the gap to macroscopic models. The challenge is to apply and assess the model capabilities for the transient solidification process with continuously decreasing temperature gradient and increasing growth velocity. Interestingly, this scenario, which is so typical for casting, has not yet been analysed systematically with respect to the history dependence of spacing evolution. More simple scenarios have been addressed experimentally [16] and by a combined cellular automaton–finite difference model [17], e.g. constant velocity and varying temperature gradient.

(iii) A volume-averaging solidification model that accounts for the centrifugal and Coriolis accelerations in the non-inertial rotating reference frame has been developed at the Institut Jean Lamour and was implemented in the framework of the OpenFOAM finitevolume platform. The current macro-scale model has been applied to simulate the columnar growth stage in the LDC-II-experiments and is further being developed to include equiaxed grain nucleation, growth and motion. Results will be presented by one of the authors, M. Cisternas, directly at the S&G2018 conference. A second volume-averaging solidification model has been implemented in the OpenFOAM finite-volume platform by one of the authors, Can Huang. This model includes the full furnace enabling to simulate macroscopic flow in the liquid during melting and solidification of the LDC-experiments. The model refers to the columnar growth stage only. Model equations and results will be presented directly at the S&G2018 conference. Finally the partners from Trinity College Dublin developed a previous front tracking model to include the solution of Navier-Stokes equations in order to predict thermal convection in the liquid region as well as in the columnar mush. A parametric study of the directional solidification process on ESA's centrifuge was performed [18] and compared to predictions derived from non-dimensional considerations.

## References

- [1] B.P. Bewlay, M. Weimer, T. Kelly, A. Suzuki, P.R. Subramanian, The Science, Technology, and Implementation of TiAl Alloys in Commercial Aircraft Engines, *MRS Proc.* 1516 (2013) 128-135.
- [2] B. P. Bewlay, S. Nag, A. Suzuki, M. J. Weimer, TiAl alloys in commercial aircraft engines, *Mater. High Temp.* 33(4) (2016) 549-559.
- [3] N. T. Reilly, B. Rouat, G. Martin, D. Daloz, J. Zollinger, Enhanced dendrite fragmentation through the peritectic reaction in TiAl-based alloys, *Intermetallics* 86 (2017) 126-133.
- [4] R.P. Mooney, S. McFadden, M. Rebow, D. J. Browne, A front tracking model of the MAXUS-8 microgravity solidification experiment on a Ti-45.5at.% Al-8at.%Nb alloy, *IOP Conf. Ser. Mat. Sci. Eng.* 27(1), (2012): 012020.



- [5] J. W. A. van Loon, J. Krause, H. Cunha, J. Goncalves, H. Almeida, P. Schiller, The large diameter centrifuge, LDC, for life and physical sciences and technology, Proc. of the “Life in Space for Life on Earth Symposium”, Angers, France (2008) 22-27.
- [6] N. T. Reilly, Hétérogénéités de fabrication des aluminures de titane : caractérisation et maîtrise de leurs formations en coulée centrifuge, PhD thesis, Université de Lorraine 2016
- [7] C.A. Schneider, W.S. Rasband, K. Eliceiri, NIH Image to ImageJ: 25 years of image analysis, Nature Methods 9 (2012) 671-675.
- [8] C.C. Bataille, R.N. Grugel, A.B. Hmelo, T.G. Wang, The effect of enhanced gravity levels on microstructural development in Pb-50 wt pct Sn alloys during controlled directional solidification, Metal. Mater. Trans. A 25 (1994) 865-870.
- [9] H.-J. Diepers, I. Steinbach, Interaction of interdendritic convection and dendritic primary spacing: Phase-field simulation and analytical modeling, Mater. Sci. Forum 508 (2006) 145-150.
- [10] M. Apel, H. J. Diepers, I. Steinbach, On the effect of interdendritic flow on primary dendrite spacing: A phase field study and analytical scaling relations, Modeling of Casting, Welding and Advanced Solidification Processes – XI, Ch. A. Gandin and M. Bellet (Eds.), TMS (2006) 505-512.
- [11] I. Steinbach, Pattern formation in constrained dendritic growth with solutal buoyancy, Acta Mat. 57(9) (2009) 2640-2645.
- [12] P. Lehmann, R. Moreau, D. Camel, R. Bolcato, A simple analysis of the effect of convection on the structure of the mushy zone in the case of horizontal Bridgman solidification: Comparison with experimental results, J. Cryst. Growth 183 (1998) 690-704.
- [13] T. Pusztai, L. Rátkai, A. Szállás, L. Gránásy, Phase-Field Modeling of Solidification in Light-Metal Matrix Nanocomposites, Magnesium Technology 2014, M. Alderman et al. (Eds.), (2014) Min., Met. & Mat. Soc., Online ISBN: 9781118888179
- [14] A. Viardin, R. Berger, L. Sturz, M. Apel, U. Hecht, Phase-field modelling of  $\beta$ (Ti) solidification in Ti-45at.%Al: columnar dendrite growth at various gravity levels, IOP Conf. Ser. Mat. Sci. Eng. 117 (2016) 012007.
- [15] M. Založnik, A. Viardin, Y. Souhar, H. Combeau, M. Apel, Mesoscopic modelling of columnar solidification, IOP Conf. Ser. Mat. Sci. Eng. 117 (2016) 012013.
- [16] D. Ma, Development of dendrite array growth during alternately changing solidification condition, J. Cryst. Growth 260 (2004) 580-589.
- [17] H. Dong, W. Wang, P.D. Lee, Simulation of the thermal history dependence of primary spacing during directional solidification, Superalloys 2000 (2004) 925-931.
- [18] S. Battaglioli, A.J. Robinson, S. McFadden, Influence of natural and forced gravity conditions during directional columnar solidification, Int. J. Heat Mass Transfer 126 (2018) 66-80.

## Acknowledgements

The National Funding Agencies and ESA are gratefully acknowledged for funding the project through distinct funding schemes. We wish to thank ESA / ESTEC and Airbus Defense & Space for implementing and running the experiments on ESA’s Large Diameter Centrifuge and on the MAXUS-9 sounding rocket. We would like to thank Jack van Loon, Antonio Verga, Neil *Melville-Kenney*, *Andreas Schütte* and Burkhard Schmitz for the good cooperation, technical advices and many enlightening discussions.

## **Thermophysical Properties of Electrical Steels under Microgravity conditions**

Antonia Betzou, Michael Auinger, Sridhar Seetharaman, Begona Santillana,  
Prakash Srirangam

**Keywords:** Viscosity, Casting, Solidification, Microgravity

### **Abstract**

Two types of FeSi alloys are being tested in terms of their viscosity against the effect of superheat, the shear rate and the alloys composition. Thermophysical properties of metals play such a significant role in casting processes with one of the most critical which is viscosity. The viscosity results were fitted upon the Arrhenius equation, which shows the relation between viscosity and temperature. One more effect on viscosity that would be investigated in this project is microgravity, in collaboration with the European Space Agency, FeSi alloys would be tested in International Space Station and in ESA parabolic flights. FeSi alloys or Electrical steels are mainly used in aerospace and electronics industrially, due to their low electrical resistivity and their magnetic properties. Viscosity as a property, is the most important one in terms of flow behaviour and as a result viscosity plays a critical role in casting and solidification processes. The viscosity of Fe3Si and Fe10Si were being measured using a rotational high temperature viscometer with DCC geometry, which allows to conduct viscosity measurements altering the shear rate, in order to test how viscosity of liquid metals changes with the alteration of shear rate. The non-Newtonian behaviour of metals is clearly visible in the experiments, despite the fact that metal melts are considered Newtonian liquids. All the set of alloys that were tested exhibit a non-Newtonian behaviour. A study on the viscosity of these alloys and how it is influenced, contribute to identify and quantify the relations between alloys microstructure and physical properties. Analysis on the oxides that formed during the measurements and their effect on the viscosity of melt is conducted using Scanning Electron Microscopy with Energy Dispersive Spectroscopy and Laser Scanning Confocal Microscopy.

## **Space for science: ESA's microgravity research programme on materials science**

Wim Sillekens

**Keywords:** Metals, solidification, microgravity

### **Abstract**

Over the past decades, the European Space Agency (ESA) has developed and employed a suite of microgravity platforms that enables scientific and industrial communities to conduct space-relevant investigations for the physical as well as for the life sciences. These platforms include drop towers, parabolic flights, sounding rockets, and the International Space Station (ISS), each with their particular features and hence application areas.

This paper gives an overview of the research programme on materials science using ESA's microgravity platforms, thereby drawing from the various projects that are conducted by (European) research teams in this domain. Examples are on solidification studies – in which melt flow, sedimentation and floatation are effectively suppressed – by amongst others the use of X-ray imaging equipment, and the study of solidification kinetics and the measurement of thermo-physical property data by means of an electromagnetic levitator. Results from these investigations provide for unique benchmark data for the testing and validation of fundamental theories and for modelling and simulation of (solidification) processes. This is to further enhance science-based predicting capabilities across the various material classes, relating to the formation of microstructures and defects in castings, the microstructural control for designed mechanical and physical properties, and so on.

## **Microgravity Materials Science Solidification Studies – An American Perspective**

Richard Grugel

**Keywords:** Microgravity, Alloy Solidification, International Space Station

### **Abstract**

A historical overview of solidification studies conducted in a microgravity environment, primarily from an American perspective, is presented. Past, current, and future investigations are described in view of the microgravity platform utilized. Results, and challenges, are discussed and a novel paradigm to conducting microgravity experiments on the International Space Station is introduced.

## **The effect of magnetically controlled fluid flow on microstructure evolution in cast technical Al-alloys: The MICAST project**

Sonja Steinbach, Lorenz Ratke, Gerhard Zimmermann, Laszlo Sturz, Andras Roosz, Jeno Kovács, Yves Fautrelle, Olga Budenkova, Jacques Lacaze, Sadik Dost, Gerd-Ulrich Grün, Nils Warnken, Menghuai Wu, Wim Sillekens

**Keywords:** solidification, Al-alloys, fluid flow, forced convection, magnetic field

### **Abstract**

The ESA-MAP research program MICAST (Microstructure Formation in CASTing of Technical Alloys under Diffusive and Magnetically Controlled Convective Conditions) focuses on a systematic analysis of the effect of convection on microstructure evolution in cast Al-alloys. Questions are, for example, how intensity of convection and flow direction act on the evolution of the mushy zone, on macro- and micro-segregations, on dendrite morphology, on the growth mode and on spatial distribution of intermetallic precipitates.

In order to simplify the complex interactions between heat and mass transport and microstructure evolution, the experiments performed by the MICAST team are carried out under well-defined thermally and magnetically controlled convective boundary conditions using directional solidification. They are analysed using advanced diagnostics and theoretical modelling, involving micro-modelling and global simulation of heat and mass transport.

The MICAST team uses binary, ternary (enriched with Fe and Mn) and technical alloys of the industrially relevant Al-Si cast alloys family. In the frame of the MICAST project solidification experiments were performed on the International Space Station (ISS) in the ESA payload Materials Science Laboratory (MSL) with a low gradient furnace (LGF) and a high(er) gradient one (SQF, Solidification and Quenching Furnace) to complement the scanning of a range of solidification times. Binary Al-7wt.%Si and ternary Al-7wt.%Si-1wt.%X (X=Fe, Mn) alloy samples were directionally solidified under both purely diffusive and stimulated convective conditions induced by a Rotating Magnetic Field (RMF). This contribution gives an overview on recent experimental results and theoretical modelling of the MICAST team and gives an outlook for the upcoming years of ISS experimentations by the team and the questions to be addressed with future experiments.

### **Acknowledgements**

The MICAST team gratefully acknowledges financial support by ESA under contract No. 14347/00/NL/SH within the ESA-MAP project 'MICAST' AO-99-031, CNES, DLR and the Hungarian Space Office. This work was supported by Hydro Aluminium Rolled Products GmbH (D), Inotal (HU), Alcoa-Köfém (HU) and Nemak (HU).

## Overview of the $\mu$ g-Foam ESA MAP project

F. Garcia-Moreno, T. Neu, P. Kamm, F. Bülk, S. Hutzler and J. Banhart

### Abstract

Metal foams are already found in commercial applications, but beside costs there are still other aspects hindering their breakthrough in the market. The main one is the sometimes unsatisfactory quality of the foam structure represented by the pore size distribution and density homogeneity. It is hard to cope with this due to the lack in understanding basic phenomena ruling foaming and in the availability of data for simulations. To overcome these problems there is a need to understand bubble nucleation, foam growth and evolution and cell wall stabilization in the liquid state, as they determine the cellular structure after solidification. For this purpose, non-destructive methods and different gravity levels are required to measure liquid foam properties in-situ.

X-ray radioscopy is known to be a powerful tool for qualitative and quantitative in-situ analyses in materials science in general and especially for metal foams. The method was used under microgravity in the ESA MAP project ' $\mu$ g-Foam' for the first time and enabled studies of liquid foam evolution, drainage, bubble coarsening, diffusion of alloy constituents, liquid metal imbibition and foam solidification. We will review the highlights of the 46<sup>th</sup> and 51<sup>st</sup> ESA Parabolic Flight Campaigns and of the ESA Sounding Rocket Maser 11, but concentrate on recent results obtained during the 65<sup>th</sup> and 67<sup>th</sup> ESA Parabolic Flight Campaigns.

On Earth, gravitational flow induces changes of foam structure such as liquid metal drainage during and after the growth process and make fabrication of foams with homogeneously distributed liquid fractions difficult. The latter influences liquid film thickness and consequently the bubble rupture rate, bubble size distribution and gas interdiffusion. Liquid drainage under 1 g and 1.8 g followed by liquid metal imbibition of a foam during  $\mu$ g is evaluated. The imbibition ability of evolving liquid metal foams is demonstrated at 1.8 g and explained by a balance of capillary and gravitational forces. The role of liquid foam viscosity of aluminium-based metal foams prepared by the Formgrip method with 5, 10 and 20 vol% of SiC particles is presented. The resulted density profiles of the foams during gravity transitions were used to obtain non-destructively quantitative data about properties of liquid metal foams such as their effective viscosity and surface tension by solving the foam drainage equation. The foam coalescence rate was analysed during parabolic flights but also for more than 6 minutes microgravity. The unexpected conclusion was that not only gravity but also the external blowing agent contribute to liquid film rupture. This encouraged the MAP team to develop an external blowing agent free alloy which gives rise to an improved cellular structure and a reduced coalescence rate as demonstrated recently in a parabolic flight.

# Melting in Microgravity: How crystalline shape changes led to new insights about interface dynamics

Martin Eden Glicksman

## Abstract

Microgravity experiments allowed quantitative measurements on the shape evolution of melting ellipsoidal-shaped crystals of pivalic anhydride (PVA), an FCC substance. Crystallites of PVA initially melted self-similarly, maintaining a nearly constant major-to-minor axial ratio. However, when these crystallites melted to about 5 mm in length and 250-500 microns in diameter, their axial ratios suddenly fell by an order-of-magnitude, from about 10-20 to unity. Without interference from sedimentation and convection, needle-like crystals melting under diffusion-controlled conditions were observed to spheroidize spontaneously.

In the 6 years since these experimental observations were reported, we determined that solid-liquid microstructures support capillary-mediated fields that redistribute small rates of thermal energy along curved interfaces. These scalar fields locally modulate an interface's mean motion, and deterministically auto-stimulate pattern evolution at spatial scales from 100 nm up to several millimeters. The presence of capillary energy fields was predicted theoretically by rigorous application of the Leibniz-Reynolds transport theorem, which imposes *omnimetric* energy conservation, i.e., higher-order local energy balance at *all* continuum length scales. Surprisingly, the standard paradigm—the Stefan balance—for interfacial energy/mass conservation in solidification problems excludes capillarity and fails to provide the desired omnimetric balances. Stefan balances, in fact, prevent identifying what causes microstructure formation in solidification. As a result, selective amplification of noise, proposed over 40 years ago, is still accepted as the fundamental microscopic physics for interfacial pattern formation in both natural crystal growth and technical solidification processes.

Capillary energy fields have recently been “exposed” and measured using phase-field simulation of solid-liquid grain boundary grooves constrained by a thermal gradient. The presence of energy fields introduces a small non-linear component in the groove's interface thermo-potential. Subtracting the uniform gradient's linear potential distribution from the measured interfacial thermo-potential produces a “residual” that is proportional to the interfacial field strength. The distribution of interface residuals was measured for a variety of stationary grain boundary grooves to an accuracy of +/-5 ppm using multiphase-field simulation. Capillary fields so revealed confirm analytic predictions of persistent capillary “bias fields” derived from sharp-interface thermodynamics. Phase-field simulations provide the first independent quantitative support for the presence of predicted capillary-mediated fields along solid-liquid interfaces. These results, prompted by observations made in microgravity help to answer a long-standing question in materials science: *What fundamental mechanism stimulates dynamic formation of diffusion-limited microstructures, and provides the relevant physics to improve microstructure-level control in alloy casting and additive manufacturing?*

# **Gravity Dependent Columnar-to-Equiaxed Transition in TiAl alloys: Solidification of Ti-46Al-8Nb in hyper gravity and Multi-physics modelling**

Can Huang, Ulrike Hecht, Julien Zollinger, Miha Založnik, Alexandre Viardin,  
Martín Cisternas

Keywords: TiAl, columnar-to-equiaxed transition, solidification microstructure, centrifuge, hypergravity, microgravity, dendrites, multi-physics modelling

## **Abstract**

Low pressure turbine blades (LPT) made by centrifugal casting from titanium aluminides require demanding process control, as to achieve desired solidification microstructures. The columnar-to-equiaxed transition (CET) and the related texture are of special interest. In the joint European Project “GRADE CET” this transition was investigated in  $\mu g$ , 1g and hyper-g conditions. We will present results for the alloy Ti-46Al-8Nb, (all at.%) gained from experiments in EAS’s Large Diameter Centrifuge (LDC), and from numerical modelling of melting/solidification coupled with thermo-solutal convection in both the mushy zone and the melt. We will describe the experimental set-up and integration into ESA’s LDC and outline the experimental parameters.

We will show that CET sensitively depends on centrifugal forces and Coriolis forces. With increasing angular velocity the equiaxed grain formation is promoted, while also depending on alloy composition and the alloy’s solidification pathway. Modelling is an essential contribution to understanding the hyper-g experiments. Our numerical model handles thermal radiation and conduction in the entire furnace, the transient steps of melting and the subsequent solidification while being limited to the columnar solidification region. Furthermore, we used motion of “tracer particles” to mimic the motion of equiaxed nuclei in the thermo-solutal convective flow under centrifugal condition. This was done by Lagrange particle models and was one-way coupled with solidification. Taken together the simulation results reveal that the centrifugal forces and Coriolis forces affect the flow pattern and the magnitude of the flow thus changing the growth conditions at the columnar front as well as the undercooling ahead of the columnar front. The CET conditions based on Hunt’ model are met more early, when the angular velocity in the LDC increases. Accordingly the length of the columnar region decreases when the angular velocity in the LDC increases in good agreement with experimental observations. Distinct scenarios about the origin of equiaxed grains will be set forth and discussed.

# **Solidification of Al-Ni melts under terrestrial and microgravity conditions**

Marcus Reinartz, Stefan Burggraf, Matthias Kolbe, Phillip Paul, Peter Galenko, Dieter M. Herlach, Markus Rettenmayr

Keywords: Crystal growth, Rapid Solidification, Al-rich Al-Ni alloys, Microgravity, Microstructure

## **Abstract**

During solidification of an undercooled melt, the dendrite growth velocity generally shows a monotonous increase for increasing initial undercoolings. In Al-rich Al-Ni alloys, however, the opposite behavior, i.e. a decreasing growth velocity for increasing undercoolings has been observed [1]. Different hypotheses were discussed, and experiments under terrestrial and microgravity conditions on board the International Space Station (ISS) were carried out to investigate this anomalous behavior. The experiments reproduced the terrestrial results concerning the reverse trend of growth velocity and undercooling. Microstructural studies revealed that a different growth mechanism acts in this type of alloy. It is conjectured that the observed front is a front of multiple nuclei propagating along the sample surface. From the multiple nucleation sites, dendrites grow towards the center of the sample, as can be clearly seen by the orientation of the primary dendrites. The idea of a feedback mechanism is put forward to explain the decreasing velocity for higher undercoolings: nucleation and growth lead to the release of heat and rejection of solute from the solid/liquid interface. The increase in temperature and change in composition influence the active layer of nucleation around the growing dendrite. This apparently leads to a higher nucleation probability, and the numerous nucleation events slow down the front propagation. Further details and mechanisms will be discussed.

## **Acknowledgements**

This work was financially supported by the DFG project HE 1601/26-3 and ESA-MAP project AO-2009-0829.

## **References**

[1] R. Lengsdorf, D. Holland-Moritz, D. M. Herlach, *Scripta Materialia* 62 (2010) 365-367





## CHAPTER 2: PHASE FIELD MODELLING



# Free Energy vs. Grand Potential Energy formulations in phase field modelling of alloy solidification

P.C. BOLLADA<sup>1</sup>, A.M. MULLIS<sup>1</sup> P.K. Jimack<sup>2</sup>

<sup>1</sup>School of Chemical and Process Engineering, University of Leeds, Leeds LS2 9JT, UK

<sup>2</sup>School of Computing, University of Leeds, Leeds LS2 9JT, UK

Corresponding author p.c.bollada@leeds.ac.uk

**Keywords:** phase field, free energy, grand potential, alloy solidification

**Abstract.** We review and compare the [Wheeler-Boettinger-McFadden Phys. Rev A 45, 1992] (WBM), free energy based, phase field formulation of alloy solidification, with the grand potential energy formulation (GPF) of [Plapp Phys. Rev E 84, 2011] and so, by association, the two phases approach of [Kim-Kim-Suzuki Phys. Rev. E 60, 1999]. We ask what the effective differences are between these approaches: are they equivalent? We then advocate an approach that lies within the WBM scheme, yet remains consistent with the GPF. This has the flexibility to apply, with some modification, to arbitrary bulk free energies, including CALPHAD-type descriptions such as Redlich-Kister relations for solution phases and sub-lattice models for non-stoichiometric intermetallics. The proposed model avoids some inherent complications implicit in the grand potential formulation, e.g. inverting the relation between chemical potential and solute concentration.

## Introduction

The phase field modelling of binary alloy solidification involves the specification of a free energy functional,  $F = \int f(\phi, \nabla\phi, c, T) dV$  of the independent variables: phase,  $\phi$ , concentration  $c$ , and temperature  $T$ . Then, by specifying diffusion parameters the functional is optimally minimised to give the dynamic equations for  $\phi, c$  and  $T$ . The free energy density,  $f$ , consists of a surface bulk contribution:  $f = f_{surf} + f_{bulk}$ . However, this paper is largely concerned with the bulk free energy density construction, which we abbreviate:  $f_{bulk} \equiv f_B$ .

Databases such as SGTE [1] provide free energy densities of particular phases of matter as a function of  $c$  and  $T$ . Phase field modelling combines these bulk densities with the phase parameter to give the bulk free energy of the combined mixture, so that just as  $c$  provides the alloy concentration,  $\phi$  provides the proportion of the two phases at any point in the domain.

In phase field the interface may be formally identified at the value of  $\phi = 0.5$  intermediate between the bulk values, here solid at 0, and liquid at 1. To maintain a finite and slowly varying value of  $\phi$  at the interface, a gradient  $\nabla\phi$  and potential well are introduced, and in doing so the phase field model can accommodate measured surface energy parameters.

This paper concerns the phase field modelling advocated by [2] as an improvement on [3] on the construction of bulk free energy rather than surface energy. In turn [2] shows that their formulation is equivalent to that of [4] and so gives that model a firmer theoretic foundation.

Let us assume that we have two free energy densities for the liquid and solid phases:

$$f_L = f_L(c, T), f_S = f_S(c, T). \quad (1)$$

A natural way to combine these densities into a bulk free energy density,  $f_B$ , using  $\phi$  as a weight is:

$$f_B = f_B(\phi, c, T) = \phi f_L(c, T) + (1 - \phi) f_S(c, T). \quad (2)$$

The driving force for phase change is then

$$\frac{\partial f_B}{\partial \phi} = f_L - f_S. \quad (3)$$

This is independent of  $\phi$  and thus also, by implication, there is a force in the bulk. But we know that the driving force for phase change can only originate at the surface (the bulk states are metastable). The standard way to address this issue, e.g. [3], is to introduce an interpolation function,  $g(\phi)$  with gradients,  $g'(\phi)$ , that vanish at the extreme values  $\phi = 0, 1$  and write

$$f_B = g(\phi) f_L(c, T) + g(1 - \phi) f_S(c, T), \quad (4)$$

where it is assumed  $g(0) = 0, g(1) = 1$ . A cubic interpolation function,  $g(\phi)$ , can be found such that given,  $\phi = 1/2 \left[ 1 + \tanh\left(\frac{x-V_t}{\delta}\right) \right]$ , we have  $\phi \propto g'(\phi)$ . The driving force,  $\frac{\partial f_B}{\partial \phi} = g'(\phi)(f_L - f_S)$ , where, for pure metals  $f_L - f_S \approx \text{const}$ , and at equilibrium (melting temperature), vanishes, but the WBM model does not have an analogous feature. This led Plapp [2] to explore the use of the chemical potential,  $\mu = \frac{\partial f}{\partial c}$  as a variable in order to define the bulk grand potential term (dropping  $T$  from hereon):

$$\omega_B(\phi, \mu) = g(\phi)\omega_L(\mu) + g(1 - \phi)\omega_S(\mu), \quad (5)$$

where the chemical potentials,  $\omega_L, \omega_S$ , have the property  $\omega_L(\mu_e) = \omega_S(\mu_e)$  for equilibrium chemical potential  $\mu_e$ . Similar to the bulk free energy density, the grand potential energy density,  $\omega_B$ , forms the bulk part of the grand potential energy density,  $\omega = \omega(\phi, \mu)$ .

$$\left. \frac{\partial \omega_B(\phi, \mu)}{\partial \phi} \right|_{\mu=\mu_e} = 0, \quad (6)$$

we have a model which resembles the pure metal,

$$\left. \frac{\partial f_B(\phi, T)}{\partial \phi} \right|_{T=T_e} = 0. \quad (7)$$

There is a major stumbling block with this approach: databases do not routinely give energy densities in terms of chemical potential. However, this problem can easily be overcome in situations where the free energy densities,  $f_L$  and  $f_S$  are quadratic in  $c$ , and indeed most if not all applications of the grand potential formulation use quadratic approximation about the equilibrium concentrations of the true free energy densities.

The key to understanding the approach of [2] is that, for each phase

$$\begin{aligned} \omega_L &= f_L - \mu_L c_L \\ \omega_S &= f_S - \mu_S c_S \end{aligned} \quad (8)$$

where the chemical potentials are

$$\mu_L = \left. \frac{\partial f_L(c, T)}{\partial c} \right|_{c=c_L}, \mu_S = \left. \frac{\partial f_S(c, T)}{\partial c} \right|_{c=c_S}. \quad (9)$$

Their idea is to set

$$\mu_L = \mu_S, \quad (10)$$

and refer to this as *the* chemical potential,  $\mu$ . These last equations allow us to find solutions,  $c_L = c_L(\mu), c_S = c_S(\mu)$ , and so allow us to write  $\omega$  as a function of  $\phi, \mu$ . There is a subtlety here in that it appears,  $\omega \neq f - \mu c$ , the true Legendre transformation from  $f$  to  $\omega$ . But we can, in principle, construct  $f$  from  $\omega$  by using  $f = \omega + \mu c$  to find the equivalent free energy construction. What we find is that the value of  $f$  intermediate between the pure phases interpolate (as a function of  $\phi$ ) in such a way as to have a common tangent throughout. If we can show, therefore, that the Legendre transformation from free energy to grand potential leaves the underlying system unchanged, it follows that using the approach of [2] is equivalent to a specific manner of interpolation of the pure phases.

### The relation between Grand potential and Free energy formulation in phase field

Assume the free energy is a functional of  $\phi, c$

$$F = \int f(\phi, \nabla \phi, c) dV, \quad (11)$$

and the grand potential is a functional of a phase field  $\psi$  and chemical potential,  $\mu$

$$\Omega = \int \omega(\psi, \nabla \psi, \mu) dV. \quad (12)$$

The relation between the two potentials is given by

$$\omega = f - \mu c, \quad (13)$$

where

$$\mu = \frac{\delta F}{\delta c} = \frac{\partial f}{\partial c}, c = -\frac{\delta \Omega}{\delta \mu} = -\frac{\partial \omega}{\partial c}, \quad (14)$$

As a consequence the functionals are related

$$\Omega = F - \int \mu c dV \quad (15)$$

or

$$F = \Omega + \int \mu c \, dV \quad (16)$$

The transformation between the two potentials assumes that  $\phi = \psi$ , but we find it clearer to keep the notation for the phase distinct because

$$\left. \frac{\partial}{\partial \phi} \right|_c \neq \left. \frac{\partial}{\partial \psi} \right|_\mu. \quad (17)$$

In fact, by the chain rule

$$\frac{\partial}{\partial \phi} = \frac{\partial \psi}{\partial \phi} \frac{\partial}{\partial \psi} + \frac{\partial \mu}{\partial \phi} \frac{\partial}{\partial \mu} = \frac{\partial}{\partial \psi} + \frac{\partial \mu}{\partial \phi} \frac{\partial}{\partial \mu} \quad (18)$$

we also have

$$\frac{\partial}{\partial \nabla \phi} = \frac{\partial}{\partial \nabla \psi} + \frac{\partial \mu}{\partial \nabla \phi} \frac{\partial}{\partial \mu}, \quad (19)$$

which implies

$$\begin{aligned} \frac{\delta \Omega}{\delta \phi} &= \frac{\partial \omega}{\partial \phi} - \nabla \cdot \frac{\partial \omega}{\partial \nabla \phi} \\ &= \left( \frac{\partial \omega}{\partial \psi} + \frac{\partial \mu}{\partial \phi} \frac{\partial \omega}{\partial \mu} \right) - \nabla \cdot \left( \frac{\partial \omega}{\partial \nabla \psi} + \frac{\partial \mu}{\partial \nabla \phi} \frac{\partial \omega}{\partial \nabla \mu} \right) \\ &= \frac{\partial \omega}{\partial \psi} - \nabla \cdot \frac{\partial \omega}{\partial \nabla \psi} + \frac{\partial \mu}{\partial \phi} \frac{\partial \omega}{\partial \mu} - \nabla \cdot \left( \frac{\partial \mu}{\partial \nabla \phi} \frac{\partial \omega}{\partial \mu} \right) \\ &= \frac{\delta \Omega}{\delta \psi} + \frac{\partial \mu}{\partial \phi} \frac{\partial \omega}{\partial \mu} - \nabla \cdot \left( \frac{\partial \mu}{\partial \nabla \phi} \frac{\partial \omega}{\partial \mu} \right). \end{aligned} \quad (20)$$

Applying this to Eq. (16) (in the second line below) gives

$$\begin{aligned} \frac{\delta F}{\delta \phi} &= \frac{\delta \Omega}{\delta \phi} + \frac{\delta \int \mu c}{\delta \phi} \\ &= \left( \frac{\delta \Omega}{\delta \psi} + \frac{\partial \mu}{\partial \phi} \frac{\partial \omega}{\partial \mu} - \nabla \cdot \left[ \frac{\partial \mu}{\partial \nabla \phi} \frac{\partial \omega}{\partial \mu} \right] \right) + \frac{\delta \mu c}{\delta \phi} \\ &= \frac{\delta \Omega}{\delta \psi} + \frac{\partial \mu}{\partial \phi} \frac{\delta \Omega}{\delta \mu} - \nabla \cdot \left[ \frac{\partial \mu}{\partial \nabla \phi} \frac{\delta \Omega}{\delta \mu} \right] + c \frac{\partial \mu}{\partial \phi} - \nabla \cdot c \frac{\partial \mu}{\partial \nabla \phi} \\ &= \frac{\delta \Omega}{\delta \psi} - \frac{\partial \mu}{\partial \phi} c + \nabla \cdot \left[ \frac{\partial \mu}{\partial \nabla \phi} c \right] + c \frac{\partial \mu}{\partial \phi} - \nabla \cdot c \frac{\partial \mu}{\partial \nabla \phi} \\ &= \frac{\delta \Omega}{\delta \psi} \end{aligned} \quad (21)$$

where we have assumed no gradient of  $\mu$  in  $\omega$  (as is the case in [2]) so that

$$\frac{\delta \Omega}{\delta \mu} = \frac{\partial \omega}{\partial \mu} \quad (22)$$

However, we have allowed that  $\mu = \mu(\phi, \nabla \phi, c)$ . The above calculation infers that

$$\phi = -M \frac{\delta F}{\delta \phi} \quad (23)$$

is identical to

$$\psi = -M \frac{\delta \Omega}{\delta \psi}, \quad (24)$$

since,  $\phi = \psi \Rightarrow \dot{\phi} = \dot{\psi}$ . If we can show that the field equation for  $\mu$  appearing in [2] is indistinguishable from the standard equation for solute

$$\dot{c} = \nabla \cdot D \nabla \frac{\partial f}{\partial c}, \quad (25)$$

then we will have established that the GPF gives identical physics, and so an identical phase profile to WBM. The construction of the equation for  $\mu$  in [2] is achieved by using the chain rule

$$\dot{c} = \frac{\partial c}{\partial \psi} \dot{\psi} + \frac{\partial c}{\partial \mu} \dot{\mu} \quad (26)$$

plus Eq. (25). Since there is no freedom to choose the coefficients of  $\dot{\psi}$  and  $\dot{\phi}$  the resulting equation for  $\mu$  must be equivalent to the equation for  $c$ . This might appear to counter the claim, in [2], that the equilibrium phase profile is different in the two formalisms. This apparently paradoxical statement is resolved in the next section by a simple worked example.

### The paradox resolved by example

We have seen that the GPF is formally identical to WBM, and yet clearly the model in [2] is different. The resolution of this is seen in the examples given in [2] where the chemical potential,  $\mu$  is not defined via  $\mu = \frac{\partial f}{\partial c}$  where  $f$  is defined as in WBM. The definition of  $\mu$  in [2] can be made compatible with  $\mu = \frac{\partial f}{\partial c}$  by changing the definition of  $f$  in WBM. When this is done, we see that GPF is identical with WBM. To illustrate this, define example free energies:

$$\begin{aligned} f_L &= (c - 0.25)^2 \\ f_S &= (c - 0.75)^2 + 0.1c \end{aligned} \quad (27)$$

For this toy example we find using Eq. (8) that

$$\begin{aligned} \omega_L &= 0.0625 - c_L^2 \\ \omega_S &= 0.5625 - c_S^2 \end{aligned} \quad (28)$$

By setting  $\mu = \mu_L = \mu_S$ , we can invert these to give two values of  $c$  (the two points where the tangents on each curve are equal to  $\mu$ ):

$$\begin{aligned} c_L &= 0.25 + 0.5\mu \\ c_S &= 0.7 + 0.5\mu \end{aligned} \quad (29)$$

These are then inserted into Eqs. (28) as follows

$$\begin{aligned} \omega_L(c_L(\mu)) &= 0.0625 - c_L^2 = -0.25\mu - 0.25\mu^2 \\ \omega_S(c_S(\mu)) &= 0.5625 - c_S^2 = 0.0725 - 0.7\mu - 0.25\mu^2 \end{aligned} \quad (30)$$

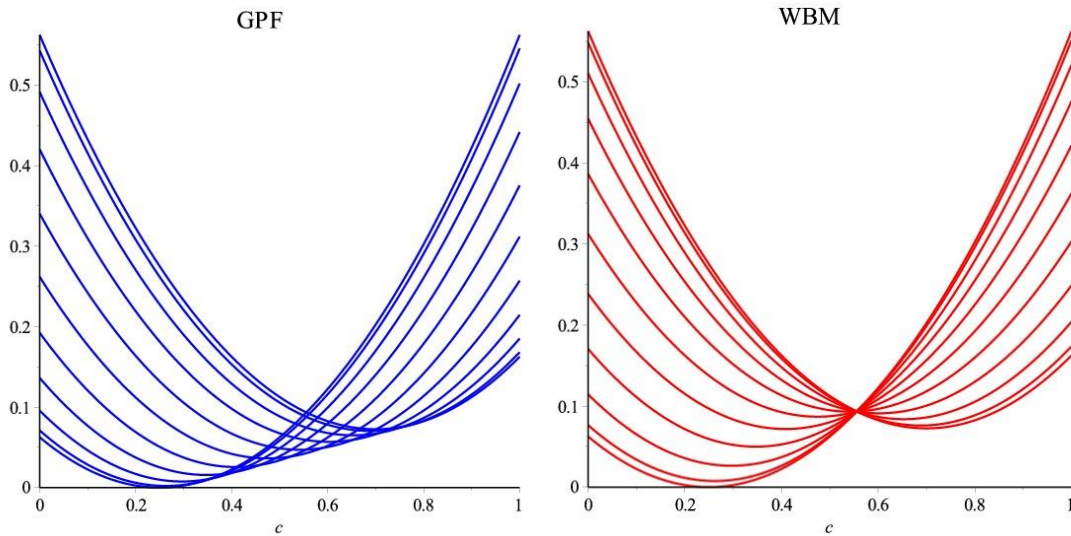
We can solve  $\omega_L(c_L(\mu)) = \omega_S(c_S(\mu))$  to obtain, for example, the slope of the common tangent at equilibrium,  $\mu_e = 0.16111$ . The solute concentration is given by the relation Eq. (14) and Eq. (5), with  $g = 3\phi^2 - 2\phi^3$ , giving:  $c = 0.7 + 0.9\phi^3 - 1.35\phi^2 + 0.5\mu$ . This may be inverted to give

$$\mu = -1.8\phi^3 + 2.7\phi^2 - 1.4 + 2c. \quad (31)$$

Now using the Legendre transformation,  $f = \omega + \mu c$ , we obtain

$$f = .81\phi^6 - 2.43\phi^5 + 1.8225\phi^4 - 1.8\phi^3 c + 2.7\phi^2 c + c^2 + 1.405\phi^3 - 2.1075\phi^2 + .5625 - 1.4c. \quad (32)$$

It is instructive to examine this as a series of 11 superimposed plots at fixed values of  $\phi \in [0,1]$ , shown below Fig. 1 in blue, and to be compared with the equivalent WBM curves in red. We see that GPF preserves the common tangent but not the point of intersection. This illustrates that the GPF method in [2] is effectively a method of interpolating the free energy curve for each phase, which keeps a common tangent, and thus suggests that the same result can be achieved directly.



**Figure 1.** Illustration of the way the two methods interpolate between the pure phases: (a) GPF keeps the common tangent and (b) WBM keeps the common point. The GPF keeps a common tangent for all intermediate free energy curves

## A direct approach to bulk free energy construction

We end with a more direct way of defining the free energy that is equivalent to the above for this example. The idea is to translate the pure phase curve,  $f_L$  such that the point  $(c_L^e, f_L(c_L^e))$  moves in a straight line, to a point  $(c_S^e, f_S(c_S^e))$  as a function of  $\phi$ , where  $c_L^e, c_S^e$  are the common tangent equilibrium concentrations. We denote this function by  $\bar{f}_L(\phi, c)$  and thus, by design, it has the property that  $\bar{f}_L(\phi = 0, c = c_S^e) = f_S(c_S^e)$ , and also  $\bar{f}_L'(\phi = 0, c = c_S^e) = f_S'(c_S^e)$ . Similarly with  $\bar{f}_S(\phi, c)$ . Thus the barred functions are given by

$$\begin{aligned}\bar{f}_S(\phi, c) &= f_S[c - g(\phi)(c_L^e - c_S^e)] + g(\phi)[f_L(c_L^e) - f_S(c_S^e)], \\ \bar{f}_L(\phi, c) &= f_L[c - g(1 - \phi)(c_S^e - c_L^e)] + g(1 - \phi)[f_S(c_S^e) - f_L(c_L^e)].\end{aligned}\quad (33)$$

Since these two functions both have a common tangent with  $f_L, f_S$  it follows that an interpolation of the two will also have a common tangent. Thus the function

$$f(\phi, c) = g(\phi)\bar{f}_L(\phi, c) + g(1 - \phi)\bar{f}_S(\phi, c), \quad (34)$$

creates a set of interpolating curves with a common tangent as in the above figure in blue. We find that the functional gradients are

$$\begin{aligned}\frac{\partial f}{\partial c} &= g f_L'(c - g\Delta c + \Delta c) + (1 - g) f_S'(c - g\Delta c), \\ \frac{\partial f}{\partial \phi} &= g'(f_L(c) - g\Delta c + \Delta c) - f_S(c - g\Delta c) - \Delta c \frac{\partial f}{\partial c},\end{aligned}\quad (35)$$

where  $\Delta c = c_L^e - c_S^e$ . These relations are valid for any functions,  $f_L, f_S$ , and there is no need for function inversion. However, the database functions  $f_L, f_S$  are not defined outside the interval  $c \in [0, 1]$  and so the above construction only works if these functions are extended beyond this interval, for example, by constructing a quadratic function about the equilibrium point with a common tangent and second derivative.

## Conclusions

We have shown the equivalence of GPF and WBM phase field models, and that the apparent difference lies with free energy construction. GPF modelling inevitably involves compromise of the database function in the metastable regions. Despite this, GPF modelling has many attractive features and explains its adoption in many multiphase models, e.g. [5], which extends the idea to a multiphase context.

## Acknowledgements

This research was funded by EPSRC Innovative Manufacturing Research Hub in Liquid Metal Engineering (LiME), Grant No. EP/ N007638/1.

## References

- [1] Scientific Group Thermodata Europe, see [www.sgte.net/en/about-sgte](http://www.sgte.net/en/about-sgte).
- [2] Mathis Plapp. Unified derivation of phase-field models for alloy solidification from grand-potential functional, *Phys.Rev. E* 84, 031601 2011
- [3] A.A. Wheeler, W. J. Boettinger, and G. B. McFadden. Phase-field model for isothermal phase transitions in binary alloys, *Phys. Rev. A* 45, 7424 1992
- [4] Seong Gyoon Kim, Won Tae Kim, and Toshio Suzuki. Phase-field model for binary alloys, *Phys. Rev.E* 60, 7186 1999
- [5] Abhik Choudhury and Britta Nestler, Grand-potential formulation for multicomponent phase transformations combined with thin-interface asymptotics of the double-obstacle potential, *Phys. Rev. E* 85, 021602 2012



# Meshless Phase Field Modeling of Dendritic Growth

TADEJ Dobravec<sup>1</sup>, BOŠTJAN Mavrič<sup>1,2</sup>, and BOŽIDAR Šarler<sup>1,2</sup>

<sup>1</sup>Laboratory for Simulation of Materials and Processes, Institute of Metals and Technology, Lepi pot 11, 1000 Ljubljana, Slovenia

<sup>2</sup>Laboratory for Fluid Dynamics and Thermodynamics, Faculty of Mechanical Engineering, University of Ljubljana, Aškerčeva cesta 6, 1000 Ljubljana, Slovenia  
bozidar.sarler@imt.si

**Keywords:** solidification, dendritic growth, phase field, meshless methods

**Abstract.** A two-dimensional model to simulate the dendritic growth in pure melt is developed. Phase field model is used to derive the system of partial differential equations describing the temporal evolution of the solid-liquid interface and temperature field. Quantitative simulations are assured by the use of model parameters obtained by the thin-interface limit of the phase field model. Meshless local radial basis function collocation method and explicit Euler scheme are used for the spatial and temporal discretization of the phase field equations, respectively. The spatial convergence of the method is verified on the regular node arrangement. Dendrite morphologies at different preferential growth directions are compared among each other in order to assess the directional independence of the numerical approach. Advantages and shortcomings of the novel numerical method as well as further developments are discussed.

## Introduction

The dendritic growth is one of the most commonly observed phenomena in the solidification of metals. The dendritic morphology has large impact on the material properties of the solidified material [1–3], consequently, it is very important to understand the key physical mechanisms, determining the final microstructure.

Theoretical studies represent a powerful tool for the prediction of microstructure evolution in the solidifying material. In 1980s phase field (PF) method [4,5] was introduced in the field of modeling free boundary problems in materials science for the purpose of studying dendritic growth from a pure melt [6–8]. The method introduces an order parameter or PF, a continuous field representing phases. For example,  $PF=1$  and  $PF=-1$  represent the solid and the liquid phase, respectively, as PF continuously varies between these two values in the thin solid-liquid boundary layer, while the position of the solid-liquid interface is determined by  $PF=0$ . A link between PF and other thermodynamic variables is given by a free energy functional. A system of partial differential equations, determining the spatial-temporal evolution of PF and other thermodynamic variables, is obtained by a dissipative minimization of the functional [9–11].

Numerical implementations [12–14] of first PF models for dendritic growth in pure materials [6–8] are straightforward, since PF models do not require explicit tracking of the solid-liquid interface. First models are, however, unable to simulate the important physical limit, where the attachment kinetics undercooling can be neglected. Another limitation of first PF models is the requirement of very thin interface widths and consequently time consuming simulations on large computational domains. The derivation of thin-interface limit of PF model [15,16] removed both limitations, allowing quantitative simulations of dendritic growth in pure materials, however, experimentally relevant situations were still difficult to simulate, due to the large stiffness of non-linear PF equations. To overcome this problem, a large number of different computational approaches have been developed in the last twenty years [17,18].

In this paper, meshless local radial basis function collocation method (LRBFCM) [19] is used for the spatial discretization of PF equations, while simple explicit Euler scheme is used for the temporal discretization. Considering transient problems, LRBFCM was first applied for the diffusion problems [19] and was later successfully used for studying many different scientific and engineering problems

[20–24]. The simulation of dendritic growth from a pure melt by using LRBFCM is, to the best of our knowledge, reported for the first time in this study.

### Governing equations

**Phase field model.** PF model for dendritic solidification from a pure melt is given by a set of two coupled partial differential equations for PF  $\phi$  and the temperature  $T$ . Generally, the temperature at the solid-liquid interface depends on the capillary length  $d(\mathbf{n})$  and the interface kinetic coefficient  $\beta(\mathbf{n})$ , where  $\mathbf{n}$  is the normal to the solid-liquid interface in the direction of the liquid phase. In this paper, the case with zero interface kinetics  $\beta(\mathbf{n})=0$  is studied, hence only the anisotropic capillary length  $d(\mathbf{n})=d_0a(\mathbf{n})$  has to be considered, where  $d_0$  is constant capillary length and  $a(\mathbf{n})$  stands for the anisotropy function. In case of the solid phase with cubic crystal structure it is usually given as

$$a(\mathbf{n}) = (1 - 3\check{n}_4) \left( 1 + \frac{4\check{n}_4}{1 - 3\check{n}_4} (\check{n}_x^4 + \check{n}_y^4) \right), \quad (1)$$

where  $\check{n}_4$  stands for the anisotropy strength.  $\mathbf{n}=(\check{n}_x, \check{n}_y)$  is calculated as  $\mathbf{n}=\mathbf{R}(\theta_0)\mathbf{n}_0$ , where  $\mathbf{R}(\theta_0)$  is the rotation matrix and  $\mathbf{n}_0=(\cos\theta_0, \sin\theta_0)$ ,  $\theta_0 \in [0, \pi/2)$  is one of the preferential growth directions.

The interface width  $W$  is according to the thin interface limit of PF model [16] with  $\beta(\mathbf{n})=0$  given as  $W(\mathbf{n})=W_0a(\mathbf{n})$ .  $W_0=d_0\lambda/a_1$  is the constant interface width, where  $\lambda=\rho L^2/(Hc_pT_m)$  is a constant, determining  $\phi-T$  coupling where  $\rho$ ,  $L$ ,  $H$ , and  $c_p$  stand for the density, the latent heat of fusion, the energy jump in the free energy between the two stable phases at the melting temperature  $T_m$ , and the specific heat at constant pressure, respectively. The characteristic time of attachment of atoms at the interface is in the thin interface limit [16] with  $\beta(\mathbf{n})=0$  given as  $\tau(\mathbf{n})=\tau_0a^2(\mathbf{n})$ , where  $\tau_0=a_2\lambda W_0^2/\alpha$ , where  $\alpha$  is the thermal diffusivity. The constants  $a_1$  and  $a_2$  depend on the functions  $g(\phi)$ ,  $p(\phi)$  and  $h(\phi)$ , determining the two stable phases at the melting temperature,  $\phi-T$  coupling, and excess heat production during solidification, respectively.

It is convenient to write PF model in a non-dimensional form by introducing dimensionless temperature  $u=(T-T_m)/(L/c_p)$  and rescaling spatial and temporal coordinates as  $\bar{t}=t/\tau_0$ ,  $\bar{x}=x/W_0$ ,  $\bar{y}=y/W_0$ . The governing equations for the dendritic solidification from a pure melt with zero interface kinetics are finally given as

$$a^2(\mathbf{n})\partial_{\bar{t}}\phi = -g'(\phi) - \lambda u p'(\phi) + \bar{\nabla} \cdot (a^2(\mathbf{n})\bar{\nabla}\phi) + \sum_{\xi=x,y} \partial_{\bar{\xi}} \left( |\bar{\nabla}\phi|^2 a(\mathbf{n}) \frac{\partial a(\mathbf{n})}{\partial(\partial_{\bar{\xi}}\phi)} \right), \quad (2)$$

$$\partial_{\bar{t}}u = \bar{D}\bar{\nabla}^2u + h'(\phi)\partial_{\bar{t}}\phi, \quad (3)$$

where  $\bar{\nabla}=(\partial/\partial\bar{x}, \partial/\partial\bar{y})$  and  $\bar{D}=\alpha\tau_0/W_0^2$ . The choice of functions

$$g'(\phi)=-\phi-\phi^3, \quad p'(\phi)=(1-\phi^2)^2, \quad h'(\phi)=\frac{1}{2}, \quad (4)$$

yields  $a_1 = 0.8839$ ,  $a_2 = 0.6267$  [16] and operating window for PF  $\phi \in [-1, 1]$ .

**Initial and boundary conditions.** The systems of PF equations is solved in the computational domain  $\Omega$  with boundary  $\Gamma$ . Initial condition for the temperature field is given as

$$u(\mathbf{r}, \bar{t} = 0) = -\Delta, \quad \mathbf{r} = (\bar{x}, \bar{y}) \in \Omega + \Gamma, \quad (5)$$

where  $\Delta$  stand for the initial undercooling, and for PF

$$\phi(\mathbf{r}, \bar{t} = 0) = -\tanh\left(\frac{|\mathbf{r} - \mathbf{r}_0|^2 - R_0^2}{\sqrt{2}}\right), \quad \mathbf{r} = (\bar{x}, \bar{y}) \in \Omega + \Gamma, \quad (6)$$

where  $\mathbf{r}_0$  and  $R_0$  stand for the position of nuclei and the initial size of the solid phase, respectively. Zero flux Neumann boundary conditions are used for PF and temperature field.

### Numerical methods

The equations are solved on a regular node distribution with the constant spacing between two neighboring computational points equal to  $h$ . A simple explicit Euler scheme is used for the temporal discretization of PF equations. The time step of integration is set to [25]

$$\Delta \bar{t} = 0.7 \Delta \bar{t}_0, \quad \Delta \bar{t}_0 = \frac{1}{4} \frac{h^2}{\max(\bar{D}, 1/a(\mathbf{n}))}. \quad (7)$$

Meshless LRBFCM [19] is used for the spatial discretization of PF equations. The method is finite-difference-like, meaning that the differential operator is approximated by the weighted sum of field values from a local sub-domain. The method however employs nodes that are not necessary confined to the coordinate lines. The general procedure for the calculation of the weights is formulated in the following section.

**LRBFCM.** The spatial discretization of  $\Omega + \Gamma$  is given by node distribution  ${}_1\mathbf{r} \in \Omega + \Gamma, l = 1, \dots, N$ , where  $N$  is the number of computational points. For each  ${}_1\mathbf{r}$ , a local sub-domain  ${}_1\Omega$  is generated, containing  ${}_1\mathbf{r}$  and its  ${}_1N - 1$  nearest neighbors. For a point  $\mathbf{r}$  closest to  ${}_1\mathbf{r}$ , a general scalar field  $\eta(\mathbf{r})$  is approximated as

$$\eta(\mathbf{r}) \approx \sum_{i=1}^{{}_1N} {}_1\alpha_i {}_1\Phi_i(\mathbf{r}) + \sum_{i=1}^m {}_1\alpha_{{}_1N+i} p_i(\mathbf{r}) = \sum_{i=1}^{{}_1N+m} {}_1\alpha_i \Psi_i(\mathbf{r}), \quad (8)$$

where  $m$  is the number of augmentation monomials  $p_i(\mathbf{r})$  and  ${}_1\Phi_i(\mathbf{r})$  is multiquadric (MQ) radial basis function, defined as

$${}_1\Phi_i(\mathbf{r}) = \sqrt{\frac{{}_1\check{h}^2}{{}_1h^2} |\mathbf{r} - {}_1\mathbf{r}_i|^2 + 1}, \quad {}_1h = \sqrt{\sum_{i=2}^{{}_1N-1} \frac{|{}_1\mathbf{r}_i - {}_1\mathbf{r}_1|^2}{{}_1N-1}}, \quad (9)$$

where  $\eta$  stands for the shape parameter. If  $\mathbf{r} \in \Gamma$ , linear boundary condition is applied to Eq. 8. By evaluating Eq. 8 in each node  $\mathbf{r}_j$  from  $\Omega$  one obtains a system of linear equations for the interpolation weights  $\alpha_i$

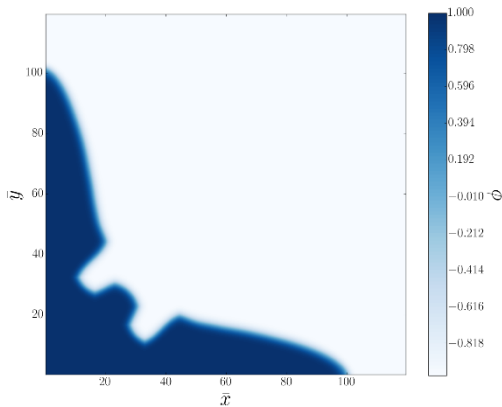
$$\sum_{i=1}^{N+m} A_{ji} \alpha_i = \gamma_j, \quad (10)$$

where  $A_{ji}$  is either MQ, monomial or on MQ applied operator of boundary condition.  $\gamma_j$  is either the field value or the value of the boundary condition. The shape parameter  $\eta$  in each sub-domain is chosen according to the targeted value of the condition number  $c_{\text{num}} = 10^{20}$  of matrix  $\mathbf{A}$  from Eq. 10. An arbitrary differential operator  $D$  in the computational point  $\mathbf{r}$  is evaluated as

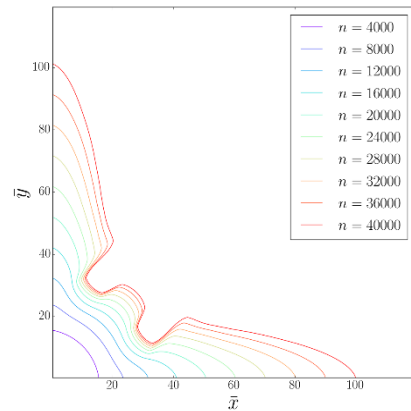
$$D\eta(\mathbf{r}) = \sum_{k=1}^N \gamma_k w_k, \quad w_k = \sum_{i=1}^{N+m} A_{ik}^{-1} D\Psi_i(\mathbf{r}). \quad (11)$$

## Numerical results

Numerical simulations are performed on a regular distribution of  $N = M \times M$  computational points. Each local sub-domain consists of considered node  $\mathbf{r}_1$ , four nearest nodes  $\mathbf{r}_j, j = 2, 3, 4, 5$  with  $|\mathbf{r}_1 - \mathbf{r}_j| = h$ , and randomly chosen next nearest node  $\mathbf{r}_6$  with  $|\mathbf{r}_1 - \mathbf{r}_6| = \sqrt{2}h$ . Non-dimensional spacing is set to  $h = 0.3$  in Figs. 1, 2 and 3, while three different values of  $h$  are used in Fig. 4, where the spatial convergence of LRBFCM is verified.  $M$  is set to  $M = 400$  in Figs. 1 and 2, to  $M = 500$  in Fig. 3, while different values of  $M$  are used in Fig. 4, according to the limitation  $hM = \text{const}$ . The center of initial circular nuclei with radius  $R_i = 10h$  and preferential growth direction angle, respectively, are set to  $\mathbf{r}_0 = (0, 0)$  and  $\theta_0 = 0$  in Figs. 1, 2 and 4, while  $\mathbf{r}_0 = (250h, 250h)$  is used in Fig. 3, where the dendritic morphology at three different  $\theta_0$  is studied. Time is discretized as  $\bar{t} = n\Delta\bar{t}$ , where  $n$  is the iteration number.



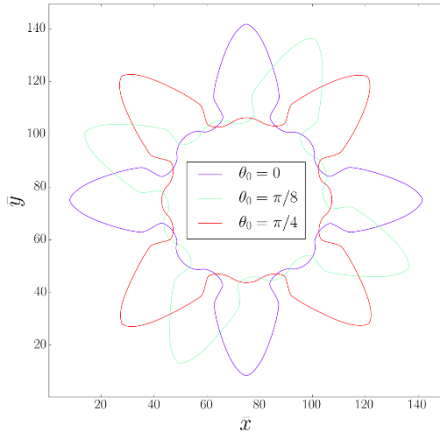
**Figure 1.** Phase field at  $n = 40000$ .



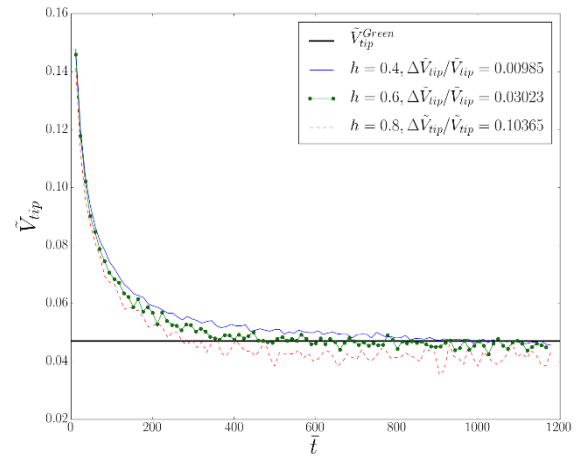
**Figure 2.** Solid-liquid interface evolution.

The spatial and temporal coordinates are scaled with  $W_0 = 1$  and  $\tau_0 = 1$ , leaving  $\bar{D}$  as the only free parameter in the thin interface limit of PF model [16]. In Figs. 1, 2 and 3 parameters  $\bar{D} = 6.267$ ,  $\eta_4 = 0.06$  and  $\Delta = 0.55$  are used, while parameters  $\bar{D} = 1$ ,  $\eta_4 = 0.05$  and  $\Delta = 0.65$  are used in Fig. 4, where the spatial convergence of LRBFCM is verified. One can see in Fig. 1 how phase field is

equal to  $PF=1$  and  $PF=-1$ , respectively, in the solid and liquid phase, while the solid-liquid interface is determined by the contour  $PF=0$ . The temporal evolution of the solid-liquid interface is shown in Fig. 2. The initial circular shape of nuclei eventually becomes unstable due to the anisotropic interfacial energy, yielding evolution of the dendrite. The dendrite tip velocity decreases with time and approaches the steady state solution as seen in Fig. 4. The velocity is rescaled as  $\tilde{V}_{tip} = V_{tip} d_0 / \alpha$  in order to obtain a numerical solution independent of PF parameters [16]. The analytical steady state solution  $\tilde{V}_{tip}^{Green}$  is obtained by the Green function method [26]. The numerical growth velocity is calculated at different values of  $h$  in order to assess the spatial convergence of LRBFCM. A very good agreement between analytical and numerical solution is observed at  $h=0.4$ , where the relative error is equal to  $\Delta\tilde{V}_{tip} / \tilde{V}_{tip} \approx 1\%$ . The solid-liquid interface at different values of the preferential growth direction, determined by  $\theta_0$ , is shown in Fig. 3, where one can see, how the dendrite morphology is independent of crystal orientation  $\theta_0$ .



**Figure 3.** Solid-liquid interface at three different values of  $\theta_0$ .



**Figure 4.** Dendrite's tip velocity as a function of time at different values of  $h$ .

## Summary

A two dimensional meshless PF model for the simulation of dendritic growth from a pure melt has been developed. Meshless solver is capable of solving highly non-linear PF equations and obtaining accurate results in comparison with the analytical steady state solution of dendritic growth. Also, dendritic morphology is independent of the preferential growth direction. The node arrangement can be arbitrary as can be seen in the choice of only  $N=6$  nodes in non-symmetric local sub-domain. The main disadvantage of the numerical model is the requirement for the computationally expensive search of the optimal shape parameter in each local sub-domain.

In our further work, the random noise will be firstly added to PF equations in order to analyze the evolution of the secondary dendrite arms. Also, the dendritic growth in binary and multi-component alloys will be considered. An  $h$ -adaptive framework adjacent to the previously developed  $r$ -adaptive framework [27] will be developed in order to assure a high density of computational points only in the regions where the phase field varies. Computationally efficient and accurate results will be assured in that way.

## Acknowledgements

This work was founded by Slovenian research agency (ARRS) in the framework of applied research project J2-7384, program group P2-0162 and MARTINA project. Project J2-7384 is cofounded by Store Steel, d.o.o. company.

## References

- [1] J.A. Dantzig, M. Rappaz, Solidification, EFPL Press, 2009.
- [2] W. Kurz, D.J. Fisher, Fundamentals of solidification, Trans Tech Publications, 1986.
- [3] M.E. Glicksman, Principles of Solidification, Springer New York, New York, NY, 2011.
- [4] L.-Q. Chen, Phase-Field Models for Microstructure Evolution, Annu. Rev. Mater. Res. 32 (2002) 113–140.
- [5] W.J. Boettinger, J.A. Warren, C. Beckermann, A. Karma, Phase-Field Simulation of Solidification, Annu. Rev. Mater. Res. 32 (2002) 163–194.
- [6] G.J. Fix, Phase field methods for free boundary problems, (1982).
- [7] J.B. Collins, H. Levine, Diffuse interface model of diffusion-limited crystal growth, Phys. Rev. B Condens. Matter. 31 (1985) 6119–6122.
- [8] J.S. Langer, Models of Pattern Formation in First-Order Phase Transitions, Dir. Condens. Matter Phys. Ser. Ser. Dir. Condens. Matter Phys. ISBN 978-9971-978-42-6 WORLD Sci. Ed. G Grinstein G Mazenko Vol 1 Pp 165-186. 1 (1986) 165–186.
- [9] J.W. Cahn, J.E. Hilliard, Free Energy of a Nonuniform System. I. Interfacial Free Energy, J. Chem. Phys. 28 (1958) 258–267.
- [10] J.W. Cahn, On spinodal decomposition, Acta Metall. 9 (1961) 795–801.
- [11] J. Cahn, S. Allen, A microscopic theory for domain wall motion and its experimental verification in Fe-Al alloy domain growth kinetics, J. Phys. Colloq. 38 (1977) C7-51-C7-54.
- [12] R. Kobayashi, Modeling and numerical simulations of dendritic crystal growth, Phys. Nonlinear Phenom. 63 (1993) 410–423.
- [13] A.A. Wheeler, B.T. Murray, R.J. Schaefer, Computation of dendrites using a phase field model, Phys. Nonlinear Phenom. 66 (1993) 243–262.
- [14] S.L. Wang, R.F. Sekerka, Computation of the dendritic operating state at large supercoolings by the phase field model, Phys. Rev. E Stat. Phys. Plasmas Fluids Relat. Interdiscip. Top. 53 (1996) 3760–3776.
- [15] A. Karma, W.J. Rappel, Phase-field method for computationally efficient modeling of solidification with arbitrary interface kinetics, Phys. Rev. E Stat. Phys. Plasmas Fluids Relat. Interdiscip. Top. 53 (1996) R3017–R3020.
- [16] A. Karma, W.-J. Rappel, Quantitative phase-field modeling of dendritic growth in two and three dimensions, Phys. Rev. E. 57 (1998) 4323–4349.
- [17] X. Dong, H. Xing, K. Weng, H. Zhao, Current development in quantitative phase-field modeling of solidification, J. Iron Steel Res. Int. 24 (2017) 865–878.
- [18] A. Karma, D. Tournet, Atomistic to continuum modeling of solidification microstructures, Curr. Opin. Solid State Mater. Sci. 20 (2016) 25–36.
- [19] B. Šarler, R. Vertnik, Meshfree explicit local radial basis function collocation method for diffusion problems, Comput. Math. Appl. 51 (2006) 1269–1282.
- [20] R. Vertnik, B. Šarler, Local Collocation Approach for Solving Turbulent Combined Forced and Natural Convection Problems, Adv. Appl. Math. Mech. 3 (2011) 259–279.
- [21] K. Mramor, R. Vertnik, B. Šarler, Simulation of laminar backward facing step flow under magnetic field with explicit local radial basis function collocation method, Eng. Anal. Bound. Elem. 49 (2014) 37–47.
- [22] G. Kosec, B. Šarler, Simulation of macrosegregation with mesosegregates in binary metallic casts by a meshless method, Eng. Anal. Bound. Elem. 45 (2014) 36–44.
- [23] B. Mavrič, B. Šarler, Application of the RBF collocation method to transient coupled thermoelasticity, Int. J. Numer. Methods Heat Fluid Flow. 27 (2017) 1064–1077.
- [24] U. Hanoglu, B. Šarler, Multi-pass hot-rolling simulation using a meshless method, Comput. Struct. 194 (2018) 1–14.
- [25] N. Provatas, K. Elder, Phase-Field Methods in Materials Science and Engineering, 1st ed., Wiley-VCH, 2010.

- [26] D.I. Meiron, Selection of steady states in the two-dimensional symmetric model of dendritic growth, *Phys. Rev. A.* 33 (1986) 2704–2715.
- [27] I. Kovačević, B. Šarler, Solution of a phase-field model for dissolution of primary particles in binary aluminum alloys by an r-adaptive mesh-free method, *Mater. Sci. Eng. A.* 413–414 (2005) 423–428.

## **Phase-field modeling of complex polycrystalline structures**

László Gránásy, Tamás Pusztai

**Keywords:** phase field, polycrystalline freezing, nucleation modes, multiple and disordered dendrites, spherulites

### **Abstract**

Results from an orientation-field-based phase-field model will be reviewed. First I briefly present a phase-field model developed during the past decade that incorporates homogeneous and heterogeneous nucleation of growth centers, and several mechanisms for the formation of new grains at the perimeter of growing crystals, a phenomenon termed as growth front nucleation (GFN). This approach enables the modeling of complex polycrystalline structures including disordered ("dizzy") dendrites, crystal sheaves, spherulites, and fractallike aggregates. Possible control of solidification patterns via external fields, confined geometry, particle additives, scratching/piercing thin films, etc. via phase-field modeling will also be addressed. Microscopic aspects of GFN, quantitative simulations, and possible future directions will also be discussed briefly.

## **Equiaxed growth of Al-Cu dendrites : 3D phase-field simulations**

Ahmed Kaci BOUKELLAL, Jean-Marc DEBIERRE

**Keywords:** Al-Cu, solidification, 3D simulations, phase-field, dendrites.

### **Abstract**

We report on equiaxed solidification of Al-Cu dendrites under isothermal conditions. The sample is cooled down at zero temperature gradient. The study focuses on the dendrite growth and the interaction between two primary arms growing toward each other [1]. A 3D phase-field code taking into account the experimental conditions is developed to study these phenomena [2]. As the chemical capillary length  $d_0$  scales as the inverse of the nominal concentration of the alloy, the experimental concentrations studied in [1] cannot be simulated because of large memory and time costs. For this reason, the growth and interactions of dendrites at lower concentrations have been simulated and scaling laws obtained. The simulation results have been extrapolated to the experimental concentrations [2]. Comparison between the extrapolated numerical results [2] and the experimental ones [1] gives a good quantitative agreement.

### **References**

- [1] Bogno A, Nguyen-Thi H, Reinhart G, Bilia B, and Baruchel J. Acta. Mater, 61:1303–1315, (2013).
- [2] Boukellal A.K, Debierre J-M, Reinhart G and Nguyen-Thi H. Scaling laws governing interaction of equiaxed Al-Cu dendrites : a study combining experiments with phase-field simulations.



# Grain coarsening in two-dimensional orientation-field-based phase-field models

Tamás Pusztai, Bálint Korbuly, Hervé Henry, Mathis Plapp, Markus Apel,  
László Gránásy

**Keywords:** grain coarsening, limiting grain size distribution, phase-field modelling, orientation field

## Abstract

Contradictory results have been published in the literature regarding the form of the limiting grain size distribution (LGSD) that characterises the late stage grain coarsening in (quasi-)two dimensional polycrystalline systems. While experiments and the phase-field crystal (PFC) model provide a lognormal distribution, other works including theoretical studies and the multi-phase-field (MPF) models yield significantly different LGSD. We show that while the distribution predicted by the orientation-field based phase-field models are very similar to the theoretical and MPF results, the partial detection of the small angle grain boundaries leads to a lognormal distribution close to those seen in the experiments and the PFC simulations. This indicates that the LGSD is critically sensitive to the details of the evaluation process, and raises the possibility that the differences among the LGSD results from different sources may originate from differences in the detection of small angle grain boundaries.

## CHAPTER 3: IN SITU OBSERVATION



# In-situ observation of the effects of gravity direction on directional solidification of the transparent alloy NPG-35wt%-DC

Turlough HUGHES<sup>1</sup>, Shaun MCFADDEN<sup>1,2</sup>, Anthony Robinson<sup>1</sup>

<sup>1</sup>Trinity College Dublin, Department of Mechanical and Manufacturing Engineering, Dublin 2, Ireland

<sup>2</sup>Ulster University, School of Computing Engineering and Intelligent Systems, BT48 7JL, N. Ireland  
s.mcfadden2@ulster.ac.uk

**Keywords:** Directional Solidification, Gravity, Convection, Columnar to Equiaxed Transition, Fragmentation

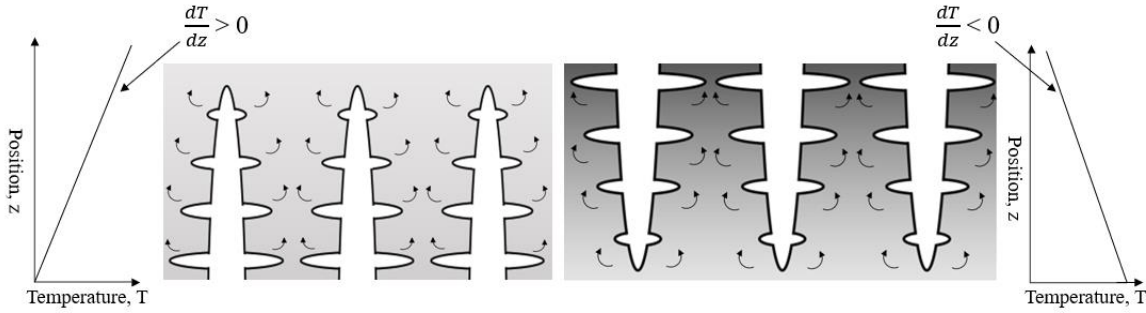
**Abstract.** Directional solidification scenarios that are in-line with gravity but in different directions (solidifying upwards or downwards) provide two qualitatively different scenarios for the study of microstructure formation. The approach has been used to investigate the influence of thermosolutal convection on dendrite arm spacing while the role of solute and thermal distributions on the mechanisms of nucleation and growth are well documented. Here, an experimental setup consisting of a long cylindrical crucible of 8mm inner diameter, which facilitates control of temperature gradient, cooling rate and, hence, isotherm velocity, was used to study directional solidification in the transparent model alloy neopentyl glycol-35wt.%(d)camphor. The rig was initially aligned vertically in-line with gravity and then inverted to study solidification in the opposing direction. In the case of upwards direction (defined as solidification in opposition to the gravity vector), classical Columnar to Equiaxed Transition behaviour was observed. In the downwards direction (solidification aligned with gravity), the situation changed considerably with copious amounts of dendrite-arm fragmentation producing single equiaxed crystals; but, moreover, with large fragments breaking from the coherent mush producing clusters of equiaxed crystals. Some crystals growing from the sidewall also provided mechanical support structure for fragments and clusters that should have tended to settle as sediment at the bottom of the sample. This fragmentation as clusters may have important consequences on macrosegregation formation in castings. This presentation will show these distinct differences that the gravity direction made to the directional solidification behaviour of the NPG-35wt%-DC alloy observed in-situ.

## Introduction

In-situ experiments using transparent analogues have helped to further knowledge on the fundamental laws and mechanisms of dendritic solidification since they were first used by Jackson et. al. in 1965 [1]. Early experimental results had been used to validate the dendrite tip radius and undercooling relationship as well as the relationship between dendrite growth velocity and undercooling [2]. One important phenomenon first observed in transparent analogues [3] and subsequently confirmed using x-ray synchrotron radiography with Al-20wt.%Cu [4], was fragmentation. Ruvalcaba [5] later demonstrated the fragmentation mechanism with XRSM, showing solute enriched liquid that partitioned at the solid liquid interface accumulating in pockets between tertiary arms, and initiating solute-enrichment-driven remelting at the base of the arm which leads to detachment.

Upwards and downwards directional solidification experiments provide two qualitatively different scenarios for a comparative study of how microstructure forms under different thermosolutal conditions. Figure 1 depicts how in one scenario, solute enriched interdendritic liquid of lower density, being more buoyant, tends to float out of the mushy zone during directional solidification upwards. A second scenario depicts the same alloy directionally solidifying downwards, where more buoyant solute enriched liquid floats upwards and accumulates in the mushy zone. Buoyancy driven thermosolutal flow and the direction of solidification with respect to gravity, therefore, play an important role in fragmentation. Fig. 1 also depicts a positive temperature gradient imposed along the z-axis during directional solidification upwards which has a stabilizing effect on the liquid flow,

where thermal expansion results in lighter liquid above heavier colder liquid. In contrast a negative temperature gradient destabilizes the fluid flow and gives rise to gravity-driven convection.

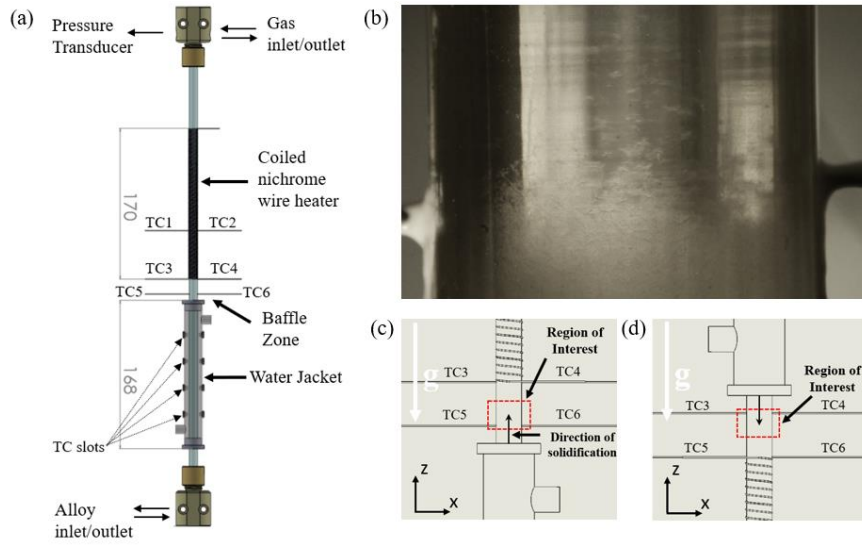


**Figure 1.** Schematic representation of thermosolutal flow at the front of the mushy zone during directional solidification upwards (left) and downwards (right), in an alloy where the solute is of lower density than the solvent.

Upwards and downwards directional solidification (DWDS) was first comparatively studied in 1976 by Burden and Hunt, where a clear effect on the primary dendrite arm spacing was demonstrated in transparent analogue  $\text{NH}_4\text{Cl}/\text{H}_2\text{O}$ . Since then DWDS experiments in the literature have been scarce. The different gravity-driven thermosolutal flows have been studied for their effect on primary and secondary dendrite arm spacings [6]–[12], freckle defects in single crystal castings [13], and potential application for thin shell castings [14]. Importantly, the recent works cited have all been ex-situ. Here, a comparative study of microstructure formation for upwards and downwards directional solidification is conducted in-situ, using transparent analogue neoptenyl-glycol-35wt.%(d)camphor. The objective of the study is to present the differences in the mechanisms of microstructure formation for upwards and downwards directional solidification with the same imposed temperature gradients and for a range imposed liquidus isotherm velocities.

## Experimental Setup & Procedure

The experimental setup, shown in Figure 2, consisted of a cylindrical sapphire crucible of length 500mm, with 8mm inner diameter and 10mm outer diameter. Sapphire, being optically transparent, allowed visualization of the top of the mushy zone and, due to its high thermal conductivity ( $\sim 23$  W/mK), facilitated heat transfer to and from the material with low ( $< 1$  K) temperature difference across the crucible wall. A resistively heated coiled nichrome wire, wrapped tightly around the outer tube, acted as a heat source on the crucible. A power supply was connected at each end and modulated with a dedicated computer providing PI temperature control, where the average of TC1 and TC2 provided the control variable. Heat was extracted from the crucible with a 168 mm long water jacket and shell type heat exchanger using a precision chiller which facilitated controlled cooling rates of 0.1, 0.2 and 1 K/min.



**Figure 2.** (a) Schematic of experimental setup (dimensions in mm) and orientation for upwards DS (b) Image capture of the region of interest during experiments. (c)-(d) Configurations and reference coordinates for directional solidification experiments upwards and downwards, respectively.

A series of 0.5mm diameter wells were drilled along the wall of the sapphire tube in diametrically opposed pairs where T-type thermocouples, shown in Figure 2, were seated with thermal paste. Differential thermocouples signals were acquired at 1 Hz via LabView and subsequently exported to MatLab for processing. End caps on the sapphire tube provided sealed inlet and outlet valves for filling the transparent analogue and for pressure compensation. These were fixed to an aluminium frame not shown in Figure 2. A camera (with variable 1.4x to 13x zoom lens) was fixed to the aluminium frame with its optical axis orthogonal to the region of interest and captured images continuously during experiments at a nominal frequency of 0.6Hz. Camera and computer clocks were synchronised in order to correlate the temperature data with a given image.  $T_H$ , the average of TC1 and TC2, was set to maintain a constant temperature difference between  $T_H$  and the temperature of the sapphire tube wall at the water jacket, which was controlled by the precision chiller. The temperature gradient,  $dT/dz$ , that was recorded for experiments was then measured locally in the baffle zone using thermocouples TC3 - TC6. Constant temperature gradient and cooling rates were applied for each round of directional solidification which resulted in a constant liquidus isotherm velocity  $V_l = \dot{T}(dT/dz)$ , where  $\dot{T}$  is the cooling rate. For DWDS, the sapphire crucible was removed from the end caps and inverted, and the rig was filled with a fresh sample of transparent analogue. In each case, the alloy was prepared in a sealed glovebox under argon atmosphere and transferred to the rig and a gas tight glass syringe. Initially, temperatures of the heater and chiller were set to bring the solidification front near the region of interest, then constant ramp down cooling was implemented to

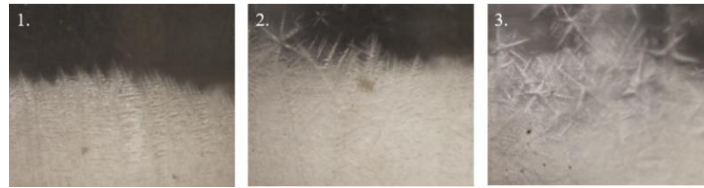
start directional solidification and a period of >10 mins was allowed before imaging to ensure for quasi-steady state directional solidification.

**Table 1.** List of experiments with temperature gradient and isotherm velocities

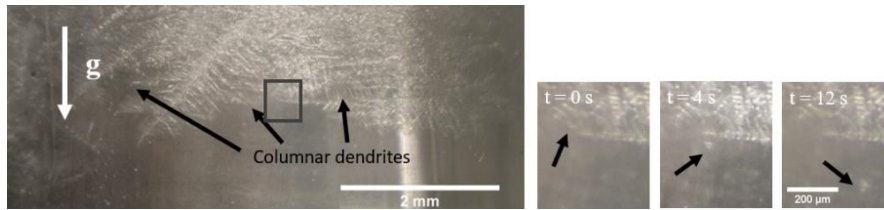
Experiment Number	$dT/dz$ [K/cm]	$V_I$ [ $\mu\text{m/s}$ ]	Direction
1	$8.8 \pm 0.4$	$1.55 \pm 0.07$	up
2	$8.7 \pm 0.4$	$3.41 \pm 0.30$	up
3	$9.2 \pm 0.3$	$14.17 \pm 0.56$	up
4	$-9.2 \pm 0.9$	$-1.75 \pm 0.17$	down
5	$-10.2 \pm 1.2$	$-3.7 \pm 0.43$	down
6	$-9.5 \pm 1.3$	$-16.2 \pm 2.3$	down

## Results

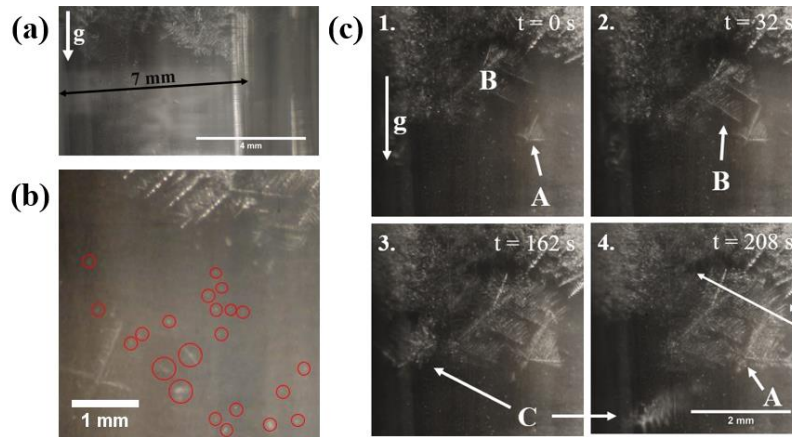
Six rounds of directional solidification were conducted, three upwards and three downwards. Details of the temperature gradient and liquidus isotherm velocities are provided in Table 1. For directional solidification upwards, with increasing  $V_I$  and relatively constant  $dT/dz$ , morphology progressed from fully columnar, mixed columnar and equiaxed, to fully equiaxed. For DWDS, exp 4 which had lowest magnitude  $V_I$  downwards, exhibited columnar dendritic growth, see Figure 4. However compared with its upwards counterpart the individual columnar grains were misaligned. Copious fragmentation was also observed in this experiment. A small increase in isotherm velocity from  $-1.75$  to  $-3.7 \mu\text{m/s}$  resulted in large clusters of equiaxed crystals fragmenting from the coherent mushy network during DWDS with clusters up to 7mm in length, see Fig. 5. While crystals which nucleated on the crucible wall provided mechanical support and prevented fragments and clusters from sedimenting, see Figure. 5 and Figure. 6.



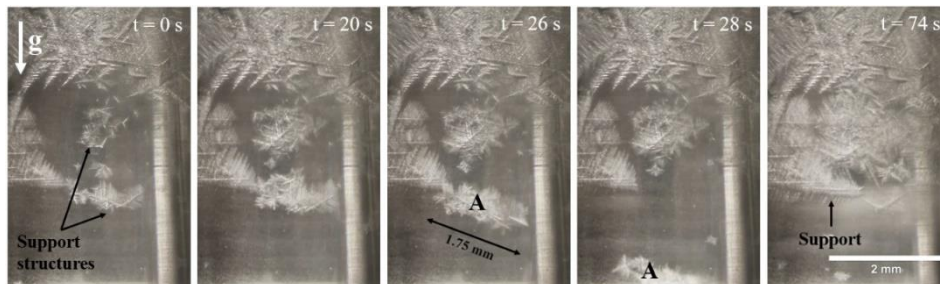
**Figure 3** (Exp. 1 – 3, see table 1.) Upward directional solidification shows a transition from columnar to equiaxed growth morphologies for increasing isotherm growth velocity



**Figure 4** (Exp. 4) shows columnar growth similar to exp 1, however the columnar grains are not well aligned with each other. A fragment ( $\sim 35\mu\text{m}$ ) is shown detaching in the image



**Figure. 5** (Exp. 5) (a) shows a 7mm cluster fragmenting from the mushy zone while (b) highlights some of the large amounts of fragmentation seen in experiments. (c) Sequence of 4 images; here crystal ‘A’, which nucleated on the crucible wall provided support for ‘B’ (image 1-2). ‘C’, however, had no support and continued down into the heater section following its fragmentation from the mushy network. Most fragments continued down into the heater in the same way as C, whereas B crystals survived and formed part of the final solid structure



**Figure. 6** (Exp. 6) Large clusters fragmenting from the mushy network. Mechanical support is provided by crystals which nucleated on the wall of the crucible. The clusters that sedimented on the support structures can be seen growing from  $t = 0$  to  $t = 26$  s until support A fragmented. A second cluster can be seen getting mechanical support at  $t = 74$  seconds.

## Conclusions

A marked difference in the mechanisms of microstructure formation during directional solidification upwards compared with DWDS was observed. The most notable was the copious amounts of fragmentation (Figure. 5 (a)) with fragments of from 35  $\mu$ m to large clusters of equiaxed crystals (Figure. 5 and Figure. 6) up to 7mm in length breaking from the mushy zone. This mass break up of the mushy zone could have important consequences for macrosegregation in castings. Thermosolutal flow will have caused solute enriched liquid to accumulate in the mushy zone for DWDS, as described in Figure 1, and the mass fragmentation observed during DWDS and not upwards, particularly that shown in Figure. 5 (b), is likely resulting from this. This proposed as the dominant cause for enhanced fragmentation. The different solidification directions could be studied further as a method for grain refinement for example in high purity castings where seed ceramic particles may not be used. The experiment highlights the effect of thermosolutal flow and in turn, solidification direction with respect to gravity, on fragmentation and the mechanisms of microstructure formation during solidification.



## References

- [1] K. A. Jackson and J. D. Hunt, Transparent compounds that freeze like metals, *Acta Metall.*, vol. 13, no. 11, pp. 1212–1215, 1965.
- [2] S. C. Huang and M. E. Glicksman, Overview 12: Fundamentals of dendritic solidification-I. Steady-state tip growth, *Acta Metall.*, vol. 29, no. 5, pp. 701–715, 1981.
- [3] J. Hutt and D. StJohn, The origins of the equiaxed zone -Review of theoretical and experimental work, *Int. J. Cast Met. Res.*, vol. 11, no. 1, pp. 13–22, Jul. 1998.
- [4] R. H. Mathiesen, L. Arnberg, P. Bleuet, and A. Somogyi, Crystal fragmentation and columnar-to-equiaxed transitions in Al-Cu studied by Synchrotron x-ray video microscopy, *Metall. Mater. Trans. A Phys. Metall. Mater. Sci.*, vol. 37, no. 8, pp. 2515–2524, 2006.
- [5] D. Ruvalcaba, In situ observations of dendritic fragmentation due to local solute-enrichment during directional solidification of an aluminum alloy, vol. 55, pp. 4287–4292, 2007.
- [6] C. Brito *et al.*, Upward and downward unsteady-state directional solidification of a hypoeutectic Al-3wt.%Mg alloy, *Ciência Tecnol. dos Mater.*, vol. 29, no. 1, pp. e65–e70, Jan. 2017.
- [7] J. E. Spinelli, O. Fernandes, L. Rocha, and A. Garcia, The Influence of Melt Convection on Dendritic Spacing of Downward Unsteady-State Directionally Solidified Sn-Pb Alloys, *Mater. Res.*, vol. 9, no. 1, pp. 51–57, 2006.
- [8] M. H. Burden and J. D. Hunt, Some observations on primary dendrite spacings, *Met. Sci.*, vol. 10, no. 5, pp. 156–158, 1976.
- [9] J. E. Spinelli, I. L. Ferreira, and A. Garcia, Influence of melt convection on the columnar to equiaxed transition and microstructure of downward unsteady-state directionally solidified Sn – Pb alloys, vol. 384, pp. 217–226, 2004.
- [10] J. E. Spinelli, D. M. Rosa, I. L. Ferreira, and A. Garcia, Influence of melt convection on dendritic spacings of downward unsteady-state directionally solidified Al-Cu alloys, *Mater. Sci. Eng. A*, vol. 383, no. 2, pp. 271–282, 2004.
- [11] J. E. Spinelli, M. D. Peres, and A. Garcia, Thermosolutal convective effects on dendritic array spacings in downward transient directional solidification of Al-Si alloys, *J. Alloys Compd.*, vol. 403, no. 1–2, pp. 228–238, 2005.
- [12] F. Wang, D. Ma, J. Zhang, L. Liu, S. Bogner, and A. Bührig-Polaczek, Effect of local cooling rates on the microstructures of single crystal CMSX-6 superalloy: A comparative assessment of the Bridgman and the downward directional solidification processes, *J. Alloys Compd.*, vol. 616, pp. 102–109, 2014.
- [13] F. Wang, D. Ma, J. Zhang, and A. Bührig-Polaczek, Investigation of segregation and density profiles in the mushy zone of CMSX-4 superalloys solidified during downward and upward directional solidification processes, *J. Alloys Compd.*, vol. 620, pp. 24–30, 2015.
- [14] D. Ma, H. Lu, and A. Bührig-Polaczek, Experimental trials of the Thin Shell Casting (TSC) technology for directional solidification, *IOP Conf. Ser. Mater. Sci. Eng.*, vol. 27, no. 1, 2011.
- [15] E. Liotti *et al.*, A synchrotron X-ray radiography study of dendrite fragmentation induced by a pulsed electromagnetic field in an Al15Cu alloy, 2014.

# Real-time and full-field quantification of buoyant convection during multi-component solidification

Virkeshwar KUMAR, Atul SRIVASTAVA, Shyamprasad Karagadde

Department of Mechanical Engineering,  
Indian Institute of Technology, Bombay  
Powai, Mumbai, India-400076  
s.karagadde@iitb.ac.in

**Keywords:** Buoyancy-driven convection, Multi-component solidification, Double-diffusive-convection, Interferometry, PIV

**Abstract.** In solidification, the thermal and compositional gradients simultaneously arise from externally imposed boundary conditions as well as from the solidification characteristics such as latent heat and solute rejection at the solidifying interfaces. These gradients lead to interacting flow behavior due to thermal and solutal buoyancy in the liquid. The buoyancy-driven flow in the fluid not only leads to complex flow patterns such as double-diffusive convection but also results in the formation of defects such as freckles, and other kinds of non-homogeneity in the system. The aim of this study is to understand the influence of gravity-driven convection on the solidification characteristics and the transport phenomena in the liquid. Bottom-cooled solidification of pure water and aqueous ammonium chloride solutions was performed to investigate the evolution of solidifying front and flow behavior.

During *in situ* experimental observations of bottom-cooled (maintained at a constant temperature - 21°C) solidification, the plumes were originated at microstructural length scales and later developed into freckle defects. The measurement of whole-field temperature and velocity in the liquid phase during solidification of Water-NH<sub>4</sub>Cl mixture was performed using a Mach-Zehnder interferometer and Particle image velocimetry (PIV) respectively. The composition of NH<sub>4</sub>Cl in the mixture has been varied between 0–25 wt%. Mach-Zehnder interferometer is a refractive index based optical technique which works on the principle of relative change in the path length of the two coherent light beams and provides temperature and/or concentration field after extraction from the images. The PIV gives the velocity field of the plume and the bulk fluid. In the present work, a brief analysis of the temperature distribution has been discussed. The results show, how gravity plays a role in forming the convective patterns at different regimes of solidification, namely (i) convection in pure water between 0-4°C, (ii) conduction during hypo-eutectic solidification of Water-NH<sub>4</sub>Cl alloy (iii) convection during hyper-eutectic solidification of Water-NH<sub>4</sub>Cl alloy.

## Introduction

The density of the multi-component liquid depends on the temperature and concentration of the alloying elements. Convective motions occur in a fluid during solidification either by a localized density variation caused due to the rejection of solute and by established thermal boundary conditions [1–3]. The process of solidification of pure materials is influenced by temperature or heat diffusion [4]. Bottom cooled solidification of water leads to convection due to the anomalous expansion behaviour of water (maximum density at 4°C) between 4°C and 0°C. Tankin and Farhadieh reported interferometric study of bottom cooled solidification of water and employed dye to visualize the convective flow during the process [5]. Kowalewski and Cybulski reported temperature and flow fields during top-cooled solidification of water by using thermochromic liquid crystal (TLC) and particle image velocimetry (PIV) respectively [6]. Large and Andreck observed different convective profile from different planes of view using schlieren [7].

Solidification of multi-component materials is controlled by implemented thermal condition and solute rejection during the process. Flow and heat transfer phenomena during bottom cooled solidification depend on the density of the residual liquid. Baraga and Viskanta reported temperature and concentration profiles, interface positions in conduction dominated regime for the aqueous salt system [8]. Copely et al. reported that the fragmentation in the hyper-eutectic salt system by the plumes increases with decreasing thermal gradient and decreasing growth rate [9]. They also reported that the freckle formation is more susceptible to higher Lewis number and low viscous fluid. Magirl and Incropera [10] reported the formation of the plume and double-diffusive layer in hyper-eutectic bottom cooled salt solution solidification. They also reported experimentally plume velocity, the wavelength of plumes and suggested that channels develop due to initial perturbation on liquid interface cause re-melting on the interface. Chen [11] reported the dependency of the number of plumes and double-diffusive layers with the bottom cooled temperature in 29 wt%  $\text{NH}_4\text{Cl}$  salt solutions.

From the literature, it is to be seen that a lot of research has been carried out to understand the phenomenon of solidification experimentally as well as through numerical approaches. However, there is a paucity of *in situ* study using interferometry and flow visualization techniques during solidification. The intended objective of the present work is to experimentally visualize the transport phenomena during bottom cooled solidification of pure material (water), hypo-eutectic and hyper-eutectic of water- $\text{NH}_4\text{Cl}$  mixture. The anomalous density behaviour of water and rejection of less dense solute in hyper-eutectic salt solution leads to convective flow in the form of rolls and plumes respectively. The convective and conductive regime in solidification was observed by the interferometer for temperature/concentration study. The flow field was captured using particle imaging velocimetry (PIV) techniques.

## Experimental setup and instrumentation

For *in situ* studies of the bottom-cooled solidification, rectangular solidification cell was used. The experimental system consists of a Mach-Zehnder interferometer (He-Ne laser with a wavelength of 632.8 nm), solidification cell, cooling system (peltier with their TEC controller and heat exchanger), and data acquisition system. The schematic diagram of the experimental system is shown in Fig. 1. The solidification cell (110 mm in height and 50 mm in width, shown in the inset of Fig. 1) was made of 8 mm thick acrylic. A cover cell was placed on it to avoid heat loss and condensation during the experiment. For interferometry experiments, transparent high-quality optical glasses (50 mm×50 mm) were fixed in the center of the two opposite walls of the cell. The solidification cell was mounted on a copper plate which was maintained at  $-21^\circ\text{C}$  using the peltier module. The hot side of peltier was attached to a heat exchanger to extract the heat. Uniform salt-solution was filled in the solidification cell at an initial temperature of  $25.5^\circ\text{C}$ .

Mach-Zehnder interferometer (one of the refractive index base optical techniques) was employed for the evaluation of temperature/concentration field. The collimated laser beam was arranged in a rectangular configuration using beam splitters and mirrors, as shown in Fig. 1. Change in thermal or concentration gradient from initial condition led to relative change in the path lengths of beams BS1-M1-BS2 and BS1-M2-BS2. Change in path length led to creating interference patterns, which contain information about the temperature/concentration. In this work, the method of obtaining two-dimensional concentration distribution in the liquid field from the recorded interferograms is discussed in the references [12–16].

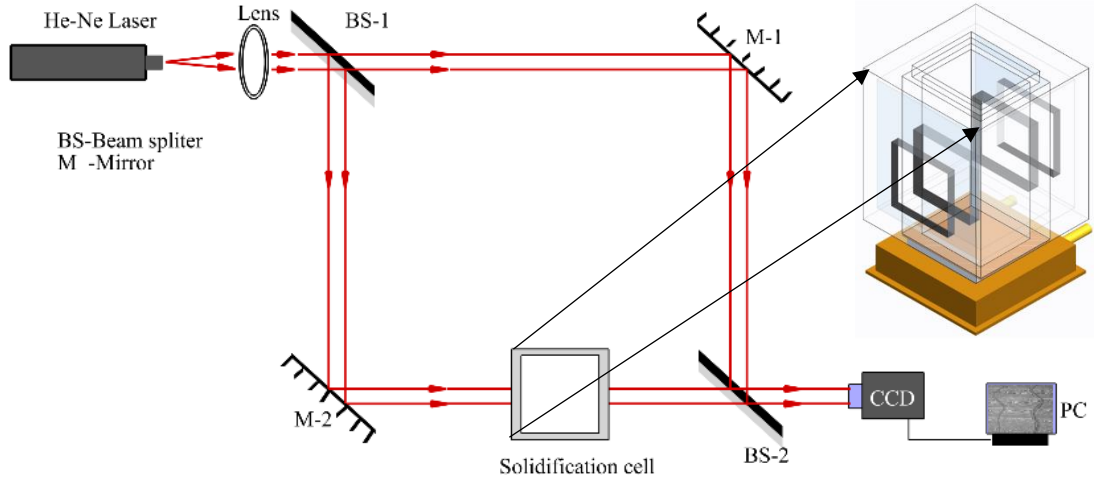


Figure 1. Schematic of experimental setup consisting Mach-Zehnder interferometer, Solidification cell, and data-acquisition system.

For flow visualization, Particle image velocimetry (PIV) technique was employed and consists of a DPSS laser ( $\lambda = 532\text{nm}$ ) to illuminate the flow. Hollow glass bead particles (mean diameter of  $10\mu\text{m}$ ) were incorporated into the salt solution and were assumed to be effectively neutrally buoyant. The fluid flow was recorded using a CCD camera (resolution  $2456 \times 2048$ ) and more details were reported in reference [17]. Both PIV and interferometric experiments were performed separately while ensuring similar experimental conditions.

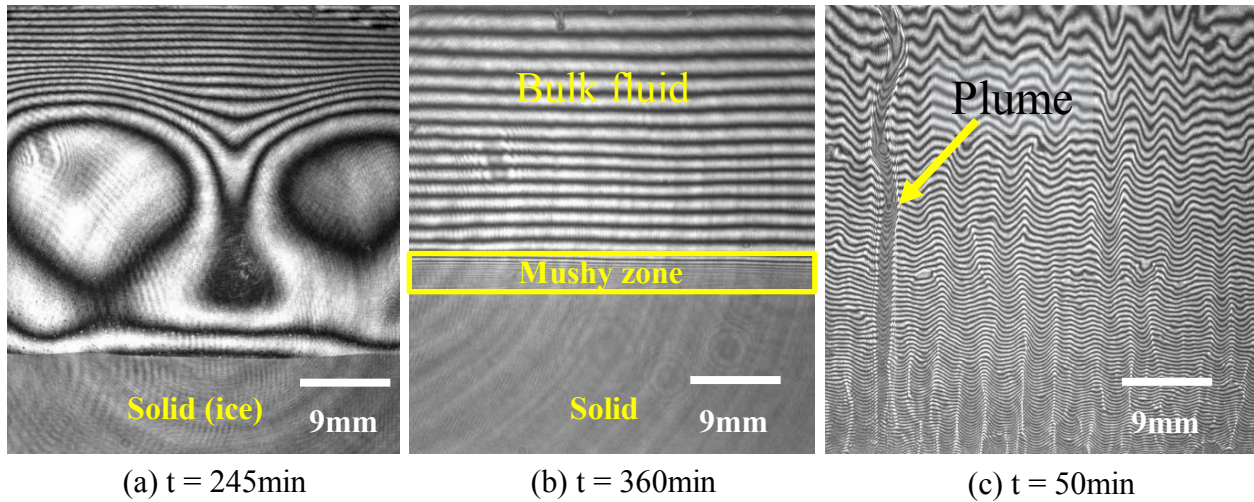
## Results and discussions

### Interferometry-based measurements

The bottom-cooled solidification of Water-0 wt%  $\text{NH}_4\text{Cl}$  leads to convective flow in  $0-4^\circ\text{C}$  due to anomalous density expansion behaviour of water. Fig. 2a shows the interferogram for water solidification at 245 min. Black curve/lines represent isotherms or iso-concentration or iso-refractive index and named as fringes. In water experiment, interferogram indicates the convective flow in the form of a pair of the roll. Convective rolls oriented in the downward direction at center leads to an interpretation of dense fluid ( $4^\circ\text{C}$ ) moving downward and rises from the sides after mixing with cold fluid ( $0^\circ\text{C}$ ). Above the  $4^\circ\text{C}$  isotherm, straight fringes were observed, which indicates the conduction dominated heat transfer mode in the fluid.

The similar interferometric experiment was conducted with water-5 wt%  $\text{NH}_4\text{Cl}$ . From phase diagram of salt solutions, the partition coefficient is zero in hypo-eutectic regime which means pure water-ice forms in solid. It is important to note here that interferogram fields contain coupled information regarding temperature and concentration. However,  $\partial n / \partial C$  (change of refractive index with concentration) is  $\approx 40$  times higher than  $\partial n / \partial T$  (change of refractive index with temperature) for the water-salt system. In view of this, it can be reasonably inferred that these interferograms are more sensitive to concentration map rather than temperature. The process of rejection of solute as salt (higher density than bulk fluid) led to conductive heat transfer mode in liquid during bottom cooled solidification. Fringes near the interface are very closely spaced due to the accumulation of heavier solute that leads to the higher gradient, as observed in Fig. 2b. The change in the composition of the bulk fluid is very less so it has low gradient region (higher spaced fringes) in bulk fluids, as shown in Fig. 2b. Higher gradient regime is termed as mushy zone.

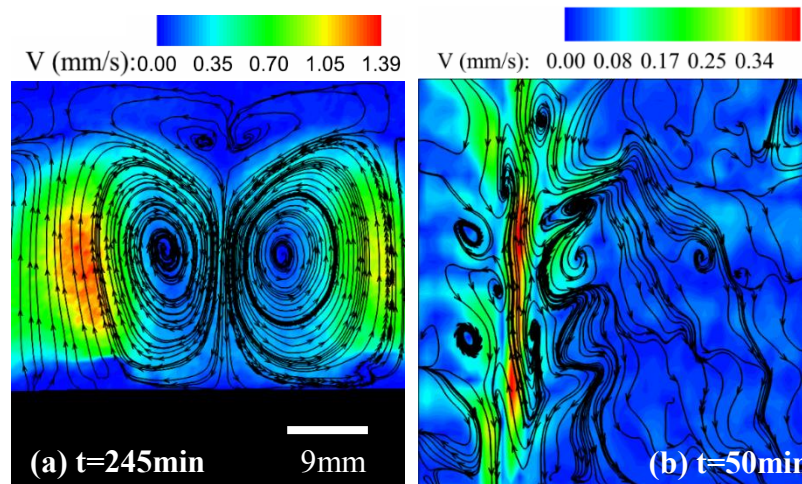
Water-enriched (less dense) liquid was rejected during bottom cooled solidification of the water-25 wt%  $\text{NH}_4\text{Cl}$  system (Fig. 2c). As time progressed, the amount of residual solute increased which led to the formation of convective plumes that clearly be seen in Fig.2c. Plumes transported water enriched salt solution to the top of the cell and reduced the concentration of bulk fluid at the top. The plume was originated from cold solid, during its movement in bulk fluid, the plume gained heat from surroundings, which in turn result into the development of thermal gradient in the horizontal direction. Location of plumes in the solid-mushy zone was observed as known defect generally termed as freckle. The interferogram contains path integrated information of temperature or concentration in the direction of cell depth (along the direction of the probe beam), hence the local plume concentration information can't be evaluated from interferograms.



**Figure 2.** Interferograms during bottom cooled solidification of (a) Water-0 wt%  $\text{NH}_4\text{Cl}$  at 245min (b) water-5 wt%  $\text{NH}_4\text{Cl}$  at 360 min (c) water-25 wt%  $\text{NH}_4\text{Cl}$  at 50min.

### PIV-based measurements of velocity field

Fig. 3a shows the streamlines and velocity contours during solidification of water at 245min. Streamlines show a pair of rolls in the downward direction at the center of the cell, which is similar to the phenomena observed in 0-4°C region from the corresponding interferograms. Two different flows, one being the plume and other being bulk fluid, was observed in bottom-cooled solidification of water-25 wt%  $\text{NH}_4\text{Cl}$  using Particle image velocimetry (PIV) technique as shown in Fig.3b. At  $t = 50$  min (correspond to Fig. 2c), maximum upward velocity was observed in the plume region (greenish region of Fig. 3b) and low downward velocity (bluish region in Fig. 3b) in the bulk field. A circulation zones was observed near the bending of the plume as shown in Fig. 3b. Due to the local mixing of the plume with the bulk fluid, temperature of the plume eventually reached the bulk temperature at the top of solidification cell.



**Figure 3.** Streamline and velocity contours during the bottom-cooled solidification of (a) Water-0 wt%  $\text{NH}_4\text{Cl}$  at 245min (b) water-25 wt%  $\text{NH}_4\text{Cl}$  at 50min.

## Conclusions

Experimental investigation using Mach Zehnder interferometer and particle image velocimetry techniques were conducted to investigate the bottom-cooled solidification process in pure water, hypo-eutectic and hyper-eutectic salt solutions. The convection and conduction dominated heat transfer modes in liquid were clearly observed with deformation of fringes in interferograms. Closely spaced straight fringes near the solid interface indication of accumulation of rejection of heavier salt solution in stable thermal and solutal condition for water-5 wt%  $\text{NH}_4\text{Cl}$ . In the stabilized thermal field, convective flow field was observed in multi-component alloys in case (i) due to anomalous density behaviour of water in pure material solidification and (ii) due to the rejection of less dense solute and form convective plumes in water-25 wt%  $\text{NH}_4\text{Cl}$ . This work will set-up the basis for validating the solute and thermal field in fluid zone and will be extended to ternary system solidification.

## Acknowledgment

Authors gratefully acknowledge the financial support from the Department of Science and Technology (DST), India (Grant No. EMR/2015/001140). The partial support from another DST project (Grant No. SR/S3/MERC/0030/2012) for the Mach-Zehnder interferometer.

## References

- [1] H.S. Davis, H.E. Huppert, E. Muller, M.G. Worster, P. Ehrhard, D.S. Riley, P.H. Steen, *Interactive Dynamics of Convection and Solidification*, Springer Science & Business Media, 2001.
- [2] D. Vikas, S. Basu, P. Dutta, In-situ measurements of concentration and temperature during transient solidification of aqueous solution of ammonium chloride using laser interferometry, *Int. J. Heat Mass Transf.* 55 (2012) 2022–2034.
- [3] M.G. Worster, J.S. Wettlaufer, Natural Convection, Solute Trapping, and Channel Formation during Solidification of Saltwater, *J. Phys. Chem. B.* 101 (1997) 6132–6136.
- [4] Porter D A; Easterling K E, *Phase Transformations in metals and alloys*, second ed, Springer-science Business Media, B.V., 1992.
- [5] R. Farhadieh, R.S. Tankin, Interferometric Study of Freezing of Sea Water, *J. Geophys. Res.* 77 (1972) 1647–1656.
- [6] T.A. Kowalewski, A. Cybulski, Experimental and Numerical investigations of Natural convection in Freezing Water, in: *Int. Conf. Heat Transf. with Chang. Phase Mech.*, 1996: pp. 7–16.
- [7] E. Large, C.D. Andereck, Penetrative Rayleigh-Bénard convection in water near its maximum



- density point, *Phys. Fluids*. 26 (2014) 094101(1)-094101(18).
- [8] S.L. Braga, R. Viskanta, Solidification of salt solutions on a horizontal surface, III ENCIT-Itapema. 1 (1990) 683–687.
  - [9] S.M. Copley, A.F. Giamei, S.M. Johnson, M.F. Hornbecker, The origin of freckles in binary alloys, *Metall. Trans.* 1 (1970) 2193–2204.
  - [10] C.S. Magirl, F.P. Incropera, Flow and Morphological Conditions Associated With Unidirectional Solidification of Aqueous Ammonium Chloride, *J. Heat Transfer*. 115 (1993) 1036–1043.
  - [11] F. Chen, Formation of double-diffusive layers in the directional solidification of binary solution, *J. Cryst. Growth*. 179 (1997) 277–286.
  - [12] R.J. Goldstein, G.E. Ernst, *Measurement Techniques in Heat Transfer*, Second edi, Taylor & Francis group, 1996.
  - [13] D. Mishra, K. Muralidhar, P. Munshi, Performance evaluation of fringe thinning algorithms for interferometric tomography, *Opt. Lasers Eng.* 30 (1998) 229–249.
  - [14] D.S. Jain, S. Srinivas Rao, A. Srivastava, Rainbow schlieren deflectometry technique for nanofluid-based heat transfer measurements under natural convection regime, *Int. J. Heat Mass Transf.* 98 (2016) 697–711.
  - [15] V. Kumar, A. Srivastava, S. Karagadde, Real-time observations of density anomaly-driven convection and front instability during solidification of water, *J. Heat Transfer*. 140 (2018) 042503(1)-042503(12).
  - [16] A. Srivastava, K. Muralidhar, P.K. Panigrahi, Comparison of interferometry, schlieren and shadowgraph for visualizing convection around a KDP crystal, *J. Cryst. Growth*. 267 (2004) 348–361.
  - [17] V. Kumar, M. Kumawat, A. Srivastava, S. Karagadde, Mechanism of flow reversal during solidification of an anomalous liquid, *Phys. Fluids*. 29 (2017) 123603(1)-123603(11).



# Observation of dendrite evolution in Fe-C system by using time-resolved X-ray tomography

Hideyuki Yasuda<sup>1</sup>, Yuta Tomiyori<sup>1</sup>, Takuya Kawarazaki<sup>1</sup>, Yuichi Kato<sup>1</sup>, Kohei Morishita<sup>1\*</sup>

<sup>1</sup>Department of Materials Science and Engineering, Kyoto University, Japan

\*Present address: Department of Materials Science and Engineering, Kyushu University, Japan  
yasuda.hideyuki.6s@kyoto-u.ac.jp

**Keywords:** In-situ observation, radiography, tomography, steel, dendrite morphology

**Abstract.** Time-resolved tomography were performed during solidification in a conventional carbon steel (Fe-0.45mass%C-0.6mass%Mn-2mass%Si) at a cooling rate of 0.17 K/s. A monochromatized X-ray of 37.7 keV was used. The specimen with dimension of 0.8 mm in diameter and 3-5 mm in height was rotated at 0.25 rps (4 s/rotation) in a vacuum furnace and transmission images (edge length of pixel is 6.5  $\mu\text{m}$ ) were acquired at a frame of 100 fps. Reconstruction was performed using 200 projections over 180 deg rotation. Although dendrite morphology was recognized on the reconstructed images, the images were degraded by noise. The reconstructed images were significantly improved by filtering procedures, which smooth images with simultaneous edge-enhancement. Development of dendrites and coarsening of the secondary arms were clearly observed even in the carbon steel. This study showed that the time-resolved tomography could be used for characterizing dendrite morphology in conventional alloys such Fe-C alloys.

## Introduction

In-situ observations of solidification and related phenomena help us to understand microstructural evolution, defect formation, and to build physical models for numerical simulations. In the third-generation facilities such as SPring-8 (Hyogo, Japan) [1], time-resolved and in-situ observations using hard X-rays were performed for low-melting-temperature alloys (Sn, Zn, Al) [2-6] and high-melting-temperature alloys (Fe-based alloys) [7-11].

In Fe-C system, it has been considered that  $\gamma$  phase (FCC) was produced by the peritectic reaction between  $\delta$  phase (BCC) and liquid phase. According to the time-resolved and in-situ observations of Fe-C alloys [10,11], the massive-like transformation was dominantly selected, in which the  $\delta$  phase transformed to  $\gamma$  phase in the solid state. In addition to the radiography, laser-scanning confocal microscopy also showed the massive-like transformation [12]. It is valuable to understand the  $\delta/\gamma$  transformation during / after solidification for controlling solidification structure and coarsening of  $\gamma$  grains.

There are some limitations in the time-resolve and in-situ observations (X-ray transmission imaging). For example, solute diffusion and development of dendrites are constrained in the thin specimen. The limited space can influence curvature of S/L interface. Thus, it is rather difficult to characterize solidification structure.

Ultrafast X-ray tomography using synchrotron radiation X-rays at ESRF was applied to observe evolution of microstructure in Al-4mass%Cu alloys [13]. A white beam (Max 40 keV) was used to increase transmission X-ray intensity. A specimen (1 mm in diameter and 3 mm in height) was cooled at 0.1K/s and 500 projections were taken over 180 deg rotation (interval between reconstruction: 10s). The study showed formation of solid grains isolated by liquid phase, change in solid fraction during cooling, shrinkage due to solidification and S/L area ( $f_s > 0.7$ ). The results successfully proved that the time-resolved X-ray tomography was a powerful tool to investigate solidification phenomena. Coarsening of dendrite arms was also observed by time-resolved tomography (monochromatized X-ray: 30keV, 721 projections over 180 deg, edge length of voxel: 1.4  $\mu\text{m}$ ) and the results were

compared with Phase-Field simulations [14]. Recently, dendrite morphology at the early stage of solidification in Al-24mass%Cu alloys (1 mm in diameter) was also observed by time-resolved tomography (interlaced view sampling, interval between reconstruction: 1.8 s, edge length of voxel: 0.65  $\mu\text{m}$ ) [15]. Morphology of the primary and the secondary dendrite arms were well reconstructed by the TIMBIR method. Time-resolved CT was also applied to investigate semi-solid deformation of Al-15mass%Cu alloys (3 mm in diameter, 720 projections over 180 deg, interval between reconstruction: 4s) [16]. The study showed that the transgranular liquation cracking of grains isolated by remaining liquid phase could occur even at low stress (1-40 MPa) [CT06].

Time-resolved CT was also used to observe solidification structure in high-temperature alloys (1.8mm in diameter) such as Ni-14mass%Hf, Fe-11mass%Hf and Co-18mass%Hf [17]. Higher contrast between the solid and the liquid phases on transmission images were achieved using high energy X-rays (65-80 keV) due to Hf rejection to the liquid phase at the S/L interface and the absorption edge of Hf (65.351 keV).

To the best of the author's knowledge, however, there are still limitations for the time-resolved CT. For example, time-resolved tomography was not performed for conventional carbon steel (Fe-C-Mn-Si alloy), because of high X-ray absorption coefficient and small difference in the X-ray absorption between the solid and the liquid phase. It is of great interest to develop time-resolved tomography technique for carbon steel, stainless steel and Ni-based superalloys. This paper demonstrates time-resolved tomography for observing dendrite morphology in Fe-0.45mass%C-0.6mass%Mn-2mass%Si alloys.

## Experiments

Time-resolved tomography experiments were performed at a beamline BL20XU of SPring-8 (synchrotron radiation facility, Hyogo, Japan). The light source of BL20XU was hybrid-type "in-vacuum" planar undulator. X-rays were monochromatized by the double crystal monochromator of Si (111), which was placed at 46 m from the source point. The experimental hatch was located at about 200 m from the light source. X-ray energy was selected at 37.7keV. An X-ray beam monitor at a pixel size of 6.5  $\mu\text{m}$  was used for transmission images. Fig. 1 shows an outlook of time-resolved tomography apparatus and setup of specimen. The specimen was rotated at 0.25rps (4s / rotation) and the transmission images were obtained at 100 fps. 200 projections over 180deg rotation were used for reconstruction.

Conventional carbon steel (Fe-0.45mass%C-0.6mass%Mn-2mass%Si) was chosen for time-resolved tomography. Dimension of specimen was 0.8 mm in diameter and about 5 mm in height.

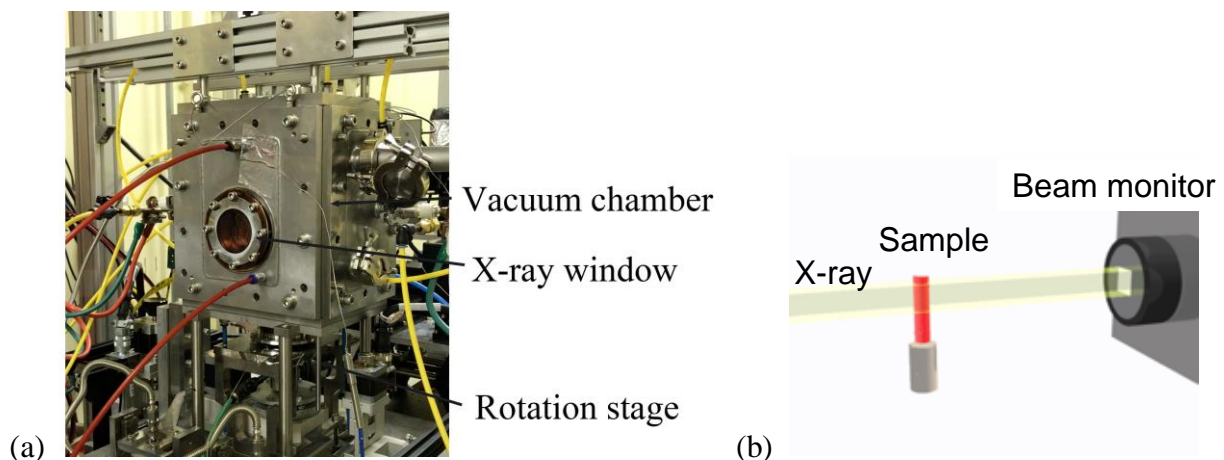


Figure 1. (a) Outlook of time-resolved tomography apparatus and (b) setup of specimen. Graphite heater and specimen inserted into  $\text{Al}_2\text{O}_3$  pipe were placed in the vacuum chamber (approximately 1 Pa). Rotation of specimen was controlled by a rotation stage placed outside the chamber. Distance between specimen and beam monitor was approximately 0.5 m.

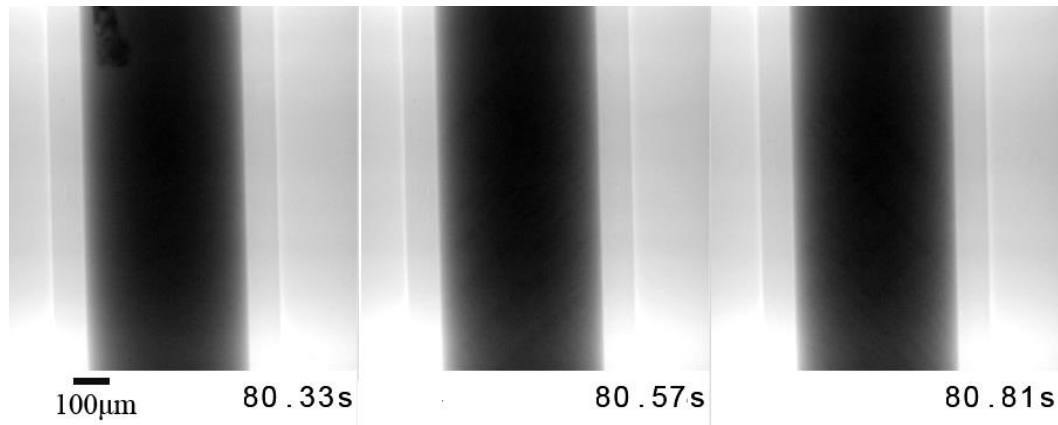


Figure 2. Examples of transmission images during time-resolved tomography experiments.

The specimen rod was inserted into sintered  $\text{Al}_2\text{O}_3$  pipe (inner and outer diameters were 1 mm and 3mm, respectively). The specimen was heated in a vacuum atmosphere (about 1 Pa). The temperature gradient at the specimen was less than 1 K/mm. The melt was cooled at a cooling rate of 0.17K/s. A series of X-ray tomographic images were obtained during the cooling procedure.

## Results

Fig. 2 shows examples of X-ray transmission images during the time-resolved tomography experiments at a cooling rate of 0.17 K/s. The transmission images were processed and the intensity (brightness) in the figure was proportional to the product of X-ray linear absorption coefficient and thickness. Due to the high X-ray absorption and low contrast between solid and liquid phases, it was rather difficult to identify dendrite arms / solidification structure in the specimen from the

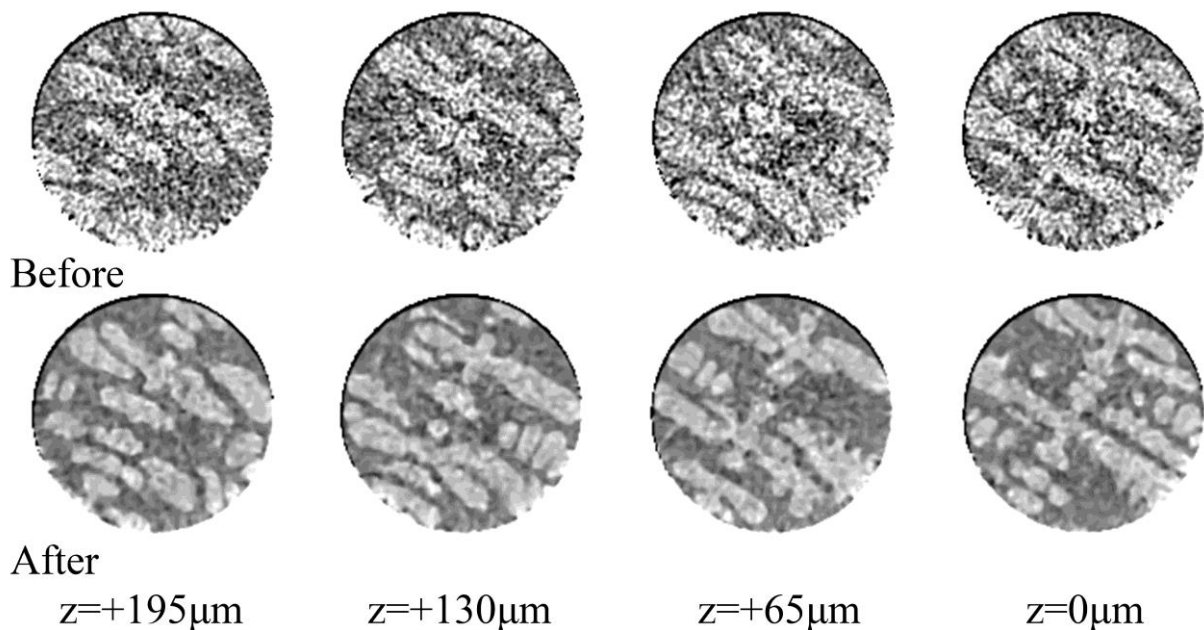


Figure 3. Reconstructed slice images and the filtered slice images at 200 s. The original images

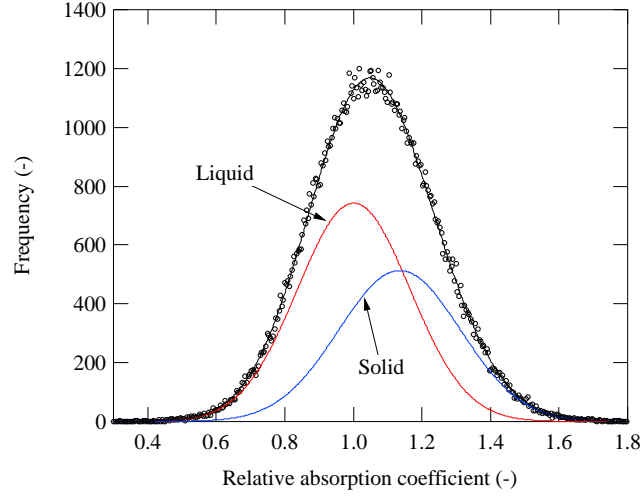
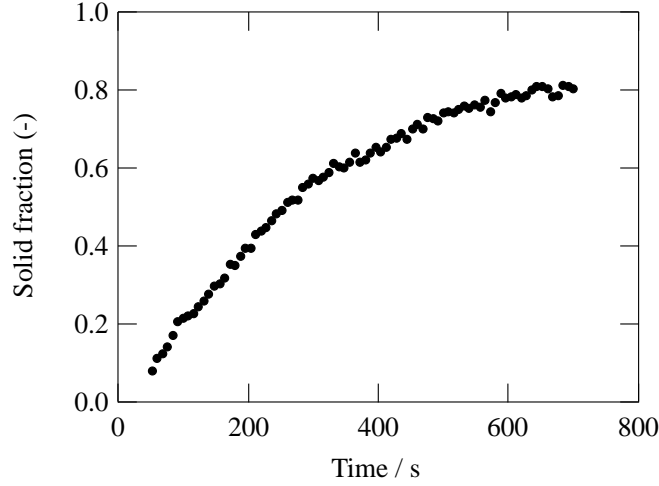


Figure 4. Distribution of X-ray absorption coefficient at 200 s. The absorption coefficient was normalized by that of liquid phase before solidification.



transmission images. However, the dendrite arms were still recognizable on the transmission images at 80.57 s of solidification time.

Reconstruction was performed using the conventional Convolution Back-Projection (CBP) method. 200 projections were used for the reconstruction. The upper images in Fig. 3 are the examples of slice images reconstructed from 200 projections at 200 s. The dendrite arms (bright region) could be somehow detected on the slice images. However, it was rather difficult to trace the solid / liquid interface precisely. Thus, image processing was required to trace the S/L interface and to reconstruct 3D microstructure. The followings are the procedures performed in this study.

The solid fraction was estimated from the distribution of X-ray absorption coefficient before the image processing. The absorption coefficients of solid and liquid phases were determined by the reconstructed data before and after solidification, respectively. Fig. 4 shows the distribution of absorption coefficient normalized by that of the liquid phase before solidification (200 s). The obtained distribution was fitted by using two Gaussian functions (solid and liquid phases), as shown in Fig.4. The solid fraction was simply evaluated from the areas of the two Gaussian functions. Fig. 5 shows the estimated solid fraction as a function of solidification time. The solid fraction follows the square-root law. The solid fraction was used as a condition of constraint for the filtering procedures.

Although one recognizes typical dendrite morphology on the cross-sections as shown in the upper images of Fig. 3, the reconstructed images were largely degraded by noise. Thus, it is required to perform image processing for restoring growing dendrite morphology. In this study, two filtering

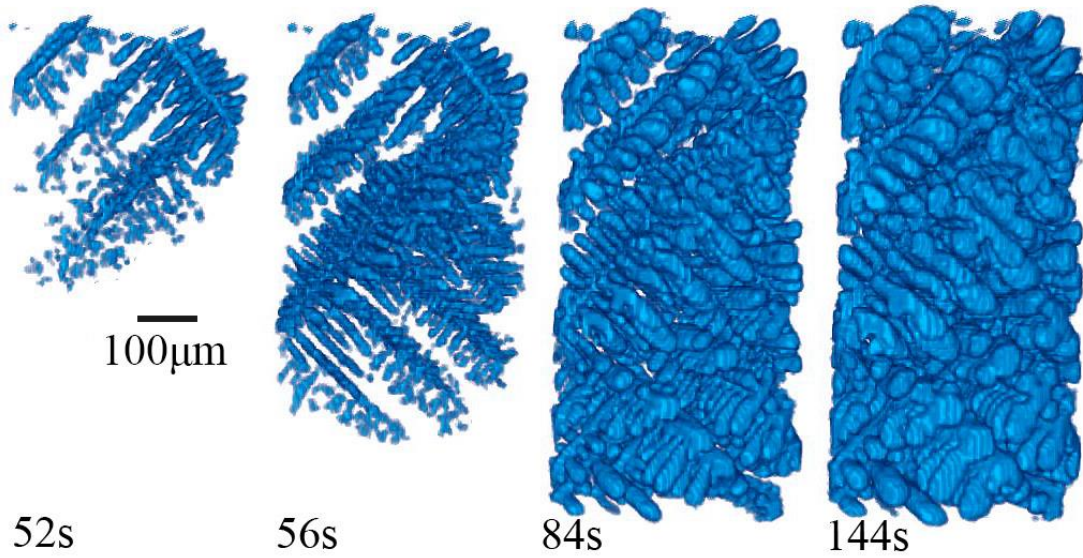
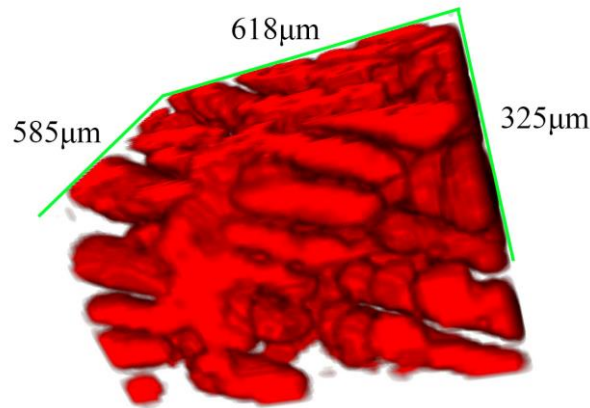


Figure 6. 3D images of dendrites in Fe-0.45mass%C-0.6mass%Mn-2mass%Si at a cooling rate of 0.17K/s. The images were constructed from the filtered slice images as shown in Fig. 3.



techniques were used to reduce noise. One is Gaussian smoothing, which blurs images by a Gaussian function. It was effective to reduce noise and to smooth pixels / voxels. However, it also blurred boundary between solid and liquid phases. The other is anisotropic diffusion filter, which smooths images with simultaneous edge-enhancement [18]. The noise in the original images were significantly reduced by the filtering procedures, as shown in lower images in Fig. 3.

Fig. 6 shows the 3D images of dendrite structure in Fe-0.45mass%C-0.6mass%Mn-2mass%Si at a cooling rate of 0.17K/s. In this observation, dendrites grew from the top to the bottom. Development of dendrite arms was clearly observed even at the low solid fraction region (for example, 54 s). Coarsening of the secondary dendrite arms was also observed. The present results proved that time-resolved tomography allowed us to observe solidification structure in conventional carbon steel. Thus, the 3D time-evolution data on the solidification structure are expected to be used for characterization of dendrite shape (i.e. permeability of melt in semisolid state, microsegregation between dendrite arms, coarsening due to curvature effect).

It is to say that there are not a few choices to perform the filtering techniques. In other words, filtering procedures, which is based on a physical principle, are required for further improvement of reliability. An image filtering technique, which is developed on the basis of growth principle such as thermodynamics and kinetics, is examined for characterizing dendrite structure and solidification phenomena [19].

## Summary

The time-resolved tomography experiments were performed at a beamline BL20XU of Spring-8. Although the 3D observation of solidification structure in carbon steel is still challenging, the following results were obtained:

- (1) The tomography experiment was performed for Fe-0.45mass%C-0.6mass%Mn-2mass%Si (0.8 mm in diameter and 3 mm in height). The specimen was rotated at 0.25 rps (4 s/rotation) and 200 projections over 180 deg rotation were obtained. X-ray energy was 37.7 keV and edge-length of pixel was 6.5  $\mu\text{m}$ .
- (2) The dendrite morphology was recognized on the images reconstructed from 200 projections over 180 deg. However, the images were degraded by noise.
- (3) The filtering procedures significantly improved image quality. Time-evolution of 3D dendrite shape was observed in Fe-0.45mass%C-0.6mass%Mn-2mass%Si at a cooling rate of 0.17 K/s. Development of dendrite arms and coarsening of secondary arms were clearly observed.
- (4) This study proved that the time-resolved tomography could be used for characterizing solidification structure in conventional carbon steel.
- (5) Filtering technique, which is based on a physical principle, will be expected to improve the time-resolved tomography.

## Acknowledgements

The synchrotron radiation experiments were performed as general projects at a beamline BL20XU at Spring-8 (JASRI), Japan. The time-resolved tomography was initially developed by Collaborative Research Based on Industrial Demand Technology (JST). The observation technique including image processing is also supported by a Grant-in-Aid for Scientific Research (S) (No. 17H06155).

## Summary

If you follow the “checklist” your paper will conform to the requirements of the publisher and facilitate a problem-free publication process.

## References

- [1] <http://www.spring8.or.jp/>
- [2] R.H. Mathiesen, L. Arnberg, F. Mo, T. Weitkamp, A. Snigirev, *Phys. Rev. Lett.*, **83** (1999) 5062.
- [3] H. Yasuda, I. Ohnaka, K. Kawasaki, A. Sugiyama, T. Ohmichi, J. Iwane, K. Umetani, *J. Cryst. Growth*, **262** (2004) 645.
- [4] N. Mangelinck-Noel, H. Nguyen-Thi, G. Reinhart, T. Schenk, V. Cristiglio, M.D. Dupouy, J. Gastaldi, B. Billia, J. Hartwig, *J. Phys. D*, **38** (2005) A28.
- [5] B. Li, H.D. Brody, D.R. Black, H.E. Burdette, C. Rau, *J. Phys. D*, **39** (2006) 4450.
- [6] T.M. Wang, J.J. Xu, T.Q. Xiao, H.L. Xie, J. Li, T.J. Li, Z.Q. Cao, *Phys. Rev. E*, **81** (2010).
- [7] H. Yasuda, Y. Yamamoto, N. Nakatsuka, T. Nagira, M. Yoshiya, A. Sugiyama, I. Ohnaka, K. Umetani, K. Uesugi, *Int. J. Cast Met. Res.*, **22** (2008) 15.
- [8] H. Yasuda, T. Nagira, M. Yoshiya, N. Nakatsuka, A. Sugiyama, K. Uesugi, K. Umetani, *ISIJ Int.* **51** (2011) 402.



- [9] T. Nagira, C. M. Gourlay, A. Sugiyama, M. Uesugi, Y. Kanazawa, M. Yoshiya, K. Uesugi, K. Umetani, H. Yasuda, *Scr. Mater.*, **64** (2011) 1129.
- [10] H. Yasuda, T. Nagira, M. Yoshiya, A. Sugiyama, N. Nakatsuka, M. Kiire, M. Uesugi, K. Uesugi, K. Umetani, K. Kajiware, *IOP Conf. Ser.: Mater. Sci. Eng.*, **33** (2012) 012036.
- [11] T. Nishimura, K. Morishita, T. Nagira, M. Yoshiya, H. Yasuda, *IOP Conf. Ser.: Mater. Sci. Eng.*, **84** (2015) 012062
- [12] S. Griesser, M. Reid, C. Bernhard, R. Dippenaar, *Acta Mater.*, **67**(2014)335–341
- [13] O. Ludwig, M. Dimichiel, L. Salvo, M. Suery, P. Falus. *Metall Mat Trans A*, **36A** (2005) 1515-1523.
- [CT02]R. Daudin, S. Terzi, P. Lhuissier, L. Salvo, E. Boller, *Mater. Des.*, **87** (2015) 313-317.
- [14] L. K. Aagesen, J. L. Fife, E. M. Lauridsen, P. W. Voorhees, *Scr. Mater.*, **64** (2011) 394-397.
- [15] J. W. Gibbs, K. A. Mohan, E. B. Gulsoy, A. J. Shahani, X. Xiao, C. A. Bouman, M. De Graef, P. W. Voorhees, *Scientific Reports*, **5** (2015) art. no. 11824.
- [16] B. Cai, S. Karagadde, L. Yuan, T.J. Marrow, T. Connolley, P.D. Lee, *Acta Mater.*, **76** (2014) 371-380.
- [17] B. Cai, J. Wang, A. Kao, K. Pericleous, A. B. Phillion, R. C. Atwood, P. D. Lee, *Acta Mater.*, **117** (2016) 160-169.
- [18] P. Perona, J. Malik, *IEEE Transactions on Pattern Analysis and Machine Intelligence*, **12** (1990) 629 – 639/
- [19] H. Yasuda, Y. Tomiyori, K. Morishita, in preparation.

# Analysis by in situ X-radiography of the impact of growth velocity on the grain structure during solidification of a refined Al-20wt.%Cu alloy

Hadjer Soltani<sup>1-2</sup>, Guillaume Reinhart<sup>2</sup>, Mohamed Chérif Benoudia<sup>3</sup>, Moussa Zahzouh<sup>1</sup>, Henri Nguyen-Thi<sup>2</sup>

<sup>1</sup> Aix Marseille Univ, CNRS, IM2NP, UMR 7334, Campus Scientifique de Saint-Jérôme, Case 142, 13397 Marseille Cedex 20, France

<sup>2</sup> Badji Mokhtar University, P.O. Box 12, 23000, Annaba, Algeria

<sup>3</sup> Laboratoire Mines Métallurgie Matériaux (L3M), Ecole Nationale Supérieure des Mines et de la Métallurgie (ENSMM), Annaba, Algeria  
guillaume.reinhart@im2np.fr

**Keywords:** Solidification, grain structure, equiaxed growth, dendritic grains.

**Abstract.** To study the impact of growth rate on the grain structure formation, an in-situ study of the solidification of a refined Al-20wt.%Cu alloy at a fixed temperature gradient and under a wide range of cooling rates has been carried out using the SFINX (Solidification Furnace with in situ X-radiography) laboratory facility. A special attention has been paid to the variation of the grain number density and the dendritic grain morphology. It is revealed that, as the growth rate increases, the nucleation rate augments and the grain morphology evolve from elongated towards isotropic equiaxed grain.

## Introduction

The mechanical properties of metal alloys strongly depend on the grain structure forming during the solidification step, so a precise control of the growth process is crucial in engineering. Two types of grain structures are commonly obtained during metal alloy solidification: a columnar grain structure with anisotropic properties, or an equiaxed grain structure with more uniform and isotropic properties that is required in most applications of aluminum-based alloys. The latter equiaxed grain structure is usually obtained by adding refining particles acting as preferential sites for heterogeneous nucleation. The efficiency of the refining particles depends on several characteristics: type, amount, size distribution. These particles are activated in undercooled liquid regions [1] and then promote the formation of an equiaxed grain structure.

The present communication reports on the horizontal directional solidification of a refined Al-20wt.%Cu alloy observed in-situ using the SFINX (*Solidification Furnace with IN-situ X-radiography*) laboratory device. The SFINX facility is dedicated to the in-situ observation of the solidification of aluminum-based alloys by X-radiography. Indeed, As most of the phenomena involved during solidification are dynamic, in-situ and real-time X-radiography imaging is the method of choice to follow this phase transition [2]. The solidification of the samples was carried out under a fixed temperature gradient  $G$ , and with different cooling rates  $R$ . Quantitative measurements of the final grain number density were performed. In addition, a quantitative characterization of the grain shape with respect to the growth velocity was also achieved.

## Experimental details

### SFINX facility

The SFINX facility is a duplicate of the device used during the MASER-12 sounding rocket mission [3] and parabolic flight campaigns [4]. These facilities were developed within the framework of the ESA MAP named XRMON (In-situ X-ray monitoring of advanced metallurgical processes under micro gravity and terrestrial conditions), devoted to the application of X-radiography during microgravity experiments [5].



The X-radiography system figures a micro-focus X-ray source with a molybdenum target (3  $\mu\text{m}$  focal spot), which provides a sufficient photon flux with two peaks of energy 17.4 keV and 19.6 keV that ensure a good image contrast to study Al–Cu based alloys. The camera system is made of a scintillator plate and a digital camera with a CCD-sensor. Due to the X-ray beam divergence, a geometric magnification of the object is observed at the detector, which is the ratio of the source-detector by source-sample distances (Fig.1). In this work a magnification of approximately 5 was used, for a Field-of-View (FoV) of about  $5 \times 5 \text{ mm}^2$  leading to an effective spatial resolution of  $\sim 4 \mu\text{m}$ . The acquisition rate was set to 2 frames per second.

The solidification furnace consists of two heaters, separated by a gap, that impose a longitudinal temperature gradient  $G_{app}$  (Fig.1). The gradient furnace enables directional solidification with applied temperature gradient within the range of 5–15 K/mm and cooling rates  $R$  within the range of 0.01–1.5 K/s.

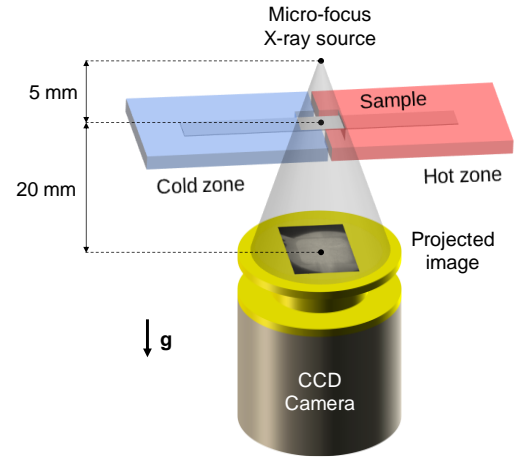


Fig. 1: Schematic layout of the SFINX device for horizontal solidification.

In the present work, the studied alloy was Al-20wt%Cu inoculated with 0.1wt.% AlTiB. A sheet-like rectangular sample with dimension of 5 mm  $\times$  50 mm in area and about 250  $\mu\text{m}$  in thickness was used. The sample was placed in the middle of stainless steel spacers sandwiched between two flexible glassy carbon sheets sewn together with a silica thread. The crucible was enclosed inside the furnace and meets both sides to achieve the expected thermal profile.

Table 1: parameters applied in the present solidification experiments.

Samples	Al-20wt%Cu inoculated with 0.1wt.% AlTiB						
G (K/mm)	10						
R (K/s)	0.05	0.1	0.15	0.3	0.45	0.9	1.35
V ( $\mu\text{m/s}$ )	4	10	15	30	50	100	140

The furnace was set in a position allowing the horizontal solidification of the sample, with its main surface perpendicular to the gravity vector  $\mathbf{g}$  (Fig.1). This configuration was chosen to minimize the gravity related-phenomena such as buoyancy and thermo-solutal convection [6]. In our experiments, a fixed temperature gradient was applied between the heaters ( $G_{app} = 15 \text{ K/mm}$ ), which gave an actual temperature gradient in the sample  $G$  of 10 K/mm [3]. Hereafter, this latter value used for our analyses. The sample was solidified by applying the same cooling rate  $R$  (Table 1) to both heaters, which kept the temperature gradient constant. For each cooling rate  $R$ , the average growth rate  $V$  of the equiaxed front (Table 1) was measured from the recorded image sequences.

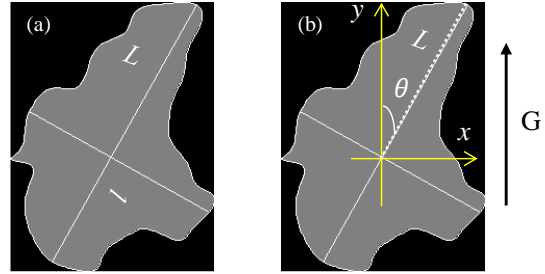
### Image processing and analysis

During the whole solidification experiment, the X-radiography system recorded a stack of raw images. The grey level variations in the acquired images are related to the attenuation coefficient of each different parts of the sample. Image legibility is enhanced by applying “flat-field” correction,

which consists in dividing each frame by a reference image recorded just before solidification. This procedure reduces the noise and removes defects related to the detector and crucible [7]. After applying the image processing, the bright regions in the processed radiograph are solid Al-grains whereas the dark regions are the Cu-rich liquid regions.

Quantitative information were obtained from the radiograph sequences by applying a semi-automatic image analysis developed with the ImageJ software [8]. Two macros were programmed and used to characterize quantitatively the effect of the growth rate on the grain structure formation. The first macro allows to determine the total grain number in the field of view at any time. The second one, allows to determine two key parameters. Firstly, the aspect ratio  $\phi$  (Fig.2a), defined as the ratio between the length  $L$  of the longest segment inscribed within the grain and the length  $l$  of the longest segment orthogonal to the first one [9].  $\phi$  can vary from unity for a perfect equiaxed grain, to value larger than two for elongated grain according to Hunt's criterion [10]. The second parameter is the tilt angle  $\theta$  ( $-90^\circ < \theta < 90^\circ$ ), defined as the angle between the longest segment inscribed within the grain and the temperature gradient direction  $G$  (Fig.2b).

Fig 2: (a) Representation of the two longest perpendicular segments inscribed within a grain. (b) Tilt angle  $\theta$  of a grain.



## Results and discussion

### Example of radiograph sequence recorded during a solidification experiment

It has been shown in the framework of the ESA-MAP entitled XRMON [3] that, for a non-refined Al-20wt.%Cu alloy, the solidification with the same temperature gradient of 10 K/mm and the same range of growth rate gave columnar microstructures. With the addition of refining particles, we observed the propagation of an equiaxed front from the cold zone to the hot zone of the sample, as illustrated in Fig.3. Firstly, grains nucleated first in the cold zone of the field of view where they formed a compact grain structure and for which it is possible to define an effective front that separates the upper limit of the equiaxed structure and the bulk liquid phase (dashed yellow line in Fig.3). This effective front is slightly tilted in the FoV, which is the consequence of a residual transverse temperature gradient from the right to the left side of the sample. The effect of this transverse temperature gradient diminished with the increase of the the cooling rate.

As the sample cooling continued, a new layer of equiaxed grains nucleated in the undercooled liquid ahead of the effective front. This mechanism is repeated over time (Fig.3b), which lead to the propagation of the effective front until the field of view is full of grains (Fig.3c).

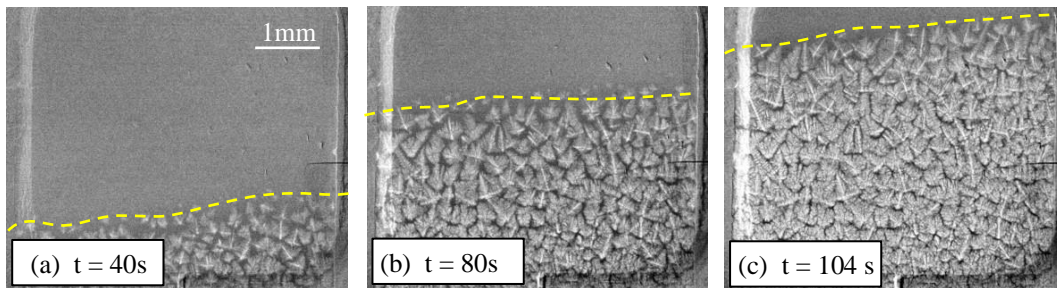


Fig. 3: Sequence of images showing the propagation of the equiaxed front at three different times of a refined Al-20wt. %Cu solidification experiment ( $G = 10$  K/mm and  $V = 50$   $\mu\text{m/s}$ )

### Impact of growth rate on grain number density

In our experiments, the final grain number density  $n_{final}$  increases with the measured growth rate (Fig.4a), which is in agreement with a recent paper of Xu et al. [6]. This variation can be explained by considering the amplitude of the maximum undercooling in the undercooled region, which is the zone ahead the solidification front where the actual temperature of the liquid  $T_L(z)$  is lower than the equilibrium temperature of the liquid  $T_{eq}(z)$  as represented in (Fig4b). In this figure, the undercooled liquid regions are drawn for two different growth rates,  $V_1 < V_2$ . The larger the growth rate, the larger the maximum undercooling. According to the size distribution of refined particles [1], an increase of the maximum undercooling will promote the activation of smaller refining particles, which augments the number of nucleated grains [11].

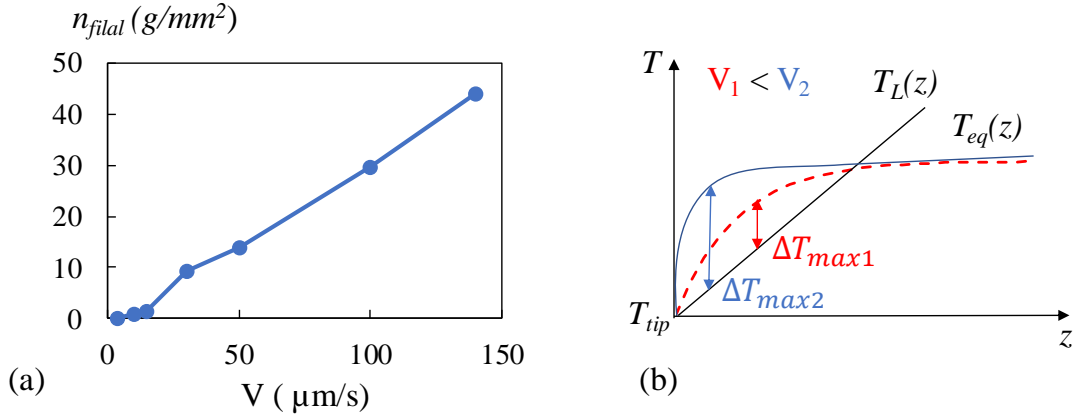


Fig. 4: (a) Variation of the final grain number density with the growth rate  $V$  (for a temperature gradient  $G = 10$  K/mm) and (b) Undercooled liquid regions for two different growth rates.

### Impact of growth rate on grain shape

In this section, the analyzes will be focused on the influence of the growth rate on the grain shape parameters, namely the aspect ratio  $\phi$  and the tilt angle  $\theta$ . For high cooling rates ( $R \geq 0.9$  K/s), accurate measurements of both parameters were difficult because grains were very small and often superimposed on each other in the sample thickness. Nevertheless, the grains looked equiaxed and we thus assumed that their aspect ratio is close to unity. For experiments with low cooling rates ( $R \leq 0.45$  K/s), the two grain parameters were measurable.

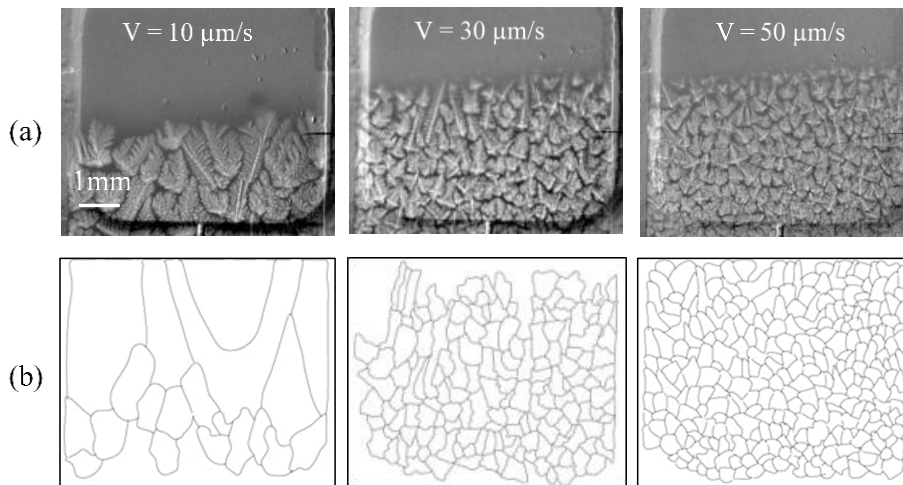


Fig. 5: (a) Images showing the grain shape changing from elongated grains at low growth rate to isotropic equiaxed grains for high growth rate. (b) Boundaries of the grains for each experiment.

Fig.5a confirms visually that the grain number density increased with the growth rate, in agreement with (Fig.4a). In addition, the significant change of the grain shape is qualitatively perceptible as growth rate increases, from elongated grains to more and more isotropic equiaxed grains. For a sake of quantitative comparison, the boundaries of all the grains in the final structure were determined for each experiment (Fig.5b). Based on these images, we evaluated for each grain its aspect ratio  $\phi$  and tilt angle  $\theta$ .

The normalized histograms of  $\phi$  as a function of the growth rate is represented in (Fig.6). The red dashed line corresponds to  $\phi = 2$ , the threshold between equiaxed and elongated grains. The red classes at the right side in (Fig.6a) and (Fig.6b) are the sum of all the grains with an aspect ratio  $\phi > 4$ . Indeed, a few grains are very elongated or pass through the FoV (see Fig.5b). For the lowest growth rate (Fig.6a), a mix of equiaxed and elongated grains was observed. Equiaxed grains nucleated on the cold zone side of the sample (Fig.5a and Fig. 5b) whereas elongated grains occupied the main part of the FoV. This in situ observation suggests that the temperature gradient was not uniform in the FoV. As the growth rate increases, the number of equiaxed grains augments and there is gradually the formation of a peak with a maximum close to unity.

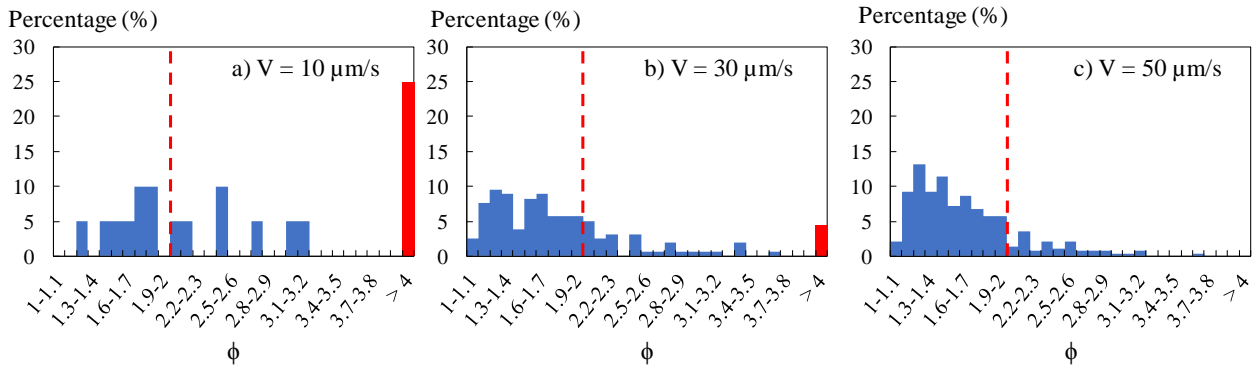


Fig. 6: Histograms of aspect ratio  $\phi$  for three increasing growth rates.

For the mean grain orientation, the normalized histograms of  $\theta$  as a function of the growth rate is represented in (Fig.7). The red dashed line corresponds to  $\theta = 0^\circ$ , when the grain growth is perfectly aligned with the temperature gradient direction. For the three histograms, the grain orientations were distributed rather evenly on both left and right directions, which confirmed the random process of nucleation. However, as growth rates increased, the  $\theta$  – distributions became flatter and flatter, with a range increasing from  $[-20^\circ-20^\circ]$  at low growth rate (Fig. 7a,  $V= 10 \mu\text{m/s}$ ) to nearly all directions for the highest growth rate (Fig. 7c,  $V= 50 \mu\text{m/s}$ ).

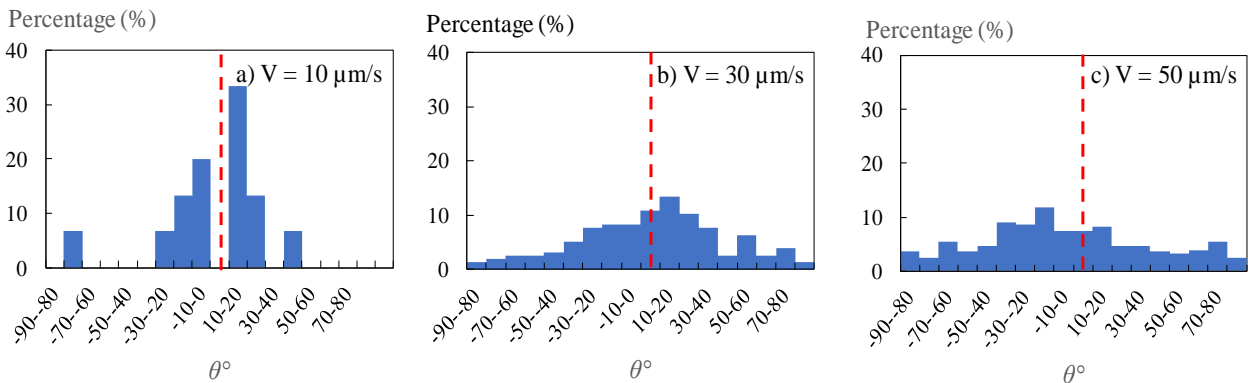


Fig. 7: Histograms of tilt angle of grains with respect to the temperature gradient  $G$  for three growth rates  $V$ .

## Conclusion

A study of equiaxed growth of a refined Al-20wt.%Cu alloy in a horizontal temperature gradient was successfully carried out using in-situ X-radiography with the SFINX apparatus. Quantitative results on the impact of growth rate on grain number density, the shape and the orientation of the grains were determined. A quantitative study of the temperature gradient impact on the grain structure formation will be the subject of future works.

## Acknowledgements

This work is supported by the XRMON project (AO-2004-046) of the MAP programme of the European Space Agency (ESA), by the French National Space Agency (CNES) and the French-Algerian doctoral fellowship program PROFAS B+. The authors would also like to thank the Swedish Space Corporation (SSC) for the development of the SFINX facility and the technical support.

## References

- [1] T. E. Quested and A. L. Greer, The effect of the size distribution of inoculant particles on as-cast grain size in aluminium alloys, *Acta Mater.*, vol. 52, no. 13, pp. 3859–3868, 2004.
- [2] H. Nguyen-Thi *et al.*, On the interest of synchrotron X-ray imaging for the study of solidification in metallic alloys, *Comptes Rendus Phys.*, vol. 13, no. 3, pp. 237–245, 2012.
- [3] H. Nguyen-Thi *et al.*, XRMON-GF experiments devoted to the in situ X-ray radiographic observation of growth process in microgravity conditions, *Microgravity Sci. Technol.*, vol. 26, no. 1, pp. 37–50, 2014.
- [4] L. Abou-Khalil, G. Salloum-Abou-Jaoude, G. Reinhart, C. Pickmann, G. Zimmermann, and H. Nguyen-Thi, Influence of gravity level on Columnar-to-Equiaxed Transition during directional solidification of Al – 20 wt.% Cu alloys, *Acta Mater.*, vol. 110, pp. 44–52, 2016.
- [5] D. J. Browne *et al.*, Overview of In Situ X-Ray Studies of Light Alloy Solidification in Microgravity in: K.N. Solanki, D. Orlov, A. Singh, N.R. Neelameggham (Eds.) Magnesium Technology 2017, in *Springer International Publishing, Cham*, 2017, pp. 581–590.
- [6] Y. Xu, D. Casari, Q. Du, R. H. Mathiesen, L. Arnberg, and Y. Li, Heterogeneous nucleation and grain growth of inoculated aluminium alloys: An integrated study by in-situ X-radiography and numerical modelling, *Acta Mater.*, vol. 140, pp. 224–239, 2017.
- [7] A. Buffet *et al.*, Measurement of Solute Profiles by Means of Synchrotron X-Ray Radiography during Directional Solidification of Al-4 wt% Cu Alloys, *Mater. Sci. Forum*, vol. 649, pp. 331–336, 2010.
- [8] M. D. Abràmoff, P. J. Magalhães, and S. J. Ram, Image processing with ImageJ Part II, *Biophotonics Int.*, vol. 11, no. 7, pp. 36–43, 2005.
- [9] V. B. Biscuola and M. A. Martorano, Mechanical blocking mechanism for the columnar to equiaxed transition, *Metall. Mater. Trans. A Phys. Metall. Mater. Sci.*, vol. 39, no. 12, pp. 2885–2895, 2008.
- [10] J. D. Hunt, Steady state columnar and equiaxed growth of dendrites and eutectic, *Mater. Sci. Eng.*, vol. 65, no. 1, pp. 75–83, 1984.
- [11] A. G. Murphy, W. U. Mirihanage, D. J. Browne, and R. H. Mathiesen, Equiaxed dendritic solidification and grain refiner potency characterised through in situ X-radiography, *Acta Mater.*, vol. 95, pp. 83–89, 2015.

# **Real-time dynamics of rod-like eutectic growth patterns on board the ISS : first results from TRANSPARENT ALLOYS**

Silvère Akamatsu, Sabine Bottin-Rousseau

**Keywords:** eutectics, in situ experiments, microgravity

## **Abstract**

Directionally solidified rod-like eutectics are self-organized composite materials with controllable microstructural features. They are typically made of an arrangement of thin fibers (or rods) of a crystal phase in a continuous matrix of the other phase. In nonfaceted binary eutectic alloys (e.g. Al-Ni), their formation results from a diffusion controlled dynamics of coupled-growth front patterns that basically present a hexagonal stacking, at least locally. The average inter-rod spacing varies as  $V^{-1/2}$  with the solidification rate  $V$ , in order of magnitude. In practice, however, the hexagonal order rarely extends over large distances, and small well-ordered domains separated by long-lived stacking defects are observed. In addition, while rod-like microstructures are clearly favored in alloys such that one of the solid phases has a volume fraction substantially smaller than the other, rods and lamella, or more complex shapes, can be observed to coexist in a given sample. In order to investigate the spatio-temporal phenomena at play, we have developed an in-situ experimentation method that allows one to follow optically the real-time evolution of coupled-growth front patterns in model transparent binary-eutectic alloys. In the succinonitrile-camphor system, we could evidence that hexagonal patterns exist for values of the interrod spacing varying in a finite interval, at given  $V$ . We identified and locate the stability limits of that interval. The lower limit is determined by a rod-elimination instability. The upper limit corresponds to the threshold of a rod splitting instability, which approximately follows a  $V^{-1/2}$  scaling law. We also brought to light the forcing effect of a large-scale curvature of the isotherms, which is due to the different heat conductivities of the media in contact (liquid, solid, container walls). This induces a slow global stretching of the pattern, but leads to a statistical selection of the rod spacing distribution when the pattern stretching is dynamically counterbalanced by rod splittings. These conclusions could be drawn from laboratory experiments during which thermo-solutal convection in the liquid was negligible, if not absent. This markedly limited the range of explorable parameters (composition, thermal field, sample size), and prevented us to undertake a systematic study of, in particular, the so-called lamellar-to-rod transition. Circumventing this obstacle is the aim of the ESA science-in-microgravity project TRANSPARENT ALLOYS (TA). An essentially automatic apparatus for in situ directional solidification experiments in large samples on board the ISS (MSG) has been designed, built, and eventually sent to the ISS (Dec. 2017). The binary-eutectic solidification (SEBA) program of that project is performed in collaboration with U. Hecht's group at Access (Aachen, Germany). We will present preliminary results of the first TA/SEBA campaign (January-March 2018).

# **Interface dynamics and microstructure selection during directional solidification of transparent bulk alloy conducted on DECLIC-DSI**

Fatima Mota, Jorge Pereda, Younggil Song, Damien Tournet, Rohit Trivedi, Alain Karma, Nathalie Bergeon

**Keywords:** DECLIC, directional solidification, phase field, microstructure formation, alloys

## **Abstract**

The study of solidification microstructure formation is of utmost importance for the design and processing of materials, as solid-liquid interface patterns largely govern mechanical and physical properties. Pattern selection occurs under dynamic conditions of growth in which the initial morphological instability evolves nonlinearly and undergoes a reorganization process. This dynamic and nonlinear nature renders in situ observation of the solid-liquid interface an invaluable tool to gain knowledge on the time-evolution of the interface pattern. In this framework, the materials of choice for direct visualization of interface dynamics are transparent organic analogs that solidify like metallic alloys. Extensive ground-based studies of both metallic and organic bulk samples have established the presence of significant convection during solidification processes that alters the formation of cellular and dendritic microstructures. The reduced-gravity environment of Space is therefore mandatory for fluid flow elimination in bulk samples.

To study the fundamental physical mechanisms in the dynamical formation of two-dimensional arrays of cells and dendrites under diffusive growth conditions, several series of microgravity experiments of directional solidification in a model transparent alloy - succinonitrile – 0.24 wt% camphor - have been conducted onboard the International Space Station using the Directional Solidification Insert (DSI) of DECLIC (Device for the Study of Critical Liquids and Crystallization) facility. This facility was developed by the French Space Agency (CNES) in collaboration with NASA. These experiments offered the very unique opportunity to in situ observe and characterize the whole development of the microstructure in extended 3D patterns. In such large samples, the situation of a single crystal ideally orientated with a perfectly flat interface is out of reach. Moreover, the furnace and crucible characteristics lead to a quite complex thermal field, far from usual theoretical or modeling approximations.

A selection of some of the most striking results will be presented regarding the dynamics of primary spacing selection. We will first see how sub-boundaries may generate noticeable heterogeneities of primary spacing even if sub-grains misorientations are very low. We will also discuss quantitative comparisons of the experiments with phase-field simulations that highlight the major influence of the complexity of the thermal field on the dynamics of primary spacing selection and the resulting accuracy of numerical simulation results.

# **In-situ observation of growth and interaction of equiaxed dendrites in microgravity**

Laszlo Sturz, Martin Hamacher, Janin Eiken, Gerhard Zimmermann

**Keywords:** Solidification, equiaxed dendrite growth, crystallographic orientation

## **Abstract**

Within the ESA-map CETSOL the experiment MEDI (Multiple equiaxed dendrite interaction) was performed in 2015 to characterize equiaxed dendritic growth and interaction of multiple equiaxed grains during solidification. About 6 minutes reduced gravity environment on the sounding rocket MASER-13 provides conditions with negligible convection and sedimentation to study nucleation, growth and solutal interaction of equiaxed dendrites in the transparent alloy Neopentylglycol-30wt.-%(d)Camphor. Applying a constant small thermal gradient and defined cooling conditions to the homogenized melt we obtain multiple dendritic equiaxed crystals with the primary dendrite arms growing along the  $\langle 111 \rangle$  crystallographic orientation, which was confirmed by phase-field simulations. Results are presented for the dendrite morphology evolution, kinetic law, nucleation characteristics, evolution of dendrite density and interaction of dendrite pairs. For interpretation of the results, a new nucleation progenitor function approach was developed by project partners and applied successfully to the MEDI-experiment. This approach will be presented in a related contribution entitled "The Nucleation Progenitor Function (NPF) approach: An alternative approach to modelling equiaxed solidification".



## **Equiaxed dendrite growth in non-refined Al-base alloys in real-time**

Florian Kargl, Maike Becker, Joerg Drescher, Mareike Wegener, Christoph Dreissigacker

**Keywords:** binary Al-base alloys; equiaxed growth; X-ray radiography; morphological transition

### **Abstract**

Numerical computer simulations of microstructure evolution during dendritic solidification require reliable experimental data for comparison. In the last two decades X-ray radiography was shown to be a powerful method to in real-time monitor dendritic solidification in thin samples. Here, we present data on equiaxed dendritic growth of fcc-Al dendrites in non-grain refined Al-Ge and Al-Cu alloys. The disc-shaped samples of up to 12 mm diameter and between 200 and 350  $\mu\text{m}$  thickness were processed in a near-isothermal furnace at constant cooling rates of 1 to 3 K/min. We compare dendrite tip velocities determined in horizontally aligned samples on ground with data acquired during two recent microgravity experiments using DLRs X-RISE facility aboard the sounding rocket MAPHEUS. Furthermore, the evolution of solute concentration field evolution in the interdendritic liquid is measured and discussed. The velocity data are compared with theoretical dendrite growth models.

## **Comparison of x-ray radiography of equiaxed alloy solidification in grain-refined Al-3.5wt.-%Ni with dendrite needle network modeling.**

Laszlo Sturz, Angelos Theofilatos

**Keywords:** Solidification, equiaxed dendrite growth, dendrite needle network modelling

### **Abstract**

We investigate multiple dendritic equiaxed grain formation during directional solidification of grain-refined Al-3.5wt.-%Ni at various solidification conditions. This is achieved by comparison of in-situ x-ray radiographic observations in thin samples reported in literature to multi-scale dendrite needle network (DNN) modeling. The model takes into account heterogeneous nucleation, branched dendritic growth and solutal interaction between branches and multiple equiaxed grains in a 2D modeling approach valid at low Péclet numbers. The decrease in equivalent circular diameter of the final average grain size with pulling velocity, which is observed in the Bridgman-type experiments, is well captured by the modeling results, as well as is the ratio of activated nucleation seeds. The effect of confinement of dendrites in a thin sample is currently investigated using a model extension to 3D and to higher Péclet number.

# High resolution synchrotron imaging of dendritic coarsening in Ga – In alloys

Natalia Shevchenko, Joerg Grenzer, Olga Keplinger, Hieram Neumann-Heyme, Alexander Rack, Kerstin Eckert, Sven Eckert

**Keywords:** coarsening kinetics, synchrotron radiography, fragmentation, Ga - In alloy

## Abstract

The dendrite coarsening kinetics and dendrite morphology have been of great interest in the solidification science and casting industry. A detailed analysis of particular solidification phenomena (coalescence, fragmentation etc.) requires X-ray techniques with a high spatial and temporal resolution. High resolution experimental data are also very important for the verification of the existing microstructural models. The synchrotron radiography experiments with solidifying Ga - In alloys were performed at BM20 and ID19 (ESRF, Grenoble) at a spatial resolution of  $< 1 \mu\text{m}$ . The temporal dynamics of morphological transitions such as retraction, coalescence and pinch-off of the sidearms were studied in-situ. Recently, we showed that the combination of numerical modelling [1] and experiments [2,3] performed at the ESRF synchrotron X-ray source in Grenoble has allowed to improve the understanding of the pinch-off process of dendritic sidearms and to obtain material information that is relevant for quantitative modelling.

In this work, a Ga–In alloy was solidified in vertical direction starting from the top of the solidification cell at a controlled cooling rate of 0.002 K/s and at a vertical temperature gradient of  $\sim 2 \text{ K/mm}$ . In general, all fragmentation events are located in the deceleration zone that is formed during the initial phase of solidification. Behind an advancing growth front, under slow growth conditions that are almost close to steady state conditions, the coarsening in the mushy zone does not involve a significant detachment of sidearms.

A detailed and advanced image analysis in combination with the high temporal and spatial resolution data of the experiment, allowed us to identify an additional migration process that is influenced by the existing temperature gradient. This Temperature Gradient Zone Melting (TGZM) process is characterized by a sidearm migration rate of  $0.01 \mu\text{m/s}$ . Interestingly, the results of our analysis suggest that this process does not play a significant role for the sidearm detachment process itself.

## References

1. H. Neumann-Heyme, et al. PHYS. REV. E, 92 (2015) 060401
2. Shevchenko et al., IOP Conf. Series: Mat. Sci. and Eng. 228 (2017), 012005
3. Neumann-Heyme, Shevchenko et al., Acta Mater. 146 (2018) 176

## CHAPTER 4: GRAIN REFINEMENT



# Roles of Mn in refining the grains of magnesium alloys with SiC inoculations

Jian GU, Yuanding HUANG\*, Karl Ulrich Kainer, Norbert Hort

MagIC-Magnesium Innovation Centre, Helmholtz-Zentrum Geesthacht, Max-Planck-Str. 1, 21502 Geesthacht

\*Yuanding.huang@hzg.de

**Keywords:** Magnesium alloys, grain refinement, Mg-Zn alloy, nucleants, microstructure

**Abstract.** A homogeneous microstructure of as-cast magnesium alloys is desired to improve the formability during their subsequent thermomechanical processing. Owing to its similar crystal structure to Mg, the part of Zr formed by peritectic reaction during solidification was considered to be the most effective nucleant for  $\alpha$ -Mg. However, regarding the Al-containing magnesium alloys, up to now no suitable and effective external nucleants were found for them. Recently, it was demonstrated that the additions of SiC worked in refining both Mg-Al and Mg-Zn alloys. The present work investigated the effects of SiC particle additions on the grain refinement of Mg-Zn alloys. The microstructures were characterized using XRD, SEM and EDS. It was found that the additions of SiC particles could refine the grains of Mg-Zn alloys. The responsible mechanism is attributed to the formation of (Mn, Si)-enriched intermetallics by the interactions between SiC and impurity Mn in alloys. This conclusion was further supported by using the high pure Mg instead of commercial Mg during preparation of Mg-Zn-SiC alloys. Due to very low amount of impurity Mn in high pure Mg, the grain refinement in Mg-Zn alloys were not observed after the additions of SiC particles. Under this situation the formation of (Mn, Si)-intermetallics was suppressed due to the deficiency of Mn.

## Introduction

Due to its hcp crystal structure, magnesium has a poor room temperature formability. Previous investigations indicate that alloying with rare earths elements and microstructural refinement can improve its formability effectively. Microstructural refinement not only increases its ductility but also its yield strength. For Al-containing magnesium alloys, carbon inoculation was considered to be one of the most successful processes to refine the casting microstructure at present [1]. The responsible refinement mechanism for carbon inoculation is owing to the formation of  $\text{Al}_2\text{MgC}_2$ , which has a very close crystal structure to that of magnesium [2]. Regarding the Mg-Zn alloys, the alloying element Zr with a similar crystal structure to Mg was found to be an effective nucleants for  $\alpha$ -Mg during solidification [3]. The part of Zr is formed from Mg-Zr melts by peritectic reaction only acts as the effective nuclei to improve the nucleation possibility of  $\alpha$ -Mg. Unfortunately, Zr is an expensive alloying element.

Recently, it was found when the external SiC particles were added to Mg-Zn alloys their grains were refined. Interestingly, Cao et al. successfully prepared Mg-Zn/SiC nano-composites by ultrasonic cavitation-based solidification processing [4, 5]. Their results also showed that the grain size of Mg-Zn alloy was reduced considerably by the addition of SiC nanoparticles. They attributed the grain refinement to SiC nanoparticles served as nuclei for heterogeneous nucleation, but no direct evidence was obtained. Luo studied the heterogeneous nucleation and grain refinement in cast AZ91/SiCp alloys [6]. A number of SiC particles were found within the primary Mg grains suggesting a possible heterogeneous nucleation mechanism for grain refinement. Luo also found that some of the SiC particles were pushed away to the grain boundaries [7]. Therefore, the grain refinement of SiC may also be attributed to the reduced growth rate of the primary phase since the presence of SiC particles around the growing Mg crystals. Inem et al. investigated the nucleation and crystallographic orientation of both the Mg matrix and the eutectic  $\text{Mg}(\text{ZnCu})_2$  phase at the  $\beta$ -SiC particle surface in ZC63 and ZC71 Mg matrix composites [8, 9]. They found that the eutectic nucleates at the particle surface with an identical crystallographic orientation, but no distinct crystallographic orientation of  $\alpha$ -Mg with SiC particle has been resolved.

In summary, previous investigations show that the grain refinement of Mg-Zn alloys caused by the addition of SiC particles is due to their physical effects. The present work is to investigate the possible other mechanisms responsible for the grain refining effect of SiC additions in Mg-Zn alloys.

### Experimental procedures

Mg-Zn alloys with different Zn contents inoculated with different contents of SiC were prepared using commercial purity Mg or high purity Mg and Zn (Table 2). SiC particles (supplied by Alfa Aesar GmbH & Co KG, Germany) with an average size of 2  $\mu\text{m}$  were used as refiner. Mg and Zn ingots were melted at 700 °C in an electrical resistance furnace using a mild steel crucible under a protective gas mixture of high pure Ar + 0.2% SF<sub>6</sub>. The melt was manually stirred for 2 min and then its surface was skimmed. SiC particles preheated to 500 °C under Ar atmosphere were added into the melt directly. After that the melt was stirred vigorously at 100 rpm for 5 min to ensure a good dispersion of SiC particles. Before casting the melt was held at 700 °C for 15 min. Each ingot was cast by pouring the melt into a steel mold preheated to 200 °C with a diameter of 70 mm at the bottom and 80 mm at the top and a height of 250 mm.

Metallographic samples were transversally sectioned from the same position of 20 mm from the bottom of the castings. They were prepared according to a standard procedure. The samples for optical observations were etched with a solution of 8 g picric acid, 5 ml acetic acid, 10 ml distilled water, and 100 ml ethanol. The average grain size was measured by the linear intercept method from the micrographs taken using polarized light in an optical microscope. A Zeiss Ultra 55 (Carl Zeiss GmbH, Oberkochen, Germany) scanning electron microscope (SEM) equipped with energy dispersive spectroscopy (EDS) was also used to observe the microstructures of selected samples. X-ray diffraction (XRD) investigations were also carried out using a Siemens diffractometer operating at 40 kV and 40 mA with Cu radiation. Measurements were obtained by step scanning from 20 to 90° with a step size of 0.02°. A count time of 3 seconds per step was used. PANalytical X'pert HighScore software with the International Center for Diffraction Data (ICDD) PDF2-2004 database was used to analyze the diffraction peaks of identified phases based on crystal structures.

Table 2. Measured chemical compositions of source materials (wt%)

Alloys	Zn	Al	Zr	Mn	Fe	Cu	Ca	Ni	Mg
Mg	0.003	0.006	<0.001	0.030	0.007	<0.001	0.0001	<0.0002	Bal.
HP Mg	0.003	0.004	<0.001	0.001	0.005	<0.001	<0.0001	<0.0002	Bal.
HP Zn	99.999	—	—	—	—	—	—	—	Bal.
Al	—	99.930	—	—	—	—	—	—	Bal.

### Results and discussion

**Influences of SiC Particles on Grain Refinement of Commercial Mg-Zn Alloys.** Figure 7 shows the optical micrographs of as-cast Mg-3Zn-0.2SiC, Mg-3Zn-0.5SiC and Mg-3Zn-10SiC alloys. Homogeneous equiaxed grain morphologies were obtained in both Mg-3Zn-0.5SiC and Mg-3Zn-10SiC alloys. Compared with Mg-3Zn-0.2SiC and Mg-3Zn-0.5SiC alloy, SiC clusters marked with black arrows in Figure 7(c) were observed in Mg-3Zn-10SiC alloy, indicating that SiC is not well inoculated in Mg-Zn alloy with high content of SiC. Conversely, SiC can be added into the melt well and distributed uniformly within the matrix when its content is less than 0.5%. Figure 7(d) clearly demonstrates a slight decrease of average grain size from  $330 \pm 12$  to  $285 \pm 10$   $\mu\text{m}$  with increasing the SiC content from 0 to 0.2%. A sharp decrease of average grain size from  $285 \pm 10$  to  $180 \pm 9$   $\mu\text{m}$  was obtained with increasing SiC content from 0.2% to 0.3%. After that, the average grain size remains relatively stable with the increase of SiC content, even up to 10% SiC.

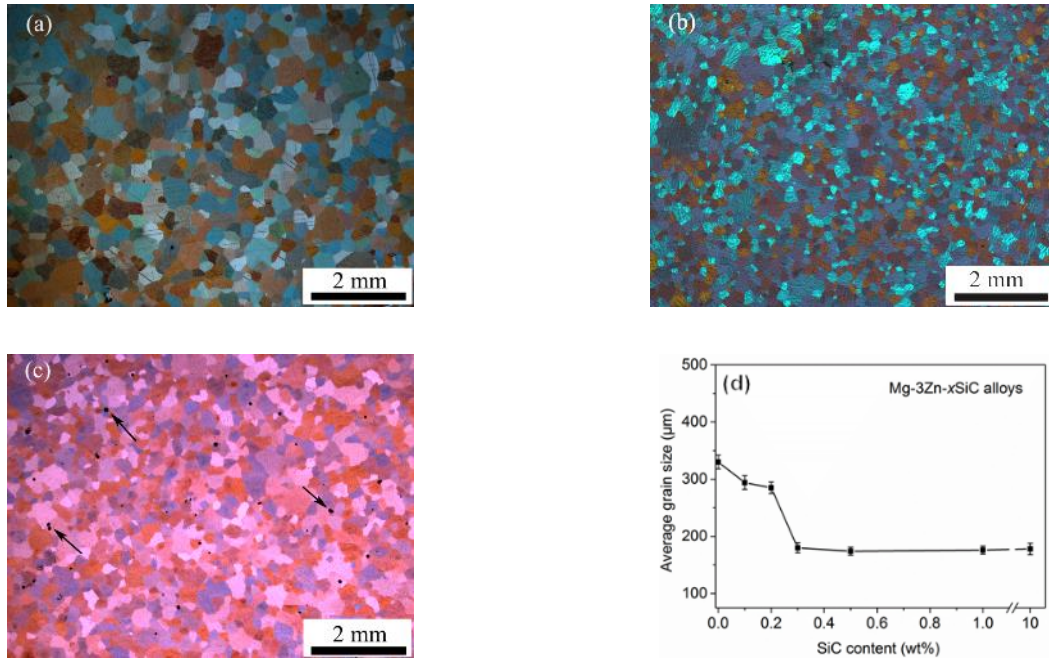


Figure 7. Optical micrographs of as-cast alloys: (a) Mg-3Zn-0.2SiC; (b) Mg-3Zn-0.5SiC; (c) Mg-3Zn-10SiC; (d) average grain size as a function of SiC content.

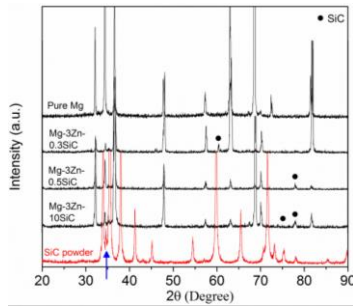


Figure 8. XRD patterns of Mg-3Zn alloys inoculated with different contents of SiC. Patterns of pure Mg and SiC powder are included for comparison. The peaks corresponding to Mg were not labeled.

**Microstructural Characterizations.** Figure 8 shows the XRD patterns of as-cast Mg-3Zn alloys inoculated with different contents of SiC. Two phases Mg matrix and SiC were identified. It is indicated that after the addition of SiC no other phases were formed except for these two phase. It is also possible that the other phase has a too low content to be detected by XRD. SEM observations frequently found that inside the grains some particles with several micrometers exist. They seem to be the nucleants for the formation of  $\alpha$ -Mg during solidification. Figure 9 presents such a typical particle inside the grain in Mg-3Zn-0.5SiC alloy and its EDS line analysis. The grain boundaries were indicated by the white arrows. Under the back-scattered mode, the black part enriched with Si and C can be confirmed as a SiC particle. Firstly, this particle has even darker contrast than that of Mg matrix suggesting that its average atomic number is less than that of Mg matrix. In addition, the length of black part particle is about 3  $\mu\text{m}$ , which is close to the original size 2  $\mu\text{m}$  of the SiC particle. The inside white part is enriched with Fe and Mn, indicating that SiC is likely to associate/react with Fe and Mn to serve as nuclei for  $\alpha$ -Mg grains. In addition, Zn enriched area was also detected by EDS line-scan analysis at the bottom of the right corner, which is closely attached to the SiC particle.

**Influences of SiC Particles on Grain Refinement of High Purity Mg-Zn Alloys.** Figure 10 shows the corresponding optical micrographs of the comparison experiments. Compared with the remarkable grain refining effect of 0.3% SiC in commercial purity Mg-3Zn alloy, its grain refining effect in HP Mg-3Zn alloys can be neglected. The grain sizes of commercial purity Mg-3Zn alloy (Figure 10 (a)), HP Mg-3Zn alloy (Figure 10 (b)) and HP Mg-3Zn-0.3SiC alloy (Figure 10 (d)) keep in the same level. In addition, no such nucleation sites can be observed in HP Mg-3Zn-0.3SiC alloy

by SEM characterizations. Also, similar results occurred for 0.5% SiC inoculated in commercial purity Mg-3Zn or HP Mg-3Zn alloys Figure 10 (e) and (f). Therefore, it is reasonable to conclude that Mn and Fe appeared in the commercial purity alloy are very important for the grain refining process with SiC inoculant in Mg-Zn alloys.

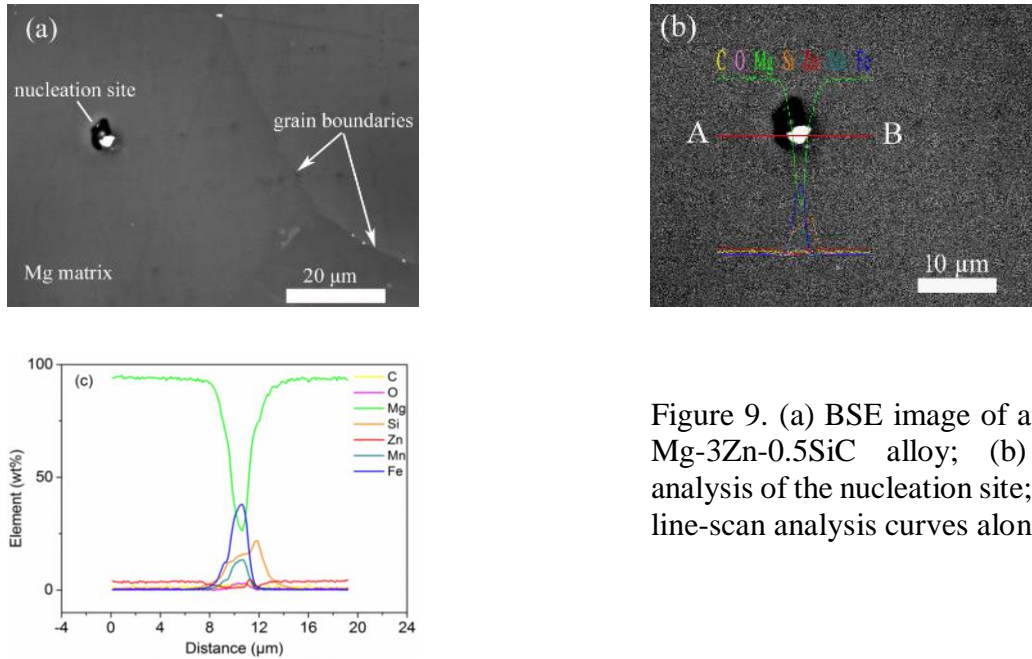


Figure 9. (a) BSE image of a nucleation site in Mg-3Zn-0.5SiC alloy; (b) EDS line-scan analysis of the nucleation site; (c) corresponding line-scan analysis curves along line A-B in (b).

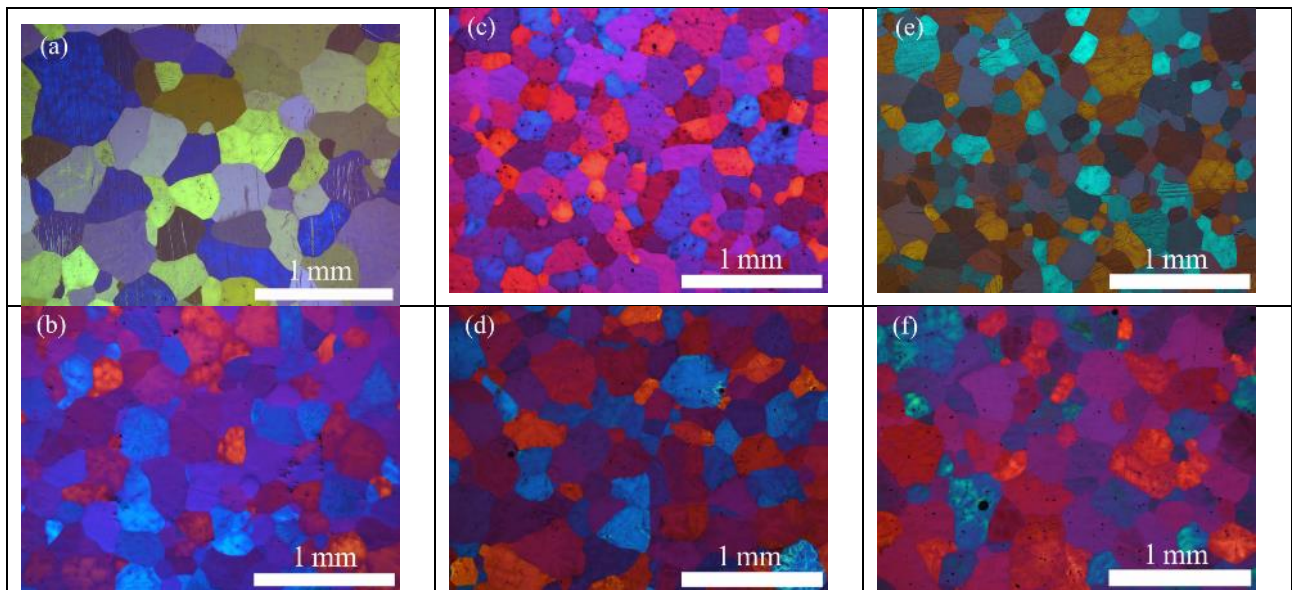


Figure 10. Optical micrographs of as-cast alloys: (a) Mg-3Zn; (b) HP Mg-3Zn (c) Mg-3Zn-0.3SiC; (d) HP Mg-3Zn-0.3SiC; (e) Mg-3Zn-0.5SiC; (f) HP Mg-3Zn-0.5SiC.

**Roles of Mn in Grain Refinement.** Figure 11 shows the influence of Al addition on the grain size of Mg-3Zn-0.3SiC alloy. After adding small amount of 0.05% Al, the grain size of Mg-3Zn-0.3SiC increases. With further increasing the content of Al to 0.1 or 0.2%, the grain size increases to 348 μm or 319 μm, respectively. The above results indicates that the addition of Al may remove or poison these nucleants formed by the interaction of SiC with those impurities such as Mn and Fe (Figure 9). As known, Al element has a very strong affinity to Mn. They can form the intermetallics  $Al_8Mn_5$  [10]. It can then be concluded that after the addition of small amount of Al the impurity Mn was removed in the matrix by the formation of  $Al_8Mn_5$ . Consequently, the remained manganese was not



enough to interact with SiC to form enough effective nucleants for  $\alpha$ -Mg. The grain size of  $\alpha$ -Mg then increases.

It is proposed that the poisoning effect of small amount addition of Al is due to the formation of  $\text{Al}_8(\text{Mn,Fe})_5$ , which interferes with the reaction between SiC and Mn (Fe) to form potent Fe-Mn-Si nuclei. The comparative test of HP Mg-3Zn-0.3SiC-0.1Al alloy with no poisoning grain refinement effect in Figure 10 directly supports this point. Zhang et al. predicted that the  $\text{Al}_8(\text{Mn,Fe})_5$  intermetallic compound has the lowest efficiency as a nucleant for Mg grains based on E2EM model calculation [11]. In addition, Wang et al. investigated that  $\text{Al}_8\text{Mn}_5$  intermetallic particles can be in-situ formed within the AZ91D alloys with different Mn addition [12]. Their extensive TEM examinations on the  $\text{Al}_8\text{Mn}_5/\alpha$ -Mg interfaces revealed that there is no crystallographic orientation relationship between the  $\text{Al}_8\text{Mn}_5$  and  $\alpha$ -Mg crystals. Therefore, they concluded that  $\text{Al}_8\text{Mn}_5$  particles are unlikely to act as effective nucleants for the  $\alpha$ -Mg grains during solidification. In the present study, when small amount of Al addition was added into Mg-3Zn-0.3SiC alloy system, part of the Al captured the Mn (Fe) elements that originated from commercial purity Mg source to form  $\text{Al}_8(\text{Mn,Fe})_5$ . This prevents the contact between Mn (Fe) elements and SiC inoculants, leading to the disappearance of the grain refining effect.

It should be also noted that some previous researches also reported that Mn is a grain refiner for Mg-Al alloy system [13-16], but the grain refining mechanisms are attributed to the formation of  $\epsilon$ -AlMn or  $\tau$ -AlMn phase in the Mn-Al alloys, not to the  $\text{Al}_8\text{Mn}_5$  phase. Furthermore, Cao et al. verified that different Mn-containing sources would lead to different grain refining effects [15]. However, no such phases were detected in the present study. Therefore, the grain coarsening effect is most likely attributed to a decrease in nucleation potency when effective Fe-Mn-Si intermetallic phase transformed to lower potent  $\text{Al}_8(\text{Mn,Fe})_5$  intermetallic phase.

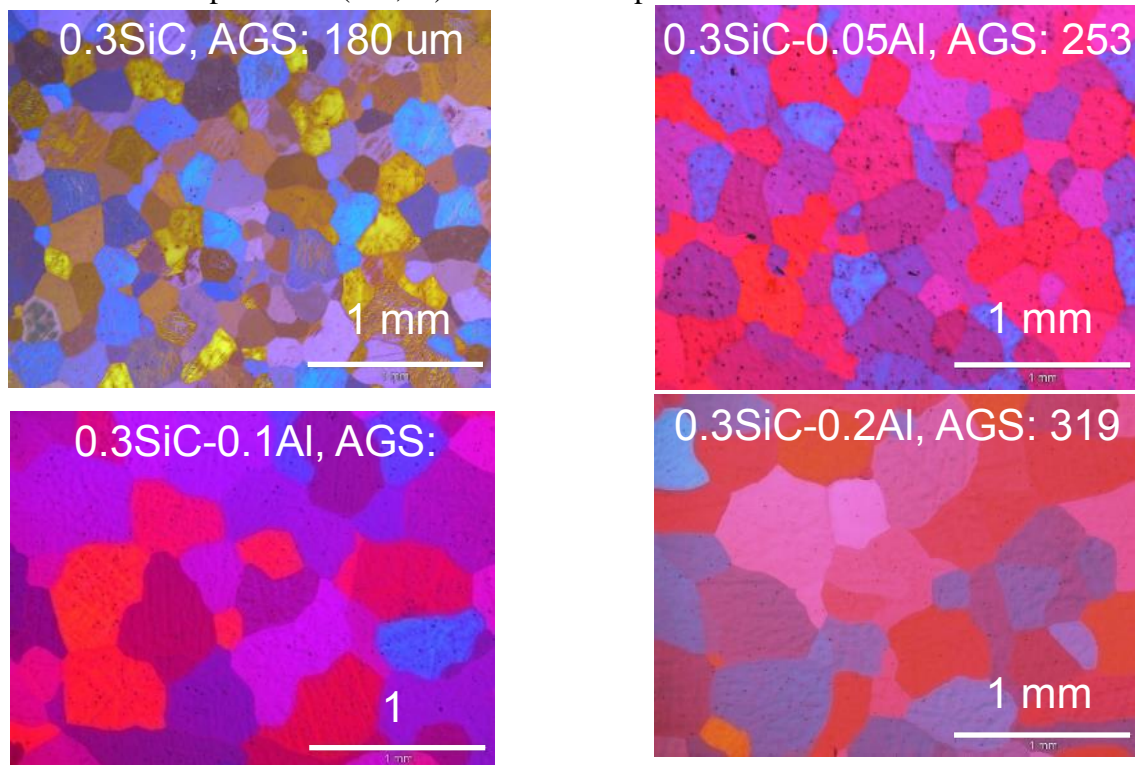


Figure 11. Optical micrographs of as-cast Mg-3Zn-0.3SiC-xAl alloys: (a)  $x = 0.05\%$ ; (b)  $x = 0.1\%$ ; (c)  $x = 0.2\%$

## Summary

SiC particle can be used as a good grain refiner in Al-free Mg-Zn alloys. The responsible grain refinement mechanism is attributed to the formation of (Si, Mn, Fe)-containing intermetallics caused by the interaction of SiC particles with impurities Fe and Mn in matrix, which can promote the

nucleation of  $\alpha$ -Mg. The grains of Mg-3Zn-0.3SiC alloy system are dramatically coarsened when the addition of Al is less than 0.1%. The poisoning effect of small amount addition of Al is due to the formation of low potent  $\text{Al}_8(\text{Mn,Fe})_5$  phase, which interferes with the reaction between SiC and Mn (or Fe) to form potent nuclei. The comparative test of high purity (HP) Mg-3Zn-0.3SiC-0.1Al alloy with no poisoning grain refinement effect supports this result well. Due to very low amount of impurity Mn in high pure Mg, the grain refinement in Mg-Zn alloys was not observed after the additions of SiC particles. Under this situation the formation of (Mn, Si)-intermetallics was suppressed due to the deficiency of Mn.

## References

- [1]. D.H. Stjohn, M.A. Easton, M. Qian and J.A. Taylor, Grain Refinement of Magnesium Alloys: A Review of Recent Research, Theoretical Developments, and Their Application, *Metallurgical and Materials Transactions* 44A (2013) 2935-2949.
- [2]. Y. Huang, K.U. Kainer and N. Hort, Mechanism of grain refinement for Mg-Al alloys by SiC inoculation, *Scripta Materialia* 64 (2011) 793-796.
- [3]. M. Qian, Z.C.G. Hildebrand and D.H. StJohn, The Loss of Dissolved Zirconium in Zirconium-Refined Magnesium Alloys after Remelting, *Metallurgical and Materials Transactions A* 40 (2009) 2470-2479.
- [4]. G. Cao, H. Choi, H. Konishi, S. Kou, R. Lakes and X. Li, Mg-6Zn/1.5%SiC nanocomposites fabricated by ultrasonic cavitation-based solidification processing, *Journal of Materials Science* 43 (2008) 5521.
- [5]. G. Cao, J. Kobliska, H. Konishi and X. Li, Tensile Properties and Microstructure of SiC Nanoparticle-Reinforced Mg-4Zn Alloy Fabricated by Ultrasonic Cavitation-Based Solidification Processing, *Metallurgical and Materials Transactions A* 39 (2008) 880-886.
- [6]. A. Luo, Development of Matrix Grain-Structure during the Solidification of a Mg(AZ91)/SiC(P) Composite, *Scripta Materialia* 31 (1994) 1253-1258.
- [7]. A. Luo, Heterogeneous nucleation and grain refinement in cast Mg(AZ91)/SiCp metal matrix composites, *Canadian Metallurgical Quarterly* 35 (1996) 375-383.
- [8]. B. Inem, Crystallography of the 2nd-Phase/SiC Particles Interface, Nucleation of the 2nd-Phase at Beta-SiC and Its Effect on Interfacial Bonding, Elastic Properties and Ductility of Magnesium Matrix Composites, *Journal of Materials Science* 30 (1995) 5763-5769.
- [9]. B. Inem and G. Pollard, Interface Structure and Fractography of a Magnesium-Alloy, Metal-Matrix Composite Reinforced with SiC Particles, *Journal of Materials Science* 28 (1993) 4427-4434.
- [10]. M. Asgar-Khan and M. Medraj, Thermodynamic Description of the Mg-Mn, Al-Mn and Mg-Al-Mn Systems Using the Modified Quasichemical Model for the Liquid Phases, *Materials Transactions* 50 (2009) 1113-1122.
- [11]. M.X. Zhang, P.M. Kelly, M.A. Easton and J.A. Taylor, Crystallographic study of grain refinement in aluminum alloys using the edge-to-edge matching model, *Acta Materialia* 53 (2005) 1427-1438.
- [12]. Y. Wang, M. Xia, Z. Fan, X. Zhou and G.E. Thompson, The effect of  $\text{Al}_8\text{Mn}_5$  intermetallic particles on grain size of as-cast Mg-Al-Zn AZ91D alloy, *Intermetallics* 18 (2010) 1683-1689.
- [13]. J. Du, J. Yang, M. Kuwabara, W.F. Li and J.H. Peng, Effects of manganese and/or carbon on the grain refinement of Mg-3Al alloy, *Materials Transactions* 49 (2008) 139-143.
- [14]. D. Qiu, M.X. Zhang, J.A. Taylor, H.M. Fu and P.M. Kelly, A novel approach to the mechanism for the grain refining effect of melt superheating of Mg-Al alloys, *Acta Materialia* 55 (2007) 1863-1871.
- [15]. P. Cao, M. Qian and D. Stjohn, Effect of manganese on grain refinement of Mg-Al based alloys, *Scripta Materialia* 54 (2006) 1853-1858.
- [16]. G.W. Qin, Y. Ren, W. Huang, S. Li and W. Pei, Grain refining mechanism of Al-containing Mg alloys with the addition of Mn-Al alloys, *Journal of Alloys and Compounds* 507 (2010) 410-413.

# **The Nucleation Progenitor Function (NPF) approach: An alternative approach to modelling equiaxed solidification**

Robin P. MOONEY<sup>1</sup> and Shaun MCFADDEN<sup>1,2</sup>

<sup>1</sup>Department of Mechanical and Manufacturing Engineering, Trinity College Dublin, Ireland

<sup>2</sup>School of Computing, Engineering, and Intelligent Systems, Ulster University, BT48 7JL, N. Ireland

Corresponding author: s.mcfadden2@ulster.ac.uk

**Keywords:** Nucleation, Equiaxed crystal growth, Dendrites, Microgravity

**Abstract.** Predictive models of equiaxed crystal nucleation and growth are essential for predicting grain refinement in casting. An alternative method for modelling polycrystalline equiaxed development during solidification, called the Nucleation Progenitor Function (NPF) approach, was described in recent literature. The NPF approach attempts to define functional progenitor-progeny relationships between seed activation and real and phantom nucleation events. The NPF approach was applied to the microgravity Multiple Equiaxed Dendrite Interaction (MEDI) experiment, which used a transparent material to observe equiaxed nucleation and growth in real time. The NPF approach was able to model the evolution of equiaxed solidification during the microgravity phase of the experiment on a volumetric and an areal basis. The difference between the volumetric and areal outputs was due to a stereological correction for the bulky transparent sample viewed under transmitted light conditions. In addition, the NPF approach modelled the thermal evolution of the MEDI with good agreement and was able to compensate for the temperature gradient and its influence on the overall statistics for the nucleation data.

## **Introduction**

Predictive models of equiaxed crystal nucleation and growth are essential for predicting grain refinement in solidification processes such as casting. Grain refinement is a significant topic in metallurgy because it leads to smaller average grain sizes. Smaller grains give improved mechanical properties through grain boundary strengthening. During solidification, nucleation and growth are described as being interdependent upon each other. Nucleation occurs in the first instance, but if nucleation is delayed or proceeds progressively, then the growth in the initial stages of transformation can suppress the nucleation rate in the latter stages. This interdependence has been explained in several literature sources, for example [1–3]. A recent approach to modelling equiaxed solidification called the Nucleation Progenitor Function (NPF) approach has been established [4] which accounts for this interdependence between nucleation and growth by defining functional progenitor-progeny relationships between seed activation rate and real nucleation rate. This manuscript summarizes the NPF approach and discusses its application to a microgravity solidification experiment called the Multiple Equiaxed Dendrite Interaction or MEDI experiment. The perceived benefits of the NPF approach are highlighted and discussed.

## **Microgravity Experimental Method and Material**

A microgravity solidification experiment into polycrystalline equiaxed nucleation and growth was performed onboard the MASER-13 sounding rocket and was reported in reference [5]. The experimental alloy used was Neopentylglycol-30wt.%(d)Camphor, which is a hypoeutectic alloy with face-centred cubic lattice structure in the primary dendritic phase. This alloy is transparent in the liquid state, whereas, the primary dendritic phase is opaque. The experiment allowed in-situ observation of polycrystalline equiaxed nucleation and growth under high-quality microgravity conditions; hence, buoyancy driven effects were negligible. A controller allowed fixed cooling conditions (0.75 K/min) to be set under a low temperature gradient (approximately 0.3 K/mm). Three thermocouples recorded temperatures within the sample that were used for thermal validation. A full thermal characterization of the MEDI experiment was reported in [6]. Thermal boundary conditions

were investigated using a bespoke model of solidification. The model used in reference [6] was closely related to the NPF model presented in [4] and used the same input data. Observations of the solidification were made in-situ and in real-time using optical magnification methods. The MEDI campaign was conducted as part of the European space agency CETSOL (Columnar-to-Equiaxed Transition in SOLidification Processing) programme [7].

### Mathematical Method for the NPF Approach

The NPF approach may be described in stepwise fashion as follows.

The first step is to define the progenitor function to describe the collective nucleation potency of all inoculant particles. This step relies on the fact that a Probability Density Function (PDF) can be used to describe the nucleation potency. In this case a Gaussian distribution is assumed.

$$\frac{dN}{d(\Delta T)} = \frac{N_o}{\Delta T_\sigma \sqrt{2\pi}} \exp \left[ -\frac{1}{2} \left( \frac{\Delta T - \Delta T_o}{\Delta T_\sigma} \right)^2 \right] \quad (1)$$

$\frac{dN}{d(\Delta T)}$  is the athermal nucleation density distribution based on undercooling,  $\Delta T$ ;  $N_o$  is the volumetric nucleation density of all possible nucleation sites; undercooling is given as  $\Delta T = T_L - T$  (where  $T_L$  is the equilibrium liquidus temperature);  $\Delta T_o$  is the mean nucleation undercooling for all potential seeds and  $\Delta T_\sigma$  is the standard deviation of the distribution.

The second step is to apply a co-ordinate transformation that changes the progenitor function from the undercooling domain,  $\Delta T$ , to the time domain,  $t$ , as follows

$$\dot{N}(t) = -\dot{T} \frac{dN}{d(\Delta T)} \quad (2)$$

Equation (2) is described as given a time instance of the progenitor function provided in equation (1).

The third step is to apply the principles of the Kolmogorov approach, based on probability theory, to develop progeny functions. Two progeny functions can be established at any given position in the sample. The first progeny function gives the volumetric nucleation rate of real nucleation events and is given by

$$\dot{N}_{REAL}(t) = \dot{N}(t) \cdot (1 - \zeta_V) \quad (3)$$

where volume fraction is given by  $\zeta_V$  and is derived through the classic Avrami equation

$$\zeta_V = 1 - \exp(-\zeta_{V,EX}) \quad (4)$$

The term  $\zeta_{V,EX}$  is known as the extended volume fraction and is given by the equation

$$\zeta_{V,EX}(t) = \frac{4\pi}{3} \int_0^t \dot{N}(t_n) \left[ \int_{t_n}^t v_t dt' \right]^3 dt_n \quad (5)$$

where  $v_t$  is the crystal growth rate. The subscripts  $n$  refers to time since nucleation.

The second progeny function is the observed nucleation rate where a stereology correction is automatically applied to account for over-projection in bulky transparent samples, and it is given as

$$\dot{N}_{OBS}(t) = \dot{N}(t_n) \cdot D \cdot (1 - \zeta_A) \quad (6)$$

$\zeta_A$  is the area fraction observed on the viewing plane and  $D$  is the thickness in the viewing direction. The area fraction is calculated using the extended area fraction  $\zeta_{A,EX}$  through the following equation

$$\zeta_A = 1 - \exp(-\zeta_{A,EX}) \quad (7)$$

And the extended area fraction at any time is given as

$$\zeta_{A,EX}(t) = \pi D \int_0^t \dot{N}(t_n) \left[ \int_{t_n}^t v_t dt' \right]^2 dt_n \quad (8)$$

The principles behind the stereology correction are explained in detail in reference [8]. Each of the progeny functions given in equations (3) and (6) are called time instances of the respective progeny function. A measure of the total number of nucleated seeds is obtained by integrating. Integration of equation (3) over all time and over the volume will give the total number of nuclei. Integration of equation (6) over all time and over the observation plane will give the total number of observed nuclei.

The fourth step is to apply reverse co-ordinate transformations to the time-instance progeny functions to convert from the time domain,  $t$ , into the undercooling domain,  $\Delta T$ . The progeny function related to real nucleation events is given by.

$$\frac{dN_{REAL}(\Delta T)}{d(\Delta T)} = -\frac{\dot{N}_{REAL}(t)}{\dot{T}} \quad (9)$$

and the progeny function related to observed nucleation events is given by

$$\frac{dN_{OBS}(\Delta T)}{d(\Delta T)} = -\frac{\dot{N}_{OBS}(t)}{\dot{T}} \quad (10)$$

The fifth step is to normalize the progeny functions to give representative PDFs for each progeny case. The PDF for the real nucleation events is

$$p_{REAL}(\Delta T) = \varphi_{REAL} \frac{dN_{REAL}(\Delta T)}{d(\Delta T)} \quad (11)$$

and the PDF for the observed nucleation events is

$$p_{OBS}(\Delta T) = \varphi_{OBS} \frac{dN_{OBS}(\Delta T)}{d(\Delta T)} \quad (12)$$

The terms  $\varphi_{REAL}$  and  $\varphi_{OBS}$  are known as normalization constants and they are obtained by integration. The requirement is that the any integral equation involving a progeny function is equated to unity and the normalization constants are solved.

The sixth step refers to the interrogation of the PDF function for standard statistical measures such as average undercooling or standard deviation. The expected value equation is a standard method for calculating a mean value from a PDF and it can be further used to calculate standard deviations, skewness, etc. Information on the expected value equations and how they are used are provided in [4]. Interestingly, the PDF function in equations (11) and (12) can be calculated at different positions and may vary due to inhomogeneity in the domain, for example, variation in undercooling due to a temperature gradient. In this case, the PDF functions generated at each reference position can be combined using the principles of convolution to give a single PDF for the entire domain  $p_{global}(\Delta T)$ . This is summarized in the following equation where the operator  $\otimes$  represents the standard convolution process and the subscripts, 1, 2,  $n$  represent different control volume positions.

$$p_{global}(\Delta T) = p_1(\Delta T) \otimes p_2(\Delta T) \otimes \dots p_n(\Delta T) \quad (13)$$

The NPF approach was coupled to a calculation of the energy equation as follows

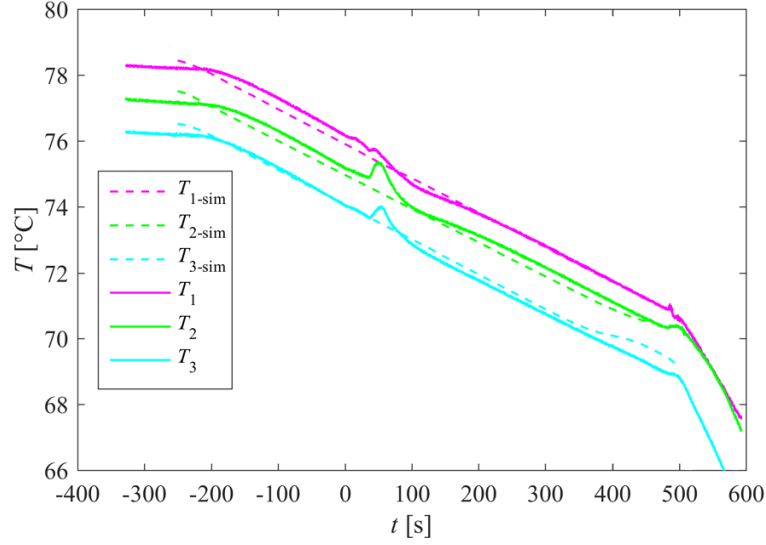
$$\frac{\partial(\rho c_p T)}{\partial t} = \nabla \cdot (k \nabla T) + \rho L \zeta_v \frac{\partial g_s}{\partial t} + \rho L g_s \frac{\partial \zeta_v}{\partial t} \quad (14)$$

Where the coupling was achieved by including volume fraction  $\zeta_v$  and its relationship to volumetric latent heat  $L$ . Local solid fraction is given by  $g_s$  and was calculated using both a Scheil formulation and a Rappaz-Thévoz model [9] for comparison. Minor differences were observed between Scheil and Rappaz-Thévoz models due to the low diffusivity of solute in the liquid; hence, all of the following simulated results used the Scheil approach.

## NPF Applied to the Microgravity MEDI Experiment with Results

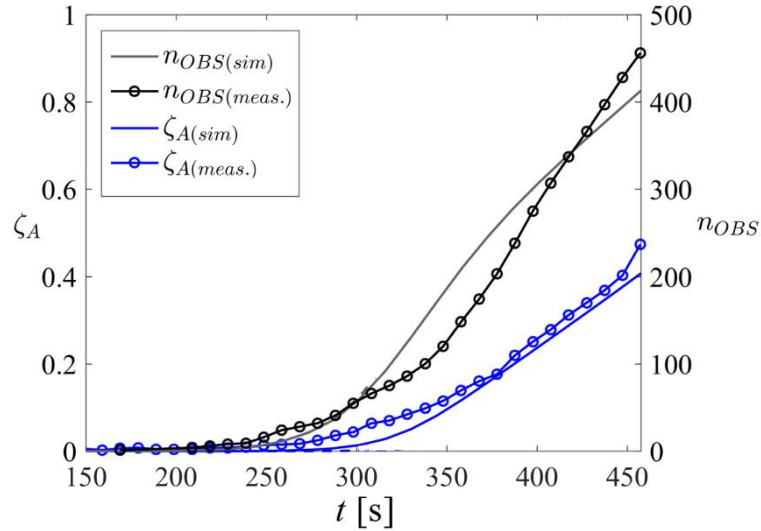
Input data for the experiment and the simulation are provided elsewhere [4,6]. Fig. 1 shows the recorded thermal history from three thermocouples located inside the sample material during the microgravity experiment. The simulated temperatures are shown for comparison. The thermal characterization to make this comparison possible was reported in reference [6]. Generally, good

agreement between measured and simulated temperatures was achieved with reported differences between all three thermocouples calculated to within 1 K.



**Figure. 1.** Measured and simulated thermal histories at three thermocouple locations within the sample. The time datum,  $t = 0$  s, refers to lift off for the sounding rocket.

Fig. 2 shows the measured and simulated values for area fraction,  $\zeta_A$ , and the number of observed nuclei on the projection plane,  $n_{OBS}$ , plotted against time. Area fraction data was extracted from the experimental video sequences by applying a threshold value to the pixel values in color-mapped timeframe images. The number of observed crystal nuclei was measured by counting all new crystals at the moment they became observable. The simulated number of crystals was calculated by integrating equation (6) over the entire observation area and with respect to time.

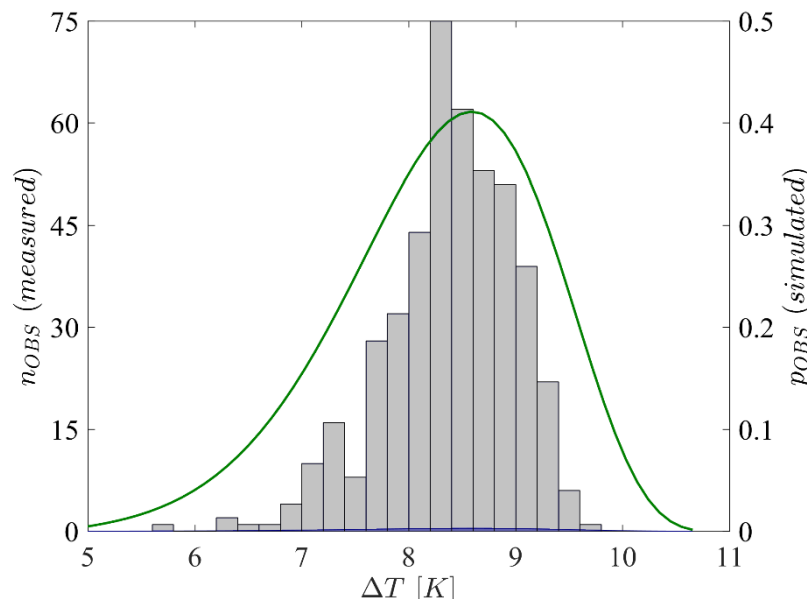


**Figure. 2.** Area fraction and observed nucleation events plotted against time. Experimentally measured (*meas.*) and simulated (*sim*) data shown for comparison.

Fig. 3 shows a bar chart with the results for all observed nucleation events showing the distribution of the estimated nucleation undercooling at the time the crystals were first observed. The overall or global PDF (calculated through equation (13)) for the entire observation plane is plotted for reference. The correlation between the discrete data in the bar chart and the continuous PDF is clear. Further calculations showed that the mean observed undercooling from the experiment was 8.4 K and the mean observed undercooling as calculated by the NPF was 8.7 K. In addition, the observed standard



deviation was 0.6 K as measured from the experimental data and calculated as 0.3 K from the NPF approach.



**Figure 3.** Overall distribution of the observed nucleation events as a function of the undercooling and the PDF of observed nucleation undercooling over the entire domain.

## Conclusion

In this paper, the Nucleation Progenitor Function approach was reviewed. The application of the NPF approach to the MEDI microgravity experiment was summarized. The NPF approach has outlined as a stepwise approach to modelling the interdependence between nucleation and growth in equiaxed growth. The NPF approach was coupled to the energy equation through the terms that deal with the latent heat. Advantages of the NPF approach include the ability to account for stereology corrections in bulky transparent alloy experiments, the ability to deal with temperature gradients using the principle of convolution, and the ability to interrogate the calculated nucleation data for statistical information such as mean and standard deviation for the nucleation undercooling. The NPF offers an additional advantage in that the statistical data can be obtained in both formative mode, as running statistics, or in a summative mode, as final statistics.

## References

- [1] A.L. Greer, Overview : Application of heterogeneous nucleation in grain-refining of metals Overview : Application of heterogeneous nucleation in grain-refining of metals, *J. Chem. Phys.* 145 (2016) 1–14. doi:10.1063/1.4968846.
- [2] M.A. Easton, M. Qian, A. Prasad, D.H. Stjohn, Recent advances in grain refinement of light metals and alloys, *Curr. Opin. Solid State Mater. Sci.* 20 (2016) 13–24. doi:10.1016/j.cossms.2015.10.001.
- [3] D.H. Stjohn, M. Qian, M.A. Easton, P. Cao, The Interdependence Theory : The relationship between grain formation and nucleant selection, *Acta Mater.* 59 (2011) 4907–4921. doi:10.1016/j.actamat.2011.04.035.
- [4] S. McFadden, R.P. Mooney, L. Sturz, G. Zimmermann, A Nucleation Progenitor Function approach to polycrystalline equiaxed solidification modelling with application to a microgravity transparent alloy experiment observed in-situ, *Acta Mater.* 148 (2018) 289–299. doi:10.1016/j.actamat.2018.02.012.
- [5] L. Sturz, M. Hamacher, G. Zimmermann, In-situ observation of equiaxed dendritic growth and interaction in microgravity, in: Z. Fan (Ed.), 6th Decenn. Int. Conf. Solidif. Process., 2017: pp. 300–303.
- [6] R.P. Mooney, L. Sturz, G. Zimmermann, S. McFadden, Thermal characterisation with

modelling for a microgravity experiment into polycrystalline equiaxed dendritic solidification with in-situ observation, *Int. J. Therm. Sci.* 125 (2018) 283–292. doi:10.1016/J.IJTHERMALSCI.2017.11.032.

- [7] G. Zimmermann, L. Sturz, H. Nguyen-Thi, N. Mangelinck-Noel, Y.Z. Li, C.A. Gandin, R. Fleurisson, G. Guillemot, S. McFadden, R.P. Mooney, P. Voorhees, A. Roosz, A. Ronaföldi, C. Beckermann, A. Karma, C.H. Chen, N. Warnken, A. Saad, G.U. Grün, M. Grohn, I. Poitroult, T. Pehl, I. Nagy, D. Todt, O. Minster, W. Sillekens, Columnar and Equiaxed Solidification of Al-7 wt.% Si Alloys in Reduced Gravity in the Framework of the CETSOL Project, *JOM*. 69 (2017) 1269–1279. doi:10.1007/s11837-017-2397-4.
- [8] R.P. Mooney, S. McFadden, Theoretical analysis to interpret projected image data from in-situ 3-dimensional equiaxed nucleation and growth, *J. Cryst. Growth*. 480 (2017) 43–50. doi:10.1016/j.jcrysgro.2017.10.002.
- [9] M. Rappaz, P. Thévoz, Solute diffusion model for equiaxed dendritic growth, *Acta Metall.* 35 (1987) 1487–1497. doi:10.1016/0001-6160(87)90094-0.



# A first-principles study of the formation of atomically rough {111} MgO surface and its effect on prenucleation of Mg

C. M. FANG<sup>1,a</sup> and Z. FAN<sup>1,b</sup>

<sup>1</sup>BCAST, Brunel University London, Kingston, Uxbridge, UB8 3PH, UK

<sup>a</sup> [Changming.fang@brunel.ac.uk](mailto:Changming.fang@brunel.ac.uk) <sup>b</sup> [zhongyun.fan@brunel.ac.uk](mailto:zhongyun.fan@brunel.ac.uk)

Key words: Prenucleation, MgO{111} surface, Atomic roughness; *Ab initio* MD simulations

**Abstract.** Based on the recent studies of the effects of lattice misfit and substrate chemistry on prenucleation, we investigate the interface between liquid Mg and MgO{111} using an *ab initio* molecular dynamics simulation (A/MD) technique. Our study reveals the formation of an atomically rough Mg layer on the {111}MgO surface when MgO is in contact with Mg melt. This atomically rough substrate surface deteriorates significantly the atomic ordering in the liquid adjacent to the liquid/substrate interface. Consequently, it reduces the potency of MgO as a substrate for heterogeneous nucleation.

## Introduction

Grain refiners have been widely used in casting of light metals to improve the mechanical properties of the products. Traditionally, grain refinement is achieved by enhancing heterogeneous nucleation through addition of potent solid particles [1,2]. Recently, it has been suggested that the most effective grain refinement can be achieved by the least potent particles if no other more potent particles of significance exist in the melt [3]. The role of MgO in nucleation of Mg is a good model system to demonstrate this theory [3]. Magnesia (MgO) exists in Mg melts due to the high affinity between O and Mg. Experiments showed that oxidation of the Mg alloys occurs at high temperature and MgO is the major products [4-6]. The naturally occurring MgO particles behave as nucleation sites and attribute to refinement of Mg alloys [5]. The misfit between MgO{111} and Mg{0001} is large (8.1%), which makes the L-Mg/MgO{111} a good case to study the structural effect on prenucleation.

Prenucleation refers to the atomic ordering in the liquid adjacent to the substrate at temperatures above the nucleation point. Men and Fan performed atomistic MD simulations of the structural effect (lattice misfit between the substrate and metal) on the prenucleation. A substrate of a smaller misfit provides better structural templating for prenucleation [7], in agreement with the epitaxial nucleation model [6]. Recently we explored the chemical effect of substrates on the prenucleation of light metal adjacent to potent substrates and revealed that a chemical affinitive substrate promotes prenucleation, whereas a chemical repulsive substrate reduces it [8]. Based on these studies, here we investigate the prenucleation in the liquid Mg adjacent to the MgO{111} substrate using a parameter-free *ab initio* MD technique. Both Mg-terminated and O-terminated MgO{111} surfaces were used as starting configurations. Our simulations show a general trend of prenucleation phenomena in Mg liquid induced by the MgO{111} substrates. The obtained information is not only helpful to understand the prenucleation of Mg alloys, but also to get some insight into solidification processes in general.

## Details of Computations

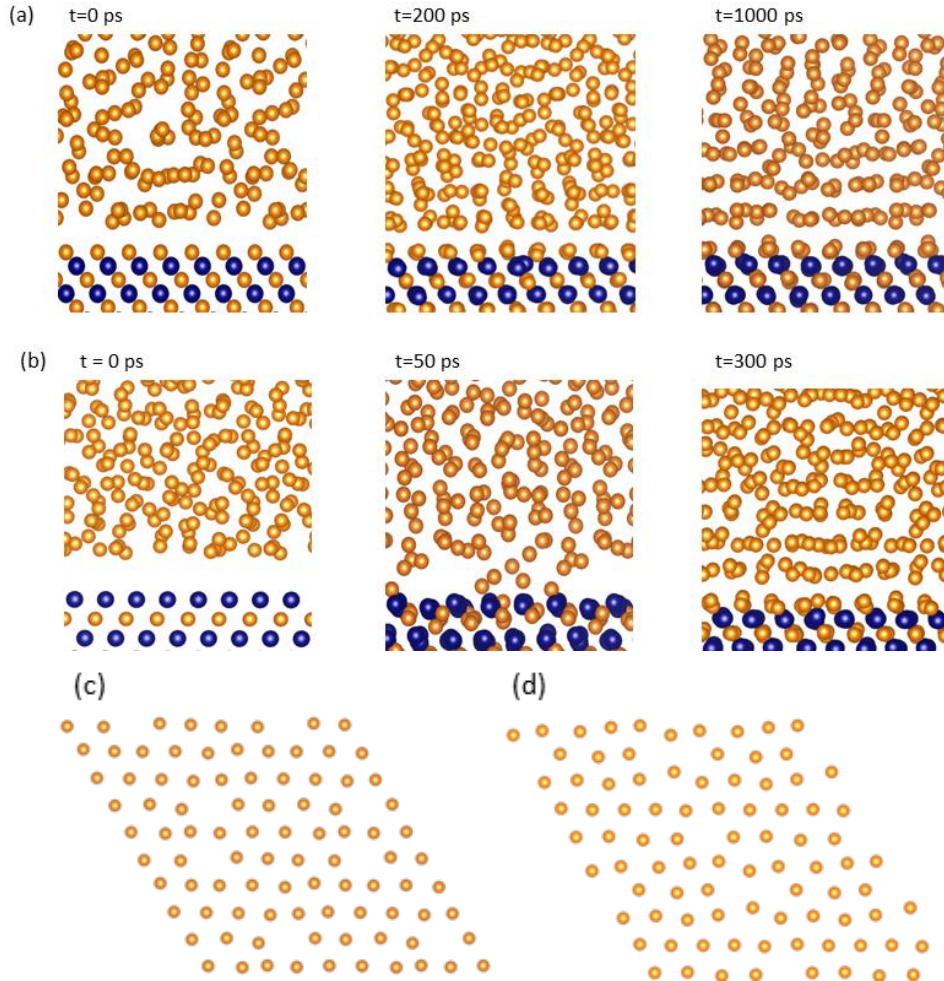
The simulation technique uses the periodic boundary conditions (PBC). Sizable supercells were built for producing meaningful results of *ab initio* MD simulations. A hexagonal supercell with  $a = 5a_h$ , here  $a_h = (\sqrt{2}/2)a_o$  and  $a_o$  is the lattice parameter of MgO was built for the L-Mg/MgO{111} systems. The substrate is composed of four O layers and three Mg layers (O-terminated) or five Mg layers (Mg-terminated). The length of  $c$ -axis is set according to the density of liquid Mg.

We employed the first-principles code VASP (Vienna *Ab initio* Simulation Package) [9] which uses the *ab initio* density functional theory (DFT) within the projector augmented-wave (PAW) framework [10]. The exchange and correlation terms were described using the generalized gradient

approximation (GGA) [11]. For *ab initio* MD simulations, we employed a cut-of energy of 320 eV and the  $\Gamma$ -point in the Brillouin zone.

Mg melt was generated by equilibrating for 6000 to 8000 steps (1.5 fs/step), or 10 picoseconds (ps) at 3000 K. Then the liquid was cooled to the designed temperature. The obtained liquid Mg was used to build the Mg(liquid)/substrate systems, which were heated at the designated temperature for about 7000 steps or  $\sim 10$  ps to ensure equilibrium by checking the configurations and the total energies of the systems. In order to obtain results of meaningful statistics [8,12], we used several different starting configurations and employed the time-averaged atomic position method, using sampling for 2000 to 3000 steps (4 to 6 ps). All substrate/liquid atoms were fully relaxed during the simulations.

## Results and Discussions



**Figure 1.** Snapshots showing the formation processes (a, b) and the resultant atomic arrangements of the newly formed Mg layer on the  $\text{MgO}\{111\}$  substrates with Mg- (a, d) and O-termination (b, c). The orange spheres represent Mg, dark blue for O.

First we address formation processes of the  $\text{MgO}\{111\}$  surface in liquid Mg by means of *ab initio* MD simulations using the O- and Mg-terminated  $\text{MgO}\{111\}$  substrates. The simulations showed that on the O-terminated substrate the liquid Mg atoms adjacent to the substrate were moving quickly and approaching to terminating O layer, as shown in Fig. 1b. Then a new Mg layer was formed on the substrate. This movement is accompanied by the movements of other adjacent Mg atoms, gradually forming layers of Mg on the substrate. This process happens in a rather short time (0.1 to 0.3 ps). Careful analysis shows that there are vacancies at the newly formed Mg layer (Fig. 1c). For the liquid Mg on the Mg-terminated  $\text{MgO}\{111\}$  substrate, during the MD simulations some of the terminating Mg atoms/ions were gradually moving into the liquid, leaving vacancies at the terminating Mg layer (Figs. 1a and 1d). Analysis showed no notable difference for the simulated systems from the O-

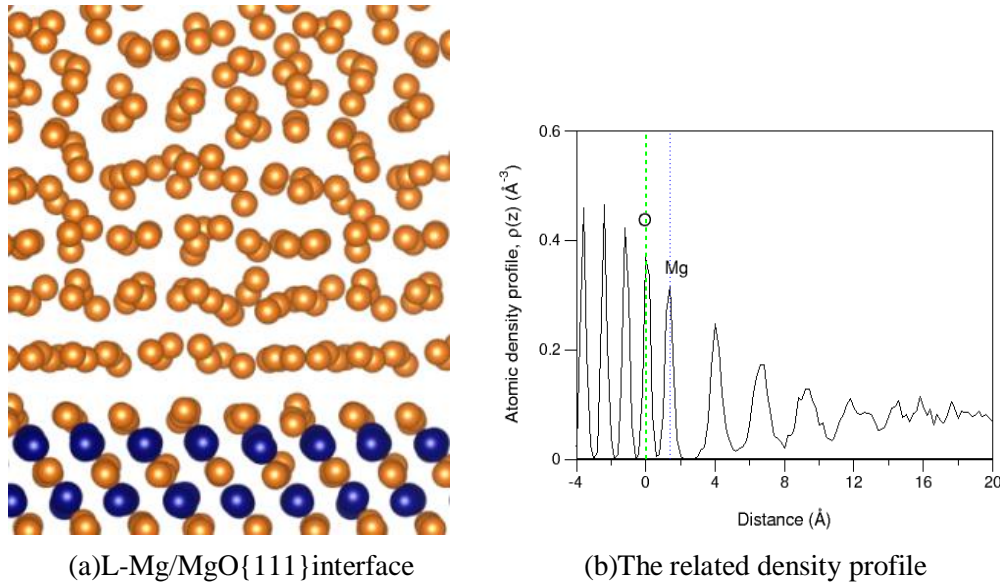
termination or Mg-termination  $\text{MgO}\{111\}$  in liquid Mg with the resultant atomic arrangements of the metal layer (Fig. 1).

Fig.1c and 1d show that the atoms in the newly formed Mg layer are ordered, forming a 2-dimensional (2D) structure containing vacancies. Analysis showed the concentration of the vacancy is 8 % for both cases (Fig.1c and 1d). These vacancies cause roughness of the substrate surfaces at atomic level.

Root mean square (RMS) has been widely used to measure the roughness of a solid surface. For the newly formed Mg layer, the surface roughness mainly comes from the Mg vacancies. Therefore, using the RMS relation,  $R_{\text{RMS}} = [\sum(\Delta z/d_0)^2/n]^{1/2} \times 100\%$ , here  $\Delta z$  is the height difference of one atom with respect to the averaged plane and  $d_0$  the interlayer spacing,  $n$  is the number of atoms in the area.  $(\Delta z/d_0) = 0$  for an occupied site and  $(\Delta z/d_0) = 1$  for an unoccupied site. In this way we obtain  $R_{\text{RMS}} = 28\%$  for the newly formed Mg substrate surface.

Next we investigate the impact of the rough substrate surface on atomic ordering in the adjacent liquid Mg. Fig. 2a shows a snapshot of the equilibrated L-Mg/MgO{111} interfaces.

The density profile of liquid perpendicular to a substrate,  $\rho(z)$  provides a clear statistic description of the atomic layering phenomenon [7,8]. We analysed the density profile for the integrated configurations of the simulated systems for over 3 ps. The density profile,  $\rho(z)$  is plotted and shown in Fig. 2b.



**Figure 2.** Snapshot for an equilibrated L-Mg/MgO{111} interface (a) and the related atomic density profile,  $\rho(z)$  (b) simulated at 1000 K. In 2a, the orange spheres represent Mg atoms/ions, the dark blue for O ions. The vertical dotted lines in 2b are used to indicate the important density peaks.

The density profile corresponds well to the related snapshot of the L-Mg/MgO{111} interface. The outmost O layer has a sharp peak (the dotted green line). The newly formed Mg layer has also a rather sharp peak (the dotted blue line) though its peak height is lower than that of the outmost O layer. On this Mg layer, there are four recognizable liquid Mg layers. The first liquid Mg layer is well separated from the newly formed Mg layer of the substrate with an interlayer spacing of 2.61 Å which is close to the interlayer spacing along the  $[0001]_{\text{Mg}}$  axis. It is noted that there is a small shoulder at the left side of the first Mg peak. Analysis showed that the atoms at the shoulder of the first Mg peak are mainly positioned at the top of the vacancies of the newly formed Mg layer. This is understandable that the vacancies at the 2D Mg structure produce local potential wells which attract liquid Mg atoms. Fig. 2b also showed that the heights of the peaks decrease with going deeper into liquid.

Atomic in-plane ordering of liquid in the layers adjacent to the substrates, or in-plane ordering coefficient is a good indicator for the description of localization of the atoms [7,8]. Here we analyse the in-plane ordering for the newly formed substrate surface layer and the liquid Mg layers adjacent

to the substrates for the integrated configurations from simulations of over 6 ps. The analysis produced that the newly formed Mg layer has a high in-plane ordering coefficient,  $S(z)$  being 0.65.  $S(z)=0.003$  for the first Mg peak, indicating liquid-like nature of these Mg atoms.  $S(z)$  is approaching zero for Mg atoms at the rest Mg layers.

MgO has the NaCl-type structure. The stable surface of MgO at ambient conditions is MgO{001}. A smooth MgO{111} surface is polar and unstable. The situation is different for MgO in a (liquid) metal. The free-electron-see of a metal enhances the occupation of the sites by Mg on the O layer at the MgO{111} substrate. This occupation is also balanced by the interactions between the substrate and the liquid metals. For MgO{111} in liquid Mg, the newly formed Mg surface layer contains vacancies due to the strong chemical interaction between the outmost O layer and the liquid Mg. These vacancies at the terminating Mg layer result in formation of a rough surface of the substrate. This atomically rough surface strongly weakens the templating effect of the substrate.

The epitaxial nucleation theory suggests that heterogeneous nucleation proceeds by a layer-by-layer growth mechanism through structural templating [6]. The lattice misfit has influences on the nucleation undercooling and therefore, can be considered as a direct measure of potency of nucleating particles [7]. This also indicates that heterogeneous nucleation can be controlled by manipulating the lattice misfit between the substrate and the metal. A good example is the recent observation of formation of the 2-dimensional compound (2DC) TiAl<sub>3</sub> on the TiB<sub>2</sub>{0001} surface. This newly formed 2DC TiAl<sub>3</sub> decreases the lattice misfit from 4.22% to 0.09 %. This is responsible for the good performance of the Al-5Ti-1B grain refiners [2]. Our recent study also showed chemical factor of substrate on prenucleation phenomenon [8]. A chemical affinitive/repulsive substrate promotes/impedes the prenucleation in the liquid metal adjacent to the substrate. Recent HR-TEM observations revealed formation of a 2DC ZrTi<sub>2</sub> on TiB<sub>2</sub> substrate in Al, the L-Al/TiB<sub>2</sub> (2DC ZrTi<sub>2</sub>) interface system [13]. This causes the restoring of the lattice misfit from 0.09 to 4.2 % [13]. *Ab initio* MD simulations discovered that at the L-Al/TiB<sub>2</sub> (2DC ZrTi<sub>2</sub>) interface, the surface Zr atoms intrude about 0.45 Å into liquid Al. This causes atomic roughness of the substrate surface. Therefore, the Zr poisoning effect originates from the combination of the lattice mismatch and the surface roughness at atomic level [14]. In the current study we investigated the geometry of MgO{111} surface of thermally equilibrated L-Mg/MgO{111} systems. In liquid Mg, the MgO{111} substrate is terminated by one Mg layer which displays ordering but has vacancies. These vacancies result in atomic roughness of the substrate surface, which reduces the layering and diminishes the in-plane ordering of the liquid Mg adjacent to the substrate. Consequently such atomically rough surface weakens prenucleation at temperatures above nucleation temperature and impedes subsequent heterogeneous nucleation, leading to a larger nucleation undercooling. This study indicates that by manipulation of the atomic roughness of the substrate surface, one may control the nucleation processes of metallic liquid to obtain alloys of desired microstructures.

## Summary

A/MD simulations revealed the formation of an Mg layer at the MgO{111} substrate in liquid Mg. This newly formed Mg layer exhibits atomic ordering but contains vacancies. The calculation provided a RMS roughness of 28%. This atomic roughness of the substrate surface weakens layering and diminishes strongly the in-plane ordering of the adjacent liquid Mg, and therefore reduces the templating effect of the substrate. The surface roughness can be considered as the third factor affecting the atomic ordering of liquid metals adjacent to the substrate, beyond the structural [7] and chemical [8] factors. Rough substrate surface may be used as a practical means to manipulate heterogeneous nucleation for more effective grain refinement.

**Acknowledgements:** Financial support from EPSRC (UK) under grant number EP/N007638/1 is gratefully acknowledged.

## References

1. K.F. Kelton, A.L. Greer, Nucleation in condensed Matter: Applications in materials and biology, Elsevier, Amsterdam, 2010.
2. Z. Fan, Y. Wang, Y. Zhang, T. Qin, X. R. Zhou, G. E. Thompson, T. Pennycook, T. Hashimoto, Grain refining mechanism in the Al/Al-Ti-B system, *Acta Mater.* 84 (2015) 292-304.
3. B. Jiang, Z. Fan, Grain initiation: Progressive vs. explosive, *Proc. 6<sup>th</sup> decennial intern. Conf. on solidification processing*, 25-28 (2017) 61-65.
4. Z. Fan M. Xia, S. Arumuganathar, Enhanced heterogeneous nucleation in AZ91D alloy by intensive melt shearing, *Acta Mater.* 57 (2009) 4891-4901.
5. H. Men, J. Bo, Z. Fan, Mechanisms of grain refinement by intensive shearing of AZ91 alloy melt, *Acta Mater.* 58 (2010) 6526-34.
6. Z. Fan, An epitaxial model for heterogeneous nucleation on potent substrates, *Metall. Mater. Trans. A* 44 (2013) 1409-1418.
7. H. Men, Z. Fan, Atomic ordering in liquid aluminium induced by substrates with misfits, *Comput. Mater. Sci.*, 85 (2014) 1-7.
8. C. M. Fang, H. Men, Z. Fan, Effect of substrate chemistry on prenucleation, to be published.
9. G. Kresse, J. Hafner, *Ab initio* molecular dynamics simulation of the liquid-metal-amorphous-semiconductor transition in germanium, *Phys. Rev. B* 49 (1994) 14251-69.
10. P.E. Blöchl, Projector augmented-wave method, *Phys. Rev. B* 50 (1994) 17953-79.
11. J. P. Perdew, K. Burke, M. Ernzerhof, Generalized gradient approximation made simple, *Phys. Rev. Lett.* 77 (1996) 3865-68.
12. L. E. Hintzsche, C. M. Fang, M. Marsman, G. Jordan, M. W. P. E. Lamers, A. W. Weeber, G. Kresse, Defects and defects healing in amorphous  $\text{Si}_3\text{N}_{4-x}\text{H}_y$ : An *ab initio* density functional theory study, *Phys. Rev. B* 88 (2013) 155204.
13. Y. Wang, C. M. Fang, L. Zhou, Z. Fan, T. Hashimoto, X. Zhou and Q. M. Ramasse, Mechanisms for Zr poisoning of Al-Ti-B based grain refiners, to be published.



# Effect of grain refinement and the solid/liquid interface velocity on the microstructure of Al-20wt% Cu alloy

Arnold RÓNAFÖLDI, András ROÓSZ

MTA-ME Materials Science Research Group  
H-3515 Miskolc-Egyetemváros, Miskolc, Hungary  
rarnold@digikabel.hu

**Keywords:** unidirectional solidification, Al-20%Cu alloy, grain refinement, CET

**Abstract** By using Al-20wt%Cu alloys with- and without grain refining material, solidification experiments were performed by unidirectional solidification in a Bridgman-type furnace in earth circumstances. In the course of one experiment, two different sample movement velocities ( $v_{\text{sam}}$ ) were used such a way that the sample movement velocity was suddenly increased tenfold as compared to the initial value of velocity (i.e. from 0.02 mm/s to 0.2 mm/s) during the solidification process. The melt was not stirred during solidification.

The aim of experiments was to investigate the effect of rapid and sudden increase of sample movement velocity on the solid/liquid interface velocity ( $v$ ). Moreover the effect of solid/liquid interface velocity and the effect of the presence of grain refining material on the microstructure and grain structure of solidified samples were also investigated.

## Introduction

The character of grains (columnar or equiaxial) and their sizes are the most characteristic structural parameters of materials made by solidification technology which highly influence the mechanical properties. Both parameters can be influenced by the temperature gradient ( $G$ ) developing at the solid/liquid interface and by the interface-velocity ( $v$ ) as well as by the small particles added to the melt which cause heterogeneous nucleus formation (i.e. by the inoculation of melt). In case of Al-alloys, the most widespread inoculation material is the Al-5wt% Ti-1wt%B alloy in which the particle performing the inoculation is  $\text{TiB}_2$  [1,2]. The effectiveness of inoculation can significantly be influenced by the interface-velocity at a given temperature gradient. In case of low velocity, a columnar structure can develop in spite of the inoculation and by increasing the velocity, the inoculation material exerts its effect as a consequence the columnar structure transforms to an equiaxial one (Columnar Equiaxed Transition, CET). From the point of view of the practical technologies, it is very important to know the exact parameter-values at which the inoculation becomes effective.

The critical interface velocity can be investigated by using three different experimental technologies at a given  $G$ -value:

- (i) the sample is moved by a constant velocity (in this case, it is necessary to perform several experiments)
- (ii) the sample is moved by a changing (decreasing or increasing) velocity (the decreasing velocity is the nearest the practical technologies)
- (iii) the velocity of sample is suddenly and rapidly changed

This later method was chosen for performing our experiments.

## Experiments

### Alloy

The Al-20wt%Cu (Sample 1) and Al-20wt%Cu+Gr (Sample 2) alloy were produced from 99.99wt% Al and Cu by vacuum metallurgy process. Gr means: grain refinement material, Al-5wt% Ti-1wt%B.

## Samples

The sample diameter was 8 and the length was 110 mm. The sample was inserted to an alumina capsule. The temperature distribution was measured at 13 places on the surface of alumina capsules by using "K" type thermocouples. The alumina capsule with thermocouples was put in a quartz holder. At the bottom of the quartz tube, a copper cooling core was connected to it in order to increase the unidirectional heat removal. Under the body of furnace, there was a water cooling chamber into which the cooling core was immersed during the experiments [3,4].

## Solidification experiments

The experiments were performed in a 4-zone Bridgmann tube furnace of vertical arrangement. Owing to the profile of furnace-temperature, the samples had to move through a length of 176 mm in the Bridgman-type furnace in order that the entire 110 mm length of samples can be solidified. The temperature of the end of sample became lower than the solidus temperature after a displacement of 176 mm. During the first 50 mm of the 176 mm of sample movement, the sample movement velocity ( $v_{sam}$ ) was 0.02 mm/s. (The first 19 mm of sample solidified during the movement of 50 mm). After 50 mm of sample movement, the sample movement velocity was immediately (during 0,01 s) increased to a value of 0.2 mm/s and it was kept at a constant value up to the end of solidification. The solidification of alloy started by  $\alpha$  aluminium solid solution at a temperature of 610°C and completed by the solidification of  $\alpha$ +Al<sub>2</sub>Cu eutectic at a temperature of 548°C. After the solidification had completed, the sample consisted of ~50-50 wt%  $\alpha$  solid solution and eutectic.

## Determination of the solidification parameters

The thermal parameters (cooling rate, temperature gradient and the solid/liquid interface velocity at the liquidus (610°C) and solidus (548°C) temperatures) were calculated as a function of the sample-distance ( $G_{sol}$ ,  $G_{lig}$  and  $v_{sol}$ ,  $v_{lig}$ ) from the cooling curve measured by 13 thermocouples. These parameters were identical at both samples. The functions of thermal parameters are demonstrated in Figures 1a-d. The titles of Figures are as follows: "Interface from the bottom of the sample vs Time" (Fig. 1a); "Average cooling rate during solidification vs distance from the bottom of sample" (Fig. 1b); "Interface velocity vs distance from the bottom of the sample" (Fig. 1c); and "Temperature gradient vs distance from the bottom of the sample" (Fig. 1d).

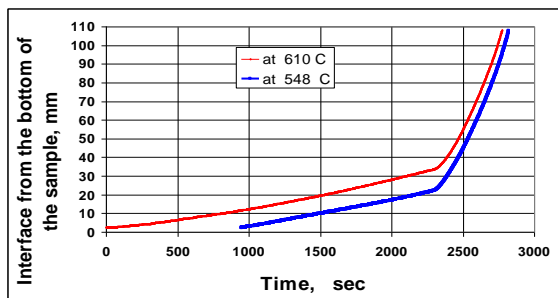


Fig.1a.

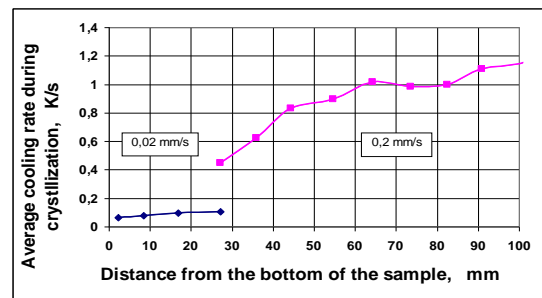


Fig. 1b.

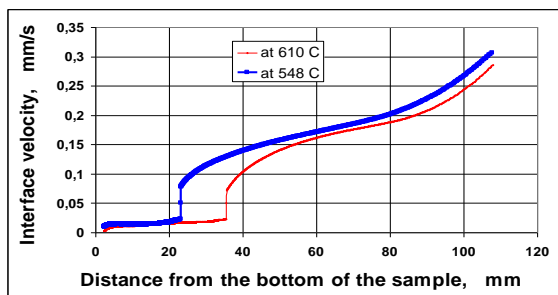


Fig.1c.

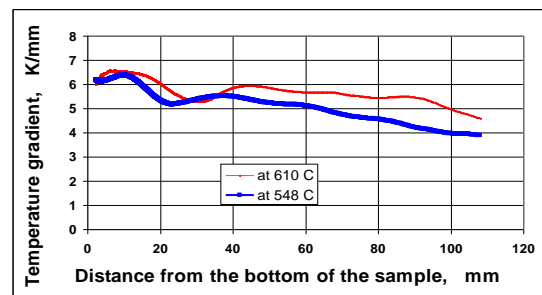


Fig. 1d.

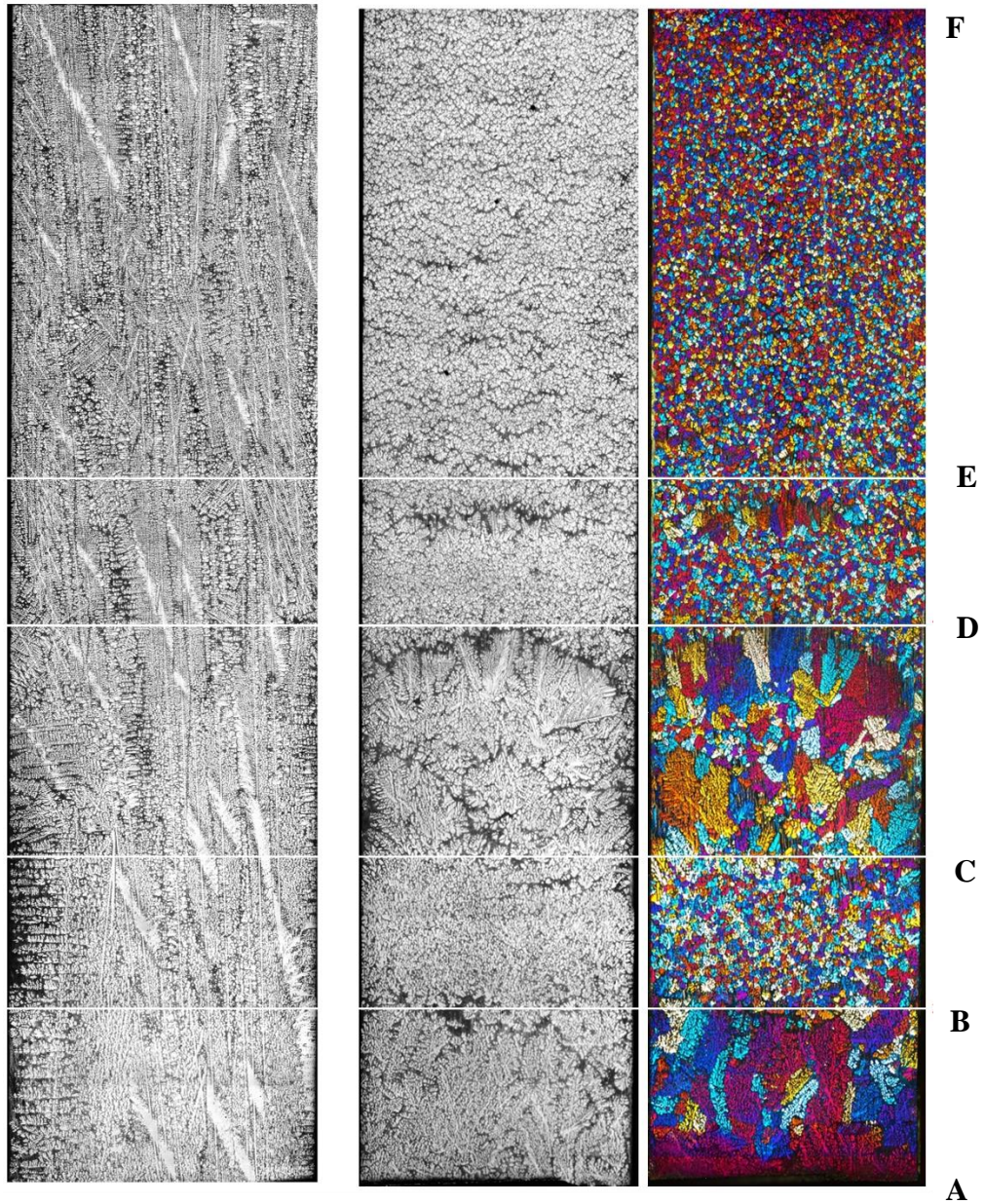


Figure 2.  
Grain structure of  
Sample 1 HF etching

Figure 3.a.  
Grain structure of  
Sample 2 HF etching

Figure 3.b.  
Grain structure of Sample 2  
Barker etching

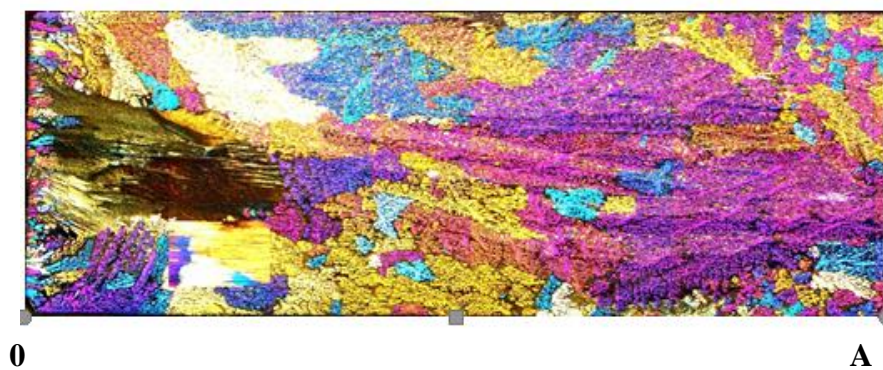


Figure 4. Grain structure of Sample 2 before the mushy zone



The values of  $v_{lig}$  and  $v_{sol}$  at the 0,02 sample movement velocity were constant and approximately equal to the sample movement velocity. Under the influence of the sudden and rapid change of sample movement velocity (increase from 0.02 mm/s to 0.2 mm/s), the solid/liquid interface velocities increased suddenly first from 0.02 mm/s to  $\sim 0.075$  mm/s (Fig. 1.b). Then they increased slowly - about  $\sim 1000$  sec was necessary to reach the value of 0.2 mm/s. At the end of the sample (at 110 mm), the movement velocity of liquidus isotherm (i.e. the start of solidification) was  $\sim 0.27$  mm/s and the movement velocity of eutectic isotherm (the end of solidification) was 0.32 mm/s – both values were higher than the sample movement velocity (0.2 mm/s). The temperature gradient decreased in a small extent during the solidification process. In case of a sample movement velocity of 0.02 mm/s, the cooling rate was  $\sim 0.1$  K/s ( $v_{liq} \cdot G_{liq} = 0.02 \text{ mm/s} \cdot 5 \text{ K/mm} = 0.1 \text{ K/s}$ ). In the transition zone, the cooling rate increased from 0.1 K/s to 0.45 K/s within some mm then it increased slowly and its value was  $0.3 \text{ mm/s} \cdot 4 \text{ K/mm} = 1.2 \text{ K/s}$  at the end of sample.

### Preparation of samples

Longitudinal sections parallel with the axis of sample and cross-sections perpendicular to the axis of sample were made of both samples. In order to investigate the dendritic microstructure, the sections were etched by using HF and the Barker-type electrochemical etching method was used for preparing the investigations of grain structure. The dendritic structure and grain structure of sections were investigated by means of a Zeiss Axio Imager m1M type light microscope.

### Results and discussion

The microstructure developing in the transition zone of Sample 1 (from 19 mm to 52 mm) after HF etching is shown in Fig. 2 on the longitudinal section and Figures 5.a-c demonstrate the grain structure developing in the cross-section after Baker etching at different distances from the bottom of sample. Fig. 3.a shows the microstructure developing on the longitudinal section of Sample 2 after HF etching and Fig. 3.b shows the grain structure developing in the transient zone after Baker etching. The grain structure of Sample 2 immediately before the transient zone can be seen in Fig. 4 (between „0” and „A” points). The grain structure developed on the cross section at different distances from the bottom of sample after Baker etching can be seen in Figures 6.a-c. In Figures 2 and 3, „A” indicates the end of mushy zone ( $548^\circ\text{C}$ ) and „C” indicates the beginning of mushy zone ( $610^\circ\text{C}$ ) at the moment when the movement velocity of sample changed from 0.02 mm/s to 0.2 mm/s in  $\sim 0.01$  s. Table 1 contains the distances of points indicated in Figures 2 and 3 measured from the bottom of sample as well as the values of  $v_{lig}$  belonging to the solidus at these points. The sample movement velocity could be changed quickly by means of the step motor used for moving the sample. The acceleration value of sample was  $\sim 18 \text{ mm/s}$  (in the period of the fast change of sample movement velocity).

The average secondary dendrite arm spacing (av.SDAS) belonging to a given „Interface velocity” ( $v_{lig}$ ) measured in the vicinity of the axis of samples as well as the average primary dendrite arm spacing (av.PDAS) are contained in Table 2. Moreover the sizes of grains developed at these values of „Interface velocity” are also shown in this Table. Obviously, the value of PDAS cannot be measured in Sample 2 (equiaxial structure) the value of SDAS couldn't be measured either owing to the insufficient resolution of light microscope.

In case of a sample-movement velocity of 0.02 mm/s, a columnar dendritic structure develops up to point „A” in both samples. At a velocity-value of 0.02 mm/s  $v_{lig}$ , the grain refining material has got only a minimum effect on PDAS and SDAS – both values decrease only in a small extent. It has got a bit greater effect on the grain size - it decreased from  $1.7 \text{ mm}^2$  to  $0.61 \text{ mm}^2$  i.e. to the third but the grain structure remained quasy columnar.

In case of Sample 1, the microstructure remained a columnar dendritic one even in case if the value of  $v_{lig}$  was high (0.3 mm/s). The values of PDAS and SDAS decrease significantly, the grain structure becomes finer (Figures 5.a-c, Table 1). However the effect of rapid, sudden increase of velocity can be observed gradually; it is in accordance with the fact that the value of  $v_{lig}$  increases also gradually following an initial fast increase.

In case of Sample 2, the columnar structure between „0” and 'A' points (see Fig. 4) remained up to the middle of mushy zone existing at the moment of rapid change of sample velocity (between „A” and „B” points in Fig. 3.b). Under the influence of the rapid change of velocity, the originally columnar structure transformed into an equiaxial one in the second half of mushy zone (between „B” and „C” points in Fig. 3b). The melt being in front of the mushy zone solidified to a basically coarse, mainly columnar structure containing some fine grains up to the „D” point ( $v_{lig} = 0.128$  mm/s). Here the grain structure became a very fine equiaxial one by a sharp transition and this structure remained up to the end of sample (Figures 6.b and c).

**Table 1.**

Name of points	A	B	C	D	E	F
Distance of points from the bottom of sample [mm]	19.00	24.51	28.85	35.19	38.65	52.00
$v_{lig}$ measured at the points [mm/s]	0.016	0.09	0.110	0.128	0.136	0.160

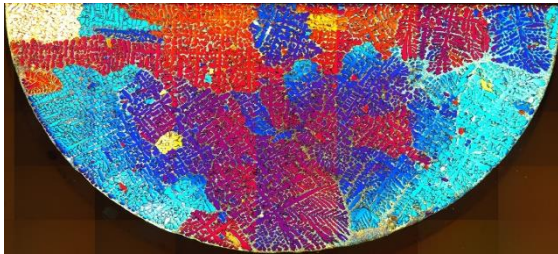


Figure 5.a. 11 mm

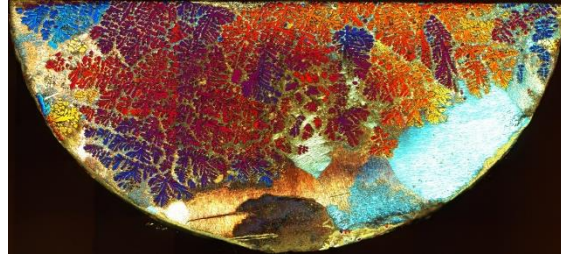


Figure 6.a. 11 mm

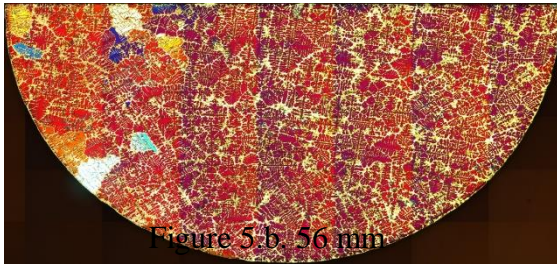


Figure 5.b. 56 mm

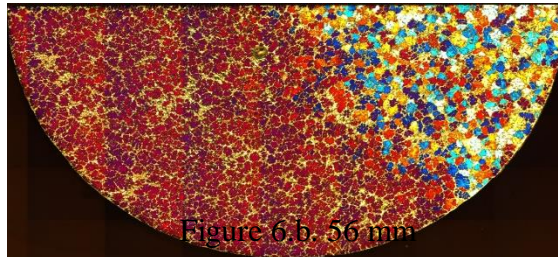


Figure 6.b. 56 mm

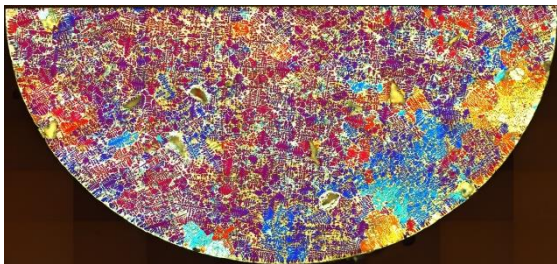


Figure 5.c. 105 mm

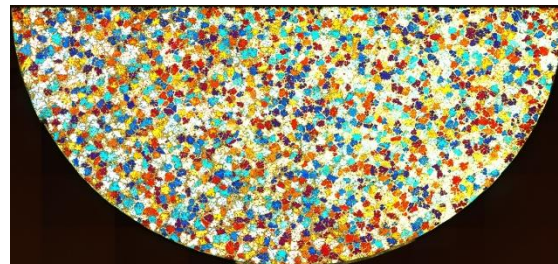


Figure 6.c. 105 mm

Figure 5. Cross section of sample 1 at different length of sample

Figure 6. Cross section of sample 2 at different length of sample

**Table.2.**

	Al-20wt%Cu		Al-20wt%Cu+Gr	
$v_{int}$ , [mm/s]	0.015	0.275	0.0136	0.275
av.SDAS, [mm]	0.101	0.035	0.076	-----
av.PDAS, [mm]	0.366	0.242	0.322	-----
Grain average, [mm <sup>2</sup> ]	~1.70	~0.32	~0.61	~0.008

The special behaviour of mushy zone developed before the rapid change of velocity can be explained by the brake of very soft dendrites under the influence of the rapid change of velocity when the sample “falls down” by an acceleration of  $\sim 18 \text{ mm/s}^2$  up to about 0.01 s, then it moves on by a velocity of 0.2 mm/s. As a consequence, an upward force due to the inertia of sample occurs. At the beginning of mushy zone where there is a lot of melt but little solid phase, this effect „breaks” the dendrites resulted many small solid particles, which will become heterogeneous nuclei, so fine equiaxed structure develops in this part of mushy zone. Because these small particles cannot move to the liquid phase which exist before this mushy zone, in the other parts of melt a columnar structure develops again. The columnar grain structure will change into a fine equiaxed grain structure when the velocity of solid/liquid front reaches the velocity necessary for CET (in this case 0.128 mm/s). It must be to note again that at this velocity, CET merely develops in the sample containing grain refining material; the grain structure of samples that do not contain grain refining material remains columnar even at 0.3 mm/s.

### Acknowledgements

Authors would like to express their thanks to the ESA for the financial support of the research working frame of the MICAST-HUNGARY MAP International Project.

### References

- [1] M. Easton, C. Davidson and D. StJohn, Grain Morphology of As-Cast Wrought Aluminium Alloys, The Japan Institute of Light Metals, pp. 173-178,
- [2] S.A. Kori, B.S. Murty, M. Chakraborty, Development of an Efficient Grain Refiner for Al-7Si Alloy, Materials Science and Engineering, A280 (2000) 58-61.]
- [3] A. Rónaföldi, J. Kovács, and A. Roósz, Proceedings of MicroCAD 2007, pp. 91-102
- [4] J. Kovács et al., Trans. Indian Inst. Met. Vol.60., 2-3, 2007, pp. 149-154

# **An Overview on Recent Advances in Understanding Early Stages of Solidification**

Fan, Zhongyun

**Keywords:** solidification, prenucleation, heterogeneous nucleation, grain refinement

## **Abstract**

Solidification of single phase alloys occurs in a number of distinctive stages during the cooling process. For isothermal solidification these may include prenucleation (atomic ordering in the liquid adjacent to the liquid/substrate interface), heterogeneous nucleation, grain initiation, spherical growth, morphological instability, dendritic growth and particle impingement. Here we define early stages of solidification as the process between prenucleation and the point of morphological instability. Since the majority of the most of the historic research has been concentrated on dendritic growth, our current understanding on early stages of solidification has been very limited albeit it contributes dominantly to the formation of the final solidified microstructure. In the recent years BCAST has been devoting its research efforts to understand the early stages of solidification and has made good progress. In this paper we offer an overview of the recent advances in understanding early stages solidification, grain initiation and their effect on grain refinement.

## **Heterogeneous Nucleation by Structural Templating**

H. Men, Z. Fan

**Keywords:** Interface, nucleation, MD simulation

## **Abstract**

It has been recently realized that atomic ordering in the liquid adjacent to the substrate (i.e., prenucleation) has a significant implication on the subsequent heterogeneous nucleation process. In this paper, we report an atomistic mechanism of the heterogeneous nucleation through structural templating. Using molecular dynamics (MD) simulation, we investigated the process of heterogeneous nucleation in the system of liquid Al and fcc substrates with  $\langle 111 \rangle$  surface orientation and varied lattice misfit (between the substrate and the corresponding solid phase). We used the EAM potential for Al, developed by Zope and Mishin to model the interatomic interactions. Our study revealed that the solid clusters in the ordered structure continue the lattice of surface layer of the substrate in either fcc or hcp stacking sequence, namely structure templating. During the nucleation process, solid clusters in the 2nd interfacial layer merge to form the new phase at the nucleation temperature. Simultaneously, the Shockley partial dislocations with predominant screw component were generated between the 1st and 2nd interfacial layers in the new phase, leading to a twist of the new phase relative to the substrate. The generation of the partial screw dislocations accounts for the major part of the nucleation barrier. In this study, for the first time we revealed the process of the heterogeneous nucleation at atomic level through a mechanism of structural templating. This mechanism would be generally applicable to other substrates with varied structures and chemistry.

## **Heterogeneous nucleation on oxide in Al alloys**

Feng Wang, Zhongyun Fan

**Keywords:** Al alloy, oxide, heterogeneous nucleation, TEM, grain refinement

### **Abstract**

The heterogeneous nucleation on native oxide particles in commercial-purity Al alloys has been investigated by analytical electron microscopy assisted with melt filtration and focused ion beam sample preparation techniques. The crystallographic features including the crystal structure and exposed broad plane has been determined using selected area diffraction pattern and high resolution transmission electron microscopy combined with electron energy loss spectroscopy. In addition, the orientation relationship and the corresponding interface between the oxide particles and Al grains have also been determined. Furthermore, the potency of the oxide as nucleation substrate for Al grain has been evaluated by calculating the lattice misfit between the oxide particles and Al grains. Based on the experimental results and theoretical calculation, the role of oxide particles in grain refinement of Al -alloys has been discussed.

## **A novel grain refiner for effective grain refinement Al-alloys**

Z.P. Que, Y. Wang, Z. Fan

**Keywords:**  $\alpha$ -Al, TiB<sub>2</sub>, de-poisoning, heterogeneous nucleation

### **Abstract**

Al-Ti-B based grain refiners have been used successfully for grain refinement of Al-alloys for many decades, but the exact mechanisms for grain refinement was attributed only recently to the formation of (112) 2-dimensional compound (2DC) on (0001) TiB<sub>2</sub> surface. However, when the Al alloys contain alloying elements, such as Zr, Cr and Si, the Al-5Ti-1B grain refiner is no longer effective due to the poisoning effect of such elements. In this study, a novel grain refiner was developed to overcome such shortcomings of the traditional Al-5Ti-1B grain refiner. The new grain refiner has been tested with commercial purity (CP) Al and various Al alloys, including those containing Zr and/or Si. The segregation of Ni and Si on the (0001) TiB<sub>2</sub> surface was identified by extensive examinations of the TiB<sub>2</sub>/Al interface using state-of-the-art highresolution transmission electron microscopy (HRTEM) and aberration (Cs)-corrected scanning transmission electron microscopy (STEM). In this paper we report the preparation of the novel grain refiner, chemical composition and crystal structure of the segregated layer and the detailed mechanisms for heterogeneous nucleation.

## **Segregation of Ca at the Mg/MgO interface and its effect on grain refinement**

Shihao Wang, Yun Wang, Quentin Ramasse, Zhongyun Fan

**Keywords:** MgO, Mg, solidification, grain refinement, adsorption, STEM, EELS.

### **Abstract**

Recently, native MgO particles were reported to be potential nucleation substrates for grain refinement of Mg and Mg alloys, even though it shows that MgO has high lattice misfit with Mg matrix (8.01%). Previous studies showed that many factors, such as size, size distribution, number density, cooling rate and alloy compositions, may affect the performance of native MgO particles for grain refinement. In addition, recent studies on modifying MgO surface showed evidence of Zr segregation on MgO{111} resulting in a significant reduction of lattice misfit. Similarly, addition of Ca has been shown to improve grain refinement. In this work, we employ Scanning Electron Microscope (SEM), Conventional Transmission Electron Microscope (TEM) equipped with Energy Dispersive X-ray (EDX) detector and Super TEM with Electron Energy Loss Spectroscopy (EELS) to study the segregation of Ca at the Mg/MgO interface in Mg-Ca alloys with varying Ca contents. Our results show that there is a distinguished layer around MgO particles on both {111} and {001} planes. Specifically, EDS and EELS analysis suggests that this interfacial layer contains Al, N and Ca, with only several layers with thickness around 1nm. However, this layer was not observed in CP Mg. In this paper, we report the nature of the Ca-rich layer at the Mg/MgO interface and its effect on grain refinement.

## **Effect of agglomeration of potent nucleant particles on grain size in the as-cast microstructure**

F. Gao, Z Fan

### **Abstract**

Predicting grain size of the solidified microstructure is of both scientific and technological importance. The current models for predicting grain size of isothermally solidified microstructures assume that the total number of grains in the solidified microstructure equals to the number of grains initiated at the temperature of recalescence. We have confirmed that the predicted grain size is significantly smaller than the ones determined by experiments. In this work, we have numerically simulated the solidification processes of Al-alloys containing potent nucleant particles. We found that the discrepancy between theoretical prediction and experimental results is caused by the following two mechanisms: (1) particles that have satisfied free growth criterion will not initiate grains if they are located within the diffusion field of a growing solid particle. This has led to the concept of grain initiation free zone (GIFZ); and (2) a smaller initiated grain located in the diffusion field of a larger solid particle will re-melt back into the liquid. We developed a new numerical model for grain size prediction by taking these two mechanisms into full consideration. The potent nucleant particles are assumed to have a log-normal size distribution, and the agglomeration of nucleant particles is quantified by the mean of particle distance. The results from the numerical model suggest that agglomeration of potent nucleant particles plays a very important role in prediction of grain size when the GIFZ is considered; the re-melting after grain initiation can affect the grain size but only in very limited effect.

## Effect of surface roughness on prenucleation

B. Jiang, H. Men, Z. Fan

**Keywords:** Interface, MD simulation, surface roughness, atomic ordering

### Abstract

Prenucleation refers to the phenomenon of significant atomic ordering in the liquid adjacent to a crystalline solid substrate, and is expected to have a significant impact on the subsequent heterogeneous nucleation process. In this work, atomic ordering in the liquid adjacent to both crystalline and amorphous substrates with atomic level surface roughness was investigated systematically using molecular dynamics (MD) simulations. We artificially constructed atomic-level rough surfaces for both crystalline and amorphous substrates with varied surface roughness. The RGL potential was used in the simulation. We use the NVT ensemble, periodic boundary conditions in 3-dimensions and a time step of 1fs. We found for the first time that increasing surface roughness of a crystalline substrate reduces both atomic layering and in-plane atomic ordering in the metallic liquid adjacent to the liquid/substrate interface. In addition, our MD simulation results revealed that the rough surface of an amorphous substrate eliminates completely in-plane ordering in the liquid regardless of surface roughness and reduces/eliminates atomic layering in the liquid depending on the level of surface roughness. This reduced atomic ordering in the liquid adjacent to an atomically rough surface can be attributed to the increase in mobility of atoms in the liquid compared with the case with a smooth crystalline surface. From the point of view of heterogeneous nucleation, in addition to the effect of lattice misfit investigated in our previous studies, this work provides further confirmation of the importance of structural templating as a mechanism for both prenucleation and heterogeneous nucleation. Furthermore, this work offers a new approach to impede heterogeneous nucleation by roughening the substrate surface at the atomic level.

## Removal of oxide skin from molten aluminum surface

Zoltán Kéri, György Kaptay

**Keywords:** alumina, aluminum, liquid aluminum surface oxidation, liquid salt metal treatment, aluminum matrix composite

### Abstract

Aluminum has an excellent mechanical properties and it is produced in large quantities worldwide. Aluminum matrix composites (AMC's) becomes more important to casting technology in recent years. The extensive use of aluminum makes it possible to meet the requirements for castings in the field of composite material development. Aluminum matrix composites are better in abrasion resistance and thermomechanical properties compared to aluminum alloys without significant weight gain. Based on our preliminary investigations, it was found that the oxide skin on the melt surface deteriorates the inlet efficiency of the particles (ex-situ) and, if necessary prevent it. The formed oxide layer can cover and wrapping the reinforcing phase to be applied. The particle encapsulated in the oxide may appear as an inclusion in the casting. The article describes the formation of the oxide layer on the molten aluminum surface depending on time and temperatur. The aggregate of equimolar NaCl-KCl salt was used to remove oxide skin on molten aluminum surface. The test was carried out between 700-780°C.





## CHAPTER 5: CASTING



# **An alternative approach for the experimental verification of microsegregation models using an in-situ hot tensile test during solidification of steel**

Michael BERNHARD<sup>1</sup>, Christian BERNHARD<sup>1</sup>, Peter Presoly<sup>1</sup> and Dali You<sup>1</sup>

<sup>1</sup>Chair of Ferrous Metallurgy, Montanuniversitaet Leoben, Franz-Josef-Strasse 18, Leoben, Austria

michael.bernhard@unileoben.ac.at

**Keywords:** steel; solidification; hot tearing; microsegregation; continuous casting;

**Abstract.** The presented paper deals with the development of an alternative approach for the experimental verification of microsegregation models with the potential extension to advanced steel grades using an in-situ hot tensile test. Based on experimental results for more than 100 plain carbon steels, the presented method is generally evaluated using a 1D-FV solidification algorithm and a modified microsegregation model as suggested by Ohnaka [1,2]. The study shows that slight modifications of the input parameters for the microsegregation model show significant influence on the predicted results. The high sensibility makes it possible, to clearly identify the influence of alloying elements on the final part of solidification.

## **Introduction**

In continuous casting of steel the exact calculation of non-equilibrium solidification and solute enrichments on microscopic scale is an essential part of a successful process control. Particularly the implementation of concepts with respect to industry 4.0, adjustment of soft reduction and optimized cooling strategies requires an accurate prediction of the shell formation and the final solidification point. In the past decades various analytical and numerical microsegregation models have been published in literature [2-8]. Coupling the calculations with high precise thermodynamic databases is a powerful way to investigate solidification phenomena also for advanced steel grades.

The experimental verification of microsegregation models with respect to steel can be generally divided into two methods: *Directly* the composition along the dendritic microstructure subsequently to a controlled solidification process can be measured using Electron Microprobe Analysis [6,8]. Since carbon and other elements show quite high diffusivity in iron, results for steels are conditionally usable. Within the *indirect way* the common hot tensile test [9,10] is applied: After complete remelting, the test sample is cooled down to a given temperature and the tensile strength and hot ductility are measured. Based on the temperature dependent results, the Zero Strength Temperature (ZST) and Zero Ductility Temperature (ZDT) of the investigated steel grade can be determined assuming correlated fractions of solid. However, it is quite challenging to guarantee defined experimental conditions and literature information is limited to just a few plain carbon steels.

The objective of this work is to develop and critically evaluate an alternative approach for the experimental verification of microsegregation models with a possible application also to advanced steel grades. Several advantages of the present in-situ method are:

- Controlled heat transfer and temperature evolution,
- Defined columnar dendritic growth,
- The possibility of an accurate numerical calculation of the solidification progress and
- Conditions close to continuous casting of steel.

## **Experimental and numerical approach**

In the past decades the Submerged-Split-Chill-Tensile (SSCT) equipment, originally developed at EPF Lausanne [11] has been successfully applied for the characterization of hot tear sensitivity of various steel grades at the Chair of Ferrous Metallurgy at Leoben [12]. As a “co-product” it is possible

to correlate the position of the formed hot tears during the experiment with simulation results for the solidus isotherm in order to validate microsegregation models on laboratory scale. The experimental procedure should be described here only briefly, detailed information can be found elsewhere [13].

**In-situ hot tensile test (SSCT-test).** The cylindrical test body is made of construction steel and consists of an upper and a lower part. Two thermocouples of type k are placed 2 mm beneath the surface of the lower part to measure the temperature and to determine the heatflux during the experiment. In general the SSCT-test procedure can be divided into four stages, Figure 3 [13]:

- The test body is placed above the liquid steel at *stage I*. The melt is prepared in an induction furnace with a capacity of 25 kg.
- During *stage II* the test body is submerged into the liquid steel with a velocity of 1.2 m/min and shell growth proceeds for a specified period of time.
- At *stage III* the actual tensile test starts: The lower part moves down with a given velocity (corresponds to a given strain rate) and a predefined total strain is induced into the solidifying shell. If the strain exceeds critical values, hot tear segregations (HTS) will be formed during the experiment.
- After the tensile test has finished the test body is lifted out of the melt during *stage IV*, whereby the velocity is identical to submerging. After the specimen is cooled down to room temperature the solidified shell is cut into 16 samples for the metallographic investigations.

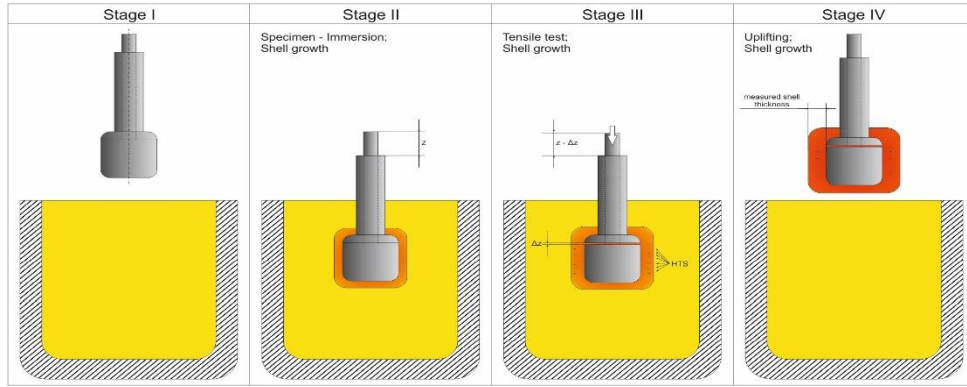


Figure 3. Different experimental stages of the SSCT-test [13]

**Correlation of hot tear statistics and numerical simulation.** The principle of correlating the metallographic results with the numerical simulation of the experiment is shown in Figure 4. A typical Low Carbon (LC) steel grade is taken as an example.

*Metallographic analysis and hot tear statistics:* The samples are etched with Bechet-Beaujard solution [14] to visualize present HTS. Within the microscopic analysis the position of HTS with respect to the test body surface as well as the shell thickness is measured Figure 4 (a). The statistical analysis of the HTS position gives the frequency maxima of start and end of HTS in the sample. In case of the LC steel most of the HTS start to form at a distance of 6.18 mm from surface and end at 7.01 mm Figure 4 (b). Since HTS only occur if the solidifying shell is mechanically loaded, the maxima correspond to the start and end of the tensile test, respectively. Under the assumption that HTS form within a preferred temperature range very close to solidus temperature ( $f_s = 0.96 - 1$ ) [15] two points for the solidus isotherm (6.18mm/18s and 7.01mm/23s) are obtained. The measured shell thickness after the SSCT-test is  $10.62 \pm 0.37$  mm and generally corresponds to a calculated fraction of solid  $f_s = 0.2$  (10.62mm/25s). Hence, three points are available to accurately reconstruct the shell growth during the SSCT-experiment and to evaluate the calculated non-equilibrium solidus isotherm as illustrated in Figure 4 (c). Regarding microsegregation models for advanced steel grades (e.g. coupling with thermodynamic databases) it is perhaps necessary to perform the tensile test under different experimental conditions (solidification time or testing time), subsequently one gets even more points for a fixed chemical composition and reproducibility is guaranteed.

*Solidification simulation and microsegregation evaluation:* An in-house 1D-FV solidification model is used to calculate the shell growth during the SSCT-test, Figure 4 (c). Input parameters for

the simulation are the superheat of the melt (typically 20-30°C) and the determined heatflux based on the measured temperature. For the general evaluation of the present approach the semi-integrated form of Ohnaka's equation according to You et al. [1] is implemented to predict the microsegregation during solidification. Note that the used microsegregation model [16] is a "stand-alone" version and therefore not as high sophisticated as the model of You et al. [1]. The advantage of the semi-integrated form is the possibility to use local partition coefficients dependent on temperature or solute enrichment. An additional tool of the software enables the plot of various temperature profiles to determine the "measured" solidus isotherm. In case of the LC steel the results of solidus temperatures from the SSCT experiment are 1492 °C and 1489 °C. Finally, the "measured" temperature is 1490.5±2°C which is in very good agreement with the calculated one using the semi-integrated Ohnaka equation [1] (1491.7 °C).

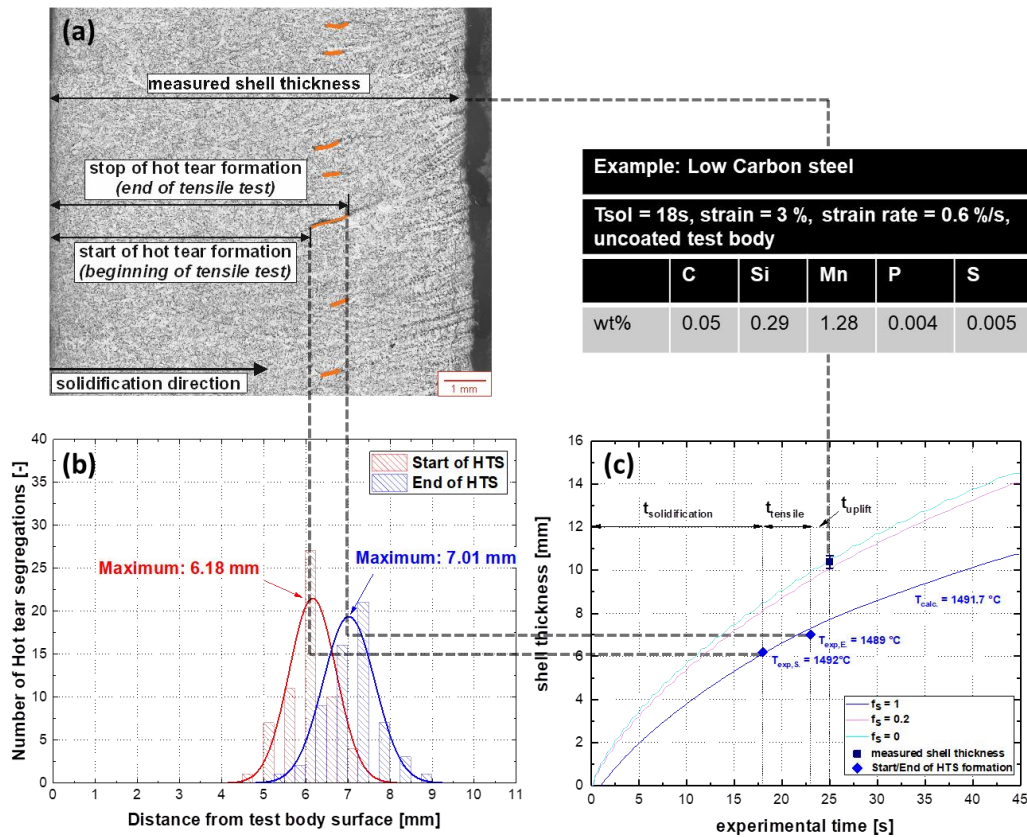


Figure 4. Principle of determining the solidus temperature from SSCT-test: (a) metallographic examination, (b) hot tear statistics and (c) correlating metallographic results with the solidification simulation

## Results and discussion

The previous explained procedure for the LC steel grade was applied for more than 100 plain carbon steels. Composition ranges of the investigated steel grades are listed in Table 3.

Table 3. Composition ranges of investigated steel grades

C [wt%]	Si [wt%]	Mn [wt%]	P [ppm]	S [ppm]
0.02-1.05	0.01-0.36	0.08-2.01	20-260	20-230

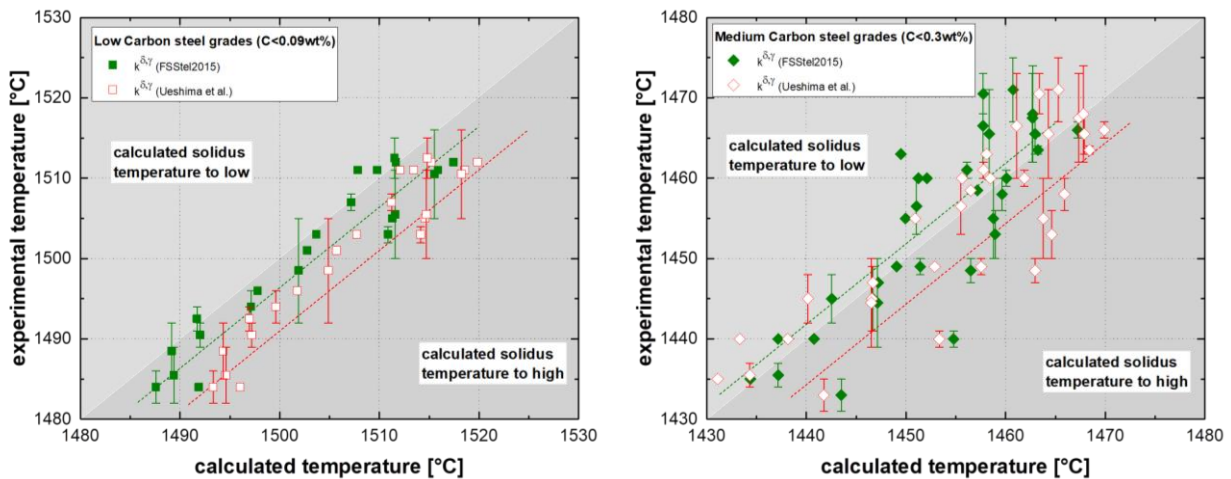
Within the first analysis the partition coefficients  $k_i$  as proposed by Ueshima et al. [6] were used to perform the microsegregation calculations. As can be seen in Figure 5 the predicted solidus temperature of LC and Medium Carbon (MC) steels is generally too high (10-15°C) compared to the "measured" temperature. In order to improve the microsegregation model the partition coefficients

were slightly modified by extracting the values for  $k_i$  from the FSSStel2015 database using the thermodynamic software FactSage [18]. In austenite the concept of a local partition coefficient for carbon is applied to define the value dependent on the carbon enrichment  $c_1(C)$  itself (Table 4). Although this procedure is not the conservative way to couple the microsegregation model with a thermodynamic database as suggested by You et al. [1], it is a simple and fast possibility to adjust the model and also to visualize the benefit of using newly assessed databases.

*Table 4. Equilibrium partition coefficients  $k_i$  used for the microsegregation calculations*

		C	Si	Mn	P	S
$\delta$	(FSSStel2015) [-]	0.17	0.70	0.70	0.32	0.04
	(Ueshima et al.)	0.19	0.77	0.76	0.23	0.05
$\gamma$	(FSSStel2015)	$0.295+0.057c_1(C)$ $-0.005c_1(C)^2$	0.83	0.70	0.16	0.02
	(Ueshima et al.)	0.34	0.52	0.78	0.13	0.035

By repeating the microsegregation calculations with the coefficients from FSSStel2015 [17] significantly better results can be obtained due to the optimized segregation description of the alloying elements. In case of LC steel grades the deviations are smaller than 5 °C. Obviously the segregation of carbon was underestimated using the coefficients from Ueshima et al. [6]. Since the concentration Phosphorus, Sulphur and Manganese of the investigated MC alloys is in a wide range, the improvement is not as clear as for the LC steel grades. The extension of local partition coefficients to all alloying elements would definitely enhance the results. Although, a better agreement between measurements and calculations can be found particularly at lower solidus temperatures the accurate description and further development of thermodynamic data for strong segregating elements (e.g. Phosphorus) is of high importance. This topic is part of recent research at the Chair of Ferrous Metallurgy at Leoben.



*Figure 5. Evaluation of calculated solidus temperature for Low Carbon and Medium Carbon steels*

The investigation of High Carbon (HC) and Ultra High Carbon (UHC) steel grades gives promising results and confirms the present approach to adjust microsegregation models based on the SSCT-test: High Carbon (HC) and Ultra High Carbon (UHC) steels with carbon concentrations between 0.5-1 wt% solidify in pure austenitic microstructure and carbon is the dominating alloying element. Due to the high initial concentration and the reduced diffusivity at lower temperatures, typical carbon

enrichment can exceed 3wt% in the interdendritic liquid. As a consequence the accuracy of the microsegregation calculation is mainly defined by the carbon segregation description. Inserting the mentioned concentration into the equation for  $k_C$  (Table 4) gives a local partition coefficient of 0.42 close to the end of solidification. Figure 6 shows the comparison of the predicted and “measured” solidus temperatures. The prediction of higher carbon segregation tendency based on the fixed carbon coefficient ( $k_C=0.34$ ) leads to a deviation of nearly 80 °C (!) whereas the prediction with adjusted microsegregation model shows only small differences to the experimental solidus temperature. This observation further indicates that already the calculation of low alloyed UHC steels requires a (partial) consideration of precise thermodynamic data (e.g. partition coefficients).

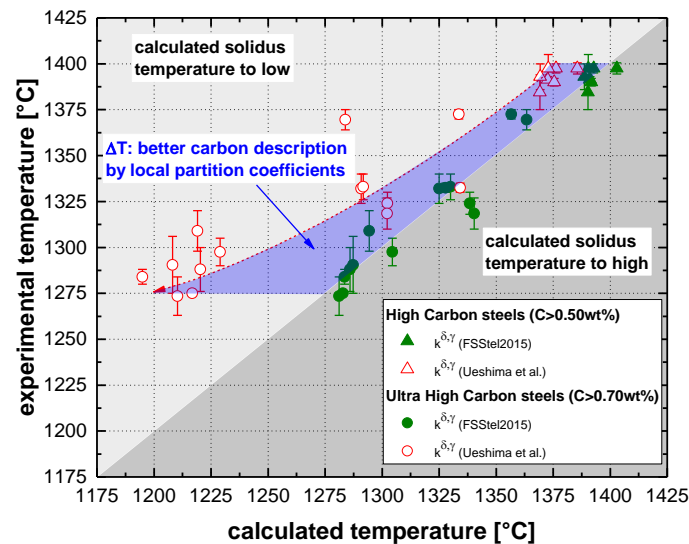


Figure 6. Evaluation of calculated solidus temperature for High Carbon and Ultra High Carbon steels

## Summary and outlook

First evaluations of a microsegregation model using the Submerged-Split-Chil-Tensile (SSCT)-test showed quite promising results. Within the analysis of more than 100 plain carbon steels, it was observed, that already slight modifications of input parameters can improve the predicted solidus temperature. As an example the partition coefficients of the alloying elements were adjusted according to the FSSel2015 [17] database. Particularly in case of High Carbon and Ultra High Carbon steel, the concept of an optimized local partition coefficient for carbon leads to a significant better agreement with the experimental results.

Future research on this topic aims to extend the present method to advanced steel grades and couple the microsegregation models with high precise thermodynamic databases. The development and investigation of thermodynamic databases for microsegregation calculations is part of a further work package within the project (Presoly, P.: “High concentrations at the final solidification of advanced steels: Thermodynamic evaluation of replicated “segregation-samples” by means of DTA/DSC-measurements”).

## Acknowledgement

Financial support by the Austrian Federal Government (in particular from Bundesministerium für Verkehr, Innovation und Technologie and Bundesministerium für Wirtschaft, Familie und Jugend) represented by Österreichische Forschungsförderungsgesellschaft mbH and the Styrian and the Tyrolean Provincial Government, represented by Steirische Wirtschaftsförderungsgesellschaft mbH and Standortagentur Tirol, within the framework of the COMET Funding Programme is gratefully acknowledged. This work is part of the ongoing K2-MPPE project P3.1 “SmartCast”.



## References

- [1] You, D., C. Bernhard, G. Wieser and S. Michelic, Microsegregation Model with Local Equilibrium Partition Coefficients During Solidification of Steels, *Steel Research International* 87 (2016), 7, 840–849.
- [2] Ohnaka, I., Mathematical analysis of solute redistribution during solidification with diffusion in solid phase, *Transactions ISIJ* 26 (1986), 12, 1045–1051.
- [3] Scheil, E., Bemerkungen zur Schichtkristallbildung, *Zeitschrift für Metallkunde* 34 (1942), 3, 70–72.
- [4] Brody, H.D. and M.C. Flemings, Solute redistribution in dendritic solidification, *Transactions of the Metallurgical Society of AIME* 236 (1966), 5, 615–624.
- [5] Clyne, T.W. and W. Kurz, Solute redistribution during solidification with rapid solid-state diffusion, *Metallurgical and Materials Transactions A* 12 (1981), 6, 965–971.
- [6] Ueshima, Y., S. Mizoguchi, T. Matsumiya and H. Kajioka, Analysis of Solute Distribution in Dendrites of Carbon Steel with delta / gamma Transformation During Solidification, *Metallurgical Transactions B* 17 (1986), 4, 845–859.
- [7] Kobayashi, S., A Mathematical Model for Solute Redistribution During Dendritic Solidification, *Transactions ISIJ* 28 (1988), 7, 535–542.
- [8] Matsumiya, T., H. Kajioka, S. Mizoguchi, Y. Ueshima and H. Esaka, Mathematical analysis of segregations in continuously-cast slabs, *Transactions ISIJ* 24 (1984), 11, 873–882.
- [9] Schmidtman, E. and F. Rakoski, Influence of the carbon content of 0.015 to 1% and the structure on the high-temperature strength and toughness behaviour of structural steels after solidification from the melt, *Archiv fuer das Eisenhuettenwesen* 54 (1983), 9, 357–362.
- [10] Seol, D.J., Y.M. Won, T. Yeo, K.H. Oh, J.K. Park and C.H. Yim, High temperature deformation behavior of carbon steel in the austenite and delta - ferrite regions, *ISIJ International* 39 (1999), 1, 91–98.
- [11] Ackermann, P., Kurz, W., and Heinemann, W., In situ testing of solidifying Aluminium and Al-Mg shells, *Materials Science and Engineering* 75 (1985), 1-2, 79-86.
- [12] Pierer, R. and Bernhard, C., The nature of internal defects in continuously cast steel and their impact on final product quality, *AIST Proceedings, Pittsburgh, USA, 2010*, 193-203.
- [13] Arth, G., S. Ilie, R. Pierer und C. Bernhard, Experimental and Numerical Investigations on Hot Tearing during Continuous Casting of Steel, *BHM* 160 (2015), 3, 103–108.
- [14] Bechet, S. and Beaujard, L., Nouveau reactif pour la mise en évidence micrographique du grain austénitique des aciers trempés ou trempés-revenus, *Revue de Metallurgie*, 92 (1995), no.10, 923–929
- [15] Bernhard, C. and Pierer, R., A new hot tearing criterion for the continuous casting process, *Proceedings of the 5th Decennial International Conference on Solidification Processing, Sheffield, UK, 2007*, 525–530
- [16] Bernhard, M., Presoly, P., Bernhard, C., Six, J. and Ilie, S., On the relevance of microsegregation models for process control in continuous casting of steel, *Proceedings of the 26<sup>th</sup> International Conference on Metallurgy and Materials, Brno, CZE, 2017*, 38-44.
- [17] Bale, C.W. et al., FactSage thermochemical software and databases, 2010–2016, *Calphad* 54 (2016), 35–53.



## Effect of Pulling Rate on the Structural Zones Localization in the Continuously Cast Brass Ingot

Waldemar WOŁCZYŃSKI<sup>1</sup>, Anna A. IVANOVA<sup>2</sup>, Piotr Kwapisiński<sup>3</sup>, and  
Krzysztof Sztwiertnia<sup>1</sup>

<sup>1</sup>Institute of Metallurgy and Materials Science, 25, Reymonta Str., 30-059 Kraków, Poland

<sup>2</sup>Institute of Applied Mathematics and Mechanics, 74, R. Luxemburg Str., 83-114 Donetsk, Ukraine

<sup>3</sup>KGHM – Polish Copper Company, 48 Skłodowskiej-Curie Str., 59-301 Lubin, Poland  
w.wolczynski@imim.pl

**Keywords:** columnar structure; equiaxed structure; continuous casting, brass ingot, pole figures

**Abstract.** An analysis of the thermal gradient field has been employed in a simplified description of both columnar and equiaxed structures creation in a large static steel ingot. It allowed to select a zone in which columnar into equiaxed structure transformation (CET) is expected. It is shown that the CET - zone is formed when the thermal gradient becomes temporarily constant. Subsequently, the method of mathematical interpretation of some functions resulting from the temperature field has been applied to structural zones prediction in the brass ingots obtained by the continuous casting. Both the velocity of liquidus isotherm movement and thermal gradient changes versus distance from the liquid brass meniscus are considered. The simulations were performed for two rates of the brass ingot passage down through the imposed crystallizer. The method of the mathematical predictions of the structural zones appearance is able to reproduce all the morphologies evinced in the brass ingot produced in the industrial condition. Two ingots: the first containing the columnar structure and the second evincing the equiaxed structure were subjected to pole figures measurement to estimate how many slip systems could be available while imposing further plastic deformation.

### Introduction

The structural modifications and in particular the  $C \rightarrow E$  (columnar into equiaxed structure) transition (CET) in solidifying alloys have already been described analytically to a high degree, [1]. This analytical description has been developed and supported by some numerical simulations which allow to localize the CET along the ingot radius or within a certain period of the ingots solidification time, [2,3,4,5,6,7,8,9].

Some of the numerical simulations are associated with the static ingot solidification and resultant prediction of the CET appearance, [2,4,6,8]. Other models try to predict the different structures formation during continuous casting of steel ingot, [3,5,7].

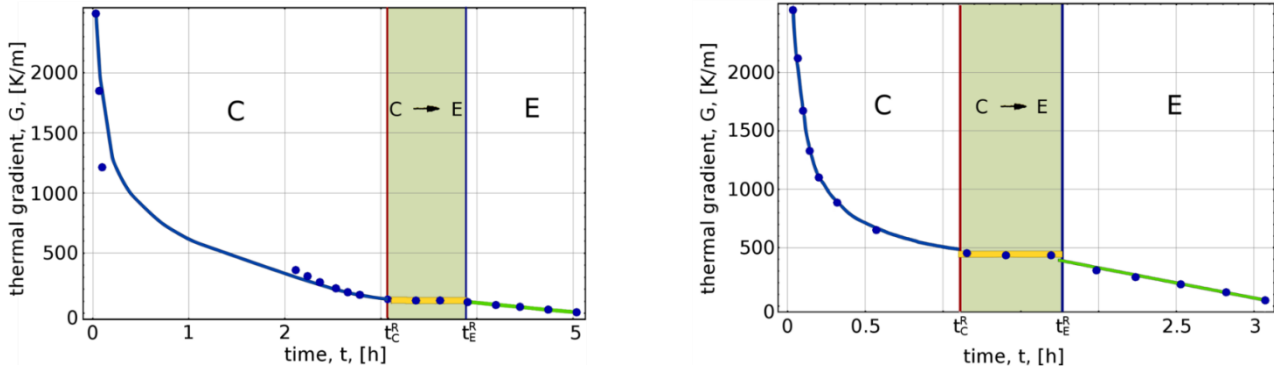
The simulations of the temperature field and the resultant mathematical prediction of the CET in the continuously cast brass ingot are connected with the analysis of hard particles motion, [9]. However, this model does not consider the effect of the pulling rate changes on the structural zones displacement. Therefore, the current simulation attempts to show how the pulling rate of the ingot decides on the appearance / localization of some structural transitions in the brass ingot.

The present study is based on the innovative mathematical method for the prediction of different structures formation. It is conceived that the proposed method for the structural zones formation / localization could be complementary to the mentioned numerical simulations, [2,3,4,5,6,7,8]. Thus, it can be applied in order to correct / modify the mentioned predictions of the CET localizations, [1,2,3,4,5,6,7,8]. The proposed method for the structural zones localization in the brass ingot is preceded by the similar forecast for the CET occurrence in the large static steel ingot. The method employs the analysis of some properties of function (yielding from the numerically simulated temperature- or thermal gradient field) as a tool to determine the CET occurrence.

### Prediction of the CET situation in a large static steel ingot

The initial simulation for the static steel solidification was performed with the use of the MAGMA program available at the Computer Center Kom-Odlew, Kraków – Poland, [10], next supported by the calculation with the application of the ABAQUS program available at the Computer Center of the AGH–University of Science and Technology, Kraków – Poland, [11].

The conversion of the obtained temperature field into the thermal gradient field allows to reveal that the thermal gradient becomes temporarily constant when the CET occurs, Fig. 1.



**Figure 1.** Thermal gradient evolution in solidification time for the 15 tons static steel ingot: a/ mold thickness equal to 0.1 m; b/ mold thickness equal to 1.0 m;  $t_C^R$  - beginning of the columnar structure disappearance, and the beginning of the equiaxed structure appearance,  $t_E^R$  - completion of the columnar structure disappearance, and the beginning of the equiaxed structure exclusive formation.

The  $G$  - thermal gradients are steep for the C – columnar structure formation, and moderate for the E – equiaxed structure appearance, Fig. 1.

### Structural zones localization in the continuously cast brass ingot

The simulation of both the temperature field and thermal gradient field were performed on the basis of the following equation formulated for the cylindrical system of co-ordination:

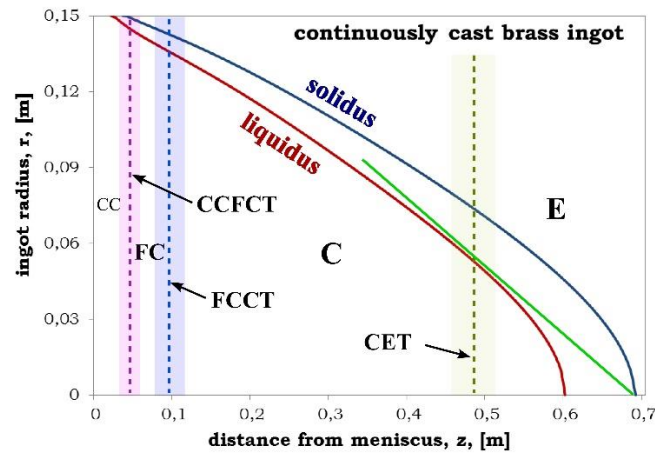
$$c_{ef}(T) \cdot \rho(T) \cdot \frac{\partial T}{\partial t} = \frac{\partial}{\partial r} \left[ \lambda(T) \cdot \frac{\partial T}{\partial r} \right] + \frac{\lambda(T)}{r} \cdot \frac{\partial T}{\partial r} + \frac{1}{r^2} \frac{\partial}{\partial \varphi} \left( \lambda(T) \frac{\partial T}{\partial \varphi} \right) + \frac{\partial}{\partial z} \left( \lambda(T) \frac{\partial T}{\partial z} \right) \quad (1)$$

$$T = T(t, r) \quad r \in [0, R_m] \quad c_{ef}(T) = \begin{cases} c_b(T), & T < T_s \\ c_b(T) + \frac{L}{T_L - T_s}, & T_s \leq T \leq T_L \\ c_b(T), & T > T_L \end{cases} \quad (1a)$$

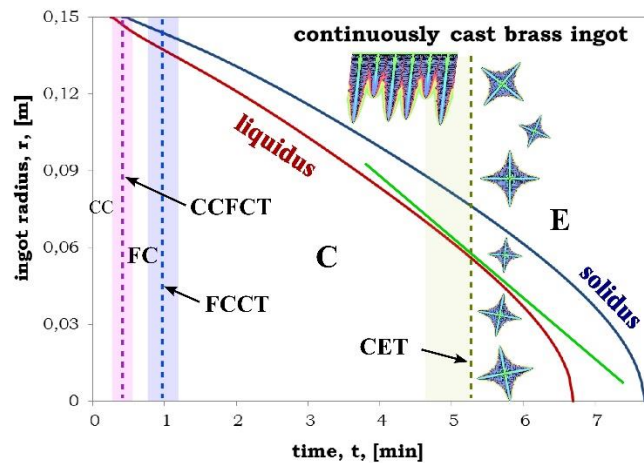
$c_b$  - specific heat of brass;  $c_{ef}$  - effective heat;  $L$  - latent heat of solidifying alloy;  $r$  - current radius of the solidifying ingot;  $r, \varphi, z$  - co-ordinates;  $t$  - time;  $T$  - temperature;  $T_L$  - liquidus temperature;  $T_s$  - solidus temperature;  $\lambda$  - thermal conductivity;  $\rho$  - density of brass.

The simulations of heat transfer performed with the application of Eq. (1) allow to analyze the temperature field for the solidifying brass ingot. Consequentially, different functions like: behavior of the solidus and liquidus isotherms along the ingot radius or along the distance from the liquid brass meniscus can be subjected to the detailed mathematical interpretation for the pulling rates equal to 90 mm/min, Fig. 2, and to 250 mm/min, Fig. 3. Crystallizer height was assumed as equal to 0.8 m.

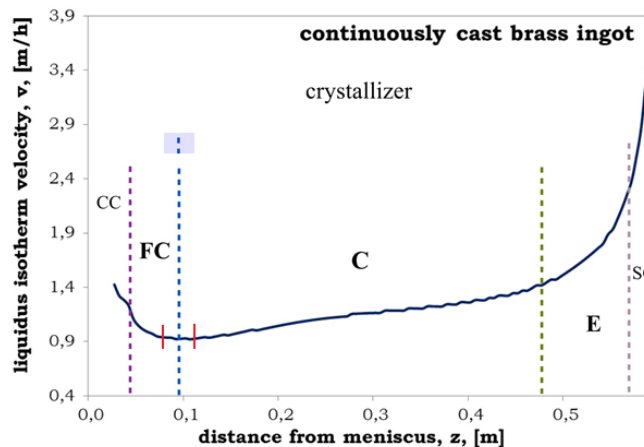
As a result, the following structural transformations are selected: CCFCT – chilled columnar into fine columnar structure transition, FCCT – fine columnar into columnar structure transition, CET – columnar into equiaxed structure transition, ESCT – equiaxed structure into single crystal transition.



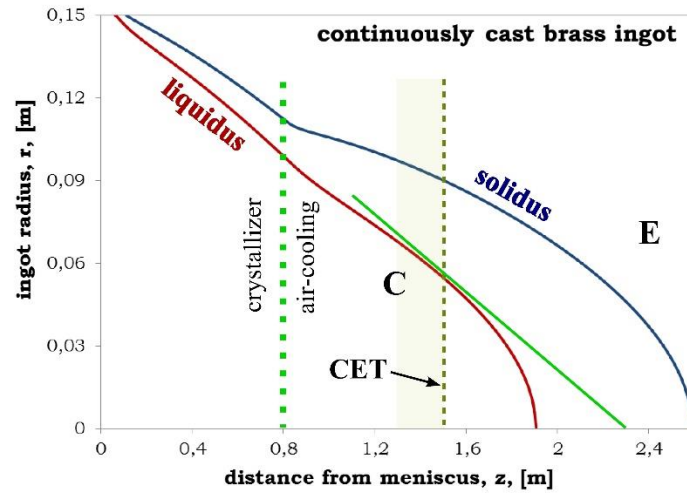
**Figure 2a.** Liquidus, and solidus isotherms situation in the map: ingot radius – distance from meniscus; CCFCT – at the point of inflection, FCCT – at the point (segment) of inflection, CET – within the range defined by the tangent, ESCT – at the beginning of linear part.



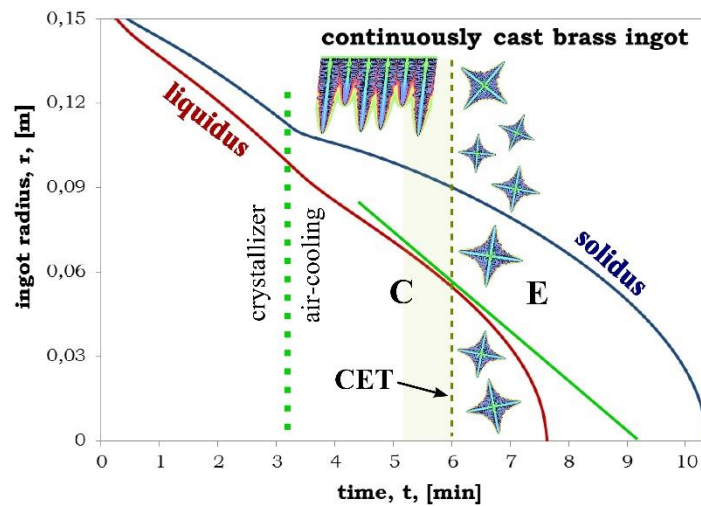
**Figure 2b.** Liquidus, and solidus isotherms situation in the map: ingot radius – solidification time; CCFCT – at the point of inflection, FCCT – at the point (segment) of inflection, CET – within the range defined by the tangent, ESCT – at the beginning of linear part.



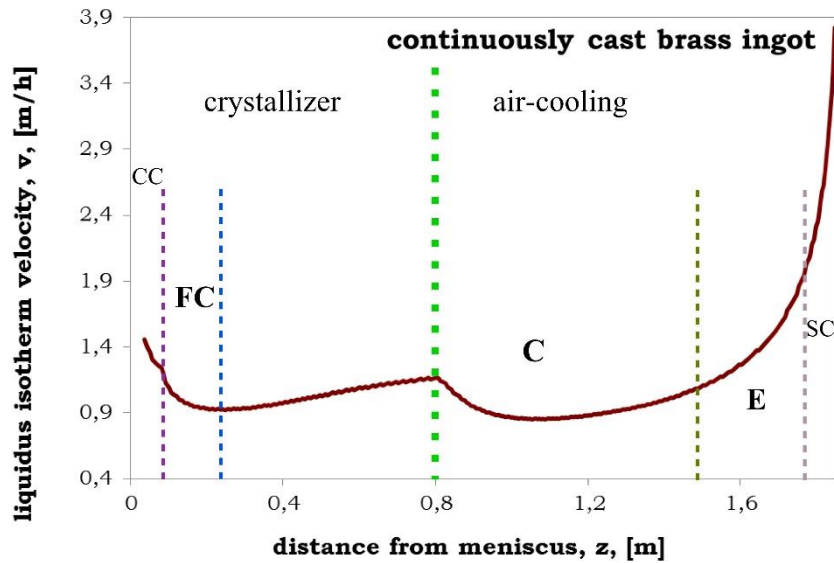
**Figure. 2c.** Velocity of the liquidus isotherm movement versus distance from meniscus; CCFCT – at the cusp of function, FCCT – within the  $v \cong const.$  - range, just before the beginning of the linear part, the CET – beginning at the end of the linear part, ESCT – at the beginning of linear part.



**Figure 3a.** Liquidus, and solidus isotherms situation in the map: ingot radius – distance from meniscus; CET – within the range defined by the tangent.

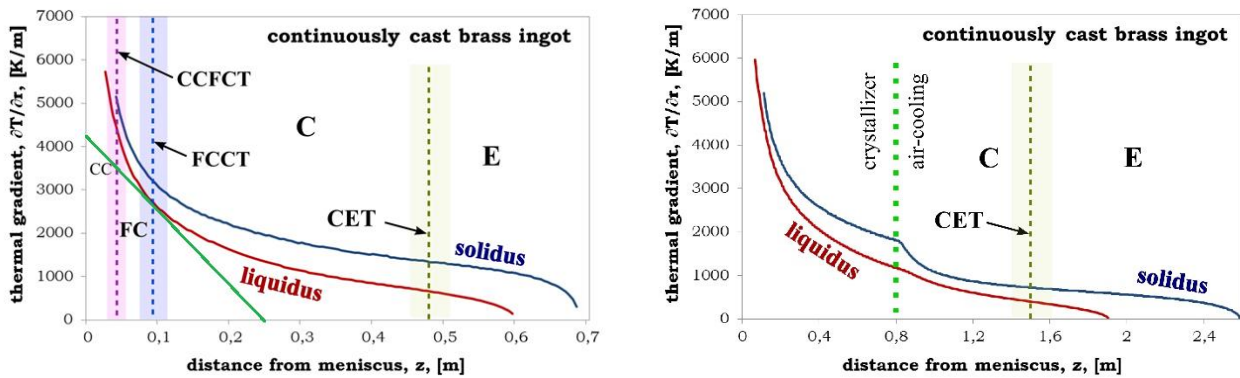


**Figure 3b.** Liquidus, and solidus isotherms localization in the map: ingot radius – solidification time; CET – within the range defined by the tangent.



**Figure 3c.** Velocity of the liquidus isotherm movement versus distance from meniscus; CCFCT – at the cusp of function, FCCT – within the  $v \cong const.$  - range, just before the beginning of the linear part, the CET – beginning at the end of the linear part, ESCT – at the beginning of linear part.

Additionally, an evolution of the thermal gradients for both pulling rates is shown in Fig. 4.



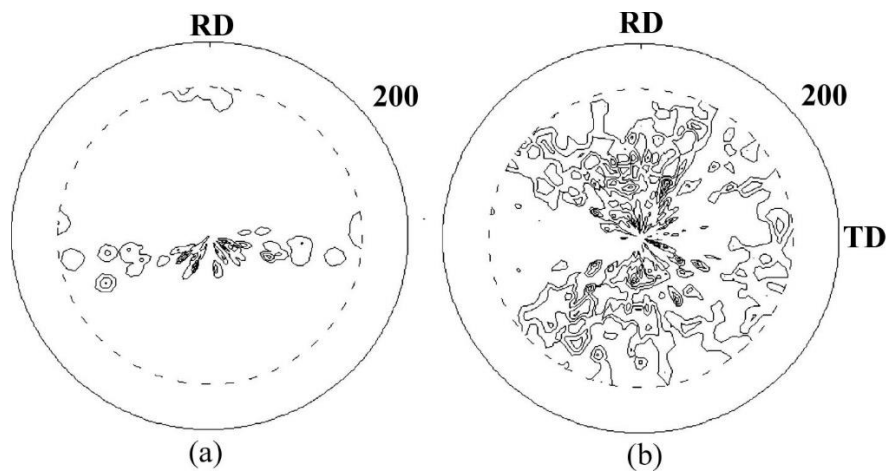
**Figure 4.** Evolution of the thermal gradient for the pulling rate equal to: a/ 90 mm/min, b/ 250 mm/min; CCFCT – at the end of linear part, FCCT – within the range defined by the tangent, CET – within the range defined by the point of inflection, ESCT – at the beginning of the linear part.

All the mathematically supposed structural transitions, Fig. 2, Fig. 3, and Fig.4, are well visible in the sections of the continuously cast brass ingot as produced in the industrial conditions, Fig. 5.



**Figure 5.** Structural zones as revealed on: a/ longitudinal section; b/ cross-section of the brass ingot.

Additionally, some pole figures were measured for two samples: the first containing the columnar structure and the second revealing the equiaxed structure only, Fig. 6.



**Figure 6.** Examples of the 200 - pole figures as measured for ingots containing: a/ columnar structure; b/ equiaxed structure; RD – rolling direction, TD – transfer direction.

### Concluding remarks

The thermal gradient is constant when the CET appears in the static ingot, Fig. 1. However, the CET appears sooner when the mold thickness is greater, Fig. 1b. So, the greater possibility of heat accumulation by the mold, the sooner CET appears.

The current mathematical prediction of structural transformations in an ingot seems informative and is able to reproduce all the structural zones visible in the continuously cast brass ingot, Fig. 5.

The brass ingot solidification is completed inside the crystallizer for the pulling rate equal to 90 mm/min, Fig. 2c. The brass ingot solidification is completed during the ingot's contact with air for the pulling rate equal to 250 mm/min, Fig. 3c.

The CET appears sooner when the pulling rate is equal to 90 mm/min, Fig. 2a, Fig. 2b, Fig. 2c and later when the pulling rate is equal to 250 mm/min, Fig. 3a, Fig. 3b, Fig. 3c. Other transitions (CCFCT, FCCT, ESCT) occur in the same manner in the relation to both imposed pulling rates.

The plastic deformation of the ingot containing columnar structure will be more difficult since limited numbers of the slip systems are available in this kind of ingot, Fig. 6a, whereas this limitation does not exist in the ingot containing the equiaxed structure (randomly oriented grains), Fig. 6b.

### Acknowledgement

The support was provided by the National Center for Research and Development in Poland under Grant No. PBS3/A5/52/2015.

### References

- [1] J.D. Hunt, Steady State Columnar / Equiaxed Growth of Dendrites and Eutectics, *Materials Science and Engineering* 65 (1984) 75-83.
- [2] M. Rappaz, Ch.A. Gandin, J.L. Desbiolles, Ph. Thevoz, Prediction of Grain Structures in Various Solidification Processes, *Metallurgical and Materials Transactions* 27A (1996) 695-705.
- [3] S. Louhenkilpi, J. Miettinen, L. Holappa, Simulation of Microstructure of As-Cast Steels in Continuous Casting, *ISIJ International* 46(6) (2006) 914-920.
- [4] S. McFadden, D.J. Browne, J. Banaszek, Prediction of the Formation of an Equiaxed Zone ahead of a Columnar Front in Binary Alloys Castings: Indirect and Direct Methods, *Materials Science Forum*, 508 (2006) 325-330.

- [5] M. Yamazaki, Y. Natsume, H. Harada, K. Ohsasa, Numerical Simulation of Solidification Structure Formation during Continuous Casting in Fe-0.7mass%C Alloy Using Cellular Automaton Method, *ISIJ International* 46(6) (2006) 903-908.
- [6] M.H. Wu, A. Ludwig, Using a Three-Phase Deterministic Model for the Columnar-to-Equiaxed Transition, *Metallurgical and Materials Transactions* 38A (2007) 1465-1475.
- [7] T. Telejko, Z. Malinowski, M. Rywotycki, Analysis of Heat Transfer and Fluid Flow in Continuous Steel Casting, *Archives of Metallurgy and Materials* 54 (2009) 837-844.
- [8] W.U. Mirihanage, H. Dai, H. Dong, D.J. Browne, Computational Modeling of Columnar to Equiaxed Structure Transition in Alloy Solidification, *Advanced Engineering Materials* 15(4) (2013) 216-229.
- [9] W. Wołczyński, A.A. Ivanova, P. Kwapisiński, E. Olejnik, Control of Structural Zones Formation and Hard Particles Motion in the Brass Ingots, *Archives of Metallurgy and Materials* 62(4) (2017) 2455-2461.
- [10] Information on: <http://www.kom-odlew.pl>
- [11] Information on: <http://www.cyfronet.krakow.pl>



**High concentrations at the final solidification of advanced steels:  
Thermodynamic evaluation of replicated “segregation-samples”  
by means of DTA/DSC-measurements**

Peter PRESOLY<sup>1</sup>, Michael BERNHARD<sup>1</sup>, Dali You<sup>1</sup>, Christian Bernhard<sup>1</sup>

<sup>1</sup> Chair of Ferrous Metallurgy, Montanuniversitaet Leoben, Franz-Josef-Strasse 18,  
8700 Leoben, Austria

[peter.presoly@unileoben.ac.at](mailto:peter.presoly@unileoben.ac.at)

**Keywords:** steel, microsegregation calculation, thermodynamic databases, DTA/DSC

**Abstract.** New demanding steel grades, complex and high alloyed grades show strong segregations during the final solidification. The validity of the used thermodynamic equilibrium data is essential for the calculation of the non-equilibrium solidus temperature, the solidification simulation (process control in continuous casting of steel, adjustment of soft reduction...) and also the prediction of non-metallic inclusion formation. However, it is still unclear whether the used thermodynamic data are valid for high concentrations at final stage of solidification.

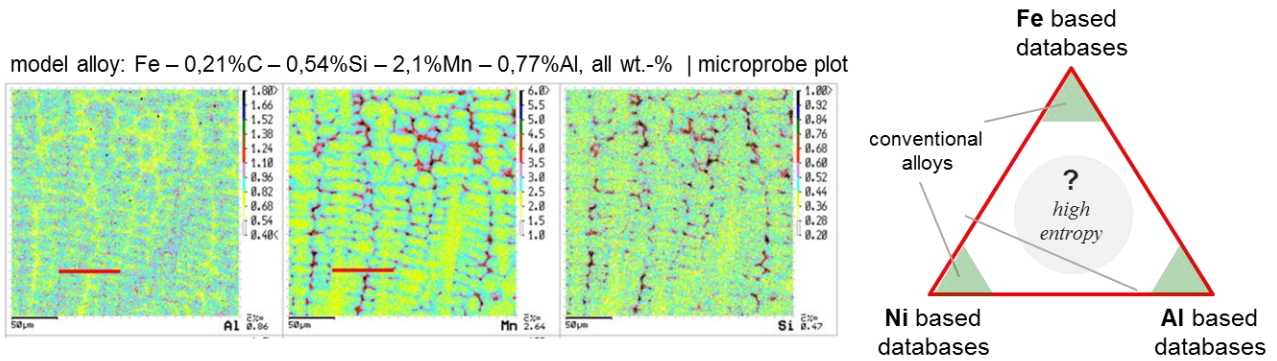
In order to verify the results of the microsegregation calculation and the validity of the used database, small laboratory melts were produced from these calculated concentrations and DTA/DSC measurements were performed to determine the equilibrium liquidus temperature. First results show good correlations between calculations and “measured segregation” for low alloyed steel grades. For high alloyed Mn-steels (Mn >6wt.-%) the performed investigations show clear deviations ( $T_{\text{Liquid}} > 10^{\circ}\text{C}$ ) at higher fraction of solid (fs). This approach of evaluating microsegregation models by using replicated “segregation-samples”, the thermal analysis and the determination of the equilibrium temperatures seems to be a promising method.

## Introduction and Motivation

Coupling thermodynamic databases with microsegregation and solidification models allows to perform the local equilibria calculation at each calculation step. Nowadays, modern steel databases (CALPHAD method) enable quite accurate calculation for the transformation temperatures of high alloyed new steels, such as e.g. Mn-steels, Dual Phase-steels, TRIP and TWIP grades. In this study an in-house developed ChemApp (FactSage) based microsegregation model (You, D. [1, 2]) is used, which can use different thermodynamic databases (FactSage, SGTE, private). At initial stage of solidification the use of different thermodynamic databases leads to similar predictions of temperatures and phase transformations. However, at high solid fraction the final result varies with the databases since the solute concentration often exceeds the validity range.

Fig. 1 (left) illustrates a microprobe plot analysis of a model alloy with a composition similar to a common TRIP steel grade (without micro alloying elements). The Mn-plot clearly visualizes primary and secondary dendrite structures drawn by high Mn enrichments (from 2 to 6 wt.-% Mn ~ factor 3x). As in the present study the investigation of manganese is of interest a typical medium-Mn steel grade with 6 wt.-%Mn was chosen. For such medium and high alloyed grades, situations with quite high solute enrichments can occur, which exceed the range of validity of the used thermodynamic database. Every thermodynamic database (e.g. for Fe-, Ni-, Al-based alloy) is optimized for one corner where the influence of the other alloying elements is taken into account. The extrapolation of different specialized databases is quite challenging.

As visualized in Fig. 1 (right), it leads to areas, where no individual database is actually valid. Even though these are still no high-entropy alloys (HEAs), high concentrations at the final solidification of advanced steels may correspond to these unknown areas (still Fe-based alloys).

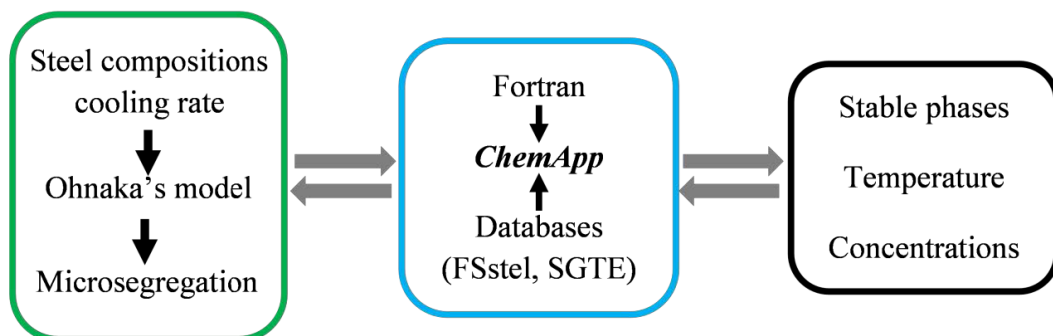


**Figure 1.** Microprobe analysis to visualize the concentration distributions (left [1]) and situation of different specialized thermodynamic databases (right [3]).

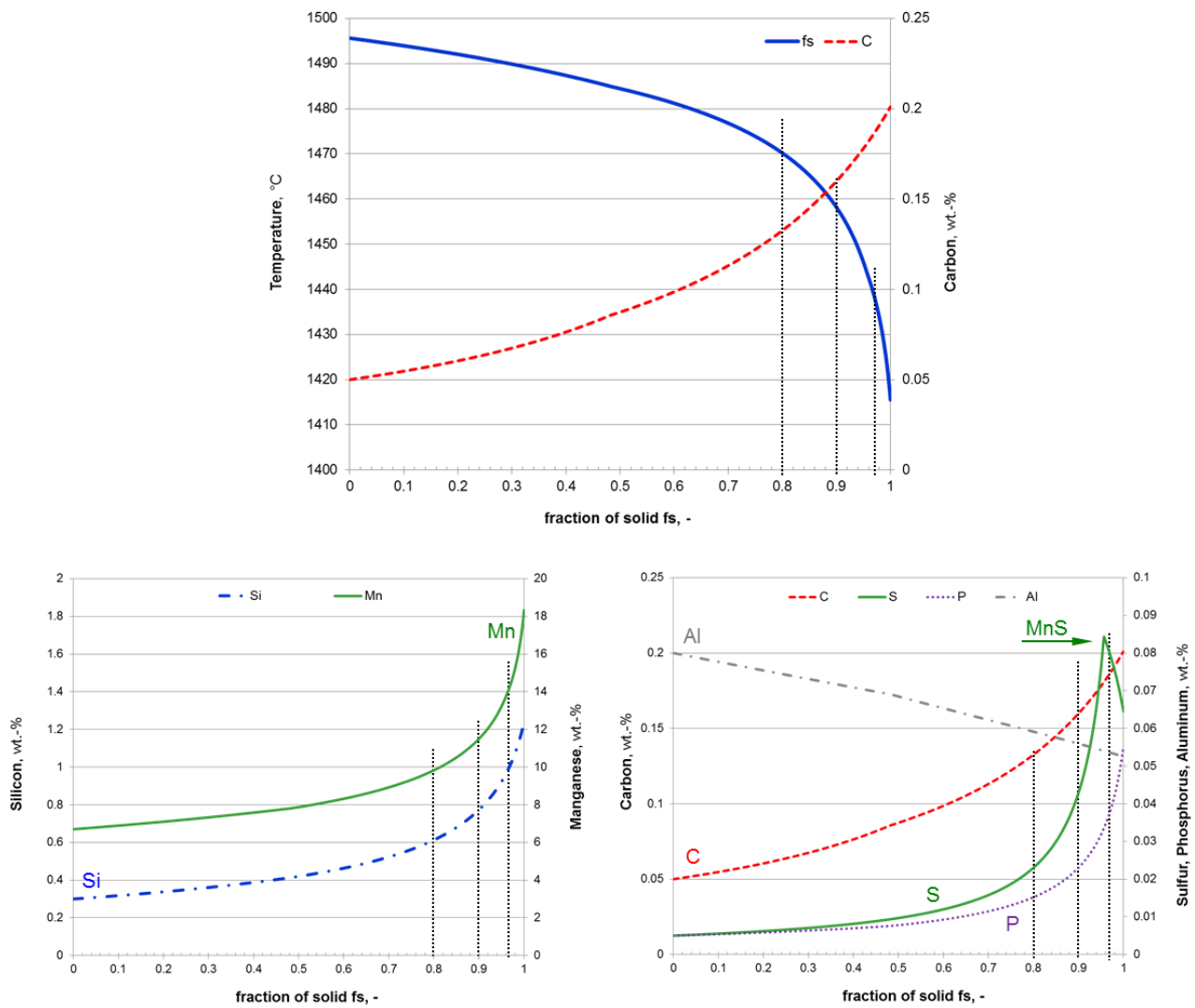
### Microsegregation calculation of a medium-Mn steel grade by ChemApp

A microsegregation model with local partition coefficients and temperature-dependent diffusion coefficients based on the model of Ohnaka [4] is proposed. In this model, multicomponent alloy effects and precipitations are considered, and the peritectic reaction can be indicated using the thermodynamic library ChemApp, visualized in Fig. 2 [1]. ChemApp is a software developed by GTT Technologies, Herzogenrath, Germany to perform thermodynamic equilibrium calculations. The secondary dendrite arm spacing is estimated by the local solidification time and initial carbon content. The full model was validated by comparing the results to calculations of other models and measured data [2].

The selected steel is a medium-Mn grade, with a chemical composition of Fe - 0.05%C – 0.3%Si – 6.7%Mn – 0.08%Al (identical to the work of [5]) and also with 0.005%P and 0.005%S (all wt.-%) which are typical values of trace elements for technical alloys. The calculation results, based on the thermodynamic database FSstel (FSstel53) from FactSage 7.0, are visualized in Fig. 2 and the chemical analyses for 4 interesting solidification stages are compiled in Tab. 1.



**Figure 2.** Schematic of the microsegregation model.



**Figure 3.** Results of the microsegregation calculation.

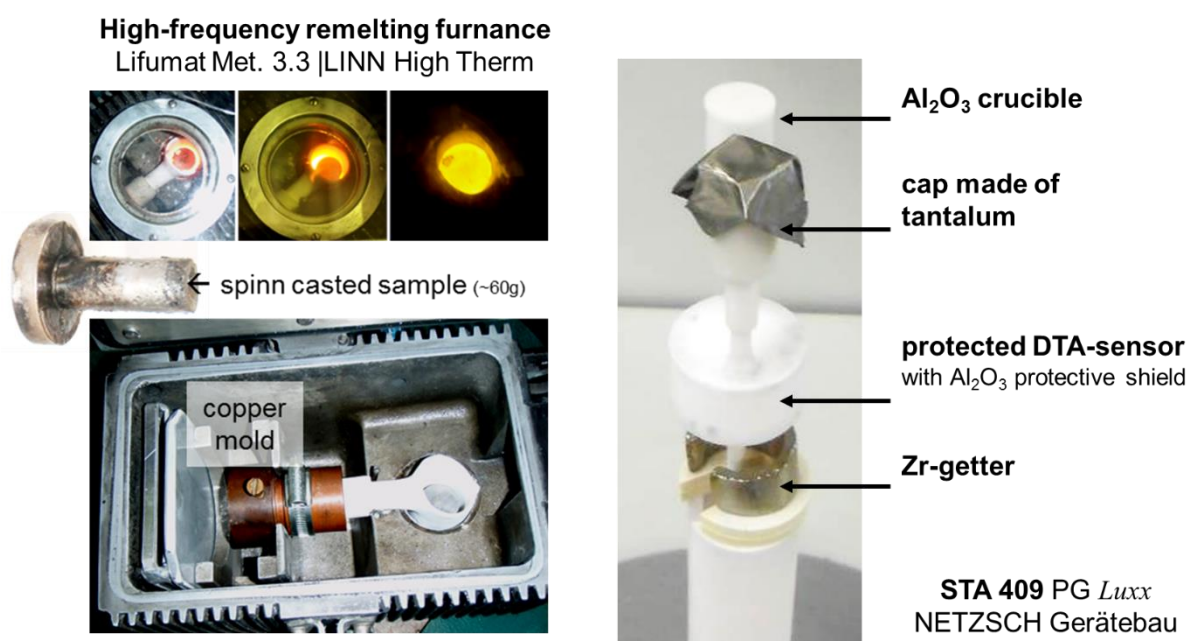
**Table 1:** Chemical composition of the initial concentration and the microsegregation calculation of the investigated medium-Mn steel grade.

Medium-Mn steel grade		alloying elements in wt.-%, rest Fe						name of the sample
		C	Si	Mn	P	S	Al	
initial concentration		0.05	0.3	6.7	0.005	0.005	0.08	
fraction of solid	fs= 0.80	<b>0.133</b>	<b>0.61</b>	<b>9.83</b>	<b>0.015</b>	<b>0.023</b>	<b>0.059</b>	Med-Mn_80
	fs= 0.90	<b>0.160</b>	<b>0.77</b>	<b>11.50</b>	<b>0.023</b>	<b>0.043</b>	<b>0.056</b>	Med-Mn_90
	fs= 0.97	<b>0.186</b>	<b>1.01</b>	<b>14.40</b>	<b>0.038</b>	<b>0.080</b>	<b>0.054</b>	Med-Mn_97
	fs= 1.00	0.201	1.24	18.33	0.055	0.065	0.053	-

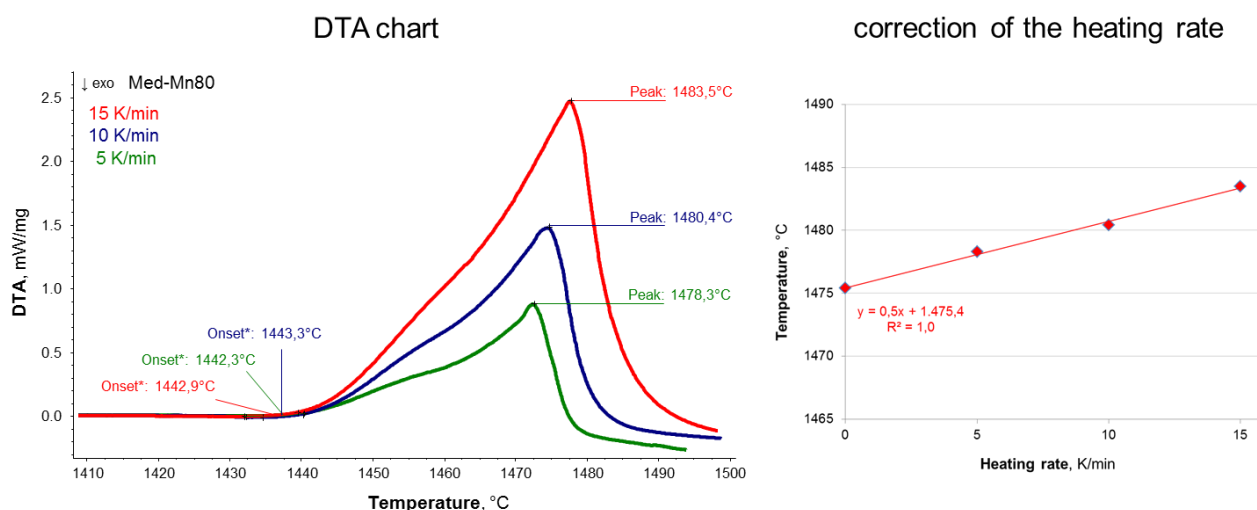
The results shown in Fig. 3 are based on a cooling rate of 1 K/s. At first the temperature of the interdendritic melt versus the fraction of solid ( $f_s$ ) is shown and then the concentration profiles of all elements in the residual liquid dependent on  $f_s$  are plotted. All elements except aluminum show strong positive segregations. The decreasing sulphur concentration close to the end of solidification can be attributed to MnS formation. The last 20% of solidification ( $f_s = 0.8$  to 1) are of particular interest, as in this region: Hot tear segregations [6], nonmetallic inclusion (e.g. MnS, oxides, nitrides) and primary carbide formation can occur. In order to verify the results of the microsegregation calculation and the validity of the used database, the concentration enrichments of selected steels were calculated at  $f_s = 0.8$ ,  $f_s = 0.9$  and  $f_s = 0.97$ , summarized in Table 1.

## Test Program – experimental work

Laboratory melts (Med-Mn\_80 / \_90 / \_97) were produced from these calculated concentrations by means of inductive melting and centrifugal spin-casting in an alumina crucible under argon protection atmosphere, visualized in Fig. 4 (left). The replicated “segregation-samples”, which are homogeneous in concentration due to the rapid solidification, were chemically analyzed (optical emission spectrometer and RFA) and small samples were produced. As the “segregation-samples” contain high amounts of manganese, which tends to evaporate and contaminate the sensitive platinum DSC sensors, a special “protective DTA” method [7] with closed crucibles was used to guarantee secured measurements without Mn-contamination of the Pt-thermocouples, visualized in Fig. 4 (right). Using a new sample for each experiment a heating rate variation (5-10-15 K/min) was performed in order to determine the equilibrium liquidus temperature with a reverse calculation to 0 K/min, visualized in Fig. 5. The good linear correlation of the liquidus peak with the different heating rates is an important quality criterion to confirm that no uncontrolled manganese evaporation takes place.

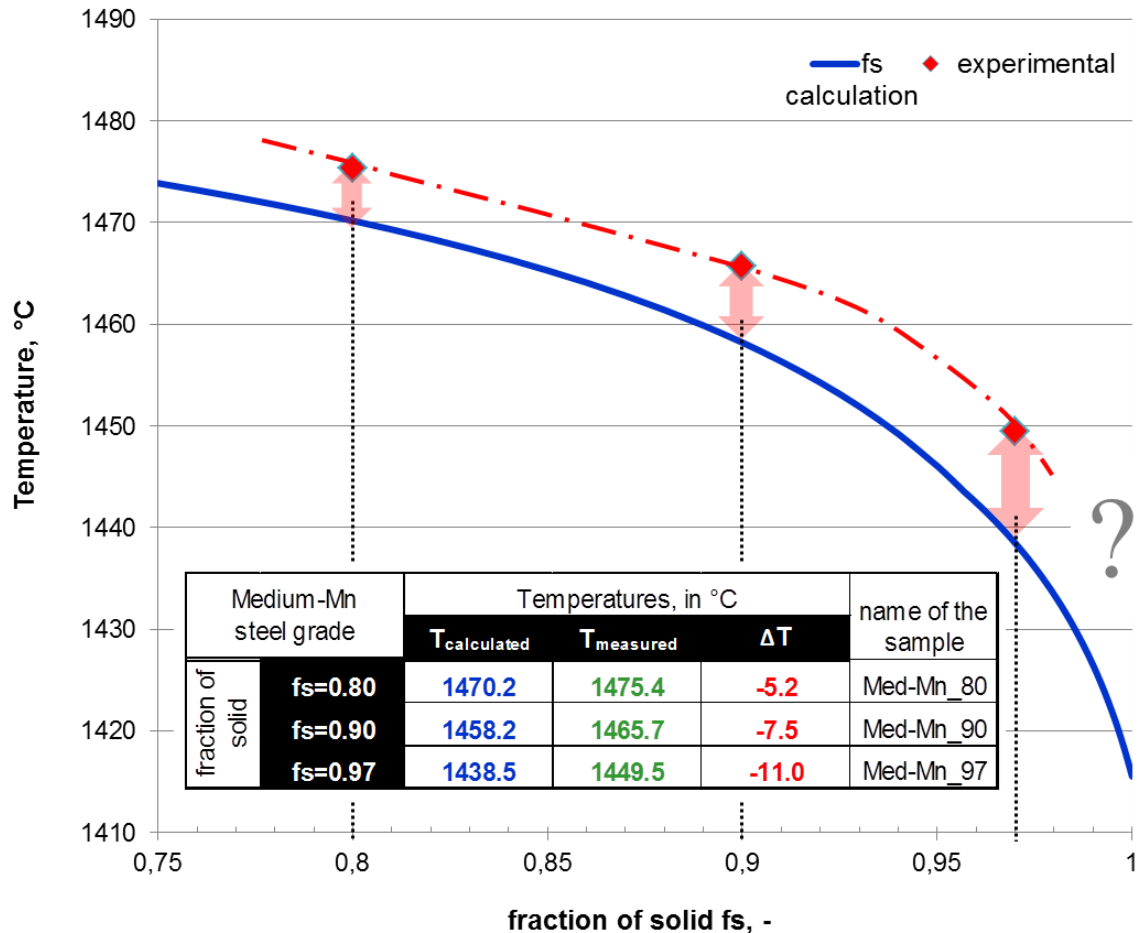


**Figure 4.** Alloy production and DTA-sensor.



**Figure 5.** DTA measurements and equilibrium calculation.

The measured liquidus temperatures were compared with the calculated solidification temperatures at corresponding solid fractions ( $f_s$ ). Investigations of the first alloy (Med-Mn\_80) show quite good correlation with the calculated temperature for  $f_s = 0.8$ , with a deviation of only  $-5.2^\circ\text{C}$ . With increasing solid fraction and concentrations, the deviation becomes higher, compiled in Fig. 6. The deviation of more than  $-10^\circ\text{C}$  for  $T_{\text{Liquid}}$  at the highest alloyed sample is significant, since normally the liquidus temperature can be calculated very accurately. This observation indicates that the used database gradually becomes invalid. The dash-dotted line in Fig. 6 shows a possible path of the temperature of the interdendritic melt versus the fraction of solid ( $f_s$ ), whereat the situation for the last 3% of residual melt is still unclear (even higher deviations of  $-20^\circ\text{C}$  might be possible).



**Figure 6.** Experimental results versus calculated.

## Summary and outlook

The present methodology of evaluating microsegregation calculation by using replicated “segregation-samples”, the thermal analysis and the determination of the equilibrium temperatures seems to be a promising approach, not only for Fe-basis alloys. Especially for high alloyed grades, the range of validity of the used thermodynamic database can be exceeded. If a higher deviation is observed, the microsegregation and also the solidification calculation seem to be inaccurate. The use of validated, or even individual optimized thermodynamic databases, as already proposed [8], is of highest importance – especially for new materials.

However, the presented method is limited and focuses only on the database, so no statements can be made about the algorithm and the parameters of the microsegregation model or its used diffusion data. This means that the transformation temperatures for the calculated compositions can be checked, but not whether the calculated concentrations really correspond to reality.

A promising method to evaluate microsegregation models is presented by Bernhard M. entitled: *“An alternative approach for the experimental verification of microsegregation models using an in-situ hot tensile test”*.

## Acknowledgments

Financial support by the Austrian Federal Government (in particular from Bundesministerium für Verkehr, Innovation und Technologie and Bundesministerium für Wirtschaft, Familie und Jugend) represented by Österreichische Forschungsförderungsgesellschaft mbH and the Styrian and the Tyrolean Provincial Government, represented by Steirische Wirtschaftsförderungsgesellschaft mbH and Standortagentur Tirol, within the framework of the COMET Funding Programme is gratefully acknowledged. This work is part of the ongoing K2-MPPE project P3.1 “SmartCast”.

## Literature References

- [1] You, D., C. Bernhard, S. Michelic, G. Wieser and P. Presoly, On the modelling of microsegregation in steels involving thermodynamic databases, IOP Conf. Ser.: Mater. Sci. Eng. 119 (2016), 12027.
- [2] You, D., C. Bernhard, G. Wieser and S. Michelic, Microsegregation Model with Local Equilibrium Partition Coefficients During Solidification of Steels, Steel Research International 87 (2016), 7, 840–849.
- [3] Ye, Y.F., Q. Wang, J. Lu, C.T. Liu and Y. Yang, High-entropy alloy: Challenges and prospects, Materials Today 19 (2016), 6, 349–362.
- [4] Ohnaka, I., Mathematical analysis of solute redistribution during solidification with diffusion in solid phase, ISIJ Int. 26 (1986), 12, 1045–1051.
- [5] Han, J. and Y.-K. Lee, The effects of the heating rate on the reverse transformation mechanism and the phase stability of reverted austenite in medium Mn steels, Acta Materialia 67 (2014), 354–361.
- [6] Pierer, R. and Bernhard, C., The nature of internal defects in continuously cast steel and their impact on final product quality, AIST Proceedings, Pittsburgh, USA, 2010, 193-203.
- [7] Zhuang, C.-l., J.-h. Liu, C. Bernhard and P. Presoly, Analysis of Solidification of High Manganese Steels Using Improved Differential Thermal Analysis Method, Journal of Iron and Steel Research, International 22 (2015), 8, 709–714.
- [8] Presoly, P., J. Six and C. Bernhard, Thermodynamic optimization of individual steel database by means of systematic DSC measurements according the CALPHAD approach, IOP Conference Series: Materials Science and Engineering 119 (2016), 1, 12013.

# Discussion on possible solidification during SEN clogging in steel continuous casting

Hadi BARATI<sup>1,2</sup>, Menghuai WU<sup>1</sup>, Abdellah Kharicha<sup>1</sup>, Andreas Ludwig<sup>1</sup>

<sup>1</sup>Chair for Modeling and Simulation of Metallurgical Processes, Department of Metallurgy, Montanuniversität, Franz-Josef Street 18, 8700 Leoben, Austria

<sup>2</sup>K1-MET, Franz-Josef Street 18, 8700 Leoben, Austria

[menghuai.wu@unileoben.ac.at](mailto:menghuai.wu@unileoben.ac.at)

**Keywords:** clogging, non-metallic inclusion, solidification, steel casting.

**Abstract.** Molten steel is conducted through the submerged entry nozzle (SEN) into the mold during the continuous casting process. Accretion inside the SEN, called clogging, is one of the major problems in continuous casting of steel. In addition to the mechanisms of attachment of de-oxidation and re-oxidation products ( $\text{Al}_2\text{O}_3$  particles) on the SEN wall, chemical reactions of the melt with the refractory material of SEN, precipitation of alumina, etc., solidification of the steel melt on the SEN wall is also considered as a possible mechanism for clogging. A transient model considering two-way coupling between clog growth (due to particle deposition) and fluid flow is upgraded to a non-isothermal model; solidification of steel during the SEN clogging in continuous casting is investigated. The results show that solidification would not occur in a SEN if the molten steel has sufficient superheat and it flows with relatively high speed through the SEN. In contrast, clogging promotes the solidification inside the clog.

## Introduction

Clogging of submerged entry nozzle (SEN) is a problematic phenomenon in steel continuous casting. As the molten steel is conducted through the SEN into the continuous casting machine, the flow path in SEN may be gradually blocked, resulting in various casting defects or operation disruptions. In Fig. 1(a), a schematic representation of SEN and clogging in steel continuous casting is presented. Clogging leads to decreased productivity of the casting, low quality of the final product, and enhanced costs. The mechanisms of clogging can be summarized in five categories: (1) attachment of de-oxidation and re-oxidation products on the SEN wall [1-3]; (2) thermochemical reactions in the melt at the SEN wall leading to in-situ formation of oxide products [4,5]; (3) negative pressure drawing oxygen through the SEN refractory pores into the inner SEN wall and reaction of oxygen with the steel melt to form oxides [6]; (4) temperature drop of the melt leading to lower solubility of oxygen in the steel melt and resulting in precipitation of alumina at SEN-steel interface [7,8]; and (5) possible solidification of the steel melt on the SEN wall [9,10].

The last mechanism, i.e. solidification of steel on the SEN wall, cannot be counted as a main mechanism, but it may promote the clogging. If the melt superheat is low, and the heat loss from the SEN wall is high, the steel may freeze on the SEN wall. Rackers and Thomas [9] stated that clogging material is a porous network of alumina (built up alumina particles). This alumina network individually is very weak and could be easily broken by the touch of finger. However, when an alumina network forms on the SEN wall, the solidified steel in the pores reinforces the whole clogging region. Therefore, the clogging material can withstand against the melt flow and cannot be washed away by the flow drag force. It is also concluded that solidification within the SEN will increase clogging rate. The practical evidence in steel plant [10] showed that increasing SEN preheating temperature reduces the deposition within SEN. It means that SEN preheating prevents or postpones solidification of steel within the clogging material. Therefore, the performance of the SEN is improved. Moreover, post-mortem microscopic analysis of clogging materials always shows solidified steel filling clog networks [11]. However, it is not clarified that the solidification of steel



has occurred during the casting process or the steel inside the clogging material was liquid and has solidified after sampling.

Theoretically, it is difficult to imagine that solidification would occur in a SEN because the steel melt temperature is around 15-20 °C higher than the liquidus temperature of the steel alloy and the flow velocity is ~ 1 m/s. The current work is a preliminary numerical study to find the answer of the main question: can solidification occur and lead to clogging in SEN?

## Model

A transient model for clogging has been developed by the current authors [12]. The original model is for isothermal conditions including different steps of clogging: transport of the particles to the wall; interactions between wall, fluid, and particles; growth of clogging material (also named *clog*) due to the particle deposition. In this model, clog is considered as a porous medium made of alumina network and steel melt fills the network pores. In the current study, the model is upgraded to a non-isothermal model and solidification of steel in the clog is considered. An enthalpy based solidification model of mixture continuum is implemented.

$$\frac{\partial}{\partial t}(\rho h) + \nabla \cdot (\rho \bar{u} h) = \nabla \cdot (\alpha \nabla T) + \rho L \frac{\partial f_s}{\partial t} \quad (1)$$

$\rho$ ,  $h$ ,  $\bar{u}$  and  $T$  are density, enthalpy, velocity, and temperature, respectively.  $\alpha$  stands for thermal conductivity.  $L$  is latent heat of solidification and  $f_s$  is the volume fraction of solid steel in a control volume. In Eq. 1, mixture values of quantities are considered. A control volume comprises three components: liquid, solid, and particle. Therefore,

$$f_s + f_\ell + f_p = 1. \quad (2)$$

In the clogging model [12], a drag force of the clog on the melt flow is applied. It is assumed that the clog is a porous medium with open pores. So, the source term of clogging materials in the momentum and turbulence equations is defined as

$$S_{\text{clog}, \phi} = \mu \frac{108(\bar{f}_p^{1/3} - \bar{f}_p)}{(1 - \bar{f}_p)(1 - \bar{f}_p^{1/3})} \frac{f_{\text{clog}}^n}{D_{\text{pore}}^2} \phi, \quad (3)$$

where  $\bar{f}_p$  is the average particle volume fraction;  $D_{\text{pore}}$  is the diameter of pores;  $f_{\text{clog}} = f_p / \bar{f}_p$  is volume fraction of clog in a control volume; and  $n$  is an interpolation correction power.

By implementation of solidification, the drag of the solidifying mushy zone on the melt has to be considered as well. Hence, a corresponding source term is defined for the mushy zone.

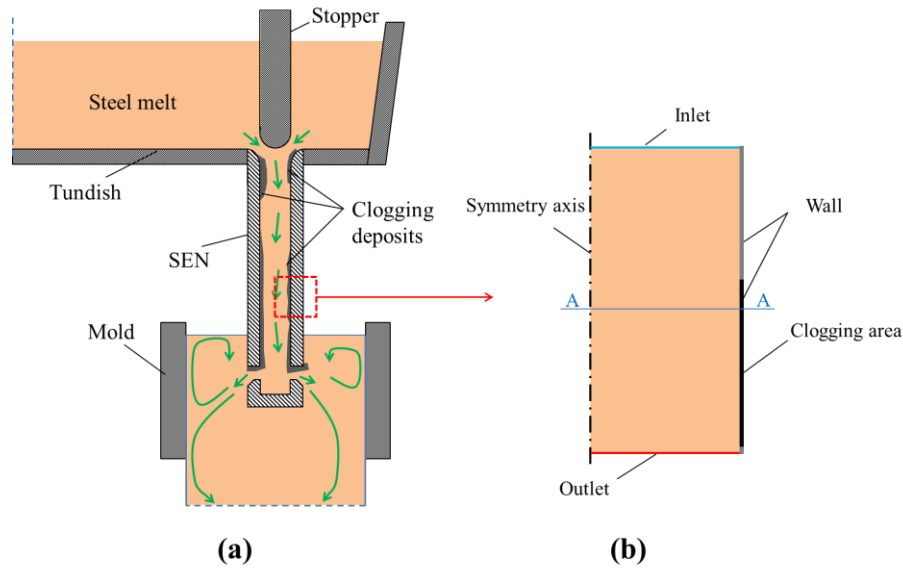
$$S_{\text{solidification}, \phi} = \frac{(1 - f_\ell)^2}{f_\ell^3} \frac{\mu}{6 \times 10^{-4} \lambda_1^2} \phi, \quad (4)$$

where  $\lambda_1$  is the primary dendrite arm spacing. In Eq. 3 and Eq. 4,  $\phi$  can be velocity, kinetic turbulence energy, and its dissipation rate.

The applied source term is an average of the clog and the solidification terms according to the particle volume fraction ( $f_p$ ),

$$S_\phi = f_p S_{\text{clog}, \phi} + (1 - f_p) S_{\text{solidification}, \phi}. \quad (5)$$

Clogging and solidification in a vertical tube relating to the SEN size is simulated. For the sake of calculation time, 2D axisymmetric conditions are considered, as shown in Fig. 1(b). The dimensions, boundary conditions, and physical properties of materials are summarized in Table 1. The heat transfer coefficient of wall is an efficient value including heat conduction through SEN wall (with ~50 mm thickness) and heat convection by air on the outer side of the SEN.



**Figure 1.** (a) Schematic presentation of continuous casting machine, (b) 2D-axisymmetric domain and boundary conditions used in the current simulation.

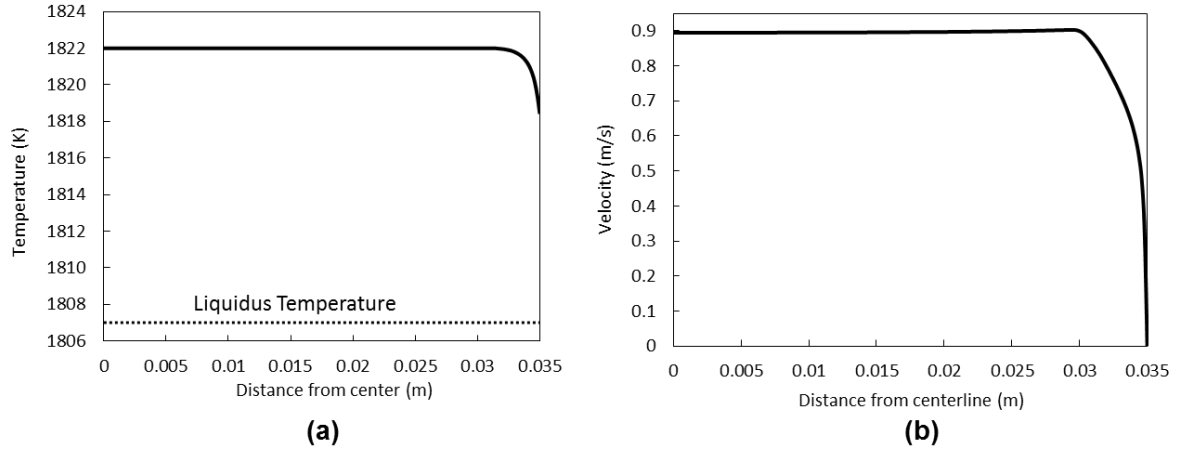
**Table 1.** The dimensions, boundary conditions, and physical properties of materials

Dimensions of domain		Physical properties	
Radius	20 mm	Steel	
Height	60 mm	Density	7020 kg/m <sup>3</sup>
Boundary conditions		Viscosity	0.0052 kg/(m.s)
Inlet		Specific heat	700 J/(Kg.K)
Velocity	0.85 m/s	Thermal conductivity	26 W/(m.K)
Temperature	1822 K	Liquidus temperature	1807 K
Turbulence kinetic energy	0.00078 m <sup>2</sup> /s <sup>2</sup>	Solidus Temperature	1780 K
Specific dissipation rate ( $\omega$ )	175.76 1/s	Latent heat	243 kJ/kg
Particle mass injection rate	0.0374 kg/s	Alumina	
Outlet		Density	3700 kg/m <sup>3</sup>
Pressure-outlet	-	Specific heat	880 J/(Kg.K)
Wall		Thermal conductivity	35 W/(m.K)
No-slip	-	Particle diameter	10 $\mu$ m
Heat transfer coefficient	100 W/(m <sup>2</sup> .K)	$\bar{f}_p$	0.55
Free stream temperature	300 K	$D_{pore}$	20 $\mu$ m

The turbulent flow is calculated by the shear stress transport (SST)  $k-\omega$  model using commercial CFD code ANSYS-FLUENT. Particle tracking is performed by Discrete Phase Model (DPM). User-defined functions (UDFs) are used for considering the particle deposition, the clog growth, and the melt solidification.

## Results and Discussion

The steady state temperature and velocity profiles along a horizontal line, when the no clogging occurs, are shown in Fig. 2. This result shows that temperature drop near the wall is about 4 K; the wall temperature is still 11 K above the liquidus temperature. Since the flow velocity is high enough to wash the cold melt close to the wall, solidification never happens on the SEN wall.



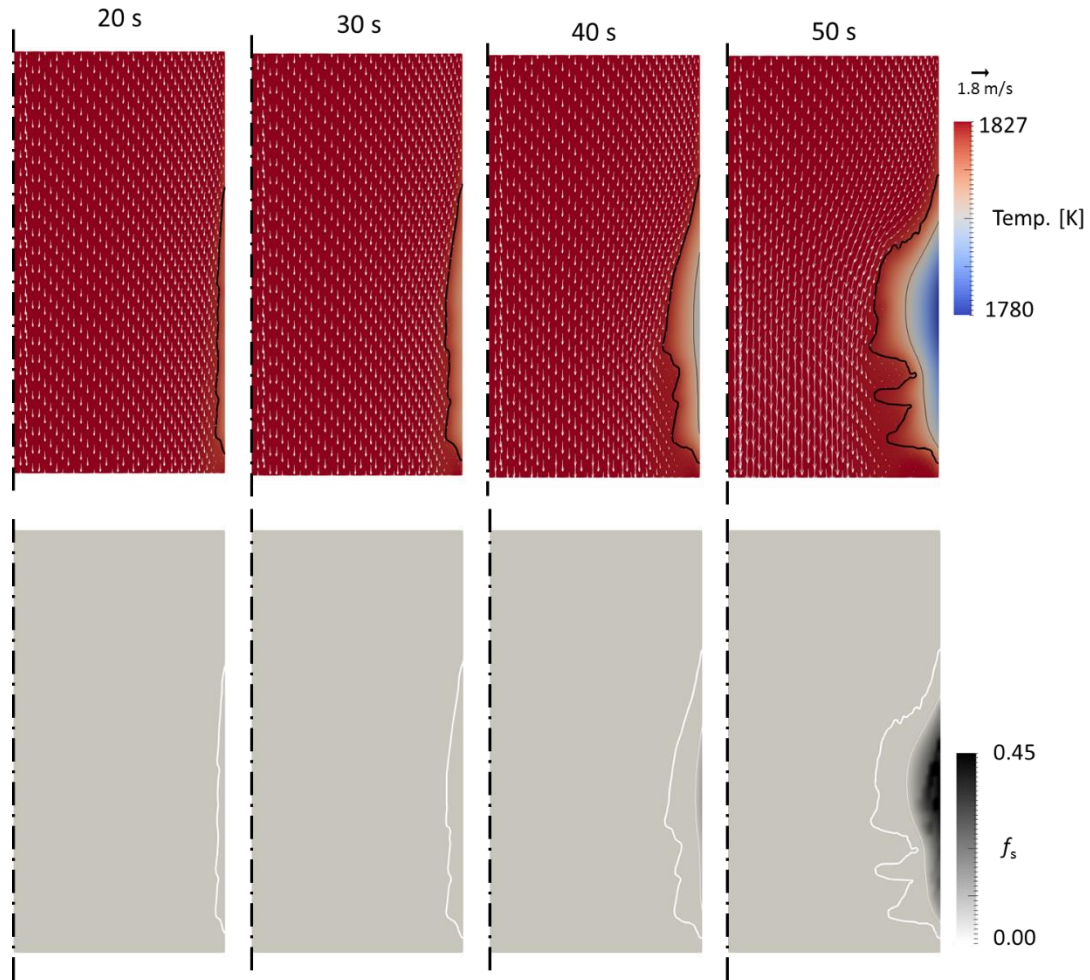
**Figure 2.** Steady state temperature (a) and velocity (b) profiles along AA line shown in Fig. 1(b).

In the practical conditions of continuous casting, clogging may happen after several hours. Therefore, simulation of real conditions is not feasible due to the too long calculation time for clogging. To overcome this problem, an exaggerated number of particles is injected in the computational domain to see the clog growth in a shorter time. Hence, the clog growth rate in the current simulation is faster than that in reality. A rough estimation shows that the real injection rate of alumina particles would be around  $8.15 \times 10^{-5}$  kg/s (particle diameter is 10  $\mu\text{m}$ ). In the current simulation, the particle injection rate is set to 0.0374 kg/s.

In Fig. 3, the evolution of clogging is depicted. On the top row, the flow and temperature fields are shown. The thick and thin solid lines represent the clog front and the liquidus isoline of the melt, respectively. On the bottom row, the solid fraction is illustrated. Note that in the clog, the average volume fraction of particle ( $\bar{f}_p$ ) is 0.55. According to Eq. 2, the maximum value of  $f_s$  can be 0.45, when all of the steel melt in a control volume solidified. The results show that the clog grows from the wall due to the continuous deposition of particles. The clog growth changes the flow field; consequently, the convective heat transfer by the fluid flow is changed. Therefore, the temperature field is adjusted by the clog growth. Due to the very low velocity of the melt in the pores of the clog, the temperature in this region decreases.

After 30, the temperature in the clog is still higher than liquidus temperature. At 40 s, a layer of steel solidifies in the clog. In Fig. 3, the liquidus temperature actually indicates the position of solidification front, considered in the simulation. At 50 s, the clog thickness increases significantly; therefore, a noticeable solidified metal shell forms in the clog. The results at 40 and 50 s declare that there always is a gap between the clog front and the solidification front (liquidus temperature). One can conclude that solidification during clogging is a consequence of weak melt flow in the clog pores. However, solidification in SEN cannot promote the clog growth because the clog front always is in a temperature close to the bulk temperature and far from the liquidus temperature.

As demonstrated in [12] and as can be seen in Fig. 3, clogging starts with covering of the nozzle wall by deposition of the particles (20 and 30 s). The growth of the clog front is not smooth. After a while, some bulges grow at different positions (40 and 50 s). Finally, bulges turn into branches. By impingement of the branches, the flow passage is blocked (this step is not shown in Fig. 3). When the bulges form on the clog front, the melt flow through the bulges is weakened. Therefore, the heating of the clog front by melt flow decreases. In this case (like 50 s), solidification front can be closer to the clog front than when the clog front is almost smooth (like 30 s).



**Figure 3.** Evolution of clogging and its interaction with solidification. The temperature and flow fields are shown on the top row and the solid fraction of steel is indicated on the bottom row. The thick and thin solid lines represent the clog front and liquidus iseline (indicating solidification front), respectively.

## Conclusions

A transient model considering two-way coupling between clog growth (due to particle deposition) and fluid flow is upgraded to a non-isothermal model. Solidification of steel during the SEN clogging in continuous casting is investigated.

- Before initiation of clogging, solidification of steel on the SEN wall is not possible due to the high velocity and high superheat of the melt in the SEN.
- Clogging promotes the solidification inside the clog.

## Acknowledgments

The authors gratefully acknowledge the funding support of K1-MET, metallurgical competence center. The research program of the K1-MET competence center is supported by COMET (Competence Center for Excellent Technologies), the Austrian program for competence centers. COMET is funded by the Federal Ministry for Transport, Innovation and Technology, the Federal Ministry for Science, Research and Economy, the provinces of Upper Austria, Tyrol and Styria as well as the Styrian Business Promotion Agency (SFG).

## References

- [1] Y. Miki, H. Kitaoka, T. Sakuraya, T. Fujii, Mechanism for separating inclusions from molten steel stirred with a rotating magnetic field, *ISIJ Int.* 32 (1992) 142-149.
- [2] L. Zhang, B.G. Thomas, State of the art in the control of inclusions during steel ingot casting, *Metall. Mater. Trans. B* 37 (2006) 733-761.
- [3] S. Basu, S.K. Choudhary, N.U. Girase, Nozzle clogging behaviour of Ti-bearing Al-killed ultra low carbon steel, *ISIJ Int.* 44 (2004) 1653-1660.
- [4] K. Sasai, Y. Mizukami, Reaction mechanism between alumina graphite immersion nozzle and low carbon steel, *ISIJ Int.* 34 (1994) 802-809.
- [5] Y. Vermeulen, B. Coletti, B. Blanpain, P. Wollants, J. Vleugels, Material evaluation to prevent nozzle clogging during continuous casting of Al killed steels, *ISIJ Int.* 42 (2002) 1234-1240.
- [6] P.M. Benson, Q.K. Robinson, C. Dumazeau, New technique for the prevention of alumina build-up in submerged entry nozzles for continuous casting, *Unitecr'93 Congr. Refract. New World Econ. Proc. Conf. Sao Paulo* (1993).
- [7] G.C. Duderstadt, R.K. Iyengar, J.M. Matesa, Tundish nozzle blockage in continuous casting, *JOM* 20 (1968) 89-94.
- [8] J.W. Farrell, D.C. Hilty, Steel flow through nozzles: influence of deoxidizers, *Electr. Furn. Proc.* (1971) 31-46.
- [9] K.G. Rackers, B.G. Thomas, Clogging in continuous casting nozzles, *78th Steelmak. Conf. Proc.* (1995) 723-734.
- [10] S. Rödl, H. Schuster, S. Ekerot, G. Xia, N. Veneri, F. Ferro, S. Baragiola, P. Rossi, S. Fera, V. Colla, et al., New Strategies for Clogging Prevention for Improved Productivity and Steel Quality (2008).
- [11] D. Janis, A. Karasev, R. Inoue, P.G. Jönsson, A study of cluster characteristics in liquid stainless steel and in a clogged nozzle, *Steel Res. Int.* 86 (2015) 1271-1278.
- [12] H. Barati, M. Wu, A. Kharicha, A. Ludwig, A transient model for nozzle clogging, *Powder Technol.* 329 (2018) 181-198.

# The Melt Cleaning Efficiency of Fluxes with Different Physical and Chemical Properties

Gábor GYARMATI<sup>1, a</sup>, György FEGYVERNEKI<sup>2</sup>, Tamás MENDE<sup>3</sup> and Monika TOKÁR<sup>4, b</sup>

<sup>1,2,4</sup>University of Miskolc, Foundry Institute, Miskolc-Egyetemváros 3515, Hungary

<sup>3</sup>University of Miskolc, Institute of Physical Metallurgy, Metalforming and Nanotechnology, Miskolc-Egyetemváros 3515, Hungary

<sup>a</sup>gygabor007@gmail.com, <sup>b</sup>monika.tokar@uni-miskolc.hu

**Keywords:** Aluminum alloy, Inclusions, Fluxes, Melt treatment, Melt quality

**Abstract.** The presence of inclusions such as oxides, carbides or refractory particles can be harmful to the mechanical and surface characteristics of castings. Inclusion-rich metals result in lower fluidity and feeding capability during casting. Nowadays, solid fluxes are widely used in foundries in order to reduce the inclusion content of aluminium melts. In this study, the effect of four different fluxes on the melt quality was studied. First, the inclusion content of the flux-treated melt, and then the properties of the fluxes (i.e. chemical composition and melting temperature) were examined.

## Introduction

Inclusions are discontinuities of the material which are non-metallic or sometimes intermetallic phases embedded in a metallic matrix [1]. Inclusions can occur in the form of solid particles, films or liquid droplets in the molten alloys [2]. The quantity and type of inclusions in the melt are determined by the quality of charge and alloying materials, as well as the melting and melt handling processes. The most common inclusions in aluminium alloys are non-metallic compounds: oxides, nitrides, carbides, and borides. Inclusions can be observed in the form of single particles, clusters and agglomerates [3]. Inclusions reduce mechanical properties by detracting from the effective cross-sectional area when stress is applied and because of the concentration of stresses at the inclusion interface. Inclusions in the melt can negatively influence melt fluidity and prevent interdendritic feeding [4].

Flux treatment usually consists of the addition of a solid blend of inorganic compounds to the melt. These compounds may perform several functions, such as the removal of non-metallic impurities from the melt, the protection of the melt surface or the refinement and/or degassing of the molten alloy [5]. The effect of fluxes is determined by their chemical composition, morphology, added quantity, as well as the temperature of the melt and the method of flux addition. It is important that the compounds in the fluxes should be able to form low-melting high-fluidity mixtures at working temperature [6]. Generally, the base flux components can be classified into four major groups based on their primary influence on the mixture: chlorides, fluorides, solvents of aluminium oxides and oxidizing compounds. Chlorides are mostly used for their fluidizing effects, but they can also be used as fillers and carriers. Fluoride salts act as surfactants and wet the interface between the inclusions and the liquid metal. Therefore, fluoride salts promote inclusion separation and metal coalescence. Oxidizing compounds are used to accelerate exothermic chemical reactions, which stimulate the coalescence of larger aluminium droplets trapped in the dross. Thus, the recovery of useful metal is facilitated. On the other hand, the heat released during the reactions promotes the interfacial reactions between the molten flux and the inclusions in the melt [5, 6].

In this study, the effects of different fluxes on the inclusion content of an aluminium alloy melt were compared. In order to find the reason for differences in melt cleaning efficiency, the chemical composition and thermal properties of the flux blends were investigated.

## Experimental Procedure

Melt treatments consisting of rotary degassing with N<sub>2</sub> gas and flux addition were executed on an Al-7Si-0.4Mg-0.5Cu alloy melt using four different fluxes (A, B, C and D). Each flux was used in 8 treatment cycles. The quantity of metal treated in one cycle was approximately 1 ton. The metal was melted in a stack smelter then transported by a transport ladle to a resistance heated holding furnace where the melt treatments were performed (Fig. 1). In each case, the melt was poured onto a lesser quantity of melt (ca. 200 kg) which remained in the holding furnace from the previous cycle. The treatment parameters and the quantity of flux added (400 g) were the same in each cycle. The N<sub>2</sub> gas flow rate was 20 L/min; the rotor revolution was 500 RPM during vortex formation and 250 RPM in the degassing phase. The treatment time was 10 minutes in each case. The molten metal temperature in the holding furnace was maintained between 740 °C and 750 °C.



**Figure 1.** The stages of melt preparation: a) pouring from melting furnace, b) melt transport to holding furnace, and c) melt processing

The inclusion content of the melts treated with different fluxes was investigated by the evaluation of K-mould samples, which were prepared in a gravity die called K-mould. The sample itself is a flat plate with four notches that act as fracture points. The fracture surface of samples can be examined either by visual inspection or with a microscope. Based on the number of inclusions, a K-value can be determined which can be used for the quantitative characterization of the melt purity (Eq. 1).

$$K = \frac{S}{n} \quad (1)$$

where  $K$  is the K-mould value,  $n$  is the number of examined samples, and  $S$  is the total number of inclusions found in  $n$  pieces [4]. The effect of different fluxes on the melt purity was evaluated using the comparison of the K-values determined before and after the melt treatments. The percentage of change in K-values ( $\Delta K$  [%]) was calculated using Eq. 2.

$$\Delta K = \frac{K_2 - K_1}{K_1} \cdot 100 \quad (2)$$

where  $K_1$  is the K-value determined before the melt treatment and  $K_2$  is the K-value determined after the melt treatment. During each melt preparation, K-mould samples were cast 3 times; the number of samples cast at once was 5. During the investigated 32 cycles (8 cycle/flux blend), 480 K-mould samples were cast. The fracture surface of K-mould samples was inspected with a stereomicroscope at a magnification of 25X. The inclusions found on the fracture surfaces were examined with scanning electron microscope (SEM) combined with energy dispersive X-ray spectroscopy (EDS analysis). In each case, the first K-mould samples were prepared from the melt in the transport ladle. After the melt was poured into the holding furnace and the produced wet dross was removed, another series of

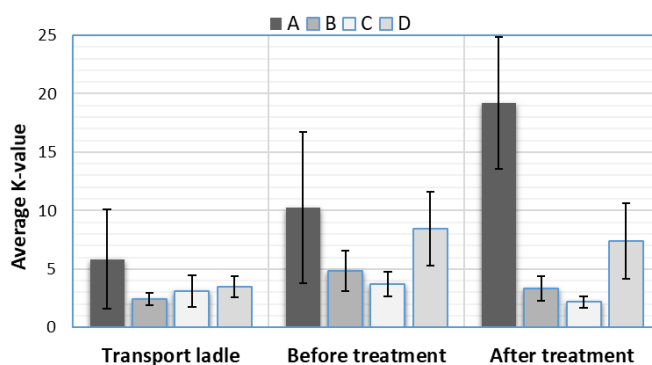


K-mould samples were prepared. The third series of samples were cast after skimming, following the fluxing and degassing treatment.

The elemental composition of the fluxes was examined with EDS analysis. The thermal properties of the fluxes were investigated with derivatographic measurements. The derivatograph is capable of performing differential thermal analysis (DTA) and thermogravimetric (TG) measurements on the same sample at the same time. During the investigations, a MOM Derivatograph-C apparatus was used with a platinum crucible, the rate of heating was 10 °C/min, the maximum temperature of the measurement was 1000 °C.  $\alpha\text{-Al}_2\text{O}_3$  was used as reference material, the mass of each flux samples was 150 mg.

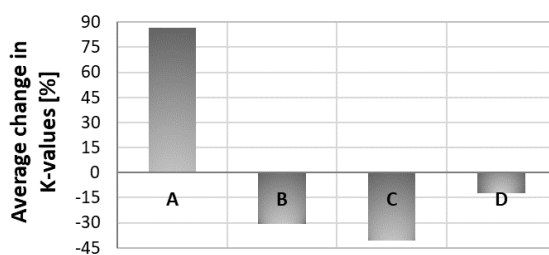
## Results and Discussion

**Inclusion Analysis.** The average K-values of the melts at the different stages of melt preparation can be observed in Fig. 2.



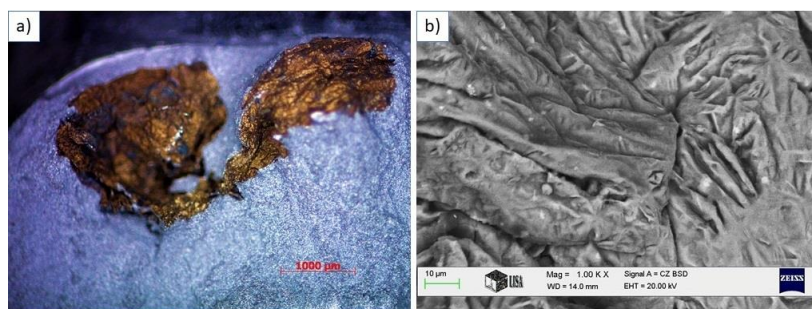
**Figure 2.** Average K-values at the different stages of melt preparation

It can be seen that the melts had different inclusion contents even in the transport ladle which was the result of the differences in the quality of charge materials. In each case, the melt in the transport ladle was poured onto a small quantity of melt remaining in the holding furnace from the previous cycle. Thus, the inclusion content of the melt was influenced by the quality of the residual melt. This way, the applied flux blends had an indirect effect on the average K-values of the melts even before the treatments were carried out. The average  $\Delta K$  values for each flux blends are illustrated in Fig. 3.



**Figure 3.** The average change in K-values ( $\Delta K$ )

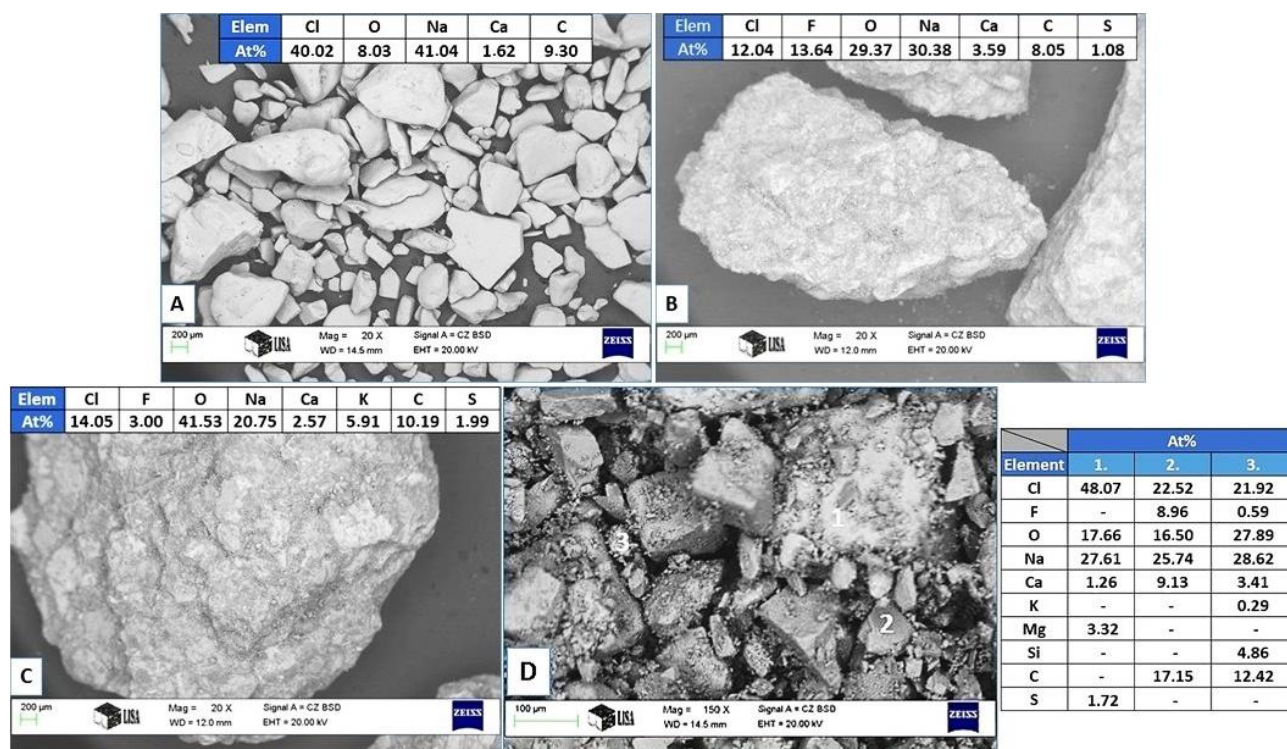
The treatments executed with flux C were the most effective in reducing the K-values and flux B was the second most efficient. Flux blend A had the poorest results. The melt treatments performed with flux A resulted in the increased inclusion content of the melt, which caused a positive change in the average K-value. An example of inclusions found during the examination of K-mould samples can be seen in Fig. 4.



**Figure 4.** Inclusion found on a fracture surface of a K-mould specimen: a) microscopic and b) SEM image

In most cases, creased film-like inclusions were found on the fracture surfaces. Based on the EDS analysis, in most cases, the inclusions had significant oxygen and nitrogen content. Therefore, the inclusions found are probably nonmetallic compounds like  $\text{Al}_2\text{O}_3$ ,  $\text{AlN}$  and  $\text{MgO} \cdot \text{Al}_2\text{O}_3$ .

**Properties of Fluxes.** The elemental composition of fluxes measured with energy dispersive X-ray spectrometer (EDS) and the SEM images of flux grains are shown in Fig. 5. The compositions presented were measured on the surface area of the flux grains. Elemental composition values of flux *D* presented in Fig. 5. were measured in case of three different grain.



**Figure 5.** The SEM images and elemental composition of flux grains

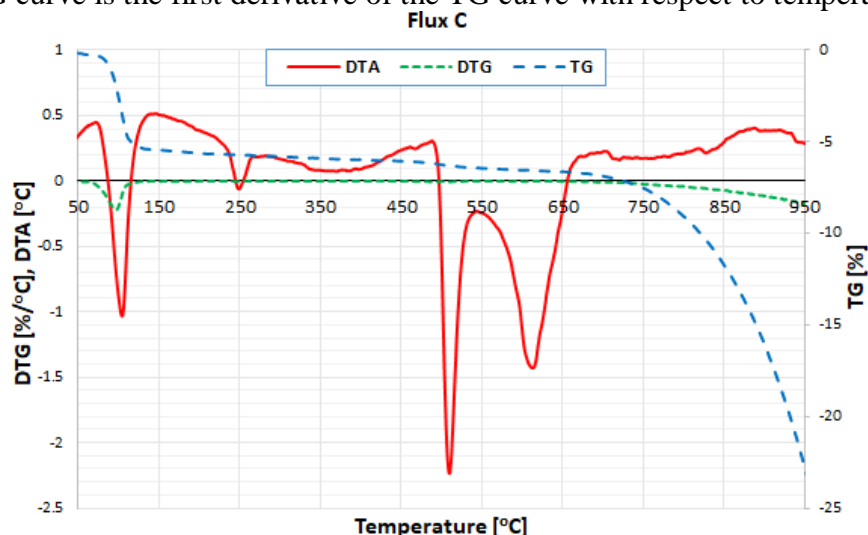
Elemental composition measurements on different flux grains were executed in case of flux *A*, *B* and *C*. It was found, that the measured composition values are almost identical. Therefore, the flux grains have consistent chemical composition. As it can be seen in Fig. 5., the grains of flux *D* have significantly different composition values, which is a common attribute of powder fluxes according to the literature [6]. The inhomogeneity of the chemical composition of flux *D* could be the main reason for the lower  $\Delta K$  values and thus the lower efficiency of melt cleaning.

The measured elemental composition values can be used to predict the quality and quantity of basic flux components like chlorides, fluorides and oxidizing compounds. Based on the chlorine and sodium content of flux *A*, the grains mainly consist of  $\text{NaCl}$ . During the analysis there was no detectable amount of fluorine in the grains, therefore probably there are no fluorides in flux *A*. The

absence of fluorides could be one of the reasons for the inefficiency of this flux regarding inclusion removal. Based on the fluorine and oxygen content of flux *B*, the flux is relatively richer in fluorides and oxidizing compounds. Flux *C* contains the highest amount of oxidizing compounds, but the fluorine and thus the fluoride content of this flux is significantly lower than in the case of flux *B*. By the comparison of the measured K-values and the elemental composition of fluxes it can be concluded that the more effective fluxes (*B* and *C*) contain reactive components (like oxidizing compounds and fluorides) at higher concentration values and their grains have consistent chemical composition.

As it can be seen in Fig. 5, the grain sizes of flux *A* and *D* is significantly smaller than the other two fluxes since they are powder fluxes while flux *B* and *C* are granular. According to *R. Gallo* and *D. Neff* [6], granular fluxes are more efficient regarding melt cleaning because of the consistency of their chemical composition. This statement is in agreement with the results of the present study.

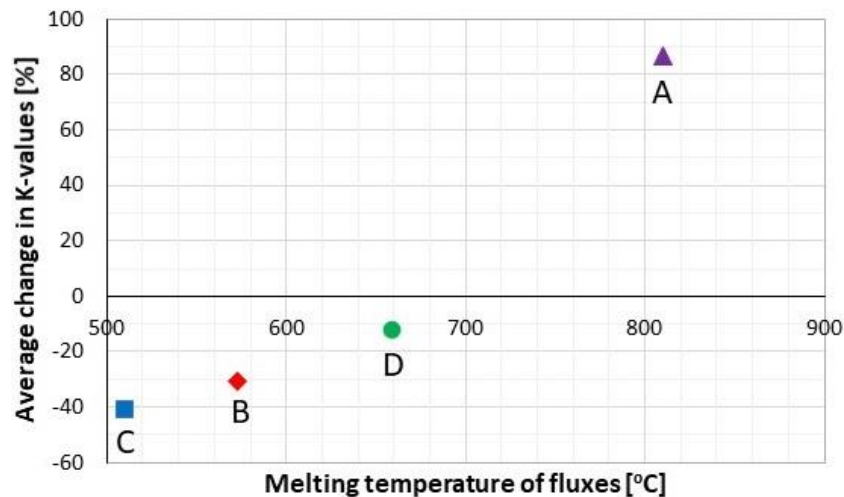
With the aid of derivatographic measurements, the melting temperature of fluxes can be determined, which is an important property that significantly influences the melt cleaning efficiency. The evaluation process of the measured data is described via the analysis of DTA, TG and DTG curves recorded during the investigation of flux *C* (Fig. 6). The DTA curve represents the temperature difference between the inert reference material and the flux sample during heating. Negative peaks on the DTA curve indicate endothermic reactions while positive peaks are the signs of exothermic reactions. The TG curve gives information about the percentage of the mass change of the flux sample. The DTG curve is the first derivative of the TG curve with respect to temperature.



**Figure 6.** The derivatographic curves of flux *C*

In order to find the melting temperature of the flux, the temperature values where strongly endothermic reactions occur according to the DTA curve, but no mass-change can be observed on the DTG curve should be identified. In case of flux *C*, two significantly endothermic reactions with no mass-change can be identified. The first one is around 510 °C and the second one is around 615 °C. The results indicate that the melting process of this flux starts at 510 °C, and the melting of another phase with higher melting temperature takes place at 615 °C.

With the aid of the evaluation process described above the melting temperature of each flux has been determined. Then, the temperature values were compared with the average change in K-values ( $\Delta K$ ) in order to find a relationship between the melt cleaning efficiency and the melting temperatures of the fluxes (Fig. 7).



**Figure 7.** The comparison of melt cleaning efficiency and the melting temperature of fluxes

Based on Fig. 7, it can be stated that in the case of the four fluxes investigated, the fluxes with lower melting temperature were more efficient regarding inclusion removal. According to *O. Majidi et al.* [7], the melt cleaning efficiency is dependent on the fluidity of molten fluxes. Since the viscosity of molten fluxes is temperature dependent, at a constant temperature the viscosity of molten fluxes with lower melting temperature is lower and their fluidity is better. During melt treatment, the molten fluxes with better fluidity can be dispersed more evenly in the molten metal which results in better melt cleaning efficiency. The described statement is in agreement with the results of the present study. Flux A has the highest melting temperature which is actually higher than the maintained melt temperature (740-750 °C), therefore the grains of flux A could not melt during melt processing. Since the flux grains were in solid state after addition, they were not capable of exposing any inclusion removing action, moreover, they contributed to the degradation of the melt quality via the entrainment of the surface oxide film of the melt during flux addition, which resulted in higher K-values. The main reason for the high melting temperature of flux A could be its chemical composition, i. e. its high NaCl content (see Fig. 5).

## Summary

From the results of the present study, it can be concluded that the melt cleaning efficiency of different fluxes is highly dependent on their chemical composition, morphology and melting temperature. Based on the results of K-mould tests, flux C was the most effective in inclusion removal. The more effective fluxes (like B and C) are granular, contain oxidizing compounds and fluorides at higher concentration values, their grains have a consistent chemical composition and they have significantly lower melting temperature than the temperature of the treated molten alloy.

## Acknowledgement

The described study was carried out as part of the EFOP-3.6.1-16-2016-00011 “Younger and Renewing University – Innovative Knowledge City – institutional development of the University of Miskolc aiming at intelligent specialisation” project implemented in the framework of the Szechenyi 2020 program. The realization of this project is supported by the European Union, co-financed by the European Social Fund.

## References

- [1] P. K. Trojan, Inclusion-Forming Reactions, in: ASM Handbook Vol. 15.: Casting, ASM International, 2008, pp. 74-83.
- [2] J. Morscheiser, P. Le Brun, M. Gökelma, M. Badowski, T. Dang, S. Tewes, Observation on Inclusion Settling by LiMCA and PoDFA Analysis in Aluminium Melts, *International Aluminium Journal* 91/4 (2015) 56–61.
- [3] R. Gallo, I have Inclusions! Determining the Best Cost Saving Approach, *Modern Casting* 107/8 (2017) 31-35.
- [4] S. W. Hudson, D. Apelian, Inclusion Detection in Molten Aluminum: Current Art and New Avenues for in Situ Analysis, *International Journal of Metalcasting* 10/ 3 (2016) 315–321.
- [5] T. A. Utigard, K. Friesen, R. R. Roy, J. Lim, A. Silny, C. Dupuis, The Properties and Uses of Fluxes in Molten Aluminum Processing, *JOM* 50/11 (1998) 38–43.
- [6] R. Gallo, D. Neff, Aluminum Fluxes and Fluxing Practice, in: ASM Handbook Vol. 15.: Casting, ASM International, 2008. pp. 230-239.
- [7] O. Majidi, S. G. Shabestari, M. R. Aboutalebi, Study of fluxing temperature in molten aluminum refining process, *Journal of Materials Processing Technology* 182. (2007) 450–455.

## **Pressure driven undercooling at solidification of hypoeutectic cast iron**

Attila Diószegi and Péter Svidró

**Keywords:** primary austenite, columnar zone, equiaxed zone

### **Abstract**

Shape casting of hypoeutectic cast iron develop a columnar and an equiaxed zone under solidification. The primary austenite in the columnar zone develop a container like domain delimiting the molding material from the internal zone of the solidification domain. Inside the container the primary phase develops as equiaxed crystals and fill the domain with a coherent solid network. The primary austenite precipitation followed by the eutectic reaction and graphite precipitation develops at different time in the columnar and equiaxed domain. The graphite precipitation in the columnar zone prior to the graphite precipitation in the eutectic zone makes cast iron different from other technical alloys without any phase expansion. The present work aims to study the influence of graphite precipitation on the volume change of the container like domain and consequently the pressure state inside the container during solidification.

## **Fabrication and properties of magnesium matrix composite obtain using thixomolding technology**

Łukasz Rogal, Bogusław Baran, Lidia Litynska-Dobrzanska

**Keywords:** AZ91 magnesium alloy, nanocomposites, thixomolding

### **Abstract**

Magnesium injection molding technology was used to obtain Mg base composites. AZ91 chips were mixed with 5 %wt. of  $\beta$ -SiC nanoparticles in solid state and next fed to the cylinder of injection molding machine (ex situ method). Using screw rotation granules were transferred to nozzle area at simultaneous intensive mixing of slurry containing reinforcement phases. Injection process was conducted at 595°C, which correspond about 90% liquid phase to steel die. Detailed characterization of microstructure were conducted using SEM and TEM microscopes. Composites microstructure consist of  $\alpha$ (Mg) globular grains with size of 20-50  $\mu\text{m}$  and volume of 7-10% surrounded by fine eutectic mixture ( $\alpha$ (Mg) +  $\beta$ -Mg<sub>17</sub>Al<sub>12</sub>). Additionally TEM-BF image showed in the matrix  $\beta$ -SiC nanoparticles with size of 20-50 nm. Applying various combinations of mixture gases and alloying elements feed during the process leads to formation of phases which reinforcement of AZ91 matrix (in situ). Hardness and compression strength of AZ91 nano-composites increased.





## CHAPTER 6: MODELLING, SIMULATION



# 3D Modelling of the impact of inlet flow on macrosegregation formation in DC casting of Aluminium alloys accounting for grain morphology and transport

Akash PAKANATI<sup>1</sup>, Mohammed M'HAMDI<sup>1,2</sup>, Hervé Combeau<sup>3</sup> and Miha Založnik<sup>3</sup>

<sup>1</sup> Department of Materials Technology, NTNU, N-7491 Trondheim, Norway

<sup>2</sup> SINTEF Materials and Chemistry, N-0314 Oslo, Norway

<sup>3</sup> Institut Jean Lamour, CNRS – Université de Lorraine, Campus Artem, 2 allée André Guinier, F-54000 Nancy, France

Corresponding Author: Mohammed.Mhamdi@sintef.no

**Keywords:** Solidification, DC Casting, Macrosegregation.

**Abstract.** Nonuniform solute distribution at the scale of the cast product is referred to as macrosegregation. This is a common defect observed in direct chill (DC) casting of aluminium alloys. Transport mechanisms such as solidification shrinkage induced flow, thermal-solutal convection and equiaxed grain motion contribute to this defect. Casting parameters, including but not restricted to inlet melt flow, affect macrosegregation formation by modifying the flow pattern. Recently, a simplified three-phase, multiscale solidification model accounting for above mentioned transport mechanisms has been published. In this study, the model is used to study the 3D macrosegregation formation of zinc in a sheet ingot during DC casting process of Al-8.375wt%Zn alloy. The impact of inlet flow and its interaction with the transport of the globular and dendritic equiaxed grains, eventually leading to macrosegregation formation is analyzed. We show that we can modify macrosegregation formation in 3D by modifying the inlet flow and that such modification is linked to grain morphology.

## Introduction

Macrosegregation is caused by various transport mechanisms during DC casting process of aluminium alloys [1]. Several numerical and experimental studies were conducted to understand the formation of macrosegregation and it is commonly believed that equiaxed grain settling is a major cause of negative segregation (solute content lower than nominal value) at the center of the ingot. Suppressing the settling could theoretically eliminate negative segregation [2]. Wagstaff and Allanore [2] experimentally observed for an Al-4.5wt%Cu alloy in a sheet ingot that a moderate inlet jet suppressed grain settling and resulted in elimination of negative segregation.

Recently Pakanati et al. [3] conducted numerical study to understand the interaction between inlet jet and the transport of equiaxed grains. They used a simplified three-phase equiaxed grain growth model proposed by Tveito et al. [4]. Pakanati et al. [3] proposed that it is easier to suspend dendritic grains and showed numerically that macrosegregation can be modified by varying the inlet jet in the case of billets.

The goal of this paper is to extend the numerical study conducted on billets [3] to sheet ingots. We investigate the interaction of inlet melt flow with both globular and dendritic grains and the resulting impact on macrosegregation formation in sheet ingot. Since flow pattern in sheet ingots is three dimensional, we conduct this study using 3D models. To perform this study we use the model proposed by Tveito et al. [4].

## Numerical Model

The simplified three-phase, multiscale numerical model [4] is an extension of the two-phase solidification model proposed by Založnik and Combeau [5] which is based on the volume averaging method [6]. For a detailed description of the model the reader is referred to these articles. Only the main model features are described here.

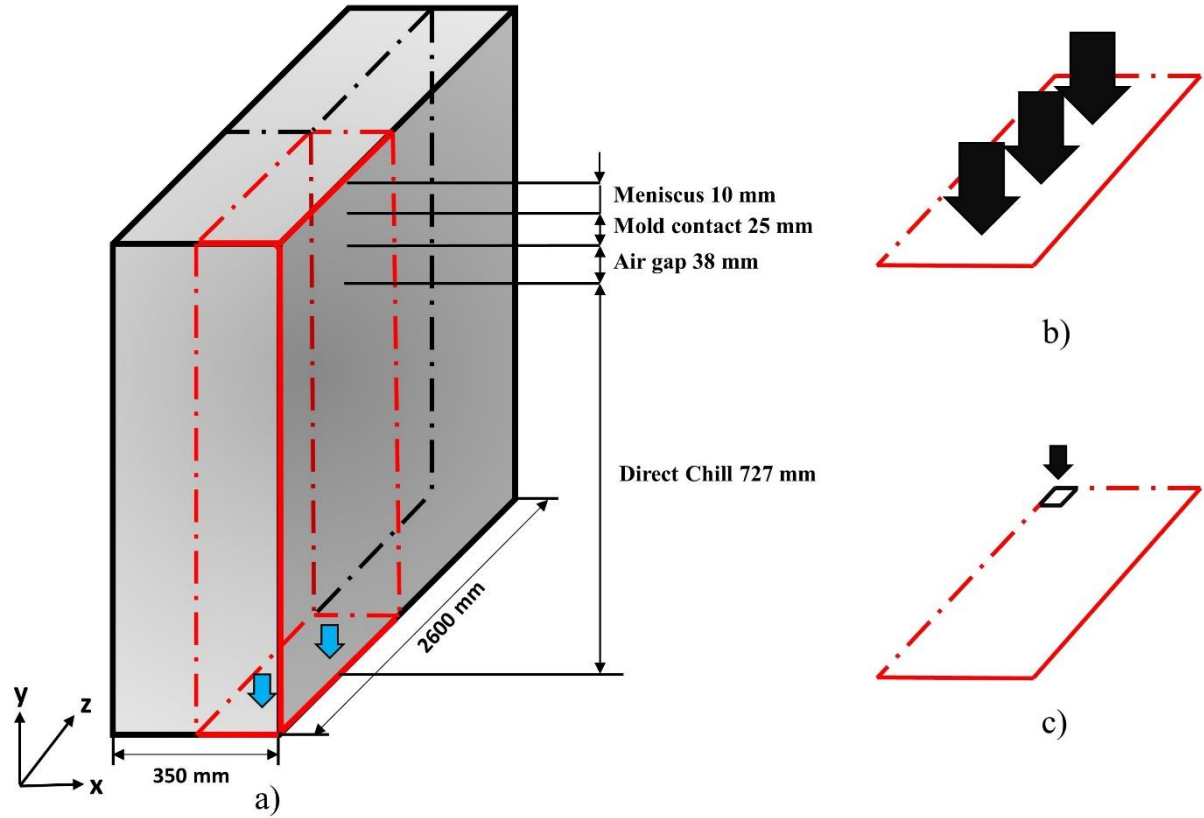
The Euler-Euler volume-averaged model considers macroscopic transport and microscopic growth. The macroscopic transport accounts for solute and heat transport coupled to mass and momentum conservation equations accounting for thermal-solutal convection and grain motion. For the sake of simplicity, solidification shrinkage is not accounted for by considering equal and constant densities in solid and liquid phases. Boussinesq approximation is used for the liquid density in buoyancy term. For the solid phase, two flow regimes are considered depending on the envelope fraction ( $g_{env}$ )[7].

For envelope fractions lower than a packing fraction ( $g_{pack}$ ) the solid (equiaxed grains) is freely floating. The interfacial drag is modeled in the same manner as in Ref. [8] for spherical particles but by considering the envelope fraction instead of the solid fraction. The measure of grain morphology can be obtained by taking the ratio of the solid fraction and the envelope fraction, called as the internal solid fraction:  $g_{intern} = g_s/g_{env}$ . The grain is globular as the  $g_{intern}$  approaches 1 and is dendritic if  $g_{intern} \ll 1$ . For envelope fractions greater than packing fractions, grains are assumed to form a rigid porous solid matrix moving with the casting velocity,  $\vec{V}_{cast}$  in this regime. The interfacial drag now is modeled by a Darcy term, where the permeability ( $K$ ) is calculated from the Kozeny Carman relation for the character size,  $l_{KC}$ . Measure of grain morphology is given by internal solid fraction ( $g_{intern}$ ). A globular morphology corresponds to internal solid fraction values close to 1, whereas dendritic morphology is associated with low internal solid fraction. A Low Rayleigh number (LRN) turbulent energy-dissipation ( $k-\epsilon$ ) model is used to address the turbulence problem.

The microscopic part is treated locally within each control volume and accounts for both nucleation and growth kinetics. Nucleation of grains is assumed to occur on grain-refiner (inoculant) particles. According to the athermal nucleation theory of Greer and co-workers [9], the critical undercooling for free growth of a grain on an inoculant particle of diameter  $d$  is given by  $\Delta T_c = 4\Gamma_{GT}/d$  where  $\Gamma_{GT}$  is the Gibbs-Thompson coefficient. The number of activated particles then depends on the size distribution of the particle population, which can be represented by an exponential distribution density function. This representation holds for the largest particles, which are activated at small undercoolings and therefore successful as nuclei. This size distribution is then discretized into  $m$  classes of inoculants. Each class  $i$  is represented by a volumetric population density  $N_{nuc}^i$  and a critical undercooling  $\Delta T_c^i$ . When the local undercooling reaches the critical undercooling of class  $i$ , its local inoculant density,  $N_{nuc}^i$ , is instantaneously added to the grain density,  $N_g$ , and  $N_{nuc}^i$  becomes locally zero. The model accounts for finite diffusion in both solid and liquid phases and local thermal equilibrium is assumed.

## Process Model

In this work, we use the DC cast geometry used by Založnik et al. [10]. The geometry with dimensions is represented in **Figure. 1a**. Due to symmetry, we consider only a quarter of the ingot marked in red. We consider two types of inlet: a simplified open inlet where liquid metal enters the domain from the top surface (**Figure. 1b**) and an inlet with a vertical jet directed towards the center of the ingot (**Figure. 1c**). The vertical jet is achieved by constricting the inlet to a 30 mm x 30 mm area (marked in black in **Figure. 1b**). The liquid metal is assumed to enter at casting temperature  $T_{cast}$ , nominal solute concentration  $C_o$  and inoculant density  $N_{nuc}^i$ . The inlet velocity is calculated based on mass balance. The solidified metal leaves the domain from outlet at the bottom (blue arrow) at predefined casting speed  $V_{cast}$  of 60 mm/min.



**Figure. 1.** a) The full isometric view of the sheet ingot. Symmetry axis is represented by dashed lines. The quarter of the ingot considered in the simulation is marked in red, b) Inlet with vertical jet and c) Simplified open inlet

Heat extraction accounts for primary and secondary cooling mechanisms and both are modelled with a Fourier condition. Primary cooling further consists of three regions: meniscus, mold and air gap. The secondary cooling heat transfer coefficient is modelled by the correlation given by Weckmann and Niessen [11]. A binary Al-8.375%Zn alloy is used, similar to Založnik et al. [10] emulating the AA7449 alloy. The thermal and physical properties (including packing fraction 0.3) are also obtained from Ref [10]. The inoculation data is taken from Ref [3].

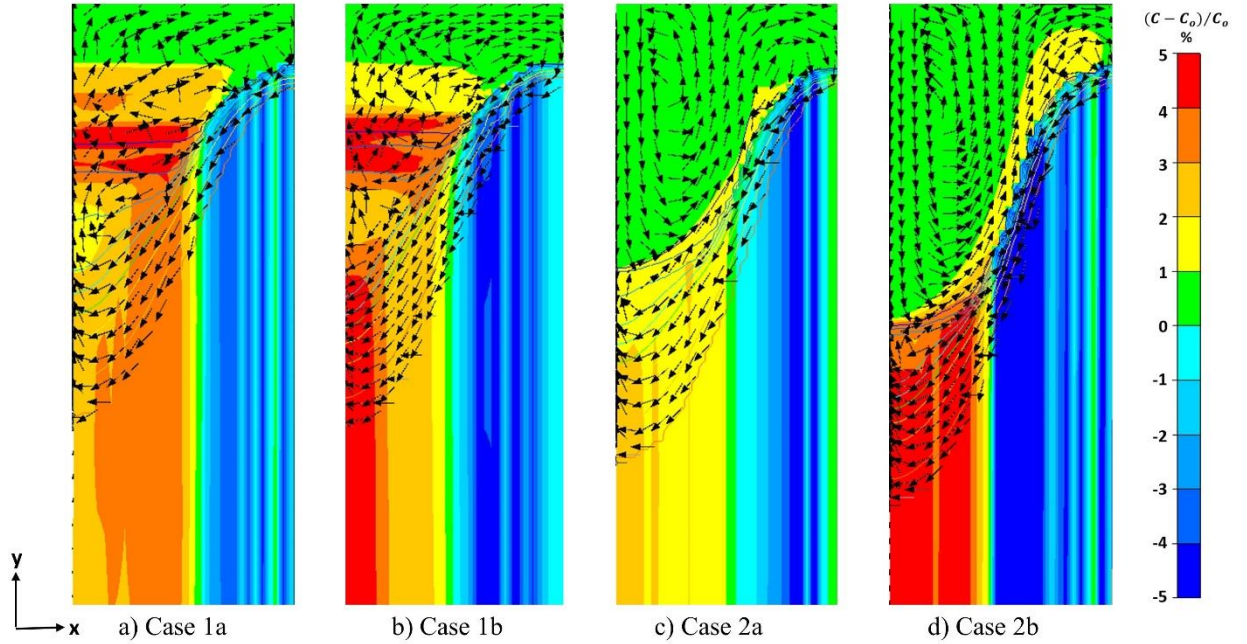
The transport equations are solved with a Finite Volume Method and the SIMPLE-algorithm for staggered grid is used for pressure-velocity coupling. The convective terms are discretized with a first-order upwind scheme and for time discretization a fully implicit first-order scheme is used. For all simulations a structured grid of 524,288 cells ( $N_x \times N_y \times N_z = 32 \times 128 \times 128$ ) is employed. A constant time step of 5 ms is used and the calculations are run until steady state is reached.

**Table 1.** Simulation Cases

Driving Mechanisms	Grain Growth Model		Inlet
	Globular	Dendritic	
Grain Motion + Thermal-Solutal convection	Case 1a	Case 1b	Simplified Open Inlet (Figure. 1b)
Grain Motion + Thermal-Solutal convection + Forced Convection	Case 2a	Case 2b	Vertical Inlet Inlet (Figure. 1c)

## Results and Discussion

A total of 4 cases based on the inlet and grain growth model are considered. They are summarized in **Table 1**. In Case 1, we simplify the inlet and assume liquid metal enters from the whole top domain. This case is subdivided into *a* and *b*. For Case 1a, we impose a globular morphology for the equiaxed grains, while for Case 1b, we consider a dendritic morphology. In Case 2, we consider the liquid metal to enter through a small opening resulting in a vertical jet directed towards the center of the ingot. This case is similarly divided into *a* and *b*, imposing globular and simulating dendritic morphology respectively. All the cases account for the same transport mechanisms: equiaxed grain motion and thermal-solutal convection. In addition to these, in Case 2 we also have forced convection due to the inlet jet. The resulting relative macrosegregation contour plots for all the cases are shown in **Figure 2** and **Figure 3**. A 2D illustration of the macrosegregation contour in the symmetric x-y plane for all cases is shown in **Figure 2**. These are over plotted with relative liquid velocity vectors ( $\vec{v}_l - \vec{v}_{cast}$ ). The quarter section of the ingot for each case along the horizontal x-z plane is presented in **Figure 3**. It can be represented as macrosegregation contour map for the entire ingot, with each quarter section showing the effect of inlet flow or grain morphology or both.



**Figure 2.** Relative macrosegregation fields and isolines of envelope fraction overplotted with vectors of liquid relative velocity ( $\vec{v}_l - \vec{v}_{cast}$ ) in the vertical x-y plane for all the cases. The symmetry axes is along the left vertical edge. The relative macrosegregation color scale is also shown in the far right.

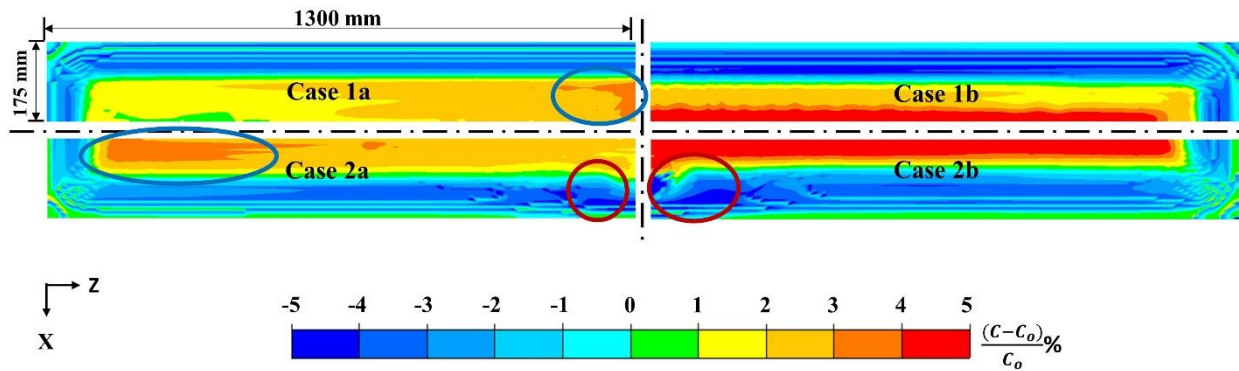
**Figure 2a** shows the macrosegregation formation and the corresponding liquid flow loop for Case 1a. Melt cooling results in a clockwise thermal flow loop and it is reinforced by the solutal flow loop as Zn is heavier than Al[10]. The settling of heavy and solute lean globular grains is towards the center of the ingot, which also results in clockwise flow loop. Combination of these two effects results in reduced settling velocities between the solid and liquid phase. The macrosegregation formation towards the center of the ingot is weakly positive due to this[3,10]. A similar flow loop can be observed in Case 1b as shown in **Figure 2b**. But the segregation at the center is strongly positive and this is attributed to the presence of dendritic grains with  $g_{intern}$  value of  $\sim 0.5$ . Unlike globular grains (Case 1a), the dendritic grains (Case 1b) carry less solid mass due to settling. Since grains are solute depleted, the amount of depletion observed due to a dendritic grain is lower than the depletion observed due to a globular grain. Also, dendritic grains are loosely packed and have high permeability [4]. This promotes the intragranular liquid flow due to thermal-solutal convection. Hence, dendritic

morphology has significant influence on the grain motion and its subsequent impact on macrosegregation formation resulting in a more positive segregation at the center of the ingot for Case 1b. We can also observe the macrosegregation contour maps along the x-z plane for Case 1a (left corner) and Case 1b (right corner) in **Figure 3**. For Case 1a, we can spot gradually increasing positive segregation as we move along the ingot width, with maximum positive segregation at the center of the ingot, indicated by the blue circle. This indicates the influence of ingot width on macrosegregation formation and emphasizes the necessity of 3D simulation.

**Figure 2c** and **Figure 2d** show a deeper mushy zone due to the presence of inlet jet for Case 2a and 2b. It is also interesting to note that solutal stratification due to grain sedimentation (observed in Case 1a and Case 1b) is not observed in these cases. The equiaxed grains are resuspended or pushed away from the center of the ingot. Macrosegregation formation for Case 2a and 2b can be further described by considering the x-z plane as shown in **Figure 3**. We can notice the relative macrosegregation contour plot for Case 2a in the bottom left corner in **Figure 3**. At the center of the ingot, along its width and thickness (represented by the red circle) we can observe severe negative segregation. This can be attributed to the inlet jet washing away the solute elements along the inclined mushy zone, a phenomena previously reported experimentally by Zhang et al. [12] and numerically by Pakanati et al. [3]. The same depletion is also observed in Case 2b, also represented by the red circle. When we compare Case 2a and 2b, we can see that the magnitude of macrosegregation is quite different for the same type of inlet. Especially along the ingot width, a large region of positive segregation is observed for Case 2b, due to the presence of dendritic grains, as discussed in previous paragraph.

Comparing Case 1a and 2a, we can study the impact of inlet flow for the same morphology (globular). In contrast to the observation in Case 1a, maximum positive segregation is observed away from the center but along the ingot width for Case 2a, also marked by blue circle. The inlet jet results in a flow loop which pushes the grains and corresponding stratified solute elements away from the center along the ingot width. This shows the important interaction of inlet jet with equiaxed grains. In the Case 2b, the grain motion effect is less dominant due to the presence of dendritic grains. Hence, we see a stronger positive segregation along the ingot width, like in Case 1b.

When compared with an open inlet, usage of inlet vertical jet results in strong modification of macrosegregation formation in its vicinity and to an extent in other parts of the ingot. The extent of modification also depends on the morphology of the equiaxed grains.



**Figure 3.** Relative macrosegregation contour plots along the horizontal x-z plane for Cases 1a, 1b, 2a and 2b. Only quarter ingot plots are shown for each case. The relative macrosegregation color scale is also shown.

## Conclusions

We have investigated macrosegregation formation in an industrial sized DC cast sheet ingot using 3D models. To do this, we used a simplified multiphase multiscale solidification model accounting for thermal-solutal convection and equiaxed grain motion. We have managed to modify macrosegregation formation by accounting for inlet melt flow. We also investigated the importance of equiaxed grain morphology and its interaction with inlet melt flow on macrosegregation formation.



Subsequent work will focus on providing a deeper understanding of the complex 3D flow pattern of solid and liquid phases and its corresponding effect on macrosegregation formation. Shrinkage induced flow which is ignored in this work also needs to be included in future studies.

## Acknowledgements

This work is conducted within the framework of PRIMAL project of which Hydro Aluminium ASA, Alcoa Norway ANS, Aleris Rolled Products Germany GmbH and Institute of Energy Technology (IFE) are the partners. This project is supported by the Research Council of Norway. A.P and M.M. acknowledge the support of NOTUR High Performance Computing program.

## References

- [1] R. Nadella, D.G. Eskin, Q. Du, L. Katgerman, Macrosegregation in direct-chill casting of aluminium alloys, *Prog. Mater. Sci.* 53 (2008) 421–480. doi:10.1016/j.pmatsci.2007.10.001.
- [2] S.R. Wagstaff, A. Allanore, Minimization of Macrosegregation in DC Cast Ingots Through Jet Processing, *Metall. Mater. Trans. B Process Metall. Mater. Process. Sci.* 47 (2016) 3132–3138. doi:10.1007/s11663-016-0718-6.
- [3] A. Pakanati, K.O. Tveito, M. M'Hamdi, H. Combeau, M. Založnik, Impact of Inlet Flow on Macrosegregation Formation Accounting for Grain Motion and Morphology Evolution in DC Casting of Aluminium, in: *Martin O. Light Met.* 2018. TMS 2018. Miner. Met. Mater. Ser. Springer, Cham, 2018: pp. 1089–1096. doi:10.1007/978-3-319-72284-9\_142.
- [4] K.O. Tveito, A. Pakanati, M. M'Hamdi, H. Combeau, M. Založnik, A Simplified Three-Phase Model of Equiaxed Solidification for the Prediction of Microstructure and Macrosegregation in Castings, *Metall. Mater. Trans. A.* 49 (2018). doi:10.1007/s11661-018-4632-1.
- [5] M. Založnik, H. Combeau, An operator splitting scheme for coupling macroscopic transport and grain growth in a two-phase multiscale solidification model: Part I - Model and solution scheme, *Comput. Mater. Sci.* 48 (2010) 1–10. doi:10.1016/j.commatsci.2009.04.036.
- [6] J. Ni, C. Beckermann, A volume-averaged 2-phase model for transport phenomena during solidification, *Metall. Trans. B---Process Metall.* 22 (1991) 349–361.
- [7] M. Rappaz, P. Thévoz, Solute diffusion model for equiaxed dendritic growth, *Acta Metall.* 35 (1987) 1487–1497. doi:10.1016/0001-6160(87)90094-0.
- [8] P.K. Agarwal, B.K. O'Neill, Transport phenomena in multi-particle systems - I. Pressure drop and friction factors: Unifying the hydraulic-radius and submergedobject approaches, *Chem. Eng. Sci.* 43 (n.d.) 2487–2499.
- [9] A.L. Greer, A.M. Bunn, A. Tronche, P. V. Evans, D.J. Bristow, Modelling of inoculation of metallic melts: application to grain refinement of aluminium by Al-Ti-B, *Acta Mater.* 48 (2000) 2823–2835.
- [10] M. Založnik, A. Kumar, H. Combeau, M. Bedel, P. Jarry, E. Waz, Influence of Transport Mechanisms on Macrosegregation Formation in Direct Chill Cast Industrial Scale Aluminum Alloy Ingots, *Adv. Eng. Mater.* 13 (2011) 570–580. doi:10.1002/adem.201000341.
- [11] D. Weckman, P. Niessen, A Numerical Simulation of the D.C. Continuous Casting Process Including Nucleate Boiling Heat Transfer, *Metall. Trans. B.* 13 (1982) 593–602. <http://link.springer.com/article/10.1007/BF02650017>.
- [12] L. Zhang, D.G. Eskin, A. Miroux, T. Subroto, L. Katgerman, Effect of Inlet Geometry on Macrosegregation During the Direct Chill Casting of 7050 Alloy Billets: Experiments and Computer Modelling, *IOP Conf. Ser. Mater. Sci. Eng.* 33 (2012) 1–8. doi:10.1088/1757-899X/33/1/012019.

# Numerical modelling of the effect of electromagnetic stirring direction in continuous casting of steel billets

MRAMOR Katarina<sup>1,2</sup>, VERTNIK Robert<sup>1,3</sup> and ŠARLER Božidar<sup>1,2</sup>

<sup>1</sup>Institute of Metals and Technology, Lepi pot 11, SI-1000 Ljubljana, Slovenia

<sup>2</sup>Faculty of Mechanical Engineering, University of Ljubljana, Aškerčeva 6, SI-1000 Ljubljana, Slovenia

<sup>3</sup>Store Steel, d.o.o., Železarska cesta 3, SI-3220 Štore, Slovenia  
katarina.mramor@imt.si

**Keywords:** Continuous casting of steel, mold electromagnetic stirring, local radial basis functions, meshless method, stirring direction

**Abstract.** The continuous casting of steel with mold electromagnetic (EM) stirring is solved in three dimensions with local radial basis function collocation meshless method (LRBFCM). The effect of periodic changing of EM stirring direction on temperature and velocity fields is studied and compared to the case with only one stirring direction. A comprehensive physical model describing the process is approximated with a set of coupled partial differential equations obtained from the mixture continuum model and takes into account an incompressible turbulent fluid flow, energy transfer, electromagnetic field and solidification. The Boussinesq approximation is used to account for the buoyancy effects in the melt, the lever rule is applied to describe the solidification and the Darcy limit is applied for the mushy zone. The method is applied on 7-noded local influence domains with multiquadric radial basis functions, whereas the pressure-velocity coupling is based on the fractional step method. The magnetic field is calculated with Elmer code. The numerical simulations show how the stirring direction and other EM parameters effect the strand temperature, velocity and the shape of the solidified shell.

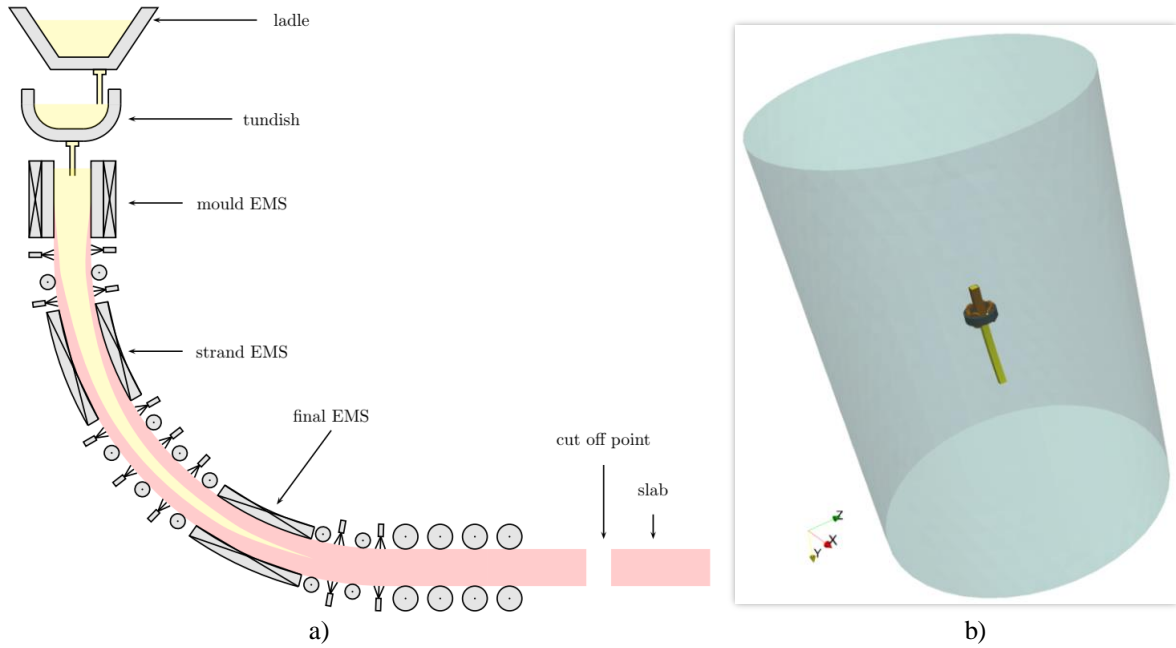
## Introduction

The mould electromagnetic (EM) stirring applied in the continuous casting (CC) [1,2] process (Fig.1) has been proven to successfully diminish the number of pin and blow holes, reduce the macrosegregation in the center of the billet, decrease the number of non-metallic subsurface inclusions and increase the heat transfer between the solidifying shell and the liquid center, thus promoting the columnar to equi-axed transition. Although, the CC process has been known to benefit from the strand and final EM stirring, mainly by accomplishing the better grain structure and elimination of the centerline segregation, the mould EM stirring seems to be superior and is therefore the most widely used.

The effects of EM field during the casting are difficult if not impossible to observe due to the complex arrangement of the stirring device and high temperatures of the melt. Furthermore, the casting experiments are time consuming and expensive and frequently do not resemble real industrial processes. It is therefore essential to build a complete and detailed numerical model that closely resembles the industrial setting. The first numerical simulations of the CC process with EM fields started in 1980s [3,4]. However, these models were crude and often semi-numerical. A more detailed models with complex geometries closely resembling industrial devices were presented in 2000s [5–8]. Today, almost two decades later, modelling of CC process is well established and widespread [9–12].

In present paper, a meshless local radial basis function collocation method (LRBFCM) was used. The method was first applied for 2D diffusive equation [13], and was later extended to a full 2D model of CC process [14–18] with EM breaking [19,20]. Afterwards, the method was used for a 3D model, first without the presence of EM field [21] and then with EM stirring [22]. In this work, mould EM stirring is investigated further. A periodic changing of stirring direction is applied and compared to the example with constant stirring direction. Since the measurements during the casting process are challenging, a parameter that indicates the history of the casting process and can be observed once

the slab is completely solid and cooled to ambient temperature, is chosen. For comparison between experiments and simulation the shape of the shell is used. In present contribution, the simulated shape of the shell is compared to the shell shape of a real cast steel billet.



**Figure 1.** a) CC process and types of EM stirring devices. b) Computational domain and geometry used in the magnetic field calculation.

### Numerical model and solution procedure

In order to devise a complete, but computationally manageable numerical model, certain assumptions have to be made. In the present study, the molten steel flow is considered as an incompressible Newtonian fluid (Eq. 1.), that has no effect on the magnetic field ( $Re_m = \nu L / \eta$ ). The temperature of the steel during the simulation is always above Curie temperature and the Joule heating is neglected. The transient term in EM force is neglected, as the characteristic time scale of magnetic field is small in comparison to the velocity field. In addition to liquid and solid phases, the mushy zone is also considered and is approximated as Darcy porous media.

The magnetic field is defined by low frequency approximation of Maxwell's equations ( $\nabla \cdot \mathbf{E} = 0$ ,  $\nabla \times \mathbf{E} = -\partial \mathbf{B} / \partial t$ ,  $\nabla \times \mathbf{B} = \mu_0 \mathbf{j}$ ,  $\nabla \cdot \mathbf{B} = 0$ ). EM force is calculated as  $\mathbf{f} = \mathbf{j} \times \mathbf{B}$ , where  $\mathbf{j}$  is EM current and  $\mathbf{B}$  is magnetic field density. The alternating current that drives the magnetic field results in real and imaginary values of  $\mathbf{j}$  and  $\mathbf{B}$ . However, as the transient term of EM is neglected, only the averaged value of the EM force ( $\mathbf{f}_{EM} = (\mathbf{f}_{Re} + \mathbf{f}_{Im}) / 2$ ) is used.

The fluid flow is described by the mass

$$\nabla \cdot \mathbf{u} = 0 \quad (1)$$

and momentum conservation equations

$$\rho \frac{\partial \mathbf{u}}{\partial t} + \rho \nabla \cdot (\mathbf{u} \mathbf{u}) = -\nabla P + \nabla \cdot [2(\mu_L + \mu_t) \mathbf{S}] - \frac{2}{3} \rho \nabla k - \mu_L K_0 \frac{(1-f_L)^2}{f_L^3} (\mathbf{u} - \mathbf{u}_s) + \mathbf{f}_b + \mathbf{f}_{EM} \quad (2)$$

where  $\mathbf{u}$  stands for velocity,  $P$  for pressure and  $\mathbf{S}$  for strain rate. Density  $\rho$  and viscosity  $\mu_L$  are constant and Boussinesq approximation  $\mathbf{f}_b = \rho [\beta_T \mathbf{g} (T - T_{ref})]$  is used to account for the buoyancy

force.  $K_0$  is morphology constant and lever rule is used to model the liquid fraction  $f_L = 1 - 1 / (1 - k_p)(T - T_L) / (T - T_m)$ , where  $k_p$  is partition coefficient,  $T$  is temperature,  $T_L$  is the liquidus temperature and  $T_m$  is the melting temperature.  $\mu_t = \rho c_\mu f_\mu k^2 / \varepsilon$  is turbulent dynamic viscosity and Abe-Kondoh-Nagano clousure coefficients ( $c_\mu, f_\mu, c_{1\varepsilon}, f_1, c_{2\varepsilon}, f_2, \sigma_T, \sigma_k, \sigma_\varepsilon$ ) are used to complete the  $k - \varepsilon$  turbulence model. The turbulent kinetic energy  $k$  and dissipation rate  $\varepsilon$  are calculated from

$$\rho \frac{\partial k}{\partial t} + \rho \nabla \cdot (\mathbf{u}k) = \nabla \cdot [(\mu_L + \frac{\mu_t}{\sigma_k}) \nabla k] + P_k - \rho \varepsilon + \rho D + \mu_L K_0 \frac{(1 - f_L)^2}{f_L^3} k \quad (3)$$

$$\rho \frac{\partial \varepsilon}{\partial t} + \rho \nabla \cdot (\mathbf{u}\varepsilon) = \nabla \cdot [(\mu_L + \frac{\mu_t}{\sigma_\varepsilon}) \nabla \varepsilon] - \rho (c_{1\varepsilon} f_1 - c_{2\varepsilon} f_2 \varepsilon) \frac{\varepsilon}{k} + \rho E + \mu_L K_0 \frac{(1 - f_L)^2}{f_L^3} \varepsilon \quad (4)$$

where  $P_k$ ,  $D$  and  $E$  source terms in  $k - \varepsilon$  equations. The energy conservation equation is modelled as

$$\rho \frac{\partial h}{\partial t} + \rho \nabla \cdot (\mathbf{u}h) = \nabla \cdot [\lambda \nabla T] - \rho \nabla \cdot (\mathbf{u}h - f_s \mathbf{u}_s h_s - f_L \mathbf{u}_L h_L) + \nabla \cdot (f_L \frac{\mu_t}{\sigma_t} \nabla h_L) \quad (5)$$

where  $h$  is enthalpy,  $f_s$  solid fraction and  $\lambda$  temperature dependent thermal conductivity. The indexes L and S stand for liquid and solid phases, respectively.

**Boundary conditions.** The calculation of the magnetic field is simplified is such a way that the CC device, coils and the surroundings are enclosed in an air filled cylinder. The boundary conditions for the magnetic field is then applied at the far off boundaries of this cylinder and are set to zero.

The velocity on the inlet is prescribed and constant, and on the outlet as fully developed flow. On the side walls, the no slip boundary condition is prescribed for the liquid velocity and the solid velocity is set to the casting velocity. The free surface flow is prescribed at the top. The temperature is prescribed on the inlet and Neumann type boundary conditions are prescribed on the side walls, with prescribed heat flux [14]. The ambient pressure is prescribed and set to zero at the outlet and the  $k$  and  $\varepsilon$  boundary conditions on the inlet are set to

$$k_{inlet} = 1.5(I_t u_{inlet,y})^2, \quad \varepsilon_{inlet} = \frac{c_\mu^{0.75} k_{inlet}^{1.5}}{0.07 d_2}, \quad I_t = 0.16 Re^{-1/8}, \quad Re = \rho u_{inlet,y} \frac{d_2}{\mu} \quad (6)$$

where  $I_t$  stands for turbulent intensity,  $d_2$  diameter of the submerged entry nozzle and Re for Reynolds number.

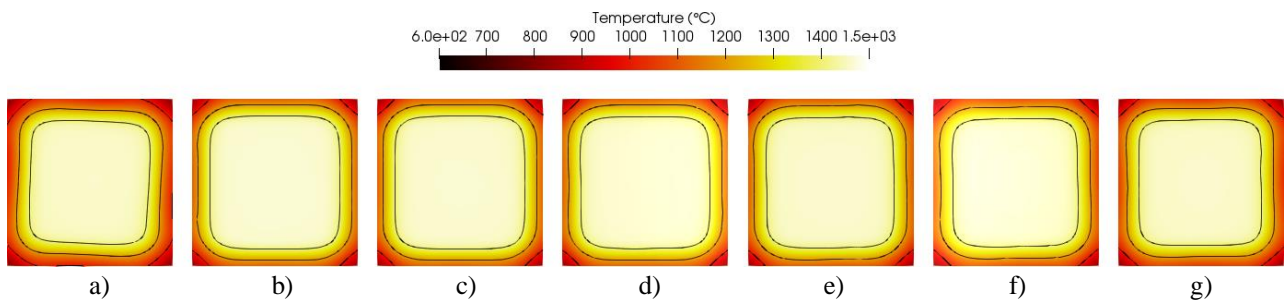
**Solution procedure.** The magnetic field is calculated in Elmer [23], an open source finite element solver. Maxwell's equations are solved in the harmonic way in **A-V** form. The averaged EM force  $f_{EM}$  is calculated at the end and interpolated to the nodes used for the calculation of fluid flow and solidification. These are solved with meshless LRBFCM method [13]. Euler explicit time-stepping is used for time discretization and Chorin's fractional step method is applied for pressure-velocity coupling.

## Numerical example and results

The CC process with EM stirring was simulated, first for the periodic changing of EM stirring direction and then for constant EM stirring direction. The stirring direction in the first case was changed every 5 s by changing the frequency, which was alternated between -2.8 Hz and 2.8 Hz. The

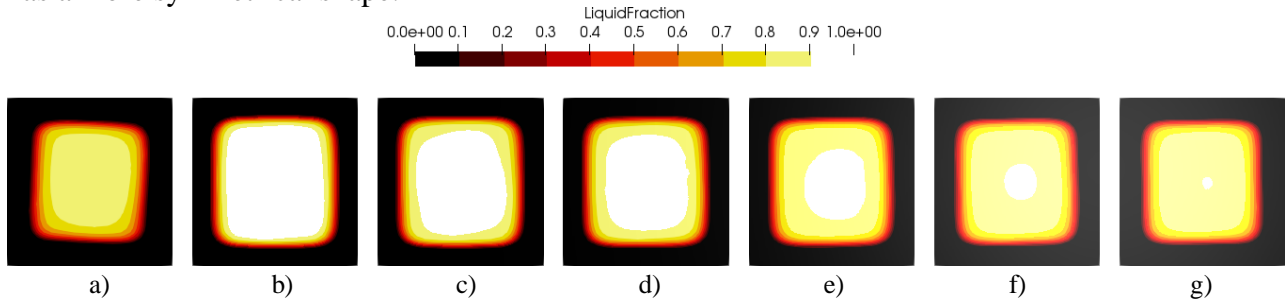
frequency of constant EM stirring direction was 2.8 Hz. The electric current in both examples was 400 A. The molten steel was poured into the mold with casting temperature of 1800 K and velocity 0.898 m/s. Casting velocity of solid phase is equal to 1.6 m/min. The radius of the casting device was 9 m and the dimension of the billets was 18 cm x 18 cm. The simulation was run on node arrangement consisting of 459159 nodes.

The time evolution of periodic changing of EM stirring is presented in Fig. 2, 3 and 4 for every 5 s and is compared to constant EM stirring. The cross-sections were observed at height 1.4 m from the top of the mold, where the mixing is not so prominent. Fig. 2 shows the temperature change. The temperature in the case with constant EM stirring (Fig. 2 a) shows isotherms that lean slightly to the right in the stirring direction. They are also slightly shifted to the right due to the curvature of the strand. The periodic changing of EM stirring (Fig. 2 b-g) causes a more homogeneous shape of the isotherms without preferential direction. The temperature difference in both cases is small. It is also apparent that the periodic changing of EM stirring reduces the shell thickness.



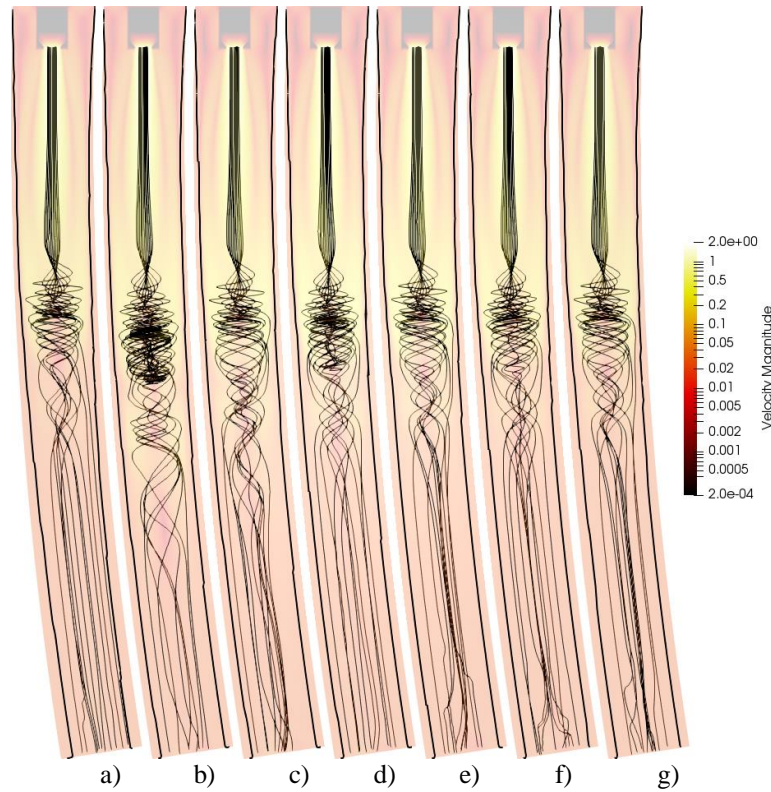
**Figure 2.** Time evolution of temperature field for constant (a) and periodic changing of EM stirring: b) 5s, c) 10s, d) 15s, e) 20s, f) 25s, and g) 30s.

Fig. 3 shows liquid fraction changes. The largest difference between constant EM stirring (Fig. 3 a) and periodic changing of EM stirring (Fig. 3 b-g) is in the shell thickness, which is thicker for constant EM stirring. The difference is also in the shape of the shell: As already mentioned, in the case of constant EM stirring, the shell leans to the right due the direction of the stirring. In the case of periodic changing of EM stirring, the effect of the stirring direction is canceled out and the shell has a more symmetrical shape.



**Figure 3.** Time evolution of liquid fraction for constant (a) and periodic changing of EM stirring: b) 0s, c) 5s, d) 10s, e) 15s, f) 20s, g) 25s, and h) 30s.

In Fig. 4 the magnitude of the velocity field is depicted together with streamlines and solid boundary. The velocity streamlines are more homogeneous for constant EM stirring.



**Figure 4.** Time evolution of velocity [m/s] for constant (a) and periodic changing of EM stirring: b) 0s, c) 5s, d) 10s, e) 15s, f) 20s, g) 25s, and h) 30s. The thick black line denotes the solid shell and the thin lines represent streamlines.

The numerical example was compared to the experimental results on 4 different test cases, 2 for periodic changing of EM stirring and 2 for constant EM stirring. It should be noted here that the experimental samples were observed after the whole strand was solidified and were not taken at the height 1.4 m from the top of the mold. Nonetheless, the experimental data confirms the change in the shape and thickness of the outer billet shell. The shape of the shell is straighter in the case of the periodic EM stirring, where the effect of stirring direction is averaged out. On the other hand, the constant EM stirring shows that the outer shell leans in the direction of the stirring.

## Conclusions

The LRBFCM method was successfully applied to coupled thermodynamic, fluid flow and EM field problem and the Elmer software was used to calculate the EM field.

The CC process with EM stirring was simulated and the comparison of different stirring regimes was made for real cast billets. The temperature, liquid fraction and velocity field show that the periodic changing of the EM stirring results in more homogeneous shell shape. Although, the numerical results cannot be directly compared to the experimental measurements, as they are taken after the process is finished, they confirm the changes in the shape of the solidified shell.

## Acknowledgements

This work was founded by Slovenian research agency (ARRS) in the framework of applied research project J2-7384, program group P2-0162 and MARTINA project. Project J2-7384 is cofounded by Store Steel, d.o.o. company.

## References

- [1] S. Kunstreich, Electromagnetic stirring for continuous casting, *Rev. Métallurgie – Int. J. Metall.* 100 (2003) 395–408.
- [2] S. Kunstreich, Electromagnetic stirring for continuous casting-Part 2, *Rev. Métallurgie–International J. Metall.* 100 (2003) 1043–1061.
- [3] K.-H. Spitzer, M. Dubke, K. Schwerdtfeger, Rotational electromagnetic stirring in continuous casting of round strands, *Metall. Mater. Trans. B.* 17 (1986) 119–131.
- [4] P. Davidson, F. Boysan, The importance of secondary flow in the rotary electromagnetic stirring of steel during continuous casting, *Appl. Sci. Res.* 44 (1987) 241–259.
- [5] K. Fujisaki, In-mold electromagnetic stirring in continuous casting, *IEEE Trans. Ind. Appl.* 37 (2001) 1098–1104.
- [6] L.B. Trindade, A.C. Vilela, M.T. Vilhena, R.B. Soares, Numerical model of electromagnetic stirring for continuous casting billets, *IEEE Trans. Magn.* 38 (2002) 3658–3660.
- [7] R. Hirayama, K. Fujisaki, T. Yamada, Dual in-mold electromagnetic stirring in continuous casting, *IEEE Trans. Magn.* 40 (2004) 2095–2097.
- [8] B. Sivak, V. Grachev, V. Parshin, A. Chertov, S. Zarubin, V. Fisenko, A. Solov'ev, MHD processes in the electromagnetic stirring of liquid metal in continuous section and bloom casters, *Metallurgist.* 53 (2009) 469.
- [9] B. Ren, D. Chen, H. Wang, M. Long, Z. Han, Numerical simulation of fluid flow and solidification in bloom continuous casting mould with electromagnetic stirring, *Ironmak. Steelmak.* 42 (2015) 401–408.
- [10] H. Liu, M. Xu, S. Qiu, H. Zhang, Numerical simulation of fluid flow in a round bloom mold with in-mold rotary electromagnetic stirring, *Metall. Mater. Trans. B.* 43 (2012) 1657–1675.
- [11] X. Geng, X. Li, F. Liu, H. Li, Z. Jiang, Optimisation of electromagnetic field and flow field in round billet continuous casting mould with electromagnetic stirring, *Ironmak. Steelmak.* 42 (2015) 675–682.
- [12] B.G. Thomas, Review on Modeling and Simulation of Continuous Casting, *Steel Res. Int.* 89 (2018) 1700312.
- [13] B. Šarler, R. Vertnik, Meshfree explicit local radial basis function collocation method for diffusion problems, *Comput. Math. Appl.* 51 (2006) 1269–1282.
- [14] R. Vertnik, B. Šarler, Simulation of continuous casting of steel by a meshless technique, *Int. J. Cast Met. Res.* 22 (2009) 311–313.
- [15] R. Vertnik, B. Šarler, Solution of a continuous casting of steel benchmark test by a meshless method, *Eng. Anal. Bound. Elem.* 45 (2014) 45–61.
- [16] R. Vertnik, B. Šarler, B. Senčič, Solution of macrosegregation in continuously cast billets by a meshless method, in: *IOP Conf Ser Mater Sci Eng*, 2012: p. 012058.
- [17] B. Šarler, R. Vertnik, K. Mramor, A numerical benchmark test for continuous casting of steel, in: *IOP Conf Ser Mater Sci Eng*, 2012: p. 012012.
- [18] R. Vertnik, B. Šarler, B. Senčič, Simulation of turbulent flow and heat transfer in continuous casting of billets by a meshless method, *na*, 2009.
- [19] K. Mramor, R. Vertnik, B. Šarler, A meshless model of electromagnetic braking for the continuous casting of steel, (2015).
- [20] K. Mramor, R. Vertnik, B. Šarler, Modelling of electromagnetic braking and electromagnetic stirring in the process of continuous casting of steel, in: *Coupled Probl. Sci. Eng. VI*, San Servolo, Venice, Italy, 2015: pp. 169–180.
- [21] R. Vertnik, B. Šarler, Three dimensional simulation of macrosegregation in steel billets by a meshless method, in: *IOP Conf Ser Mater Sci Eng*, 2016: p. 012069.
- [22] B. Šarler, R. Vertnik, M. Maček, Simulation of continuous casting of steel with EM stirring, in: *9th European continuous casting conference-ECCC*, Vienna, Austria, 2017: pp. 903–912.
- [23] CSC - Elmer, (2018). <https://www.csc.fi/web/elmer> (accessed January 12, 2018).



# Numerical simulation series for the investigation and validation of the Lorenz force field in bidirectional travelling magnetic field via thermal gradient shift effect

Csaba Nagy<sup>1,2,3</sup>, Olga Budenkova<sup>1</sup> Y. du Terrail<sup>1</sup> A. Rónaföldi<sup>2</sup> A. Roósz<sup>2</sup>

<sup>1</sup> Laboratoire SIMaP/EPM, Grenoble, France

<sup>2</sup> MTA-ME Materials Science Research Group, Miskolc, Hungary

<sup>3</sup>Starters E-Components Generators Automotive Hungary kft. Miskolc, Hungary

ntsart@gmail.com

**Keywords:** TMF, magnetohydrodynamics, travelling magnetic field, thermal gradient, convection, aluminium, multiphysics, simulation

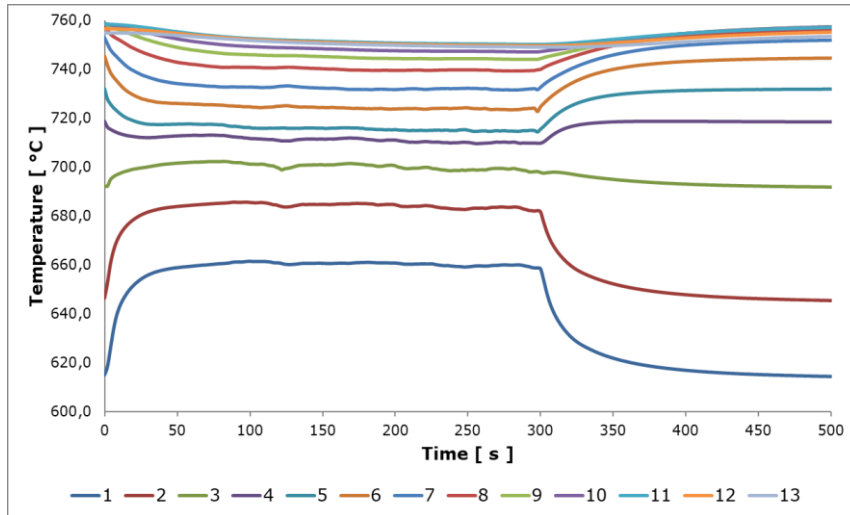
**Abstract.** A simulation series on the bidirectional Lorenz force field of a twin-head travelling magnetic field inductor was performed using Comsol Multiphysics and Ansys Fluent with an aim to use the results in later solidification simulations. The geometry of the inductor was not known in details, only magnetic field measurements were available. For the final validation, the effect of flow on the temperature distribution inside the sample is used. First, Comsol simulations were performed to gather the Lorenz force field induced inside the pure Al specimen. After electromagnetic simulations, the global thermal system of the complete TMF solidification facility was simulated to extract the heat flux appearing on the wall of the sample holding crucible. As last step, the thermal-flow model was prepared using the Lorenz force field of electromagnetic simulations and the heat flux data of the global thermal model. The results compared to measurements are discussed in the paper.

## Introduction

Solidification research including the effect of forced convection has been started many decades ago, but detailed work about the effect of electromagnetic stirring on the solidified structure was started only at the millennium. Rotating magnetic field was used in majority [1-6] since the forced convection can easily be applied on the complete melt volume. On the other hand, traveling magnetic field mixing has significantly lower skin depth and the mixing is partially driven magnetically and partially with internal shear stress. To eliminate such an effect, a twin-head inductor was designed and constructed at MTA-ME Materials Science Research Group. The innovative facility can mix the melt in several ways. The current paper discusses the effect of bidirectional mixing – pushing one side of the melt upward and the other downward – resulting in a very intensive stirring. The design of the inductor was protected by patenting, therefore minimal technical information was available. A series of simulations was provided to achieve the correct Lorenz force field for later solidification simulations. First, electromagnetic simulation had to be done to gather the Lorenz force field itself, then an indirect validation was done using the measurement of a thermal effect. A thermal model of the complete facility and a separate thermal model was performed. The work is presented in the paper.

## Thermal gradient shift effect

If a thermal gradient is set up in the stationary melt and the bidirectional TMF stirring is turned on, the gradient changes significantly. The strength of the effect is depending on the intensity of the electromagnetic induction. The colder areas warm up and the hotter cool down. The effect under 40 mT mixing is presented on Fig. 1.

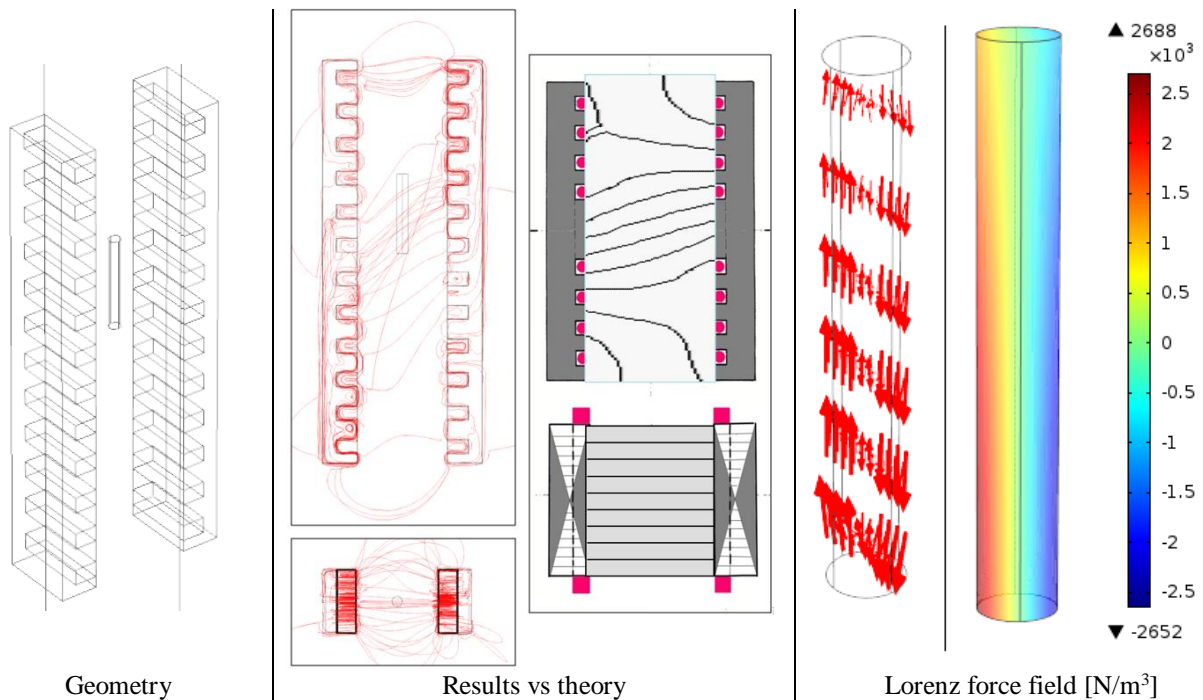


**Figure 1.** The thermal gradient shift effect in case of 40 mT bidirectional TMF stirring – 1 is for the lowest thermocouple, 13 is for the highest thermocouple

At 0 second, the stirring is turned on and 300 s it is turned off.

### Electromagnetic simulation

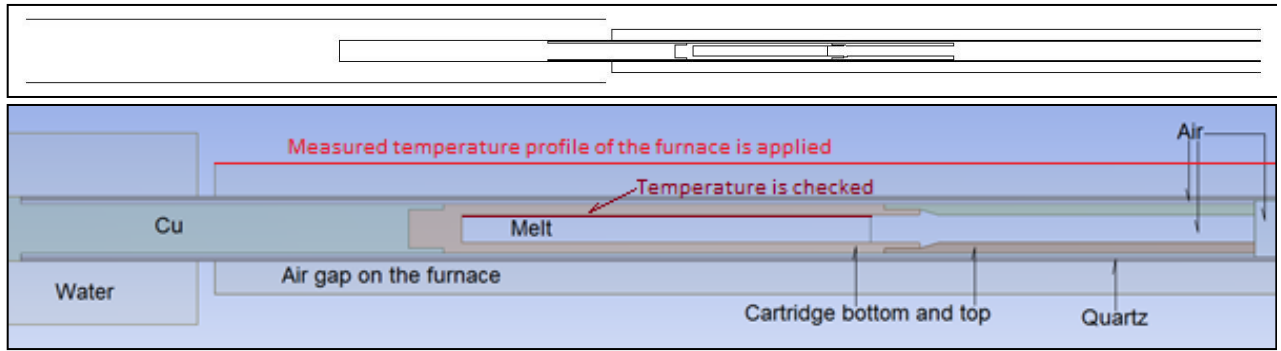
A schematic geometry was provided based on the available data. The geometry, the electromagnetic field distribution comparison and the Lorenz force field for 40 mT can be seen on Fig. 2. The quantitative accuracy is visible.



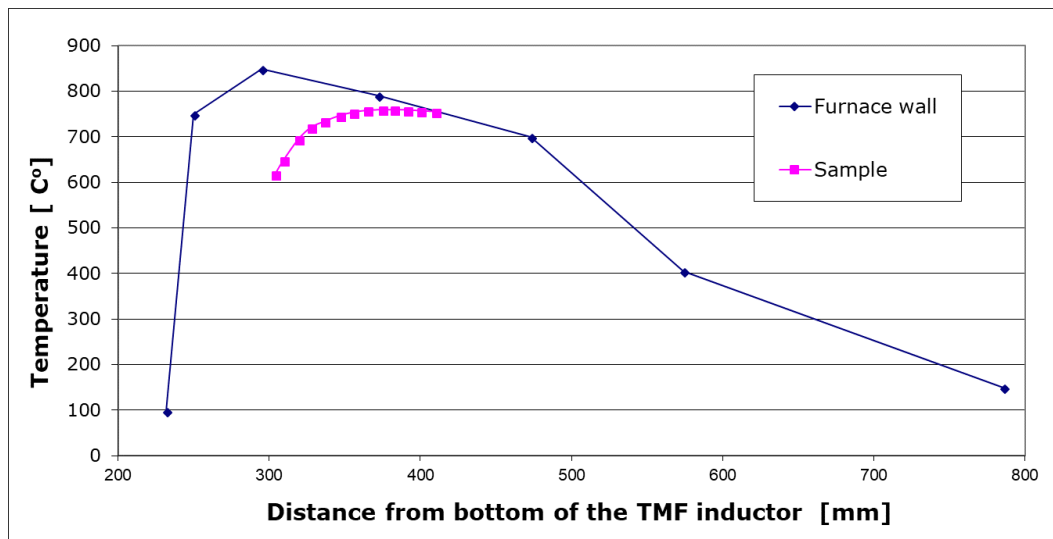
**Figure 2.** Geometry, alimentation and the results compared to theoretical data – 40 mT

### Global thermal model

The facility was completely simulated in 2D to gather the heat fluxes appearing on the wall of the sample holder crucible. The measured temperature distribution of the furnace was applied in the model – Fig. 4 and Fig. 5. The velocity of the water was set to 0,313 m/s calculated from Bernoulli equation and measured data. One should note that the highest point of the crucible has the same temperature as the furnace wall.

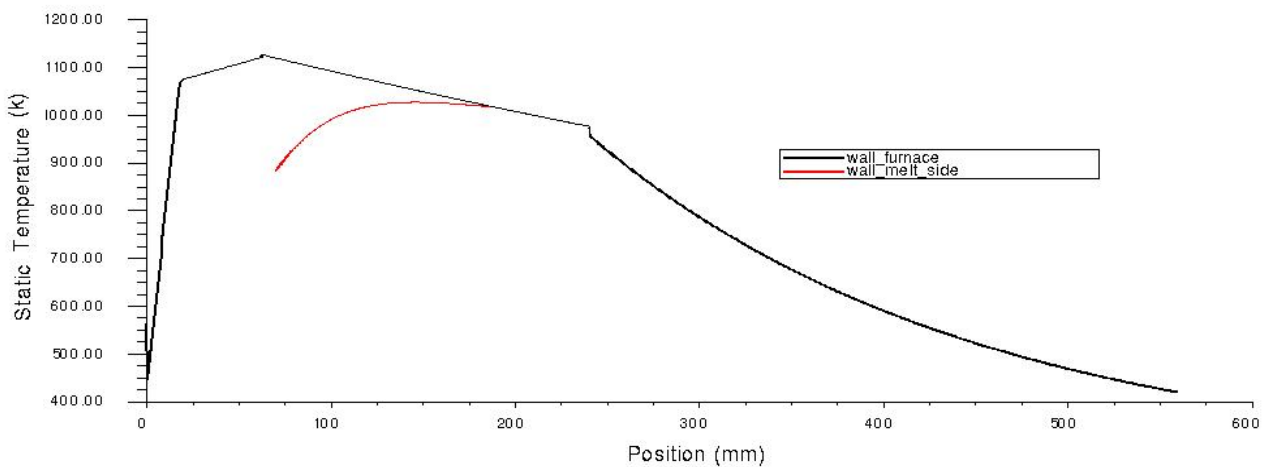


**Figure 4.** The geometry



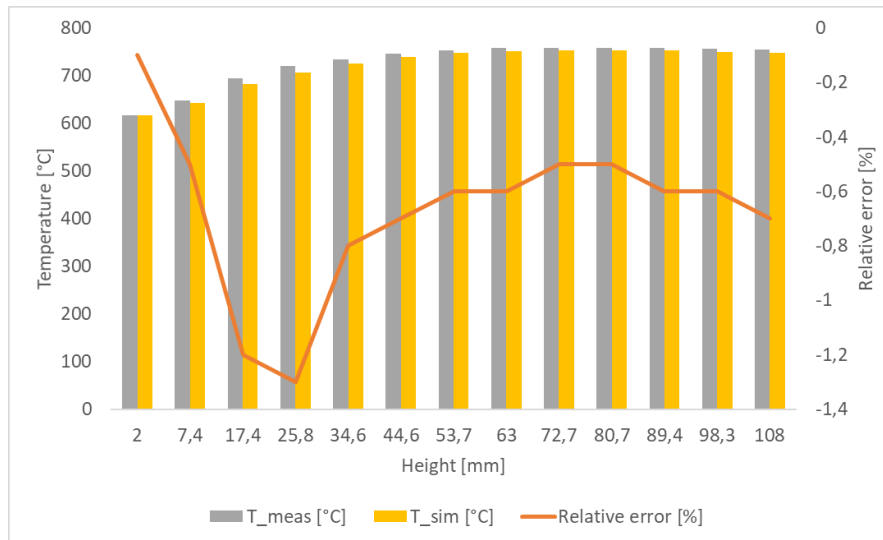
**Figure 5.** Temperature distribution of the furnace and the surroundings

The temperature distribution of the 13 thermocouples were monitored and the final stable result was compared with the measurement. Fig. 6 presents the simulated temperature distribution as in the measurement. The temperature on the top position is identical with the furnace wall, which proves the validity of the thermal model.



**Figure 6.** Simulated temperature distribution on the wall of the furnace and the crucible

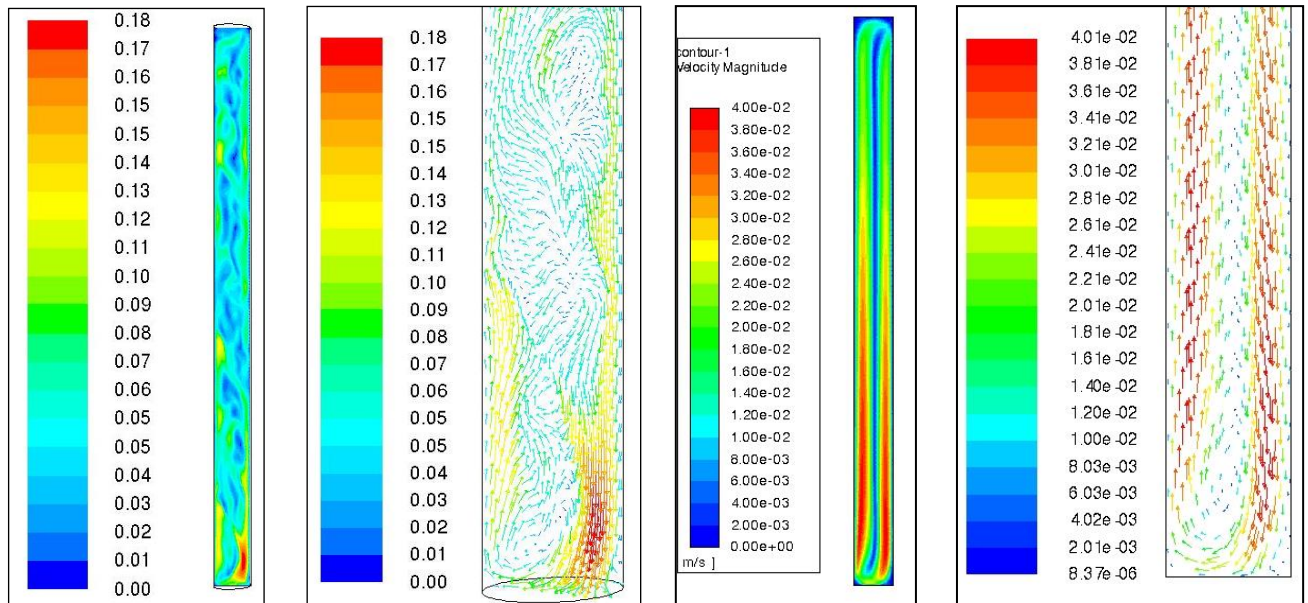
Fig. 7 presents the results. Qualitative and quantitative correspondence is visible.



**Figure 7.** Results of the simulation compared to the measurement of the 13 thermocouples

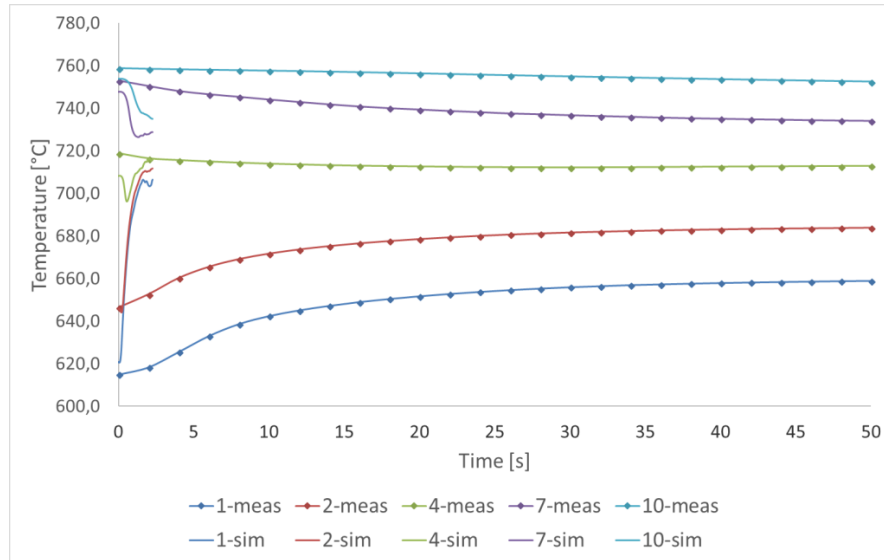
### Thermal flow modelling

The final model had a very simple geometry: a cylinder of 8 mm diameter X 100 mm height. The boundary condition was the heat flux data provided in the global thermal model. The flow was induced by the Lorenz force field simulated in the electromagnetic model. The force field was exported from Comsol and imported into Ansys Fluent. The simulation was transient 3D and single phase using pure aluminium melt. The flow pattern is presented on Fig. 8. The bidirectional mixing appears, but the flow becomes turbulent and accelerates very fast. If the comparison of the measured and simulated temperature distribution is done, it is obvious that the Lorenz Force field is too strong. Since the alimentation and the geometrical data was not accessible, a reduction factor of 0.1 was applied to achieve the desired flow.

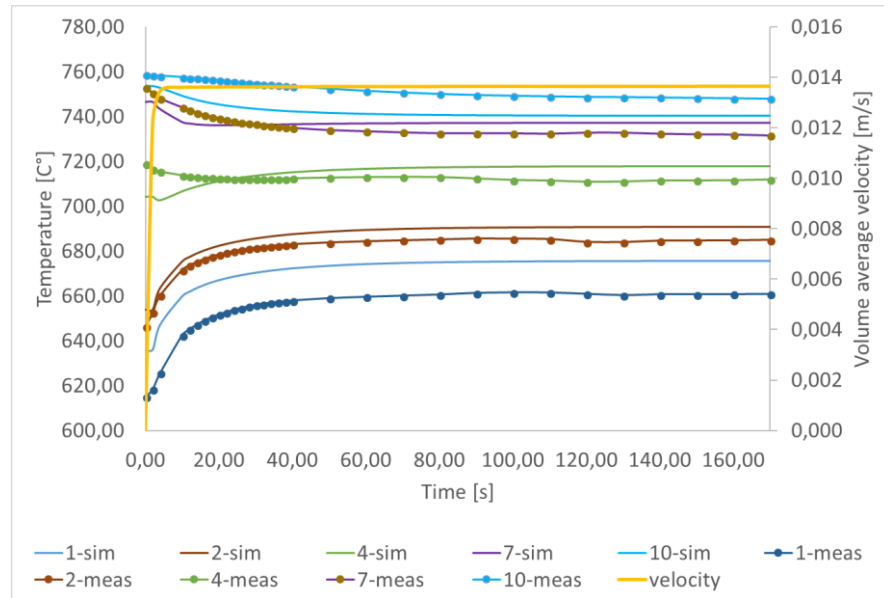


**Figure 8.** Flow pattern of the first trial and after adjustment of the force field

The thermal gradient shift effect with original and reduced Lorenz force field is presented of Fig. 9-10.



**Figure 9.** Thermal gradient shift with original Lorenz force field



**Figure 10.** Thermal gradient shift with reduced Lorenz force field and the settlement of the flow

Using the reduction factor the measured thermal effect could be simulated with qualitative and quantitative accuracy.

## Summary

A series of simulations was presented with the aim of providing the correct Lorenz force field for future solidification simulations. The electromagnetic simulation was not exact since the detailed technical data of the inductor was not accessible, but qualitative accuracy could be achieved. The global thermal simulation of the complete system was successful and useful thermal data was provided for the thermal-flow simulations. The final results show good correlation with the measurement if the reduction factor is applied. The reduced Lorenz force field can be used directly for solidification simulation, on the other hand the adjustment of the electromagnetic simulation should be done.

## References

- [1] Z. Yan, X. Li, Z. Cao, X. Zhang, Tingju Li: Grain refinement of horizontal continuous casting of the CuNi10Fe1Mn alloy hollow billets by rotating magnetic field (RMF). *Materials Letters*, vol. 62, p. 4389-4392. 2008
- [2] S. Steinbach, L. Ratke: The effect of rotating magnetic field on the microstructure of directionally solidified Al-Si-Mg alloys. *Materials Science And Engineering A* 413-414, p. 200-204. 2005
- [3] S. Eckert, B. Willers, P.A. Nikirtyuk, K. Eckert, U. Michel, G. Zouhar: Application of a rotating magnetic field during solidification of Pb-Sn alloys: Consequences of CET. *Materials Science And Engineering A* 413-414, p. 211-216. 2005
- [4] J. Kovács, A. Rónaföldi, A. Roósz: Unidirectional Solidification of Binary and Ternary Aluminium Alloys in a Rotating Magnetic Field. 6th International Conference on Electromagnetic Processing of Materials (EPM), Forschungszentrum Dresden-Rossendorf, ISBN978-3-936104-65-3, p. 664-667. Dresden, Germany. 2009. october 19-23.
- [5] C. Nagy, A. Rónaföldi, A. Roósz: Comparison of measured and numerically simulated angular velocity of magnetically stirred liquid Ga-In alloy. *Materials Science Forum* Vol. 752 (2013) pp 157-166
- [6] C. Nagy, Y. Fautrelle, O. Budenkova, A. Rónaföldi, A. Roósz : Numerical simulation of the RMF stirring of molten Ga-In alloy using RANS k- $\epsilon$  and LES turbulence models. *Materials Science Forum* Vols. 790-791 (2014) pp 402-407

# A 3-phase equiaxed solidification numerical model for binary alloy coupling macroscopic transport and grain growth

Tao WANG<sup>1,2</sup>, Olga BUDENKOVA<sup>2</sup>, Yves Delannoy<sup>2</sup>, Yves Fautrelle<sup>2</sup> and Engang Wang<sup>1</sup>

<sup>1</sup>Key Laboratory of Electromagnetic Processing of Materials (Ministry of Education), Northeastern University, P. R. China

<sup>2</sup>SIMAP, CNRS, Grenoble INP, University Grenoble Alpes, at Grenoble, 38000, France

[epm\\_wangtao@163.com](mailto:epm_wangtao@163.com); [olga.budenkova@simap.grenoble-inp.fr](mailto:olga.budenkova@simap.grenoble-inp.fr);  
[yves.delannoy@simap.grenoble-inp.fr](mailto:yves.delannoy@simap.grenoble-inp.fr); [yves.fautrelle@simap.grenoble-inp.fr](mailto:yves.fautrelle@simap.grenoble-inp.fr);  
[egwang@mail.neu.edu.cn](mailto:egwang@mail.neu.edu.cn)

**Keywords:** Solidification, Macrosegregation, Grain growth, Multiphase flows, Modeling.

**Abstract.** Modeling equiaxed solidification plays an important role in comprehension of solidification of metallic alloys and serves for prediction of the final solid structure and components' segregation. In the work, a 3-phase model which couples heat, mass, solute and momentum transportation for both grain phase and extradendritic liquid phase is presented for equiaxed solidification. A special attention is given to the calculation of the diffusion length at the interface between interdendritic and extradendritic liquid phases as well as to the momentum exchange coefficient between the liquid and grain phases. It is demonstrated that both the two parameters have critical effect on simulation results. The model is tested using a case of solidification of a binary alloy in a rectangular cavity. The results obtained in simulations are compared with other numerical results.

## Introduction

Numerical analysis for equiaxed dendritic solidification with convection basically need to solve two issues: (1) crystal growth method inside an undercooled melt at each growing stage, governed and affecting the mass, heat and chemical species transfer through the interfaces between phases for a single grain; (2) macroscopic scale movement of different phases and corresponding transport of concentration, energy and nuclei density, which is fundamental to the formation of the equiaxed zone and structural inhomogeneity induced by sedimentation or flotation of free crystals. For predicting the structure and composition of solidifying material various numerical models have been developed. The early models of solidification where the grain growth rate was controlled both by thermal balance and solute diffusion assumed solidification happens for a single grain in a stagnant melt zone [1,2], then the volume averaging technique was adopted to combine microstructural properties with macroscopic phenomena [3]. Following this, melt convection and solid-phase transport was accounted, the first attempting for this was made by Ni and Beckermann [4], who presented a 2-phase model that incorporated momentum exchange equations into previous globular solidification model and with this model some phenomena during the solidification of an Al-4%Cu alloy in a side-cooling cavity were successfully predicted [5]. Further, the 2-phase (liquid and solid) equiaxed model was expanded to 3 phases (interdendritic and extradendritic liquid and solid), and drag correlation for a wide range of solid volume fractions in equiaxed solidification was introduced after an extensive comparison of several main interfacial drag models [6,7].

Since then, equiaxed solidification models have been evolved [9–14]. Ciobanas and Fautrelle [9] derived an expression to calculate solute diffusion length with the respect of thermal equilibrium at the scale of the grain and the local homogeneity hypothesis. They also transposed the statistical phase averaging procedure generally accepted for gas-liquid models [15] into modeling of solidification. In simulation, the time step for solidification was different from the one used to solve the transport equation. Double time scheme was introduced in [16] to resolve and integrate globally the convection terms at first and then resolve and integrate locally the contributions of the grain growth kinetics. Wu



and Ludwig [13] included both globular and dendritic growth method in equiaxed solidification model to adapt it better to real physical process. Besides, in order to calculate the species exchange between phases, surface concentration was improved according to the shape factor theory of Nielsen et al [11].

This article presents a 3-phase multiscale solidification model to incorporate descriptions of fundamental microscopic phenomena, mainly the evolution of nuclei and dendrite growth during equiaxed alloy solidification, into macroscopic heat, solute and fluid flow calculations. After brief description of the governing equations and solution algorithm, some results obtained for solidification of a binary alloy in a rectangular cavity is discussed.

## Model description

Current model is built based on an averaging technique [6], through which macroscopic transport equations for each phase are obtained. It is appropriate to remind that both averaging procedures, the one over a representative volume or a statistical one over an ensemble, results in similar macroscopic equations provided some restrictions are fulfilled [15]. Then, the macroscopic equations related to the transport of mass, momentum, heat, solute along with phase fraction and variable grain density, in average, account for the interphase exchange at microscopic scale.

Similar to [6], [9] and [13] in the present model three phases are distinguished: liquid outside the envelope of equiaxed dendrite (*l*-phase), interdendritic liquid (*d*-phase) and the solid dendrite (*s*-phase) that gives for the corresponding fractions  $f_d + f_s + f_l = 1$ . Modelled mass transfer and solute diffusion between the three phases handle the growth kinetics for the grain envelope and the solidification of the interdendritic melt. Lipton–Glicksman–Kurz (LGK) tip growth kinetics is applied to estimate the evolution of the grain envelope. The solidification of interdendritic melt is driven by the difference between equilibrium liquid concentration and interdendritic liquid concentration. More details about the grain growth model and macroscopic conservation can be seen in [13]. Besides, solute diffusion length in the extradendritic liquid is updated according to appendix A in [9].

In terms of momentum transport, *s*-phase and *d*-phase are treated as union, which is literally the dendritic structure or grain phase, whose fraction is defined as  $f_e: f_e = f_d + f_s$ . Interdendritic liquid and solid dendrite share same velocity field. The equiaxed solidification interfacial drag model proposed in [8] (Eq. (26)) is adopted, however, flow partitioning effect between the interdendritic and extradendritic liquid is neglected for simplicity. Notice that this partitioning effect would be important when internal flow of dendrite is obviously stronger than external flow of dendrite, for instance, liquid flow can only happen in *d*-phase when  $f_l$  approach 0.

## Solution method

The processes happen at macroscopic and microscopic scale are modelled with different time steps, the solution procedure is shown in Fig. 1. A larger time step  $dt$ , used for the calculation of the transport phenomena at the macro-sale is divided by  $N$  time sub-steps for the calculation of the processes within the grain (diffusion, solidification) and the grain growth. Each sub-step calculation iterates until all the relevant variables converge. Once all the  $N$  time sub-steps are finished, we integrate the phase change rate and concentration transfer rate over time  $dt$ . The obtained values are used as source term for solving global transport equations. The macroscopic calculation, including multiphase flow field and transport of energy, solute and nuclei density, are solved by ANSYS FLUENT® software with the time step  $dt$ .

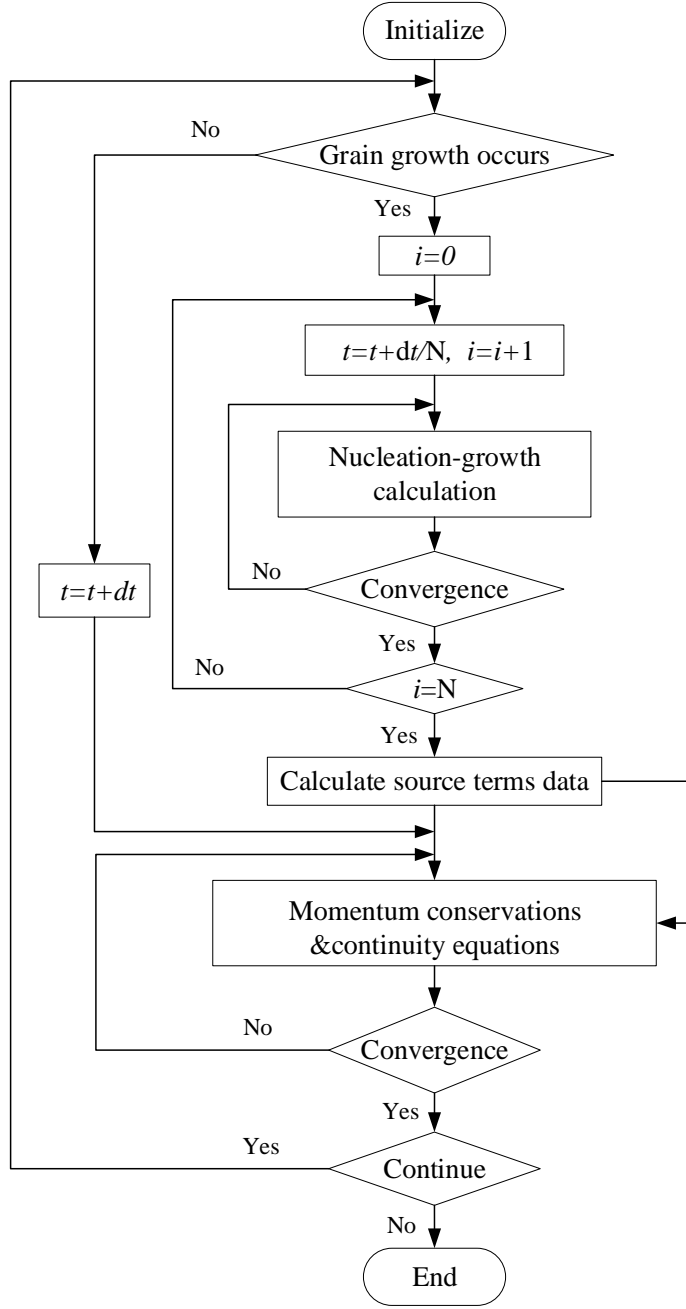


Figure 1. Solution algorithm

### Test case and results

The verification of current model is performed on a well-known Hebditch–Hunt benchmark solidification problem of Sn-5wt%Pb [17] with principal physical parameters and boundary conditions implemented in the same way as in [16]. The nucleation is also assumed to occur at fixed temperature equal to the one chosen in [16]. Equiaxed envelope shape factors are determined as suggested in [13] as well as the grain packing limit fraction  $f_e^c = 0.637$ .

In our calculations, similar to [16,17], because of thermal and solutal buoyancy effect, the liquid alloy at the cooled side is heavier and thus flows downward that eventually forms a global counterclockwise motion flow. According to the chosen properties, the density of the solid phase is

constant and larger than the density of the liquid if the concentration of Pb rejected to the liquid is less than 8.85wt%. At the initial stage of solidification, as seen in Fig. 2, both the grain phase ( $e$ ) and liquid phase ( $l$ ) can move freely, however, the grain phase always has tendency to sediment despite that solid contains less Pb while the pure liquid becomes enriched with Pb while it passes through grains from a colder to warmer wall and then goes upward near the right boundary.

At grain fraction  $f_e = f_e^c$ , as shown by the isline in Fig. 2, the grain phase becomes packed. Due to rapidly increasing flow resistance in the packed grains, liquid flow appears too weak to influence the solute distribution in this region. A packed grains layer which is poorer in Pb gradually heaps up from the bottom of cavity until the top. Sometimes the grains reach packing limitation before arrive to right part, which explain the formation of a gently slope toward east.

Finally, a higher concentration of the Pb present at the top of the sample which could seem unusual, and slightly negative segregated layer presented at the bottom, as shown in the final macrosegregation map (Fig.3).

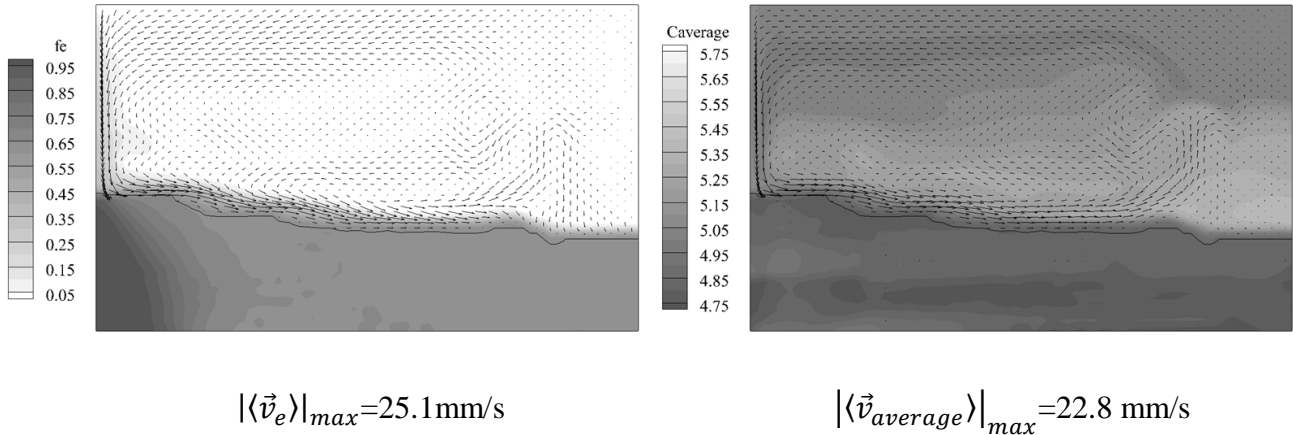


Figure 2. Results obtained after 50s of solidification – grain phase fraction ( $f_e$ ) and grain phase velocity ( $\langle \vec{v}_e \rangle$ ) distribution (left); averaged mass concentration ( $C_{average}$  in wt. %Pb) and averaged velocity ( $\langle \vec{v}_{average} \rangle$ ) distribution (right)

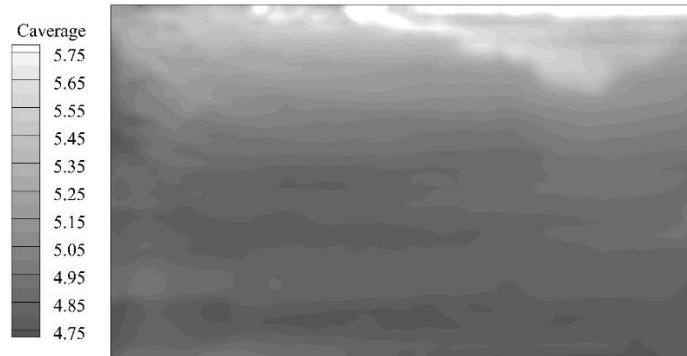


Figure 3. Final macrosegregation map (wt. %Pb) in the cavity

Compared with the results from 2- phase model in [16], current results do not predict a severe segregation channel at the bottom wall and the predicted segregation at the top is weaker. The differences may arise because of two reasons:

(1) In the present case, the growth of grain envelope happens much faster compared to the evolution of the solid/liquid interface (solidification) in 2-phase model, especially at the initial stage of solidification. The grains' packing criteria in present model is achieved earlier than that in [16], where the grains become packed at solid fraction  $f_s^c = 0.3$ . In the grain-packed region, interdendritic flow stops while extradendritic flow is damped. Consequently, the liquid flow has less time to bring away solute from the solidification frontier through the porous zone before it is blocked by packed grains, thus the enrichment at the top is lighter than in [16].

(2) In 2-phase model, interdendritic and extradendritic liquid phase share same concentration field and flow field, which implies that their concentration is always completely mixed. In the present model, the introduced interdendritic liquid phase serves as a transition area between pure liquid and inner solid. With this way solute transport between solid and liquid is limited compared with the condition in 2-phase model.

## Summary

A 3-phase equiaxed solidification model is proposed where detailed kinetic grain growth model is coupled with macroscale transport. A multi- time step resolution algorithm is applied to accelerate the calculation. A Hebditch-Hunt test of solidification of a binary Sn-5wt%Pb alloy is modelled and results are compared with numerical simulations performed in [16]. The grain fraction distribution, liquid flow field and macrosegregation map have shown similarity, yet the segregation predicted in this work is lighter and concentration distribution is more uniform. The difference may arise from rapidly growing packed grains bed as well as the inhibiting effect of concentration transport by interdendritic liquid phase.

## Acknowledgements

This work is a joint cooperation between SIMAP laboratory of Grenoble INP (France) and Key Laboratory of EPM of Northeastern University (P. R. China). The authors gratefully acknowledge financial support from China Scholarship Council (no. 201706080074) and ESA-MAP project MICAST (contract number ESA-AO-99-031).

## References

- [1] M. Rappaz, P.H. Thévoz, Solute diffusion model for equiaxed dendritic growth: Analytical solution, *Acta Metall.* 35 (1987) 2929–2933.
- [2] P. Thévoz, J.L. Desbiolles, M. Rappaz, Modeling of equiaxed microstructure formation in casting, *Metall. Trans. A* 20 (1989) 311–322.
- [3] C.Y. Wang, C. Beckermann, A unified solute diffusion model for columnar and equiaxed dendritic alloy solidification, *Mater. Sci. Eng. A* 171 (1993) 199–211.
- [4] J. Ni, C. Beckermann, A volume-averaged two-phase model for transport phenomena during solidification, *Metall. Trans. B* 22 (1991) 349–361.
- [5] J. Ni, C. Beckermann, Modeling of globulitic alloy solidification with convection, *J. Mater. Process. Manuf. Sci.* 2 (1993) 217–231.
- [6] C.Y. Wang, C. Beckermann, A multiphase solute diffusion model for dendritic alloy solidification, *Metall. Trans. A* 24 (1993) 2787–2802.
- [7] C.Y. Wang, C. Beckermann, Equiaxed dendritic solidification with convection: Part I. Multiscale/multiphase modeling, *Metall. Mater. Trans. A* 27 (1996) 2754–2764.
- [8] C.Y. Wang, S. Ahuja, C. Beckermann, H.C. de Groh, Multiparticle interfacial drag in equiaxed solidification, *Metall. Mater. Trans. B* 26 (1995) 111–119.
- [9] A.I. Ciobanas, Y. Fautrelle, Ensemble averaged multiphase Eulerian model for columnar/equiaxed solidification of a binary alloy: I. the mathematical model, *J. Phys. D. Appl. Phys.* 40 (2007) 3733–3762.
- [10] N. Leriche, H. Combeau, C.A. Gandin, M. Založnik, Modelling of columnar-to-equiaxed and equiaxed-to- columnar transitions in ingots using a multiphase model, *IOP Conf. Ser. Mater. Sci. Eng.* 84 (2015) 1–8.
- [11] Nielsen, B. Appolaire, H. Combeau, A. Mo, Measurements and modeling of the microstructural morphology during equiaxed solidification of Al-Cu alloys, *Metall. Mater. Trans. A Phys. Metall. Mater. Sci.* 32 (2001) 2049–2060.
- [12] B. Appolaire, H. Combeau, G. Lesoult, Modeling of equiaxed growth in multicomponent alloys accounting for convection and for the globular/dendritic morphological transition, *Mater. Sci. Eng. A* 487 (2008) 33–45.
- [13] M. Wu, A. Ludwig, Modeling equiaxed solidification with melt convection and grain sedimentation—II. Model verification, *Acta Mater.* 57 (2009) 5632–5644.
- [14] M. Založnik, H. Combeau, An operator splitting scheme for coupling macroscopic transport and grain growth in a two-phase multiscale solidification model: Part I – Model and solution scheme, *Comput. Mater. Sci.* 48 (2010) 1–10.
- [15] D.A. Drew, Mathematical modeling of two-phase flow, *Annu. Rev. Fluid Mech.* 15 (1983) 261–291.
- [16] M. Založnik, A. Kumar, H. Combeau, An operator splitting scheme for coupling macroscopic transport and grain growth in a two-phase multiscale solidification model: Part II – Application of the model, *Comput. Mater. Sci.* 48 (2010) 11–21.
- [17] D.J. Hebditch, J.D. Hunt, Observations of Ingot Macrosegregation on Model Systems., *Met. Trans* 5 (1974) 1557–1564.

# Numerical Simulation of Heat Transfer and Fluid Flow in Electroslag Remelting Process

Hao SHI<sup>1</sup>, Houfa SHEN<sup>1</sup>

<sup>1</sup> Key Laboratory for Advanced Materials Processing Technology, Ministry of Education, School of Materials Science and Engineering, Tsinghua University, Beijing 100084, China

shen@tsinghua.edu.cn

**Keywords:** Electroslag remelting; numerical simulation; two-phase flow; metal droplet; multi-physics coupling

**Abstract.** Electroslag remelting (ESR) is thought as a promising method for the production of high-quality ingots of special steels or nickel-based superalloys. In ESR process, the formation and movement of droplets plays an important role in heat transfer and fluid flow in slag. Limited to the complexity of the mechanism, high temperature and high trial costs, it is very difficult to make experimental observations of the phenomena occurring within the molten slag. In this paper, the droplet formation and movement during ESR process is simulated by means of a magnetohydrodynamic (MHD) and slag-metal multiphase flow approach with Re-Normalisation Group (RNG)  $k$ - $\varepsilon$  turbulence model. The computational domain includes a layer of slag and a layer of liquid steel. The two-phase flow is tracked with the volume of fluid (VOF) method. Results show that a strong interaction between the electromagnetic field and the phase distribution occurs. Since the metal has a higher electrical conductivity, the electric current travels through the liquid metal in priority and the current density around the droplet is higher than that in the periphery of the electrode. Hence, the maximum Joule heat and Lorentz force occur in the slag around the metal droplet. Under the electrode, a thin metal liquid film is formed first and then the droplet is formed. In the industrial scale ESR process, the position where the droplets fall down is distributed randomly at the bottom of electrode. The droplet falling causes strong flow in the slag and melt pool. The maximum velocity in the slag layer is approximately 0.5 m/s. The droplet size increases with the increase of the surface tension.

## Introduction

High-quality ingots are becoming more important in aerospace, metallurgy, mining, machinery and electricity with the rapid development of industry. Electroslag remelting (ESR), a method of refining a consumable metal electrode through a molten slag that is electrically heated, is thought as a promising method for the production of high-quality ingots because non-metallic inclusions and sulfur dissolved in the metal can be removed efficiently and compact structure can be obtained [1]. ESR has been widely used in the production of high-quality ingots of special steels or nickel-based superalloys.

Due to the high trial costs, the complexity of the mechanism and high temperature, it is very difficult to make industrial scale experimental observations of the phenomena occurring within the molten slag. It is widely accepted that the development of heat and mass transfer at the slag/droplet interface affects the process of the non-metallic inclusion removal and desulfurization directly. Moreover, when the droplet falls through the slag and into the metal pool, it will cause violent flow, which affects the distribution of the temperature field and the heat transfer between the slag and metal. Thus, for fundamental and technical reasons, investigations of how the droplets form at the tip of consumable electrodes and how they behave in the slag pool are important to validate the mechanism and provide value direction to the production. However, it is difficult to observe and measure the ESR process due to the opaque materials, high temperature and strong electric current. Hence, many fundamental aspects of this process are still unclear and subject of controversy. During the past decades, many researchers have devoted significant efforts to understand the electromagnetic phenomenon and slag-metal two phases flow during the ESR process. Some physical models similar

to the ESR process have been established to investigate the formation of droplets. J. Campbell [2] used a slag containing a transparent substances, such as LiCl-KCl, NaOH, to remelt an electrode comprising low-melting metals. Similar models have also been reported by Jiang et al [3]. An oscilloscope was used to detect the occurrence of a droplet departure in conventional nontransparent slag by monitoring the curve of the voltage. By counting droplets and measuring the weight change of ingot, an approximate size of each droplet was determined [4]. Zhong et al. set up a transparent model to explore the effect of transverse static magnetic field on the droplet behavior in ESR process. Molten  $\text{ZnCl}_2$  was as the slag and low-melting-point zinc bar was selected as electrode. Although these physical experiments can be used to study the formation and detachment of droplets, understanding the real conditions of the ESR process is still needed.

In recently years, mathematical models, much faster and easier than experiments, have been widely used to simulate the ESR process benefited from the fast development of the computer and the results of the experiments. A. Kharicha et al. [6] simulated the electromagnetic field considering influences of the movement of slag-melt pool interface and dripping of droplets through the slag, which showed the interaction among electromagnetic field, fluid flow and heat transfer. However, such simulation was computationally expensive. He et al. [8] established a 3D mathematical model to describe the effects of the slag-metal two-phase flow on the distribution of Joule heat and Lorentz force. Dong et al. [7] built a two-dimensional axisymmetric model and simulated the electrode melting and droplet falling in the slag. However, it is difficult to use the two-dimensional axisymmetric model to predict the asymmetrical phenomena of falling droplets.

The purpose of the present work is to understand the formation and drop of metal droplets in slag bath of electros slag remelting processes based on the three-dimensional model with the primary variables of two-phase flow field. Non-uniform mesh and adaptive time step are employed to speed up the calculation of programs. At the same time, parametric studies are also conducted with the effect of surface tensions in the ESR system.

**Table 1.** Physical properties of metal and slag

Parameter	metal	slag
Density, $\text{kg/m}^3$	7200	2850
Dynamic viscosity, $\text{Pa}\cdot\text{s}$	0.006	0.01
Thermal conductivity, $\text{W/m}\cdot\text{K}$	30.52	10.46
Specific heat, $\text{J/kg}\cdot\text{K}$	752	1255
Electrical conductivity, $\Omega^{-1}\cdot\text{m}^{-1}$	714000	250
Thermal coefficient of cubical expansion, $\text{K}^{-1}$	0.0001	0.0004

**Table 2.** Operating and boundary conditions

Parameter	value	BCs	value
Current, A	1500	$h_{\text{slag-mold}}$ , $\text{W/m}^2\cdot\text{K}$	400
Melting rate, $\text{kg/s}$	0.01	$h_{\text{ingot-mold}}$ , $\text{W/m}^2\cdot\text{K}$	400
Temperature of water and environment, K	298.15	$h_{\text{air-slag}}$ , $\text{W/m}^2\cdot\text{K}$	188
Frequency, Hz	50	$\epsilon_{\text{slag}}$	0.6
Interfacial tension, N/m	0.2/0.5/1.0		
Thermal coefficient of cubical expansion, $\text{K}^{-1}$	0.0001		

## Mathematical Model

The complex ESR process involves a range of physical phenomena and their coupling interaction: heat transfer with phase change and fluid convection, the interaction between the turbulent flow and electromagnetic field known as magnetohydrodynamics (MHD). The general transport equation for AC electromagnetic fields could be expressed by the magnetic diffusion equation. The Lorentz force and Joule heat obtained from the electromagnetic field calculation affect the flow and temperature distribution in slag pool respectively. The temperature field affects the fluid flow equations through the buoyancy term and the knowledge of the velocity field and of the turbulence parameters is required in the solution of the convective heat transfer equation. Meanwhile, the slag-metal two-phase



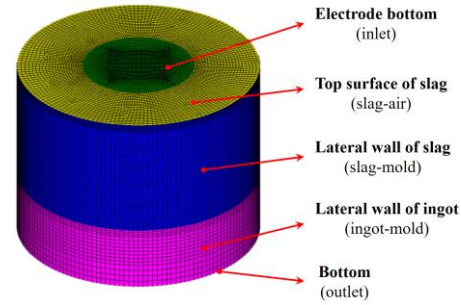
flow affects the electromagnetic field as a result of the significant different electric conductivity between the slag and the metal. The geometrical parameters, physical properties of the metal and slag, as well as the process parameters are listed in Tabs. 1-2.

The interface between the molten slag and liquid steel melt is tracked with the geometric reconstruction VOF technology. A single set of momentum equations is shared by all fluids. The motion of the slag and liquid metal is turbulent. Consequently, the flow is modeled using Reynolds-averaged Navier-Stokes equations, which has been shown to give a satisfactory reproduction of the time averaged velocity field.

Considering that the solidification in the metal pool has little effect on the multiphase flow in the slag pool, the solidification process is ignored in this work.

**Table 3.** Geometrical parameters

Geometry	value
Electrode diameter, m	0.055
Immersion depth of electrode, m	0.0
Ingot diameter, m	0.12
Slag height, m	0.06
Metal height, m	0.032



**Figure 1.** Computational model and mesh

## Solution Procedure

The governing equations were discretized based on the Finite Volume Method (FVM) and solved by means of the commercial software FLUENT. Firstly, the mesh size was set about 0.8mm to ensure tracking the interface of the slag and metal accurately and non-uniform grid was employed to save computing time (Fig. 1). The dimensions of the whole model was listed in Table 3. Then the governing equations for the electromagnetic phenomena, two-phase flow and heat transfer were solved simultaneously. Before advancing to the next time step, the iterative procedure continued until all normalized unscaled residuals were less than  $10^{-5}$ . The adaptive time step was determined by the dynamic of the metal and slag interface through a chosen maximum courant number 0.24. Depending on the droplet falling speed, the typical calculation time step was in the range of  $10^{-3}$ - $10^{-4}$  second. The calculations were performed using 16 cores of Intel Xeon 2.40GHz.

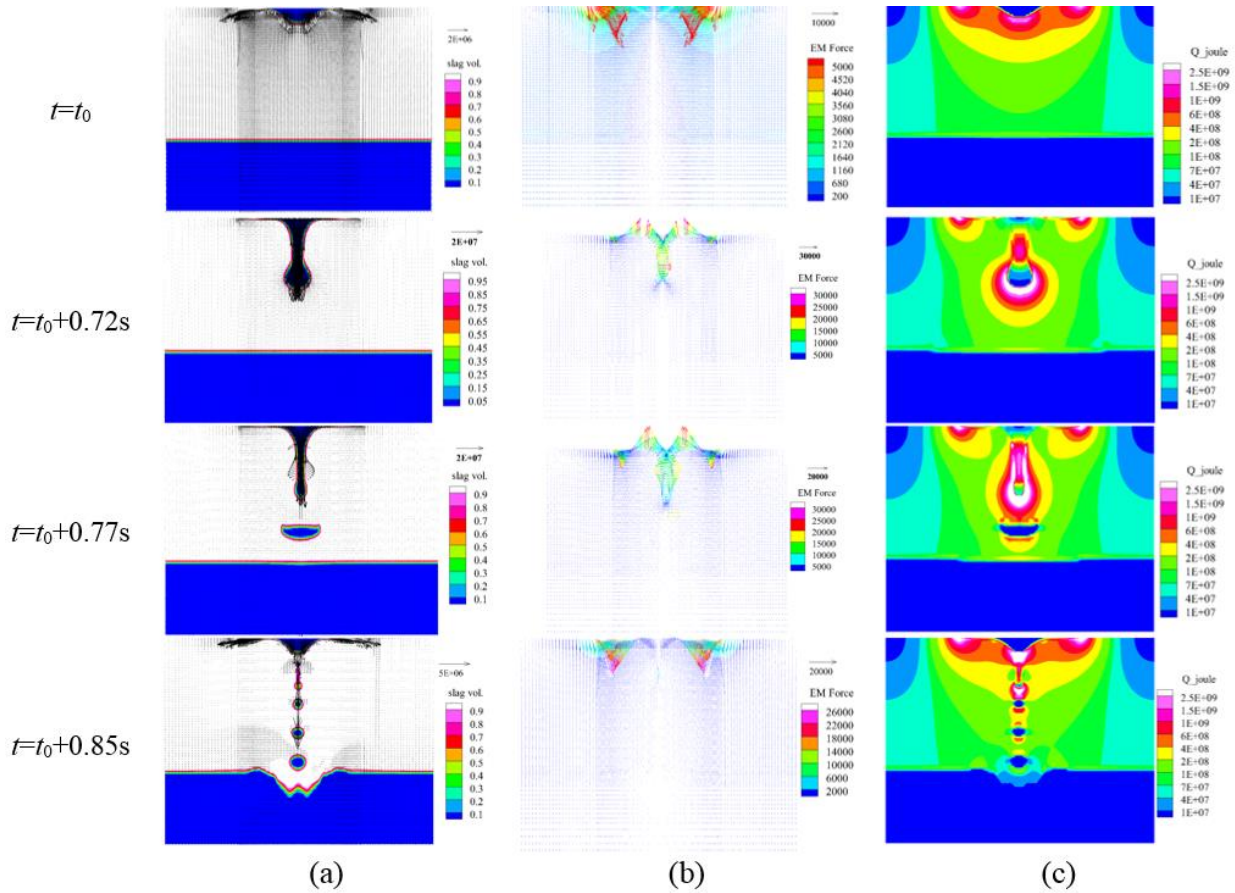
## Results and discussion

There are three cases, named Case 1, Case 2 and Case 3, to simulate the droplets behaviors for three different interfacial tension coefficients 1N/m, 0.5N/m and 0.2N/m, respectively. Fig. 2 shows the field variations of electromagnetic quantities in ESR process for Case 1 and the interfacial tension coefficient is equal to 1N/m. It is obvious that there are three stages for the droplet motion: (1) formation of droplets at the electrode tip; (2) droplets falling through the slag, and (3) collection of the droplets in a metal pool at the top of the ingot.

At the time of  $t_0$ , Fig. 2 (a) shows that a larger current density occurs at the edge of electrode and droplet tip. It is because the current always choose preferentially to flow through the metal droplet to minimize the electric resistance and the current usually aggregates at the conductor tips. Interacting with magnetic field, the current creating the maximum Lorentz force, nearly  $30\ 232\text{N/m}^3$ , at the edge of electrode. The Joule heat is concentrated at the edge of electrode and droplet tip due to the high current density.

As the electrode melting and the liquid metal accumulating at the bottom electrode, an elongated faucet forms (shown in Fig. 2) and the necking phenomenon takes place at the time  $t_0+0.72\text{s}$  under the effect of gravity, Lorentz force and interfacial tension. Almost all of the current passes through the metal faucet to the slag, thus the current from the edge of electrode flows towards the center, which

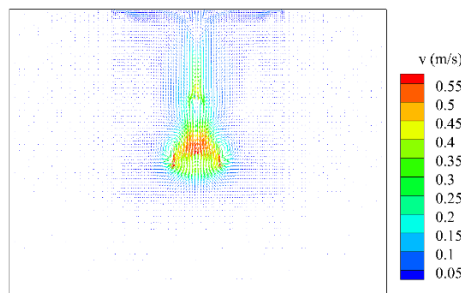
raises the upward Lorentz force as shown in Fig. 2 (b). As a result of large amount of current passing through the faucet, a lot of Joule heat is generated in the faucet.



**Figure 2.** Field variables of the electromagnetic quantities  
(a) the slag volume fraction, (b) Lorentz force, (c) Joule heat

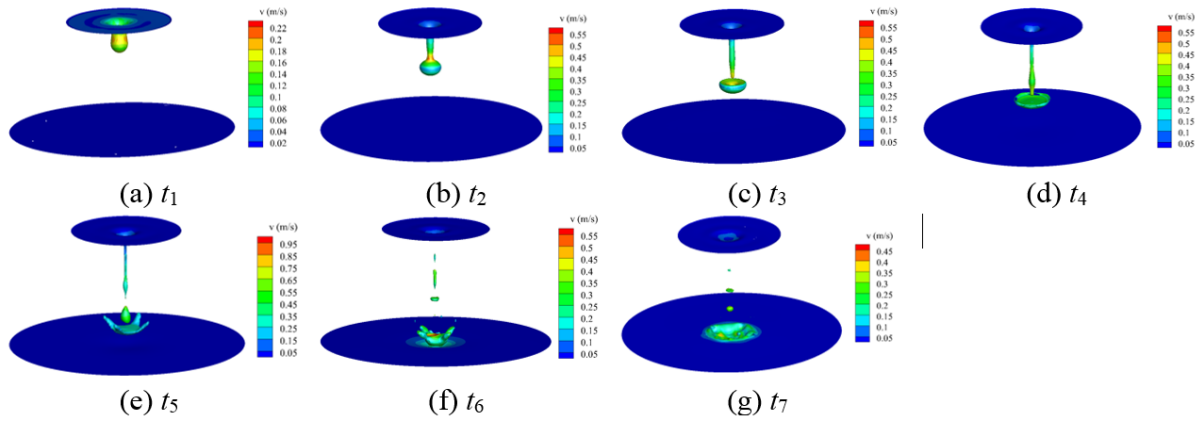
When the liquid metal at the electrode bottom accumulates to a certain critical value, the gravity of liquid metal is greater than interfacial tension and the formation of droplets occurs. At  $t_0+0.77s$ , the departure of the first droplet occurs and a slag gap forms between the droplet and the remaining faucet, shown in Fig. 2 (a). The diameter of the first droplet is about 15mm. Obviously, the surface area of the remaining faucet decreases due to the droplets formation, thus the current density is increasing at the slag-metal surface which cause the generation of Joule heat increasing.

During droplets falling down, the shape of the droplet changes from ball to flat ball under the effect of relative movement between the slag and droplets. Meanwhile, a strong flow in the slag is created by the falling of the droplets (Fig. 3) and this flow drags the remaining faucet. Under the effect of slag flow and interfacial tension, the remaining faucet is broken into several little droplets and a little of liquid metal remains at the bottom of the electrode to form a stable liquid film.



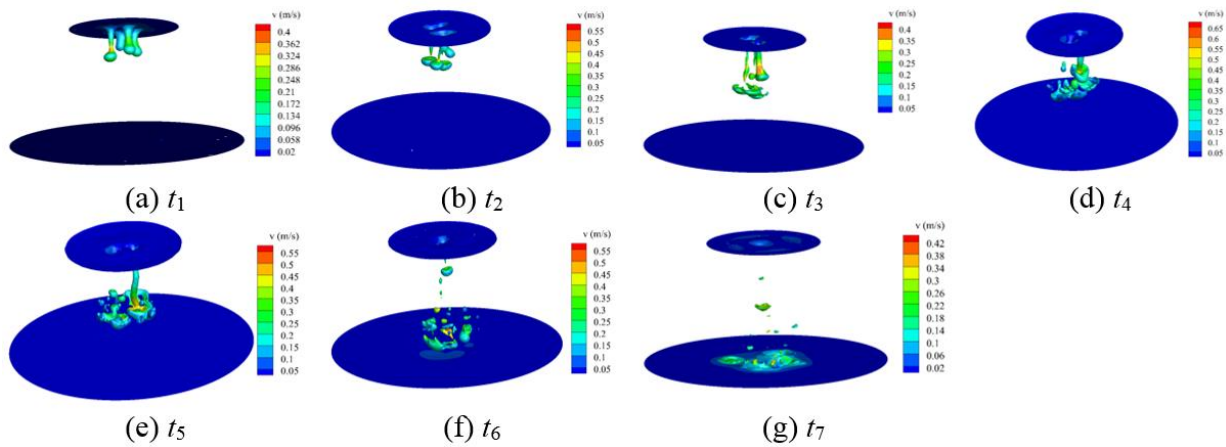
**Figure 3.** Flow field during droplet falling

Fig. 4 shows the droplets formation and movement of Case 2 and the interfacial tension coefficient is equal to 0.5N/m. Compared with Case 1, the diameter of the first droplet in Case 2 is about 11mm, a bit less than that of Case 1. When the droplet detaches from the faucet and falls down through the slag, the deformation of the droplets is large and the shape of the droplet changes from spherical liquid drop to liquid film because the interfacial tension cannot withdraw the resistance in the slag. At the time  $t_5$ , the droplet begins to break up and forms some little droplets at the edge area. However, these small droplets cannot be observed in this simulation because their size is smaller than the mesh size.



**Figure 4.** Views of the slag/metal interfaces colored by velocity with interfacial tension of 0.5N/m  
(a, b) formation of the liquid faucet, (c, d, e) droplets formation and detachment,  
(f, g) droplets impact and deformation of the slag/pool interface

For Case 3, the droplets behavior is a little different from the other two cases at the droplet formation stage. Four faucets form simultaneously in four different positions shown as Fig. 5 (a) and these four faucets finally merge into one faucet like Figs. 5 (g). The necking phenomenon takes place as soon as the faucets are formed because the interfacial tension cannot withstand the gravity force and the electromagnetic pinch force. After detaching the faucets, the droplets deform quickly and greatly. Firstly, the droplets flatten and develop a crescent shape (Figs. 5 b-c). Then under the effect of slag flow, these droplets are totally broken up into plenty of small droplets. Therefore, the diameter of the droplets are smaller than that in the other cases. These small drops have small effects on the metal pool and provide large surface area which the removal of inclusion and desulfurization.



**Figure 5.** Views of the slag/metal interfaces colored by velocity with the interfacial tension of 0.2N/m  
(a, b) formation of the liquid faucet, (c, d, e) droplets formation and detachment,  
(f, g) droplets impact and deformation of the slag/pool interface

## Summary

A 3-D VOF model coupled with a magneto-hydrodynamic model was proposed to simulate the droplet formation and movement during Electroslag Remelting (ESR) process. The model can predict the electric and magnetic field distribution in function of the metal distribution in the low electric conductivity slag. In addition, the effect of the interfacial tension coefficient on the droplets behavior was investigated.

(1) As the melt is a much better conductor than the molten slag, most of the current provided by the electrode chooses to flow through the metallic path. According to the simulation results, the slag-metal two-phase flow influences the current distribution greatly. The Joule heat reaches maximum where current flows from metal into slag.

(2) With larger interfacial tension, less faucet forms and larger droplets are released. After the droplets depart from the faucet, the faucet is broken into several small droplets under the pinch force, gravity and viscous force between slag and liquid metal.

(3) For a small interfacial tension, two to three faucets appear at the bottom of electrode. In addition, the large droplets are broken into small droplets during falling down. Therefore, the space between the electrode and the liquid pool surface is filled with many small droplets, which promote the heat and mass transfer as well as the inclusions removal.

## Acknowledgement

This work was financially supported by the project of green manufacturing system integration of MIIT China (2016-64).

## References

- [1] B. Hernandez-Morales, A. Mitchell, Review of Mathematical Models of Fluid Flow, Heat Transfer, and Mass Transfer in Electroslag Remelting Process, *Ironmak. Steelmak.* 26.6 (1999) 423-438.
- [2] J. Campbell, Fluid Flow and Droplet Formation in the Electroslag Remelting Process, *JOM* 22.7 (1970) 23-35.
- [3] Y. Cao, Y. Dong, Z. Jiang, et al., Research on Droplet Formation and Dripping Behavior during the Electroslag Remelting Process, *Int. J. Miner. Metall. Mater.* 23.4 (2016) 399-407.
- [4] E. Schlienger, J.M. Robertson, et al. United States Patent 6019811. Metals Processing Control by Counting Molten Metal Droplets. 2000
- [5] H. Wang, Y. Zhong et al., Influences of the Transverse Static Magnetic Field on the Droplet Evolution Behaviors during the Low Frequency Electroslag Remelting Process, *ISIJ Int.* 57.12 (2017) 2157-2164.
- [6] A. Kharicha, A. Ludwig, A. Wu, 3D Simulation of the Melting during an Electro-Slag Remelting Process, *Epd Congress* (2011) 771-778.
- [7] A. Kharicha, M. Wu, A. Ludwig, et al., Simulation of the Electric Signal During the Formation and Departure of Droplets in the Electroslag Remelting Process, *Metall. Mater. Trans. B* 47.2 (2016) 1427-1434.
- [8] L. Shuang, H. Zhu, H. Cai, et al., Numerical Simulation of the Formation and the Dripping of Droplet in the Electroslag Remelting Process, *Therm. Sci.* 14.00 (2017) 70-70.
- [9] Y. Dong, Z. Jiang, J. Fan, et al., Comprehensive Mathematical Model for Simulating Electroslag Remelting, *Metall. Mater. Trans. B* 47.2 (2016) 1475-1488.

# The Simulation of Special Gravity Filling Conditions

Daniel MOLNAR<sup>1</sup>, David HALAPI<sup>1</sup>, Marianna Bubenko<sup>1</sup>

<sup>1</sup>Institute of Foundry Engineering, Department of Materials Science and Engineering,  
University of Miskolc, Hungary  
[daniel.molnar@uni-miskolc.hu](mailto:daniel.molnar@uni-miskolc.hu)

**Keywords:** gravity casting, tilt casting, computer simulation, Control Volume

**Abstract.** Fluidity of metal melts is an important property of casting technology which fundamentally determines the adequacy of castings. In this paper different factors of fluidity are discussed among others the application of the limited Bernoulli's equation, viscosity in the mushy zone and the application of Darcy's law. A commercial Control Volume model is used to simulate a special gravity casting case, called tilt casting.

## Introduction

Reliable fluidity data for aluminium alloys are not readily available however such data are important in mould filling calculations. Fluidity is used to indicate the distance of a molten metal can flow before it solidifies and it is not only the inverse of viscosity, but depends upon many factors. The fluidity equation based on Flemings is: [1]

$$L_f = \frac{(A \cdot \rho \cdot v)(k \cdot H_f + c \Delta T)}{S \cdot h \cdot (T - T_r)} * \left(1 + 0,5 * \frac{h \cdot \sqrt{\pi \cdot \alpha \cdot \Delta X}}{k \cdot \sqrt{v}}\right) \quad (1)$$

Where: ( $L_f$ ) final length – fluidity, ( $A$ ) mould surface area, ( $\Delta X$ ) choking range, ( $T$ ) liquid metal temperature, ( $T_r$ ) room temperature, ( $h$ ) heat transfer coefficient at mould-metal interface, ( $S$ ) circumference of mould channel, ( $\Delta T$ ) superheat, ( $k$ ) thermal conductivity of the mould, ( $\rho$ ) density of metal, ( $v$ ) velocity of metal flow, ( $H_f$ ) heat of fusion of metal, ( $c$ ) specific heat of metal.

Fluidity factors can be categorized as follows:

1. Metal variables: chemical composition, solidification behaviour and range, viscosity, heat of fusion.
2. Mould and metal variables: heat transfer coefficient, thermal conductivity, mass density, specific heat, surface tension.
3. Pouring method variables: gravity casting, tilt casting, LPDC, HPDC.

By carefully selection of the combination of these variables, fluidity can be controlled. This plays a key role for thin walled castings because e.g. misruns are a result of insufficient fluidity of the liquid metal. It is not easy to control fluidity due to the large number of variables involved. However, if variations in fluidity due to uncontrolled factors can be estimated, defect problems, such as unexpected misruns and cold shuts, can be overcome and process costs reduced.

## Description of flow, the Bernoulli's equation

The application of Bernoulli's equation in foundry calculations is limited. In ideal case a simplified form of Bernoulli's equation can be used:

$$\frac{v^2}{2} + gh + \frac{p}{\rho} = \text{constant} \quad (2)$$

Where: ( $v$ ) velocity, ( $g$ ) value of gravity, ( $h$ ) height, ( $p$ ) pressure, ( $\rho$ ) density. The velocity of the melt in the gating system is not only altered by the hydrodynamic laws, but the quantity of the metal which depends on the losses and the degree of solidification. To achieve Newtonian fluid behaviour, the melt density during filling must be constant, thus the cavity must be filled before solidification occurs. The wall friction ( $\Delta h_1$ ), tapers and directional changes ( $\Delta h_2$ ) occurs as pressure drops:

$$\Delta h_1 = \lambda \frac{l}{d} \frac{v^2}{2g} \quad (3)$$

$$\Delta h_2 = \xi \frac{v^2}{2g} \quad (4)$$

Where: ( $\lambda$ ) drag coefficient, ( $l$ ) channel length, ( $d$ ) channel diameter, ( $\xi$ ) empirical resistance number. Thus the Bernoulli's equation in mould filling cases can be used as: [2,3]



$$\frac{2g(h-\Delta h_1-\Delta h_2)}{2} + g(h - \Delta h_1 - \Delta h_2) + \frac{p}{\rho} = \text{constant} \quad (5)$$

In general, however, the application of the Bernoulli equation to gating systems is not quite so straightforward. There are various reasons for this.

1. In general, Bernoulli's equation relates to steady state flow. However, of course, in gating systems most of the interest necessarily lies in the priming of the flow channels. In this situation the surface tension of the advancing meniscus can be important, as described in the Weber number, where ( $\sigma$ ) is the surface tension:

$$We = \frac{\rho l v^2}{\sigma} \quad (6)$$

If  $We < 1$  the liquid surface is tranquil, and if  $We > 1$  surface turbulence is expected. If the priming is not carried out well, the casting is likely to suffer severely.

2. The surface tension of liquid metals is over ten times higher than that of water. Thus pressures due to surface tension have been neglected and are neglectable for such common room temperature liquids on which most flow research has been conducted. The additional pressure generated because of the curvature of the meniscus at the flow front, and the curvature at the sides of a flow stream, affect the behaviour of metals in many examples involved in the filling of molds. For instance at the critical velocity that is targeted in mould filling, the effects of surface tension and flow forces are equal. At velocities lower than this, surface tension dominates.
3. The presence of the oxide on the surface of an advancing liquid is a further complication, and is not easily allowed for. The flow adopts a stick-slip motion as the film breaks and re-forms. The advance of the unzipping wave is a classic instance that could not be predicted by a purely liquid model such as that described by Bernoulli.
4. The frictional losses during flow, which can be explicitly cited in Bernoulli's equation, are known to be important. However, in general, although they are assumed to be known, they have been little researched in the case of the flow of liquid metals.
5. The presence of oxide films floating about in suspension is another uncertainty that can cause problems. The density of such defects can easily reach levels at which the effective viscosity of the mixture can be very much increased, although viscosity does not appear explicitly in the Bernoulli equation. The suppression of convection in such contaminated liquids is common. Flow out of thick sections and into very thin sections can be prevented completely by blockage of the entrance into the thin section.

From the above list it is clear that the application of Bernoulli equation is more accurate for thicker section flows where surface effects and internal defects in the liquid are less dominant. As filling systems are progressively slimmed, and casting sections are thinned, Bernoulli's equation has to be used with greater caution.

### **Description of flow, viscosity**

Viscosity is a fundamental characteristic property of all liquids. When a liquid flows, it has an internal resistance to flow. Viscosity is a measure of this resistance to flow or shear. Viscosity is expressed in two distinct forms: dynamic viscosity and kinematic viscosity. [4] Viscosity of molten metals is quite low and has a significant effect on fluidity. Fluidity of metals is a factor of metal composition, overheating of the melt, surface tension, degree of oxidation and pouring conditions. The ratio of solid phase has a significant effect on the viscosity of the melt in the mushy zone:

1. Under 10% of solid phase ratio, the melt behaves as a Newtonian fluid. In continuum mechanics, a Newtonian fluid is a fluid in which the viscous stresses arising from its flow, at every point, are linearly proportional to the local strain rate, the rate of change of its deformation over time. [5]

- Between 10-20% of solid phase ratio, the melt behaves as a non-Newtonian fluid. A non-Newtonian fluid is a fluid that does not follow Newton's law of viscosity and the viscosity is dependent on shear rate. In this case the value of viscosity must be re-calculated as relative viscosity:

$$\eta_r = (1 - 2,5\varphi)^{-1}\eta_0 \quad (7)$$

- Between 20-40% of solid phase ratio, the melt behaves as non-Newtonian fluid and the value of viscosity must be re-calculated as modified relative viscosity:

$$\eta_{r_{mod}} = (1 - 2,5\varphi - a\varphi^2 + b\varphi^3)^{-1}\eta_0 \quad (8)$$

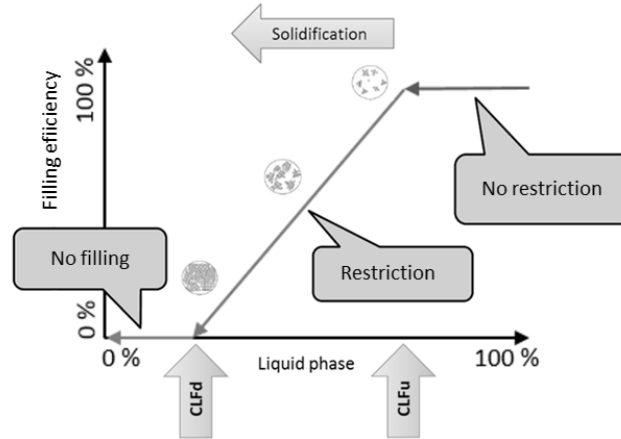
- Over 40% of solid phase ratio, the metal melt doesn't behave as a fluid.

Where: ( $\eta_0$ ) viscosity of the Newtonian liquid, ( $\eta_r$ ) relative viscosity, ( $\eta_{r_{mod}}$ ) modified relative viscosity, ( $\varphi$ ) solid phase ratio, (a,b) constants.

### Description of flow, Darcy's law

In our model the behaviour of the melt in the mushy zone is defined as can be seen in Fig. 1. Regarding how the fluidity calculation is made the following thresholds are defined:

- Fluidity threshold ( $CLF_u$ ). Value of the liquid phase fraction above which the Navier-Stokes equations are applicable. The stress in the fluid is the sum of a diffusing viscous term and a pressure term. In this case the nucleated crystals in the liquid volume freely flow together with the melt. [6]
- Percolation threshold ( $CLF_d$ ). The value of the liquid phase fraction below which the melt flow is absent without plastic deformation.
- Between  $CLF_u$  and  $CLF_d$  the Darcy's law works, part of the solid phase became fixed and puts up resistance to the melt flow.



**Figure 1.** Behaviour of the melt in the mushy zone

Darcy's law is an equation that describes the flow of a fluid through a porous medium:

$$Q = - \frac{\kappa A (p_b - p_a)}{\mu l} \quad (9)$$

The (Q) total discharge is equal to the product of the ( $\kappa$ ) intrinsic [permeability](#) of the medium, the (A) cross-sectional area to flow and the ( $p_b - p_a$ ) total pressure, all divided by the ( $\mu$ ) [viscosity](#), and the (l) length over which the pressure drop is taking place. [7] It relies on the fact that the amount of flow between two points is directly related to the difference in pressure between the points, the distance between the points, and the interconnectivity of flow pathways between the points.

### Simulation model

In this paper a commercial Control Volume model (NovaFlow&Solid) is used to simulate a special gravity casting case, called tilt casting. [8,9] The casting process itself is the point in manufacture



when most of the defects are introduced into the cast part. In case of gravity casting the most problematic factor is the metal velocity. The critical velocity of technical alloys, to avoid turbulence, is between 0.29-0.5 m/s, for aluminium alloys ~0.5 m/s.

Tilt casting solutions for gravity pouring can be described as damage limitation exercises. Only tilt, level transfer and counter-gravity can produce ideal transfer of metal into the mould, thus manufacturing the best quality of castings. The main factors of tilt casting can be described as follows. If tilt casting is initiated from a tilt orientation at or below the horizontal, during the priming of the runner the liquid metal accelerates downhill at a rate out of the control of the operator. The metal runs as a narrow jet. In addition, the velocity of the liquid at the far end of the runner is almost certain to exceed the critical condition for surface turbulence. Once the mold is initially inclined by more than 10° below the horizontal at the initiation of flow, it is no longer possible to produce reliable castings by the tilt casting process.

Tilt casting operations benefit from using a sufficiently positive starting angle that the melt advances into an upward sloping runner. In this way its advance is stable and controlled. This mode of filling is characterized by horizontal liquid metal transfer, promoting a mould filling condition free from surface turbulence.

Tilt filling is preferably slow at the early stages of filling to avoid the high velocities at the far end of the gating system. However, after the gating system is primed, speeding up the rate of rotation of the mould greatly helps to prevent any consequential non-filling of the castings. [2]

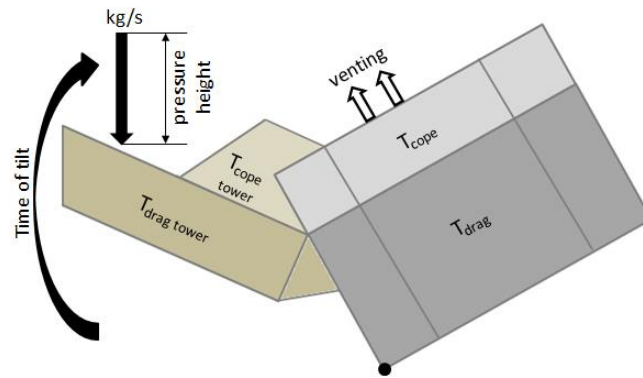
Technological steps of tilt casting are:

1. Pouring all the required melt to the pouring ladle by controlling the following parameters: Gating position of the melt, diameter of the entering metal stream, angle of the entering metal stream, pressure height of the melt, flow of pouring, friction factor, filling stop criteria.
2. Achieving the tilt movement by controlling the following parameters: Downtime after filling, initial position of the mould, direction of rotation, centre point of rotation, axis of rotation, time of tilt, tilt angle.
3. Solidification calculation by controlling the following parameters: Material properties, pouring temperature, mould temperature, time of removal.

During simulation constant and variable parameters were altered to achieve cavity filling. A standard aluminium alloy was poured into a permanent metal die made of alloyed steel. The cores were produced with cold-box technology on 200°C. The environment was air on 30°C. During filling the diameter of the liquid alloy stream was 80 mm and the tilt angle was 55°. Variable parameters can be seen in the DoE in Table 1. The model geometry can be seen in Fig. 2.

**Table 1.** Design of Experiments

Experiment	Melt	Mould	Drag tower	Cope tower	Pressure height	Pouring velocity	Poured metal	Time of tilt	Venting
	Temperature								
	°C	°C	°C	°C	mm	kg/s	kg	s	
1	730	400	320	400	2	1.6	2	5	No
2	730	400	320	400	5	2.55	1.5	5	No
3	730	400	320	400	5	3.33	2.8	3	No
4	730	400	320	400	4	2.98	2.3	3	No
5	730	400	320	400	4	2.98	2.3	4	No
6	730	400	320	320	4	2.98	2.3	4	No
7	750	450	420	420	4	2.34	2.37	4.5	Yes
8	750	450	450	450	4	2.98	2.37	4.5	Yes
9	750	450	420	420	4	2.98	2.37	3	Yes



**Figure 2.** Tilt casting model

### Post-processing

In Experiment 1-2. not enough metal was poured into the pouring ladle. The pouring flow was too low and the melt solidified in the gating system. The entire casting cavity was unfilled. Pouring velocity and the quantity of the melt were increased to avoid freezing.

In Experiment 3. the enlarged melt quantity helped to fill the cavity but unfilled areas detected in the lower and upper part of the geometry. Pressure height, pouring velocity and the quantity of melt were changed to reach better filling of the cavity.

In Experiment 4-6. the time of tilt was changed and it was determined that without venting the geometry cannot be filled completely.

In Experiment 7-9. venting is defined to ensure the filling of the cavity. Venting is accomplished in the area of the riser head. The temperature of the die elements were increased to keep warm the melt and to avoid cold flows. The amount of the poured metal was increased till the technology limit and the time of tilt was determined correspondently to the measurements.

Using the determined technological parameters the complete cavity is filled without turbulences. Both critical parts of the cavity can be filled without significant air entrapment. Venting is effective, the geometry of the venting channel is adequate and the position of venting is applicable. In Fig. 3. representation of the mould filling can be seen. Target is achieved while all air entrapment managed to eliminate from the cavity.



**Figure 3.** Mould filling

## Summary

If we consider adequacy of simulation, the following process parameters are identified.

1. Geometrical adequacy: height of the pouring basin, cross-section of the basins' nose, geometry of the flow channel between the basin and the gating system.
2. Pouring conditions: consideration of liquid contraction, cross-section of the melt stream, definition of pressure height to avoid splashing.
3. Material properties and temperature adequacy: definition of the material and the temperature of the basin, application of refractory coatings to avoid melt cooling.
4. Tilt conditions: filling stop criteria, rotation options, downtime after filling, time of tilt, tilt angle.

The described article was carried out as part of the EFOP-3.6.1-16-2016-00011 “Younger and Renewing University – Innovative Knowledge City – institutional development of the University of Miskolc aiming at intelligent specialisation” project implemented in the framework of the Szechenyi 2020 program. The realization of this project is supported by the European Union, co-financed by the European Social Fund.

## References

- [1] J.E. Niesse, AFS Transactions 67. p.685, Illinois (1959)
- [2] John Campbell, Complete Casting Handbook, Butterworth-Heinemann, UK (2011)
- [3] Nándori Gyula, Elméleti öntészet, Tankönyvkiadó, Budapest (1975)
- [4] Dabis S. Viswanath, Viscosity of Liquids, Springer, The Netherlands (2007)
- [5] Ronald L. Panton, Incompressible Flow, John Wiley&Sons, Hoboken (2013)
- [6] Philip Drazin, The Navier-Stokes Equations, Cambridge University Press (2006)
- [7] Donald A. Nield, Convection in Porous Media, Springer, Auckland (2006)
- [8] Jesper Hattel, Fundamentals of Numerical Modelling of Casting Processes, Polyteknisk, Lyngby (2005)
- [9] NovaFlow&Solid User Guide, Novacast Systems AB, Ronneby (2016)

# Investigation of the effect of asymmetric thermal conditions on stresses during continuous casting of steel with the use of meshless travelling-slice model

BOŠTJAN Mavrič<sup>1,2</sup>, TADEJ Dobravec<sup>1</sup>, ROBERT Vertnik<sup>1,3</sup> and BOŽIDAR Šarler<sup>1,2</sup>

<sup>1</sup>Institute of Metals and Technology, Lepi pot 11, 1000 Ljubljana, Slovenia

<sup>2</sup>Faculty of Mechanical Engineering, University of Ljubljana, Aškrčeva 6, 1000 Ljubljana, Slovenia

<sup>3</sup>Štore Steel, Železarska cesta 3, 3220 Štore, Slovenia

bostjan.mavric@imt.si

**Keywords:** solid mechanics, continuous casting of steel, travelling-slice model, meshless methods.

**Abstract.** The purpose of this paper is to develop a travelling-slice model for solid mechanics with intent of modelling hot-tearing susceptibility. The thermomechanical model is formulated with meshless method considering temperature dependent material parameters, viscoplastic deformation of the mushy zone and thermal strains accumulated in the material. The results are used to predict the hot-tearing susceptibility, the stress field and the shape of the solid shell. The results of the numerical method are presented for symmetric field, tilted field and field caused by more intense cooling on one strand face.

## Introduction

The continuous casting of steel is well established process for producing steel billets, blooms and slabs used as semi-products for further downstream processing, however, there still exist details of the process that are difficult to control. One of such things is the possibility of asymmetric cooling that can occur in the mold because of deformations of the strand or because of asymmetric temperature profile, caused by electromagnetic stirring. Such asymmetric thermal conditions can lead to significant deformation of the strand and increased occurrence of hot-tears.

The travelling-slice model is particularly useful for efficient modelling of the continuous casting process [1,2]. It assumes that thermal diffusion and deformation of the strand in the casting direction are negligibly small and that advection is the principal way of transferring information along the casting direction. These assumptions allow one to model the strand as a two-dimensional slice of material traveling in the casting direction making the model computationally very effective [3,4].

In this work we present the addition of a solid mechanics model to complement the existing traveling slice model of heat transport, solidification and grain growth [5]. The solid mechanics model is stated in plane stress formulation and a two-phase model is used to determine the stress equilibrium of the inhomogeneous material. The liquid phase is modelled as an elastic solid with very small Young's modulus while an elasto-viscoplastic material model is used to describe the behavior of the solid and the consolidated part of the mushy zone.

The governing equations are discretized by a local RBF collocation method, augmented by first order monomials [6]. The shape parameter is determined automatically by adjusting the condition number of the interpolation matrix. The implicit Euler method is used to perform the time stepping.

The results in this contribution are focused on the impact of asymmetric temperature fields on the distribution of stress, deformation of the billet and the probability for the occurrence of hot-tears in the material. We consider two possible sources of asymmetry. Firstly, the asymmetry can stem from asymmetric cooling conditions on the strand sides, which can be the result of the design of the caster or suboptimal setting of the water cooling. Secondly, we consider the state that is obtained by tilting the originally symmetric temperature profile by a small angle around axis parallel with the casting direction. Such perturbation is usually caused by the electromagnetic stirring of the melt.

## Governing equations

Since the total strain of the strand are expected to be small we use additive strain decomposition to write the total strain  $\varepsilon$  as the sum of thermal strain  $\varepsilon^t$ , viscoplastic strain  $\varepsilon^{vp}$  and elastic strain  $\varepsilon^e$ .

The thermal strain is the driving term of the model and is given by

$$\varepsilon^t = I \int_{T_s}^T \alpha(T) dT, \quad (1)$$

where  $T_s$  is the solidus temperature and  $\alpha(T)$  is the temperature dependent coefficient of thermal expansion obtained from JMatPro. The viscoplastic strain is calculated from the rate equation

$$\dot{\varepsilon}^{vp} = \frac{3\tau}{2\sigma_e} A \exp\left(-\frac{Q}{RT}\right) \left(\frac{\sigma_e}{\sigma_0}\right)^n, \quad (2)$$

where  $\tau$  is the deviatoric stress calculated from the stress tensor  $\sigma$  as  $\tau = \sigma - I \text{tr} \sigma / 3$ . The effective stress is given by  $\sigma_e = \sqrt{2\tau : \tau / 3}$ . The parameters of the constitutive equation are reference strain rate  $A$ , reference stress  $\sigma_0$ , stress exponent  $n$ , activation energy  $Q$  and the general gas constant  $R$ . The stress equilibrium equation is stated in terms of total displacement vector  $\vec{u}$  to obtain the following equilibrium equation

$$0 = G \nabla \vec{u} + (G + \lambda) \nabla (\nabla \cdot \vec{u}) + \nabla \lambda (\nabla \cdot \vec{u}) + \nabla G (\nabla \vec{u} + (\nabla \vec{u})^T) - \nabla \cdot (2G \varepsilon^p) - \nabla ((3\lambda + 2G) \varepsilon^t) - \nabla (f_l p), \quad (3)$$

where  $G$  and  $\lambda$  are Lamé parameters calculated from temperature dependent Young's modulus and Poisson's ratio. The interaction of the liquid melt and the solid shell is introduced through the term  $\nabla (f_l p)$ , where  $f_l$  is the liquid fraction and  $p$  the metallosstatic pressure at the position of the center of the slice.

The probability for occurrence of hot-tears is estimated by Lahaie-Bouchard (LB) hot-tearing model [7]. It is chosen because it represents a sophisticated model that does not use any information about the flow field. The model calculates critical stress as

$$\sigma_c = \frac{4\gamma}{3h} \left( 1 + \left( \frac{f_s^m}{1 - f_s^m} \right) \varepsilon_{\square} \right)^{-1}, \quad (4)$$

which is derived from considering the stress required to overcome the surface tension force in a mushy- zone-like structure. In the formula  $h$  is the grain size,  $\gamma$  is the surface tension, and  $\varepsilon_{\square}$  is the strain in the direction of maximum principal stress. The microstructure is described by the exponent  $m$ , which is set to 1/2 for columnar and to 1/3 for equiaxed grains.

The hot-tearing susceptibility is given by  $HCS = \sigma_{max} / \sigma_c$ , where  $\sigma_{max}$  is the largest positive principle stress. Susceptibility at a position in the strand is time dependent. To obtain a time-independent information about hot-tearing susceptibility the accumulated susceptibility is defined as

$$AHCS(n\Delta t) = \sum_{i=0}^n HCS(i) \Delta t \quad (5)$$

at each point in the strand.

## Solution procedure

Since the interaction of the strand with rolls and mold is neglected in the present development, the strand is traction free on all four sides. This results in degenerated system of equations for mechanical equilibrium (3). To remedy that, Lagrange multipliers corresponding to the three degrees of freedom of rigid-body motion are introduced to the problem.

To discretize the governing equations, the meshless local radial basis collocation method has been used. It was first developed to solve transport problems [8] and has been recently expanded to deal with thermomechanical problems [6,9]. The time stepping is performed by implicit Euler method, where the resulting system of nonlinear equations is solved by modified Bouaricha method [10]. The code implementing the method is written in Fortran 2008, parallelized in OpenMP and run on an Intel Xeon processor.

## Numerical examples

**Driving fields.** The driving of the model is in this paper achieved by a manufactured temperature field and the solidification results are designed in a way that correspond to a typical result for temperature and structural history obtained by a slice model. The temperature field is given by

$$T(\vec{r}) = T_0 + \frac{\Delta T}{2} \left[ 1 + \tanh \left( \frac{s_0(t) - s(\vec{r})}{S(t)} \right) \right] \quad (6)$$

where  $T_0 = 900^\circ\text{C}$  and  $\Delta T = 600^\circ\text{C}$ . The center of the solidification front  $s_0(t)$  and its width  $S(t)$  are tuned in such a way that they correspond to typical evolution of a temperature field during continuous casting. The shape of the solidification front is determined by

$$s(\vec{r}) = \sqrt[p(t)]{|x|^{p(t)} + |y|^{p(t)}}, \quad (7)$$

where the shape of the front is determined by the value of parameter  $p$ . When it is equal to 2, the front has circular shape and as it is increased, the front becomes more and more rectangular with beveled corners and sides parallel to coordinates axes. At the start of the simulation  $p$  is set to 10 and then gradually decreased to 2 to obtain a circular shape of the solidification front.

The values of the solid fraction are determined from the temperature by the following relation

$$f_s(T) = \frac{1}{2} \left( 1 + \tanh \left( \frac{T_f - T}{\Delta T_f} \right) \right), \quad (8)$$

where  $T_f = 1400^\circ\text{C}$  and  $\Delta T_f = 40^\circ\text{C}$ , resulting in solidification range similar to some spring steels.

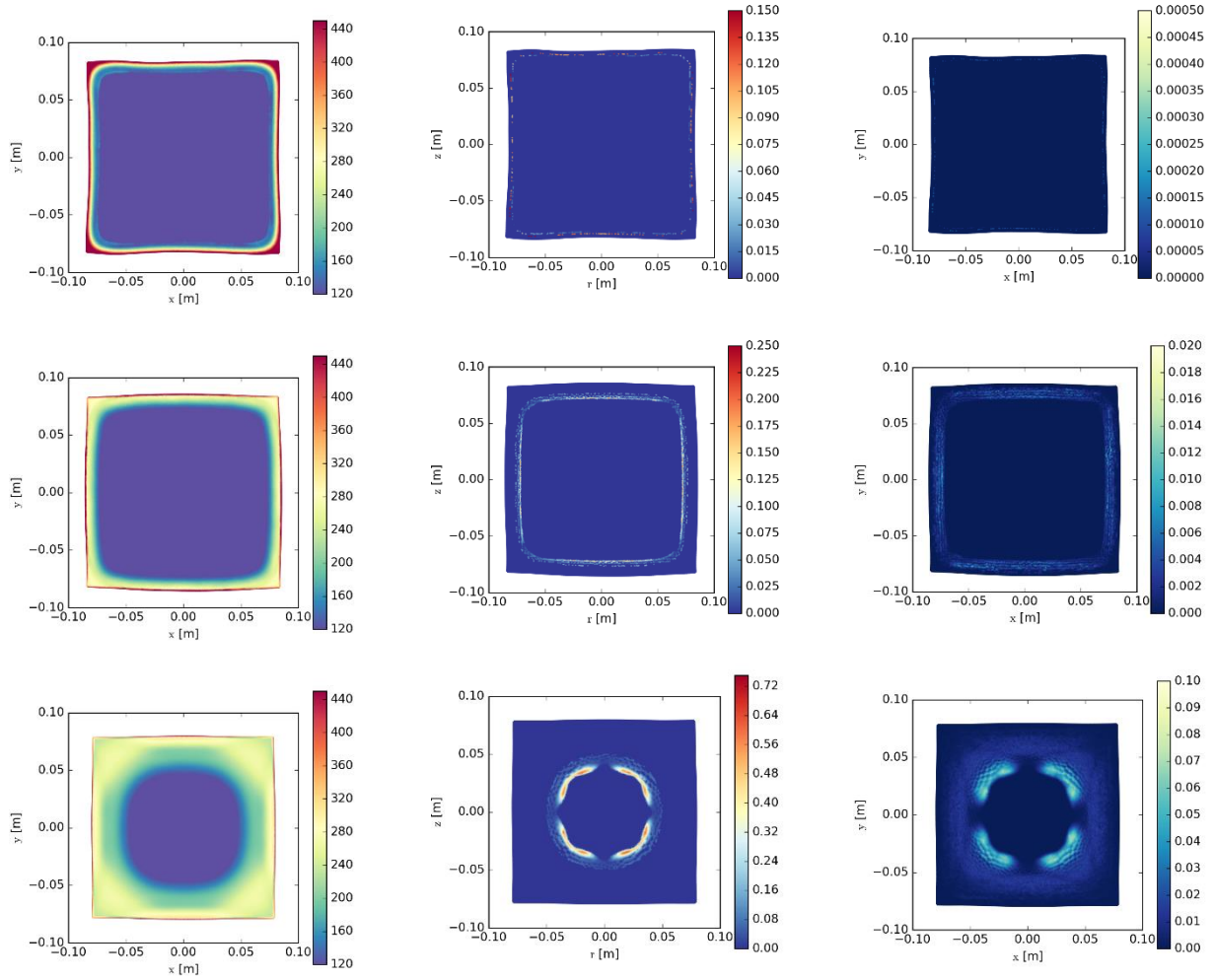
### Symmetric temperature field.

This is the reference case studied with driving fields implemented as defined in the previous subsection. The results are given in Fig. 1 with plots of effective stress, HCS and AHCS. The deformations of the strand are amplified by a factor of 20 to make the resulting strand shape more apparent. The plots are given at three times: 4, 40 and 160 s after the start of the simulation. The times were selected to demonstrate three different regimes that can be observed during the casting process at:  $t = 4$  s the shell is very thin and it caves in at the sides because of thermal stresses in the corners. The area where hot tearing is possible is very thin and distributed uniformly along the solidifying region. At  $t = 40$  s the metallostatic pressure causes the strand to bulge, which increases the stresses in the solidifying region and in turn results in increased probability of hot-tearing in the centers of the sides. At  $t = 160$  s the solid shell is strong enough to support the metallostatic pressure and the sides of the strand straighten again. The solidifying front at this point is circular and the probability for hot tearing is increased at the areas of the solidification front that are close to the strand.

Effective stress [MPa]

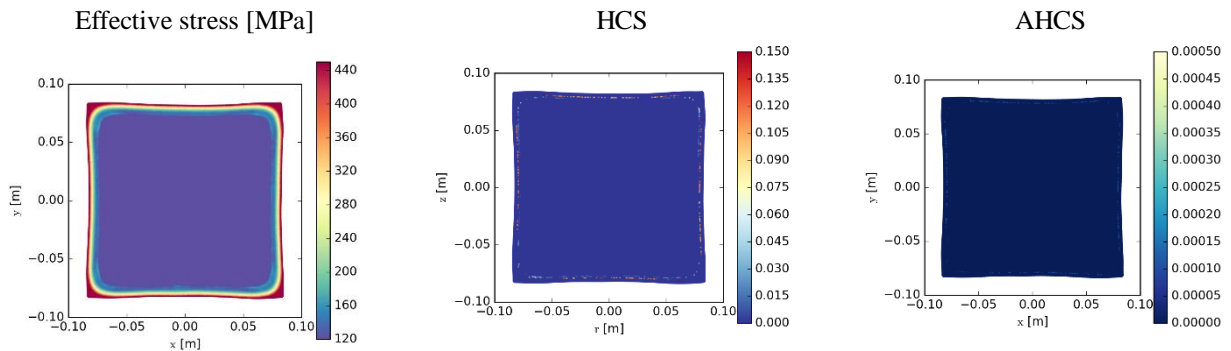
HCS

AHCS

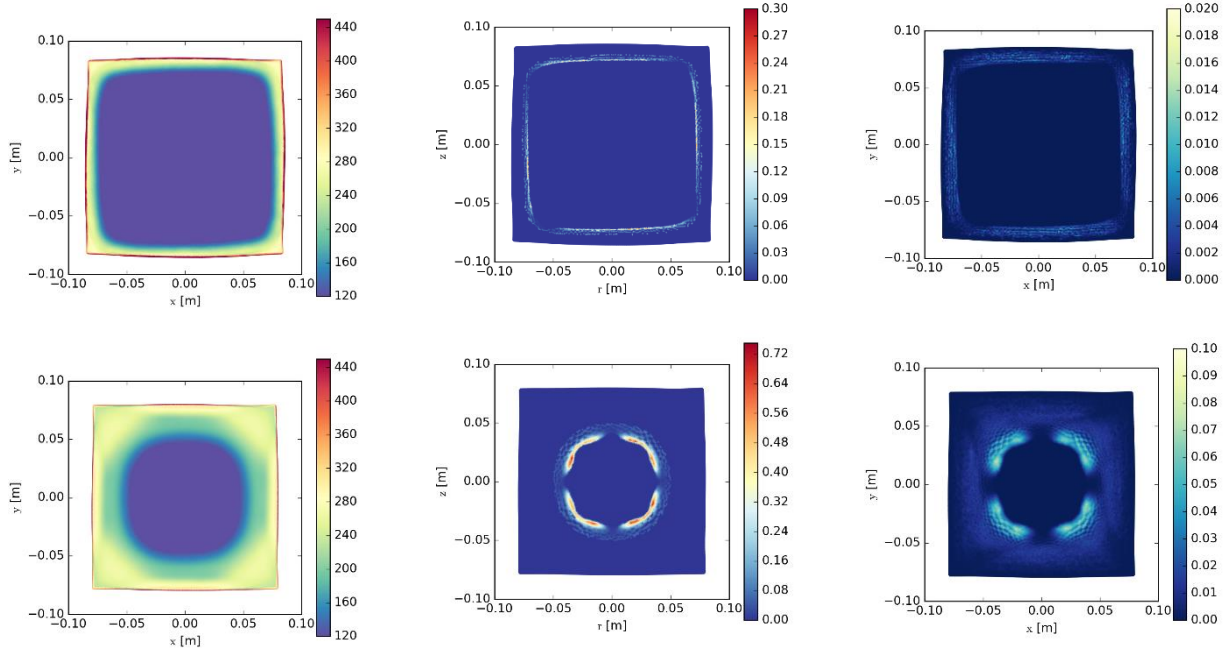


**Figure 1.** The results for symmetric temperature field showing (from left to right) the effective stress, HCS and AHCS. The results in the top row are given at 4, in the middle row at 40 and in the bottom row at 160 s.

**Tilted temperature field.** This example aims to model the temperature field in the strand when the electromagnetic stirrers are used to increase the convection in the melt, which results in the temperature profile being tilted in the direction of the stirring. In this model such a temperature field is achieved by rotating the vector  $\vec{r}$  from formula Eq. 6 by a small, time dependent amount. The results are shown in Fig. 2 where we can notice two impacts of the tilted temperature profile. Firstly, the deformations of the surface are not symmetric with respect to the centerline of the surface and the bulge is shifted in the direction of stirring. Secondly, the hot-tearing susceptibility is increased in the areas where the solid shell is thicker due to the tilted temperature field, which is also reflected in the accumulated susceptibility.





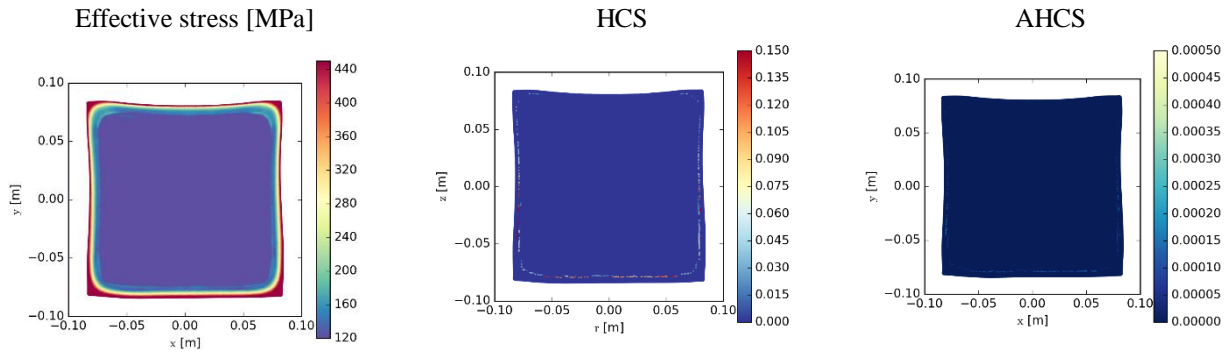


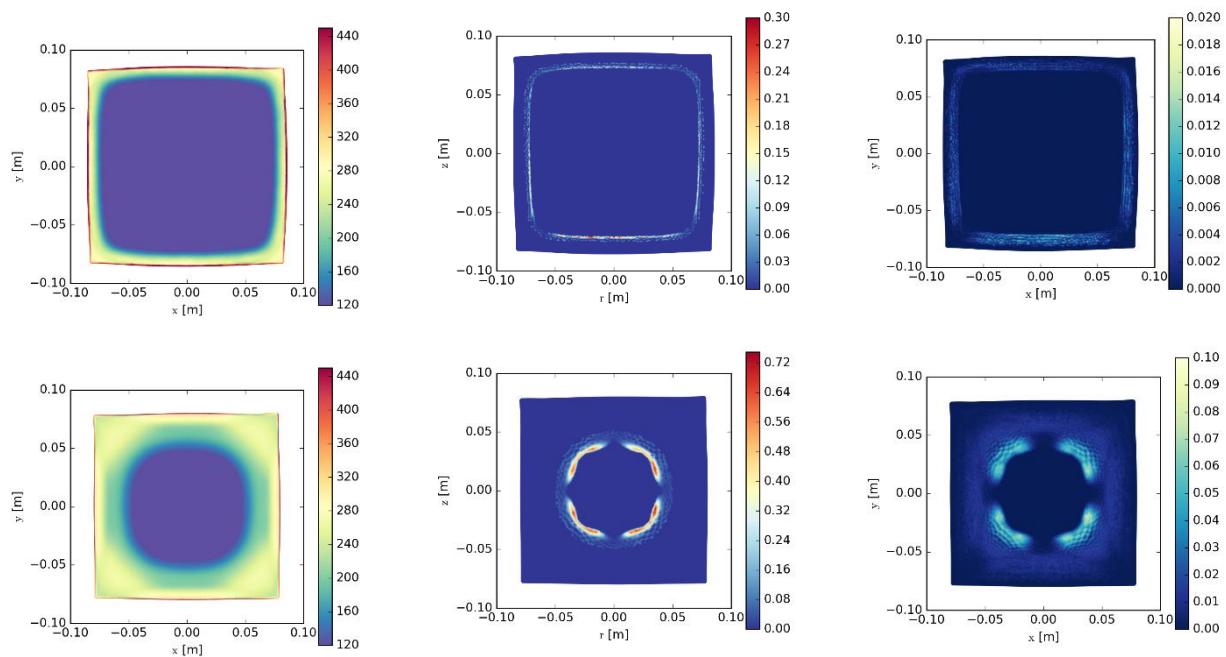
**Figure 2.** The results for tilted temperature field showing (from left to right) the effective stress, HCS and AHCS. The results in the top row are given at 4, in the middle row at 40 and in the bottom row at 160 s.

**Asymmetric temperature field.** This example aims to show the effect of increased cooling on the bottom side of the strand. This is modelled by replacing the vector  $\vec{r}$  in the Eq. 6 with vector  $\vec{r}'$  obtained from vector  $\vec{r}$  as

$$\begin{aligned} x' &= x - axy \\ y' &= y - ay^2 \end{aligned} \quad (9)$$

with  $a = 0.2$ . The results of such temperature field are shown in Fig 3. The increased cooling of the bottom side destroys the symmetry in the deformation of the strand. Additionally, the solidifying area near the cooler side appears to be more susceptible to hot tearing. This is reflected in both HCS and AHCS plots.





**Figure 3.** The results for asymmetric temperature field showing (from left to right) the effective stress, HCS and AHCS. The results in the top row are given at 4, in the middle row at 40 and in the bottom row at 160 s.

## Conclusions

The mechanical travelling slice model that is presented in this paper was used to study the impact of several asymmetric temperature fields on the hot-tearing susceptibility. The cases considered were the symmetric temperature field, the tilted temperature field and the asymmetric temperature field. The results provide interesting insight in the mechanical phenomena during the casting process. In the future this model will be integrated with the microstructure slice model. Additionally, the interaction with the mold and rolls will be added.

## Acknowledgments

This work was funded by Slovenian research agency (ARRS) in the framework of applied research project J2-7384, program group P2-0162 and MARTINA project. Project J2-7384 is cofunded by Store Steel, d.o.o. company.

## References

- [1] A.Z. Lorbiecka, R. Vertnik, H. Gjerkeš, G. Manojlovič, B. Senčič, J. Cesar, B. Šarler, Numerical modeling of grain structure in continuous casting of steel, *Computers, Materials & Continua*. 8 (2009) 195–208.
- [2] I. Vušanović, R. Vertnik, B. Šarler, A simple slice model for prediction of macrosegregation in continuously cast billets, *IOP Conference Series: Materials Science and Engineering*. 27 (2012) 012056. doi:10.1088/1757-899X/27/1/012056.
- [3] C. Ji, C. Wu, M. Zhu, Thermo-Mechanical Behavior of the Continuous Casting Bloom in the Heavy Reduction Process, *JOM*. 68 (2016) 3107–3115. doi:10.1007/s11837-016-2041-8.
- [4] J. Song, Z. Cai, F. Piao, M. Zhu, Heat Transfer and Deformation Behavior of Shell Solidification in Wide and Thick Slab Continuous Casting Mold, *Journal of Iron and Steel Research, International*. 21 (2014) 1–9. doi:10.1016/S1006-706X(14)60112-6.
- [5] T. Dobravec, B. Mavrič, R. Vertnik, B. Šarler, Meshless modelling of microstructure evolution in the continuous casting of steel, in: *Coupled Problems VII : Proceedings of the VII International Conference on Coupled Problems in Science and Engineering*, International Center for Numerical Methods in Engineering (CIMNE), Rhodes Island, 2017: pp. 156–166.

- [6] B. Mavrič, B. Šarler, Local radial basis function collocation method for linear thermoelasticity in two dimensions, *International Journal of Numerical Methods for Heat & Fluid Flow*. 25 (2015) 1488–1510. doi:10.1108/HFF-11-2014-0359.
- [7] D.J. Lahaie, M. Bouchard, Physical modeling of the deformation mechanisms of semisolid bodies and a mechanical criterion for hot tearing, *Metallurgical and Materials Transactions B*. 32 (2001) 697–705.
- [8] B. Šarler, R. Vertnik, Meshfree explicit local radial basis function collocation method for diffusion problems, *Computers & Mathematics with Applications*. 51 (2006) 1269–1282. doi:10.1016/j.camwa.2006.04.013.
- [9] B. Mavrič, B. Šarler, Application of the RBF collocation method to transient coupled thermoelasticity, *International Journal of Numerical Methods for Heat & Fluid Flow*. 27 (2017).
- [10] A. Bouaricha, *Solving Large Sparse Systems of Nonlinear Equations and Nonlinear Least Squares Problems Using Tensor Methods on Sequential and Parallel Computers*, University of Colorado at Boulder, 1992.

# Macroscopic modeling of solidification of TiAl alloys in hypergravity

Martín Cisternas, Miha Založnik and Hervé Combeau

**Keywords:** Solidification, modeling, centrifugal casting, hypergravity, convection

## Abstract

Hypergravity conditions are used for casting TiAl alloys in order to improve mold filling and to prevent porosity defects. One way to generate hypergravity on Earth is through the use of centrifuges, by the combination of the normal terrestrial gravity and centrifugal acceleration. To be able to control the structure of the castings (CET, grain size, grain morphology) and the macrosegregation defects it is of prime importance to understand the process-scale transport phenomena in the casting: thermosolutal convection of the liquid, and the motion of grains and grain fragments. Under centrifugal conditions the flow structure is determined by the combined effect of the centrifugal and Coriolis accelerations.

To investigate the influence of hypergravity on the structure of TiAl alloys under centrifugal conditions, directional solidification experiments in the ESA Large Diameter Centrifuge (LDC) were conducted in the framework of the GRADECET project. Cylindrical Ti-Al samples (8 mm diameter, 120 mm length) were solidified in well controlled conditions under five different gravity levels (1 g – 20 g), with the apparent gravity aligned with the cylinder centerline.

We present a numerical model study of the flow during the solidification of the LDC samples. The modeling supports and complements post-mortem characterizations of the microstructure and macrosegregation. 3D simulations were performed with a volume-averaging solidification model that accounts for the centrifugal and Coriolis accelerations in the non-inertial rotating reference frame. The model was implemented in the OpenFOAM finite-volume-method framework and was validated for the simulation of macrosegregation and of natural convection in rotating systems.

The simulations of the centrifugally solidified samples indicate that the Coriolis acceleration plays a fundamental role in the thermosolutal convection because it breaks the symmetry of the flow structure. The macrosegregation pattern is therefore entirely modified in comparison with a sample solidified under terrestrial gravity conditions. The modified flow structure can also have an influence on the microstructure distribution in the samples.

## **Simulation of mechanical deformation during dendritic solidification**

Bogdan Nenchev, Dr. Simon Gill

**Keywords:** Solidification of binary alloy, cellular automata, mechanical deformation, hot cracking, simulation

### **Abstract**

A new approach to hot cracking investigation has been proposed. Aimed to describe the phenomena at a micro scale level, it combines micro-CAFE (Cellular Automata with Finite Difference) dendritic simulation with Newtonian mechanics for a two-phase medium. The solidification model adopts previously proposed methodology for a solute steady state interface balance, directed by a modified decentred algorithm and a cellular automata (CA) in order to specify the new cell capturing rules and account for the mesh anisotropy. The CAFE model is capable of simulating grains with random orientation making it well suited to calculate deformation in fine grain alloys. A mass balance, based on a diffusional flow in three phases: liquid, solid and S/L interface, is calculated concurrently with the solute diffusion for a binary alloy. It finds the shrinkage contribution dependant on thermal gradient, permeability and viscosity, evaluated with reference to an equilibrium state value. Tensile deformation in the solid skeleton is also introduced leading to complex effects such as visco-plastic deformation of the dendrite network and induced liquid pressure. All effects from the phenomena are resolved by a force balance equation for an identical to the CA control volume. A control system with springs (solid) and dampers (liquid) is used to model the system in a simple and yet open to further development approach. The calculation of pressure drop is based on a form of Darcy's equation where lack of liquid feeding in liquid pockets or narrow channels in the interdendritic network would lead to a formation of a hot crack. The model sets up for a comprehensive framework of modelling mechanical deformation in solidifying metal at a micro scale level.

## **Phase-field modeling of mobile dendrites in melt flow**

László Rátkai, Tamás Pusztai, László Gránásy

**Keywords:** phase-field modeling, mobile dendrites, melt flow, columnar to equiaxed transition

### **Abstract**

The Phase-Field and Lattice Boltzmann Methods have been combined to simulate the growth of solid particles moving in melt flow. To handle the mobile particles, an overlapping multi-grid scheme was developed, in which each individual particle has its own moving grid, with local fields attached to it. Using this approach we are able to simulate simultaneous binary solidification, solute diffusion, melt flow, solid motion, effect of gravity, and collision of the particles. The method has been applied for describing columnar to equiaxed transition in the Al-Ti system.

# **A quantitative benchmark of multiscale models for dendritic growth**

Sabrine Ziri, Laszlo Sturz, Alexandre Viardin, Miha Založnik, Damien Tournet

**Keywords:** Dendritic growth, Multiscale modeling, Phase field modeling

## **Abstract**

Dendritic growth is a key phenomenon in the selection of solidification microstructures. The emergence of dendritic patterns originates from an interplay of phenomena across a wide range of length and time scales — from the atomic structure of the solid-liquid interface to the macroscopic transport of heat and species, for instance by gravity-induced liquid buoyancy. Because the integration of all these scales matter, quantitative simulations at the scale of experiments or processes remain challenging, even considering modern models, implementations, and computers. For this reason, a range of multiscale modeling approaches have been proposed that aim at scaling up simulations of dendritic growth. However, a direct, quantitative, and critical comparison of such models is yet to be performed.

We present a quantitative benchmark of multiscale dendritic growth simulation methods. We specifically focus on approaches based on (i) Phase-Field [1], (ii) Dendritic Needle Network [2], and (iii) Dendritic Envelope dynamics [3]. We compare their similarities and differences in the modeling of: (i) Steady and transient isothermal growth of an equiaxed grain in a supersaturated liquid in 3D, as well as the predicted macroscopic grain envelope shape; (ii) Primary spacing selection in directional solidification in 3D, using realistic experimental parameters for a succinonitrile-acetone alloy; (iii) Isothermal growth of an equiaxed grain in a supersaturated liquid in the presence of forced flow in 2D. Results are also directly compared to experimental data and corresponding scaling laws when available.

In light of this benchmark, we discuss the capabilities and limitations of each approach in quantitatively and efficiently predicting transient and steady states of equiaxed and columnar dendritic growth. We provide key insight into how to select numerical parameters that provide the best compromise between accuracy and computational efficiency in multiscale needle-based and envelope-based models. We expect that these results will guide further developments and utilization of these models, and ultimately pave the way to a quantitative understanding of the effect of convection, e.g. gravity-driven liquid buoyancy, in the selection of microstructures at a scale relevant to entire experiments and solidification processes.

## **References**

- [1] A. Karma, Physical Review Letters 87, 115701 (2001); B. Echebarria, et al., Physical Review E 70, 061604 (2004).
- [2] D. Tournet and A. Karma, Acta Materialia 61, 6474-6491 (2013); D. Tournet and A. Karma, Acta Materialia 120, 240-254 (2016); L. Sturz and A. Theofilatos, Acta Materialia 117, 356-370 (2016).
- [3] I. Steinbach, et al., Acta Materialia 47, 971-982 (1999); Y. Souhar, et al., Computational Materials Science 112, 304-317 (2016); Viardin, et al., Acta Materialia 122, 386-399 (2017).

# Numerical simulation of chill cooling and solidification of a levitated steel droplet in microgravity

Ayoub Aalilija, Elie Hachem, Charles-André Gandin

**Keywords:** Solidification, microgravity, finite element modeling, Level-Set method, surface tension

## Abstract

The present work is a part of the Microgravity Application Promotion (MAP) program of the European Space Agency. It involves the projects entitled Non-Equilibrium Solidification, Modelling for Microstructure Engineering of Industrial Alloys (NEQUISOL) and Chill Cooling for the Electromagnetic Levitator in relation with Continuous Casting for steels (CCEMLCC). The goal is to reach a better understanding of solidification of steel products and associated defects. The solidification of a freely suspended steel droplet in reduced-gravity conditions is triggered by a ceramic chill plate that represents the mould in a continuous casting process, thus extracting the heat from the sample.

In this work, we propose a numerical simulation of the levitated steel droplet. The numerical framework is based on the use of a single Eulerian mesh for both the steel droplet and the surrounding gas. The contact between the sample and the chill plate is implicitly taken into account via a boundary condition. A monolithic formulation of total mass, momentum and energy conservation enables the resolution of a single set of equations in the whole domain. Only the metal's species conservation equation is considered. A Variational Multi-Scale stabilized finite element method [1] is proposed to solve Navier-Stokes equations. Assuming that the solid phase is fixed, the momentum equation is enriched by accounting for solidification shrinkage [2], surface tension [3] and Marangoni effect [4] acting at the liquid-gas interface. The level set method is used for tracking the evolution of the metal-gas boundary. The liquid-solid interface is implicitly represented by the volume averaging methodology. We test the numerical framework on a specific steel grade and compare to the existing experimental data of a sounding rocket experiment [2].

## REFERENCES

- [1] E. Hachem, B. Rivaux, T. Kloczko, H. Dignonnet, T. Coupez, Stabilized finite element method for incompressible flows with high Reynolds number, *Journal of Computational Physics*, Volume 229, 2010, Pages 8643-8665
- [2] A. Saad, Numerical modelling of macrosegregation formed during solidification with shrinkage using a level set approach, Ph.D. thesis, MINES ParisTech, PSL - Research University, 2016
- [3] M. Khalloufi, Y. Mesri, R. Valette, E. Massoni, E. Hachem, High fidelity anisotropic adaptive variational multiscale method for multiphase flows with surface tension, *Computer Methods in Applied Mechanics and Engineering*. Volume 307, 2016, Pages 44-67
- [4] Q. Chen, G. Guillemot, C.-A. Gandin, M. Bellet, Three-dimensional finite element thermomechanical modeling of additive manufacturing by selective laser melting for ceramic materials, *Additive Manufacturing*, Volume 16, 2017, Pages 124-137



# **3D mesoscopic modeling of isothermal equiaxed dendritic solidification of Al-20 wt%Cu**

Antonio Olmedilla, Miha Založnik, Hervé Combeau

Keywords: equiaxed dendritic solidification, binary alloy, three-dimensional simulation

## **Abstract**

A 3D mesoscopic envelope model is used to numerically simulate the experimental X-ray observations of the equiaxed dendritic isothermal solidification of a thin sample of Al-20 wt%Cu alloy with x, y and z dimensions of 4124, 2746 and 200, respectively. Once the calibration of the mesoscopic model is carried out we show the growth evolution of the multi-grain system composed by 15 grains accentuating the effect that the thin third dimension, z, has on the growth kinetics, mainly focusing on three aspects: (i) the impact of incorporating the third dimension to the solute diffusion, for that we compared a 3D simulation to a 2D simplified simulation with the solute diffusion in the x-y middle plane ( $z=0$ ), (ii) the influence of the grain orientation about an axis contained in the x-y plane, and (iii) the influence of the grain centroid position along the sample thin dimension.

The 3D grain structure is shown to play an important role in the description of the dendritic grain growth kinetics. The consideration of the 3D solutal diffusion on the model is fundamental in order to obtain realistic grain kinetics. The dendritic grain kinetics increases by a factor of two when the thin third dimension is considered. We determine that the grain morphology and kinetics are extensively influenced by the grain orientation about an axis contained in the x-y plane. For that three simulations are carried out where a reference grain (approximately located at the center of the sample) is rotated 15, 30 and 45. Considering the projection view of the rotated reference grain on the middle x-y plane, the projected primary arms perpendicular to the rotation axis shorten with rotation. Additionally, the effect of the grain centroid position along the sample thickness on the grain morphology and kinetics is investigated by means of other three simulations where the centroid of the reference grain is located at a z coordinate of 50, 75 and 100. We prove that the grain kinetics are faster the further the centroid is with respect to the sample middle plane.

The numerical model is calibrated by means of a single parameter --confocal distance, - that is not very influential on the grain morphology for the case under study. The mesoscopic model is capable of describing solutal grain interactions down to short distances between grains.

# Monte Carlo Simulations of Chemical Segregation at the Liquid/Substrate Interface

H. Tetlow, Z. Fan

**Keywords:** Atomistic Simulations, Segregation, Monte Carlo, solid-liquid interface

## Abstract

One of the most widely used examples of grain refinement is the addition of Al-Ti-B refiners during solidification of Al-alloys. Experimental studies of this system have revealed that a single atomic layer of (112)  $\text{Al}_3\text{Ti}$  is formed at the liquid/ $\text{TiB}_2$  (0001) interface, produced due to the segregation of solute Ti to the interface. Furthermore, the creation of this layer has been suggested to increase the potency of  $\text{TiB}_2$  for the heterogeneous nucleation of  $\alpha$ -Al. The formation of the  $\text{Al}_3\text{Ti}$  layer itself has been shown to be highly dependent on both the concentration of Ti in the liquid, the holding temperature and time.

A Lennard Jones based potential suitable for describing the system of interest is constructed, which allows the first ever large scale simulations of the  $\text{TiB}_2/\text{Al}$  system. Monte Carlo (MC) simulations are run at various temperatures and the stability of the  $\text{Al}_3\text{Ti}$  layer at the interface is confirmed. Using semi-grand canonical Monte Carlo simulations the Ti segregation process is fully investigated, allowing for changes in the solute concentration. Evidence for the segregation of Ti to the  $\text{TiB}_2/\text{Al}$  interface is found and the conditions which favour the formation of  $\text{Al}_3\text{Ti}$  are determined. Motivated by the success of Al-Ti-B refiners, we search for other liquid/substrate systems where solute segregation is prevalent, and where this may lead to increased nucleation potency. The MC methods used for  $\text{TiB}_2/\text{Al}$  are applied to these other systems to determine the solute concentration and temperature conditions which promote solute segregation.

# Multiscale modelling of dendritic growth by a combination of three methodologies

Romain Fleurisson, Gildas Guillemot, Charles-André Gandin

**Keywords:** multiscale modelling, dendritic growth, multigrid, alloys

## Abstract

Multiscale modelling of solidification processes is of great interest for industries. However coupling the multiple scale phenomena to reach a quantitative simulation applied to a large domain is challenging. In the present contribution, this is achieved using a combination of three methodologies: the Finite Element (FE) method, the Cellular Automaton (CA) method and the Dendritic Needle Network (DNN) method.

The FE method provides a solution of the conservation equations, written for volume average quantities, that is suitable for computation applied to a large domain. It serves for macroscopic description of heat and mass transfers. The CA method tracks the development of the envelope of each individual dendritic grain at a mesoscopic scale. The coupling of these two methods is the CAFE model and was demonstrated to provide efficient and quantitative simulations of the columnar-to-equiaxed transition, macrosegregation and freckles, competition taking place among columnar dendritic grains and the resulting formation of crystallographic textures. However, the dendrite tip growth kinetics could be improved since it was based on the analytical Ivantsov solution.

The DNN is another mesoscopic method recently introduced. It uses solute mass balance considerations in the vicinity of the tip of the dendrites to compute accurately the growth kinetics. Because it relies on a direct estimation of the composition gradient at the solid-liquid interface, steady state growth regime is no longer assumed. Its implementation with a FE method to solve the solute flow is extensively validated against analytical results given by the Ivantsov solution [1] for different temperatures and grain orientations.

Coupling CAFE with DNN computed growth kinetics provides a unique solidification model. The CA grid handles both the shape of the grain envelopes and branching mechanisms. The FE mesh is used to solve flux and conservation of mass and energy at both the scale of the dendrite tip solute layer and the domain dimensions. It is possible thanks to adaptive remeshing strategies and use of multiple FE meshes. Capabilities of the model are demonstrated by simulating an experiment documented by Bogno et al. [2].

[1] G. P. Ivantsov. Temperature field around the spherical, cylindrical and needle crystals which grows in supercooled melt. *Doklady akademii Nauk SSSR* 58 (1947), 567.

[2] A. Bogno et al. Growth and interaction of dendritic equiaxed grains: In situ characterization by synchrotron X-ray radiography. *Acta Materialia* 61 (2013.), 1303.

## CHAPTER 7: SOLIDIFICATION OF DENDRITE



# A Large-Scale 3D Computer Tomography analysis of Primary Dendrite Arm Spacing Response to Withdrawal Velocity Change Using Dendrite Centre Tracking

J. E. MILLER<sup>1</sup>, L. STURZ<sup>2</sup>, S. Steinbach<sup>3</sup>, G. Zimmermann<sup>2</sup>, and N. Warnken<sup>1</sup>

<sup>1</sup>Department of Metallurgy and Materials, University of Birmingham, United Kingdom, B15 2TT

<sup>2</sup> ACCESS e.V., Intzestr. 5, 52072 Aachen, Germany

<sup>3</sup> Institut für Materialphysik im Weltraum, Deutsches Zentrum für Luft- und Raumfahrt (DLR), 51170 Köln, Germany

Email of corresponding author: N.Warnken@bham.ac.uk

**Keywords:** Directional Solidification; Computerised Tomography; Primary Dendrite Arm Spacing; Changing Withdrawal Velocities; 3D Metallography; Dendrite Centre Tracking; Aluminium 10 wt% Copper

**Abstract.** Directional solidification of alloys is an extremely important process to understand due to the many high value products that are produced in this manner, *e.g.* turbine blades. Controlling how the columnar dendrites grow and pack together is an important aspect of increasing the strength and longevity of these components. As such 3D examination of a 200 mm in length and 6 mm diameter aluminium 10 wt % copper rod solidified under varying withdrawal rates (40  $\mu\text{m/s}$  then a jump to 80  $\mu\text{m/s}$ ) has been undertaken in a lab based computerised tomography (*CT*) machine. Novel image analysis techniques involving active contours and skeletonisation have been used to track the dendrites through the sample itself. Sites of dendrite initiation and termination have been identified automatically within the dataset. These points of dendrite creation or deletion were found to be most prevalent after a step change in the withdrawal rate. Information on the array packing and primary dendrite arm spacing (*PDAS*,  $\lambda$ ) for each grain within the sample has been obtained. The results show that there is a distance delay after the withdrawal rate change and the onset of a *PDAS* restructuring.

## Introduction

With the advent of lab based computerised tomography (*CT*) scanners there has been an increase in the options available for 3D metallography that researchers can undertake. *CT* scanners allow for the non-destructive analysis of components and castings and can build up a 3D virtual view of the internal microstructure of a component. This has allowed for the quick and relatively easy evaluation of microstructures in three dimensions where previously the only avenue available to researchers was the use of tedious serial sectioning.

Moreover with the increase of computation power available greater volumes of data can be now analysed swiftly and cost effectively. As such now is the first time that the large volumes associated with *CT* analysis can be effectively analysed and giving a greater understanding of how a dendritic array evolves in a directionally solidified sample giving a stable *PDAS*.

Many equations for *PDAS* calculation have been put forward including the Trivedi equation which takes account of the marginal stability criterion [1]:

$$\lambda = 2.83 m(k - 1)D\Gamma LC^{0.25}v^{-0.25}G^{-0.5} \quad (1)$$

Where:  $m$  is the liquidus slope [K/wt%];  $k$  is the partition coefficient;  $D$  is the diffusivity of solute in the liquid [ $\text{m}^2\text{s}^{-1}$ ];  $\Gamma$  is the Gibbs-Thomson coefficient [mK];  $L$  is a constant which depends upon the harmonic perturbations which is set to 28 [1];  $C$  is the bulk composition [wt%];  $v$  is the solidification front velocity; and  $G$  is the thermal gradient [K/m].

Eq. 1 has proven adapt in producing predictions for the *PDAS* in steady state solidification. However not quite as adapt in the unsteady state. In this type of situation, the dendritic array restructures to compensate for changing solidification conditions resulting in either the creation or termination of primary dendrite arms [2-5]. Ma [2 & 3] set the stable limit for the *PDAS* to  $\lambda_{\min} = 2/3 \lambda$  to  $\lambda_{\max} = 4/3 \lambda$ . If the *PDAS* becomes too small a dendrite is outcompeted and killed off and the microstructure readjusts increasing the *PDAS*. Conversely if the *PDAS* is too large then a new primary dendrite arm will fill a gap in the array formed from the growth of a tertiary arm from one of the surrounding dendrites.

This array restructuring is easy to see in two dimensional samples especially in transparent model alloys [2-4]. However, it is much more difficult in 3D. When calculating the *PDAS* in a solidified sample it must first be sectioned and the number of individual dendrites (*N*) counted, then using the equation:

$$\lambda_B = \sqrt{\frac{A}{N}} \quad (2)$$

the bulk *PDAS* can be calculated for that transverse section of the sample if the area of the slice, *A*, is known [6-8]. The drawback of this method is that it only gives an average value for the *PDAS* so no statistical analysis can be undertaken using it. Methods such as the Warnken-Reed and Voronoi *PDAS* calculations can however be used to find the local *PDAS* across a sample [6-8].

Therefore, in order to test how microstructures readapt in 3D to changing solidification conditions, an Al-10 wt% Cu sample was directionally solidified under a constant *G* of 10 K/m with an instantaneous velocity jump from 40  $\mu\text{m/s}$  to 80  $\mu\text{m/s}$ . It was then imaged in a CT and examined using custom algorithms developed by the authors in Matlab to calculate the local and bulk *PDAS* and find instances where new dendrites are created.

## Methodology

An Al-10wt% Cu master alloy billet was cast from commercially pure aluminium and copper at the University of Birmingham Casting lab. It was then *EDMed* into a 200 mm length rod with a 6 mm diameter in the Netshape Laboratory, Birmingham. The sample was then directionally solidified in the lab-scale CARLO Bridgman furnace at ACCESS e.V. Germany under a constant withdrawal of 40  $\mu\text{m/s}$  for 60 mm with an instantaneous velocity jump to 80  $\mu\text{m/s}$  which was then constant for 30 mm. The bottom 90 mm of the sample was used to hold the sample in place and top 20 mm was assumed to be unusable. These lengths for the 40 and 80  $\mu\text{m/s}$  sections were chosen to give each section an equal number of diffusion lengths ( $800L_d$  in each instance) for the usable 90 mm of sample where:  $L_d = D/v$ . Which is an  $L_d$  of 75  $\mu\text{m}$  and 37.5  $\mu\text{m}$  respectively (using parameters in Table 1).

The sample was then *CTed* at the Institut für Materialphysik im Weltraum at the German Aerospace Centre (DLR), using a GE Phoenix nanotom microCT scanner with an acceleration voltage of 100 kV and a current of 110  $\mu\text{A}$ . The resulting voxel size was 2  $\mu\text{m}^3$ . The images were then analysed using a series of author written applications within Matlab to: binarise and segment the images using active contours; then find the centre of each dendrite using the skeleton centre method [9]. The dendrite centres of each slice were then joined up forming lines that followed the primary arm of a dendrite producing a “forest” of separate dendrite trunks. The coordinates of a newly initiated dendrite were found by locating where these traced lines branched. This branching indicates a situation where a tertiary arm from the original primary trunk has become stable and formed a new primary trunk.

The bulk *PDAS* for each slice in the sample was calculated using equation 2 above. The local *PDAS* along the length was also calculated using the Voronoi and Warnken-Reed methods which are described by Tschopp et al. [6 & 7] and Warnken and Reed [8]. The average number of nearest neighbours for these two methods was also calculated. In the Warnken-Reed method the authors used



an  $\alpha$  value of 1.5. The results of this were compared with calculations for the *PDAS* using Eq. 1 and the parameters given in Table 1.

**Table 1.** Table of parameters used

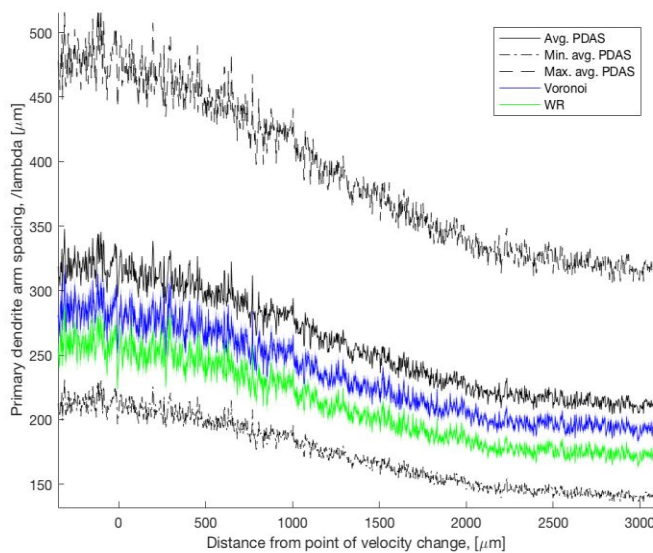
in Eq. 1 to calculate the *PDAS* [10]

## Results

Parameter	Value
$C$	10 [wt% Cu]
$D$	$3 \times 10^{-9}$ [ $\text{m}^2 \text{s}^{-1}$ ]
$G$	10 000 [ $\text{K m}^{-1}$ ]
$k$	0.14
$L$	28
$m$	-3.37 [ $\text{K wt}^{-1}$ ]
$v_1$	40 [ $\mu\text{m s}^{-1}$ ]
$v_2$	80 [ $\mu\text{m s}^{-1}$ ]
$\Gamma$	2.41 [K $\mu\text{m}$ ]

The *PDAS* was determined along the length of the manipulated and binarised *CT* volume (Fig. 1, with two of the *CT* slices before and after the transition shown in Fig. 2) using each of the different methods described above *i.e.* the bulk, Warnken-Reed, and Voronoi. As can be seen in Figure 1 the bulk *PDAS* method gives the highest value for the *PDAS* along the sample with the Voronoi and then Warnken-Reed below that. The evolving dendrite array takes approximately 2500  $\mu\text{m}$  (equivalent to 66  $L_d$ ) until the *PDAS* stabilises and does not decrease further. After which it remains relatively constant. The minimum and maximum stable *PDAS* has also been calculated and shown on Fig. 1. These values were calculated for each slice using  $\lambda_{\min} = 2/3 \lambda$  to  $\lambda_{\max} = 4/3 \lambda$ .

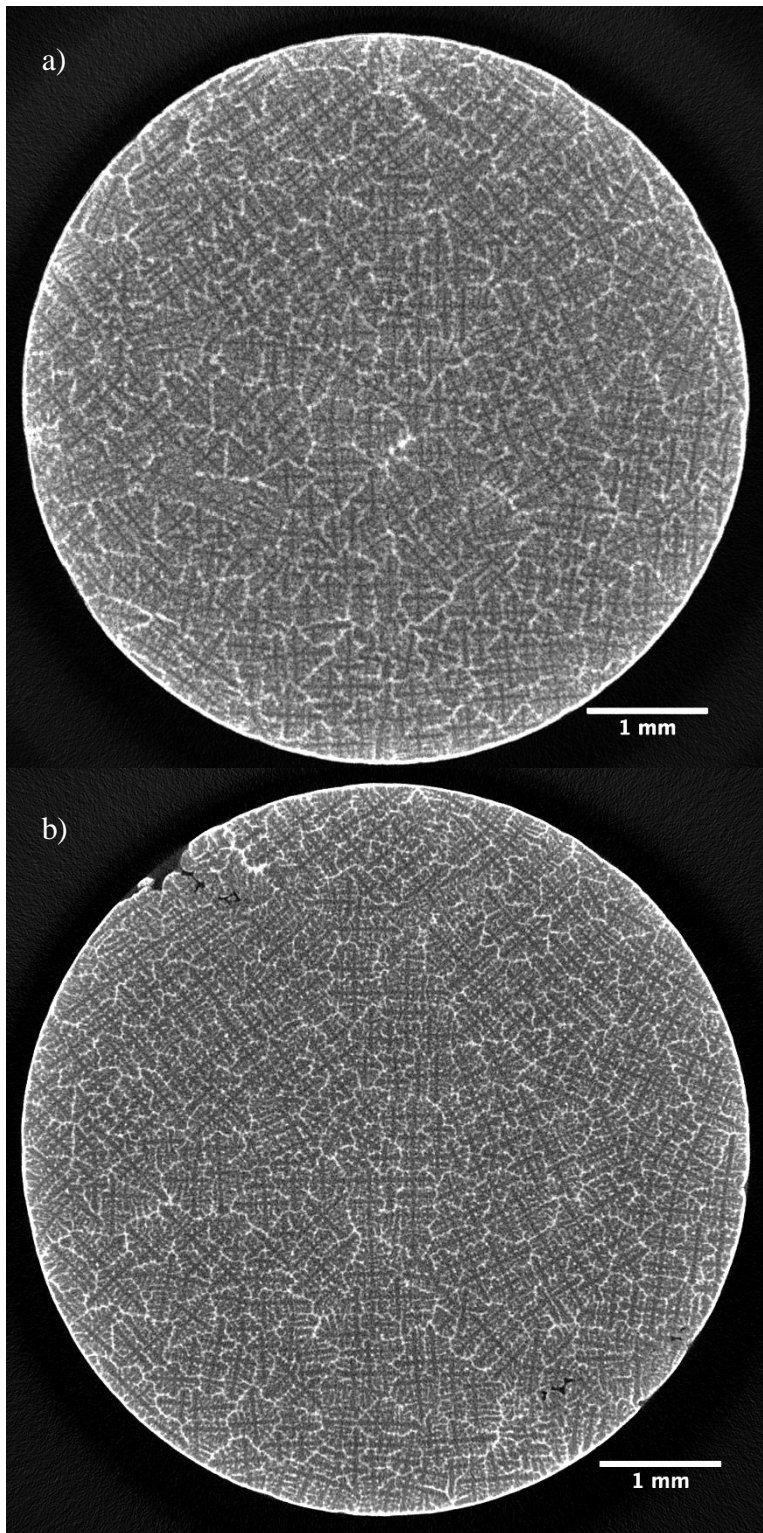
Fig. 3 shows that along the length of the sample there was a slight increase in the number of nearest neighbours in the Warnken-Reed method on the order of 0.05 neighbours. Whereas the Voronoi method shows an increase of approximately 0.2 new neighbours. In both instances there is a steady increase after the velocity change until it plateaus after 2500  $\mu\text{m}$ .



**Figure 1.** *PDAS* along the length of the sample from the velocity change

Fig. 4 shows the cumulative number of created or outcompeted dendrites along the length of the sample. As can be seen there is a relatively constant rise in the number of new dendrites being formed after the velocity change. Whereas after 1000  $\mu\text{m}$  there begins to be dendrites which are eliminated.

The calculated values for the *PDAS* using Eq. 1 and the parameters in Table 1 were 310  $\mu\text{m}$  and 260  $\mu\text{m}$  at 40  $\mu\text{m/s}$  and 80  $\mu\text{m/s}$  respectively. The former value shows good agreement with the results in Fig. 1 prior to the velocity change (distance < 0  $\mu\text{m}$ ). Whereas the calculated value for the *PDAS* of 260  $\mu\text{m}$  at 80  $\mu\text{m/s}$  (distance > 2500  $\mu\text{m}$ ) is



**Figure 2.** CT micrographs of the sample 1 mm before the velocity change (a) and 3 mm after the transition (b)

restructuring as new tertiary dendrite arms fill gaps within the dendritic array.

Moreover Fig. 4 and 5 show that there are some instances of dendrites being out competed and “killed off”. The last such instance of a dendrite being out competed coincides with the levelling off in the number of nearest neighbours seen in Fig. 3. After this levelling of the *PDAS* remains constant and so too does the approximate number of total dendrites.

incorrect by 40  $\mu\text{m}$  as the stabilised *PDAS* in this region is 220  $\mu\text{m}$ . However Eq. 1 is just one of many *PDAS* calculation models.

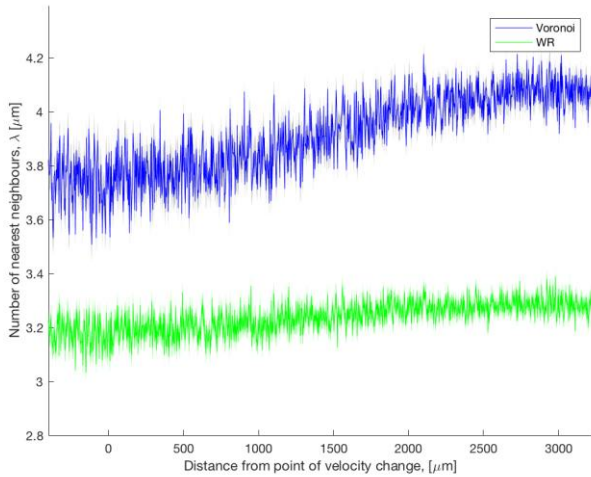
Using information from Fig. 4 the location of the initiations and deletions was found. Fig. 5 shows the stabilisation and deletion of dendrites within the array after 1700  $\mu\text{m}$  and every 200  $\mu\text{m}$  afterwards until 2300  $\mu\text{m}$ . In both cases of stabilisation and deletion the dendritic array readjusts itself around the new or removed dendrite.

## Discussion

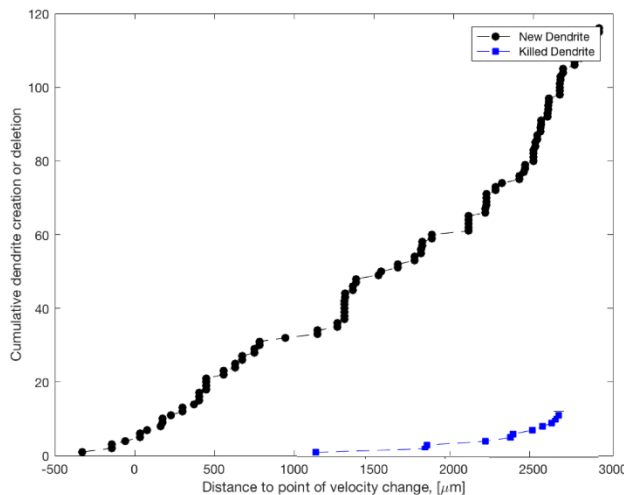
The results of the experiment show that the microstructural array rearranges itself with changing solidification conditions. In this instance, an increase in the velocity from 40 to 80  $\mu\text{m/s}$ . The *PDAS* decreased when calculated using Eq. 2, and with the Voronoi and Warnken-Reed methods for each slice along the length of the sample. This reduction in *PDAS* was expected due to the expectation that the evolving microstructural array would adapt to a lower value (as shown by comparing Fig. 2a and 2b). This re-adaption was achieved by means of a production of new primary dendrite trunks which formed from the stabilisation of tertiary dendrite arms (Fig. 5). As can be seen in Fig. 4 there is a continual increase in the number of new primary dendrite arms after the velocity change. Including after this graph shows that the dendrite array restructuring was not due to a columnar to equiaxed transition (*CET*) but rather a gradual

Fig. 5 also implies that the misorientation between the dendrites may play a role in the deletion of the dendrites. The outcompeted dendrite is misorientated by  $45^\circ$  to all the surrounding nearest neighbours.

A clear feature of Fig. 1 is that the *PDAS* adjustment is not an instantaneous process but takes place over several mm. In this instance, approximately 2.5 mm. This distance corresponds to approximately 70 times the diffusion length in the  $80 \mu\text{m/s}$  regime. It is possible that the diffusion length  $L_d$  plays an intrinsic part in the restructuring of a dendritic microstructure. As it may be possible that a certain number of  $L_d$  need to be reached before the array reaches a stable and unchanging *PDAS* after a velocity change. However more experiments will need to be undertaken to see if this or another parameter plays a role in the time taken for a dendritic array to re-stabilise.



**Figure 3.** Change in nearest neighbour number along the length of the sample



**Figure 4.** Cumulative dendrite creation or deletion along the length of the sample

be used to predict the length that the array adjustment occurs over until a new stable *PDAS* is reached. For this sample, approximately  $66 L_d$  at  $80 \mu\text{m/s}$  were reached before the array stabilised at a *PDAS* of  $230 \mu\text{m}$ .

## Conclusions

A directionally solidified Al-10 wt% Cu rod was solidified under a  $40 \mu\text{m/s}$  withdrawal rate which was instantaneously changed to  $80 \mu\text{m/s}$  after 60 mm. This was achieved to promote dendritic array restructuring by the promotion of tertiary arms stabilising into primary arms.

The solidified rod was *CTed* and analysed using image analysis algorithms written by the authors to trace the centre of the dendrites using the Skeleton Centre method [9]. The *PDAS* was calculated along the length of the sample using the bulk, Voronoi, and Warnken-Reed methods showing in each case that it took approximately 2.5 mm for the array structure to return to steady state with a continuous *PDAS*.

During this transition, new dendrites were created via the promotion of tertiary arm growth and tracked within the 3D *CT* volume. The creation of these new primary arms gives credence to the extension of 2D dendrite array restructuring [2-5] in 3D. Moreover, sites where primary trunks were out competed were also found along the length of the sample showing that the microstructure is continuously adjusting the array to bring it into a stable configuration.

The authors tentatively put forward that the diffusion length  $L_d$  may in some way



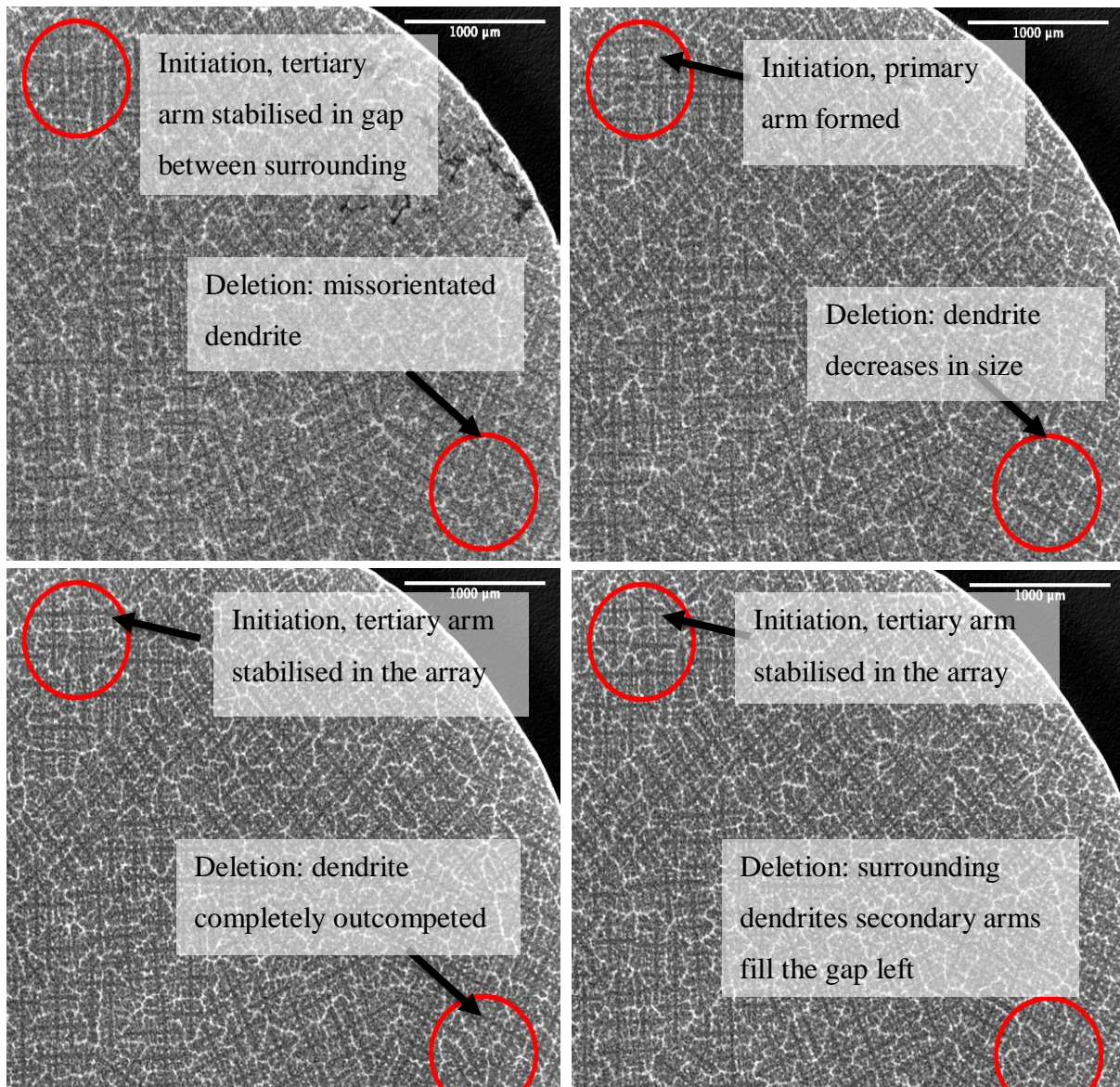


Figure 5. Sites of dendrite initiation and deletion. The images are a) 1700 μm b) 1900 μm, c) 2100 μm and d) 2300 μm from the velocity change.

## Acknowledgments

This work forms part of the Microstructure Formation in Casting of Technical Alloys under Diffusive and Magnetically Controlled Conditions (MICAST) project. The authors would like to thank the ESA for funding as part of the MICAST project and support with this work. With special thanks to Adrian Caden and Peter Cranmer for help casting the master alloy; Amanda Field and Sam Crutchely for the help with EDMing the sample; Christoph Pickmann at Acces e.V. for running the Bridgman furnace; and Vanessa Indrizzi for help with the Matlab code.

## References

- [1] R. Trivedi. Interdendritic spacing: Part ii. a comparison of theory and experiment. *Metallurgical and Materials Transactions A*, 15(6):977–982, Jun 1984.
- [2] D. Ma. Development of dendrite array growth during alternately changing solidification condition. *Journal of Crystal Growth*, 260:580–589, 2004.
- [3] D. Ma. Response of primary dendrite spacing to varying temperature gradient during directional solidification. *Metallurgical and Materials Transactions B*, 35B:735–742, 2004.

- [4] E. Üstün, E. Çadırli, and H. Kaya. Dendritic solidification and characterization of a succinonitrile–acetone alloy. *Journal of Physics: Condensed Matter*, 18(32):7825, 2006.
- [5] V. Indrizzi, N. Warnken, and D. Putman. Computational study of spacing selection in directionally growing dendritic arrays. In SP17, 07 2017.
- [6] M. A. Tschopp, J. D. Miller, A. L. Oppedal, and K. N. Solanki. Characterizing the local primary dendrite arm spacing in directionally solidified dendritic microstructures. *Metallurgical and Materials Transactions A*, 45(1):426–437, 2014.
- [7] M. A. Tschopp, J. D. Miller, A. L. Oppedal, and K. N. Solanki. Evaluating local primary dendrite arm spacing characterization techniques using synthetic evaluating local primary dendrite arm spacing characterization techniques using synthetic directionally solidified dendritic microstructures. *Metallurgical and Materials Transactions A*, 46A:4610–4628, October 2015.
- [8] N. Warnken and R. C. Reed. On the characterization of directionally solidified dendritic microstructures. *Metallurgical and Materials Transactions A*, 42(6):1675–1683, 2011.
- [9] J. E. Miller, M. Strangwood, S. Steinbach, and N. Warnken. Skeletonisation to find the centre of dendrites traced from a 2d microstructural image. In Z. Fan, editor, *Solidification Processing 2017*, 2017.
- [10] M. Gündüz and E. Çadırli. Directional solidification of aluminium–copper alloys. *Materials Science and Engineering: A*, 327(2):167 – 185, 2002.

# Tunable concentration gradients generated by controlled changes in the solidification conditions

Hannes ENGELHARDT, Dorothea MEY and Markus Rettenmayr

Otto Schott Institute of Materials Research, Friedrich-Schiller-Universität Jena (Germany)  
Hannes.Engelhardt@uni-jena.de

**Keywords:** directional solidification, segregation, concentration gradient, temperature gradient, graded material.

**Abstract.** Directional solidification in a temperature gradient with enhanced and reduced melt convection was examined with respect to generating a sequence of tunable concentration gradients. Segregation effects that occur during directional solidification and isothermal holding in a temperature gradient of binary and ternary alloys were investigated using different pulling velocities. In conclusion, a solidification technique for samples with multiple gradients is presented. Position, shape and slope of concentration fluctuations that are comprised of gradients of steeply increasing and decreasing solute concentrations are adjustable. The solidified samples are entirely single phase.

## Introduction

Samples with multiple gradients are valuable e.g. as diffusion samples; no internal interfaces or possible oxide layers disturb the determination of diffusion parameters. The objective of the present work is to produce rod shaped samples that exhibit a sequence of steep concentration gradients without artificial internal interfaces and that are entirely single phase after solidification.

During directional solidification, a variety of parameters are affecting the formation of (macro-) segregations and thus the concentration distribution of the alloying elements along the solidification direction. When an alloy sample is cooled at one end and heated at the other end until it is melted at the hot end, the solid/liquid mushy zone appears between the completely liquid and the completely solid part. During holding of the sample in the temperature gradient, the mushy zone resolidifies completely, and a concentration gradient is created in the solid. The solute concentrations along the resolidified mushy zone follow a section of the solidus line (binary case) or a path on the solidus surface (ternary and higher order) [1-3]. Eventually, a planar solid/liquid interface develops. During subsequent directional solidification with the planar interface, convection in the melt directly influences the segregation behavior [4]. The influence of melt convection and solidification velocity was particularly investigated in this work.

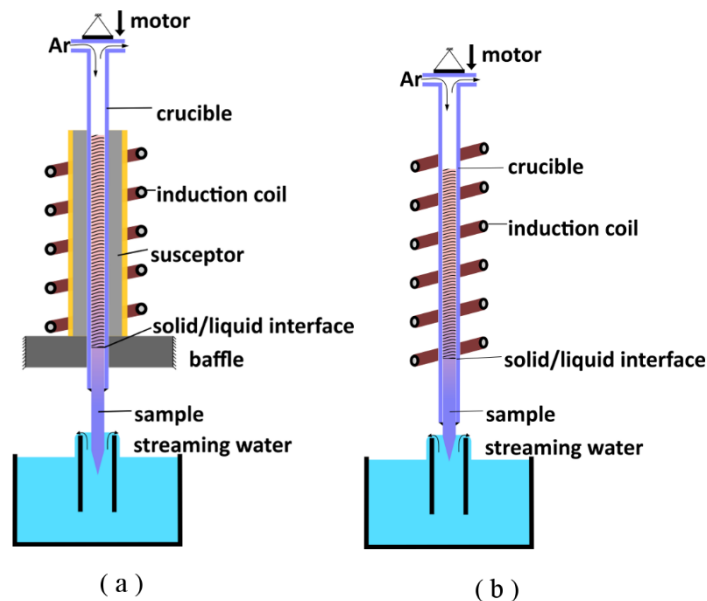
When directional solidification is performed with enhanced convection of the melt, there is complete mixing in the melt, and, due to the sample dimensions, negligible diffusion in the solid. Thus, *Scheil* conditions are fulfilled. *Scheil* type solidification results in pronounced macrosegregation. The concentration profile starts flat with almost constant solute concentrations and exhibits an increasing slope towards the maximum solubility, which theoretically will always be reached [5].

However, if melt convection is suppressed during directional solidification, solute piles up in front of the propagating solid/liquid interface and is transported into the melt solely by diffusion. After an initial transient with increasing solute concentration, a steady state concentration profile at the solid/liquid interface is established and the solidifying composition is constant. The length of the initial transient depends on the solute partitioning coefficient, the solute diffusion coefficient in the melt and the solidification velocity [6,7]. An abrupt change of the solidification velocity during steady state solidification leads to concentration fluctuations, while the concentration profile at the interface adjusts to the new conditions [6-8] and finally reaches steady state again. An increase of the velocity causes fluctuations toward higher solute concentrations, a decrease results in momentarily lower concentrations. Such concentration fluctuations and the initial transient may exhibit considerably steep concentration gradients [6]. In this work we investigate how the segregation effects in the convective and diffusive regimes can be utilized to generate samples with multiple concentration gradients.

## Experiments

The binary and ternary alloys Al – 1.5 at% Cu and Al – 3.5 at% Mg – 1 at% Zn were induction melted from the pure elements Al, Mg, Zn and Cu with a purity of 99.99 at% and cast into rod-shaped molds with 5 mm and 8 mm diameter for the binary and the ternary alloy, respectively. For directional solidification, the samples were placed in tube shaped alumina crucibles (5 and 8 mm inner diameter for Al-Cu and Al-Mg-Zn, respectively). The gap between the sample and the tube was sealed with silicone. The crucible was evacuated and flowed with Ar. The tip of the sample protruded out of the crucible for heat extraction by streaming water, while the upper part of the sample was heated. The temperature gradient was adjusted to  $\sim 15 \text{ K mm}^{-1}$  by adapting the distance between the water bath and the heated zone. Heating was performed differently for the two samples. The Al-Cu sample was heated by radiation from a steel tube that was heated inductively. Below the steel tube, an insulating baffle guarantees a steep temperature gradient (Fig. 1(a)). During directional solidification, the solid/liquid interface is located inside the baffle. The homogeneous heat radiation into the sample results in a uniform temperature distribution in the melt and therefore reduced thermal convection.

For the ternary Al-Mg-Zn sample, heating was performed inductively. This assures good mixing of the melt by forced convection. The skin effect and the electromagnetic forces inside the coil promote melt stirring (Fig. 1(b)). For both set-ups, the directional solidification was performed by moving the crucible through the heater into the streaming water. With a linear motor, the velocities can be varied in a wide range.



**Figure 1.** experimental set-ups for directional solidification with reduced melt convection (a) and forced melt convection (b)

For the Al-Cu sample in set-up (a), the crucible was maintained in its position for thermal stabilization for 3 h after the temperature gradient was established. Then pulling was performed with a velocity of  $3.2 \mu\text{m s}^{-1}$  for 30 mm. Subsequently, the velocity was changed abruptly to  $2 \mu\text{m s}^{-1}$  (Fig. 2 upper graph). Solidification was then proceeded for further 30 mm.

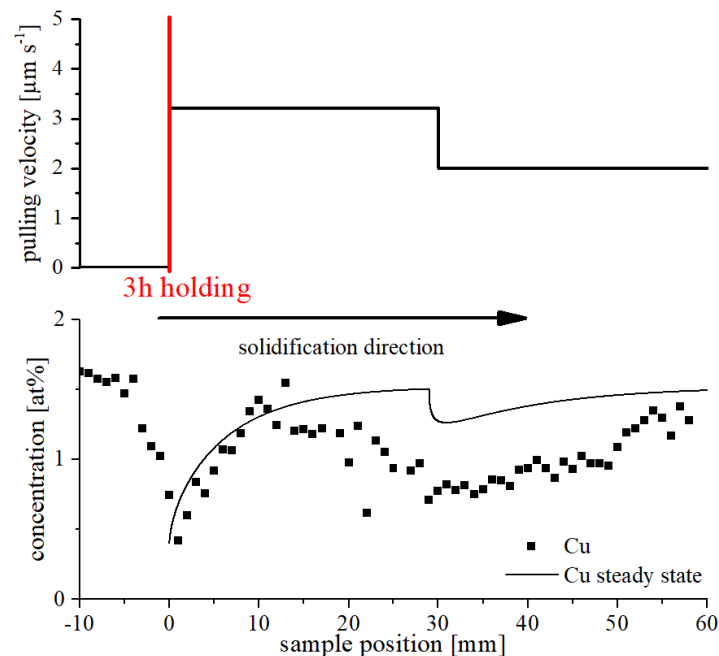
The ternary Al-Mg-Zn sample in set-up (b) was also maintained in the starting position for 3 h. Directional solidification was then started with  $1 \mu\text{m s}^{-1}$ . After a distance of 20 mm, the velocity was abruptly changed to  $10 \text{ mm s}^{-1}$  for 10 mm. Subsequently, the sample was again maintained in the current position for 3 h. Afterwards, fast pulling with  $10 \text{ mm s}^{-1}$  for 10 mm and subsequent holding for 3 h was repeated two more times. The final solidification step was then again slow directional solidification with  $1 \mu\text{m s}^{-1}$  for 20 mm. The remaining melt was quenched by turning off the heating device for both samples.



Longitudinal sections of the samples were prepared metallographically. The composition distribution along the sample axis and the occurrence of secondary phases were investigated by SEM equipped with EDX.

## Results and Discussion

**Solidification with reduced melt convection:** During solidification of primary (Al), the solute elements are piled up in front of the propagating solid/liquid interface. For the Al–Cu sample, the solute element (Cu) is of a higher density than Al and will form stable layering in the melt in front of the interface (that moves upwards). The stable layering together with the choice of the heating set-up for a homogeneous temperature distribution in the melt and a reduced crucible diameter of 5 mm were expected to reduce melt convection sufficiently to reach steady state solidification. A concentration profile assuming solely diffusive solute transport in the melt was calculated applying the equations of Smith et al. [7]. Experimental solidification velocities, positions of velocity changes and a constant partition coefficient of 0.12 were considered. The calculated profile is plotted in Fig. 2 together with the results of the elemental analysis in the sample.



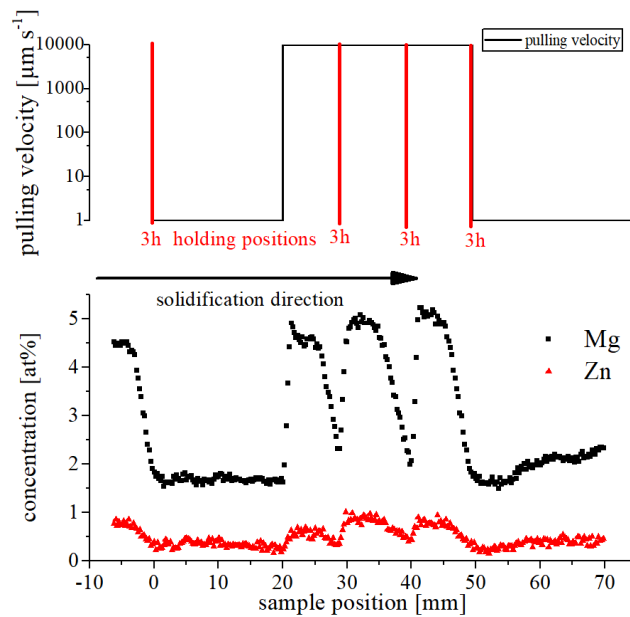
**Figure 2.** pulling velocities (upper graph) and Cu concentration along the sample with overall composition Al – 1.5 at% Cu together with calculated profile for completely suppressed convection.

The measured concentration profile starts with the overall composition of ~1.5 at% Cu in the as-cast microstructure. In the region where the mushy zone was situated and which resolidified during the initial holding time, a concentration gradient with decreasing Cu concentration developed. The concentrations follow the decreasing solidus concentrations with increasing temperature along the sample axis in the temperature gradient. The position 0 mm is set to the position where the planar solid/liquid interface developed. It started to move when the pulling of the sample began with a velocity of  $3.2 \mu\text{m s}^{-1}$ . Judging from the evaluation of Mullins and Sekkerka [9], the planar front may have been in an unstable regime at this velocity. However, the microstructure was found to be single phase, and no lateral microsegregation was observed, as it would be the case for long cells or dendrites. Within the first 15 mm, the concentrations fairly fit to the initial transient of the calculated concentration profile. For the rest of the investigated solidification length, the Cu concentration is lower than predicted by the calculation. This indicates that convective flow in the melt was not fully suppressed. Remaining convection resulted in the partial depletion of the diffusion layer in front of the moving interface. The expected effect of an abrupt velocity change on the concentration profile

is severely diminished. It has been shown elsewhere that a sample diameter of 5 mm is still too large for pure diffusive solute transport [10]; the influence of convection on the evolution of the solute profile is still quite drastic.

**Solidification with enhanced melt convection:** The set-up used for the solidification of the ternary sample promotes strong convection in the melt by inductive heating of the sample. Therefore, sufficient mixing of the solute elements in the melt is assured regardless of their individual density. The final concentration profile of the Al-Mg-Zn sample is shown in Fig. 3. Starting with the overall composition of the alloy, the concentrations of both alloying elements decrease linearly along the solidification direction within a transient of  $\sim 5$  mm length. This is the region where the first solid/liquid mushy zone was situated and resolidified during the first holding time. During the holding time, eventually a planar solid/liquid interface developed. This was the initial condition for the directional solidification step with a planar front.

During the first pulling with  $1 \mu\text{m s}^{-1}$ , the planar solidification front was stable. The melt in front of the solid/liquid interface is not constitutionally supercooled [9]. Considering the large diffusion distance in the solid and the slow solid diffusion, the solidification conditions are close to *Scheil* conditions [5]. Solidification proceeded with a concentration distribution close to the initial section of a *Scheil* distribution. Thus, for the first  $\sim 20$  mm of the directionally solidified zone, the samples exhibit almost constant solute concentration.



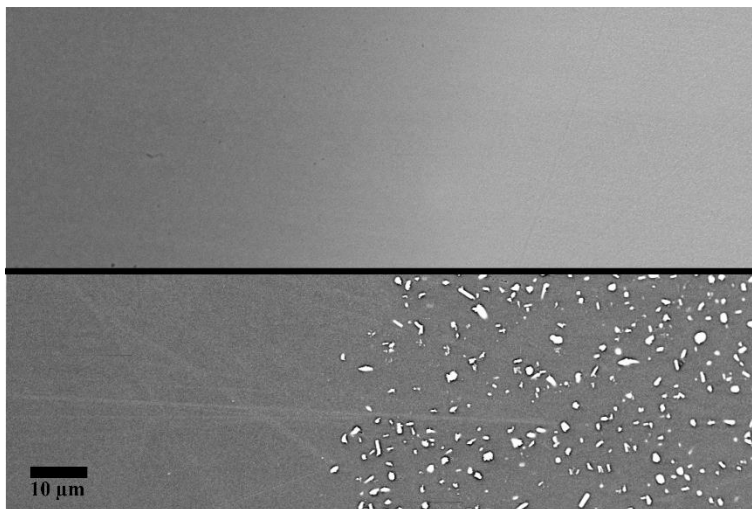
**Figure 3.** pulling velocities (upper graph) and Mg and Zn concentrations along the sample with overall composition Al–3.5at% Mg–1at% Zn.

At the moment when the solidification velocity is abruptly changed to  $10 \text{ mm s}^{-1}$ , the solidification front becomes unstable. A fine dendritic structure develops. However, SEM investigations show a single-phase microstructure at this position (upper part of Fig. 4), interdendritic eutectic or microsegregation were not observed. The concentration profile exhibits an abrupt increase for Mg and Zn at the position of the velocity jump. At this position, the higher melt composition is built into the solid phase to a higher degree. During the holding period subsequent to 10 mm of fast pulling, the dendrites homogenize to a microsegregation free structure that is single-phase. A new mushy zone forms during the fast pulling, which resolidifies quickly over the period of subsequent holding time. Resolidification is accelerated by the initial high density of solid/liquid interfaces in the dendritic structure. Liquid film migration (LFM) and temperature gradient zone melting (TGZM) [11-13] contribute to a fast solute transport out of the mushy zone into the remaining melt. Again, a steep concentration gradient evolves at the position of the second resolidified mushy zone.

Each time when the sequence of fast pulling for 10 mm with  $10 \text{ mm s}^{-1}$  and holding the sample in the temperature gradient is repeated, a new graded zone with steeply increasing and decreasing solute concentration is generated. For the Al-Mg-Zn sample shown in Fig. 3, the sequence was executed three times.

The concentration interval of the peaks and the length of concentration gradients along the profile depend on the initial alloy composition and the temperature gradient.

The last part of directional solidification was again conducted under conditions near *Scheil* with a pulling velocity of  $1 \text{ } \mu\text{m s}^{-1}$ . Thus, adjacent to the concentration peaks, the sample exhibits another region of low solute concentration. The solute concentration increases more distinctly during the final solidification step as compared to the first section, because the solute enrichment is more pronounced in the remaining melt pool that is significantly shorter than at the earlier steps.



**Figure 4.** SEM images with backscattered electrons contrast of a position where Zn and Mg concentrations increase steeply towards the right hand side. Lower image at the same position after precipitation annealing.

All the concentration gradients that were produced due to effects at the solid/liquid interface were 'frozen' as solidification proceeded, because they were transferred to lower temperatures in the temperature gradient upon pulling. Diffusional changes of the concentration profile in the solid state are negligible over the period of solidification time.

The solidification routine with forced melt convection is capable to produce samples with multiple concentration gradients. The concentration profiles can be tailored regarding the space between the peaks by intermediate sections of *Scheil* type solidification and regarding the height of the concentration peaks. For this, the length of faster solidification sequences must be shorter than the mushy zone length. Thus, the maximum peak composition will be lower than the melt composition at this moment. Furthermore, the peak width is adjustable by adapting the temperature gradient.

The specifically graded samples that are now accessible are candidates for graded materials with sequentially changing properties. The variability of mechanical properties due to the solution strengthening can be further enhanced by precipitation annealing – precipitates are occurring only locally with varying density and size due to varying supersaturation. The localized precipitation is shown exemplarily at the position of a steep concentration gradient in the Al-Mg-Zn sample after aging for 5 h at  $250^\circ\text{C}$  in the lower part of Fig. 4.

In diffusion data mining, samples featuring a specific concentration distribution designed with the elaborated solidification routine are a valuable starting condition for diffusion experiments in a temperature gradient. Such diffusion experiments aim at the determination of mobility parameters including their temperature dependence in a single diffusion heat treatment [14].

## Summary

Selected effects that cause macrosegregation and that may result in considerable concentration gradients in directionally solidified samples were evaluated. For the solidification conditions with

reduced melt convection it has been shown that in the initial transient zone, the experimental solute distribution approaches the theoretical concentration profile, while perfect steady state solidification is not attained in the studied sample length.

For the solidification conditions with forced melt convection, a routine to create a sequence of concentration gradients was successfully elaborated. A combination of mushy zone resolidification, *Scheil* type solidification conditions performed with a planar front, and dendritic growth conditions were found to produce concentration profiles with a sequence of concentration gradients along the solidification direction.

## Acknowledgements

We gratefully acknowledge financial support of the Deutsche Forschungsgemeinschaft (DFG) under grant reference EN 1159/1-1.

## References

- [1] H. NguyenThi, B. Drevet, J.M. Debierre, D.Camel, Y.Dabo, B. Billia, Preparation of the initial solid/liquid interface and melt in directional solidification, *J. Cryst. Growth*. 253 (2003) 539–548.
- [2] A. Löffler, K. Reuther, H. Engelhardt, D. Liu, M. Rettenmayr, Resolidification of the mushy zone of multiphase and multicomponent alloys in a temperature gradient- experiments and modeling, *Acta Materialia* 91 (2015) 34–40.
- [3] H. Engelhardt, B. Hallstedt, M. Drüe, A. Löffler, M. Schick, M. Rettenmayr, Solvus composition paths in multicomponent alloys- experimental approach and correlation with calphad calculations for the example Al-Mg-Si, *Adv. Eng. Mat.* 14 (2012) 319–323.
- [4] B. Siber, Seigerungsbildung und Konvektion bei gerichteter Erstarrung von Aluminiumlegierungen, PhD thesis, TU Darmstadt, Herdecke, 1999.
- [5] E. Scheil, Bemerkung zur Schichtkristallbildung. *Z. Metallkd.* 34 (1942) 70–72.
- [6] W.A. Tiller, K.A. Jackson, J.W. Rutter, B. Chalmers, The redistribution of solute atoms during the solidification of metals, *Acta Metall.* 1 (1953) 428–437.
- [7] V.G. Smith, W.A. Tiller, J.W. Rutter, A Mathematical Analysis of Solute Redistribution during Solidification, *Canadian Journal of Physics*, 33 (1955) 723–745.
- [8] S. Li, H. Fu. Liquid concentration distribution and planar interface instability at an abruptly changing pulling velocity in directional solidification, *Sci. China, Ser. E*, 50 (2007) 118–126.
- [9] W.W. Mullins, R.F. Sekerka, Stability of planar interface during solidification of dilute binary alloy, *Journal of Applied Physics* 35 (1964) 444–451.
- [10] R. Trivedi, H. Miyahara, P. Mazumder, E. Simsek, SN Tewari, Directional solidification microstructures in diffusive and convective regimes, *J. Cryst. Growth*. 222 (2001) 365–379.
- [11] D.J. Allen and J.D. Hunt, Temperature Gradient Zone Melting and Microsegregation in Castings. In *Solidification and Casting of Metals: Proceedings of the International Conference on Solidification*, pages 39–43, London, 1979. Metals Society Book.
- [12] T.A. Lograsso and A. Hellawell. Temperature gradient zone melting: Approach to steady state, *J. Cryst. Growth*. 66 (1984) 531–540.
- [13] S. Fischer, M. Založnik, J. M. Seiler, M. Rettenmayr, H. Combeau, Experimental verification of a model on melting and resolidification in a temperature gradient, *J. Alloys Compd.* 540 (2012) 85–88.
- [14] H. Engelhardt, M. Rettenmayr, Diffusion in a temperature gradient - a single cycle method to determine frequency factor and activation energy of solid diffusion coefficients in alloys, *Acta Materialia*, 95 (2015) 212–215.

# **Influence of nucleation and dendrite fragmentation on as-cast structure of Sn-10wt.%Pb benchmark**

Yongjian ZHENG<sup>1</sup>, Menghuai WU<sup>1, 2</sup>, Abdellah Kharicha<sup>1, 2</sup>, Andreas Ludwig<sup>1</sup>

<sup>1</sup>Chair of Modeling and Simulation of Metallurgical Processes, University of Leoben, Austria

<sup>2</sup>Christian Doppler Lab for Advanced Simulation of Solidification and Melting, University of Leoben, Austria

E-mail: menghuai.wu@unileoben.ac.at

**Key words:** solidification, heterogeneous nucleation, dendrite fragmentation, simulation.

**Abstract:** A laboratory benchmark casting experiment on the Sn-10 wt.%Pb alloy has shown an equiaxed zone in the up-left region of the casting [Hachani et al., Int. J. Heat Mass Transfer, 85 (2015), 438-454]. It is not clear if the equiaxed crystals originate from heterogeneous nucleation or dendrite fragmentation. The current work is to use a three-phase mixed columnar-equiaxed solidification model to study its solidification process by assuming different crystal origins, due to either the heterogeneous nucleation, dendrite fragmentation, or a combination of them. Simulations are performed, and compared with the as-cast structure. The modeling results show that when the nucleation is considered as the sole origin of equiaxed crystals, it is difficult to ‘reproduce’ the experimental result, i.e. the calculated equiaxed zone is much narrower than the one of the as-cast structure. When the fragmentation is considered as the origin of equiaxed crystals, the shape of equiaxed zone seems closer to experimental one. The case with combination of nucleation and fragmentation show the best agreement with the experiment. Based on this modeling study, fragmentation seems to play a dominant role in the origin of equiaxed crystals.

## **Introduction**

The laboratory solidification experiments were widely used to investigate the formation of as-cast structure and related phenomena [1, 2]. Recently, an experiment setup with precise control of cooling rate and temperature gradient was designed [3], and a series of solidification experiments and post-mortem metallographic analyses of as-solidified benchmarks were performed at the SIMAP Laboratory in Grenoble, France [4]. It reported that there was an equiaxed zone in the up-left region of the benchmark under normal gravity condition. A hypothesis is that solute-rich liquid rises through the mushy zone and causes re-melting and fragmentation, which may explain the origin of equiaxed crystals. Based on the theoretical study on local remelting of the mushy zone [5, 6], the authors have proposed a simple formula to consider the fragmentation phenomenon in a mixed columnar-equiaxed solidification model [7, 8]. The fragmentation rate is dependent on the local melt concentration gradient and the interdendritic flow. A preliminary study has shown that the equiaxed zone in the benchmark casting is reproducible by the numerical model if the fragmentation mechanism is considered [9]. It is also well known that the heterogeneous nucleation is an important crystal origin of many engineering castings [10]. Therefore, new questions arise: can the aforementioned as-cast structure be reproduced if only the heterogeneous nucleation is considered, and how does the as-cast structure look like if both fragmentation and heterogeneous nucleation are considered? To address above questions, the current work tries to use the same three-phase mixed columnar-equiaxed solidification model to analyze the solidification process with the emphasis on the transport of equiaxed crystals. Simulations are made with assumption of different crystal origins, due to either the heterogeneous nucleation, fragmentation, or a combination of them. The calculated mixed columnar-equiaxed structure is compared with the as-cast structure, hence to get some indications about the most probable mechanism of the origin of the equiaxed crystals.

## **Model descriptions**

The three-phase mixed columnar-equiaxed solidification model was described previously [8]. The three phases are the primary melt ( $\ell$ ), equiaxed (e) and columnar phases (c). Their volume fractions are quantified by  $f_\ell$  [-],  $f_e$  [-], and  $f_c$  [-], and  $f_\ell + f_e + f_c = 1$ . Both the liquid and equiaxed phases are

moving phases, and the corresponding Navier-Stokes equations are solved. The columnar phase is assumed to be rigid and stationary. Nucleation of equiaxed crystals is assumed to occur following a classical Gaussian heterogeneous nucleation law. The inoculants ( $n_{em}$  [ $m^{-3}$ ]) serve as nucleation sites, which are activated as equiaxed crystals ( $n_{eq}$  [ $m^{-3}$ ]) by undercooling ( $\Delta T$  [K]) as follows:

$$N_{nu} = \frac{n_{em}}{n_{max}} \cdot \frac{D(\Delta T)}{D(t)} \cdot \frac{dn_{eq}}{d(\Delta T)} \quad (1)$$

$$\frac{D(\Delta T)}{D(t)} = \frac{\partial T}{\partial t} + u_\ell \cdot \left( m \cdot \frac{\partial c_\ell}{\partial x} - \frac{\partial T_\ell}{\partial x} \right) + v_\ell \cdot \left( m \cdot \frac{\partial c_\ell}{\partial y} - \frac{\partial T_\ell}{\partial y} \right) \quad (2)$$

$$\frac{dn_{eq}}{d(\Delta T)} = \frac{n_{max}}{\sqrt{2\pi} \cdot \Delta T_\sigma} \cdot e^{-\frac{1}{2} \left( \frac{\Delta T - \Delta T_N}{\Delta T_\sigma} \right)^2} \quad (3)$$

$N_{nu}$ ,  $N_{max}$ ,  $\Delta T_N$ ,  $\Delta T_\sigma$  mean heterogeneous nucleation rate [ $m^{-3} s^{-1}$ ], initial inoculant number density [ $m^{-3}$ ], Gaussian distribution width [K] and undercooling for maximum grain production rate [K], respectively.  $u_\ell$ ,  $v_\ell$ ,  $c_\ell$ ,  $T_\ell$ ,  $m$  indicate x component of liquid velocity [ $m s^{-1}$ ], y component of liquid velocity [ $m s^{-1}$ ], liquid concentration [-], liquid temperature [K], and liquidus slope [-], respectively. The method to treat dendrite fragmentation in the mixed columnar-equiaxed solidification model was described elsewhere [7]. The fragmentation-induced mass transfer rate ( $M_{ce}$  [ $kg m^{-3} s^{-1}$ ]) from columnar to the equiaxed is calculated:

$$M_{ce} = -\gamma \cdot (\vec{u}_\ell - \vec{u}_c) \cdot \nabla c_\ell \cdot \rho_e \quad (4)$$

$\gamma$ ,  $\rho_e$  are the fragmentation coefficient [-] and equiaxed phase density [ $kg m^{-3}$ ].  $\vec{u}_\ell$  and  $\vec{u}_c$  denote liquid and columnar velocity vectors [ $m s^{-1}$ ]. Note that fragmentation occurs only with remelting, i.e. for the case of  $M_{ce} > 0.0$ . For the case of solidification (calculated  $M_{ce}$  has a negative value), we set  $M_{ce} = 0.0$ , i.e. no fragmentation should occur. The mass integral of all fragments as produced per time is proportional to the increase rate of constitutional supersaturation as caused by the interdendritic flow. The diameter of the fragment ( $d_{e,frag}^0$  [m]) is proportional to the secondary dendrite arm space ( $\lambda_2$  [m]) and the volume fraction of the columnar phase ( $f_c$ ):

$$d_{e,frag}^0 = \lambda_2 \cdot f_c \quad (5)$$

Hence the rate of the fragment production ( $N_{frag}$  [ $m^{-3} s^{-1}$ ]) can be calculated as:

$$N_{frag} = \frac{M_{ce}}{\rho_e \cdot \frac{\pi}{6} (d_{e,frag}^0)^3} \quad (6)$$

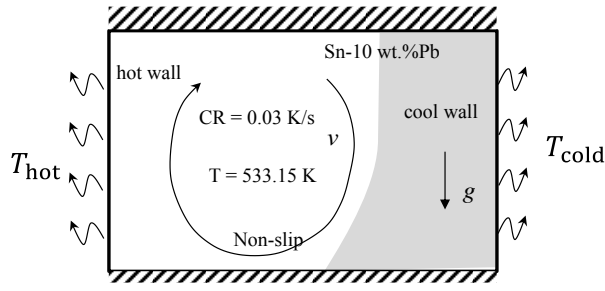
The transport of equiaxed inoculants is calculated as follows [11, 12].

$$\frac{\partial}{\partial t} n_{em} + \nabla \cdot (\vec{u}_\ell n_{em}) = -N_{nu} \quad (7)$$

As the columnar dendrite structure and the equiaxed grains (crystals) are treated as two separated solid phases, evolutions of them by solidification are calculated explicitly. The amounts of them are quantified by their volume fractions,  $f_c$  and  $f_e$ . The columnar phase is stationary ( $\vec{u}_c = 0$ ). The motion of equiaxed crystals,  $\vec{u}_e$ , is calculated by solving corresponding momentum conservation equation. Transport of the number density of the equiaxed crystals,  $n_{eq}$ , must be calculated with

$$\frac{\partial}{\partial t} n_{eq} + \nabla \cdot (\vec{u}_e n_{eq}) = N \quad (8)$$

by considering a source term  $N$  [ $m^{-3} s^{-1}$ ].  $N$  should include the contribution of the heterogeneous nucleation,  $N_{nu}$ , and the fragmentation,  $N_{frag}$ .



**Figure 1.** Simulation settings for the benchmark casting: geometry and boundary conditions.

Fig. 1 shows the configuration and settings of the simulation, as is in accordance with the experiment from Hachani et al. [4]. Sn-10 wt.%Pb alloy is considered. The thermodynamic and physical parameters can be found in reference [9]. 5 cases are calculated (Table 1). Case 1 assumes only the fragmentation as sole origin of equiaxed crystals, while Case 5 assumes heterogeneous nucleation as only origin. Case 2 to Case 4 consider both fragmentation and heterogeneous nucleation, with different nucleation parameters.

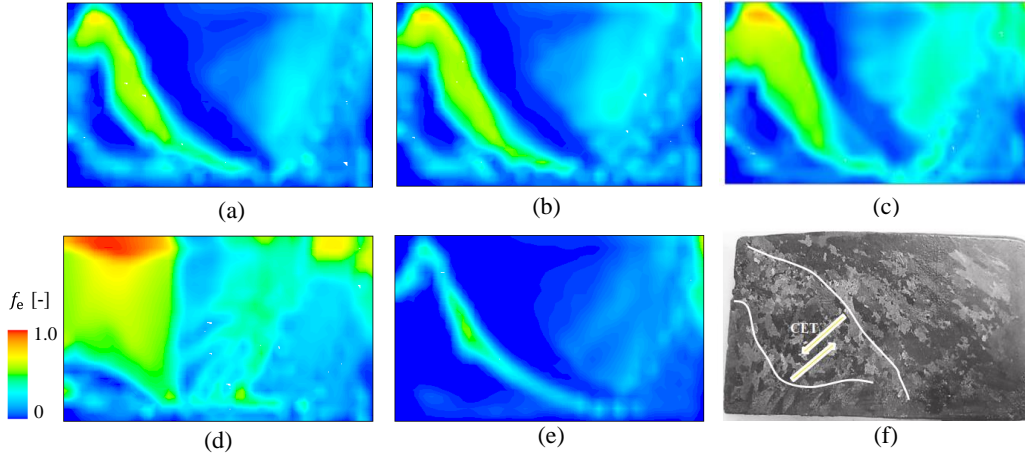
**Table 1.** Numerical parameter study and different simulation cases.

origin of equiaxed crystals		parameters
Case 1	fragmentation only	$\gamma = 1.0$
Case 2	fragmentation + nucleation	$N_{\max} = 5.0 \times 10^8 \text{ m}^{-3}$ , $\Delta T_N = 3.0 \text{ K}$ , $\Delta T_\sigma = 3.0 \text{ K}$ , $\gamma = 1.0$
Case 3	fragmentation + nucleation	$N_{\max} = 1.0 \times 10^9 \text{ m}^{-3}$ , $\Delta T_N = 3.0 \text{ K}$ , $\Delta T_\sigma = 3.0 \text{ K}$ , $\gamma = 1.0$
Case 4	fragmentation + nucleation	$N_{\max} = 5.0 \times 10^9 \text{ m}^{-3}$ , $\Delta T_N = 3.0 \text{ K}$ , $\Delta T_\sigma = 3.0 \text{ K}$ , $\gamma = 1.0$
Case 5	nucleation only	$N_{\max} = 5.0 \times 10^9 \text{ m}^{-3}$ , $\Delta T_N = 3.0 \text{ K}$ , $\Delta T_\sigma = 3.0 \text{ K}$

## Results and discussion

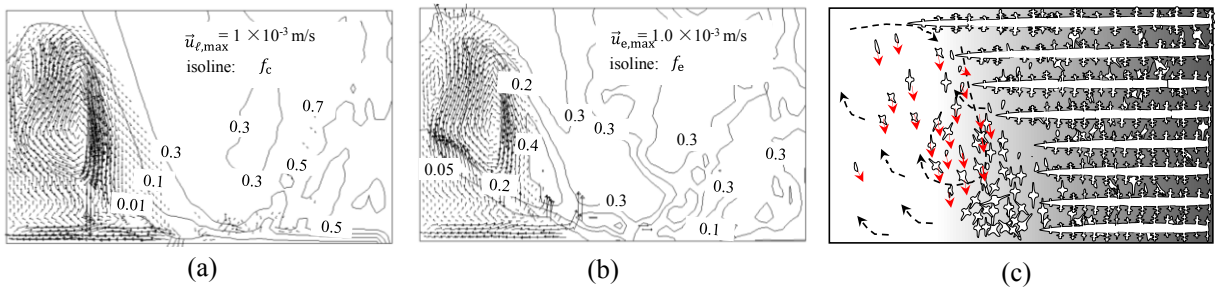
Fig. 2 shows the simulated equiaxed zone in the as-solidified benchmark casting for different cases, as well as the as-cast structure of experiment observation. Contour in Fig. 2(a) shows the result of Case 1 (only fragmentation). There is an equiaxed zone in the up-left region, extending to the middle of the bottom. There is a small portion of equiaxed crystals which are scattered in the right part of the benchmark. The equiaxed crystals are set to be detached from the columnar trunk and some of them are embedded in the space between different columnar dendrites. If both fragmentation and nucleation are considered in the solidification process (Case 2-4), the position of equiaxed zone would not change significantly, locating in the up-left corner. However, the equiaxed area becomes broader as the initial inoculant number density  $n_{\max}$  increases (Fig. 2(b)-(d)). When the initial inoculants number density is considered as  $n_{\max} = 5 \times 10^9 \text{ m}^{-3}$  (Case 4), the equiaxed zone is too large in comparison with the experiment (Fig. 2(d), (f)). The simulation result of Case 3 seems to show best agreement with the experiment using  $n_{\max} = 1 \times 10^9 \text{ m}^{-3}$  (Fig. 2(c), (f)). The fragmentation of dendrite plays a significant role in the formation of the equiaxed zone. The numerical analysis shows that without dendrite fragmentation, Case 5 even with a very large initial inoculant number density  $n_{\max} = 5 \times 10^9 \text{ m}^{-3}$  would not be able to reproduce the experiment result, i.e. the calculated equiaxed zone is too narrow (Fig. 2(e)).





**Figure 2.** Calculated as-solidified equiaxed volume fraction contour for different cases with various parameters for equiaxed crystal origin and the as-cast structure of the experiment: (a) with fragmentation (Case 1), (b) with fragmentation and nucleation using  $n_{\max} = 5 \times 10^8 \text{ m}^{-3}$  (Case 2), (c) with fragmentation and nucleation using  $n_{\max} = 1 \times 10^9 \text{ m}^{-3}$  (Case 3), (d) with fragmentation and nucleation using  $n_{\max} = 5 \times 10^9 \text{ m}^{-3}$  (Case 4), (e) only with nucleation using  $n_{\max} = 5 \times 10^9 \text{ m}^{-3}$  (Case 5) and (f) as-solidified structure observed from experiment [4].

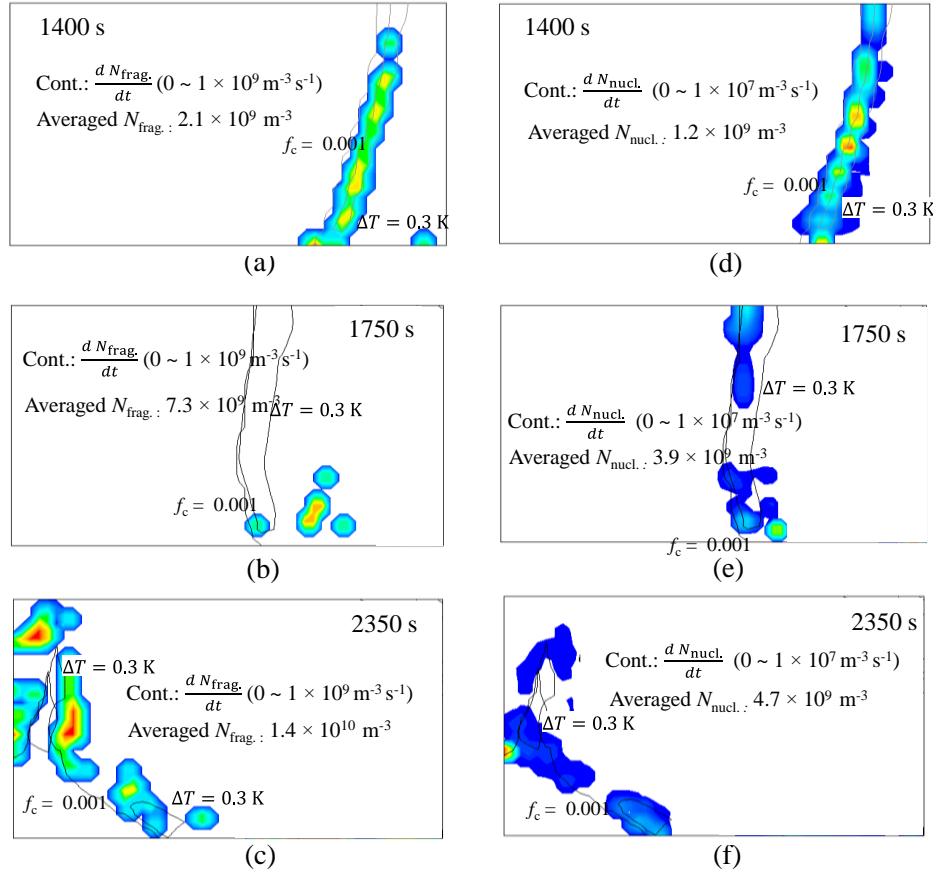
The subsequent analyses are based on Case 3. As shown in Fig. 2(f), an accumulated equiaxed zone was obtained in the up-left corner region of the as-solidified benchmark casting, and this region extends to the middle bottom. The transport of the equiaxed crystals is responsible for this distribution. Equiaxed crystals are produced near the solidification front. Subsequently, they tend to sediment along the columnar tip front due to the density difference between liquid and solid crystals. Meanwhile, the melt flow also tries to bring them into the bulk region (left side) and a large portion of equiaxed crystals would move into the melt bulk. As moving in the melt, those crystals continue to grow if the melt is still undercooled, or they might be melted if they are brought into the overheated or supersaturated region. As the density of the melt is strongly dependent on the solute enrichment of the melt [9], the equiaxed crystals are with different capability of settling due to the different density variation between solid and melt all over the benchmark.



**Figure 3.** Analysis of the crystals movement for Case 3 during solidification at 2300 s: (a) liquid velocity field overlaid with  $f_c$  isoline; (b) equiaxed velocity overlaid with  $f_e$  isoline; (c) schematic of melt flow and equiaxed movement (black dash lines indicate the circulation of melt flow and red arrows indicate the relatively moving direction of equiaxed crystals).

A detailed analysis of the crystal movement for the moment at 2300 s is shown in Fig. 3. A clockwise liquid convection is observed in the melt. The intensity of the liquid flow is at the magnitude of  $1 \times 10^{-3} \text{ m s}^{-1}$  (Fig. 3(a)). Due to the drag force between liquid and equiaxed crystals, the equiaxed crystals also form a clockwise convection (Fig. 3(b)), similar as that for the liquid. Equiaxed crystals tend to

move downwards relative to the liquid (Fig. 3(c)). The convection cell gradually shrinks and moves to the up-left corner, till the end of solidification. It is essential for the formation of final as-cast structure and the details are discussed in [9]. It is worth mentioning that no matter where the crystals come from, nucleation or fragmentation, the movement of crystals obeys a same pattern. It is impossible to figure out the origin of the crystal once it is formed.



**Figure 4.** Comparison of different equiaxed crystal origin mechanisms (Case 3): (a)-(c) contours of fragmentation rate at 1400 s, 1750 s and 2350 s, respectively; (d)-(e) contours of heterogeneous nucleation rate at 1400 s, 1750 s and 2350 s, respectively.

Comparison of the differences equiaxed crystal origins, fragmentation or heterogeneous nucleation, are made in Fig. 4. At 1400 s, the solidification front advances to about  $\frac{1}{4}$  length of the benchmark from right cold wall. Crystals form slightly behind the solidification front, either by the mechanisms of fragmentation or nucleation. The fragment production rate is about 100 times larger than heterogeneous nucleation rate (Fig. 4(a), (d)). When the solidification front evolves to the middle part of the benchmark (1750 s), the fragmentation is witnessed only in some special locations, e.g. bottom and segregated channels. This phenomenon is connected to the local liquid flow conditions. According to Eq. 4, the fragmentation is not available when the dot production of liquid concentration gradient  $\nabla c_\ell$  and liquid velocity  $\vec{u}$  is equal or greater than zero. At this moment, the solidification front is nearly vertical (Fig. 4(b)), as would lead to a similar direction of liquid velocity. It would result in the unfavorable condition for fragmentation. However, the nucleation mechanism takes effect continuously (Fig. 4(e)) with a relatively low production rate with the magnitude  $1 \times 10^7 \text{ m}^{-3} \text{ s}^{-1}$ . At the late age of the solidification (2350 s), the fragmentation of dendrite plays an important role to produce equiaxed crystals in the mush zone. It happens in a wide area slightly behind the solidification front (Fig. 4(c)). Heterogeneous nucleation, by contrast, makes a contribution to the formation of equiaxed crystals near the front (Fig. 4(f)). The combined effect of fragmentation and nucleation would result in finally an enrichment equiaxed zone, as is close to the experiment observation. Even though the nucleation takes effect from the beginning to the end of solidification,

it is fragmentation that makes the dominant contribution to the crystals origination in the solidification process.

## Summary discussion

Effects of heterogeneous nucleation and dendrite fragmentation on the formation of equiaxed zone in a solidifying Sn- 10% Pb benchmark were investigated by a three-phase mixed columnar-equiaxed solidification model. With undercooling the inoculants in the melt will be activated as equiaxed nuclei, and they can develop into equiaxed crystals. Remelting is the main mechanism for the origin of equiaxed fragments. Once the crystal is formed, it tends to settle down in the melt, interacting with the melt flow through the drag force. A clockwise convection cell shrinks and moves gradually to the up-left corner at the late age of solidification, as is responsible for the formation of equiaxed zone in the up-left part of the benchmark. It is difficult to reproduce the equiaxed zone properly only through the contribution of heterogonous nucleation. Even though the case only considering fragmentation can reproduce the shape and position of equiaxed zone, it is the case that properly considering both nucleation and fragmentation fits best with the experiment. Fragmentation plays the dominant role in the production of equiaxed crystals. Since the simulations were made in 2D, some details about the location of the crystal production were not properly revealed. For heterogonous nucleation, the Gaussian distribution width and undercooling for maximum grain production rate are given as fixed values. Additionally, a fixed value of 0.1 is assigned to fragmentation coefficient  $\gamma$ . Those parameters require further theoretic studies and experimental validations.

## References

- [1] D. Hebditch, J. Hunt, Observations of ingot macrosegregation on model systems, *Metall. Mater. Trans.*, 5 (1974) 1557-1564.
- [2] J. Sarazin, A. Hellawell, Channel formation in Pb-Sn, Pb-Sb, and Pb-Sn-Sb alloy ingots and comparison with the system  $\text{NH}_4\text{Cl-H}_2\text{O}$ , *Metall. Mater. Trans. A*, 19 (1988) 1861-1871.
- [3] X. Wang, Y. Fautrelle, An investigation of the influence of natural convection on tin solidification using a quasi two-dimensional experimental benchmark, *Int. J. Heat Mass Transfer*, 52 (2009) 5624-5633.
- [4] L. Hachani, K. Zaidat, Y. Fautrelle, Experimental study of the solidification of Sn-10 wt.%Pb alloy under different forced convection in benchmark experiment, *Int. J. Heat Mass Transfer*, 85 (2015) 438-454.
- [5] M.C. Flemings, G.E. Nereo, Macrosegregation : Part I, *Trans. Metall. Soc. Aime*, 239 (1967) 1449-1462.
- [6] T. Campanella, C. Charbon, M. Rappaz, Grain refinement induced by electromagnetic stirring: A dendrite fragmentation criterion, *Metall. Mater. Trans. A*, 35 (2004) 3201-3210.
- [7] Y. Zheng, M. Wu, A. Kharicha, A. Ludwig, Incorporation of fragmentation into a volume average solidification model, *Model. Simul. Mater. Sci. Eng.*, 26 (2018) 015004
- [8] M. Wu, A. Ludwig, A three-phase model for mixed columnar-equiaxed solidification, *Metall. Mater. Trans. A*, 37A (2006) 1613-1631.
- [9] Y. Zheng, M. Wu, E. Karimi-Sibaki, A. Kharicha, A. Ludwig, Use of a mixed columnar-equiaxed solidification model to analyse the formation of as-cast structure and macrosegregation in a Sn-10 wt% Pb benchmark experiment, *Int. J. Heat Mass Transfer*, 122 (2018) 939-953.
- [10] M. Rappaz, Modelling of microstructure formation in solidification processes, *Int. Mater. Rev.*, 34 (1989) 93-124.
- [11] M. Wu, Y. Zheng, A. Kharicha, A. Ludwig, Numerical analysis of macrosegregation in vertically solidified Pb-Sn test castings-Part I: Columnar solidification, *Comp. Mater. Sci.*, 124 (2016) 444-455.
- [12] Y. Zheng, M. Wu, A. Kharicha, A. Ludwig, Numerical analysis of macrosegregation in vertically solidified Pb-Sn test castings-Part II: Equiaxed solidification, *Comp. Mater. Sci.*, 124 (2016) 456-470.

# Effect of temperature and heating rate on dissolution of a 3003 core by a 4004 clad during vacuum brazing

JACQUES Bruno<sup>1,2</sup>, LACAZE Jacques<sup>2</sup>, MAZET Thierry<sup>1</sup>,  
VYNNYCKY Michael<sup>3</sup> and DEZELLUS Olivier<sup>4</sup>

<sup>1</sup>Fives Cryo, 25 bis rue du Fort – B.P. 87 88194 Golbey Cedex, France

<sup>2</sup>CIRIMAT, ENSIACET, 4 allée Emile Monso – CS44362, 31030 Toulouse Cedex 4, France

<sup>3</sup>Department of Materials Science and Engineering, KTH Royal Institute of Technology,  
Brinellvägen 23, 100 44 Stockholm, Sweden

<sup>4</sup>LMI-UMR CNRS 5615 Université Lyon 1, 43 Bd du 11 novembre 1918, 69100 Villeurbanne,  
France

bruno.jacques@ensiacet.fr

**Keywords:** Vacuum brazing, Heat exchanger, Aluminium alloys, Dissolution

**Abstract.** High capacity aluminium heat exchangers are composed of many layers of brazing plates and fins and are brazed under vacuum. Brazing sheets consist of a core material clad with an Al-Si alloy that melts at much lower temperature than the core and provides the liquid needed to fill the joints by capillarity. Due to the size of the heat-exchangers, the temperature in the assembly cannot be homogeneous at any time, meaning that hotter and colder areas can exist during the brazing cycle which must be properly controlled to ensure a safe final assembly.

In the present study, melting and re-solidification of the clad material has been investigated on disc samples machined out of a brazing sheet and processed under secondary vacuum using a lamp furnace. The re-solidified clad layers were observed on a diametrical section of the samples. As expected, higher brazing temperature increases the amount of liquid formed which evidences a dissolution stage following melting of the clad. Further, solid-state diffusion of silicon to the core during heating to the brazing temperature, and thus the change in the amount of liquid available at brazing temperature, was demonstrated by carrying out the experiments for two strongly differing heating rates.

## Introduction

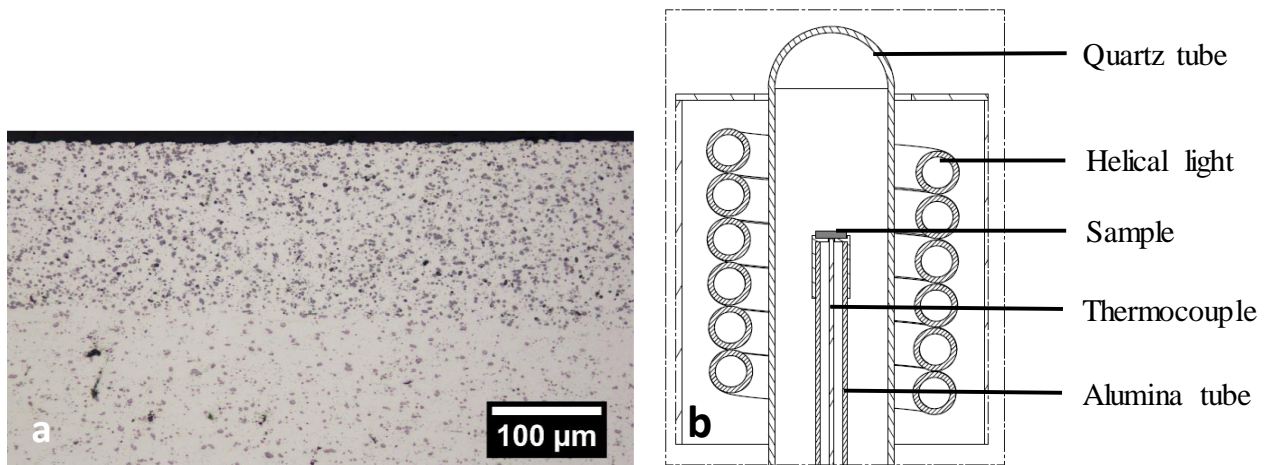
Aluminium heat-exchangers are commonly used for low temperature gas processing and liquefaction plants. They are often manufactured by controlled atmosphere brazing (CAB) using a flux to destroy the oxide film and thus to allow the filler metal to flow. In contrast, high capacity heat exchangers are assembled by vacuum brazing owing to their size. In this case, the filler metal contains magnesium or a similar element to disrupt the alumina film and to trap the oxygen or water left in the vacuum chamber [1].

Brazing sheets consist of a sandwich material, typically an Al-Mn core alloy clad on one or both sides with an Al-Si alloy with a lower melting point than the core. At the brazing temperature, capillarity displaces the liquid clad to the joints where it will solidify upon cooling thus ensuring mechanical assembly. However, interactions between the clad and the core during the process can lead to serious defects affecting the mechanical strength or service capabilities of the heat exchanger. Amongst those interactions is diffusion of silicon from the clad to the core during the heating stage, which may decrease the amount of liquid available for joining and can lead to poor service properties of the assembly [2]. On the other hand, brazing at too high temperature or for too long time leads to detrimental dissolution of the core by the liquid clad, as emphasized by Zhao and Woods in their review [3].

This study investigates the effect of maximal temperature and of heating rate on the amount of liquid at the maximum brazing temperature. This is achieved by using 2 significantly different heating rates and 5 brazing temperatures, between 595°C to 625°C. The experiments were conducted on discs processed in a light furnace.

## Materials and methods

The samples consist of discs 9.8 mm in diameter machined out from a brazing sheet 1.5 mm in thickness made of a core in 3003 alloy clad on one side with 150  $\mu\text{m}$  of 4004 alloy. The nominal compositions of the alloys are given in Table 1. Fig. 1-a shows a metallographic transverse section of the as-received brazing sheet: dispersed precipitates in the core alloy are Mn-bearing phases, while populated precipitates in the clad alloy are silicon particles. At higher enlargement, it would be possible to note that 3003 alloy presents precipitates and dispersoids of  $\alpha\text{-Al}(\text{Mn,Fe})\text{Si}$  and  $\text{Al}_6(\text{Mn,Fe})$  phases, while 4004 alloy shows also precipitates of  $\text{Mg}_2\text{Si}$  and  $\pi\text{-Al}_3\text{FeMg}_3\text{Si}$  [4].



**Figure 1.** Micrograph of the upper part of the brazing sheet in the as-received state (a) and schematic of the experimental set-up (b).

**Table 1.** Nominal composition (wt.%) of 3003 and 4004 alloys.

Alloy	Si	Fe	Cu	Mn	Mg	Zn	Other
3003	0.6	0.7	0.05-0.2	1.0-1.5	-	0.1	0.05
4004	9-10	-	-	-	1-2	-	0.05

The samples were processed in a light furnace under a secondary vacuum better than  $5 \cdot 10^{-5}$  mbar before starting heating. Fig. 1-b shows a schematic of the experimental set-up in which the sample is isolated from the environment by a quartz tube. Heating is achieved by means of an helical lamp and controlled by a thermocouple penetrating half-way within the sample.

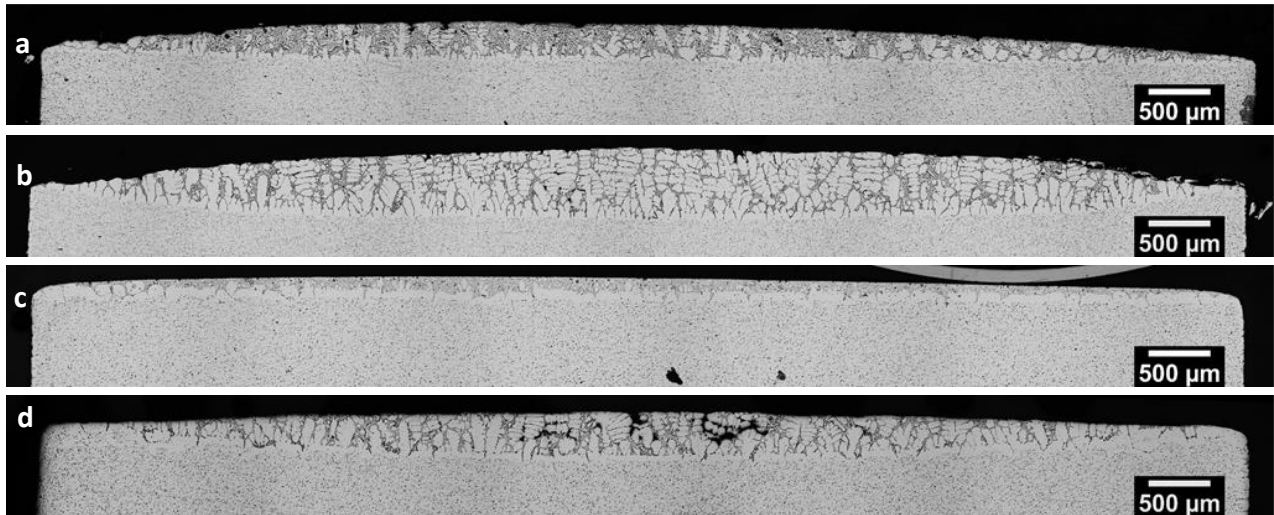
The temperature cycles consisted in heating at constant rate to a maximum hold temperature at which the clad alloy was melted. Five hold temperatures were used, namely 595°C, 605°C, 610°C, 615°C and 625°C. Two heating rates have been used, a fast heating rate (FHR) of  $\approx 120^\circ\text{C}/\text{min}$  and a slow heating rate (SHR) of  $0.6^\circ\text{C}/\text{min}$ . In both cases, the samples were held for 5 min at the maximum temperature and then finally cooled down by turning off the lamp. The cooling rate was  $\approx 50^\circ\text{C}/\text{min}$  from 600°C to 300°C.

Each sample was sectioned along a diametrical section, mounted, polished and then observed with light optical microscopy.

## Results and discussion

Fig. 2 shows the cross section of the FHR-595°C (a), FHR-625°C (b), SHR-595°C (c) and SHR-625°C (d) samples. All samples exhibit on the upper part a dendritic microstructure with a more or less overall lens shape that is associated with the re-solidified clad layer. It is clearly seen that the higher the hold temperature was, the greater the amount of re-solidified clad that shows a dissolution effect. Further, at a given hold temperature, and as would be expected, the quantity of re-solidified clad appears larger for rapid heating rate than for slow heating rate, because there is less time for the silicon to diffuse to the core.





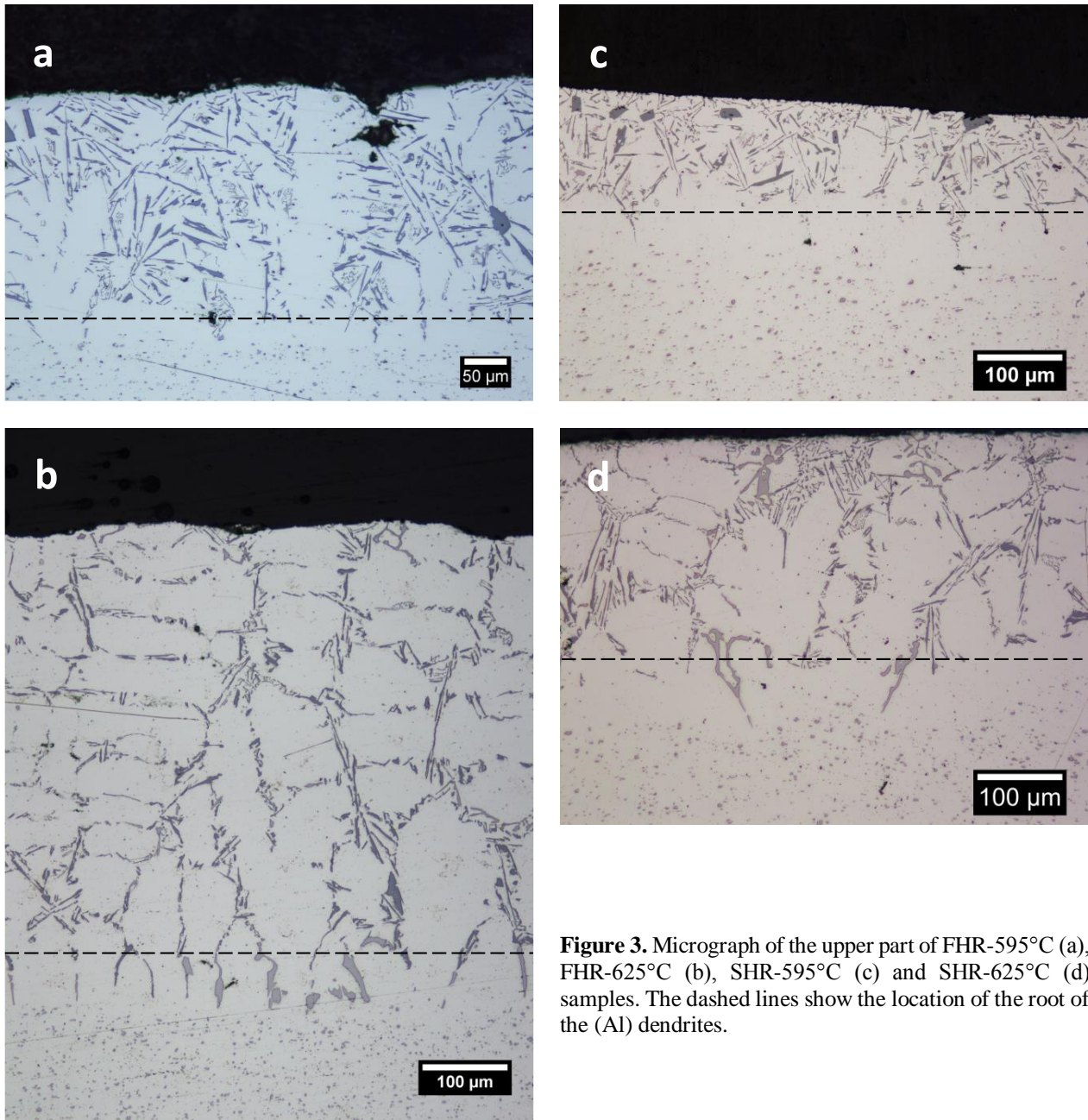
**Figure 2.** Mosaic images of the upper part of FHR-595°C (a), FHR-625°C (b), SHR-595°C (c) and SHR-625°C (d) samples.

Fig. 3 compares the microstructure of the re-solidified clad layers at an enlargement allowing for better differentiating the various phases. As a general observation, it was seen that the amount of minor phases – i.e. eutectic phases – is higher at the top of the re-solidified layer than at the bottom, with the exception of sample FHR-625°C, which shows a more even distribution. This observation suggests that re-solidification of the liquid clad proceeded from the bottom in contact with the core to the outer surface.

A second observation is that one may notice a few dark-grey blocky precipitates that are silicon precipitates in the two samples held at 595°C (Figs. 3-a and 3-c). The size and shape of these precipitates contrast with the thin lamellae corresponding to eutectic silicon precipitating during re-solidification. In agreement with similar previous observations [5], it is postulated that these are precipitates which did not have enough time to fully dissolve within the 5-minute hold at 595°C. A close examination of the whole section of all samples showed the number of these precipitates decreases with holding temperature and increases with heating rate.

As this hold temperature of 595°C is only slightly higher than the liquidus of the clad alloy [4], no or very little dissolution could have taken place during the process. Accordingly, the so-called depleted zone [2] due to solid-state diffusion of silicon from the clad to the core during heating should be present between the core and the clad. Indeed, comparing Figs. 3-a and 3-c shows that an area without small-sized precipitates is effectively observed which is much larger in the SHR sample than in the FHR one. The difference in thickness of these two areas must be due to the much more extensive silicon diffusion in the SHR sample than in the FHR and thus certainly represents the depleted zone. Using the time for the SHR sample to heat from 500°C to the start of melting at 577°C, namely  $t=7700$  s, and an average value for the silicon diffusion coefficient of  $D=5 \cdot 10^{-13} \text{ m}^2 \cdot \text{s}^{-1}$  [6], the value of  $(D \cdot t)^{0.5}$  is 60 µm which compares well with the 40-50 µm observed for the thickness of the depleted zone in the SHR sample. Further, this was confirmed by micro-analyses showing a local maximum in silicon content that is much alike that seen in the work by Benoit et al. [7] and that relates to the position of the core/liquid clad interface at brazing temperature.

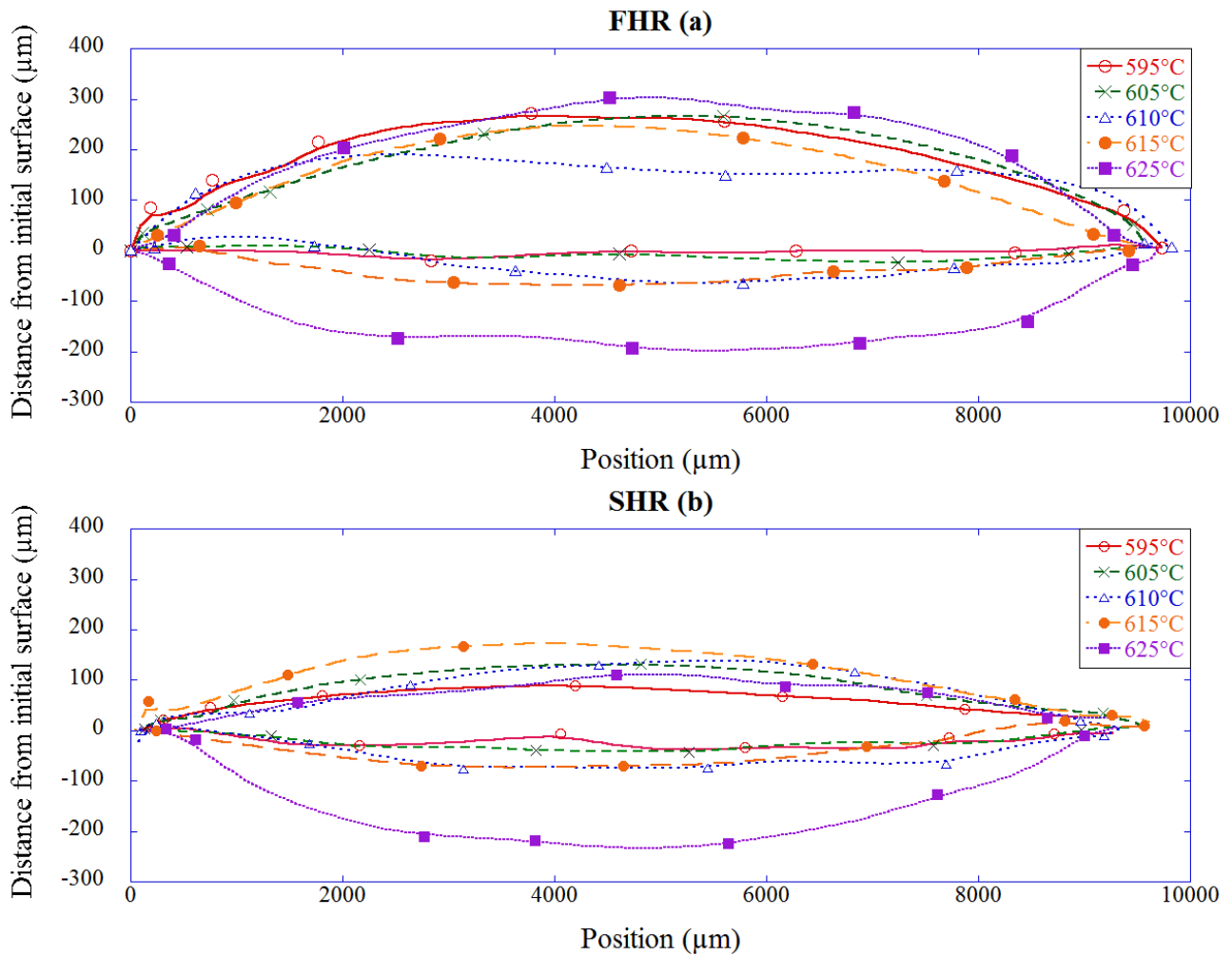
Finally, it may be seen in Figs. 3-a and 3-c that the root of interdendritic regions may go down deep inside the depleted zone, and in some cases even reach the core alloy. This suggests that these are traces of liquid penetration at grain boundaries which re-solidified at the same time that the liquid clad re-solidified. This assumption is corroborated by the fact that the intermetallic precipitates in these areas mainly consist of  $\alpha\text{-Al(Fe,Mn)Si}$ . If this part of the samples had been fully liquid - *and not only in the grooves* – then the silicon content should have been higher and silicon lamellae should be observed together with  $\alpha\text{-Al(Fe,Mn)Si}$  precipitates. An interesting feature of liquid penetration is the characteristic distance between the grooves, which is seen to be much smaller for FHR samples than for SHR samples.



**Figure 3.** Micrograph of the upper part of FHR-595°C (a), FHR-625°C (b), SHR-595°C (c) and SHR-625°C (d) samples. The dashed lines show the location of the root of the (Al) dendrites.

From the above description, the lower limit of the liquid pool – *i.e. not considering the penetrations* - could be located: this has been illustrated in Fig. 3 with the dashed lines. Then, the shape of the liquid lens was drawn for each sample by considering the lower limit as described and the upper surface of the sample as the upper limit. Fig. 4 shows the five drawings superimposed for FHR (a) and SHR (b) samples. In both cases, it is seen that the dissolution of the core material is quite limited except for the highest temperature of 625°C.





**Figure 4.** Overall shape of the re-solidified clad for the FHR (a) and SHR (b) samples.

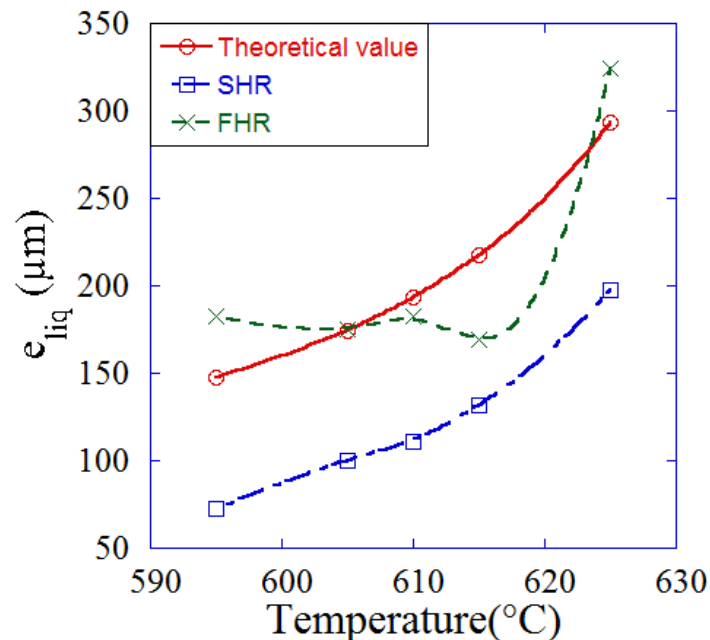
Using Fig. 4, the volume of liquid at the hold temperature has been evaluated, from which an equivalent even thickness of liquid,  $e_{liq}$ , was estimated. The results are plotted in Fig. 5. A strong contrast is seen between the two series of experimental results, with SHR data showing a smooth increase in liquid amount with the hold temperature, whilst that for FHR samples appear nearly constant for all temperatures except 625°C. In fact, the time spent with the clad fully liquid changes from 5 to 5.5 min in the FHR series, while it varies from 5 to 55 min in the SHR series. It may thus be inferred that dissolution and liquid homogenization take place in a time comparable with the full duration of the FHR experiments, leading to the observed results.

The results in Fig. 5 are compared with the theoretical values calculated assuming the composition of the liquid at the hold temperature is homogeneous and equal to that of the corresponding liquidus. For achieving the corresponding equilibrium, the liquid clad must dissolve some core material in an amount that increases with the hold temperature. The calculations were performed using data from the TCAL2 database [8] assuming the clad is a ternary Al-Mg-Si alloy with 1.5 wt.% Mg. The experimental value for the FHR-625°C sample agrees well with the theoretical predictions, while the clearly smaller amount of liquid for the SHR samples emphasizes the effect of solid-state diffusion of silicon from the clad to the core during the heating stage.

### Conclusion

The metallographic observations reported in this work suggested that some liquid penetration occurred along grain boundaries in contact with the melted clad. This was accounted for when evaluating the boundary of the liquid lens formed at the brazing temperature. As expected, it was observed that the amount of liquid available for brazing depends on the maximal temperature and on the heating rate. A slow heating rate allows silicon to diffuse from the braze metal to the core of the

brazing sheet, and thus lowers the quantity of liquid remaining at the brazing temperature. Also, a high brazing temperature leads to marked dissolution of the solid core by the liquid braze. Finally, the variability of the results in the FHR samples suggests dissolution and homogenization take place within a couple of minutes once the clad is fully liquid.



**Figure 5.** Amount of liquid versus hold temperature for the FHR and SHR samples.

## References

- [1] J.R. Terrill, C.N. Cochran, J.J. Stokes, W.E. Haupin, Understanding the mechanisms of aluminum brazing can improve results in production operations, *Welding J.* 48 (1971) 833-839.
- [2] J.R. Terrill, Diffusion of silicon in aluminum brazing sheet, *Welding J.* 45 (1966) 202s-209s
- [3] H. Zhao, R. Woods, Controlled atmosphere brazing of aluminum, in: D. P Sekulić (Ed.), *Advances in Brazing: Science, Technology and Applications*, Woodhead Publishing Ltd., Cambridge (UK), 2013, pp. 280-322.
- [4] C. Bernardi, A. Hazotte, N. Siredey-Schwaller, T. Mazet, J. Lacaze, Microstructure evolution in an aluminum clad sheet during vacuum brazing, *Mater. Sci. Forum* 790–791 (2014) 355-360.
- [5] F. Gao, D.P. Sekulic, Y.Y. Qian, J.G. Morris, Formation of microlayers of clad residue on aluminium brazing sheet during melting and resolidification in brazing process, *Mater. Sci. Tech.* 20 (2004) 577-584.
- [6] Yong Du, Y.A. Chang, Diffusion coefficients of some solutes in fcc and liquid Al: critical evaluation and correlation, *Mater. Sci. Eng. A* 363 (2003) 140-151.
- [7] M.J. Benoit, M.A. Whitney, M.A. Wells, S. Winkler, Reduction of liquid clad formation due to solid state diffusion in clad brazing sheet, *Metall. Mater. Trans. B* 47B (2016) 3501-3510.
- [8] information on [http://www.thermocalc.com/media/5982/tcal20\\_extended\\_info.pdf](http://www.thermocalc.com/media/5982/tcal20_extended_info.pdf)

# On the Primary Solidification of Fe-C Alloys: Morphological Evolution of Primary Austenite During Coarsening

Juan Carlos HERNANDO<sup>1,a</sup>, Isabel María MEDINA AGUDO<sup>1,b</sup> and Attila DIÓSZEGI<sup>1,c</sup>

<sup>1</sup>Jönköping University, School of Engineering, Department of Materials and Manufacturing, P.O. Box 1026, Gjuterigatan 5, SE-551 11, Jönköping, Sweden

<sup>a</sup>Juan-Carlos.Hernando@ju.se, <sup>b</sup>isabel.mdn.ag@gmail.com, <sup>c</sup>Attila.Dioszegi@ju.se

**Keywords:** Primary Austenite, Microstructure Evolution, Dendritic Coarsening, Ostwald Ripening, Graphitic Cast Iron, Fe-C Alloys

**Abstract.** This work studies the morphological evolution of the primary austenite developed in hypoeutectic alloys of the main three industrial cast Fe-C alloys. The solidification of three hypoeutectic alloys treated with different Mg contents to form respectively, lamellar, compacted and spheroidal graphite morphologies, is studied through a re-melting experimental technique. The evolution of the primary microstructures at the mushy zone is observed under isothermal conditions and studied at room temperature by means of interrupted solidification experiments. The application of shape independent quantitative parameters to the quenched micrographs confirms the reduction of the total interfacial area of the primary austenite as result of a coarsening process during the isothermal treatment. The three families of alloys show a similar behavior in the evolution of the primary austenite coarsening process, with a similar coarsening rate when expressed as a function of the isothermal time.

## Introduction

Dendritic growth is the most common growth mechanism for primary microstructures in hypoeutectic cast alloys [1]. The final morphology of these primary dendritic microstructures is responsible in a great manner of the final properties of the material [2] and a correct interdendritic feeding during solidification [3].

Consisting of primary trunks and secondary arms [4], the evolution of these dendritic microstructures is governed by a coarsening process which minimizes the interfacial free energy of the system [5] by reducing the solid-liquid interfacial area per volume [6]. As result of this diffusional process, the length scale of the system increases while the total interfacial area decreases [7].

The complexity of these dendritic microstructures endorsed the use of the secondary dendrite arm spacing (SDAS) [8] as a traditional parameter to characterize the coarsening process. SDAS follows a linear relation with the cube root of the time over which solid and liquid coexist,  $t^{1/3}$  for both normal and isothermal coarsening processes [1, 9]. However, the morphological changes induced under long coarsening times involve dendrite multiplication and coalescence [10] which made necessary the use of shape-independent size parameter to characterize the full microstructural evolution [4]. Three-dimensional investigations allowed the measurement of the surface area per unit volume of the entire system [2, 7] and the simulation of its evolution for a wide range of binary alloys [11]. However, the application of this three-dimensional techniques is scarce in complex industrial alloys such as the Fe-C alloys.

In the case of cast Fe-C alloys, the dendritic microstructure formed during the primary solidification in hypoeutectic melts is known as primary austenite. Whereas the primary austenite, is the most important solidification phase contributing to the mechanical strength of the material in the Fe-C alloys, it has been traditionally neglected when compared to the eutectic graphite microstructures when correlations between microstructure-mechanical have been proposed [12]. The difficulties in revealing the primary austenite on the microstructure at room temperature, as the austenite undergoes a solid-state transformation during cooling, promoted a great advance on the knowledge front of the eutectic solidification, being studies on the role of the primary austenite rare in the literature. Therefore, the study of the coarsening process of the primary austenite has received

little attention in the previous decades [13, 14]. In recent investigations, the mechanical properties in hypoeutectic melts have been found to be directly related to the final morphology of the primary dendrites in lamellar graphite cast iron (LGI) [15]. Additionally, the presence of coarsened dendrites has been reported inside shrinkage porosities for compacted graphite iron, suggesting a connection between both phenomena [16]. Consequently, it is of major importance to understand the evolution of this primary microstructures during solidification to control the mechanical properties and foresee the possible existence of solidification defects in the material.

The scope of this work is to study the morphological evolution of primary austenite under isothermal conditions for the three main families of Fe-C cast graphitic alloys with industrial applications. By re-melting experiments, the composition of the melt will be controlled to produce lamellar (LGI), compacted (CGI) and spheroidal graphitic cast iron (SGI). In combination, the application of an isothermal treatment at the mushy zone to promote a coarsening process combined with interrupted solidification experiments will allow the study of the evolution of primary austenite.

## Experimental Procedure

Two alloys have been used for this study. First, an industrial hypoeutectic LGI, with a chemical composition used to produce automotive components was cast under industrial foundry conditions. This material is the base for the LGI investigation. Second, a base hypoeutectic SGI alloy was cast within laboratory conditions with the purpose of being the base material for the SGI and CGI investigations. The chemical composition of both alloys is shown in Table 1. Cylindrical specimens of 38 mm diameter with an approximate height of 42 mm were produced from both base alloys.

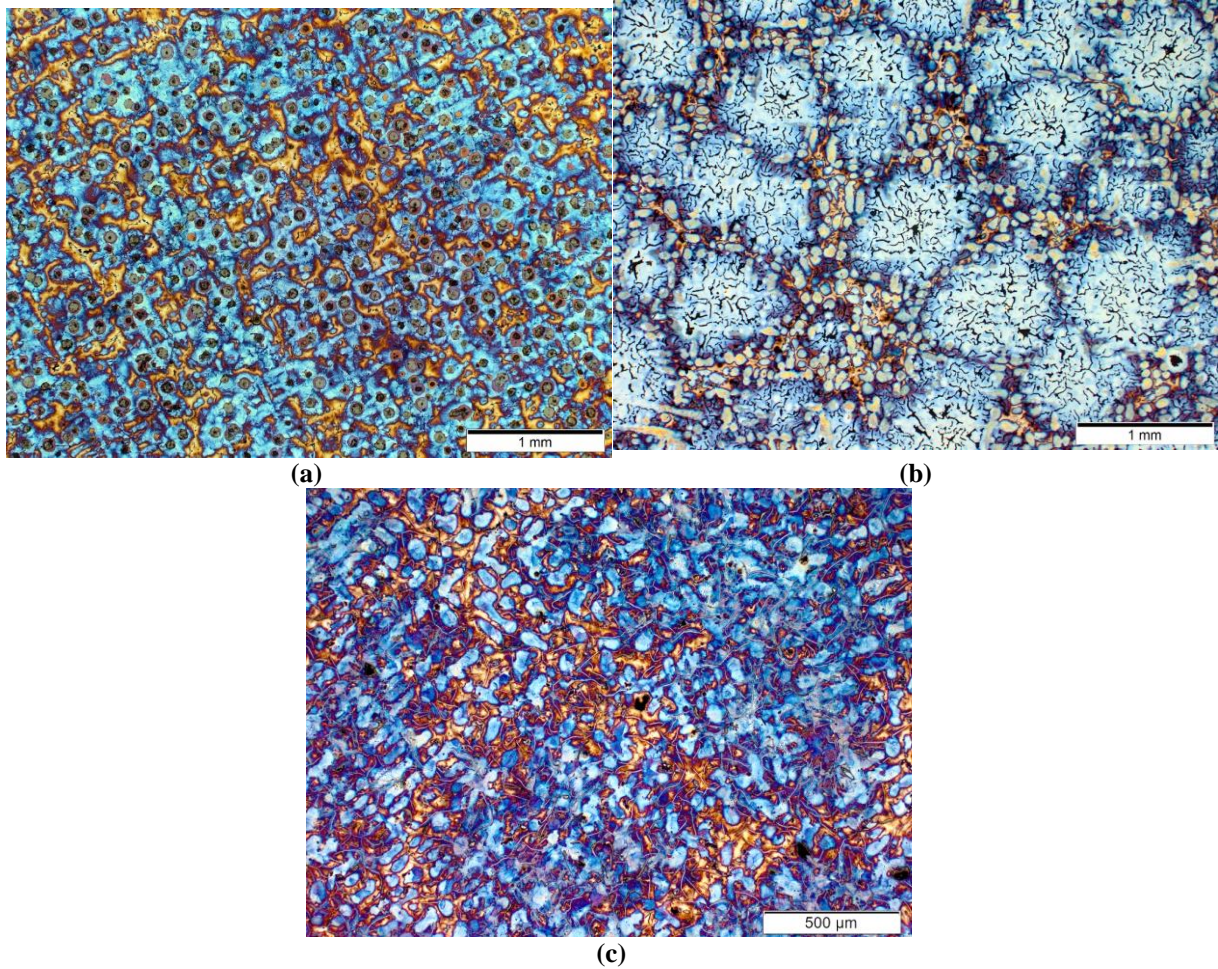
**Table 1.** Chemical composition of the base alloys.  $CE^* = C + 1/3 (Si + P)$ .

Element [wt. pct.]	C	Si	Mn	P	S	Mg	CE*
<b>Base LGI</b>	3.3	1.8	0.60	0.034	0.086	-	3.9
<b>Base SGI</b>	3.4	2.5	0.68	0.030	0.010	0.063	4.2

The cylindrical samples of the base alloys were subjected to a re-melting process inside a vertical tube electrical resistance furnace with an inner Ar neutral atmosphere. For the base LGI experiments, the re-melting process consisted on a heating cycle of 90 min from room temperature to 1723 K (1450 °C) and holding time of 30 min. For the base SGI, two different holding times were used depending on the intended final graphite morphology. The mechanism of Mg fading that influences the presence of O in the melt and thus the morphology of the final graphite particles needs to be tailored during the re-melting process [17]. This process is critical to achieving final alloys of the required compositions. For the obtention of spheroidal graphite, a holding time of 10 min was applied, while for the case of compacted graphite it was required 80 min of holding time. The base samples were then cooled down inside the furnace leading to a solidification process. Preliminary experiments were performed to acquire the thermal data required for the definition of an isothermal profile which later will enable the study of the coarsening mechanism for each alloy. These preliminary experiments the consisting in a re-melting process followed by a natural cooling process inside the furnace produced fully solidified as-cast specimens, the results can be observed in Fig 1.

The interrupted solidification experiments were performed in the following sequence. The sample was re-melting and held at 1723 K (1450 °C) for the time described above for each alloy. Then a solidification process began inside the furnace. This process was then halted after the thermal coherency when a coherent dendritic primary austenite structure has been formed. At this moment, an isothermal treatment was applied, promoting the isothermal coarsening process of the existing primary microstructure. Once the end of the isothermal treatment was reached, the sample was quenched into agitated water, interrupting the solidification and preserving the dendritic microstructures at room temperature. For each Fe-C system, isothermal times of 10, 30, 60 and 90 min were studied. An additional sample for 0 min of isothermal treatment was quenched from the thermal coherency temperature, right before the isothermal treatment starts. This allowed the observation of the original coherent dendritic microstructure.





**Figure 1.** Representative micrographs of fully solidified samples of (a) spheroidal, (b) compacted, and (c) lamellar hypoeutectic graphitic cast irons after the re-melting process, i.e. full solidification after the re-melting process.

The samples produced after the quenching were sectioned perpendicularly to the longitudinal axis at their middle section. The preparation of the surface was carried out by mechanical grinding and polishing. An additional etching process based on subsequent polishing steps [18], was applied to reveal the primary microstructures. The etched micrographs were then transformed into binary images where dendrites were represented as black color phase, as shown in Fig. 2. The fully solidified samples from the preliminary experiments followed the same preparation including an additional color-etching process with a picric acid solution, as shown in Fig. 1.

Several microstructural parameters were measured on the binary images to perform the two-dimensional quantitative analysis of the coarsening process. The fraction,  $f'_V$ , Eq.1, the perimeter,  $P_V$ , and area,  $A'_V$ , of the primary austenite are measured to later calculate the relevant morphological parameters associated with the microstructural evolution. Based on stereological relations, the modulus of primary austenite,  $M'_V$  [ $\mu\text{m}$ ], Eq.2, the hydraulic diameter of the interdendritic phase,  $D_{IP}^{\text{Hyd}}$  [ $\mu\text{m}$ ], Eq.3, and the distance to the nearest neighbor,  $D_V$  [ $\mu\text{m}$ ], measured by Olympus Stream Motion Desktop software 1.9.1, were used to the characterization of coarsening phenomena. The secondary dendrite arm spacing, SDAS, was also measured on the microstructure as it is a classical parameter used to characterize the coarsening process in the literature. The morphological parameters used for the analysis of the microstructural evolution are described as follows:

$$f'_V = \frac{V'_V}{V} = \frac{A'_V}{A} \quad (1)$$

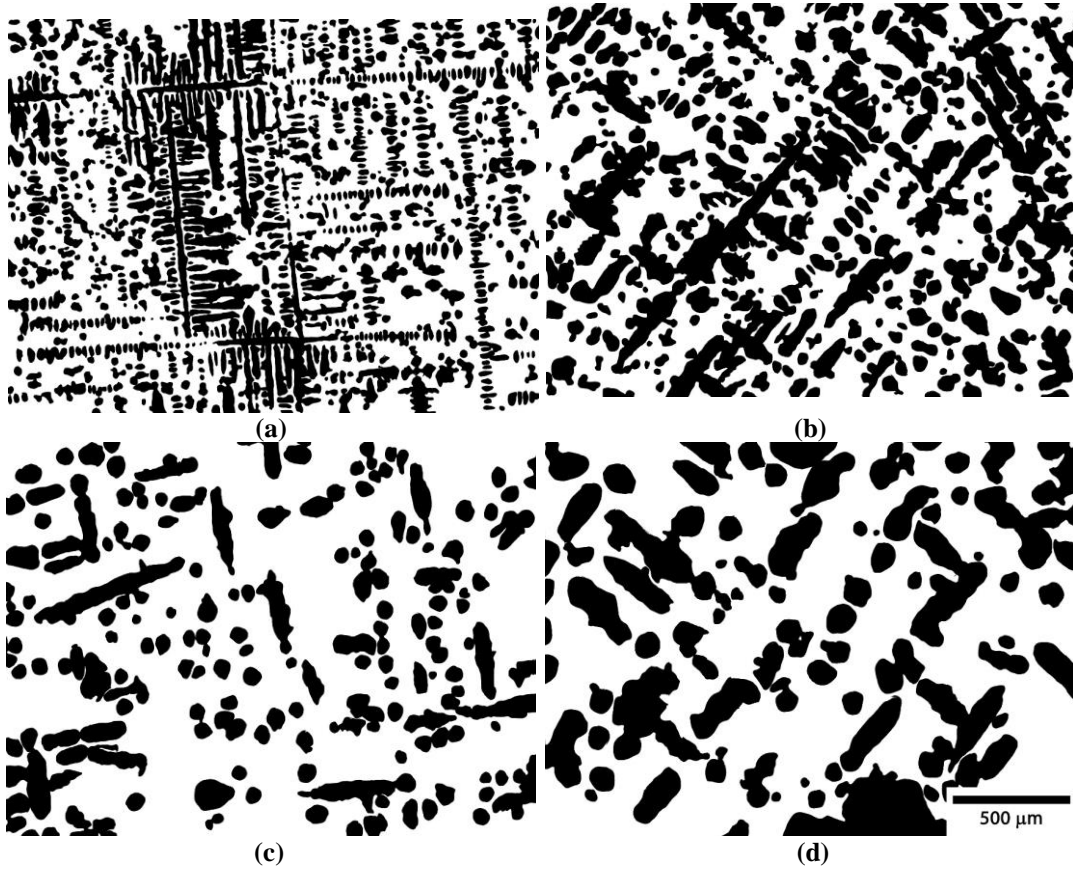
$$M'_Y = \frac{V'_Y}{S'_Y} = \frac{A'_Y}{P'_Y} \quad (2)$$

$$D_{IP}^{Hyd} = \frac{V_{IP}}{S_{IP}} = \frac{A_{IP}}{P_{IP}} = \frac{A - A'_Y}{P'_Y} \quad (3)$$

The variables V, A, S, and P stand for volume, area, interfacial surface area and perimeter, respectively. The subscripts: T,  $\gamma'$ , and IP, refer to total, primary austenite, and interdendritic phase, respectively.

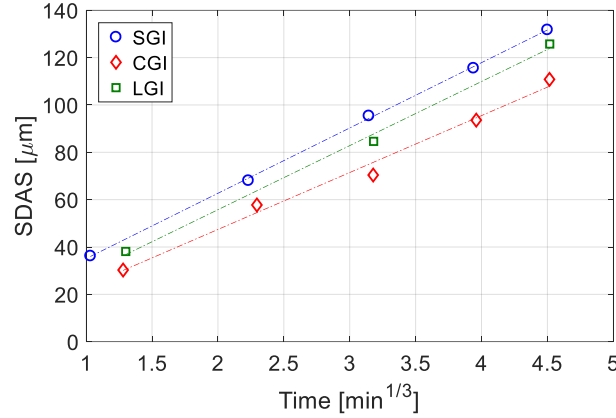
## Results and Discussion

The isothermal treatment applied to the samples promoted the coarsening of the primary austenite in the three Fe-C alloys studied. All the alloys show a similar behavior as a function of the isothermal holding time. As can be seen in Fig. 2 for the case of SGI, the original dendritic microstructure, Fig. 2 (a), starts a coarsening process, following the classical Ostwald mechanism. Ripening, Fig. 2 (b), dendrite multiplication, Fig. 2 (c) and coalescence Fig. 2 (d) are observed [10].



**Figure 2.** Binary images extracted from the quenched samples for quantitative analysis. The microstructure of the primary austenite is shown in black after (a) 0 min, (b) 10 min, (c) 30 min, and (d) 90 min of isothermal coarsening for a spheroidal graphitic Iron-Carbon melt. All images are shown at the same magnification.

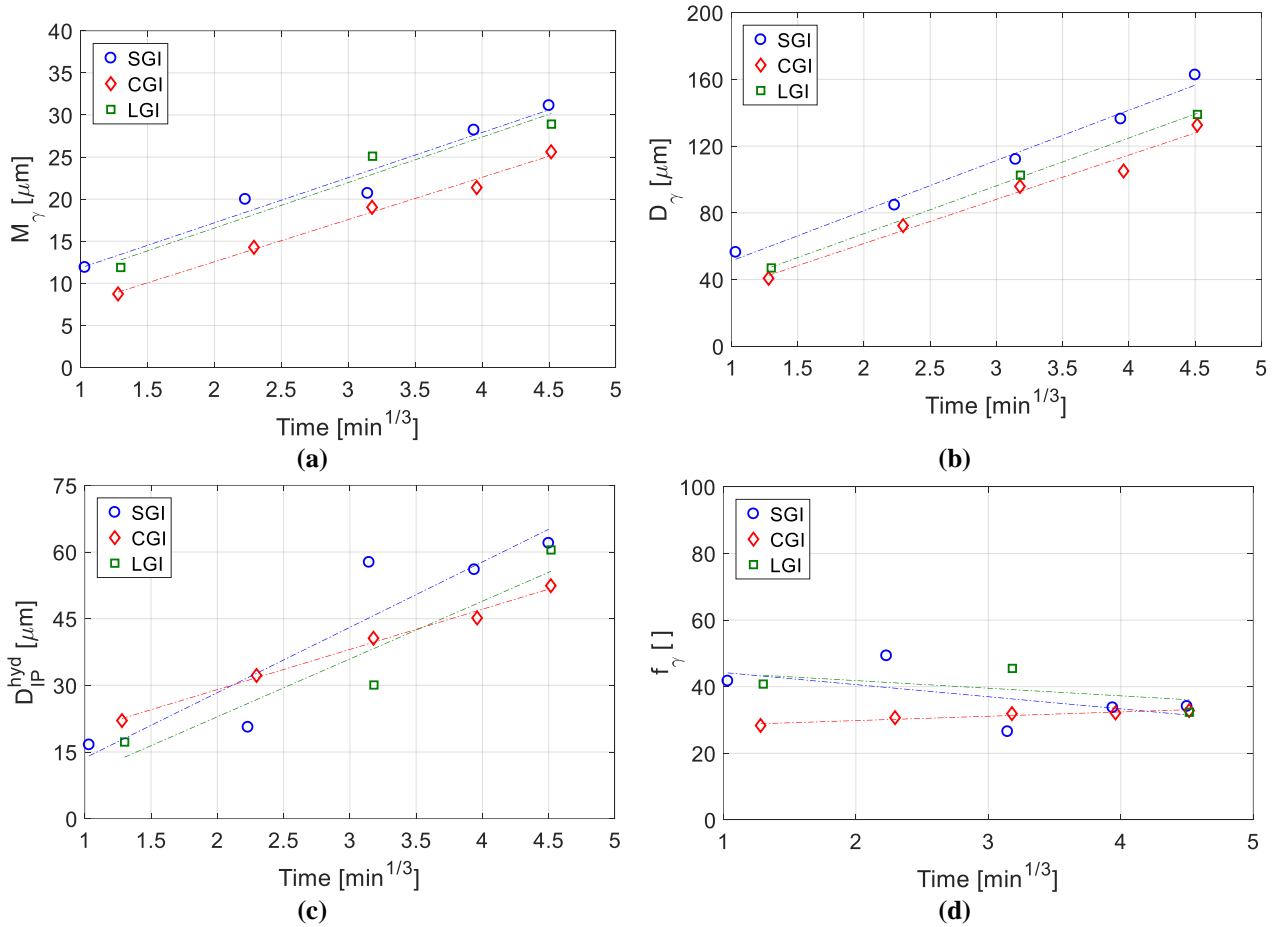
The SDAS shows a similar behavior to other technical alloys studied previously in the literature [1] with a linear relation with the cubic root coarsening time ( $t^{1/3}$ ), Fig. 3. However, the error accumulated when using SDAS, or any other local features, to characterize the coarsening, increases with longer times. This is a direct consequence of the coarsening mechanism itself. It is therefore recommended to use shape-independent parameters like those proposed in this work or in other works in literature in two-dimensional [4] or three-dimensional studies [11].



**Figure 3.** SDAS as a function of the coarsening time for SGI, CGI, and LGI.

The modulus of the primary austenite phase,  $M_\gamma$ , illustrates the reduction of surface area to volume ratio of the austenite crystals occurring during the coarsening process, Fig. 4(a). The spatial arrangement that takes places simultaneously is shown by  $D_\gamma$ , Fig. 4(b). the distance between austenite crystals, which also increases as a function of the coarsening time for SGI, CGI, and LGI.

The hydraulic diameter of the interdendritic phase,  $D_{IP}^{hyd}$ , Fig. 4(c), which illustrates the space between dendrites, follows a relation with the isothermal holding time. However, it shows a larger dispersion than the  $M_\gamma$  and the  $D_\gamma$ , due to its dependency with the austenite fraction area, which shows small variations due to the experimental restrictions of a two-dimensional investigation, Fig. 4(d).



**Figure 4.** (a) The modulus of the primary austenite phase,  $M_\gamma$ , (b) distance between austenite particles,  $D_\gamma$ , (c) hydraulic diameter of the interdendritic phase,  $D_{IP}^{hyd}$ , and (d) measured area fraction of primary austenite,  $f_\gamma$ , as a function of the coarsening time for SGI, CGI, and LGI.



## Summary

The coarsening process of the primary austenite in the three main cast Fe-C alloys with industrial applications has been analyzed under isothermal conditions. The main quantitative stereological parameters applied to the study of the coarsening process of primary austenite, SDAS,  $M_V$ ,  $D_{IP}^{hyd}$ , and  $D_V$  show a very similar behavior to that observed in other technical alloys, representing a linear relation to  $t^{1/3}$ . Despite the three different alloys studied and the varying ranges of fraction of austenite measured, the data show small scatter and similar rates when expressed as a function of  $t^{1/3}$ . These observations suggest that the coarsening process of primary austenite, occurring in the solid-liquid region during the primary solidification for the three main families is not influenced by the presence of impurities, such as O, which on the contrary, do play an important role during the eutectic solidification modifying the growth of the graphite and determining its final morphology [3].

## References

1. Kurz, W. and D. Fisher, *Fundamentals of solidification*, 1986. Trans Tech Publications, Switzerland, 1989.
2. Kammer, D. and P.W. Voorhees, *The morphological evolution of dendritic microstructures during coarsening*. Acta Materialia, 2006. **54**(6): p. 1549-1558.
3. Stefanescu, D.M., *Science and Engineering of Casting Solidification*. 2015: Springer International Publishing.
4. Marsh, S.P. and M.E. Glicksman, *Overview of Geometric Effects on Coarsening of Mushy Zones*. Metallurgical and Materials Transactions A, 1996. **27**(3): p. 557-567.
5. Voorhees, P.W., *The Theory of Ostwald Ripening*. Journal of Statistical Physics, 1985. **38**(1-2): p. 231-252.
6. Terzi, S., L. Salvo, M. Suery, A.K. Dahle, and E. Boller, *Coarsening mechanisms in a dendritic Al-10% Cu alloy*. Acta Materialia, 2010. **58**(1): p. 20-30.
7. Fife, J.L. and P.W. Voorhees, *The morphological evolution of equiaxed dendritic microstructures during coarsening*. Acta Materialia, 2009. **57**(8): p. 2418-2428.
8. Flemings, M.C., T.Z. Kattamis, and B.P. Bardes, *Dendrite Arm Spacing in Aluminium Alloys*, in *AFS Transactions*, AFS, Editor. 1991. p. 501-506.
9. V. Rontó and A. Roósz, *Investigation of Secondary Dendrite Arm Coarsening of Al-Cu-Si Alloy*. Materials Science Forum, 2000. **329-330**: p. 79-86.
10. Flemings, M.C., *Coarsening in Solidification Processing*. Materials Transactions, 2005. **46**(5): p. 895-900.
11. Neumann-Heyme, H., K. Eckert, and C. Beckermann, *General evolution equation for the specific interface area of dendrites during alloy solidification*. Acta Materialia, 2017. **140**: p. 87-96.
12. Stefanescu, D.M., *ASM Handbook, Volume 1A: Cast Iron Science and Technology*, ed. D.M. Stefanescu. 2017.
13. Lora, R. and A. Diószegi, *Dynamic Coarsening of 3.3C-1.9Si Gray Cast Iron*. Metallurgical and Materials Transactions A, 2012. **43**(13): p. 5165-5172.
14. Hernando, J.C., E. Ghassemali, and A. Diószegi, *The morphological evolution of primary austenite during isothermal coarsening*. Materials Characterization, 2017. **131**: p. 492-499.
15. Fourlakidis, V. and A. Diószegi, *A generic model to predict the ultimate tensile strength in pearlitic lamellar graphite iron*. Materials Science and Engineering A, 2014. **618**: p. 161-167.
16. Vazehrad, S., *A Study On Factor Influencing the Microstructure and Shrinkage Porosity Formation in Compacted Graphite Iron*. 2014, KTH Royal Institute of Technology: Stockholm.
17. Hernando, J.C., B. Domeij, D. González, J.M. Amieva, and A. Diószegi, *New Experimental Technique for Nodularity and Mg Fading Control in Compacted Graphite Iron Production on Laboratory Scale*. Metallurgical and Materials Transactions A, 2017. **48**(11): p. 5432-5441.
18. Domeij, B., J.C. Hernando, and A. Diószegi, *Quantification of Dendritic Austenite After Interrupted Solidification in a Hypoeutectic Lamellar Graphite Iron*. Metallography, Microstructure, and Analysis, 2016. **5**(1): p. 28-42.

# Directional Solidification of the Al-0.25 wt%Zr Overhead Line Conductor

Elif YILMAZ<sup>1</sup>, Emine Acer EROL<sup>2</sup>, Harun Erol<sup>3</sup> and Mehmet Gündüz<sup>4</sup>

<sup>1</sup>Department of Automotive, Vocational College, Kayseri University; 38039 Kayseri, Turkey

<sup>2</sup>Department of Physics, Institute of Sciences, Erciyes University; 38039 Kayseri, Turkey

<sup>3</sup>Department of Physics, Faculty of Sciences, Çankırı Karatekin University; 18200, Çankırı, Turkey

<sup>4</sup>Department of Physics, Faculty of Sciences, Erciyes University; 38039 Kayseri, Turkey

ecengiz@erciyes.edu.tr

**Keywords:** Al-Zr alloy, growth rate, microstructure

**Abstract.** Addition of small amount of Zr element to aluminum or aluminum alloys enhance their mechanical properties, thermal stability and electrical conductivity. These features are also affected by chemical component, homogeneity, processing technology and microstructures of the alloys. The alloys with smaller sized microstructures are more favorable and structures of the solidified materials change with the variation of the solidification processing parameters (namely; composition; Co, temperature gradient; G, growth rate; V). Knowing the relationship between microstructures and solidification processing parameters helps the understanding of the properties of the materials. The aim of this study is to experimentally investigate the variation of microstructural parameters with growth rates in the Al-0.25wt%Zr alloy. In this study the alloy was solidified with five different growth rates (8.3- 166  $\mu\text{m/s}$ ) under constant temperature gradient (8.50 K/mm). After metallographic examinations microstructural parameters were measured and the dependence of the microstructure parameters and growth rates were obtained with linear regression analysis. It was observed that the microstructure parameters decrease while the growth rates increase.

## Introduction

Due to their high strength-to weight ratio, aluminium and its alloy are used in a wide range of industrial applications such as transportation, particularly with aircraft and space vehicles, construction and building, containers, packaging and electrical transmission lines [1]. Aluminium and its alloys are used in all bare overhead energy transmission lines. Al-Zr heat resistant overhead energy transmission lines have higher operating temperatures and longer service life than the other overhead line conductors [2]. Zirconium additions (0.1-0.3wt%) to Al have been reduced the as-cast grain size and increased the operating temperatures of Al-Zr alloys up to 210 °C without a loss in the tensile strength [3].

It is well known that the mechanical properties of metallic materials are affected by their microstructures. The mechanical properties of directionally solidified Al-based alloys, which are important commercial materials, have been reported in several researchers [4-6]. The solidification processing parameters, (growth rate, V, temperature gradient, G, initial composition of the alloy,  $C_0$ ), of the alloys directly affect the microstructures of the alloy system, significantly influencing the mechanical behavior. Hence the effect of the solidification processing parameters and microstructure parameters, (cellular spacing,  $\lambda$ , grain size, d), on mechanical properties have been studied intensively [7-10]. So it is important to obtain more insight in to the relationship between the solidification processing parameters and the microstructure parameters.

In the steady-state directional solidification experiments, V, G,  $C_0$  can be independently controlled, so that one may investigate the dependence of microstructural parameters,  $\lambda$ , on either V at constant G or G at constant V for the constant  $C_0$ . The most experimental studies have been shown that the microstructural parameters decrease as the processing parameters increase for the constant  $C_0$ . Literature surveys show several theoretical models [11-13] use to examine the effect of solidification processing parameters on the microstructural parameters. Hunt [11], Kurz-Fisher [12], Trivedi [13]

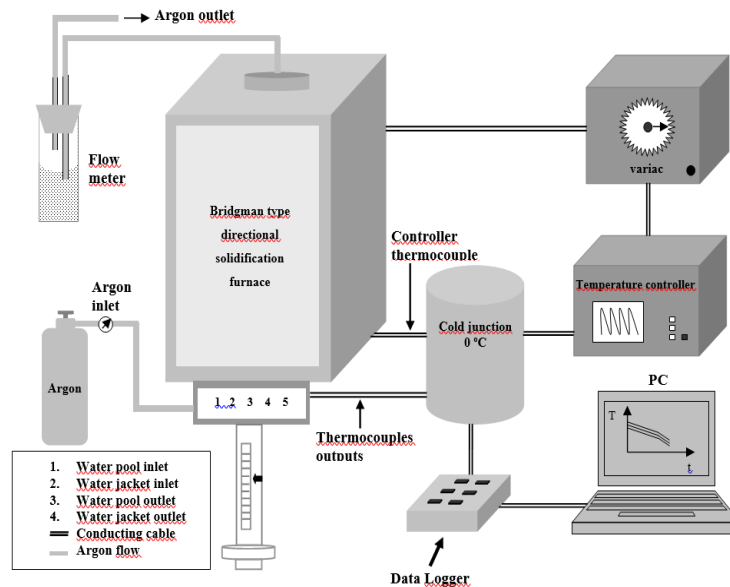
have been proposed detailed theoretical models to characterize cells and dendrite arm spacing during steady-state conditions as a function of  $G$ ,  $V$ ,  $C_0$ .

The aim of the work is to obtain more insight in to the microstructure and phase selection of the single phase and to investigate the relationship between the growth rate,  $V$ , and cellular spacing in the Al-0.25wt% Zr alloy.

## Experimental

### Controlled Solidification.

The Al-0.25wt%Zr alloy was prepared by using high purity Al ( $\geq 99.99$  wt. %) and Zr ( $\geq 99.99$  wt. %) by melting in a graphite pot inserted in a vacuum melting furnace. After allowing time for melt to become homogeneous, the molten master alloy was stirred and quickly poured into the graphite crucibles (inner diameter of 9.5 mm and 200 mm in length) and then pulled to the cold region of the furnace. The specimens were directionally frozen from bottom to the top under vacuum to avoid the occurrence of air pores. Afterwards every graphite specimen was positioned in a Bridgman type furnace. After stabilizing the thermal conditions in the furnace under an argon atmosphere the sample was withdrawn downward about 90- 100 mm with a known pulling rate by means of a synchronous motor and then the sample rapidly quenched. The block diagram of the experimental set up is shown in Fig. 1. Samples were solidified under steady state conditions with different growth rates,  $V$  (8.3-166  $\mu\text{m/s}$ ) at a constant temperature,  $G$  (8.50 K/mm) in order to see the effect of  $V$  on cell spacing,  $\lambda$ .



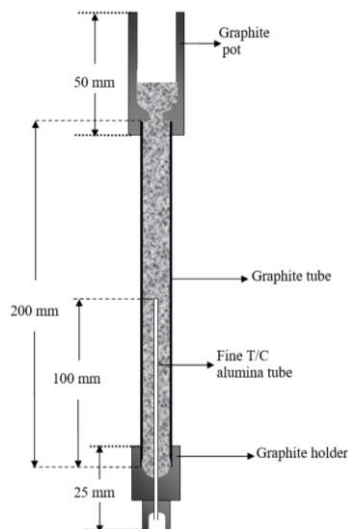
**Figure 1.** Block diagram of the directional solidification experimental setup.

**Measurement of solidification processing parameters ( $G$  and  $V$ ).** The temperature of the Bridgman type furnace was controlled by a 0.5 mm insulated K-type thermocouple placed between the heating element and alumina tube. The temperature could be controlled to about  $\pm 0.1$  K during the run. Four insulated K-type 0.5 mm diameter thermocouples with known distances were placed into a four bored alumina tube which was parallel to the heat flow direction inside the crucible. (Fig 2). All of the thermocouple leads were connected to a data logger interfaced with a computer and the temperature data recorded simultaneously. When the third thermocouple was at the solid- liquid interface and then the first and the second thermocouples in the liquid, their temperatures were used to obtain temperature gradient  $G$ .  $G$  could be kept constant during the run by keeping the temperature of the cooler part and the hotter part of the furnace constant, and the distance stable between them.

The positions of the thermocouples were measured by electronic caliper having accuracy of  $\pm 0.02$  mm after the quench. Careful experimental measurements showed that the pulling rates of the samples were equal to the magnitude of the growth rates. The solidification time and solidified distance were measured for the run and the ratio of them gives the growth rate  $V$ .

### Metallographic examination.

The unidirectionally grown quenched specimen was removed from the graphite crucible, then ground to observe the solid-liquid interface. The longitudinal sections of the samples (10 mm) which included the quenched interface were separated from the specimen and set in the cold mounting resin. The longitudinal and transverse sections of this part were ground, polished using diamond paste to a  $1\text{ }\mu\text{m}$  finish and etched within the Keller' solution to reveal the microstructure. The microstructures of the specimens were investigated by using optical microscopy.



**Figure 2.** The specimen solidified in directional solidification furnace.

**Measurement of cell spacing.** The cell spacing,  $\lambda$  was measured on the longitudinal sections of each sample by using linear intercept method. At the linear intercept method,  $\lambda$  is obtained by measuring the distance between adjacent cell tips. Totally 20-50  $\lambda$  were measured by using the mean linear intercept method on the longitudinal sections depending on the growth conditions.

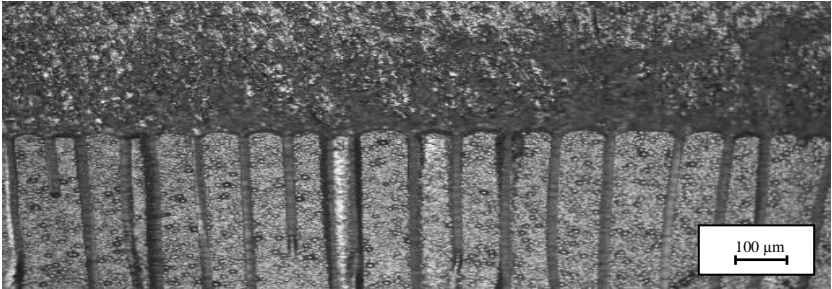
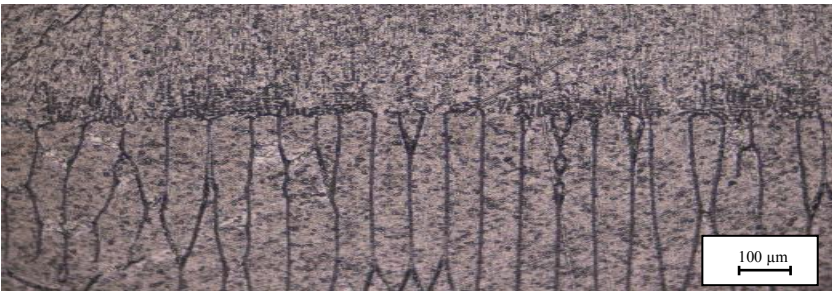
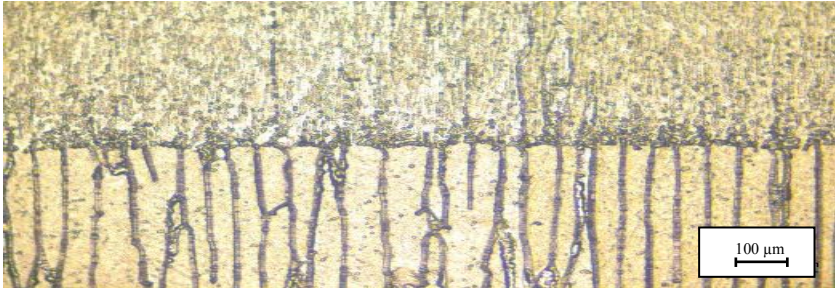

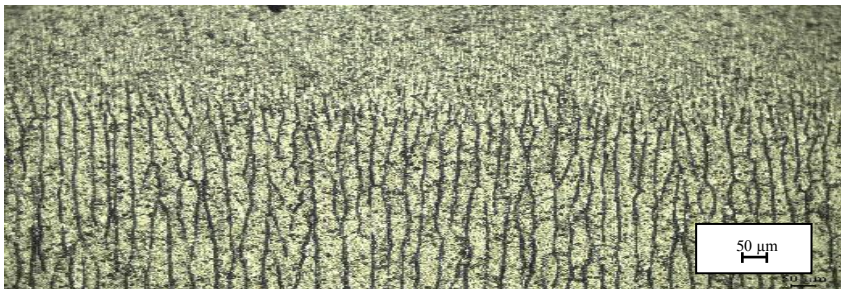
## Results and Discussion

It is well known that there is a dependency between growth rate,  $V$  and cell spacing,  $\lambda$  in directionally solidified alloys. To determine this dependency in Al-0.25wt%Zr alloy a series of directional solidification experiments were carried out at 5 different growth rates,  $V$  (8.3- 166  $\mu\text{m/s}$ ) under a constant temperature gradient,  $G$ . Figure 3 shows the typical longitudinal views of microstructures. Cellular microstructures occurred at the interfaces can be seen from these photographs.

The measured  $\lambda$  values with standard deviations are given in Table 1. The variation of  $\lambda$  with  $V$  was plotted in Figure 4 and the mathematical relationship was obtained by linear regression analysis. The result is given in Table 2. The power law dependency of  $\lambda$  on  $V$  was obtained from Figure 4. These calculations have led to the establishment of the following general relationship:  $\lambda = kV^{-a}$ , where  $k$  is proportionality constant,  $a$  is the growth rate exponent values of  $\lambda$ .

Experimental observations show that the values of  $\lambda$  decrease as  $V$  increase. As can be seen from Table 2 the value of exponent  $a$  is found to be the range of 0.40 for Al-0.25wt%Zr alloy. The theoretical models predict the growth rate exponent value of  $\lambda$  as 0.25 [11-13]. Therefore our experimental result of the growth rate of  $\lambda$  is higher than the exponent values of Hunt [11], Kurz-Fisher [12] and Trivedi [13] models.

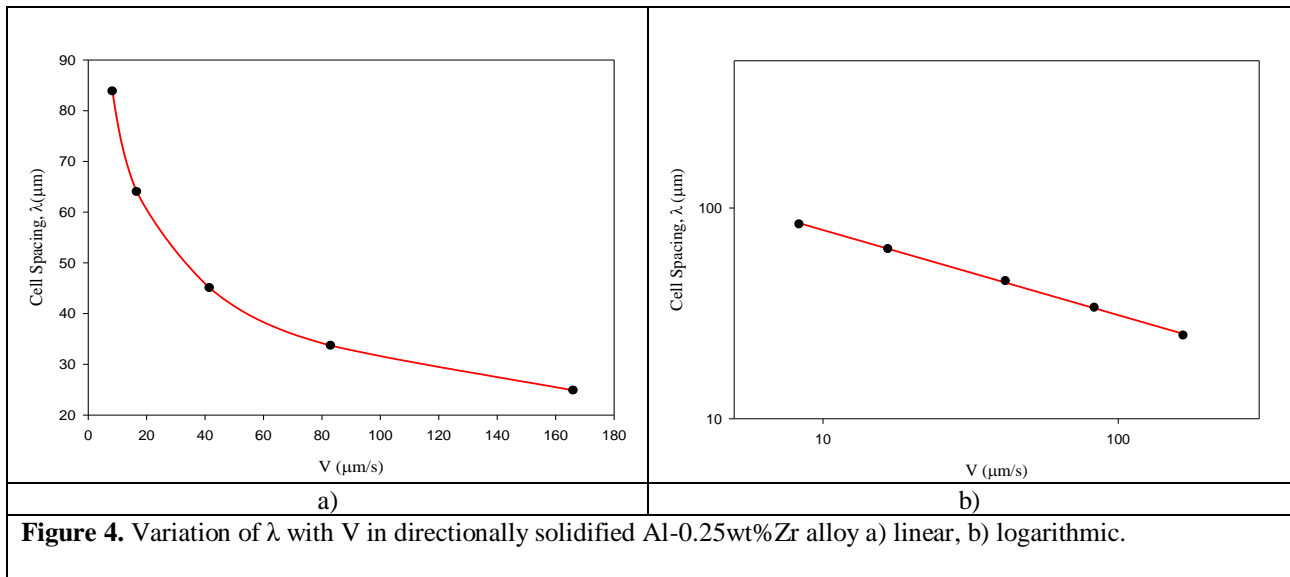


V \ G	G=8.50 K/mm
8.30 $\mu\text{m/s}$	
16.60 $\mu\text{m/s}$	
41.50 $\mu\text{m/s}$	
83.00 $\mu\text{m/s}$	
166.00 $\mu\text{m/s}$	

**Figure 3.** Microstructures of directionally solidified Al-0.25wt%Zr alloy

<b>Table1.</b> Effect of growth rates on microstructure parameter for directionally solidified Al-0.25wt%Zr alloy for a constant G (G=8.50 K/mm).	
Growth Rate, V (μm/s)	Cell Spacing, λ (μm)
8.30	83.84±9.91
16.60	64.02±7.57
41.50	45.08±5.20
83.00	33.70±3.78
166.00	24.88±2.66

<b>Table 2.</b> Dependency of λ on V at a constant G.		
$\lambda=kV^{-0.40}$	$k=199,021 \mu\text{m}^{1.52} \text{s}^{-0.52}$	$r_1=-0.999$



**Figure 4.** Variation of λ with V in directionally solidified Al-0.25wt%Zr alloy a) linear, b) logarithmic.

## Conclusions

In the present study, the Al-0.25wt% Zr alloy was solidified unidirectionally upward under different growth rates at a constant temperature gradient. The principal results can be summarized as follows:

1. Generally cellular microstructures form at low growth rates, (<10μm), the cell/dendrite transition forms at higher growth rates (<20μm) and then then the dendritic structures form at much higher growth rates. However the cellular microstructures were observed for all growth rates in the Al-0.25wt% Zr alloys.
2. It was seen that the values of λ decrease as the values of V increase.
3. The range of growth rate exponent, (a=0.40), is in good agreement with some previous experimental values [14-16] and higher than the results of the theoretical values [, (0.25), and some other experimental values [17-19]. This means that the growth rate, V, on the microstructures in Al-0.25wt%Zr alloy is more effective than some other Al-based alloys or these discrepancies might be due to the grain refining of Zr in Al.

## Acknowledgement

This project was supported by the Erciyes University (ERU) Scientific Research Project Unit under Contract No: FOA-2014-5195. The authors would like to thank ERU Scientific Research Project Unit for their financial support.

## References

- [1] R.E. Smallman, A.H.W. Ngan, Modern Physical Metallurgy, 8<sup>th</sup> Edt., Butterworth-Heinemann, New York.2014.
- [2] G. Civili, M. Handel, New types of conductors for overhead lines with high thermal resistance, Bulk Power Systems Dynamics and Control Vol.1, 2004, pp833-839.
- [3] A. Edris, High-temperature low-sag transmission conductors, Technical report, EPRI, Palo Alto, CA, 2002.
- [4] E.I. Lavernia, N. I. Grant, Aluminium-lithium alloys, J. of Mater. Sci. 22 (1987) 1521-1529.
- [5] H.A.H. Steen, A. Hellawell, Structure and properties of aluminium-silicon eutectic alloys, Acta Metall. 20 (1972) 363-370.
- [6] F. Yang, L. Peng, K. Okazaki, Microindentation of Aluminium, Metall. Mater. Trans. 35A (2004) 3323-3328.
- [7] H. Kaya, E. Çadırlı, M. Gündüz, A. Ülgen, Effect of the temperature gradient, growth rate and the interflake spacing on the microhardness in the directionally solidified Al-Sieutectic alloy, J. Mater. Eng. Perform. 12 (2003) 544-551.
- [8] N. Fatahalla, M. Hafız, M. Abdulkhalek, Effect of microstructure on the mechanical properties and fracture of commercial hypoeutectic Al-Si alloy modified with Na Sb and Sr, J. Mater. Sci. 34 (1999) 3555-3564.
- [9] X. L. Liu, M. Nagumo, M. Umemoto, The Hall-Petch relationship in nanocrystalline materials, Mater Trans., JIM 38 (1997) 1033-1039.
- [10] O. P. Modi, N. Deshmukh, D.P. Mondal, A.K. Jha, A.H. Yegneswaran, H.K. Khaira, Effect of interlamellar spacing on the mechanical properties of 0.65%C steel, Mater. Charact. 46 (2001) 347-352.
- [11] J.D. Hunt, Solidification and Casting of Metals, The Metals Society, London, 1979.
- [12] W. Kurz, D.J. Fisher, Acta Metall. 29 (1981) 11-20.
- [13] R. Trivedi, Metall. Trans. 15 (1984) 977-982.
- [14] E. Çadırlı, H. Tecer, M. Şahin, E. Yılmaz, T. Kırındı, M. Gündüz, Effect of heat treatments on the microhardness and tensile strength of Al-0.25wt% Zr alloy, J. of Alloys and Compounds 632 (2015) 229-237.
- [15] E. Çadırlı, M. Gündüz, Directional solidification of aluminium-copper alloys, Mater. Sci. and Eng. A327 (2002) 167-185.
- [16] M. Gündüz, H. Kaya, E. Çadırlı, A. Özmen, Interflake spacing and undercooling in Al-Si irregular eutectic alloy, Mater. Sci. and Eng. A369 (2004) 215-229.
- [17] S. Yang, W. Huang, X. Lin, Y. Su, Y. Zhou., Scripta Materialia 42 (2000) 543.
- [18] A.B. Kloosterman, J.T. Hosson ;J. Materials Science 32 (1997) 6201.
- [19] M. Şahin, E. Çadırlı, H. Kaya, Surface and Review Letters 17 (2010) 477.



# Undercooling studies and growth velocity measurements on multi- component FeCuNi{X} alloys

Rahul M R <sup>1a</sup>, Sumanta Samal <sup>2</sup> and Gandham Phanikumar <sup>1b</sup>

<sup>1</sup> Department of Metallurgical and Materials Engineering, Indian Institute of Technology Madras, Chennai 600036, India

<sup>2</sup> Discipline of Metallurgy Engineering and Materials Science, Indian Institute of Technology Indore, Simrol, Khandwa Road, Indore, 453552, Madhya Pradesh, India

<sup>1a</sup>rahulmr1991@gmail.com, <sup>2</sup>sumanta@iiti.ac.in, <sup>1b</sup>gphani@iitm.ac.in,

**Keywords:** Undercooling, High entropy alloys, Growth velocity

**Abstract.** High entropy alloys or complex concentrated alloys have recently gained wide attention due to their excellent high temperature properties. New alloys are also being explored for functional properties towards magnetic and thermoelectric applications. Unlike conventional alloy design, exploration of high entropy alloys involves the central region of the phase diagram. Microstructures of these alloys processed through melt route have shown multiple phases which challenge their designation as high entropy alloys. Undercooling is a possibility to obtain metastable microstructures. Solidification studies on undercooled alloys of this class are limited to only a few in the open literature. In this work, undercooling studies were carried out on FeCuNi{X} series of alloys where {X} = {Co, Sn}. Microstructure evolution was correlated to the extent of undercooling. A maximum undercooling of >200 K was achieved in these studies. During solidification, high speed video imaging was employed to measure the recalescence growth velocity as a function of undercooling. The growth velocity showed sluggish compared to Ni based alloys below 175°C undercooling temperature.

## Introduction

Multicomponent alloys with equatomic compositions have attracted many research groups for the last few years. These alloys can be called with different designations like high entropy alloys (HEAs) [1], complex concentrated alloys [2], etc. High entropy alloys with remarkable properties are reported in literature [2]. This category of alloys can be a potential candidates in different sectors such as high temperature applications [3 4], cryogenic applications [5], functional applications [6], structural applications [7] etc. For the application, the behaviour of these alloys at different processing conditions and understanding of its physical metallurgy is required. Presently different processing techniques are employed to manufacture HEAs, which include conventional castings, mechanical alloying with sintering and induction melting, etc. The study of solidification behaviour of these alloys under different conditions is limited and needed to be explored.

There are a few undercooling studies reported on HEAs such as CoCrCuFeNi [8,9] and WMoTa NbZr [10]. These studies shown the liquid phase separation phenomenon could be occurred at undercooling conditions in CoCuFe containing alloys. Liquid phase separation was reported in as cast condition of HEAs which violates the concept of HEA phase formation [11]. In case of WMoTa NbZr alloys shows stable BCC phase at all levels of undercooling [10]. HEAs behaviour at different undercooling conditions is yet to be explored. Sn added HEAs were reported to be good at corrosion properties in NaCl solution while compared to 304 stainless steel [12]. In this present study FeCoNiCuSn<sub>5</sub> HEA was taken for undercooling studies. The microstructure variation and observed growth velocity was correlated with different undercooling temperatures.

## Experimental Details

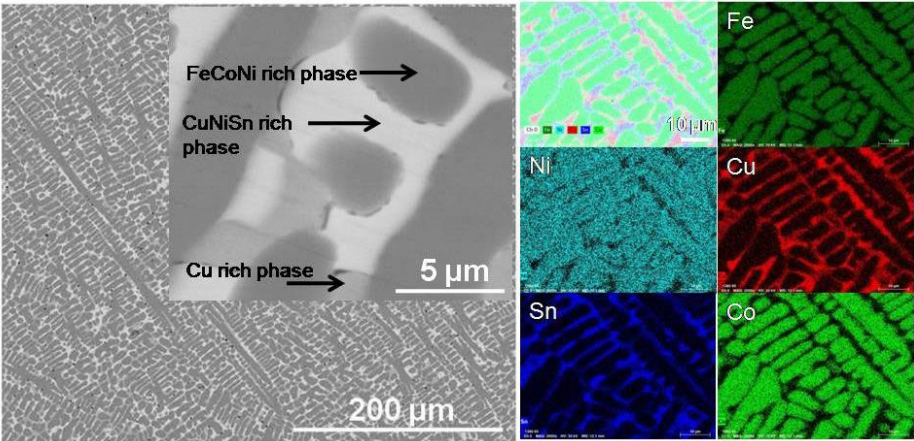
As cast samples in the form of button with a weight of 20 gm were prepared by using vacuum arc melting technique with a non consumable tungsten electrode. The pure elements (>99.9%) was

weighed based on the atomic proportion and melted in the argon atmosphere. The samples were melted for six times to get a homogeneous distribution of alloying elements and after each melting, cast buttons were flipped. The arc melted button was cut in to required quantity by using electrical discharge machining and the cut samples were polished to remove the oxide layer. The undercooling experiments were carried out using melt fluxing technique and boron tri oxide was used as a flux during experiments. Temperature data with respect to time was captured using two colour infrared pyrometer with an accuracy of  $\pm 5^{\circ}\text{C}$ . The high speed imaging of solidification process was captured by using Photron FASTCAM<sup>®</sup> high speed camera with 1 lakh frames per second and the data was analysed by using Photron FASTCAM<sup>®</sup> Viewer software. The as cast and undercooled samples were characterised by using back scattered electron imaging with EDS attachment using Quanta 400<sup>®</sup>. Structural characterisation was done by XRD using X'pert Pro PANalytical<sup>®</sup> with Cu-K $\alpha$  ( $\lambda = 0.154056\text{ nm}$ ) radiation, operated at 45 kV and 30 mA, with a step size of  $2\theta = 0.017\text{ deg}$ . Transmission electron microscopy studies were done on Technai-FEI<sup>®</sup> to identify phases in as cast samples.

## Results and discussion

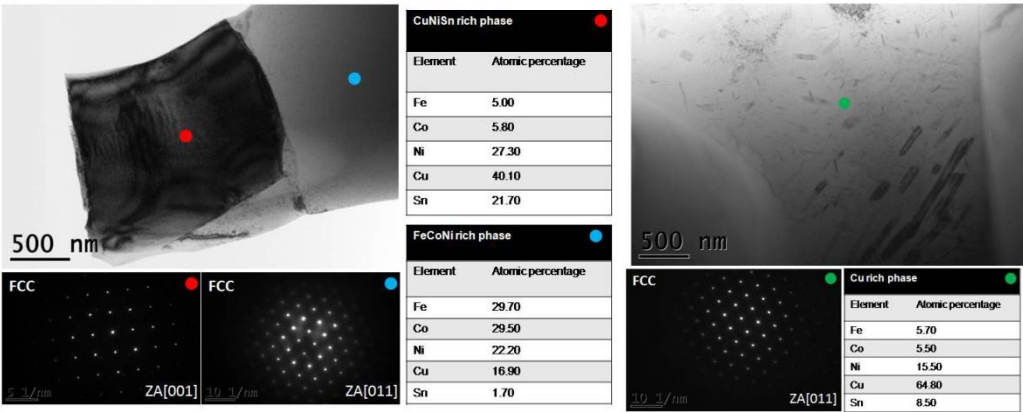
### As cast microstructure

The as cast sample consists of 3 major phases such as FeCoNi rich phase, Cu rich phase and CuNiSn rich phase. Since Cu having immiscibility with Fe and Co, it will segregate in the interdendritic region. Fig. 1 shows the existence of three phases in the present alloy.



**Figure 1.** BSE SEM image of as-cast sample and its EDS mapping

From the BSE low magnification image, it is clear that the FeCoNi phase is the primary dendritic phase with Cu rich and CuNiSn rich phases formed in the interdendritic regions. It is evident from the EDS mapping that the Fe and Co are almost absent at the interdendritic region where as Ni distribution is less in the interdendritic region but not completely depleted. TEM analysis shown in Fig. 2 confirms that the major phase in the alloy is disordered FCC.

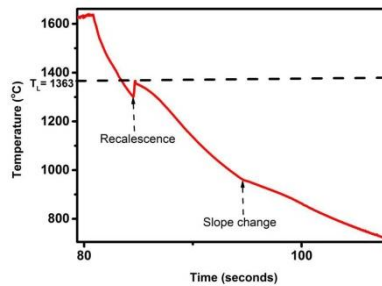


**Figure 2.** TEM micrograph and EDS quantification of as cast sample

From EDS spot analysis in TEM, it is clearly shown that the primary phase formed is FeCoNi rich and it also confirms that Ni is distributed in Cu rich and CuNiSn rich phases. The CuNiSn rich phase consists of a major amount of Cu and Ni. The TEM reveals formation of fine precipitates in the Cu rich region which may be due to the immiscible nature of Cu with Co and Fe leading to precipitation or segregation.

### Time temperature characteristics

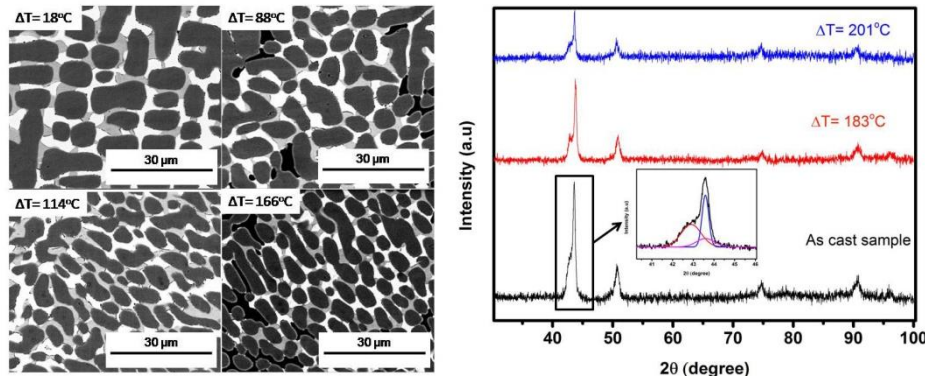
The typical temperature variation with respect to time for the alloy chosen is shown in Fig. 3. The liquidus of the studied alloy is 1363°C marked in the Fig. 3. The undercooling temperature is taken as the difference between the recalescence temperature and liquidus temperature. The curve shows a primary recalescence event which corresponds to the formation of FeCoNi rich primary dendritic phase and slope change around 950°C shows the formation of CuNiSn rich phase. The studied alloy shows a maximum undercooling of  $0.15T_L$ .



**Figure 3.** Typical time temperature characteristics of FeCoNiCuSn<sub>5</sub> during undercooling experiments

### Undercooled microstructure

SEM-BSE image shown in Fig. 4 confirms the variation of undercooled samples compared to as cast. It is clear that all phases are present in all level of undercooling and also confirms that with increasing level of undercooling there is a refinement in microstructure. There are reports on liquid phase separation of Fe and Cu rich region in Fe-Cu-Sn system at different undercooling conditions [13]. The studied alloy shows no liquid phase separation and no macro segregation at all level of undercooling.



**Figure 4.** SEM-BSE images and XRD pattern of undercooled sample

The XRD analysis confirms that the phases are stable even at deeper undercooling in the studied HEA. The deconvolution in the first peak reveals that the presence of 3 phases which are having close lattice parameters. The XRD confirms that there is no major peak shifting and also the strain due to undercooling in this system is negligible.

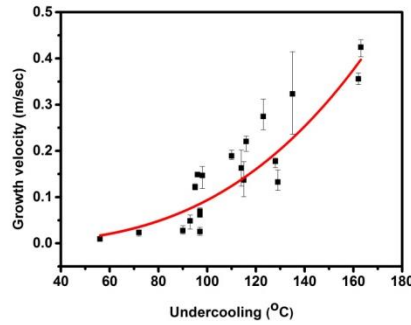
### Growth velocity

Fig. 5 shows the growth velocity calculated from the high speed video imaging confirms that the growth velocity increases with the undercooling temperature. The velocity order shown here is sluggish (at undercooling below 175°C) compared to the pure metals and conventional Ni based

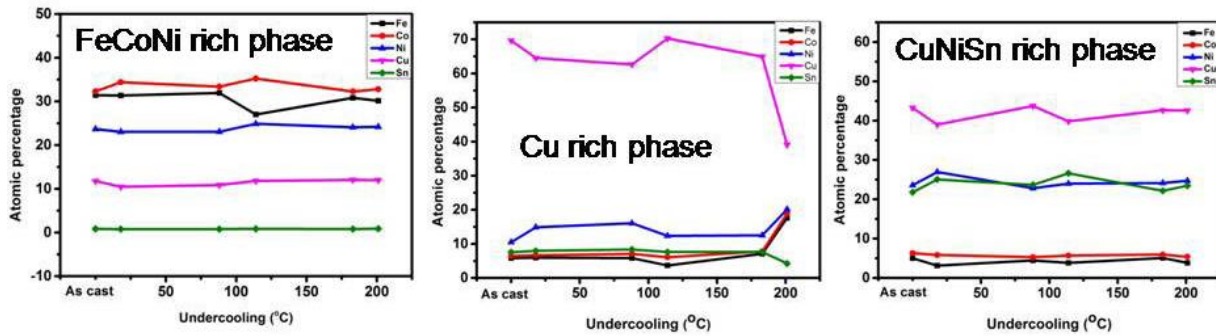
alloys. In the higher undercooling regime (above 175°C) the observed growth velocity is more than 5 m/sec (not shown in Fig. 5) may attributed to the deep undercooling achieved. The red curve shown in figure 5 confirms that the velocity variation with respect to undercooling temperature increasing non-linearly in the range of undercooling below 175°C. The dependence of growth velocity with undercooling temperature in the system can be written as

$$\text{Growth velocity (V) (m/sec)} = 1.1346 \times 10^{-7} (\Delta T)^{2.95815}$$

The growth velocity in the current system was sluggish compared to the Fe-Co binary systems [14] and comparable to the commercial tool steels [15]. The velocity domain is comparable with the reported HEAs such as CoCrCuFeNi and WMoTaNbZr. The observed velocity was comparable to intermetallic compounds [16] and lower than Ni based alloys [17]. The growth velocity of Fe-Cu-Sn system which has shown liquid phase separation [13] was lower than the studied HEA



**Figure 5.** Growth velocity Vs. undercooling temperature



**Figure 6.** Compositional variation of individual elements in different phases

The EDS analysis of individual elements in different phases plotted in Fig. 6. It shows that the individual element atomic fraction is almost equal in FeCoNi rich phase at all levels of undercooling. The Cu and Sn are slightly increasing with increase in undercooling confirms there is no significant solute trapping in the primary dendritic phase. The dip in Cu concentration in Cu rich phase at highest undercooling may be due to solute trapping in this regime. This might be the reason for high velocity in that domain.

## Summary

Undercooling studies on FeCoNiCuSn<sub>5</sub> alloy was carried out and obtained a maximum undercooling temperature of 0.15T<sub>L</sub>. The studies confirm that the phase stability of studied HEA in deep undercooling conditions. There is no metastable phase formation in this system at all levels of obtained undercooling. The growth velocity increasing non-linearly in the range of undercooling temperature below 175°C. EDS results confirms that there is no significant solute trapping with respect to undercooling in the studied alloy.

## References

- [1] J.-W. Yeh, S.-K. Chen, S.-J. Lin, J.-Y. Gan, T.-S. Chin, T.-T. Shun, et al., Nanostructured High-Entropy Alloys with Multiple Principal Elements: Novel Alloy Design Concepts and Outcomes, *Adv. Eng. Mater.* 6 (2004) 299–303. doi:10.1002/adem.200300567.
- [2] D.B. Miracle, O.N. Senkov, A critical review of high entropy alloys and related concepts, *Acta Mater.* 122 (2016) 448–511. doi:10.1016/j.actamat.2016.08.081.
- [3] T.-K. Tsao, A.-C. Yeh, C.-M. Kuo, K. Kakehi, H. Murakami, J.-W. Yeh, et al., The High Temperature Tensile and Creep Behaviors of High Entropy Superalloy, *Sci. Rep.* 7 (2017) 12658. doi:10.1038/s41598-017-13026-7.
- [4] T.K. Tsao, A.C. Yeh, H. Murakami, The Microstructure Stability of Precipitation Strengthened Medium to High Entropy Superalloys, *Metall. Mater. Trans. A Phys. Metall. Mater. Sci.* 48 (2017) 2435–2442. doi:10.1007/s11661-017-4037-6.
- [5] Y.H. Jo, S. Jung, W.M. Choi, S.S. Sohn, H.S. Kim, B.J. Lee, et al., Cryogenic strength improvement by utilizing room-temperature deformation twinning in a partially recrystallized VCrMnFeCoNi high-entropy alloy, *Nat. Commun.* 8 (2017) 1–8. doi:10.1038/ncomms15719.
- [6] D.D. Belyea, M.S. Lucas, E. Michel, J. Horwath, C.W. Miller, Tunable magnetocaloric effect in transition metal alloys, *Nat. Publ. Gr.* (2015) 1–8. doi:10.1038/srep15755.
- [7] Z. Li, K.G. Pradeep, Y. Deng, D. Raabe, C.C. Tasan, Metastable high-entropy dual-phase alloys overcome the strength-ductility trade-off., *Nature.* 534 (2016) 227–30. doi:10.1038/nature17981.
- [8] N. Liu, P.H. Wu, P.J. Zhou, Z. Peng, X.J. Wang, Y.P. Lu, Rapid solidification and liquid-phase separation of undercooled CoCrCuFeNi high-entropy alloys, *Intermetallics.* 72 (2016) 44–52. doi:10.1016/j.intermet.2016.01.008.
- [9] W.L. Wang, L. Hu, S.B. Luo, L.J. Meng, D.L. Geng, B. Wei, Intermetallics Liquid phase separation and rapid dendritic growth of high-entropy CoCrCuFeNi alloy, 77 (2016) 41–45. doi:10.1016/j.intermet.2016.07.003.
- [10] W.L. Wang, L. Hu, S.J. Yang, a. Wang, L. Wang, B. Wei, Liquid Supercoolability and Synthesis Kinetics of Quinary Refractory High-entropy Alloy, *Sci. Rep.* 6 (2016) 37191. doi:10.1038/srep37191.
- [11] A. Munitz, M.J. Kaufman, R. Abbaschian, Liquid phase separation in transition element high entropy alloys, *Intermetallics.* 86 (2017) 59–72. doi:10.1016/j.intermet.2017.03.015.
- [12] Z.Y. Zheng, X.C. Li, C. Zhang, J.C. Li, Microstructure and corrosion behaviour of FeCoNiCuSn<sub>x</sub> high entropy alloys, *Mater. Sci. Technol.* 31 (2015) 1148–1152. doi:10.1179/1743284714Y.00000000730.
- [13] W. Wang, X. Zhang, L. Li, B. Wei, Dual solidification mechanisms of liquid ternary Fe-Cu-Sn alloy, *Sci. China Physics, Mech. Astron.* 55 (2012) 450–459. doi:10.1007/s11433-012-4646-4.
- [14] J.E. Rodriguez, C. Kreischer, T. Volkman, D.M. Matson, Solidification velocity of undercooled Fe-Co alloys, *Acta Mater.* 122 (2017) 431–437. doi:10.1016/j.actamat.2016.09.047.
- [15] J. Vallotton, D.M. Herlach, H. Henein, D. Sediako, Microstructural Quantification of Rapidly Solidified Undercooled D2 Tool Steel, *Metall. Mater. Trans. A Phys. Metall. Mater. Sci.* 48 (2017) 4735–4743. doi:10.1007/s11661-017-4249-9.
- [16] D.M. Herlach, Dendrite Growth Kinetics in Undercooled Melts of Intermetallic Compounds, *Crystals.* 5 (2015) 355–375. doi:10.3390/cryst5030355.
- [17] P.K. Galenko, S. Reutzel, D.M. Herlach, S.G. Fries, I. Steinbach, M. Apel, Dendritic solidification in undercooled Ni-Zr-Al melts: Experiments and modeling, *Acta Mater.* 57 (2009) 6166–6175. doi:10.1016/j.actamat.2009.08.043.



## Phase selection in solidification of undercooled Co-B alloys

Xiuxun Wei, Wanqiang Xu, Jilong Kang, Michael Ferry, Jinfu Li

**Keywords:** undercooling, rapid solidification, metastable phase diagram, structure evolution

### Abstract

M23X6 (M-transition metal, X-nonmetal) phases widely exist in alloy steels and some other multicomponent alloys, but were seldom solidified from binary alloys. In the present work, a series Co-(18.5~20.7)at.%B melts encompassing the eutectic composition (Co81.5B18.5) were solidified at different degrees of undercooling. It is found that the metastable Co23B6 phase solidifies as a substitute for the stable Co3B phase in the alloy melts undercooled above a critical undercooling value of ~60 K, and can be retained to room temperature if the cooling rate is larger than 25 K min<sup>-1</sup>. This phase was confirmed to be the classic Cr23C6-type structure (space group Fm-3m) with a lattice parameter, measured by Rietveld refinement method, of  $a=10.4912(1)$  Å. On exposure of the metastable Co23B6 phase at a given temperature above 1208 K, it does not decompose even after several hours. But it transforms by a eutectoid reaction to  $\alpha$ -Co+Co3B at lower temperature. The Co23B6 and  $\alpha$ -Co phases make up a metastable eutectic. The corresponding eutectic composition and temperature are Co80.4B19.6 and 1343 K, respectively.

## Solidification behavior and microstructure analysis of ternary Zr-Cu-(Al/Ni) alloys

Stefanie Koch, Peter Galenko, Olga Shuleshova, Raphael Kobold, Markus Rettenmayr

**Keywords:** Electromagnetic levitation, Glass forming ability, solidification, Parabolic flight

### Abstract

Zr-Cu-Al and Zr-Cu-Ni are ternary alloy systems with high glass forming ability. Additions of Al to binary Cu50Zr50 enhance the glass forming ability up to a concentration of 8at.% Al. The Zr-Cu-Ni system is a base model system to study the glass forming ability of bulk metallic glasses. Alloys of a Cu content  $\geq 20$  at.% additionally show abnormal behavior, particularly an abrupt decrease in growth velocity with increasing growth undercooling in the high undercooling range.

By electromagnetic and electrostatic levitation were used study the solidification behavior over a wide range of undercoolings. These experiments offer the benefit to process the samples in an ultra clean environment and to determine parameters such as cooling rate, ratio of the specific heat and emissivity from the cooling curves that are measured contactless by a pyrometer.

For the Zr-Cu-Al system we compare experimental results from a Parabolic Flight, Ground experiments and in-situ X-ray experiments performed at the German Electron Synchrotron (DESY). Temperature-Time-Transformations (TTT) diagrams are constructed which give the critical cooling rate to bypass crystallization and to solidify an amorphous structure. The results are analyzed using model calculations of nucleation and crystal growth.

Growth velocities as a function of undercooling of Zr-Cu-Ni alloys are tracked with a high-speed camera. Measurements of the growth velocity versus undercooling in the environment of reduced gravity (Parabolic Flights) are compared with Ground experiments. The microstructures processed under microgravity conditions are compared with the ones observed after cold wall crucible processing, i.e. generated under near-equilibrium conditions of moderate cooling rates. Distinct differences are found. X-ray diffraction analysis confirms the presence of several phases.





## CHAPTER 8: FORCED CONVECTION



# Effect of forced convection on dendritic growth: theoretical modeling and analysis of recent experimental results

P.K. GALENKO<sup>1</sup>, D.V. ALEXANDROV<sup>2</sup>, L.V. Toropova<sup>2</sup>, M. Rettenmayr<sup>1</sup> and D.M. Herlach<sup>3</sup>

<sup>1</sup>Physikalisch-Astronomische Fakultät, Friedrich-Schiller-Universität Jena, 07743 Jena, Germany

<sup>2</sup>Department of Theoretical and Mathematical Physics, Laboratory of Multi-Scale Mathematical Modelling, Ural Federal University, Ekaterinburg, 620000, Russian Federation

<sup>3</sup>Institute of Materials Physics in Space, German Aerospace Center, 51170 Cologne, Germany  
E-mail of corresponding author: peter.galenko@uni-jena.de

**Keywords:** Dendritic growth, forced convection, selection theory, crystalline anisotropy

**Abstract.** Using currently developing model of convective transport and dendrite growth, results on theoretical modeling are presented. Analysis of experimental data obtained in solidifying Ti<sub>45</sub>Al<sub>55</sub> samples processed in electromagnetic levitator is given. It is shown that convective transport plays essential role in quantitative description of dendrite growth kinetics.

## Introduction

A dendritic shape represents the most common crystal morphology appearing during solidification processes in the vast majority of undercooled melts and supersaturated solutions [1,2]. The growth kinetics and shapes of dendrites are controlled by heat and mass transfer in combination with the anisotropic properties of the crystal/liquid interface [3-5].

Several experimental studies show that the internal structure of solidified alloys (both single crystal and polycrystal) is highly dependent on the level of undercooling (supersaturation), solidification velocity and dendrite tip radius [3,5]. Also convection plays an essential role in the growth of dendrites [4], influencing the transport of heat and matter [5], and possibly leading to mechanical deformation of dendrites [6]. The effect of convective transport on the growth kinetics has been demonstrated for different materials: Ni (a typical metal with face-centered-cubic crystal structure) [7,8], Ni<sub>2</sub>B (a congruently melting compound solidifying without chemical segregation) [5] and Ti<sub>45</sub>Al<sub>55</sub> (an alloy solidifying with chemical segregation) [9]. In these works, it was shown that convection enhances the crystal growth velocity due to shrinking of the thermal and solute boundary layers and by establishing larger thermal and chemical gradients ahead of the growing dendrite in the presence of convective flow [10].

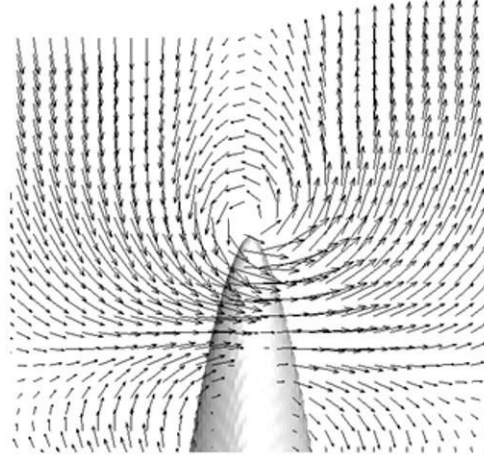
Up to present, all theoretical models known to the authors considered the conductive heat and mass transfer mechanism in the vicinity of the growing dendritic tip [4]. These models allow to describe a large variety of experimental data in the limit of low, moderate and high growth Péclet numbers. However, there is a number of experiments where fluid motions near the dendritic surface are so intensive that the mechanisms of heat and mass transfer occur in a manner different from the conductive type [11]. Such mechanisms can be described by Newton's law of heat (mass) exchange, i.e. the balance conditions for heat and mass transport at the solid/liquid interface should be changed to the convective type. This type of heat and mass exchange mechanism is considered in the present study. We analyze how the convective transport influences the solvability criterion and the sum of undercoolings at the dendrite surface. Finally, experimental data on growth kinetics of dendrites from Ti<sub>45</sub>Al<sub>55</sub> melts [9] are compared with the predictions of our model in its low velocity limit.

## Solvability criterion under convective heat and mass transfer

In this paper, we consider the so-called low-velocity solidification limit in the case of intensive fluid flows near the growing dendritic tip. Generally speaking, if we pay our attention to the case of increasing dendritic tip velocity occurring at high undercoolings, we can face a mixed mode

(convective and conductive) of heat and mass transfer in a thin boundary layer of liquid near the crystal tip. Therefore, first, we give a test for the low-velocity limit in comparison of the theory and experimental data.

The fluid velocity field in the vicinity of growing dendrites might be so intensive that it may lead to transport of heat and mass by the convective mechanism at the dendrite surface [12]. The conductive mechanism of heat and mass transfer becomes inapplicable. For developing the selection of growth mode under intensive convective conditions, we consider the corresponding theory in the presence of convective heat and mass fluxes in the liquid phase [12,13]. Such fluxes can be caused, for instance, by turbulent mixing in the oceanic boundary layer underneath the ice cover [11] or in thermo-electrical hydrodynamic flows [7,8], Fig. 1.



**Figure 1.** Schematic representation of a curl induced by intensive convective flow far from a dendrite surface [7], which induces the flow velocity  $u_*$  that represents convective heat and mass transport (see for details Ref. [14]). Arrows indicate local direction of the flow velocity.

The solvability criterion for thermo-solutal controlled growth is given by

$$\sigma^* = \frac{2d_0 D_T}{\rho^2 V} = \frac{\sigma_0 \sqrt{\alpha_d} V \beta_1}{P_g} = \frac{2\sigma_0 \sqrt{\alpha_d} D_T \beta_1}{\rho}. \quad (1)$$

Combining two different cases  $\beta_1 \ll b d_0 / V$  and  $\beta_1 \gg \sqrt{d_0 / (V D_T)}$ , we consider the generalized criterion [14]:

$$\sigma^*(\rho, P_g) = \frac{\sigma_0 \alpha_d^{5/4} (1 + b D_T \beta_1) \left(1 + \mu \tau_1^{3/2}\right)^2}{\left[1 + \nu_1 \left(\alpha_d^{3/4} \rho b + \frac{3 \alpha_d^{1/4} P_g \beta_1 D_T}{2^{1/4} d_0}\right)\right]^2} + \frac{2\sigma_0 \sqrt{\alpha_d} D_T \beta_1}{\rho}, \quad (2)$$

where

$$\tau_1(\rho, P_g) = \frac{\alpha_d^{1/4} \rho b^2 d_0}{2^{1/4} P_g (1 + b D_T \beta_1)}, \quad \beta_1 = \beta_0 + \frac{m C_i (1 - k_0)}{T_Q \alpha_m u_*},$$

$$b = \frac{\alpha_h \rho_l c_l u_*}{2k_s}, \quad v_1^2 = \frac{2^{\frac{9}{2}} 25 \sigma_0}{27}, \quad C_i = \frac{\alpha_m u_* C_{l\infty}}{\alpha_m u_* - (1 - k_0)V}$$

and  $\sigma_0$  and  $\mu$  represent selection parameters,  $\alpha_h$  and  $\alpha_m$  are the convective (turbulent) coefficients for heat and mass, so that  $\alpha_h/\alpha_m = (D_T/D_C)^n$  with  $2/3 < n < 4/5$ . Other parameters are defined in Table 1.

### Undercoolings

To obtain the dendrite tip velocity  $V$  and dendrite tip radius  $\rho/2$  we use a system of two equations representing the sum of undercoolings and the stability criterion of the dendrite tip [1]. The equation at the dendrite tip can be written out in the form

$$\Delta T = \Delta T_T + \Delta T_C + \Delta T_R + \Delta T_K \quad (3)$$

The thermal undercooling  $\Delta T_T$  is presented as

$$\Delta T_T = T_i - T_\infty = \frac{T_Q V k_s}{\alpha_h \rho_l c_l u_* D_T} \quad (4)$$

The contribution of solutal undercooling  $\Delta T_C$  due to impurity is expressed as

$$\Delta T_C = m(C_i - C_{l\infty}) = \frac{(1 - k_0)V m C_{l\infty}}{\alpha_m u_* - (1 - k_0)V} \quad (5)$$

The interface curvature (Gibbs-Thomson effect) at the dendrite tip  $\Delta T_R$  and the atom kinetics (kinetic undercooling)  $\Delta T_K$  have the form

$$\Delta T_R = \frac{4d_0 T_Q}{\rho}, \quad \Delta T_K = \frac{V}{\mu_k} \quad (6)$$

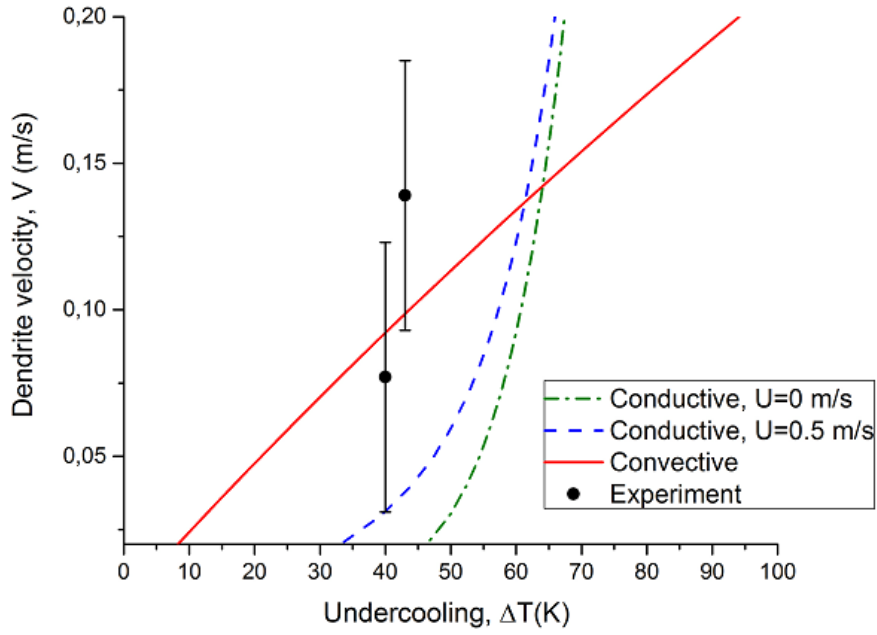
Combining Eqs. (4), (5) and (6), one can express the explicit function  $\rho(V)$  in the form

$$\rho(V) = \frac{4d_0 T_Q}{\Delta T - \Delta T_T(V) - \Delta T_C(V) - \frac{V}{\mu_k}} \quad (7)$$

Now substituting  $\rho(V)$  from (7) into (2), we come to the implicit equation for the dendrite velocity  $V$  of the form

$$\frac{\rho^2(V)V}{2d_0 D_T} \sigma^*(\rho(V), V) = 1 \quad (8)$$

where  $\sigma^*(\rho(V), V)$  is determined by the right-hand side of equation (2) after substituting  $\rho(V)$  from equation (7).



**Figure 2.** Comparison of model predictions with experimental data on the dendrite growth kinetics in  $\text{Ti}_{45}\text{Al}_{55}$ . Predictions with conductive boundary conditions in stagnant melt ( $U=0$  m/s) and under forced flow ( $U=0.5$  m/s) are taken from [15]. Predictions with convective boundary conditions are given using the present model, Eqs. (2)-(8) and material parameters from Table 1. Experimental points are taken from Hartmann et al. [9] for the smallest flow velocity at which the low-velocity limit of dendritic growth is developed in the present model with convective boundary conditions. Error bars indicate uncertainty in experimental measurements of the crystal growth velocity by high-speed camera in droplets processed in an electromagnetic levitation facility.

## Results and discussion

The solution of the system of two equations for selection criterion (2) and sum of undercoolings (3) is given for two functions: the dendrite tip velocity  $V$  and dendrite tip radius  $\rho/2$  at the given total  $\Delta T$ . This solution is compared in the present work with previous theoretical predictions under conductive boundary conditions [15] and experimental data [2] obtained on dendrite growth kinetics in  $\text{Ti}_{45}\text{Al}_{55}$  melt. Indeed, the predictions in Ref. [15] exhibit acceptable agreement with experimental data. However, at the smallest growth velocities, the error bars of the experimental data do not comprise the theoretical curves calculated for the average flow velocities of  $U=0.5$  m/s and  $U=0.75$  m/s. At such intense forced flows one can expect a transition from laminar to turbulent flow in levitated droplets [16]. For these conditions the model in Ref. [15] is not applicable due to the imposed constraint of the laminar character of the forced flow. Therefore, we recalculated the relationship of dendrite growth velocity vs. undercooling under the convective conditions as given by the system of equations (2)-(8).

Fig. 2. shows the comparison of the model predictions for the boundary conditions of the conductive and convective types as well as the experimental data on dendrite velocities obtained for solidifying  $\text{Ti}_{45}\text{Al}_{55}$ . It can be seen that the model with the stagnant melt (zero velocity of the incoming flow,  $U=0$  m/s) does not predict the experimental data. Such outcome was given in Refs. [9,15]. The model with conductive boundary condition and incoming flow with the velocity representing the highest limit of the laminar flow,  $U=0.5$  m/s (see, for details, Ref. [16]) is consistent with the lower limit of the measurements. Thus, conductive boundary conditions do not precisely represent the experiment in the low-velocity limit.

As can also be seen from Fig. 2, including of convective boundary condition in the model of dendrite growth makes it possible to describe the theoretical data of Ref. [9] within the error bars of the experimental measurements of the dendrite velocity. We have assumed that the flow in levitated

droplets was strongly turbulent and at the tips of growing dendrites intensive curls caused heat and mass conduction to occur by the convective mechanism. This made it possible to describe experimental data in the low-velocity limit of dendritic growth in  $\text{Ti}_{45}\text{Al}_{55}$  melt as described in Ref. [9].

**Table 1.** Material parameters and parameters of calculation for dendrite growth in  $\text{Ti}_{45}\text{Al}_{55}$  melts

Parameter	Symbol	Units	Value
Constant of solvability	$\sigma_0$	—	1.17
Capillary constant	$d_0$	$m$	$9.28 \cdot 10^{-10}$
Thermal diffusivity	$D_T$	$m^2/s^{-1}$	$2.50 \cdot 10^{-6}$
Liquid density	$\rho_l$	$kg/m^3$	$2.46 \cdot 10^3$
Solute partitioning coefficient	$k_0$	—	0.86
Nominal concentration	$C_{l\infty}$	at. %	55.00
Surface energy stiffness	$\alpha_d$	—	0.30
Kinetic growth coefficient	$\beta_0$	$s \cdot m^{-1}$	$1.88 \cdot 10^{-20}$
Selection parameter	$\mu$	—	$10^{-3}$
Slope of the liquidus line	$m$	$K/at. \%$	8.78
Heat capacity	$c_l$	$J \cdot kg^{-1} \cdot K^{-1}$	1237
Stability constant	$b$	$m^{-1}$	$1.04 \cdot 10^6$
Convective coefficient of heat	$\alpha_h$	—	3.55
Friction velocity of flow	$u_*$	m/s	4.00
Hypercooling	$T_Q$	K	272.64
Crystal thermal conductivity	$k_s$	$W \cdot m^{-1} \cdot K^{-1}$	29.22

## Conclusions

In this paper, the theory of dendrite growth in a binary alloy in the presence of forced convective flow has been developed and tested against experimental data. The main features of the convective flow around the dendritic tip consist in the fact that the fluid (in a thin layer near the crystal surface) moves in a disordered or even chaotic manner, so that heat and mass transfer are not conductive. They become convective, and the heat and mass balance conditions must be modified and described by Newtonian boundary conditions. Their key distinctive features are the convective heat and mass fluxes at the dendrite growing into undercooled liquid phase.

We considered the low-velocity limit to describe the stable growth of parabolic dendrites. With this aim, a new selection criterion determining a stable combination of dendrite tip velocity and dendrite tip diameter has been derived. The sum of undercoolings condition represents the second relation connecting the tip velocity and diameter for a given undercooling.

Our new analytical solutions representing two equations (selection criterion and undercooling) were compared with a previously known solution that describes dendrite growth with a forced flow within the framework of the model of conductive heat and mass transfer [15]. Considering the low-velocity limit, we experimentally verified that the present model of convective heat and mass transfer near the dendrite surface gives a better comparison with the experiments carried out by Hartmann et al. on the solidification of  $\text{Ti}_{45}\text{Al}_{55}$  [9].

The heat and mass transfer near the dendrite interface can be of a mixed type containing the convective and conductive contributions. This more complex solidification scenario requires developing a new dendrite selection theory and represents a research direction for future investigations.



## Acknowledgments

This work was supported by the Russian Science Foundation, Grant No. 16-11-10095 and German Space Center Space Management under contract number 50WM1541.

## References

- [1] R. Trivedi, W. Kurz, Dendritic growth, *Int. Mater. Rev.* 39 (1994) 49–74.
- [2] P.K. Galenko, D.V. Alexandrov, From atomistic interfaces to dendritic patterns, *Phil. Trans. A.* 376, 2113 (2018), 20170210.
- [3] S. Binder, P.K. Galenko, D.M. Herlach, Faceting of a rough solid–liquid interface of a metal induced by forced convection, *Phil. Mag. Lett.* 93 (2013) 608–617.
- [4] D.V. Alexandrov, P.K. Galenko, Dendrite growth under forced convection: analysis methods and experimental tests, *Phys.–Usp.* 57 (2014) 771–786.
- [5] S. Binder, P.K. Galenko, D.M. Herlach, The effect of fluid flow on the solidification of  $\text{Ni}_2\text{B}$  from the undercooled melt, *J. Appl. Phys.* 115 (2014) 053511.
- [6] A.M. Mullis, K. Dragnevski, R.F. Cochrane, Mechanically deformed primary dendritic structures observed during the solidification of undercooled melts, In *Solidification and crystallization*, ed. DM Herlach, Weinheim, Germany, Wiley-VCH, pp. 175–184.
- [7] J. Gao, M. Han, A. Kao, K. Pericleous, D.V. Alexandrov, P.K. Galenko, Dendritic growth velocities in an undercooled melt of pure nickel under static magnetic fields: A test of theory with convection, *Acta Mater.* 103 (2016) 184–191.
- [8] J. Gao, A. Kao, V. Bojarevics, K. Pericleous, P.K. Galenko, D.V. Alexandrov, Modeling of convection, temperature distribution and dendritic growth in glass-fluxed nickel melts, *J. Cryst. Growth.* 471 (2017) 66–72.
- [9] H. Hartmann, P.K. Galenko, D. Holland-Moritz, M. Kolbe, D.M. Herlach, O. Shuleshova, Non-equilibrium solidification in undercooled  $\text{Ti}_{45}\text{Al}_{55}$  melts, *J. Appl. Phys.* 103 (2008) 073509.
- [10] P.K. Galenko, O. Funke, J. Wang, D.M. Herlach, Kinetics of dendritic growth under the influence of convective flow in solidification of undercooled droplets, *Mater. Sci. Eng. A.* 375–377 (2004) 488–492.
- [11] D.L. Feltham, M.G. Worster, J.S. Wettlaufer, The influence of ocean flow on newly forming sea ice, *J. Geophys. Res.* 107 (2001) 3009.
- [12] M.G. McPhee, G.A. Maykut, J.H. Morison, Dynamics and thermodynamics of the ice/upper ocean system in the marginal ice zone of the Greenland Sea, *J. Geophys. Res.* 92 (1987) 7017–7031.
- [13] D.V. Alexandrov, I.G. Nizovtseva, To the theory of underwater ice evolution, or nonlinear dynamics of ‘false bottoms’, *Int. J. Heat Mass Transf.* 51 (2008) 5204–5208.
- [14] D.V. Alexandrov, P.K. Galenko, L.V. Toropova, Thermo-solutal and kinetic modes of stable dendritic growth with different symmetries of crystalline anisotropy in the presence of convection, *Phil. Trans. A.* 376, 2113 (2018) 20170215.
- [15] P.K. Galenko, D.A. Danilov, K. Reuther, D.V. Alexandrov, M. Rettenmayr, D.M. Herlach, Effect of convective flow on stable dendritic growth in rapid solidification of a binary alloy, *J. Cryst. Growth.* 457 (2017) 349–355.
- [16] R.W. Hyers, G. Trapaga, B. Abedian, Laminar-turbulent transition in an electromagnetically levitated droplet, *Metall. Mater. Trans. B.* 34B (2003) 29–36.

# Numerical simulation of fluid flow in the mushy zone under rotation magnetic field: influence of permeability

Haijie Zhang, Menghuai WU\*, Yongjian Zheng, Andreas Ludwig, Abdellah Kharicha  
Chair for Simulation and Modeling of Metallurgy Processes, Department of Metallurgy,  
University of Leoben, A-8700 Leoben, Austria  
E-mail: [menghuai.wu@unileoben.ac.at](mailto:menghuai.wu@unileoben.ac.at)

**Keywords:** fluid flow, permeability, macrosegregation, rotation magnetic field

**Abstract:** A series of directional solidification experiments on Al-Si-M alloy were performed under terrestrial condition with RMF (rotation magnetic field) stirring [Kovács *et al.*, Materials Science Forum, 2010, 263-268]. Under a certain range of process parameters, a “Christmas tree” segregation pattern was observed. The current study is to use a two-phase columnar solidification model to simulate this segregation phenomenon, focusing on (1) its formation mechanism due to the RMF-induced interdendritic flow in the mushy zone; (2) the model sensitivity to different expressions of permeability law, as proposed by literatures. The geometry configuration for the calculation is identical with the sample (diameter of 8 mm) of the unidirectional solidification experiment, and the alloy is Al-7%Si alloy. Process parameters are taken from experiments. The agreements between calculated macrosegregation patterns and the experimental results are critically evaluated. In principle, the experimentally observed “Christmas tree” of macrosegregation can be numerically reproduced, if a correct permeability law with proper parameters is chosen under forced flow condition. The mushy zone thickness decreases with the increase of permeabilities. The formation of “Christmas tree” macrosegregation can be analyzed by the flow-solidification term ( $\vec{u}_i \cdot \nabla c$ ).

## Introduction

The interaction between a developing mushy zone and the melt flow is still an unclear issue, which is responsible for the formation of macrosegregation and plays important role in the formation of microstructure. To investigate the interdendritic flow and its interaction with the microstructure and macrosegregation, a series of experiments related to the MICAST (Microstructure Formation in Casting of Technical Alloys under Diffusive and Magnetically Convection Condition) research, supported by ESA (Europe Space Agency) were performed on ground and in space [1-4]. With the increase of the magnetic induction or decrease of the cooling rate, a central channel enriched with Si transforms into a channel with a shape of “Christmas tree” [2, 4]. Qualitative explanation of this phenomenon was that the solute rejected from the dendrites was captured by multiply traveling vortices and can be brought back to the mushy zone [2]. A series of simulations related to the MICAST project were made to better understand the flow-solidification interaction during the unidirectional solidification process. Noepfel *et al.*[5] studied the effect of the RMF and TMF on macrosegregation during directional solidification of Al-based binary alloy, and they suggested that the channels formed at the junction of two meridional vortices in the liquid zone. Similar works were also done by Budenkova *et al.*[6]. A periodical structure along the sample adjacent to the central channel was presented. However, they found that the characteristic time correspond to a spatial branch was quite long when it was compared with the oscillations of the fluid flow. It seemed that there was no direct relationship between the formation of spatial branches and oscillations of the fluid flow. From the previous works, the formation of “Christmas tree” macrosegregation is not fully explained.

Currently, the two-phase model, developed by Wu *et al.* [7-9], is used to simulate the unidirectional solidification process of the binary Al-7%Si alloy both under RMF and nature convection. A 2D axisymmetric model is established. Fluid flow in the bulk liquid and mushy zone is calculated under different permeability laws/expressions. Finally, formation mechanism of channel segregation is discussed.

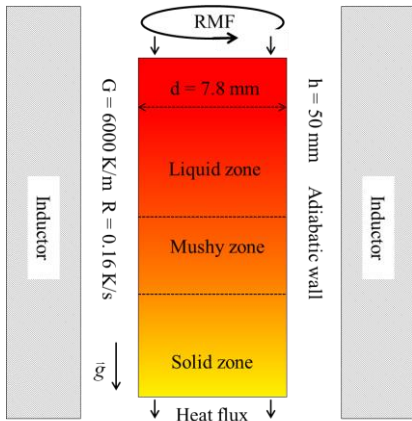
## Simulation Settings

The two-phase volume average model was described elsewhere [7-9]. A 2D axisymmetric model is established to simulate the solidification phenomenon. As shown in Figure 1, the alloy solidifies directionally with an imposed cooling rate (0.16 K/s) and temperature gradient ( $G = 6000$  K/m). An RMF inductor is installed outside the cylindrical crucible. The rotation magnetic field, with the frequency 50 Hz, magnetic induction 20 mT, is controlled with a switch. Owing to the large aspect ratio ( $H/R$ ), where  $H$  is the height of the sample and  $R$  is the radius of the sample, an analytical approximation of the azimuthal component of the electromagnetically force is assumed to be valid (Eq. (1)).

$$\bar{F}_\theta = \frac{1}{2} \sigma \omega B^2 r \left( \frac{\omega R - \bar{u}_\theta}{\omega R} \right) \bar{e}$$

(1)

where  $\bar{F}_\theta$  is the azimuthal component of the electromagnetic force (N),  $\sigma$  is the electrical conductivity of the melt ( $3.65 \times 10^6 \Omega^{-1} \text{m}^{-1}$ ),  $\omega = 2\pi f$  is angular frequency (314),  $B$  is the magnetic induction (0.02 T),  $r$  and  $R$  (4 mm) is the radial coordinate and the radius of the crucible, and  $\bar{u}_\theta$  is the practical azimuthal velocity (m/s) at a radial coordinate  $r$ . The initial temperature of the liquid is set as 1490 K, and a prospective temperature gradient is obtained by a pre-treatment. For the material properties the reader is referred to [5, 10].



**Figure 1.** Geometry configuration and boundary conditions

Two laws of the isotropic permeability, derived from the Carman-Kozeny law and reported by Ramirez[11] and Noeppel [5], are employed in this part to evaluate the effect of the permeability on the fluid flow in the mushy. Noeppel's formulation (Eq.2) is related to  $\lambda_2$ , while Ramirez's formulation is related to  $\lambda_1$  (Eq.3). Additionally, to cover the permeability range defined by different laws, two ultimate conditions, one is small enough and the other big enough, are considered. Details of four simulation cases are summarized in Table 1.

$$K = \frac{\lambda_1^2 f_\ell^3}{1667(1-f_\ell)^2} \quad (2) \quad K' = \frac{\lambda_2^2 f_\ell^3}{4\pi^2 K_c (1-f_\ell)^2} \quad (3)$$

**Table 1.** Permeability laws used for the current study

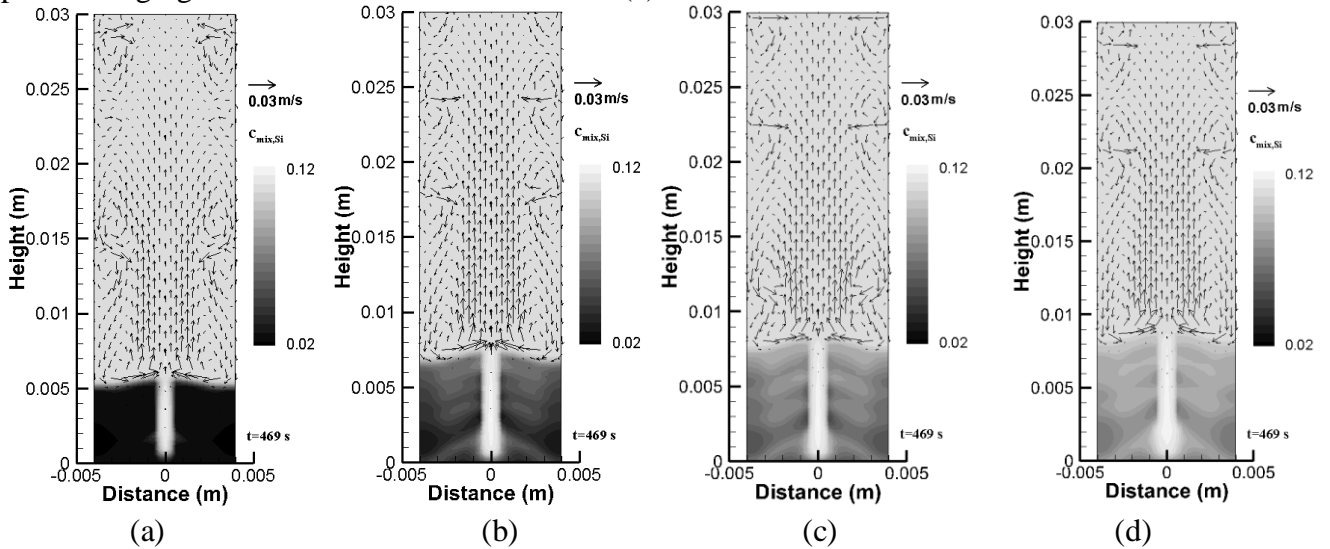
Cases	Expression	Relationship	Referred to	Parameters
a	-	10K	-	
b	$K' = \frac{\lambda_2^2 f_\ell^3}{4\pi^2 K_c (1-f_\ell)^2}$	4K	Noeppel [5]	$\lambda_1 = 300 \mu\text{m}$ and
c	$K = \frac{\lambda_1^2 f_\ell^3}{1667(1-f_\ell)^2}$	K	Ramirez [11]	$\lambda_2 = 50 \mu\text{m}$ , which are
d	-	0.1K	-	taken from experiments

## Simulation Results

As shown in Figure 2, meridional velocity and solute distribution are plotted for different cases. The vector stands for the liquid meridional velocity and the contour stands for mix solute concentration ( $c_{\text{mix}}$ ). During the solidification process, when the RMF is on, an additional force is applied on the liquid phase. A large azimuthal velocity with the value of 0.13 m/s is generated under the current magnetic condition (20 mT), superimposed by the meridional circulation. The maximum

meridional velocity is about 0.02 m/s, which is one order of magnitude smaller than the azimuthal velocity, but it is also four times larger than the velocity as induced only by buoyancy force. Some vortices are generated near the lateral wall and they move upward or downward, dissipating at the sample top surface or the solidification front. During the moving sequence of these vortices, some of the vortices aggregate to a big vortex. The generation and aggregation of these vortices seems randomly. The dissipation period of the vortex is about 1.5 s. Near the solidification front, two inward circulation flow pattern are observed. In the bulk liquid, the permeability of the mushy zone can hardly influence the velocity in the bulk liquid, so the flow pattern and flow intensity is very similar.

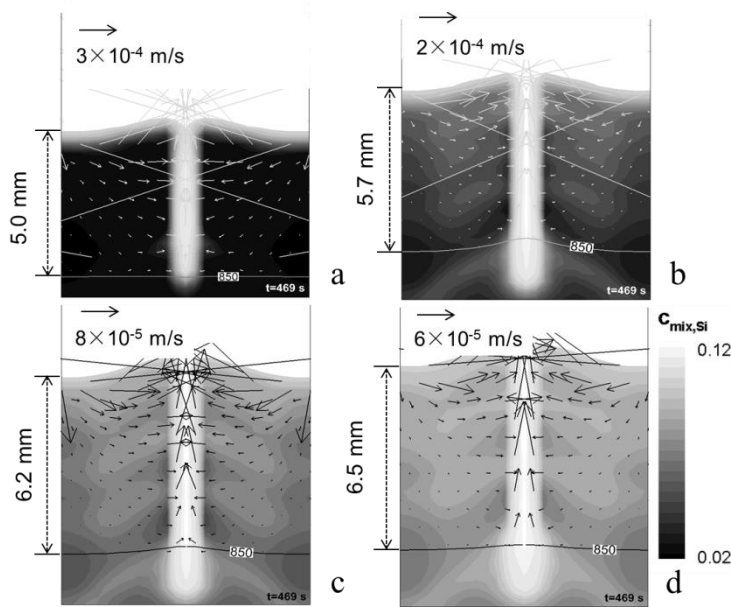
However, the segregation severity and the mushy zone thickness are highly dependent on the value of the permeability. In all cases, a central channel strongly enriched with the Si with a diameter of 1 mm is formed. Except for the case (a), all simulations present a “Christmas tree” segregation pattern adjacent to this central channel with periodical structure, which is consistent with the experimental result and other simulated result [2, 6]. A characteristic time for the periodical formation of channels is quite long (110 s), while the period of the vortex generation (1.5 s) is quite shorter. With the decrease of the permeability (from case a to case d), the segregation severity decreases significantly. Instead the formation of some channels, very strong negative segregation adjacent to the central positive segregation channel is observed in case (a).



**Figure 2.** Influence of the permeability of the mushy zone on the segregation pattern at 469 s: (a) 10K ; (b) 4K ; (c) K ; (d) 0.1K . Gray-scale shows  $c_{mix}$  with lighter showing higher concentration. Vector shows the liquid velocity in the bulk liquid. Maximum meridional liquid velocity in the bulk liquid is similar,  $v_{max} = 0.02 \text{ m/s}$ .

The fluid flow in the mushy zone ( $0 < f_\ell < 0.9$ ) is analyzed. As shown in Figure 3, the vector is the liquid velocity in the mushy zone and the solid line is the position of the eutectic temperature isotherm. Near the solidification front, the liquid volume fraction is larger and the magnitude of the liquid velocity is close to the velocity in the bulk liquid. In the deep mushy zone, the liquid velocity is weakened by the columnar dendrites, and the velocity there is two orders of magnitude smaller than that in the bulk liquid. The maximum permeability is employed in case (a), which means the lowest drag force applied on the liquid phase, leading to the biggest velocity in the mushy zone is observed. With the decrease of the permeability, the liquid velocity in the mushy zone is decreased obviously, which will suppress the solute transport in the mushy zone and reduce the segregation severity. Due to no channel formed in case (a), the velocity stream in mushy zone is very smooth, from the lateral region to the central channel. However, the velocity streams are contorted due to the formation of the channels in the case (b) to case (d), and solute-enriched liquid, rejected from the solid-liquid interface, is preferred to pass through these channels, and finally is washed into the central channel, which induces the positive segregation in the center part of the sample. The mushy zone thickness decreases with the increase of the permeability. The liquid velocity in the mushy zone is

relative large when a large permeability is employed. The intensive liquid velocity in the mushy zone promotes the energy (enthalpy) transport. The hot liquid in the top of the mushy zone can be more easily transported to the deep part of the mushy zone, increasing the temperature gradient. This should be the reason for the decrease of the mushy zone thickness when increasing the permeability.



**Figure 3.** Influence of permeability on the fluid flow in mushy zone at 469 s: (a)  $10K$  ; (b)  $4K$  ; (c)  $K$  ; (d)  $0.1K$  . Gray-scale shows  $c_{mix}$  with lighter showing higher concentration. Vector shows the liquid velocity in the bulk liquid. Solid line shows the position of the eutectic isotherm. Liquid velocity in the mushy zone decreases with the permeability.

## Discussions

Formulation given by Li and Wu [8, 9] is employed to study the formation mechanism of channel segregation.

$$\frac{\partial(c_\ell^* - c_\ell)}{\partial t} = \frac{(c_\ell - c_s^*)}{f_\ell} \frac{\partial f_\ell}{\partial t} + \frac{1}{m} \frac{\partial T}{\partial t} + \vec{u}_\ell \cdot \nabla c \quad (4)$$

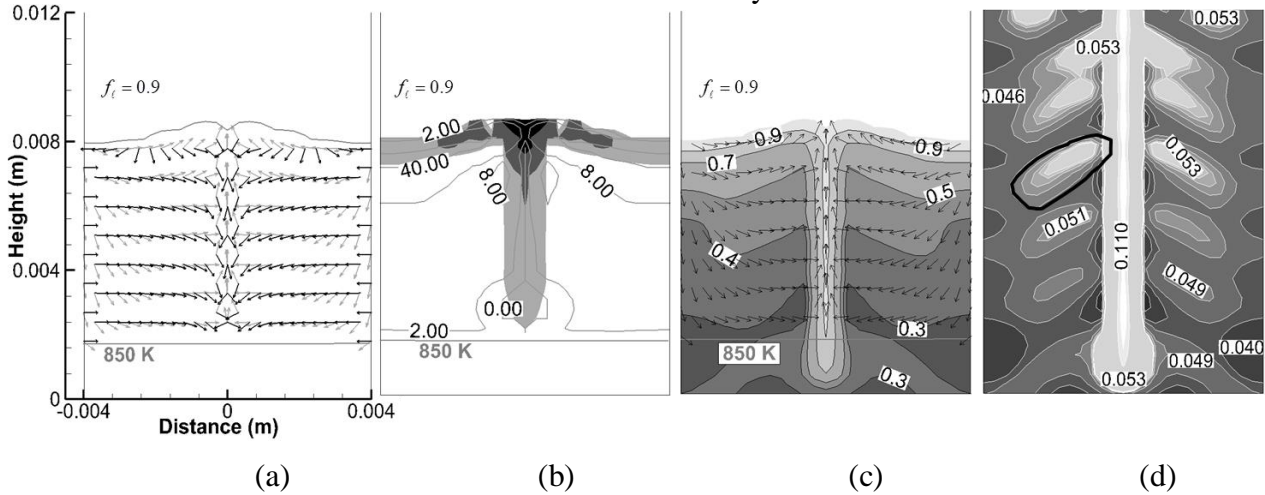
where  $f_\ell$  is liquid volume fraction,  $c_\ell$  is specie concentration in liquid phase,  $c_\ell^*$  and  $c_s^*$  is interface equilibrium species concentration, and  $m$  is liquidus slope.

As shown in Eq. 4, the local solidification/melting rate is the result of three contributions, corresponding to the three right hand side (RHS) terms of Eq. (4). The first RHS term is the solidification induced solute enrichment of the interdendritic melt, which is always negative. The second RHS term is the contribution of the cooling rate, which is always positive. The third RHS term is the flow-solidification interaction term, which can be positive or negative depending on the interdendritic flow direction. Local solidification behavior highly depends on the sign of the flow-solidification interaction.

In a region where the melt flows in the same direction as the concentration gradient, the flow-solidification interaction term is positive. The local increase in the flow velocity due to a flow perturbation accelerates solidification and as a consequence of the locally permeability ( $K$ ) becomes relatively smaller than that of neighboring zones and the interdendritic flow slows down, and channels do not form. On the contrary, in regions where the melt flows in the opposite direction of the concentration gradient, the flow-solidification interaction term is negative. The local increase in the flow velocity due to flow perturbation suppresses the solidification rate. This region with a relatively lower solid fraction has a larger permeability and the flow becomes stronger, and channels form.

As shown in Figure 4 (a), the vectors of liquid velocity and solute gradient are both plotted in gray and black respectively. When the angle between these two vectors is larger than  $90^\circ$ , the flow-solidification interaction term should be negative. The suppressed solidification zone, corresponding to negative  $\vec{u}_\ell \cdot \nabla c$ , is shown in Figure 4 (b), where the solidification rate was significantly slowed

down, especially in the center channel zone. It can be seen that in the center zone of the sample, the flow-solidification interaction term is always negative, and the mass transfer is extremely lower than neighboring cells. Near the solidification front, which corresponds negative  $\vec{u}_\ell \cdot \nabla c$ , although the mass transfer rate is large, it should be suppressed currently. The suppressed solidification rate possibly leads to the formation of the channels. Once the channel forms, the liquid prefers to pass through these channel zone with the least resistance. As shown in Figure 4 (c), these regions, where channels form, with a relatively lower solid fraction, have a larger permeability and the enriched liquid is prefers to flow through the channel zone, which decreases the liquidus of the molten alloy, then the solidification process is further suppressed. This reinforced interaction will continue until the liquid is fully solidified. The final segregation pattern is shown in Figure 4 (d) by map and isolines, and the channel colored with black solid outline is the newly formed at 469 s.



**Figure 4.** Analysis of the formation of the channel segregation at  $t = 469$  s: (a) vector of liquid velocity (gray) overlaid by vector  $c_{mix}$  (black); (b) contours of the flow-solidification interaction term  $(\vec{u}_\ell \cdot \nabla c)$  in white (positive) and black (negative) overlaid by the mass transfer rate  $(M_{lc})$  isolines; (c) liquid volume fraction  $(f_l)$  contours and isolines overlaid by vectors of liquid velocity; and (d) contour of  $c_{mix}$  and its isolines at 849 s. (Vector just stands for the direction in these figures)

## Summary

A two-phase solidification model, coupled momentum, energy, species transfer is used to “reproduce” the unidirectional solidification process of Al-7%Si alloy under RMF (Rotation magnetic field). The fluid flow induced by the nature convection and RMF is consisted of a large azimuthal velocity superimposed with a meridional circulation. The meridional velocity is one order of magnitude smaller than the azimuthal velocity. Some vortexes randomly generate near the lateral wall and move to the crucible top and bottom. For the larger difference of the time magnitude, it seems that there is no direct relationship between the vortex generation and the channel formation, supporting Bodenkova et al.[2]. In principle, the experimentally observed “Christmas tree” of macrosegregation can be numerically reproduced, if correct permeability laws with proper parameters are chosen. The segregation severity is reduced when a smaller permeability is applied. The “Christmas tree” macrosegregation can be clearer if the permeability increases in a certain range. However, when the permeability value is extremely large, the “Christmas tree” of macrosegregation is replaced by the serious negative segregation. The mushy zone thickness decreases with the increase of the permeability. The formation of channels during the solidification process can be analyzed by the flow-solidification term  $(\vec{u}_\ell \cdot \nabla c)$ .

## References

- [1] D. R. Liu, N. Mangelinck-Noël, C.A. Gandin, G. Zimmermann, L. Sturz, H.N. Thi, B. Billia, Structures in directionally solidified Al-7 wt.% Si alloys: Benchmark experiments under microgravity, *Acta Mater.*, 64 (2014) 253-265.
- [2] O. Budenkova, A. Noepfel, J. Kovács, A. Rónaföldi, A. Roósz, A.M. Bianchi, F. Baltaretu, M. Medina, Y. Fautrelle, Comparison between Simulation and Experimental Results of the Effect of RMF on Directional Solidification of Al-7wt.%Si Alloy, *Mater. Sci. Forum*, 649 (2010) 269-274.
- [3] S. Steinbach, L. Ratke, G. Zimmermann, L. Sturz, A. Roósz, J. Kovács, Y. Fautrelle, O. Budenkova, J. Lacaze, S. Dost, Investigation of the effect of fluid flow on microstructure evolution in Al-Si-Fe alloys: The MICAST project, in: *Decennial International Conference on Solidification Processing*, 2017.
- [4] J. Kovács, A. Rónaföldi, A. Roósz, Effect of the High Rotating Magnetic Field (min. 30 mT) on the Unidirectionally Solidified Structure of Al7Si0.6Mg Alloy, *Mater. Sci. Forum* 649 (2010) 263-268.
- [5] A. Noepfel, A. Ciobanas, X.D. Wang, K. Zaidat, N. Mangelinck, O. Budenkova, A. Weiss, G. Zimmermann, Y. Fautrelle, Influence of Forced/Natural Convection on Segregation During the Directional Solidification of Al-Based Binary Alloys, *Metall. Mater. Trans. B*, 41 (2010) 193-208.
- [6] O. Budenkova, F. Baltaretu, J. Kovács, A. Roósz, A. Rónaföldi, A.M. Bianchi, Y. Fautrelle, Simulation of a directional solidification of a binary Al-7wt%Si and a ternary alloy Al-7wt%Si-1wt%Fe under the action of a rotating magnetic field, in: *Materials Science and Engineering Conference Series*, 2012, pp. 012046.
- [7] M. Wu, Y. Zheng, A. Kharicha, A. Ludwig, Numerical analysis of macrosegregation in vertically solidified Pb-Sn test castings – Part I: Columnar solidification, *Comput. Mater. Sci.*, 124 (2016) 444-455.
- [8] J. Li, M. Wu, J. Hao, A. Kharicha, A. Ludwig, Simulation of channel segregation using a two-phase columnar solidification model – Part II: Mechanism and parameter study, *Comput. Mater. Sci.*, 55 (2012) 419-429.
- [9] J. Li, M. Wu, J. Hao, A. Ludwig, Simulation of channel segregation using a two-phase columnar solidification model – Part I: Model description and verification, *Comput. Mater. Sci.*, 55 (2012) 407-418.
- [10] M. Ghods, L. Johnson, M. Lauer, R.N. Grugel, S.N. Tewari, D.R. Poirier, Radial macrosegregation and dendrite clustering in directionally solidified Al-7Si and Al-19Cu alloys, *J. Cryst. Growth*, 441 (2016) 107-116.
- [11] J. C. Ramirez, C. Beckermann, Evaluation of a rayleigh-number-based freckle criterion for Pb-Sn alloys and Ni-base superalloys, *Metall. Mater. Trans. A*, 34 (2003) 1525-1536.



# The effect of electromagnetic stirring during solidification of Co-Cr alloys

Inês OLIVEIRA<sup>1</sup>, Rui SOARES<sup>1</sup>, Ricardo Paiva<sup>1</sup>, João Ferreira<sup>2</sup>, Ana Reis<sup>3</sup>,  
Rui Neto<sup>3</sup>

<sup>1</sup>Institute of Science and Innovation in Mechanical and Industrial Engineering, Rua Dr. Roberto Frias 400, 4200-465 Porto, Portugal

<sup>2</sup>Zollern & Comandita, Rua Jorge Ferreirinha, 1095 Ap. 1027 P-4470-314 Vermoim MAIA

<sup>3</sup>Faculty of Engineering of the University of Porto, Rua Dr. Roberto Frias, 4200-465 Porto, Portugal  
ioliveira@inegi.up.pt

**Keywords:** Investment Casting, Grain Refinement, Electromagnetic Stirring, Co-Cr alloys

**Abstract.** Cobalt-based alloys are one of the most attractive metallic materials for biomedical applications. Their biocompatibility, excellent corrosion and wear resistance as well as higher strengthening properties make them suitable for artificial hip and knee replacements. It is generally recognized that the grain refinement is an effective methodology to improve the quality of casted parts. Conventional grain refinement techniques involve the addition of inoculation substances, the control of solidification conditions or thermomechanical treatment with recrystallization. However, such methods often lead to non-uniform grain size distribution and the formation of hard phases, which are detrimental to both wear performance and biocompatibility.

Stirring of the melt by electromagnetic fields has been widely used in continuous castings with success for grain refinement, solute redistribution and surface quality improvement. Despite on the advantages, much attention has not been paid yet on the use of this approach on functional castings such as investment casting. Furthermore, the effect of electromagnetic stirring (EMS) fields on cobalt-based alloys is not known. In line with the gaps/needs of the state-of-art, the present research work targets to promote new advances in controlling grain size and morphology of investment cast cobalt–chromium alloys. For such purpose, a set of experimental tests was conducted. A high frequency induction furnace with vacuum and controlled atmosphere was used to cast the Co-Cr alloy in ceramic shells. A coil surrounded the casting chamber in order to induce electromagnetic stirring during solidification. Aiming to assess the effect of the electromagnetic stirring on Cr-Co alloys, the samples were subjected to microstructural analysis. The results show that electromagnetic stirring can be an effective methodology to modify the grain size on investment-cast parts.

## Introduction

Co-based alloys are finding ever-increasing applications in biomaterials due to their excellent mechanical, physical and biological performance [1]. Metallic implants are remarkably important for the reconstruction of failed hard tissue. As human life span grows, the need of implants, as hip and knee replacements, will continue to increase as well as the demand for high durability and reliability [2].

The adjustment of grain morphology has been proved to be crucial for improving the mechanical properties and the biocompatibility of cast Co-Cr alloys [3]. Several methods are known refine the grain during solidification: the addition of grain refiners [4], control of the cooling conditions [5], mechanical or electromagnetic stirring [6, 7] or ultrasonic agitation [8].

Grain refiners are widely used in the foundry industry as an effective method to achieve grain refinement. Despite on the success on the control of the grain size, such methods may origin the formation of hard phases that are detrimental to both wear performance and biocompatibility [9].

The control of cooling conditions is a common practice to minimize the occurrence of several casting defects and to regulate the size of the grain. However, it leads to non-uniform grain size distribution, and consequently, non-uniform mechanical properties [10].

Dynamic methods, based on the introduction of forced convection in the melt during solidification are known as an effective way to promote substantial grain refinement. In these processes, externally applied forces, resulting from ultrasonic/mechanical vibration or electromagnetic stirring, are used to control heat and fluid flow.

The principles underlying electromagnetic stirring EMS are simple: as alloys solidify in a temperature gradient, a solid-liquid (mushy) zone is formed between the solid skin and the liquid pool [11]. A solute gradient is formed in the mushy zone due to solute partitioning. If the solidification structure is columnar, the growing dendrites are coherent with the solid skin. If the solidification structure is equiaxed, the solid-liquid mixture remains fluid to 20-30% solid. At higher-percentage solids, the equiaxed dendrites become coherent with the solid skin. According to several authors, EMS allows the solid-liquid mixture to stay fluid to higher solid fractions. Additionally, the fluid motion causes dendrite fragmentation and grain multiplication. This can lead to a columnar-equiaxed transition and a substantial reduction in the grain size [11, 12].

Electromagnetic stirring is based on physical effects described by Maxwell, i.e. when a current is discharged through a coil, in the form of a damped sinusoidal wave, a transient magnetic field  $\mathbf{B}$  will be generated in the vicinity of the coil.  $\mathbf{B}$  induces Eddy currents  $\mathbf{J}$  in the metal placed nearby, which are responsible for limiting the penetration of the magnetic field  $\mathbf{B}$  into the metal and for the creation of its own induced currents. The metal is, therefore, subjected to electromagnetic body forces  $\mathbf{F}$ , resulted from the interaction between the Eddy currents  $\mathbf{J}$  and the magnetic field  $\mathbf{B}$  [11, 12].

Stirring of the melt by electromagnetic fields has been widely used in continuous castings with success for grain refinement, solute redistribution and improvement of the surface quality. Despite of the advantages, no attention has yet been paid on the use of this approach on functional castings, such as investment casting. Additionally, the effect of electromagnetic stirring (EMS) fields on cobalt-based alloys is not known.

The work presented in this article is part of a comprehensive study that targets the understanding of the refinement mechanisms underlying electromagnetic stirring of Co-Cr alloys. The final goal is to optimize the mechanical properties of investment casting Co-Cr components and produce reliable and durable medical implants. The current work focus on the preliminary evaluation of the influence of electromagnetic stirring (EMS) on grain refinement of ASTM F75 Alloy.

## Materials and Methods

The chemical composition, in wt.%, of the ASTM F-75 alloy, expressed in mean values, is outlined in Table 1. The analysis was performed in four samples, cut from five different zones of the ingot, by spark emission spectrometry.

**Table 1.** Chemical Composition, expressed in mean values, measured by spark emission spectrometry.

	wt.%
Chromium, Cr	29,9
Molybdenum, Mo	6,8
Nickel, Ni	0,3
Iron, Fe	0,1
Carbon, C	0,2
Silicone, Si	0,9
Manganese, Mn	0,7
Tungsten, W	<0,05
Phosphorus, P	<0,05
Sulphur, S	<0,05
Aluminium, Al	<0,05
Bor, B	<0,05
Cobalt, Co	61,0

Cylindrical specimens, standardized for tensile testing, were prepared by lost-wax casting technique. The injected wax pattern was assembled to a central wax gating system to form the so-called tree-like assembly –Figure 1 a). The radial effect of the electromagnetic field was evaluated by positioning the wax models at two different distances from the centre. As it is well known, the electromagnetic field magnitude decreases as the distance from a location to the source increases.

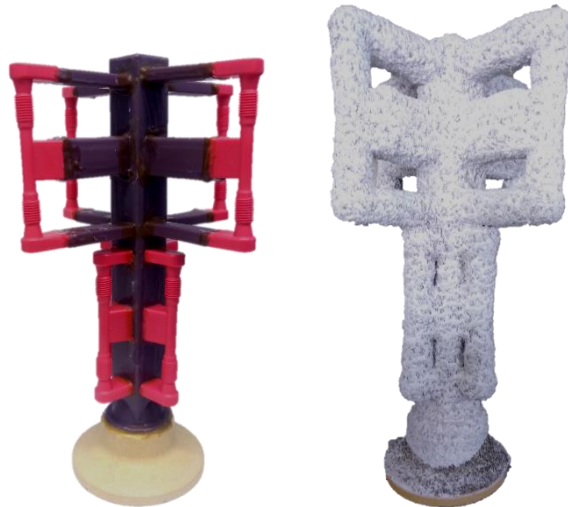
The shell mould was created by dipping the tree into a very fine ceramic slurry. After this first coating, the shell was layered with a fine ceramic refractory grain. Upon drying, the process of dipping the shell mould into the slurry and layering the sand was repeated (with coarser grains) in order to obtain a thickness equal to 8 mm – Figure 1 b).

The ceramic moulds were preheated to 1150 °C in a resistance furnace. The alloy was melted in a vacuum induction furnace and casted into the ceramic mould, placed inside the furnace chamber. The air inside the chamber was maintained at 100 mbar. Melting pouring temperatures from 1450 to 1470 °C were registered.

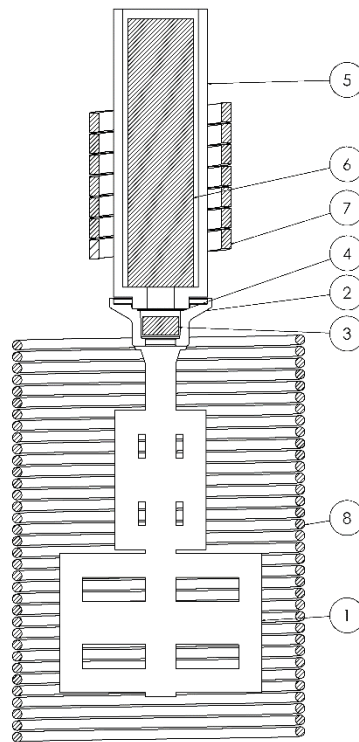
An electromagnetic stirrer, powered by a three-phase induction motor, operating at 50 Hz and 80 A was placed around the casting chamber. A schematic of the experimental set up is shown in Figure 2. After cooling, the ceramic shell was knocked off and specimens were sand blasted to clean the external surface.

A total of six castings were produced: three under electromagnetic stirring and three without, maintaining the remain cast and cooling conditions.

The cylindrical specimens were subjected to tensile testing and metallographic analysis to evaluate the effects of the electromagnetic stirring.



**Figure 1.** a) wax pattern tree; b) shell mould. The radial effect of the electromagnetic field was evaluated by positioning the wax specimens at two different distances from the centre.



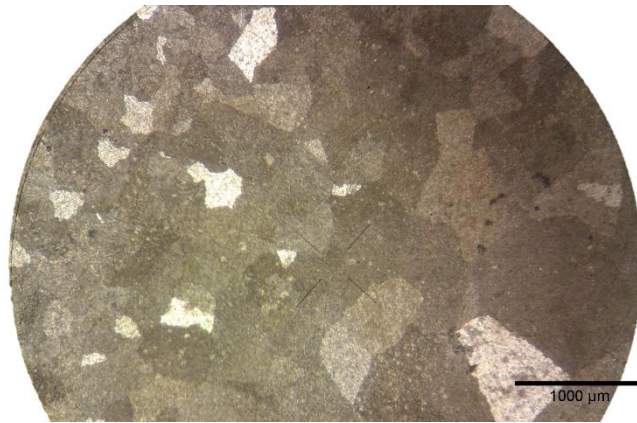
**Figure 2.** Schematic of the experimental set up used for EMS experiments. 1) shell mould; 2) cup; 3) ceramic filter; 4) penny; 5) ceramic crucible; 6) metal ingot; 7) induction coil; 8) EMS inductor.

## Results

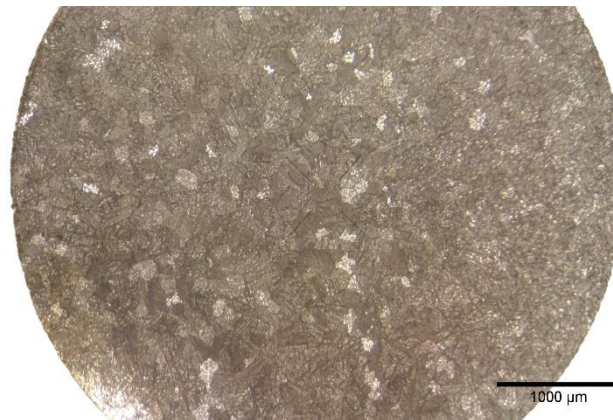
**Effect of electromagnetic stirring on the grain size of Co-Cr alloys.** Figure 3 and Figure 4 present the macrostructure of specimens cut from the centre of the casting trees, solidified without and with electromagnetic stirring. The samples were chemically etched to reveal the grain.

In the case of solidification without electromagnetic field, grains start to grow from the sidewalls towards the central region of the mould.

The effect of the electromagnetically driven melt convection on the solidified structures is shown in Figure 4. As can be seen, comparing with the Figure 3, the growth of the grains was significantly disturbed, possibly as consequence of the redistribution of the solute concentration and dendrite fragmentation due to fluid motion. In average, the grain of the samples electromagnetically stirred is approximately 30% smaller than the obtained during normal solidification. Electromagnetic stirring promotes a significant grain refinement of Co-Cr alloys, casted by investment casting.



**Figure 3.** Macrograph showing as-cast grain, without refinement technique. Sample cut from the centre of the casted tree.



**Figure 4.** Macrograph showing the effect of applying electromagnetic stirring during the solidification of a Co-Cr alloy. Sample cut from the centre of the casted tree.

**Tensile test.** Specimens solidified under both conditions, i.e., with the action of the electromagnetic agitation and without, were subjected to mechanical testing to evaluate the effect of the EMS on the mechanical properties of Co-Cr alloys. In order to study the radial effect of the electromagnetic field on the mechanical properties of the specimens, four samples per casted tree, two per radial distance, were tensioned at  $7 \times 10^{-5}$  1/s and room temperature. The results, expressed in terms of mean values, are shown in Table 2. As can be noted, in average, the samples subjected to the electromagnetic field are more ductile and have more resistance than the ones casted without EMS. Additionally, the resistance of the specimens closer to the electromagnetic inductor is higher than the ones placed farther from the coil. The increase on strength is probably a consequence of the grain size and particle strengthening effects.

**Table 2.** Results from the tensile testing. "D" and "d" correspond to the samples placed at higher and smaller diameter. "D" are, therefore, the samples closest to the electromagnetic inductor.

Specimens	Rp0,2 [MPa]	Rm [MPa]	A [%]	Z [%]
dWithout EMS	548	762	8	3
DWithout EMS	567	884	9	10
dWith EMS	561	885	12	6
DWith EMS	632	1012	11	9

## Conclusions

The effects of electromagnetic stirring on the grain size and mechanical properties of Co-Cr specimens, produced by investment casting, were examined.

Compared with conventional solidification, the microstructure is clearly refined and the mechanical properties improved. With this preliminary set of experiments, the technical viability of the approach was validated. Further tests will be hereafter conducted to study the mechanisms behind the grain refinement of Co-Cr alloys.

## Acknowledgments

Este trabalho é financiado por Fundos FEDER através do Programa Operacional Competitividade e Internacionalização – COMPETE2020 e por Fundos Nacionais através da FCT – Fundação para a Ciência e a Tecnologia no âmbito do projeto com a referência POCI-01-0145-FEDER-032460.

Este trabalho foi desenvolvido no âmbito da operação NORTE-01-0145-FEDER-000022 – SciTech – Science and Technology for Competitive and Sustainable Industries, cofinanciado pelo Programa Operacional Regional do Norte (NORTE2020), através do Fundo Europeu de Desenvolvimento Regional (FEDER)

## References

- [1] Li, Y., Yang, C., Zhao, H., Qu, S., Li, X., & Li, Y. (2014). New developments of Ti-based alloys for biomedical applications. *Materials*, 7(3), 1709-1800.
- [2] Kang, C. W., & Fang, F. Z. (2018). State of the art of bioimplants manufacturing: part I. *Advances in Manufacturing*, 1-21.
- [3] Kurosu, S., Matsumoto, H., & Chiba, A. (2010). Grain refinement of biomedical Co–27Cr–5Mo–0.16 N alloy by reverse transformation. *Materials Letters*, 64(1), 49-52.
- [4] Apelian, D., Sigworth, G. K., & Whaler, K. R. (1984). Assessment of grain refinement and modification of Al–Si foundry alloys by thermal analysis. *AFS trans*, 92(2), 297-307.
- [5] Trivedi, R. (1994). Microstructure characteristics of rapidly solidified alloys. *Materials Science and Engineering: A*, 178(1-2), 129-135.
- [6] Flemings, M. C. (1991). Behavior of metal alloys in the semisolid state. *Metallurgical transactions A*, 22(5), 957-981.
- [7] Vives, C., & Perry, C. (1986). Effects of electromagnetic stirring during the controlled solidification of tin. *International journal of heat and mass transfer*, 29(1), 21-33.

- [8] Eskin, G. I. (1998). Ultrasonic treatment of light alloy melts. CRC Press.
- [9] Lee, H. C., Wo, K. D., Kang, D. S., Lee, T., Oh, S. T., & Kang, W. J. (2015). Effect of cobalt-aluminate addition on microstructure and mechanical property of Co–Cr–Mo alloy. *Materials Research Innovations*, 19(sup1), S1-66.
- [10] Kaiser, R., Williamson, K., O'Brien, C., Ramirez-Garcia, S., & Browne, D. J. (2013). The influence of cooling conditions on grain size, secondary phase precipitates and mechanical properties of biomedical alloy specimens produced by investment casting. *Journal of the mechanical behavior of biomedical materials*, 24, 53-63.
- [11] Campanella, T., Charbon, C., & Rappaz, M. (2004). Grain refinement induced by electromagnetic stirring: a dendrite fragmentation criterion. *Metallurgical and Materials Transactions A*, 35(10), 3201-3210.
- [12] Griffiths, W. D., & McCartney, D. G. (1996). The effect of electromagnetic stirring during solidification on the structure of Al-Si alloys. *Materials Science and Engineering: A*, 216(1-2), 47-60.



# **Influence of Al-alloy composition on the potential of forced convection to reduce grain size and prevent macrosegregation**

Räbiger DIRK, Willers BERND, Eckert Sven

Helmholtz-Zentrum Dresden-Rossendorf, 01314 Dresden, Germany

d.raebiger@hzdr.de

**Keywords:** grain refinement, forced convection, electromagnetic stirring, aluminium alloy, macrosegregation

**Abstract.** This paper presents experimental investigations on the impact of forced convection on the solidification of unalloyed aluminium with different purity grade. In addition Al 7 wt% Si cast Alloy, AW EN 6082 wrought aluminum and Fe rich cast alloys were discussed. Pure aluminium (99.997 and 99.9999 wt % Al) has been solidified under the influence of both electric current pulses and a traveling magnetic field for electromagnetic melt stirring. The electric current was applied by means of two parallel electrodes immersed into the melt through the free surface. In contradistinction to well-known investigations in solute-rich alloys or recently published studies for pure aluminium in our experiments we did not observe a grain refinement effect which can be attributed to the melt treatment applied. It becomes obvious that a slight contamination of the basic raw material by an impure processing during melt preparation has a more pronounced influence on the grain structure as the melt agitation provided by applying electric currents or magnetic fields.

## **Introduction**

In addition to alloy composition, the grain size and a homogeneous phase distribution plays a major role to adjust the properties of cast and wrought aluminium alloys. To achieve grain refinement in solidification processes several methods are common: add-on of grain refiners [1], rapid cooling conditions [2], mechanical or electromagnetic stirring [3, 4], or ultrasonic treatment [5]. The generation of an additional forced flow in the melt offers the possibility to control the grain size without chemical additives.

AC magnetic fields permit a contactless method to generate such forced flow in the liquid metal. Even more: It is possible to control the flow inside the bulk and tune the grain size of the solidified metal [6, 7]. Many studies have shown the complex interaction of magnetic field and melt flow and between melt flow and solidification structure. beneficial effects like a distinct grain refinement or the promotion of a transition from a columnar to an equiaxed dendritic growth (CET) can be obtained. However, electromagnetically-driven melt convection may also produce segregation freckles on the macroscale especially in solute-rich alloys showing different equilibrium concentrations of solute in the mixed crystal and the surrounding melt [8, 9]. The achievement of superior casting structures needs a well-aimed control of melt convection during solidification, which in turn requires a detailed knowledge of the flow structures and a profound understanding of the complex interaction between melt flow, temperature and concentration field. Time-modulated rotating magnetic fields have been proposed recently to control the heat and mass transfer at the solidification front and to avoid segregation effects [10 - 12].

In this paper experimental results are shown to understand the impact of alloy composition on the grain size and phase distribution for different flow conditions. To typify different solidification behaviors we compare various compositions. For this study pure aluminium, AW EN 6082 wrought aluminium alloy and an AlSi7 cast alloy was used. Our results demonstrate the restriction of meaningful implementation in low-alloy and the potential to control the grain size in wrought and cast alloys.

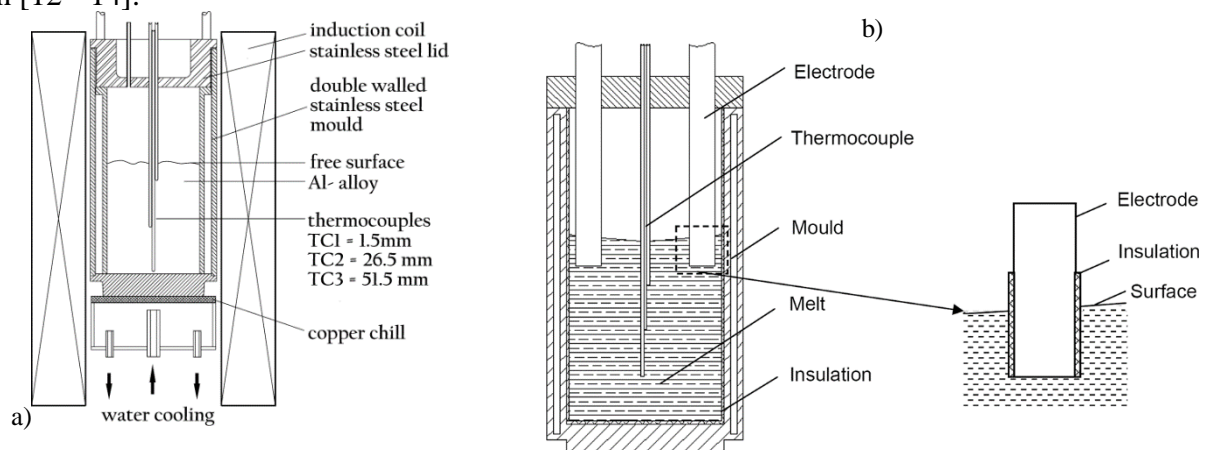
## Experimental Set-up

The present study was conducted using 99.997 wt % and 99.9999 wt % Al as two levels of pure aluminium, respectively (Hydro Aluminium High Purity GmbH). The cylindrical ingots (diameter 50 mm, height 60 mm) were directly eroded from the raw billet. The surface of specimens was ground using SiC - paper and cleaned afterwards by means of an ultrasonic cleaner. The entire preparation process was done carefully in order to avoid pollution of the material.

The cast Al 7wt% Si alloy was melted from 99.99% Al and 99.999% Si according to the designated composition. For the other investigated alloys, the wrought aluminium alloy AW EN 6082 and the A226, commercial supported material was used.

A schematic view of the experimental set-up is shown in Fig 1 (a). The specimens were prepared in a double walled, cylindrical stainless steel mould with an inner diameter of 50 mm and a height of 100 mm. The inner wall of the mould was coated with boron nitride (BN). Samples were solidified directionally from the bottom in a double-walled, cylindrical stainless steel mold. Preparatory specimens were made with a predetermined weight of 315 g corresponding to a filling height of 60 mm for the liquid in the mold. After melting the mold was positioned at a water-cooled copper chill which was kept at a constant temperature of about 20°C. In the experiments presented here the cooling of the sample and the influence of the magnetic field starts at the same time. In the case of the pure alloys, the forced convection would be generated by electro current direct in the melt. The convection to the melt is schematic presented in Fig 1 (b). After the solidification samples was sectioned longitudinally along its mid-plane for metallographic investigations.

More details for the experimental set-up and the prinziple of electro current application you can find in [12 - 14].

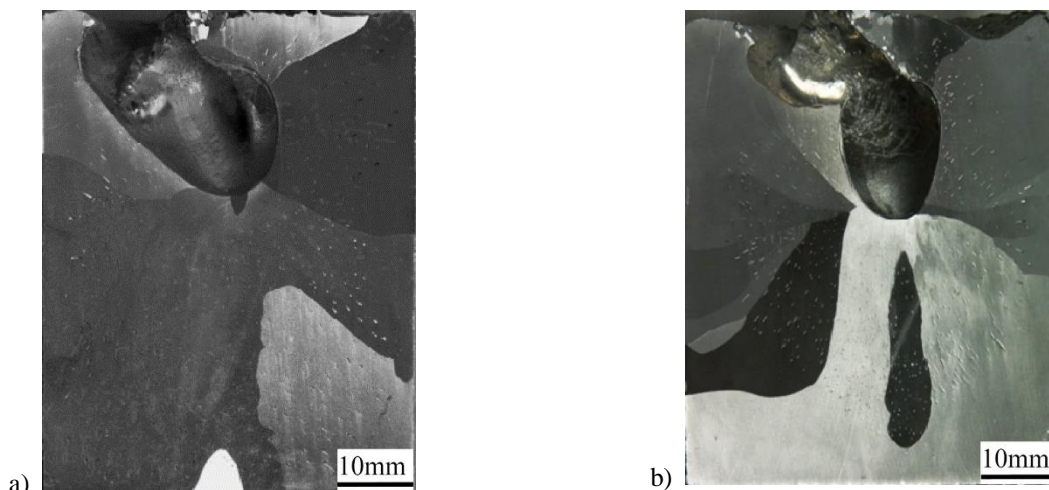


**Figure 1.** Schematic drawing of the experimental setup: a) for the electromagnetic stirring and b) an application of electro current.

## Results

The solidification experiments were performed using 99.997 wt % and 99.9999 wt% Al, respectively. Figure 2 displays the macrostructures in the longitudinal section of four samples solidified from the raw material 99.9999 wt% Al without forced convection (Fig. 2(a)) and with electric current treatment (Fig. 2(b)). The macrostructures are rather coarse and show only a few grains. A grain refining effect of the convection is not visible. Apart from the composition of the investigated material and different cooling conditions, the experimental configuration is identical like in [13], but, the corresponding solidification experiments in pure aluminium performed here do not reveal any tendency for a significant grain refinement. In order to check a potential grain refining effect by forced convection these experiments were repeated using the pure Al (99.997 wt %). The resulting macrostructures shown in Fig. 3 a) contain also very few coarse grains.

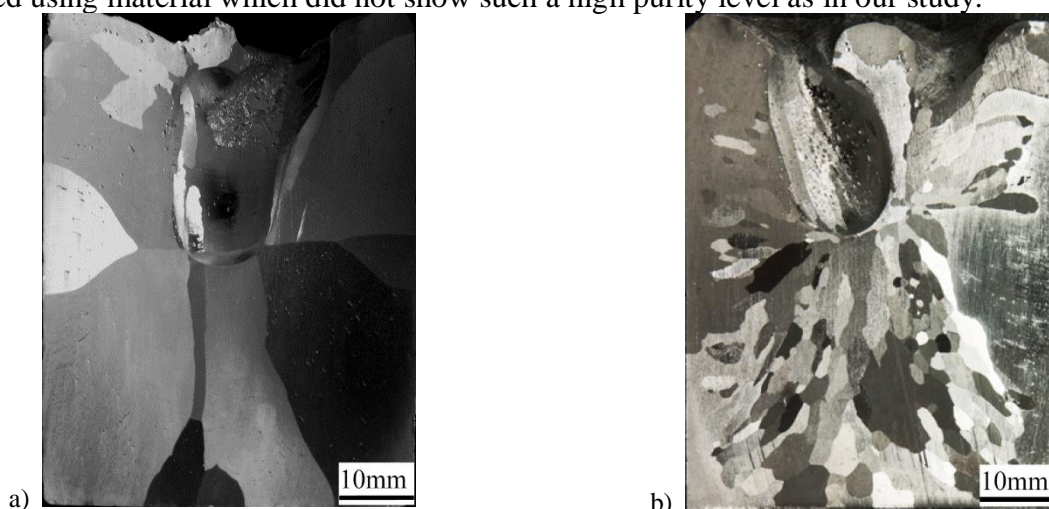
Obviously, these findings contradict the results reported by previous papers [15, 16]. One remarkable distinction is the lower purity level of the aluminium used there (99.7 wt % Al [16], 99.97 wt % Al [15]).



**Figure 2.** Macrostructures in the longitudinal section of solidified 99.9999 wt% Al a) without forced convection and b) with forced convection by using electric current and graphite electrodes.

For checking the influence of the purity level on the results we have performed an additional experiment where the material was slightly contaminated. For that purpose, the original material was melted in a clay-graphite crucible. After melting the liquid aluminium was poured into the mould made of stainless steel. The chemical analysis resulted in a purity level of 99.97 wt % Al. In particular, the amount of Si increases by a factor of about 70, the amount of Fe by a factor of about 22. The further experimental procedure was identical with those of the previous experiments. The resulted macrostructure is shown in Fig. 3b). The grain size is significant smaller as in the sample with a higher purity, but the difference between the situation with and without (is not shown here) forced convection is negligible [14].

Both electromagnetic stirring as well as the application of electrical currents produce a forced melt flow during solidification which causes distinct changes of the temperature and the concentration field in the mushy zone. The melt flow promotes grain refinement by forcing remelting and detachment of dendrite side arms by the local accumulation of solute in the mushy zone and reduction of temperature gradients in the melt. This mechanism works verifiably in solute-rich alloys [17], but, cannot be considered as an explanation for the grain refining effect in pure metals. Previous solidification studies showing significant grain refinement in pure aluminium [15, 16] were conducted using material which did not show such a high purity level as in our study.



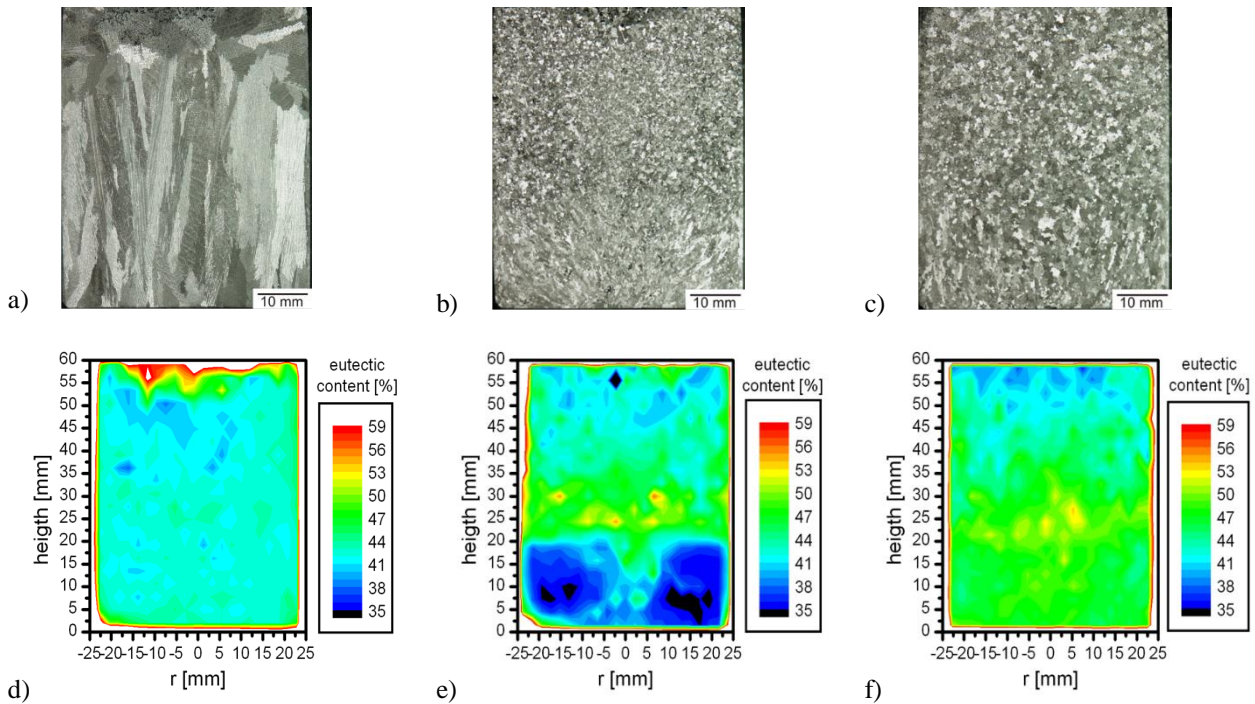
**Figure 3.** Macrostructures in the longitudinal section of solidified 99.997 wt% Al with an applied magnetic field a) eroded sample from the original ingot and b) polluted by a remelting in a clay-graphite crucible and a final purity of 99.97 wt % Al.

Moreover, the melt was solidified in sand moulds which do not guarantee a perfect control of the purity level. Melt flow could transport impurities from the wall into the bulk of the sample where

such particles, oxides, etc. can become efficient as nuclei. More details of this examination you can find in [14]. For wrought aluminium alloy AW EN 6082 with 97 wt.% Al a distinct grain refinement effect can be observed [18].

In the case of solute-rich alloys not the grain refining but rather the segregation effects of forced convection can be the problem. Many studies shows that driven melt convection may also produce segregation freckles on the macroscale [19]. Fig. 4 show the influence of forced convection on the macrostructure and the phase distribution on the solidification structure of a Al 7 wt.% Si alloy.

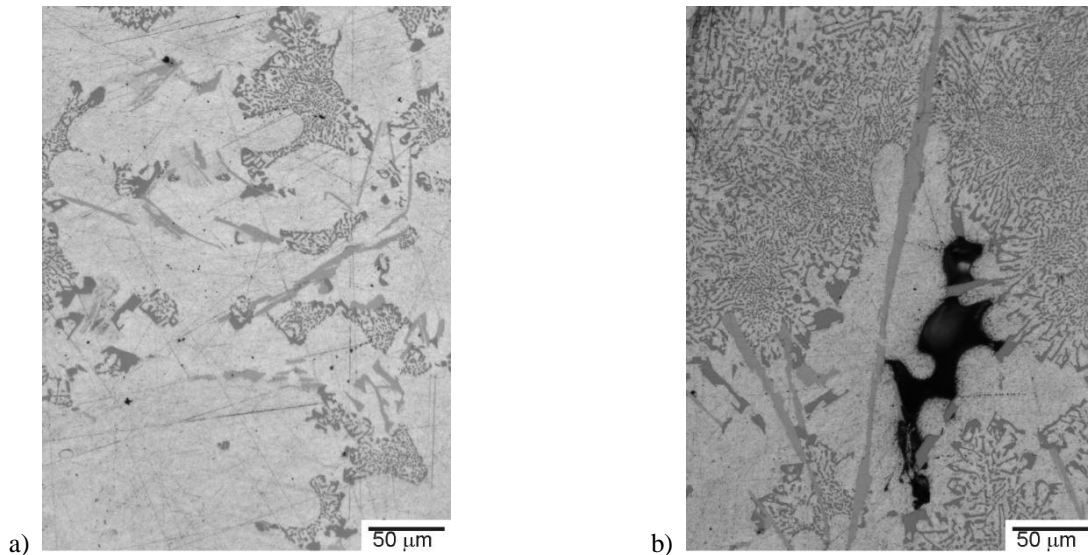
As described before a distinct grain refinement caused by the forced convection becomes visible. In Fig. 4b) a deflection of the columnar grains in the bottom part in the case of the continuous applied RMF is evident. The reason for this deflection is the permanent radial inward flow along the front of the mushy zone. To overcome these segregation effect a modulated magnetic field can be use as described in [11, 12]. With the applied modulated magnetic field in a proper way the deflection is not visible like in Fig. 4c). This macrostructure indicates a flow structure without preferred direction ahead the solidification front. This assumption is confirmed by measurements of the distribution of the eutectic content. While in the lower part of Fig. 4(e) a strong segregation can still be observed along the axis, this segregation disappears in the case of the sample solidified with a modulated magnetic field in Fig. 4(f). The horizontal segregation around the position of the CET remains visible in all cases where forced convection is applied. More details to the mechanism and the impact of the modulated magnetic field on the mechanical properties you can find in [20].



**Figure 4.** Longitudinal sections of solidified samples: (a-c) Macrostructure and (d-f) distribution of the eutectic phase for (a) and (d) without forced convection, (b) and (e) a continuous applied RMF with  $B_0 = 9.2$  mT and (c) and (f) a modulated RMF with  $f_R = 0.35$  mT and  $B_0 = 9.2$  mT.

The promotion of the CET is also caused by the mixing effect in the liquid stage. The temperature field becomes homogenized. Due to this mixing, the melt (or melt and crystals) are longer in the solidification interval. Because of this effect intermetallic phases have more time to grow. Furthermore, the flow transports fresh solute to the intermetallic phase, which allows it to grow faster. In Fig. 5 the microstructure of an A226 alloy are shown. In the case without forced convection the intermetallic phases have a maximum size of 100  $\mu\text{m}$  (Fig. 5a)). On the contrary the intermetallic phases with forced convection can grow to a length of more than 300  $\mu\text{m}$ .





**Figure 5.** Microscopic structure of an A226 alloy a) without forced and b) with forced convection.

## Summery

The present overview shows the influence of the alloy composition on the solidification structure if a forced convection is applied. It could be shown that forced flow is not always able to cause grain refining. This requires a sufficient amount of alloying components. Furthermore, it could be shown that with the help of time modulated magnetic fields grain refinement can be achieved and segregation can be prevented. With the last example, the complex interaction of flow and structure development should be underlined. This demonstrates that experience from one alloy cannot be easily transferred to other alloys with other metallographic constituent. Therefore, further experiments make sense and should be used to optimize materials.

## Acknowledgment

The research is supported by the German Helmholtz Association in form of the Helmholtz-Alliance “LIMTECH”. Furthermore we thank the TRIMET Aluminium SE for supporting the alloy and fruitful discussions.

## References

- [1] D. G. McCartney: Grain refining of aluminium and its alloys using inoculants. *International Materials Reviews*, Vol. 34, 1989, pp. 247-260.
- [2] R.K. Trivedi: Microstructure characteristics of rapidly solidified alloys. *Materials Science and Engineering A*, Vol. 178, 1994, pp. 129-135.
- [3] M.C. Flemings: Behavior of metal alloys in the semisolid state. *Metallurgical Transactions A*, Vol. 22, 1991, pp. 957-981.
- [4] C. Vives and C. Perry: Effects of electromagnetic stirring during the controlled solidification of tin. *International Journal of Heat and Mass Transfer*, Vol. 29, 1986, No. 1, pp. 21-33.
- [5] G.J. Eskin: *Ultrasound treatment of Light Alloy Melt*. Gordon and Breach, Amsterdam, 1998.
- [6] J.K. Roplekar and J.A. Danzig: A study of solidification with a rotating magnetic field, *International Journal of Cast Metals Research*, Vol. 14, 2001, No. 2, pp. 79-95.
- [7] W.D. Griffiths and D.G. McCartney: The effect of electromagnetic stirring during solidification on the structure of Al-Si alloys. *Materials Science and Engineering A*, Vol. 216, 1996, pp. 47-60.

- [8] M. Medina, Y. Du Terrail, F. Durand and Y. Fautrelle: Channel Segregation during Solidification and the Effects of an Alternating Traveling Magnetic Field. *Metall. Mat. Trans. B*, Vol 35, 2004, pp. 743-755.
- [9] P.A. Nikrityuk, K. Eckert and R. Grundmann: A numerical study of unidirectional solidification of a binary metal alloy under influence of a rotating magnetic field. *International Journal of Heat and Mass Transfer*, Vol. 49, 2006, pp. 1501-1515.
- [10] S. Kojima, T. Ohnishi, T. Mori, K. Shiwaku, I. Wakusagi and M. Ohgarni: Development of Magnetic-stirring System in Bloom-caster. *Proc. of the 66th Steelmaking Conf.*, Atlanta, ISS-AIME, Warrendale, 1983, pp. 127-131.
- [11] S. Eckert, P. A. Nikrityuk, D. Rübiger, K. Eckert and G. Gerbeth: Efficient Melt Stirring Using Pulse Sequences of a Rotating Magnetic Field: Part I. *Metall. Mat. Trans. B*, Vol. 38, 2007, pp. 977-988.
- [12] B. Willers, S. Eckert, P.A. Nikrityuk, D. Rübiger, J. Dong, K. Eckert and G. Gerbeth: Efficient Melt Stirring Using Pulse Sequences of a Rotating Magnetic Field: Part II. *Metall. Mat. Trans. B*, Vol 39, 2008, pp. 304-316.
- [13] D. Rübiger, Y. Zhang, V. Galindo, S. Franke, B. Willers, S. Eckert: The relevance of melt convection to grain refinement in Al–Si alloys solidified under the impact of electric currents. *Acta Mater*, Vol 79, 2014, pp.327-338.
- [14] Y. H. Zhang, D. Rübiger, S. Eckert: Solidification of pure aluminium affected by a pulsed electrical field and electromagnetic stirring. *J Mater Sci*, Vol 51, 2016, pp. 2153–2159.
- [15] X.L. Liao, Q.L. Zhai, J. Luo, W.J Chen, Y.Y.Gong: Refining mechanism of the electric current pulse on the solidification structure of pure aluminum. *Acta Mater* Vol 55 (9), 2007, pp. 3103-3109.
- [16] J.H. Ma, J. Li, Y.L. Gao, Q.J. Zhai: Grain refinement of pure Al with different electric current pulse modes. *Mater Lett*, Vol 63 (1), 2009, pp. 142-144.
- [17] E. Liotti, A. Lui, R. Vincent, S. Kumar, Z. Guo, T. Connolley: A synchrotron X-ray radiography study of dendrite fragmentation induced by a pulsed electromagnetic field in an Al-15Cu alloy. *Acta Mater*, Vol 70, 2014, pp. 228-239.
- [18] D. Rübiger, B. Willers, S. Eckert, M. Rosefort, T. Dang, H. Koch: Optimization of liquid metal flow pattern generated by rotating magnetic field and the effect on solidification structure of wrought aluminium alloys, *Proceedings of the XVIII International UIE-Congress*, 2017, Hannover.
- [19] P.A. Nikrityuk, K. Eckert and R. Grundmann: A numerical study of unidirectional solidification of a binary metal alloy under influence of a rotating magnetic field. *Int. J. Heat Mass Transfer*, Vol 49, 2006, pp. 1501-1515
- [20] D. Rübiger, B. Willers, S. Eckert: Flow control during solidification of AlSi-alloys by means of tailored AC magnetic fields and the impact on the mechanical properties. *Mater Sci Forum*, Vol 790-791, 2014, pp 384-389

## **The effect of magnetically controlled fluid flow on microstructure evolution in cast technical Al-alloys: The MICAST project**

Sonja Steinbach, Lorenz Ratke, Gerhard Zimmermann, Laszlo Sturz, Andras Roos, Jeno Kovács, Yves Fautrelle, Olga Budenkova, Jacques Lacaze, Sadik Dost, Gerd-Ulrich Grün, Nils Warnken, Menghuai Wu, Wim Sillekens

**Keywords:** solidification, Al-alloys, fluid flow, forced convection, magnetic field

### **Abstract**

The ESA-MAP research program MICAST (Microstructure Formation in CASTing of Technical Alloys under Diffusive and Magnetically Controlled Convective Conditions) focuses on a systematic analysis of the effect of convection on microstructure evolution in cast Al-alloys. Questions are, for example, how intensity of convection and flow direction act on the evolution of the mushy zone, on macro- and micro-segregations, on dendrite morphology, on the growth mode and on spatial distribution of intermetallic precipitates.

In order to simplify the complex interactions between heat and mass transport and microstructure evolution, the experiments performed by the MICAST team are carried out under well-defined thermally and magnetically controlled convective boundary conditions using directional solidification. They are analysed using advanced diagnostics and theoretical modelling, involving micro-modelling and global simulation of heat and mass transport.

The MICAST team uses binary, ternary (enriched with Fe and Mn) and technical alloys of the industrially relevant Al-Si cast alloys family. In the frame of the MICAST project solidification experiments were performed on the International Space Station (ISS) in the ESA payload Materials Science Laboratory (MSL) with a low gradient furnace (LGF) and a high(er) gradient one (SQF, Solidification and Quenching Furnace) to complement the scanning of a range of solidification times. Binary Al-7wt.%Si and ternary Al-7wt.%Si-1wt.%X (X=Fe, Mn) alloy samples were directionally solidified under both purely diffusive and stimulated convective conditions induced by a Rotating Magnetic Field (RMF). This contribution gives an overview on recent experimental results and theoretical modelling of the MICAST team and gives an outlook for the upcoming years of ISS experimentations by the team and the questions to be addressed with future experiments.

### **Acknowledgements**

The MICAST team gratefully acknowledges financial support by ESA under contract No. 14347/00/NL/SH within the ESA-MAP project 'MICAST' AO-99-031, CNES, DLR and the Hungarian Space Office. This work was supported by Hydro Aluminium Rolled Products GmbH (D), Inotal (HU), Alcoa-Köfém (HU) and Nemak (HU).



# Investigations of forced flow effects on dendritic solidification

Natalia Shevchenko, Olga Keplinger, Sven Eckert

**Keywords:** bottom-up solidification, electromagnetic stirring, segregation channel, Ga-In alloy

## Abstract

Many studies have demonstrated that the application of electromagnetic stirring enhances the area of equiaxed grains and reduces the mean grain size (see e.g. [1-2]). It is widely accepted that flow-induced grain refinement and the CET (columnar to equiaxed transition) in metallic alloys is triggered by the appearance of additional dendrite fragments originating from the columnar front. The mechanism for grain multiplication by melt convection is supposed to be complex and is not fully understood until now. The idea to apply electromagnetic stirring to control the defects arising from the action of natural convection is not straightforward too.

The X-ray radiography was used for an in-situ study of the effect of electromagnetic stirring during the directional bottom-up solidification of a Ga-25wt%In alloy in a Hele-Shaw cell [3]. The experimental setup was extended by a magnetic wheel, which allowed for controlled excitation of a melt flow in the liquid phase. The forced flow eliminates the solutal plumes and damps the local fluctuations of solute concentration. The induced redistribution of solute induces different effects on dendrite morphology, such as the uneven growth of primary trunks or lateral branches, remelting of single dendrites and also of larger dendrite ensembles, changes the inclination angle of the dendrites and leads to an increasing arm spacing. The uneven growth of primary dendrites at the beginning of the solidification experiment leads to the formation of Ga-rich zones near the solidification front which develop into distinct segregation freckles.

Another interesting effect can be observed during solidification experiment: the switching off the magnetic wheel leads to "repairing" of a segregation channel due to growth of equiaxed or fine dendrites in areas of Ga-rich pools. It has been demonstrated that the appearance of small equiaxed grains in the undercooled melt in the segregation pools is triggered by quick redistribution of solute after stopping the magnetic pump. A more detailed study of the "repairing" mechanisms of channels is the subject of ongoing work.

## References

1. B. Willers et al, Materials Science and Engineering A 402 (2005) 55-65
2. T. Campanella et al, Metallurgical and Materials Transactions A 35 (2004) 3201-3210
3. N. Shevchenko et al, Journal of Crystal Growth 417 (2015) 1-8

## **Phase-field modeling of melt flow and directional solidification in Ti48Al alloy**

Alexandre Viardin, Julien Zollinger, Markus Apel, Janin Eiken, Ralf Berger,  
Laszlo Sturz, Dominique Daloz, Ulrike Hecht

**Keywords:** hypergravity, TiAl, phase field, dendrites

### **Abstract**

Centrifugal casting processes of titanium aluminides are mainly used to produce parts for automotive and aircraft industries. During these processes, gravity levels can be as high as 20 nevertheless the effect of solutal convection during directional solidification of dendrite is not well known. With the aim of supporting directional solidification experiments under hyper-gravity using a large diameter centrifuge and under microgravity using sounding rocket experiments, we have applied phase field simulations in order to study the evolution of dendritic morphologies in Ti48Al during directional solidification with and without flow. The main microstructural features of TiAl alloys directionally solidified with gravity level ranging between 0 and 20 will be shown. The effect of fluid flow on the formation of dendrites will then be presented especially for spacing evolution and branching by tip-splitting of dendrites induced by flow.

## **In-situ analysis of thermoelectric magnetic effect by synchrotron X-radiography during directional solidification under static magnetic field**

Henri Nguyen-Thi, Lara Abou-Khalil, Georges Salloum-Abou-Jaoude, Jiang Wang, Mariano Garrido, Guillaume Reinhart, Xi Li, Zhong-Min Ren and Yves Fautrelle

**Keywords:** Solidification, Equiaxed grains, Static magnetic field, Thermo-Electro-Magnetic Force, X-Radiography

### **Abstract**

It is well known that the application of a magnetic field during the growth process can have pronounced effects on cast material structures and their properties, so that magnetic fields have been widely applied since the 1950's. Solidification of liquid metals contains all the ingredients for the development of the Thermo-Electric (TE) effect, namely liquid-solid interfaces and temperature gradients. Combination of TE currents with a superimposed magnetic field gives rise to Thermo-Electro-Magnetic (TEM) volume forces acting on both liquid and solid. TEM forces acting on the solid cause both fragmentation of dendrite branches and a movement of equiaxed grains in suspension. These phenomena were already unveiled by post mortem analysis of samples, but they could be analyzed in more detail by using X-radiography in situ and real-time observations. Moreover, TEM forces also act on the liquid, which results in the generation of fluid flows, which considerably modifies the morphology of the solidification front as well as that of the mushy zone (channeling effect).

In this presentation, we present a review of experimental investigations of the TEM forces induced by a permanent transverse magnetic field during columnar and equiaxed solidification of Al-Cu alloys (4wt% and 10wt%). In situ visualization was carried out by means of synchrotron X-radiography, which is a method of choice for studying dynamic phenomena in metal alloys. The presentation brings conclusive evidences of all the aforementioned effects (dendrite fragmentation, motion of solid particles, formation of segregated channels in the mushy zone).

In addition, numerical calculations of the TEM convection and Stokes drag force were performed firstly on a spherical solid and secondly on a dendrite envelope. Considering the wall confinement and the grain morphology, an excellent agreement was found between the experimental values and the numerical predictions.

## **FEM Magneto-thermo-electric modeling around a solid grain during alloy solidification under uniform AC/DC magnetic field**

Yves Du Terrail Couvat, Olga Budenkova, Thiago Takamura Yanaguissava, Annie Gagnoud

**Keywords:** finite element model, magnetic field, metallic alloy, solidification, simulation

### **Abstract**

Influence of a magnetic field applied to a metallic alloy during solidification under high temperature gradient may have a strong impact on the final micro-structure of an ingot. The observed effects due to Lorentz forces created by thermo-electric currents coupled with magnetic field, are directional movements of each equiaxed grain with dendrite arms breaking. Experiments related in literature show the effectiveness of such phenomena. Our research group at EPM focuses on a better comprehension of the magneto-thermo-electric effects through computational simulation and mathematical modeling. We have developed numerical tools simulating these phenomena. Those tools allow to calculate Temperature, thermoelectric currents, fluid motion inside a given sample and the trajectory of a unique grain. The magnetic field is considered uniform and may vary in time. Tools are based on 2D and 3D finite element model of fundamental physical coupled equations, also coupled to the dynamic fundamental equations to calculate trajectory and rotation of one grain. A domain immersion method is applied considering two coupled regions : the experimental sample considered as a liquid region and the grain domain composed of solid grain and adjusted liquid region around it. Algorithms are non linear and may be static or transient. Numerical experiments are based on various grain's morphology :

- in 2 dimension, grain may be rectangular, circular or built from X radiography image,
- in 3 dimension, grain may be spherical, hexaedral or built from tomography image.

Simulations with DC fields show that grain are moving in a preferential direction different of vertical sedimentation one, until reaching the boundary of the domain. In the case of low frequency magnetic field ( $<10\text{Hz}$ ), trajectories of grain are oscillating on a shorter distance. In both cases, a rotation may appear due to differential distribution of forces developing in dendrite arms around the mass center of the grain. The rotation and translation motion are linked to grain morphology. If frequency grows, trajectories of grains become shorter, until quasi immobility, and induced currents due to Joule effect becomes important.

The numerical tools will be presented in detail, and results of simulations will be compared, when possible, to analytical and experimental data.

## **The effect of strong melt flow induced by the rotating magnetic field on the structure of Al<sub>6</sub>Si<sub>4</sub>Cu alloy**

Jenő Kovács, Arnold Rónaföldi, Árpád Kovács, András Roósz

**Keywords:** Al<sub>6</sub>Si<sub>4</sub>Cu alloy, melt flow, rotating magnetic field, macrosegregation, secondary dendrite arm spacing

### **Abstract**

By applying the Bridgman method of vertical arrangement with bottom cooling, unidirectional solidification experiments were performed by using pure ternary Al<sub>6</sub>Si<sub>4</sub>Cu alloys in a rotating magnetic field. The length of cylindrical samples was 120 mm and their diameter was 8 mm. In the course of the solidification process, the rotating magnetic field was switched on and off twice. The magnetic induction of field was 30, 60 mT or 90, 150 mT. In each case, the frequency of field was 50 Hz. The magnetic field was generated by the CHRMF (Crystallisator with High Rotating Magnetic Field) facility planned and built at our Institute. The experiments were performed at three different types of decelerated sample-movement by which the approximately constant movement velocity of solid/liquid interface could be ensured along the entire length of sample. During the experiments, the temperature of sample was measured by using 13 pieces of NiCr-Ni thermocouples placed along the length of the sample. The position of solid/liquid interface, its movement velocity and the temperature gradient were determined from the recorded data by using an in-house software. The interface movement velocities were 0.04 mm/s, 0.08 mm/s and 0.14 mm/s and the temperature gradient was  $9 \pm 1$  K/mm along the length of samples. Under the influence of the strong melt flow developed by the rotating magnetic field, the columnar dendritic structure transformed into an equiaxial dendritic one and a “Christmas-tree”- shape macrosegregation developed in the samples. The secondary dendrite arm spacing as well as the Si- and Cu-concentration were measured along the sample length at the edge of the sample as well as in the half-radius. Relationships were determined between the concentration-change caused by the flow and the values of secondary dendrite arm spacing. The average diameter of segregated trunks, the average diameter of segregated branches as well as the average distance between the segregated branches were determined among the geometrical parameters of macrosegregation. The parameters were plotted as a function of the applied magnetic induction at different movement velocities of the solid/liquid interface.

## **Effect of Travelling Magnetic Field on the Solidified Structure of Peritectic Sn–Cd Alloy**

Maria Sveda, Anna Sycheva, Arnold Ronafoldi, Andras Roosz

**Keywords:** travelling magnetic field, directional solidification

### **Abstract**

In the course of the directional solidification experiments performed in travelling magnetic field (TMF), it was observed that the melt flow has a significant effect on the solidified structure of Sn-Cd alloys. In this paper, this effect was investigated experimentally in the case of Sn-1.6 wt. % Cd peritectic alloy. A Bridgman-type gradient furnace equipped with two different inductors was used for the experiments. One of them generates the travelling magnetic field in order to induce a flow in the melt. The microstructure was investigated by an optical and a scanning electron microscope. The Cd concentration was measured along several lines as function of the sample diameter by Energy-dispersive X-Ray microanalysis. The cell size of the primary tin phase was determined by an image analyzer on the longitudinal polished sections along the total length of the samples. To the effect of melt flow induced by TMF, the microstructure changes from banded to finer cellular microstructure.

## CHAPTER 9: COMPOUND SOLIDIFICATION



# Microstructure Characterisation of Drop Tube Processed SiGe Semiconductor alloy

Naveed HUSSAIN<sup>1</sup> and Andrew M MULLIS<sup>2</sup>

<sup>1</sup>School of Chemical & Process Engineering, University of Leeds, Leeds LS2 9JT, UK

<sup>2</sup>School of Chemical & Process Engineering, University of Leeds, Leeds LS2 9JT, UK

**Keywords:** Rapid Solidification, Microstructure, Semiconductors, Metals and Alloys

**Abstract.** Si-Ge based thermoelectric materials are of interest due to the challenges associated with energy recovery from waste heat in industrial processing. A directionally solidified, chill cast ingot of Si<sub>70</sub>Ge<sub>30</sub> was broken into pieces before being subject to rapid solidification in reduced gravity. Drop-tube processing was employed to produce a powder sample with particle diameters in the range 850-150 µm. Solidification occurred under reduced gravity conditions during free-fall down the tube. Cooling rates of between 1800 and 20000 K s<sup>-1</sup> were achieved among the various particle sizes. EDX analysis was used to confirmed that the starting material, drop-tube particles and a small amount of residual material left in the crucible were all the same composition. Scanning Electron Microscopy (SEM) was used to analyse the resulting microstructure as a function of cooling rate.

The as-solidified microstructure consists of relatively large Si-rich grains with Ge localised at the boundaries, in line with the expected solidification pathway. The Ge is found to form numerous small Ge rich grains which decorate the boundaries of the much larger Si-rich grains, resulting in highly bimodal grain size distribution. This has not previously been reported in the scientific literature. The effect of cooling rate on grain size was studied using SEM and quantitative image analysis, with grain size being found, as expected, to decrease with increasing cooling rate. Point Energy Dispersive X-Ray (EDX) was conducted on all samples at areas of interest; with the larger Si rich grains showing more Si than the original alloy composition (approx. 5-15% more). The small Ge rich grains showed relatively small amounts of Si (between 3-15%). The segregation and heterogeneity found in the microstructure of rapidly solidified particles, alongside the correlation in grain sizes determined by cooling rate, would be important in understanding and improving the conversion efficiency of SiGe whilst also maximising the cost-efficiency.

## Introduction

Due to their application in micro-electronics, semiconductors such as Si<sub>1-x</sub>Ge<sub>x</sub> are the subject of great current interest. In particular, their tuneable band gap means that the alloy proves to be more flexible than current, pure silicon based, materials [1]. High mechanical strength and a high melting point, together with a low thermal conductivity at high temperatures (900 to 1200 K) [2], means that Si<sub>1-x</sub>Ge<sub>x</sub> is often used in thermoelectrical power generation. The performance of electricity generation using heat from a thermoelectric material is determined by the dimensionless figure of merit:

$$ZT = \sigma S^2 T / \kappa. \quad (1)$$

where  $\sigma$  is the electrical conductivity,  $S$  is the Seebeck coefficient, and  $\kappa$  is the thermal conductivity. The maximum efficiency is given as a function of the figure of merit  $ZT$  [3] by:

$$\eta_{max} = \frac{T_h - T_c}{T_h} \left[ \frac{\sqrt{1 - ZT_{ave}} - 1}{\sqrt{1 - ZT_{ave}} + T_c/T_h} \right]. \quad (2)$$

where  $T_h$  and  $T_c$  are the hot- and cold-side temperatures, respectively, and  $T_{ave}$  is the average  $(T_h + T_c)/2$ . The maximum efficiency is a product of a reduction factor along with the Carnot efficiency  $(T_h - T_c)/T_h$ .

Interest in SiGe alloys in industry has been due to its ability to recover power by utilising waste heat and as a result increasing cost efficiency, particularly in steel manufacturing. One of the primary challenges in developing the next generation of SiGe thermoelectric materials is to avoid altering the



characteristics of SiGe when reducing the amount of the more expensive Ge component. SiGe alloys with compositions of  $\text{Si}_{92}\text{Ge}_8$  [4,5] and  $\text{Si}_{95}\text{Ge}_5$  [4] using a nanostructuring approach have previously been developed, this representing a lower Ge content than the commercial alloy that is available. Electromagnetic levitation studies have found that the solidification conditions can affect the development of the microstructure, so thermal conductivity of the lower Ge content materials can be decreased by departing from thermodynamic equilibrium (i.e. increasing undercooling) [7,8,9]. In a previous study, melt spinning was used to synthesise SiGe samples and they were compared against slow cooled SiGe samples of the same composition. During close to equilibrium solidification the microstructure appeared inhomogeneous, in contrast to the rapidly solidified samples which showed a greater degree of homogeneity. Increased solute trapping was thought to be the reason behind this, with the rapidly solidified samples displaying less segregation than the sample solidified close to equilibrium. The study also found that homogeneity was improved at a higher cooling rate, alongside a decrease in grain size. [5]. Another study in 2002 compared microgravity experiments conducted on SiGe samples using the Japan Microgravity Center's (JAMIC's) drop shaft and 10m drop tube with samples processed under conventional conditions. Ground-based samples showed a higher level of segregation, though segregation was not fully suppressed even in the samples produced in microgravity. Segregation was thought to have occurred due to diffusion during unidirectional solidification [6]. Both studies found that the first region to solidify was the Si-rich grains followed by Ge-rich regions forming towards the edges and boundaries of the large distinctive Si-rich grains.

## Experimental Procedure

Rapid solidification was affected by drop-tube processing. Small pieces broken from a directionally solidified, chill cast ingot of SiGe were obtained from Goodfellow. Multiple pieces of the ingot (approx. 4 g) were loaded into an alumina crucible which contained three  $\times 300\text{ }\mu\text{m}$  laser drilled holes in the base. A graphite susceptor was used to mount the crucible at the top of the drop-tube and created a gas-tight seal to allow the molten alloy to be ejected under pressure. This was placed within a twin-walled alumina heat-shield surrounded by an induction coil that is connected to a 3 kW RF generator.

Before melting the tube is flushed three times with oxygen free nitrogen at a pressure of 40 kPa after it is evacuated to a pressure of 1 Pa using an oil-filled rotary pump. A turbomolecular pump is then used to evacuate the tube to a pressure of  $10^{-4}$  Pa before it is filled again to 40 kPa with dried, oxygen free nitrogen gas. An R-type thermocouple within the melt crucible was used for temperature determination. A 95-minute heating cycle was employed to melt the material with an estimated 50 K superheat prior to ejection. Ejection is achieved by pressurising the crucible with 400 kPa of nitrogen gas. Further details of the drop-tube method can be found in Ref. [7]

The solidified particulate samples were collected then sieved into the following standard sieve sizes:  $850\text{ }\mu\text{m} < d$ ,  $500\text{ }\mu\text{m} < d < 850\text{ }\mu\text{m}$ ,  $300\text{ }\mu\text{m} < d < 500\text{ }\mu\text{m}$ ,  $212\text{ }\mu\text{m} < d < 300\text{ }\mu\text{m}$  and  $150\text{ }\mu\text{m} < d < 212\text{ }\mu\text{m}$ , with  $d$  being the particle diameter. Cooling rates for particles in free-fall were estimated from the balance of heat fluxes, following the method given in [7]. For particles of 850, 500, 300, 212 and 150  $\mu\text{m}$  in diameter the estimated cooling rates for the undercooled liquid were 1800, 3600, 7200, 12000 and 20000  $\text{K s}^{-1}$  respectively. Some SiGe melt remained in the crucible following the pressurisation, possibly due to the base of the crucible not being perfectly flat. The residue, starting material and drop-tube particles were all confirmed to be the same composition using EDS (described below).

In preparation for Scanning electron microscopy (SEM) the samples were mounted in TransOptic™ resin before being ground and polished. The samples were then sputter coated using a layer of Carbon. Full details of sample preparation for SEM analysis can be found in Ref [8]. The high-resolution settings in backscattered detection mode on the Hitachi SU8230 microscope were 5 kV accelerating voltage ( $V_{acc}$ ) and 30  $\mu\text{A}$  probe current ( $I_e$ ). Grain size distribution from the SEM backscattered micrographs was analysed using the ImageJ software [9]. Electron Dispersive X-Ray (EDX) Spectroscopy maps were obtained for each sieved sample sizes, crucible residue and starting material, with point measurements also taken at areas within the micrographs of interest.

A Scheil calculation was also conducted for Si-Ge with a starting composition of 25 at. % Ge where diffusivity was assumed to be 0 in the solid fraction and infinite in the liquid. This was conducted using the CALPHAD modelling software package MTDATA [10] with version 4.3 of the SGTE database.

## Results

**SEM Microstructure Characterisation.** A section of the starting crushed ingot was analysed using SEM backscatter to compare with rapidly solidified samples. The SEM micrograph, seen in Fig. 1a, appears to display a heterogenous microstructure with significant variations in Ge content. The microstructure of the residual crucible sample is displayed as an SEM backscatter micrograph in Fig. 1b and it also shows a heterogenous microstructure with significant variations in Ge content.

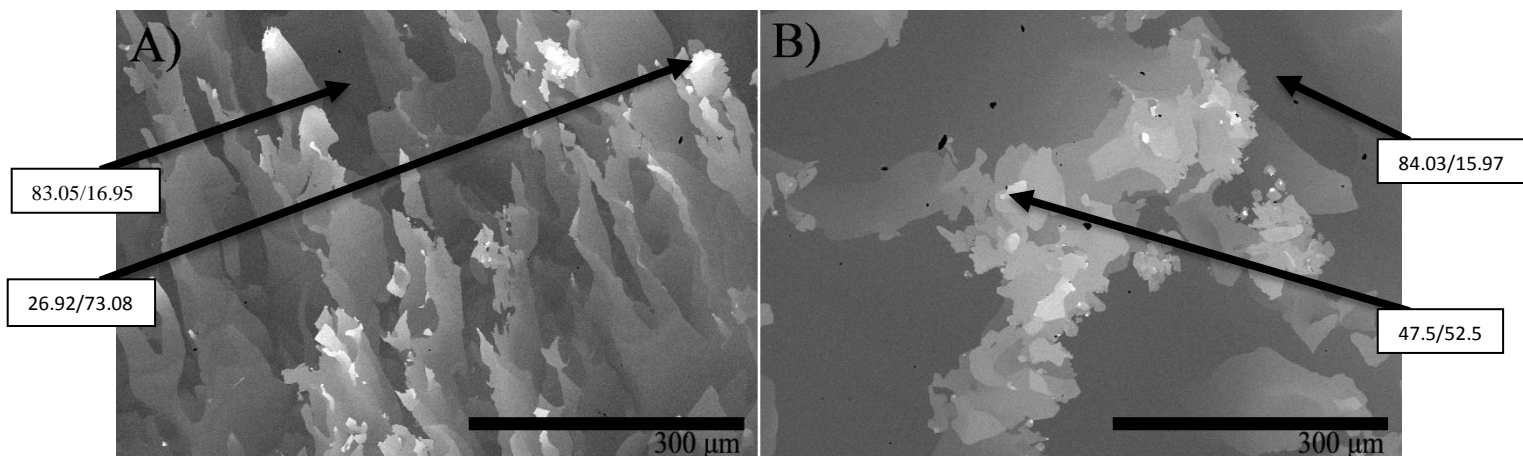
The SEM backscatter micrographs shown in Figs. 2a – 2e are associated with the drop tube processed samples of each size fraction. In contrast to previous studies we find, somewhat surprisingly, that the rapidly solidified samples show greater inhomogeneity with more visible segregation compared to either the starting or residual materials. Ge is found to be localising at the boundaries of the relatively large Si rich grains. Further investigation finds the Ge on the boundary of the large Si grains to be formed as smaller grains resulting in a bimodal grain size distribution. The segregation and Ge localisations are in line with the findings of Zhang et al [5] and Nagai et al [6], but the bimodal distribution of Si-rich grains and Ge-rich grains was not reported. Also visible are several ‘cross’ shapes, possibly a result of coring, within the Si grains which suggest the early signs of dendrite formation.

The results of grain size distribution analysis, for the rapidly solidified samples, can be seen in Table 1. The average grain area, in  $\mu\text{m}^2$ , for the Si-rich grains, Ge-rich grains and overall average grain area was investigated using a number (N) of scans at different sites within the sample(s) and this has been expressed with standard error. The average grain area can be seen to decrease as the cooling rate increases with a smaller particle size fraction.

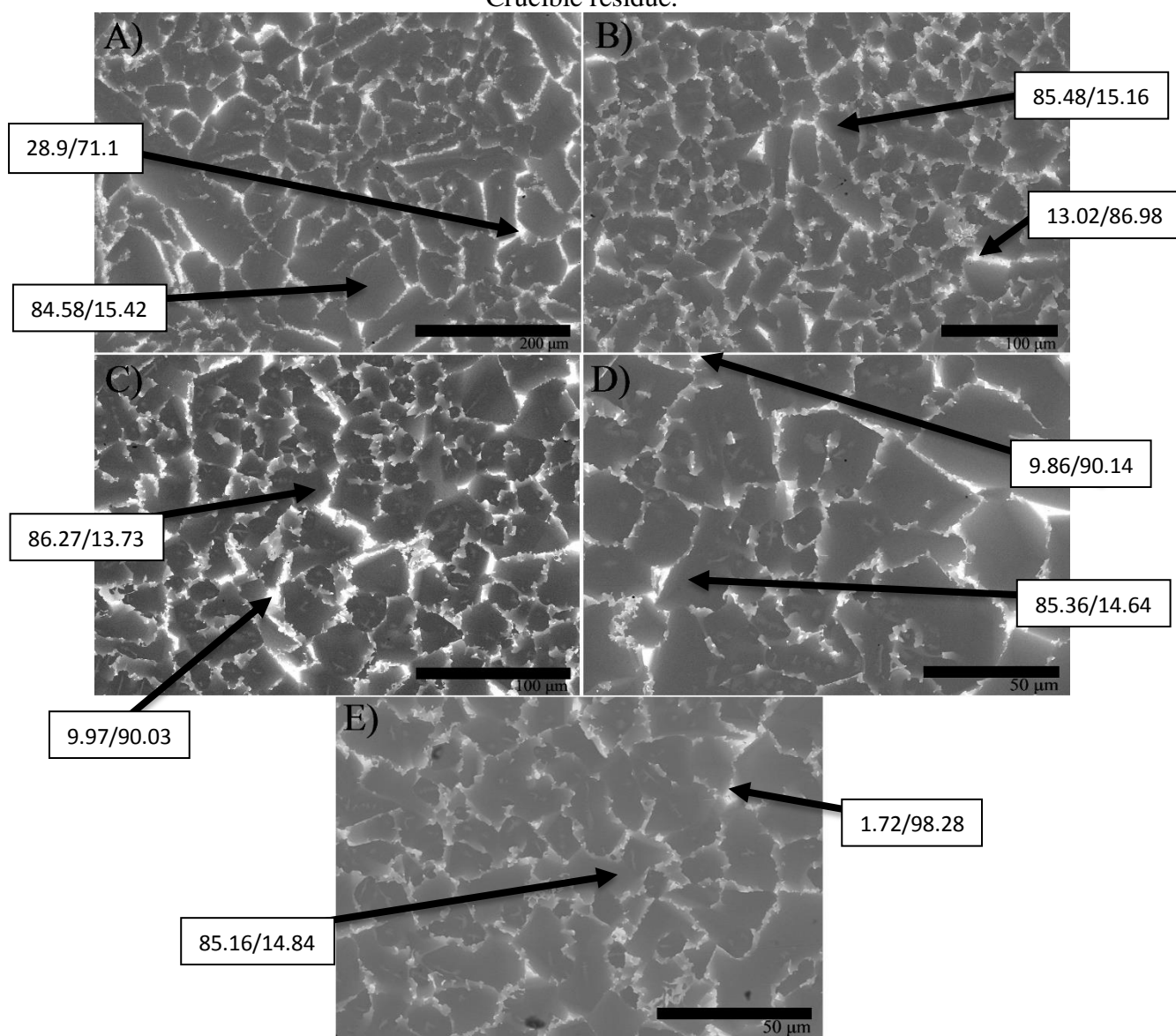
**Table 1.** Average area, in  $\mu\text{m}^2$ , of A) Si-rich grains, B) Ge-rich grains and C) Overall average grain area observed in N number of SEM backscatter micrographs.

Grain size distribution		Average grain area in [ $\mu\text{m}^2$ ] (and standard error)		
		Si-rich grains	Ge-rich grains	Overall average
850 $\mu\text{m}$ < d	N=3	844.57 (93.73)	60.74 (6.95)	264.04 (13.54)
500 $\mu\text{m}$ < d < 850 $\mu\text{m}$	N=4	812.02 (229.61)	40 (3.39)	192.26 (20.97)
300 $\mu\text{m}$ < d < 500 $\mu\text{m}$	N=3	679.4 (10.22)	24.0 (0.72)	132.81 (4.87)
212 $\mu\text{m}$ < d < 300 $\mu\text{m}$	N=4	467.31 (70.62)	17.51 (0.35)	102.47 (3.84)
150 $\mu\text{m}$ < d < 212 $\mu\text{m}$	N=3	321.81 (30.79)	9.75 (0.65)	65.21 (2.44)

**EDS Point Measurements.** EDS area mapping confirmed that all samples showed the same bulk elemental composition ( $\pm 2$  wt. %). EDS point measurements were taken for all samples at regions of maximum Si concentration and maximum Ge concentration and the results can be seen in figures 1 and 2 as wt. % of Si/Ge. The EDS point measurements confirm the higher level of segregation seen in the micrographs of the rapidly solidified samples as the Si-rich grains appear to have a higher Si content than the starting alloy, and Ge-rich grains consistently have over 70% Ge. A high diffusive flux resulting from strong segregation would also help explain the visible dendrite fragments at the centre of some grains.

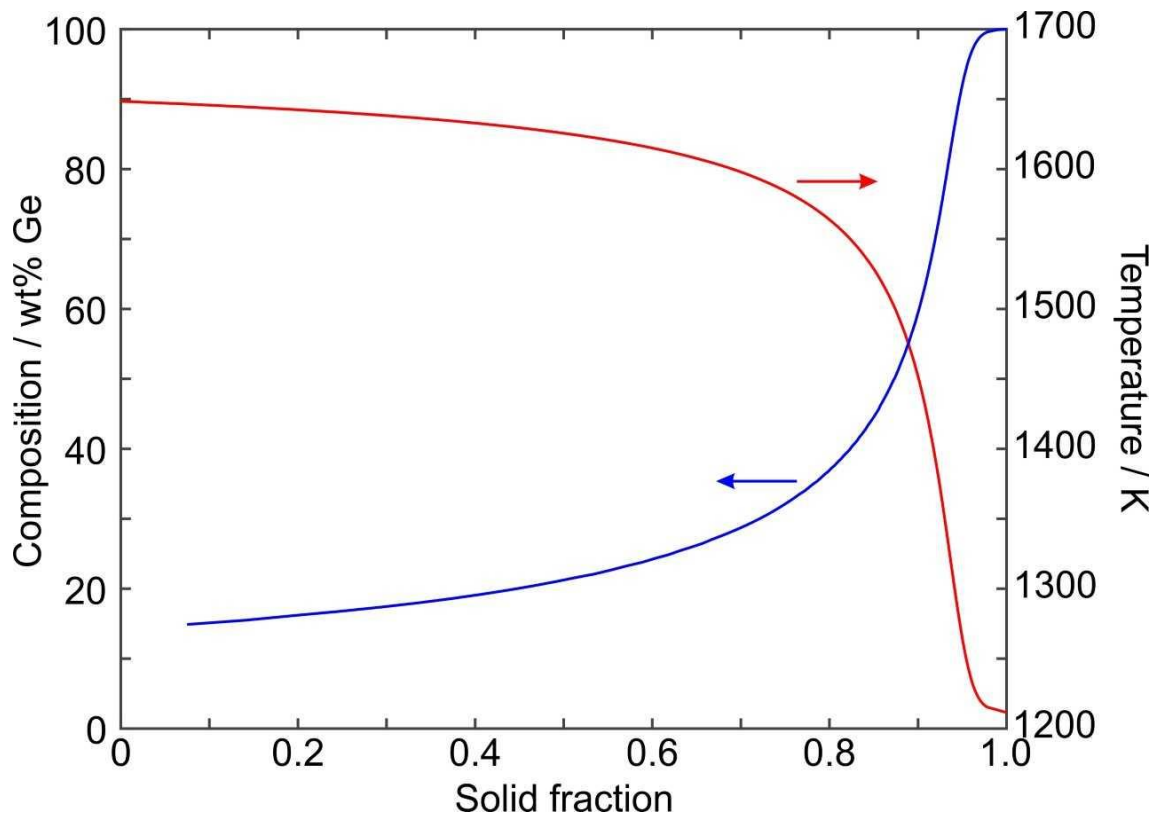


**Figure 1.** SEM backscatter micrographs with EDS point measurements of A) Starting ingot, and B) Crucible residue.



**Figure 2.** SEM backscatter micrographs with EDS point measurements of rapidly solidified samples with particle size fractions of A)  $850\ \mu\text{m} < d$ , B)  $500\ \mu\text{m} < d < 850\ \mu\text{m}$ , C)  $300\ \mu\text{m} < d < 500\ \mu\text{m}$ , D)  $212\ \mu\text{m} < d < 300\ \mu\text{m}$  and E)  $150\ \mu\text{m} < d < 212\ \mu\text{m}$ .

**CALPHAD Modelling.** Fig. 3 shows both the solid fraction (red) and the elemental composition of the growing solid (blue) as a function of solid fraction based upon a Scheil calculation. Noticeably, the solid fraction is seen to be strongly non-linear in the melting interval. The first solid formed is very Si-rich containing 84.3 wt. % Si and 14.7 wt. % Ge. Ge-rich regions are expected to solidify relatively late in the solidification sequence which is consistent with large Si-rich grains surrounded by grain boundaries high enriched in Ge, as observed in Fig. 2. Indeed, last parts of the microstructure to form would be expected to contain the highest concentration of Ge (approaching 100% Ge concentration).



**Figure 3.** Scheil solidification sequence of the growing solid fraction and Ge composition in the growing solid fraction during rapid solidification.

## Conclusion

It was found that the average grain size within the microstructure(s) correlated with the cooling rate, as a higher cooling rate resulted in a smaller average grain size. Both the microstructures found in SEM micrographs and the EDS point measurements seem to agree with the Scheil calculation with large Si grains expected to form first, and the solid fraction of the highest concentration of Ge to form at the end of solidification and occupy the Si grain boundaries. EDS point measurements also showed that the level of segregation found was higher than previously reported.

The formation of a bimodal distribution with Si-rich grains followed by Ge-rich grains was found in the SEM backscatter images but interestingly this was not previously reported despite a similar microstructure found by Zhang et al [5] and Nagai et al [6].

## References

- [1] R. R. King, N. H. Karam and M. Haddad, "Multijunction photovoltaic cells and panels using a silicon or silicon-germanium active substrate cell for space and terrestrial applications.". US Patent US 6340788 B1, 2002.

- [2] C. B. Vining, "Thermoelectric Properties of Silicides," in *CRC Handbook of Thermoelectrics*, 1 ed., N. Sullivan, Ed., CRC Press LLC, 1995, pp. 329-337.
- [3] A. F. Loffe, *Physics of semiconductors*, New York: Academic Press Inc., 1960.
- [4] G. Bernard-Granger, K. Favier, M. Soulier, C. Navone, M. Boidot, B. Deniau, P. Grondin, J. Leforestier and J. Simon, "Thermoelectric properties of an N-type silicon–germanium alloy related to the presence of silica nodules dispersed in the microstructure.," *Scripta Materialia*, vol. 93, p. 40–43, 2014.
- [5] G. H. Zhu, H. Lee, Y. C. Lan, X. W. Wang, G. Joshi, Z. W. Wang, J. Yang, D. Vashaee, H. Guilbert, A. Pillitteri, M. S. Dresselhaus, G. Chen and Z. F. Ren, "Increased Phonon Scattering by Nanograins and Point Defects in Nanostructured Silicon with a Low Concentration of Germanium," *Physical Review Letters*, vol. 102, 2009.
- [6] B. Yu, M. Zebarjadi, H. Wang, K. Lukas, H. Wang, D. Wang, C. Opeil, M. Dresselhaus, G. Chen and Z. Ren, "Enhancement of Thermoelectric Properties by Modulation-Doping in Silicon Germanium Alloy Nanocomposites.," *Nano Letters*, vol. 12, no. 4, p. 2077–2082, 2012.
- [7] L. K. Eckler and D. M. Herlach, "Evidence for Transitions from Lateral to Continuous and to Rapid Growth in Ge-lat%Si Solid Solution.," *Europhysics Letters*, vol. 32, no. 3, pp. 223-227, 1995.
- [8] R. P. Liu, T. Volkmann and D. M. Herlach, "Undercooling and solidification of Si by electromagnetic levitation," *Acta Materialia*, vol. 49, p. 439–444, 2001.
- [9] C. Panofen and D. M. Herlach, "Rapid solidification of highly undercooled Si and Si–Co melts," *Applied Physics Letters*, vol. 88, pp. 171913-171913-3, 2006.
- [10] P. Zhang, Z. Wang, H. Chen, H. Yu, L. Zhu and X. Jian, "Effect of Cooling Rate on Microstructural Homogeneity and Grain Size of n-Type Si-Ge Thermoelectric Alloy by Melt Spinning," *Journal of Electronic Materials*, vol. 39, no. 10, pp. 2251-2254, 2010.
- [11] H. Nagai, Y. Nakata, H. Minagawa, K. Kamada, T. Tsurue, M. Sasamori and T. Okutani, "Synthesis of Si–Ge Alloy by Rapid Cooling in Short-Duration Microgravity," *Japanese Journal of Applied Physics*, vol. 41, pp. 749-753, 2002.
- [12] O. Oloyede, T. D. Bigg, R. F. Cochrane and A. M. Mullis, "Microstructure evolution and mechanical properties of drop-tube processed, rapidly solidified grey cast iron," *Materials Science & Engineering A*, vol. 654, p. 143–150, 2016.
- [13] N. Hussain, A. M. Mullis and J. S. Forrester, "Effect of cooling rate and chromium doping on the microstructure of Al-25 at.% Ni Raney type alloy," *Journal of Alloys and Compounds*, vol. 744, pp. 801-808, 2018.
- [14] J. Schindelin, I. Arganda-Carreras, E. Frise, V. Kaynig, M. Longair, T. Pietzsch, S. Preibisch, C. Rueden, S. Saalfeld, B. Schmid, J.-Y. Tinevez, D. J. White, V. Hartenstein, K. Eliceiri, P. Tomancak and A. Cardona, "Fiji: an open-source platform for biological-image analysis," *Nature Methods*, vol. 9, p. 676–682, 2012.
- [15] R. H. Davies, A. T. Dinsdale, J. A. Gisby, J. A. J. Robinson and S. M. Martin, "MTDATA - Thermodynamics and Phase Equilibrium Software from the National Physical Laboratory," *CALPHAD*, vol. 26, no. 2, pp. 229-271, 2002.

# Applying directional solidification to Cu doped Bi<sub>2</sub>Te<sub>3</sub> thermoelectric materials

Dongmei LIU<sup>1</sup>, Xinzhong LI<sup>2</sup> and Markus Rettenmayr<sup>1</sup>

<sup>1</sup>Otto Schott Institute of Materials Research, Friedrich Schiller University Jena, Löbdergraben 32, D-07743 Jena, Germany

<sup>2</sup>School of Materials Science and Engineering, Harbin Institute of Technology, Harbin 150001, PR China

dongmei.liu@uni-jena.de

**Keywords:** Thermoelectrics; Bi<sub>2</sub>Te<sub>3</sub>; Directional solidification; Homogeneity.

**Abstract.** For understanding the effect of doping with Cu on the thermoelectric performance of Bi<sub>2</sub>Te<sub>3</sub> based materials, anisotropic Cu<sub>x</sub>Bi<sub>2</sub>Te<sub>3</sub> ( $x=0 \dots 0.15$ ) samples were prepared by a tailored zone melting technique. Since thermoelectric properties are extremely sensitive to alloy composition and crystal orientation, a zone melting technique with a seed crystal was developed to ensure the homogeneity of Cu along the growth direction. During directional solidification, growth of Cu<sub>x</sub>Bi<sub>2</sub>Te<sub>3</sub> with a planar interface proceeds from the seed ingot to the sample ingot. The seed alloy is of a different Cu concentration from that of the sample alloy. The seed crystal concentration is chosen from the experimentally determined solute redistribution of Cu during planar growth of Cu<sub>x</sub>Bi<sub>2</sub>Te<sub>3</sub> alloys. At low Cu concentrations, particularly  $x=0, 0.05$ , growth occurs as single phase Bi<sub>2</sub>Te<sub>3</sub>. With increasing Cu concentration ( $x \geq 0.07$ ), the Cu-rich phases Cu<sub>2</sub>Te and (Cu) form. The temperature dependent thermoelectric properties of Cu<sub>x</sub>Bi<sub>2</sub>Te<sub>3</sub> were characterized from 330 to 525 K. Cu doping and increasing Cu concentration leads to a transition from p- to n-type thermoelectric properties. Besides, Cu doping up to  $x=0.07$  contributes to enhanced electrical conductivity and reduced thermal conductivity. Further increase of Cu concentration ( $x=0.15$ ) leads to simultaneous deterioration of Seebeck coefficient and electrical conductivity. The Cu<sub>0.07</sub>Bi<sub>2</sub>Te<sub>3</sub> samples show the highest figure of merit, particularly  $zT=0.82$  at 330 K.

## Introduction

Bismuth telluride (Bi<sub>2</sub>Te<sub>3</sub>) and its alloys are widely used in thermoelectric applications in the temperature range from 200 to 350 K, both for generating power from waste heat and as Peltier cooler. There is a strong need of improving the thermoelectric properties of Bi<sub>2</sub>Te<sub>3</sub> based material for an enhanced working efficiency of thermoelectric devices. The performance of thermoelectric materials can be evaluated by the figure of merit  $zT = \alpha^2 \sigma T / k$ , where  $\alpha$  is the Seebeck coefficient,  $\sigma$  the electrical conductivity,  $T$  the absolute temperature, and  $k$  the total thermal conductivity. Owing to the layered structure of Bi<sub>2</sub>Te<sub>3</sub>, in which quintuple layers (QL) [Te1-Bi-Te2-Bi-Te1] along the  $c$ -axis are the fundamental building blocks, the thermoelectric properties of Bi<sub>2</sub>Te<sub>3</sub> are highly anisotropic. The  $zT$  value perpendicular to the  $c$ -axis,  $zT_{\perp}$ , is generally at least twice of that parallel to the  $c$ -axis,  $zT_{\parallel}$ . Hence, solidification techniques including Bridgman-type directional growth, Czochralski growth and zone melting are widely used to prepare oriented Bi<sub>2</sub>Te<sub>3</sub> samples for fully exploiting the best thermoelectric property direction.

Beside the optimization of thermoelectric properties by modifying the synthesis process, doping with donor or acceptor elements are used to optimize the charge carrier concentration, which is a key feature for excellent thermoelectric properties. Based on studies on Cu doped Bi<sub>2</sub>Te<sub>3</sub>, [1-10], Cu was shown to be a donor element, improving the thermoelectric performance of n-type Bi<sub>2</sub>Te<sub>3</sub>-based alloys. Cu ions partly intercalate between the quintuple layers of the crystal, providing an electron ( $\text{Cu} \rightarrow \text{Cu}^+ + e^-$ ) for electrical conductivity, or as inactive species [11]. It was demonstrated that the Cu atoms can also contribute to enhanced carrier mobility and reduced lattice thermal conductivity ( $k_L$ ) through the formation of Cu nanoparticles [3], resulting in enhanced  $zT$  values. The influence of Cu doping varies depending on the processing method of the sample.

Considering the intercalating behaviour of Cu atoms between Te1 and Te1 layers, the thermoelectric properties of Cu doped Bi<sub>2</sub>Te<sub>3</sub> are expected to be of a more pronounced anisotropy than the undoped material. For Cu doped Bi<sub>2</sub>Te<sub>3</sub>, both Cu concentration and crystallographic orientation play a critical role in the thermoelectric performance. For understanding the fundamentals behind the dependence of the thermoelectric performance in Cu<sub>x</sub>Bi<sub>2</sub>Te<sub>3</sub> alloys on the Cu concentration, oriented samples of

a homogeneous Cu concentration, grown with a {001} plane (quintuple layer) parallel to the growth axis need to be generated. As grain boundaries will induce (equilibrium) segregation of Cu atoms and/or exert an influence on the carrier transport, the density of grain boundaries in the anisotropic sample should be as low as possible. A planar growth interface at a low growth rate is expected to reduce the density of grain boundaries and grain boundary segregation. In the present work, a zone melting technique will be applied to prepare anisotropic  $\text{Cu}_x\text{Bi}_2\text{Te}_3$  samples. Particularly, a seed ingot will be used for achieving a constant Cu concentration throughout the oriented sample. By characterizing microstructure, concentration distribution and thermoelectric properties, a critical Cu concentration for an optimum  $zT$  value of  $\text{Cu}_x\text{Bi}_2\text{Te}_3$  is determined.

## Experiments

### Synthesis

As-cast ingots of  $\text{Cu}_x\text{Bi}_2\text{Te}_3$  ( $x=0, 0.05, 0.075, 0.10$ ) alloys were produced from pure Bi, Te and Cu ( $\geq 99.99\%$  purity) by induction melting. The mixture of the elements was loaded into a quartz tube, which was then evacuated, argon charged with up to 0.6 bar and sealed. During induction melting, strong convection in the melt contributes to an overall homogeneity of the melt. The as-cast sample is  $\sim 10$  mm in diameter and  $\sim 60$  mm in length. The recently developed seeding zone melting technique [12] was applied to grow oriented  $\text{Cu}_x\text{Bi}_2\text{Te}_3$  from the as-cast ingot. A seed of  $\text{Cu}_x\text{Bi}_2\text{Te}_3$  with a Cu concentration twice of the desired Cu concentration of the sample was used. Planar growth of  $\text{Cu}_x\text{Bi}_2\text{Te}_3$  at a growth rate of  $2 \mu\text{m/s}$  started and proceeded from the seed ingot into the sample ingot, aiming for a homogeneous Cu concentration along the growth direction. More details can be found in our previous work [12]. Microstructure and composition were characterized using a scanning electron microscope (SEM) equipped with energy dispersive X-ray spectrometer (EDX). Phase analysis was performed by powder X-ray diffraction (XRD) with Cu  $K_\alpha$  ( $\lambda=1.54056 \text{ \AA}$ ).

### Measurement of thermoelectric properties

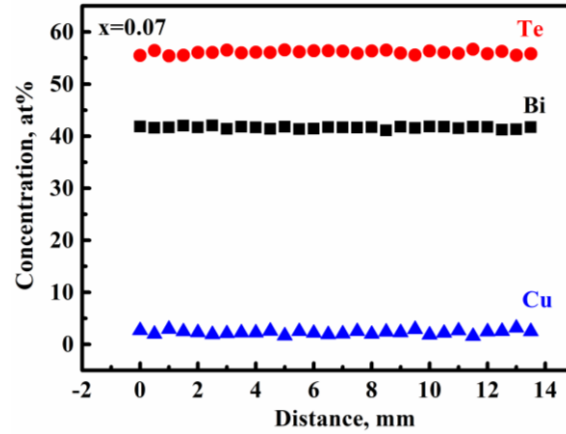
Cuboid samples of about  $3 \times 3 \times 20 \text{ mm}^2$  and disks of  $\varnothing 10 \times 2 \text{ mm}^2$  were cut from the anisotropic  $\text{Cu}_x\text{Bi}_2\text{Te}_3$  samples. Electrical conductivity ( $\sigma$ ) and Seebeck coefficient ( $\alpha$ ) were measured using an LSR-3 device (Linseis Seebeck and Resistivity) in He atmosphere with temperatures ranging from 330 to 525 K. The thermal conductivity ( $k_{\text{tot}}$ ) was calculated from the values of thermal diffusivity ( $\lambda$ ), density ( $\rho$ ) and specific heat capacity ( $C_P$ ) by the relationship  $k = \lambda \rho C_P$ . The Archimedes method was used to measure the density of the samples, yielding  $7.64 \text{ g/cm}^3$ . Thermal diffusivity ( $\lambda$ ) was measured using the laser flash method. The heat capacity,  $C_P$ , was determined by a differential scanning calorimeter (Netzsch STA-449FA). A linear relationship between  $C_P$  and temperature (in K) was suggested based on the experimental data:  $C_P = 0.16 + 4.6 \times 10^{-5} T$ . The above properties were all measured along the directional solidification direction, i.e. allowing property characterization parallel to the basal plane.

## Results and discussion

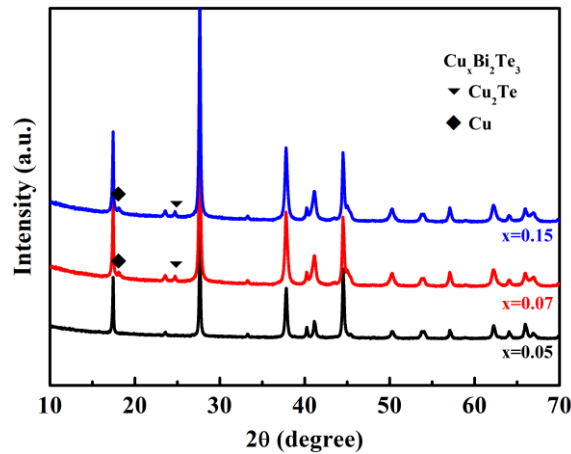
After seeding zone melting, constant concentrations of Bi, Te and Cu along the growth direction were observed. A representative concentration profile of the three elements in  $\text{Cu}_{0.07}\text{Bi}_2\text{Te}_3$  after seeding zone melting is shown in Fig. 1. The concentration of Bi is  $41.5 \pm 0.5 \text{ at\%}$ , the Te concentration is  $56.5 \pm 0.5 \text{ at\%}$ , and the Cu concentration is  $2 \pm 0.5 \text{ at\%}$ . Judging from the composition analysis by EDX, the composition of the seeding zone melting samples deviates from the ratio Bi:Te = 2:3, which may lead to the formation of additional phases or a change of crystal structure. XRD analyses of fine powders of the  $\text{Cu}_x\text{Bi}_2\text{Te}_3$  samples were performed, as shown in Fig. 2. The main diffractions peaks belong to the rhombohedral  $\text{Bi}_2\text{Te}_3$  phase, of which  $a$  is  $4.385 \text{ \AA}$ , and  $c$  is  $30.483 \text{ \AA}$ . For the sample with  $x=0.05$ , only diffraction peaks of the  $\text{Bi}_2\text{Te}_3$  phase were observed. For higher Cu concentrations, particularly  $x \geq 0.07$ , small fractions of  $\text{Cu}_2\text{Te}$  and (Cu) were detected. In comparison with previous work from Han et. al [3] in which  $x=0.08$  was suggested as the upper limit of Cu solubility, the maximum solubility of Cu in  $\text{Bi}_2\text{Te}_3$  in the present work is somewhat smaller. However, it is



consistent with the predicted upper limit of the solubility of Cu in  $\text{Bi}_2\text{Te}_3$  ( $x=0.06$ ) in previous work [12]. It is worth noting that judging from the combination of EDX and XRD results, Cu atoms are supposed to substitute Te atoms and the rhombohedral structure  $\text{Bi}_2(\text{Te,Cu})_3$  forms.

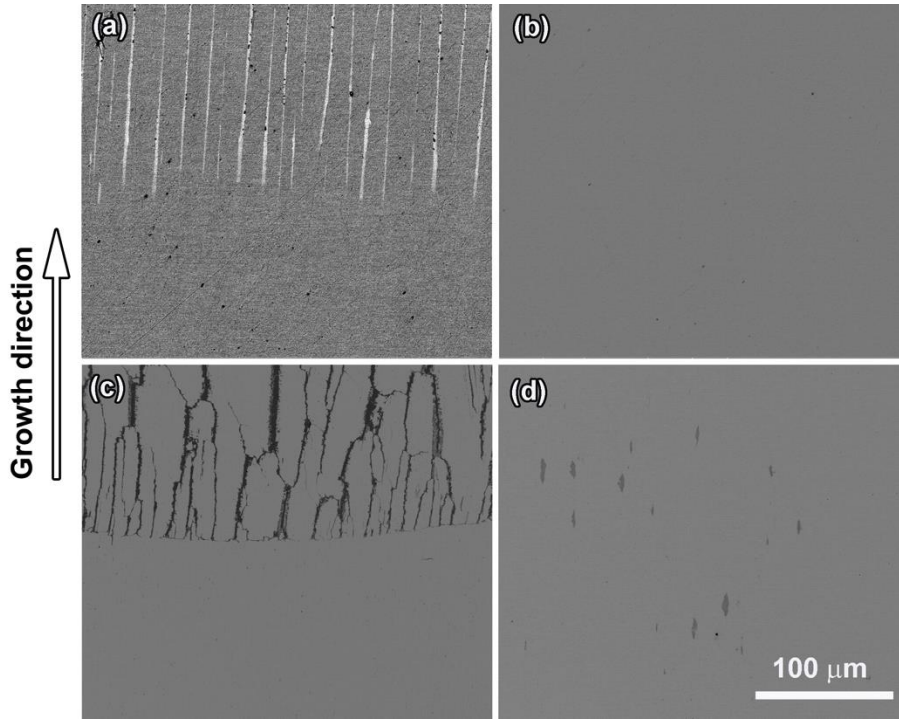


**Figure 1.** Chemical homogeneity of Cu, Bi and Te along the growth direction in anisotropic  $\text{Cu}_x\text{Bi}_2\text{Te}_3$  ( $x=0.07$ ).



**Figure 2.** XRD diffraction patterns of  $\text{Cu}_x\text{Bi}_2\text{Te}_3$  showing the influence of minor amounts of Cu on the constituent phases.

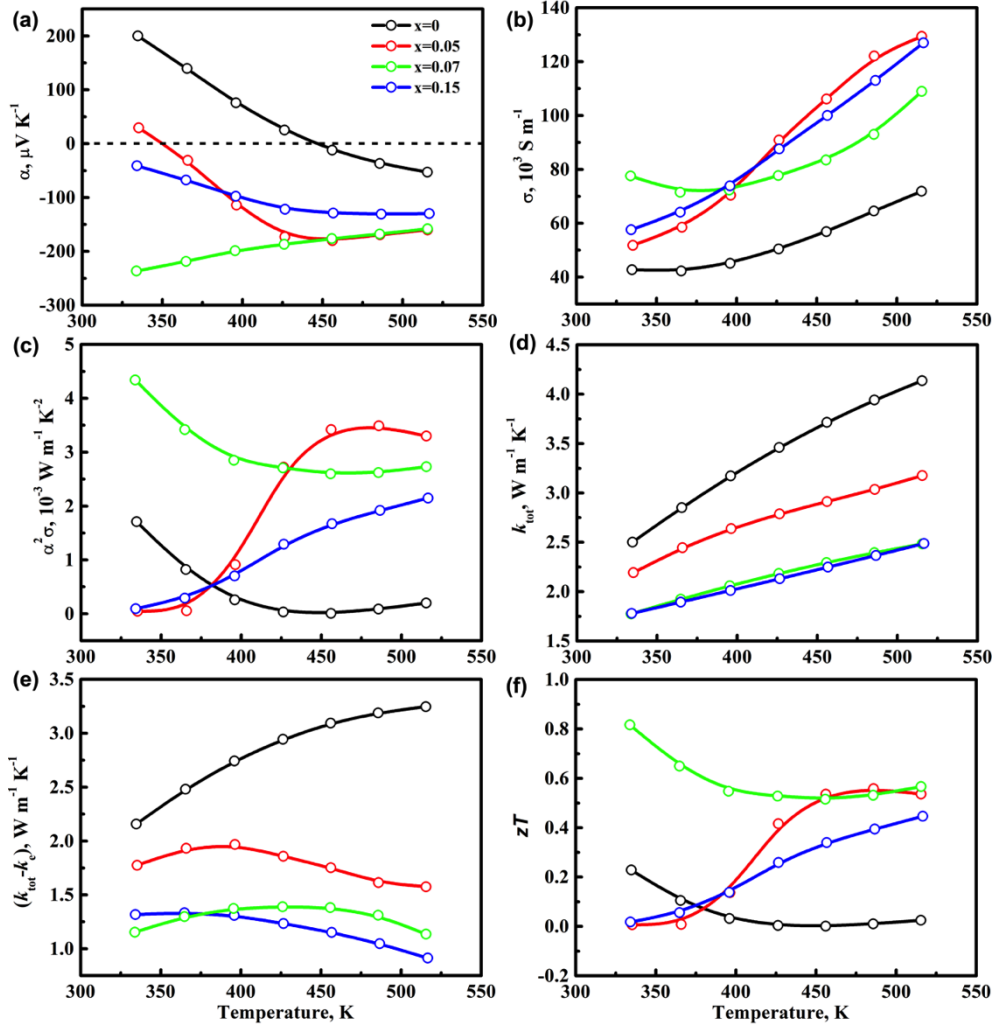
Representative microstructures of seeding zone melted  $\text{Cu}_x\text{Bi}_2\text{Te}_3$  samples grown with a velocity of  $2\text{ }\mu\text{m/s}$ , and the growth interface and the microstructure of the sample part from zone melting, are shown in Fig. 3. A planar quenched solid/liquid interface was observed for all  $\text{Cu}_x\text{Bi}_2\text{Te}_3$  samples, as shown in Figs. 2(a) and 2(c). For the alloy with  $x=0.05$ , only one phase was observed below the quenched solid/liquid interface, as shown in Fig. 3(b). For the sample with  $x=0.15$ , a randomly distributed secondary phase in the  $\text{Bi}_2\text{Te}_3$  matrix (Fig. 3(d)) was observed. It was identified as a Cu-rich phase, either  $\text{Cu}_2\text{Te}$  or (Cu), as suggested from XRD pattern.



**Figure 3.** Microstructures with the quenched solid/liquid interface (left) and zone melted region (right) of  $\text{Cu}_x\text{Bi}_2\text{Te}_3$  after seeding zone melting; (a) (b)  $x=0.05$ ; (c) (d)  $x=0.15$ .

The temperature dependent thermoelectric properties along the growth direction of seeding zone melted  $\text{Cu}_x\text{Bi}_2\text{Te}_3$  are presented in Fig. 4, including Seebeck coefficient  $\alpha$ , electrical conductivity  $\sigma$ , power factor  $\alpha^2\sigma$ , total thermal conductivity  $k_{\text{tot}}$ , ( $k_{\text{tot}} - k_e$ ) where  $k_e$  is the electronic contribution to the thermal conductivity, and the figure of merit  $zT$ .  $k_e$  is calculated based on the Wiedemann-Franz law,  $k_e = L\sigma T$ , where  $L$  is the Lorenz number,  $L=2.44 \times 10^{-8} \text{ W } \Omega \text{ K}^{-2}$ . Without Cu, i.e. for  $x=0$ ,  $\text{Bi}_2\text{Te}_3$  exhibits positive semiconductor behavior (p-type) in the temperature range from 330 to 450 K, and indeed a positive Seebeck coefficient was detected. For further increasing temperature above 450 K, a negative Seebeck coefficient indicating n-type transport behavior was observed. For  $x=0.05$ , although a positive Seebeck coefficient was detected at 330 K, the transition temperature from p- to n-type transport behavior is distinctly reduced in comparison with undoped  $\text{Bi}_2\text{Te}_3$ .  $\text{Cu}_x\text{Bi}_2\text{Te}_3$  samples with  $x \geq 0.07$  exhibit n-type semiconductor behavior in the whole temperature range from 330 to 525 K. The highest Seebeck coefficient was obtained for  $x=0.07$ , whereas with further increasing Cu concentration (e.g.  $x=0.15$ ), a deterioration of the Seebeck coefficient, especially at relatively low temperatures, was observed.

With increasing Cu concentration, the variation of the electrical conductivity of  $\text{Cu}_x\text{Bi}_2\text{Te}_3$  is more complex than that of the Seebeck coefficient. The two samples with  $x=0.05$  and  $x=0.15$  exhibit similar electrical conductivity in the whole temperature range. The other two samples with  $x=0$  and  $x=0.07$  exhibit similar temperature dependence of the electrical conductivity, and the sample with  $x=0.07$  exhibits an enhanced electrical conductivity as compared to that of the alloy with  $x=0$ . As indicated by the temperature dependent Seebeck coefficient, for  $x \leq 0.05$  two types of carriers, particularly electrons and holes, are present. The complex behavior of the temperature dependent electrical conductivity of  $\text{Cu}_x\text{Bi}_2\text{Te}_3$  alloys is due to their complex conduction band structure. As a result, the  $\text{Cu}_{0.07}\text{Bi}_2\text{Te}_3$  sample exhibits the highest power factor at 330 K, i.e.  $4.3 \times 10^{-3} \text{ W m}^{-1} \text{ K}^{-2}$ . This originates from the high Seebeck coefficient of  $-236.5 \mu\text{V K}^{-1}$ , and an electrical conductivity of  $77.6 \times 10^3 \text{ S m}^{-1}$ .



**Figure 4.** Temperature dependent thermoelectric properties of  $\text{Cu}_x\text{Bi}_2\text{Te}_3$  along the growth direction. (a) Seebeck coefficient  $\alpha$ ; (b) electrical conductivity  $\sigma$ ; (c) power factor  $\alpha^2\sigma$ ; (d) total thermal conductivity  $k_{\text{tot}}$ ; (e)  $k_{\text{tot}} - k_e$ ; and (f) figure of merit  $zT$ .

As shown in Fig. 4 (d), all four  $\text{Cu}_x\text{Bi}_2\text{Te}_3$  samples exhibit increasing total thermal conductivity with increasing temperature. Cu additions reduce the total thermal conductivity of the samples with  $x \leq 0.07$ . While  $\text{Cu}_{0.07}\text{Bi}_2\text{Te}_3$  and  $\text{Cu}_{0.15}\text{Bi}_2\text{Te}_3$  exhibit nearly the same total thermal conductivity in the whole temperature range from 330 to 525 K, with a minimum of  $k_{\text{tot}}$  of  $1.78 \text{ W m}^{-1} \text{ K}^{-1}$  at 330 K. The  $\text{Bi}_2\text{Te}_3$  sample exhibits increasing  $(k_{\text{tot}} - k_e)$  with increasing temperature, which results from the bipolar transport effect due to the coexistence of electrons and holes. Doping with Cu as electron donor and formation of  $\text{Cu}_2\text{Te}$  and/or (Cu) can suppress bipolar thermal conductivity and leads to a negative slope of  $(k_{\text{tot}} - k_e)$  vs. temperature. All Cu doped  $\text{Bi}_2\text{Te}_3$  samples exhibit significantly higher  $zT$  values in the higher temperature range (450 to 525 K) than those of undoped  $\text{Bi}_2\text{Te}_3$ . This results from the enhanced power factor and decreased thermal conductivity. Finally, in  $\text{Cu}_{0.07}\text{Bi}_2\text{Te}_3$  at 330 K along the growth direction a  $zT$  value of 0.82 was obtained as the highest  $zT$  value.

### Summary

Zone melting with a seed crystal was applied to Cu doped  $\text{Bi}_2\text{Te}_3$  alloys for enhanced chemical homogeneity of anisotropic  $\text{Cu}_x\text{Bi}_2\text{Te}_3$ . With Cu concentrations exceeding  $x \geq 0.07$ ,  $\text{Cu}_2\text{Te}$  and/or (Cu) form besides the  $\text{Bi}_2\text{Te}_3$  solid solution phase. Thermoelectric properties as a function of Cu doping in  $\text{Bi}_2\text{Te}_3$  were investigated. As electron donor, Cu of sufficient concentration ( $x=0.07, 0.15$ ) leads to change from p-type semiconductor behavior to n-type of  $\text{Cu}_x\text{Bi}_2\text{Te}_3$ . A solid solution of Cu in  $\text{Bi}_2\text{Te}_3$  and the formation of the Cu rich phase contribute to enhanced phonon scattering and reduce

bipolar conductivity. A significantly reduced thermal conductivity accompanied by an increased power factor results in an enhanced  $zT$  ( $zT=0.82$ ) of  $\text{Cu}_{0.07}\text{Bi}_2\text{Te}_3$  as compared to undoped  $\text{Bi}_2\text{Te}_3$ .

## Acknowledgment

Financial support from the German Research Foundation (DFG) under Grant Re1261/15-1 is gratefully acknowledged.

## References

1. T.E. Svechnikova, P.P. Konstantinov, G.T. Alekseeva, Physical properties of  $\text{Bi}_2\text{Te}_{2.85}\text{Se}_{0.15}$  single crystals doped with Cu, Cd, In, Ge, S, or Se, *Inorganic Materials*, 36 (2000) 677-681.
2. W. Liu, Q. Zhang, Y. Lan, S. Chen, X. Yan, Q. Zhang, H. Wang, D. Wang, G. Chen, Z. Ren, Thermoelectric Property Studies on Cu-Doped n-type  $\text{Cu}_x\text{Bi}_2\text{Te}_{2.7}\text{Se}_{0.3}$  Nanocomposites, *Adv. Energy Mater.* 1(2001) 577–587
3. M. Han, K. Ahn, H. Kim, J. Rhyec, S. Kim, Formation of Cu nanoparticles in layered  $\text{Bi}_2\text{Te}_3$  and their effect on ZT enhancement, *J. Mater. Chem.*, 21(2011)11365-11370.
4. H. Yu, M. Jeong, Y. Lim, W. Seo, O. Kwon, C. Park, H. Hwang, Effects of Cu addition on band gap energy, density of state effective mass and charge transport properties in  $\text{Bi}_2\text{Te}_3$  composites, *RSC Adv.* 4(2014)43811-43814.
5. H. Yu, M. Jeong, Y. Lim, W. Seo, O. Kwon, C. Park, H. Hwang, Effects of Cu addition on band gap energy, density of state effective mass and charge transport properties in  $\text{Bi}_2\text{Te}_3$  composites, *RSC Adv.* 4 (2014) 43811-43814.
6. K. Lee, S. Kim, H. Mun, B. Ryu, S. Choi, H. Park, S. Hwang, S. Kim, Enhanced thermoelectric performance of n-type  $\text{Cu}_{0.008}\text{Bi}_2\text{Te}_{2.7}\text{Se}_{0.3}$  by band engineering, *J. Mater. Chem. C*, 3(2015) 10604-10609.
7. F. Hao, P. Qiu, Y. Tang, S. Bai, T. Xing, H. Chu, Q. Zhang, P. Lu, T. Zhang, D. Ren, J. Chen, X. Shi, L. Chen, High efficiency  $\text{Bi}_2\text{Te}_3$  - based materials and devices for thermoelectric power generation between 100 and 300 oC, *Energy Environ. Sci.*, 9(2016)3120-3127.
8. M.K. Han, Y. Jin, D. Lee, S. Kim, Thermoelectric Properties of  $\text{Bi}_2\text{Te}_3$ : CuI and the Effect of Its Doping with Pb Atoms, *Materials*, 10(2017)1235.
9. M. Jeong, J. Tak, S. Lee, W. Seo, H. Koun Cho, Y. S. Lim, Effects of Cu incorporation as an acceptor on the thermoelectric transport properties of  $\text{Cu}_x\text{Bi}_2\text{Te}_{2.7}\text{Se}_{0.3}$  compounds, *Journal of Alloys and Compounds* 696 (2017) 213-219.
10. S. Chen, K. Cai, S. Shen, Influence of Se-doping and/or Bi addition on microstructure and thermoelectric properties of  $\text{Cu}_{0.05}\text{Bi}_2\text{Te}_3$ , *Ceramics International* 43 (2017) 599–603
11. J. Bludska, S. Karamazov, J. Navratil, I. Jakubec and J. Horak, Copper intercalation into  $\text{Bi}_2\text{Te}_3$  single crystal, *Solid State Ionics*, 2004, 171, 251-259.
12. D. Liu, H. Engelhardt, X. Li, A. Löffler, M. Rettenmayr. Growth of an oriented  $\text{Bi}_{40-x}\text{In}_x\text{Te}_{60}$  ( $x= 3, 7$ ) thermoelectric material by seeding zone melting for the enhancement of chemical homogeneity. *CrystEngComm*, 17 (2015) 3076-3081.

# **Morphology of bismuth precipitates in Zn-Bi single crystals for bactericidal applications**

Grzegorz Boczek, Paweł Pałka, Wojciech Spisak, Andrzej Chlebicki

**Keywords:** bismuth precipitates, bactericidal applications, single crystal

## **Abstract**

Bio-compatible materials used in implantation fulfill their functions in applications inside a human body. In the case of using them as elements that connect the organism with the environment, problems arise. Classical bio-compatible alloys are a place preferable for bio-film grows, which in turn leads to serious infections and as a consequence for antibiotic therapy. There are a seriously problems in long-time application these elements as catheters, tracheal tubes, dialysis connectors and other. Extending the working time of such elements would reduce patient suffering and save significant resources for the treatment of infections.

Previous research has shown that one of the most effective methods can be the use of a seemingly toxic metal that is bismuth. Its uniqueness in relation to other heavy metals is that it is not accumulated by the human body.

To verify this theory, the Zn-Bi alloy were investigated. Zinc is a metal friendly to the body, and the ability to make Zn-Bi single crystals gives access to a research material with a strictly controlled distribution of bismuth precipitates in the structure. Single crystals for the tests were prepared using the Bridgman method. The research focused on two Zn-Bi alloy compositions, with a content of 2% and 4% by weight of bismuth. This is the range of the zinc-bismuth eutectic. The solubility of bismuth in zinc is low, so the obtained material was characterized by a mono-crystalline matrix Zn(a) decorated by the precipitates of native bismuth with varying degrees of dispersion. The mechanical, structural and biological aspects of the single crystals were investigated. Mechanical properties were determined in a compression test. Microstructure were observed on SEM with EDS. Microbiological tests including the growth of bacterial and fungal colonies allowed check the most favorable structure for potential medical applications.

# **A Novel Directional Solidification of TiAl-based Alloy Using Y2O3 Mould Coupled with Electromagnetic Cold Crucible Zone Melting Technology**

Hongsheng Ding, Hailong Zhang, Haitao Huang, Ruirun Chen, Jingjie Guo, Hengzhi Fu

**Keywords:** directional solidification, TiAl-based Alloy, Y2O3 mould, microstructure, mechanical property.

## **Abstract**

Light-weight TiAl-based alloys are materials that could potentially be applied in high thrust-to-weight turbine engines in the form of either compressor blades or turbine blades. Normally, the Bridgman directional solidification process, with a ceramic mould, is an effective approach to not only improve the high temperature mechanical properties, but also enable greater geometrical complexity. However, because the high reactivity of TiAl melt it has, an interaction between molten metal and ceramic mould will be initiated during solidification. Thus, in order to decrease mould contamination, a novel directional solidification process was developed for TiAl-based alloys, where a conventional Y2O3 mould was used but the thermally gradient heating was performed coupled with electromagnetic cold crucible (EMCC) zone melting technology. To determine the characteristics of this process, the macro/microstructures and mechanical properties of directionally solidified (DS) Ti45Al2Cr2Nb ingots prepared by two kinds of directional solidification techniques, namely traditional graphite heating (control group) and EMCC heating, were extensively investigated using electromagnetic field and temperature field. Compared with the control group, this new technique can induce bigger electromagnetic force in the tangential direction, generate a more rapid heating and higher temperature gradient, and decrease the interaction between the mould and melt; however the heat transfer is altered to inclining outward owe to the lateral heat transfer. The DS sample prepared by this method can achieve finer columnar crystals growing toward to the axis. Also, it yields well-aligned  $\alpha_2/\gamma$  lamellae at higher heating powers, but lower levels of contamination with regard to Y2O3. These are beneficial to improve mechanical properties of DS TiAl-based alloys, especially as the fracture toughness and tensile properties was being concerned about.

## CHAPTER 10: EUTECTIC, PERITECTIC. MONOTECTIC, FOAM





# Reduced Gravity Processing of Cu-Co Metastable Monotectic Alloy via Drop-Tube Processing

Andrew M MULLIS<sup>1</sup>, Oluwatoyin JEGEDE<sup>1</sup> and Robert F Cochrane<sup>1</sup>

<sup>1</sup>School of Chemical and Process Engineering, University of Leeds, Leeds LS2 9JT, UK  
Corresponding author a.m.mullis@leeds.ac.uk

**Keywords:** Liquid phase separation; Core-shell structures; drop-tube processing

**Abstract.** The metastable monotectic alloy Co-Cu has been subject to rapid solidification under reduced gravity conditions via drop-tube processing. Two alloy compositions were studied, Co-50 at.% Cu and Co-31.5 at.% Cu, with the undercooling required for binodal decomposition estimated as 41 K and 143 K respectively. The resulting particles were classified into 9 size fractions between 850  $\mu\text{m}$  and 38  $\mu\text{m}$ , giving cooling rates between 850  $\text{K s}^{-1}$  and 85,000  $\text{K s}^{-1}$ . Liquid phase separation was observed in both alloys, as were fully spherical core-shell morphologies. A statistical analysis of > 3000 particles across both compositions and all size fractions was undertaken. It was found that for both alloys the incidence of liquid phase separation increased with increasing cooling rate (decreasing particle size). For the Co-31.5 at.% Cu alloy the incidence of spherical core-shell morphologies also increased with increasing cooling rate but for the Co-50 at.% Cu alloy it was found that the incidence of spherical core-shell morphologies peaked in the 106-75  $\mu\text{m}$  size fraction, wherein  $\approx 40\%$  of all particles displayed this morphology. However, with further increases in cooling rate the incidence of core-shell structures decreased rapidly. This is thought to be due to the limited time available for migration of the two melts following liquid phase separation.

## Introduction

Monotectic alloys, such as Al-Bi and Cu-Pb, undergo liquid phase separation when cooled below a critical temperature, forming two immiscible liquids. For metastable monotectic alloys this critical temperature is below the liquidus, meaning that liquid phase separation occurs only in the undercooled melt. Examples of such systems include Ag-Ge, Al-Ag [1], Cu-Fe [2] and Cu-Co [3], among others. Many monotectic systems display a large density difference between the two liquids, making processing under terrestrial conditions problematic due to rapid buoyancy induced separation of the two liquids. However, when such materials are processed in the absence of gravity, buoyancy induced flow is eliminated and a range of unique structures can be accessed. In small droplets core-shell structures, in which a spherical core of one phase is encased in a shell of the other phase, have been observed in both stable [4] and metastable monotectic systems [5].

Such structures arise due to Marangoni convection, that is, flow driven by differences in the surface tensions of the two liquids. In the absence of buoyancy, Marangoni flow may become dominant over small length scales, wherein small temperature gradients across the cooling droplet drive the higher surface tension phase towards the core and the lower surface tension phase towards the surface of the droplet. However, the effect is far from fully understood, with not only core-shell but also three- (core-shell-corona) and even multi-layer structures being observed in some systems [5]. Moreover, some authors have claimed the core is always the lower volume fraction phase [6], while others have claimed it is always the higher melting point phase [4]. Likewise, the balance between migration velocity (increasing with increasing cooling rate) and time available for migration (decreasing with increasing cooling rate) can lead to a range of intermediate states [5] which may further complicate the analysis of such structures.

A number of novel applications have recently been suggested for monotectic alloys including: the formation under rapid cooling of amorphous-crystalline [7] or amorphous-amorphous [8] composites, the fabrication of microporous metals by selective leaching of one of the demixed phases [9], Metal Matrix Composites (MMC's) in which the ceramic particles are confined to one of the demixed phases [10] and the formation of Cu or Ag based core-shell particles which have significant promise for electrical interconnects [4].

In this paper we investigate the metastable monotectic system Co-Cu, processed under reduced gravity conditions in the Leeds 6.5 m drop-tube. Liquid phase separation in undercooled Co-Cu alloys has previously been studied by electromagnetic levitation [3] and in both long- [11] and short- [12] drop-tubes. A range of structures have been reported including Co-rich spherulites [3],  $\alpha$ -Co dendrites at the surface of the droplet with Cu-rich spheres towards the centre [11] and uniformly dispersed Co-rich spheres in a Cu-rich matrix [12]. However, as far as we are aware, there have been no previous reports of core-shell type structures in undercooled Co-Cu melts.

## Experimental Methods

The Co-Cu master alloys for subsequent drop-tube experiments were produced by arc melting elemental Co and Cu together under a protective argon atmosphere. Two alloys were produced, with compositions of Co-50 at.% Cu and Co-31.5 at.% Cu. The equilibrium liquidus temperature for the two compositions, together with the undercooling required for binodal (nucleated) and spinodal (spontaneous) liquid phase separation to occur were determined using the CALPHAD method using the assessed thermodynamic data for the Co-Cu system given by [13].

Rapid solidification processing took place using the Leeds 6.5 m drop-tube facility. Samples of around 9 g were loaded into an alumina crucible which has three  $\times$  300  $\mu\text{m}$  holes laser drilled in the base. The crucible is loaded into a graphite sleeve which is mounted inside an induction coil at the top of the drop-tube. Processing takes place under an inert gas atmosphere at 40 kPa, with the sample being induction heated. When the desired temperature is attained, in this case a 50 K superheat above the notional liquidus temperature for the composition being processed, the crucible is pressurized to 400 kPa, wherein a spray of droplets is produced which subsequently cool and solidify in-flight down the tube. Further details of the drop-tube method are given in [1].

Once collected, the drop-tube powders are sieved into the following standard size ranges: > 850  $\mu\text{m}$  ( $< 860 \text{ K s}^{-1}$ ), 850-500  $\mu\text{m}$  ( $860\text{-}1680 \text{ K s}^{-1}$ ), 500-300  $\mu\text{m}$  ( $1680\text{-}3300 \text{ K s}^{-1}$ ), 300-212  $\mu\text{m}$  ( $3300\text{-}5400 \text{ K s}^{-1}$ ), 212-150  $\mu\text{m}$  ( $5400\text{-}9000 \text{ K s}^{-1}$ ), 150-106  $\mu\text{m}$  ( $9000\text{-}15400 \text{ K s}^{-1}$ ), 106-75  $\mu\text{m}$  ( $15400\text{-}26700 \text{ K s}^{-1}$ ), 75-53  $\mu\text{m}$  ( $26700\text{-}47500 \text{ K s}^{-1}$ ), 53-38  $\mu\text{m}$  ( $47500\text{-}84000 \text{ K s}^{-1}$ ) and < 38  $\mu\text{m}$  ( $> 84000 \text{ K s}^{-1}$ ). Cooling rates, which are shown in parentheses, are calculated based upon the balance of heat fluxes, using the methodology described in [i].

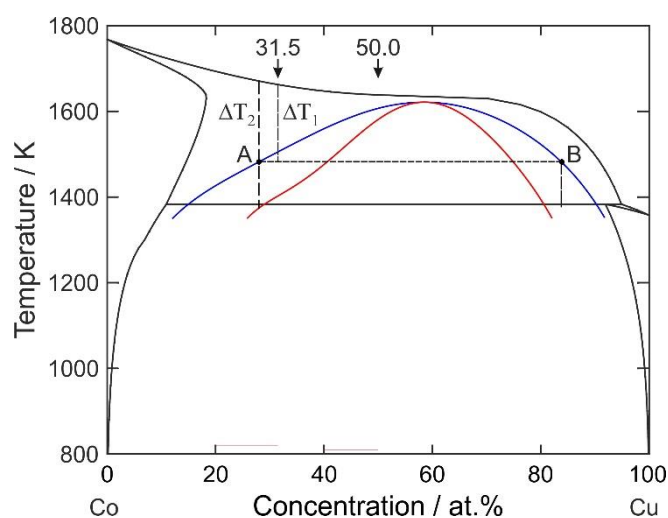
Some of the powders from each sieve fraction were used to confirm the bulk composition using ICP and for oxygen determination using LECO. The remainder were mounted in Transoptic resin and polished to a 1  $\mu\text{m}$  surface finish for microstructural examination, using an Olympus BX51 optical microscope and Carl Zeiss Evo MA15 Scanning Electron Microscope (SEM) which was used in backscatter detection mode. Prior to microstructural examination, samples were etched in Nital solution, this preferentially dissolving the Co-rich phase and thus improving contrast.

## Results

The ICP results confirm that the bulk composition of the drop-tube powders is the same as that of the starting alloy while the LECO analysis gives the oxygen content as  $< 0.02\%$ .

The calculated phase diagram, including the metastable binode and spinode lines, as given by the CALPHAD calculation is shown in Fig.1. The critical composition is 58.7 at.% Cu, wherein liquid phase separation occurs at 1623 K, an undercooling of 13 K. For the 50.0 at.% Cu composition the liquidus, binodal and spinodal temperatures were determined as 1639 K, 1595 K ( $\Delta T = 41$  K) and 1587 K ( $\Delta T = 52$  K) respectively, with the corresponding values for the 31.5 at.% Cu composition being 1662 K, 1519 K ( $\Delta T = 143$  K) and 1406 K ( $\Delta T = 256$  K).

During microstructural analysis a range of microstructures were identified. In all but the smallest sieve fractions, the majority of droplets showed no obvious features associated with liquid phase separation, comprising Co-rich dendrites in a Cu-rich matrix. However, in all size fractions and for both alloys, some particles could always be identified which did display characteristic signs of liquid phase separation. In some cases these were of the core-shell type, in other cases, although clear Co-rich and Cu-rich liquids had formed, the migration required to form separate core and shell had either not occurred or had not gone to completion. Fig. 2 shows an example of (a) a core-shell particle and (b) a liquid phase separated, but non-core-shell particle. In both cases the droplets are of the Co-50.0 at.% Cu composition, with that shown in part (a) being from the 150 – 212  $\mu\text{m}$  size fraction while that shown in part (b) is from the 75 – 106  $\mu\text{m}$  size fraction. Both micrographs are taken using backscatter imaging, wherein the Co-rich phase appears dark and the Cu-rich phase light. In the case of the non-core-shell particle shown in Fig. 2b there is clear evidence that the Co-rich region is evolving towards spherical and we believe that this particular morphology arose due to freezing of the droplet prior to spheroidisation of the core going to completion.

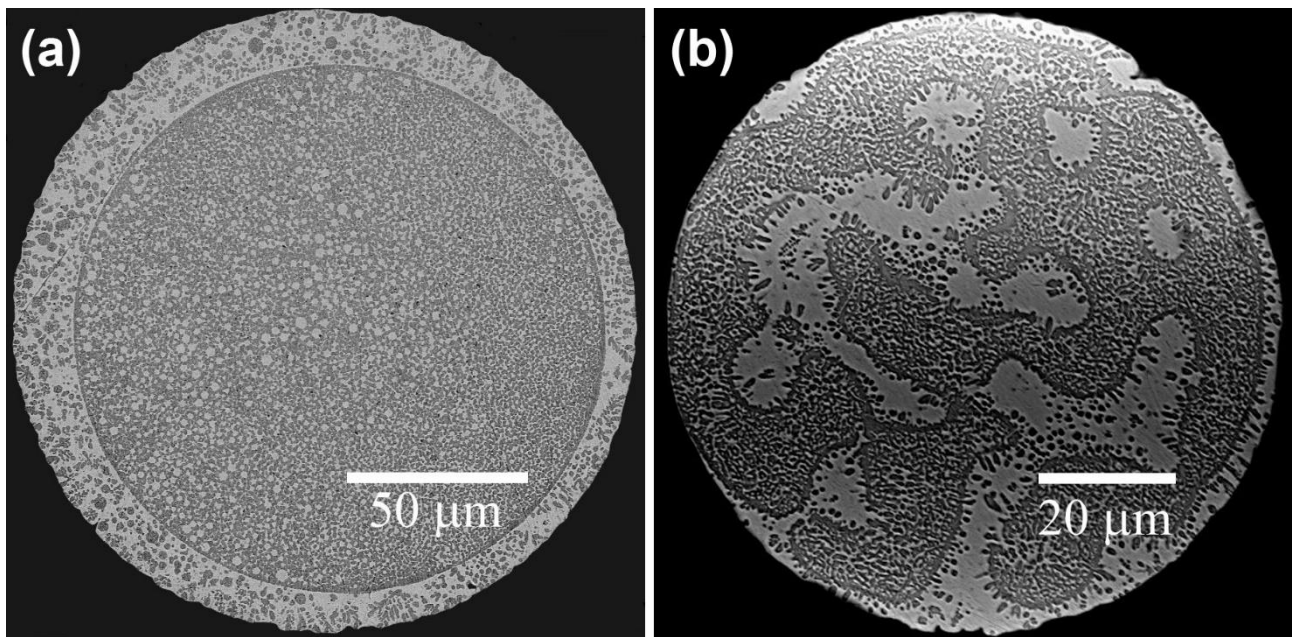


**Figure 1.** Phase diagram for the Co-Cu system showing the metastable binode (blue) and spinode (red). Also shown are the compositions of the two alloys considered in this work. Points ‘A’ and ‘B’ show the compositions of the Co- and Cu-rich liquids formed by binodal decomposition at an undercooling  $\Delta T_1$ . Due to the asymmetry of the phase diagram, further undercooling to  $\Delta T_2$  would result in secondary (spinodal) decomposition of the Co-rich, but not the Cu-rich, liquid.

One feature to note that is common to both microstructures shown in Fig. 2, is the fine dispersion of Cu-rich particles and filaments in the bulk Co-rich region. The very fine nature of this dispersion, together with its interconnected filament like nature, leads us to believe this arises due to spinodal decomposition and is indicative of both samples shown in Fig. 2 of having undergone two episodes of liquid phase separation, binodal, followed by spinodal. Interestingly, where we observe such

instances of double decomposition, we always observe a fine dispersion of Cu-rich filaments in the bulk Co-rich region but only sometimes do we observe the corresponding fine dispersion of Co-rich filaments in the bulk Cu-rich region. Fig. 2a shows both, but in Fig. 2b the fine filament type dispersion is much less widespread in the bulk Cu-rich regions than in the bulk Co-rich region. We believe this arises due to the asymmetry in the binode and spinode lines.

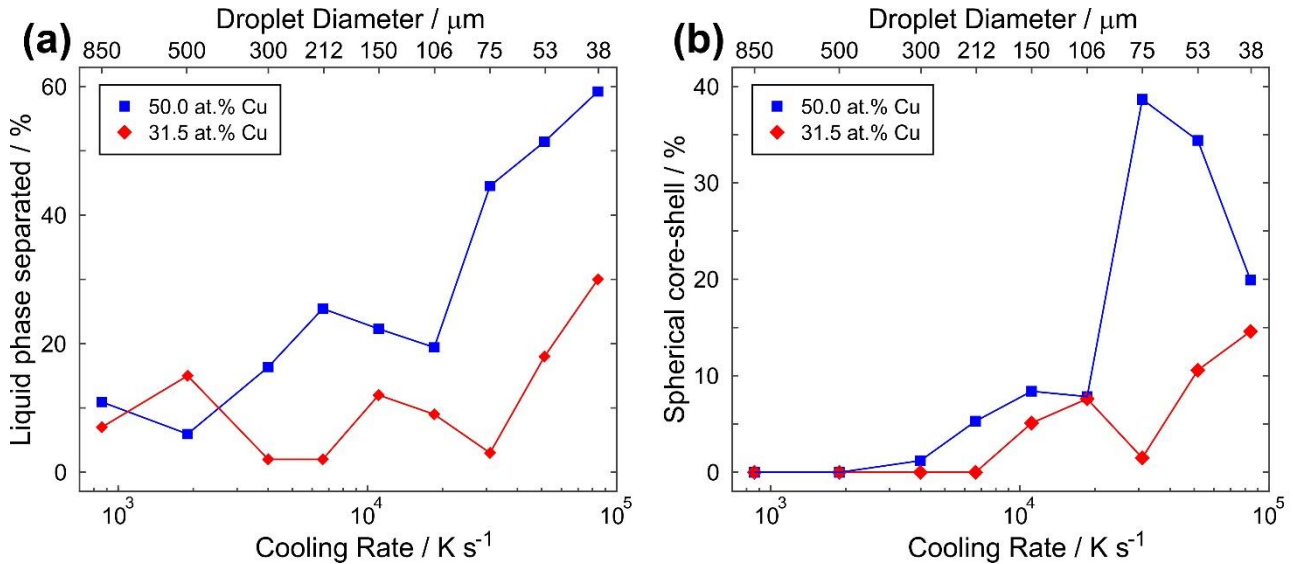
The basic mechanism is illustrated on Fig. 1, for an alloy at 31.5 at.% Cu, although the process would also work for the 50.0 at.% Cu composition. Due to rapid cooling, and the division of the melt into small droplets, the melt will undercool in-flight. As the binodal decomposition is a nucleated transition the first episode of liquid phase separation will not necessarily occur at the binodal temperature, but at some point below this, let us assume at an undercooling  $\Delta T_1$ . Binodal decomposition will result in the formation of Co- and Cu-rich liquids, the composition of which is given by the binode line of the metastable phase diagram. These points are labelled 'A' and 'B' respectively on Fig. 1. With further cooling the total undercooling could now reach a level  $\Delta T_2$ , wherein the Co-rich liquid will reach the spinodal decomposition temperature, with a second episode of spontaneous liquid phase separation occurring. However, due to the asymmetry in the phase diagram the Cu-rich liquid will still be substantially above its spinodal decomposition temperature, wherein secondary decomposition may occur in one phase only, or with sufficient undercooling, both phases.



**Figure 2.** Two liquid phase separated droplets from the Co-50 at.% Cu alloy: (a) displaying a well-developed core-shell structure and clear evidence of secondary (spinodal) liquid phase separation in both the Co-rich and Cu-rich phases and (b) a droplet frozen before full agglomeration of the Co-rich phase to form the core. Note that secondary liquid phase separation is clearly evident in the bulk Co-rich (dark) phase but much less so in the bulk Cu-rich phase.

The stochastic nature of nucleation, both for binodal decomposition and ultimately for solidification, mean that we observe a range of microstructures in all particle size fractions. The prevalence of liquid phase separation as a function of droplet size is shown in Fig. 3a for both the 50.0 at.% and 31.5 at.% Cu alloys. The data contained in the figure is based on a microstructural classification of  $> 1500$  particles for each composition, with not less than 100 particles in any size fraction. The general trend is for the proportion of such droplets to increase with decreasing droplet size, which is as expected as high cooling rates favour deep undercooling as does the lower number

of potential heterogeneous nucleation sites in the smaller droplets. Moreover, the higher undercooling required to access liquid phase separation in the 31.5 at.% Cu alloy means that the prevalence of such droplets is lower in this alloy. Fig. 3b shows, as a proportion of the total number of droplets, the prevalence of particles containing a fully spherical core, as a function of droplet size, wherein a more complex trend is apparent. For the 50 at.% Cu alloy, the incidence of core-shell structures peaks in the 75–106  $\mu\text{m}$  sieve fraction before decreasing sharply for yet smaller particles, despite the increasing incidence of liquid phase separation. This observation can be understood as, at the higher cooling rates, although the undercooling of the melt increases the time available for migration of the Co-rich melt to the core prior to solidification, decreases. Consequently, the incidence of fully spherical core-shell particles decreases. These are replaced by structures which display liquid phase separation, but have not undergone complete core-shell migration, such as that shown in Fig. 2b. The main difference between the two compositions is apparent in Fig. 3b. Specifically, the incidence of fully spherical core-shell particles continues to increase with increasing cooling rate in the Co-rich composition, rather than peaking at some intermediate undercooling, as is the case for the 50-50 (at.%) composition. This may reflect the larger core requiring less time to form as there will be significantly more Co-rich material available following liquid phase separation in the 31.5 at.% Cu alloy.



**Figure 3.** (a) Fraction of droplets, for both compositions, that are observed to undergo liquid phase separation as a function of cooling rate (droplet size) and (b) the fraction of droplets that form fully spherical cores, again as a function of cooling rate (droplet size) and for both compositions.

## Summary

Liquid phase separation has been studied in the metastable monotectic Co-Cu system. Contrary to previous work on this system we find clear evidence for the formation of core-shell structures. A statistical analysis of the prevalence of liquid phase separation and of the formation of core-shell structures has been undertaken. We find that in the 31.5 at.% Co alloy studied, liquid phase separation and core-shell structures are both most prevalent at the highest cooling rates achieved. In contrast, in the 50.0 at.% Cu, although liquid phase separation is still most common at the highest cooling rates, core-shell formation peaks at intermediate cooling rates. This is thought to reflect the time available for migration of the two separated liquids into the core and shell regions.

## References

- [<sup>1</sup>] L. Ratke, G. Korekt, S. Brück, F. Schmidt-Hohagen, G. Kasperovich, M. Köhler, Phase equilibria and phase separation processes in immiscible alloys, in: 2nd Sino - Ger. Symp. (2009).
- [<sup>1</sup>] N. Liu, Investigation on the phase separation in undercooled Cu-Fe melts, *J. Non. Cryst. Solids*. 358 (2012) 196–199.
- [<sup>1</sup>] A. Munitz, R. Abbaschian, Microstructure of Cu-Co Alloys Solidified at Various Supercoolings, *Metall. Mater. Trans. A*. 27 (1996) 4049–4059.
- [<sup>1</sup>] R. Dai, S.G. Zhang, Y.B. Li, X. Guo, J.G. Li, Phase separation and formation of core-type microstructure of Al-65.5 mass% Bi immiscible alloys, *J. Alloys Compd.* 509 (2011) 2289–2293.
- [<sup>1</sup>] C.P. Wang, X.J. Liu, I. Ohnuma, R. Kainuma, K. Ishida, Formation of immiscible alloy powders with egg-type microstructure, *Science* 297 (2002) 990–993.
- [<sup>1</sup>] R.P. Shi, C.P. Wang, D. Wheeler, X.J. Liu, Y. Wang, Formation mechanisms of self-organized core/shell and core/shell/corona microstructures in liquid droplets of immiscible alloys, *Acta Mater.* 61 (2013) 1229–1243.
- [<sup>1</sup>] J. He, H. Jiang, S. Chen, J. Zhao, L. Zhao., Liquid phase separation in immiscible Ag–Ni–Nb alloy and formation of crystalline/amorphous composite *J. Non-crystalline Solids* 357 (2011) 3561–3564.
- [<sup>1</sup>] A. Concustell, N. Mattern, H. Wendrock, U. Kuehn, A. Gebert, J. Eckert, A.L. Greer, J. Sortd, M.D. Baro, Mechanical properties of a two-phase amorphous Ni–Nb–Y alloy studied by nanoindentation, *Scripta Mater.* 56 (2007) 85–88.
- [<sup>1</sup>] H. Yasuda, I. Ohnaka, S. Fujimoto, N. Takezawa, A. Tsuchiyama, T. Nakano, K. Uesugi, Fabrication of aligned pores in aluminum by electrochemical dissolution of monotectic alloys solidified under a magnetic field, *Scripta Mater.* 54 (2006) 527–532.
- [<sup>1</sup>] I. Budai & G. Kaptay, Wettability of SiC and alumina particles by liquid Bi under liquid Al, *J. Mater. Sci.* 45 (2010) 2090–2098.
- [<sup>1</sup>] X. Luo, L. Chen, Investigation of microgravity effect on solidification of medium-low-melting-point alloy by drop tube experiment, *Sci. China Ser. E Technol. Sci.* 51 (2008) 1370–1379.
- [<sup>1</sup>] C. Cao, N. Wang, B. Wei, Containerless rapid solidification of undercooled Cu-Co peritectic alloys, *Sci. China Ser. A Math.* 43 (2000) 1318–1326.
- [<sup>1</sup>] T. Nishizawa, K. Ishida, The Co-Cu (Cobalt-Copper) system, *Bull. Alloy Phase Diagrams*, 5 (1984) 161–165.
- [<sup>1</sup>] O.R. Oloyede, T.D. Bigg, R.F. Cochrane, A.M. Mullis, Microstructure evolution and mechanical properties of drop-tube processed, rapidly solidified grey cast iron, *Mater. Sci. Eng. A*, 654 (2016) 143–150.



# Microstructure evolution and mechanical properties of Co-Fe-Ni-Ti-V eutectic high entropy alloy

Rahul M R<sup>1a</sup>, Reliance Jain<sup>2a</sup>, Sumanta Samal<sup>2b\*</sup>, Gandham Phanikumar<sup>1b</sup>

<sup>1</sup>Department of Metallurgical and Materials Engineering, Indian Institute of Technology Madras, Chennai-600036, Tamil Nadu, India.

<sup>2</sup>Discipline of Metallurgy Engineering and Materials Science, Indian Institute of Technology Indore, Khandwa Road, Simrol, Indore-453552, Madhya Pradesh, India.

<sup>1a</sup>rahulmr1991@gmail.com, <sup>1b</sup>gphani@iitm.ac.in, <sup>2a</sup>phd1701105011@iiti.ac.in, <sup>2b\*</sup>[sumanta@iiti.ac.in](mailto:sumanta@iiti.ac.in)

**Keywords:** Eutectic high entropy alloy (EHEA), Microstructure evolution, Phase equilibria, Pseudo-quasiperitectic reaction, Mechanical property.

**Abstract.** The present study is aimed at understanding the sequence of phase evolution during solidification in Co<sub>25</sub>Fe<sub>25</sub>Ni<sub>25</sub>Ti<sub>20</sub>V<sub>5</sub> eutectic high entropy alloys (EHEAs), synthesized by vacuum arc melting cum suction casting technique. The detailed X-ray diffraction (XRD) and electron microscopic (SEM and TEM) coupled with energy dispersive spectroscopic (EDS) analyses reveal the presence of BCC ( $\beta$ ), FCC\_1 ( $\alpha_1$ ), FCC\_2 ( $\alpha_2$ ) and Ni<sub>3</sub>Ti phases. For Co-Fe-Ni-Ti-V HEA, at first Ni<sub>3</sub>Ti (DO<sub>24</sub>) primary dendritic phase is formed from the liquid, followed by peritectic reaction to form FCC\_1 ( $\alpha_1$ ) phase (i.e. Ni<sub>3</sub>Ti + L  $\rightarrow$  FCC\_1 ( $\alpha_1$ )). Then the remaining liquid undergoes eutectic reaction to form FCC\_1 ( $\alpha_1$ ) and FCC\_2 ( $\alpha_2$ ) phases (i.e. coarse eutectic: L  $\rightarrow$  FCC\_1 ( $\alpha_1$ ) + FCC\_2 ( $\alpha_2$ )). Finally, the remaining liquid undergoes eutectic reaction to form BCC ( $\beta$ ), and FCC\_2 ( $\alpha_2$ ) (i.e. fine eutectic: L  $\rightarrow$  BCC ( $\beta$ ) + FCC\_2 ( $\alpha_2$ )). Therefore, based upon sequence of microstructure evolution, two pseudo-quasiperitectic reactions i.e. L + Ni<sub>3</sub>Ti  $\rightarrow$  FCC\_1 ( $\alpha_1$ ) + FCC\_2 ( $\alpha_2$ ) and L + FCC\_1 ( $\alpha_1$ )  $\rightarrow$  BCC ( $\beta$ ) + FCC\_2 ( $\alpha_2$ ) have been proposed for the investigated EHEA. It is also found that Co<sub>25</sub>Fe<sub>25</sub>Ni<sub>25</sub>Ti<sub>20</sub>V<sub>5</sub> EHEAs retains high strength at elevated temperature.

## Introduction

The complex concentrated high entropy alloys (HEAs) [1-8] consisting multiple principal elements in equiatomic or near equiatomic ratio exhibits simple microstructure of FCC and/or BCC solid solution phase. This is attributed to the several important core effects in HEAs [4, 5] such as high configurational entropy, severe lattice distortion and sluggish diffusion [9, 10]. Yeh et al. [1] first reported CuCoNiCrAl<sub>x</sub>Fe HEAs which shows good strength at elevated temperature up to 500°C. The refractory HEAs such as Nb<sub>25</sub>Mo<sub>25</sub>Ta<sub>25</sub>W<sub>25</sub> and V<sub>20</sub>Nb<sub>20</sub>Mo<sub>20</sub>Ta<sub>20</sub>W<sub>20</sub> alloys have been studied by Senkov et al. [11] which exhibits excellent mechanical properties at high temperatures. Similarly, new class of multicomponent eutectic HEAs [5, 12-14], exhibiting good high temperature strength have also been reported in the open literature. Although a lot of new and exciting research work has been done by many research groups across globe in the field of HEAs to design novel materials for possible industrial applications by choosing elements and composition judiciously in order to obtain unique microstructural features. Therefore, an attempt is made in this direction to develop novel HEA with improved mechanical properties at elevated temperature.

The objective of the present study is to understand the sequence of phase evolution during solidification and to establish new phase equilibria based upon detailed microstructural characterization as well as to evaluate the high temperature mechanical properties in the newly designed multicomponent Co<sub>25</sub>Fe<sub>25</sub>Ni<sub>25</sub>Ti<sub>20</sub>V<sub>5</sub> HEA.

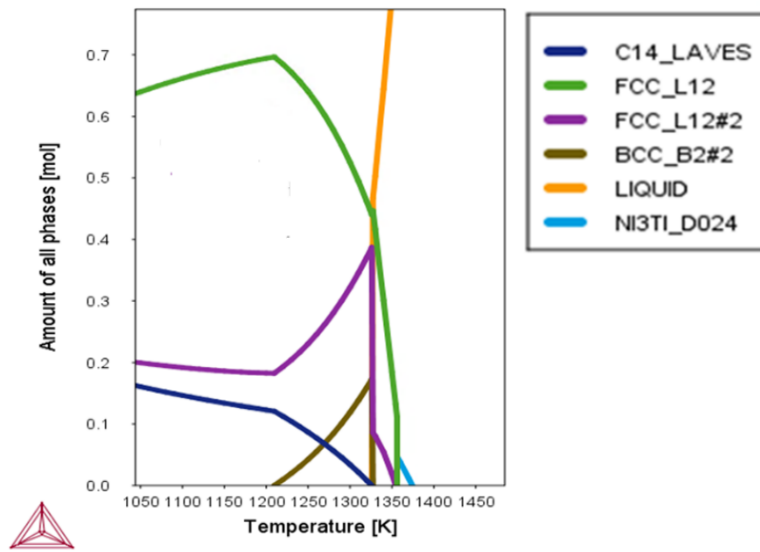
## Experimental materials and procedures

High purity commercial Co, Fe, Ni, Ti and V elements were used as the starting materials to prepare  $Co_{25}Fe_{25}Ni_{25}Ti_{20}V_5$  HEA (henceforth referred to as EHEA) by arc melting technique under ultra high purity argon gas to obtain arc melted alloy button. The structural characterization of studied high entropy alloy was carried by X-ray diffraction (XRD) (Panalytical X-pert pro instrument) with  $Cu-K\alpha$  ( $\lambda = 0.154056$  nm) radiation, operating at 45 kV and 30 mA, with step size of  $2\theta = 0.017$  deg. The peaks in the XRD pattern were identified using International Committee for Diffraction Data (ICDD) database in PCPDFWIN software. The microstructural characterization of the samples was examined using the scanning electron microscope (Inspect F) equipped with an energy-dispersive spectrometer (EDS). Isothermal hot compression tests of the cylindrical samples ( $\phi = 6$  mm and aspect ratio of 1.5:1) were carried out using Gleeble 3800® thermo mechanical simulator at deformation temperatures of 800°C (1073 K) and 1000°C (1273 K) with constant strain rates of  $10^{-1}$ .

## Results and Discussion

### Thermodynamic simulation

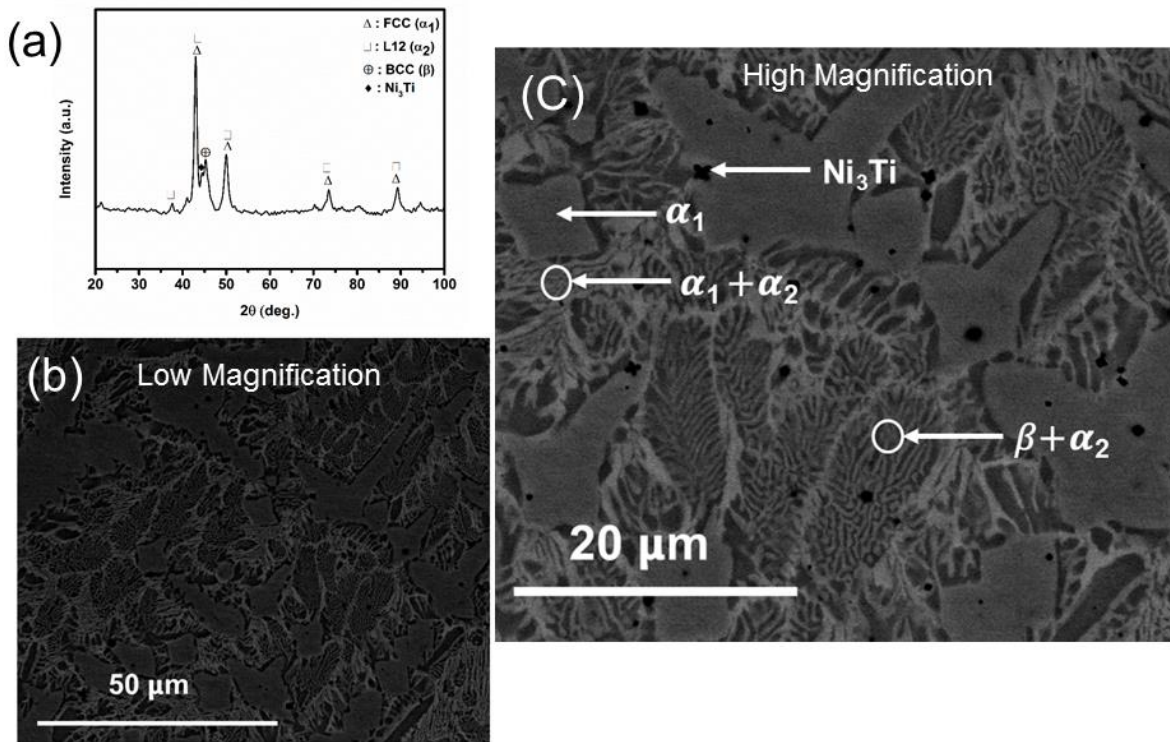
The thermodynamic simulations (as shown in Fig. 1) of studied multicomponent EHEA have been carried out to understand the phase evolution and predict the equilibrium solidification path using TCHEA database in ThermoCalc software. It is observed that there are six equilibrium phases such as Ni<sub>3</sub>Ti\_DO24, FCC\_L12, FCC\_L12#2, BCC\_B2#2, C14\_LAVES and LIQUID phases from liquidus temperature (~1101°C) to 780°C. It is to be noted that at first Ni<sub>3</sub>Ti phase is formed from the liquid, followed by formation of both FCC\_L12, FCC\_L12#2 phases and finally BCC\_B2#2 and C14\_LAVES phases are formed in this temperature range.



**Figure 1.** Thermodynamic simulation of multicomponent  $Co_{25}Fe_{25}Ni_{25}Ti_{20}V_5$  HEA.

### Structural characterization

The XRD pattern of multicomponent EHEA is shown in Fig. 2a. The XRD pattern shows the intense diffraction peaks corresponding to BCC solid solution phase ( $\beta$ ), Disorder FCC1 solid solution phase ( $\alpha_1$ ), Order FCC2(L12) solid solution phase ( $\alpha_2$ ) and ordered Ni<sub>3</sub>Ti\_DO24



**Figure 2.** (a) XRD pattern, (b) and (c) SEM micrograph of multicomponent  $Co_{25}Fe_{25}Ni_{25}Ti_{20}V_5$  HEA. **Microstructural characterization**

The detailed microstructural characterization of multicomponent EHEA was carried out using back scattered electron (BSE) imaging mode in SEM. However, the representative SEM micrograph of the studied HEA is given in Fig. 2b (low magnification image) and Fig. 2c (high magnification image) to decipher the different phases in the microstructure. The different phases in the microstructure of the studied HEA are marked based on the compositional analyses using SEM coupled with EDS. The compositional measurement of each phases in microstructure has also been carried out using TEM coupled with EDS (as shown in Table 1).

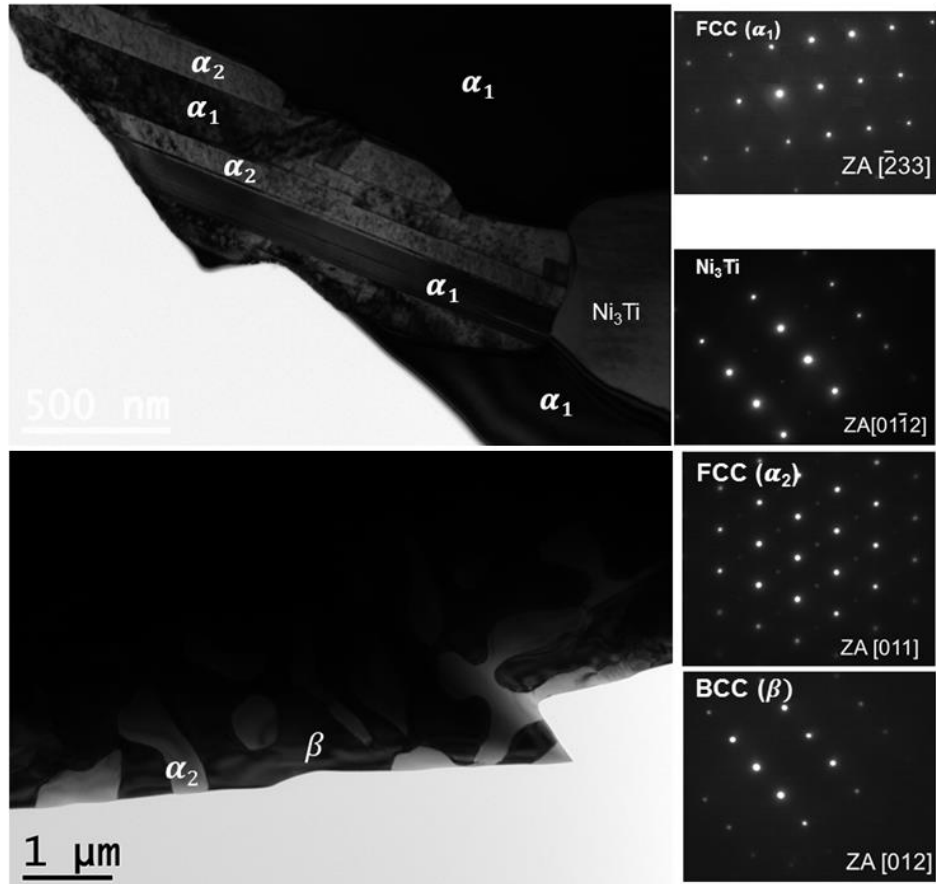
Phases	Co	Fe	Ni	Ti	V
<i>FCC (<math>\alpha_1</math>)</i>	24.20	24.30	22.20	24.40	4.90
<i>FCC (<math>\alpha_2</math>)</i>	25.10	25.70	20.60	24.50	4.10
<i>BCC (<math>\beta</math>)</i>	29.90	30.60	9.90	23.80	5.90
<i>Ni<sub>3</sub>Ti</i>	23.59	22.03	26.97	22.05	5.36

**Table 1.** EDS analysis of all the phases (composition in atomic percent) in microstructure of multicomponent  $Co_{25}Fe_{25}Ni_{25}Ti_{20}V_5$  HEA.

The microstructure of multicomponent EHEA reveals the presence of primary  $(Ni,Fe,Co)_3Ti$  with black contrast, Ni-rich (i.e. Ni-Co-rich phase) solid solution phase with bright contrast ( $\alpha_1$ ) as well as light contrast ( $\alpha_2$ ) and Ni-lean (i.e. Fe-Co-rich phase) solid solution phase gray contrast ( $\beta$ ).

A detailed TEM characterization of the suction cast ( $\phi = 6$  mm) EHEA was done to elucidate the fine scale microstructural features (shown in Fig. 3). The phases in the microstructure are identified using the obtained selected area diffraction (SAD) patterns. The microstructure reveals the presence of two eutectics i.e. (i) one eutectic is between disorder FCC1 solid solution phase ( $\alpha_1$ ) and order FCC2 solid solution phase ( $\alpha_2$ ) and (ii) other one is between order FCC2 solid solution phase ( $\alpha_2$ ) and BCC ( $\beta$ ) solid solution phase as well as two dendritic phases i.e. ordered  $Ni_3Ti_{DO24}$  and disorder FCC1 solid

solution phase ( $\alpha_1$ ). It is important to note that all the equilibrium phases predicted by thermodynamic simulation (Fig. 1) except C14\_LAVES phase are observed in the microstructure of the studied EHEA.



**Figure 3.** TEM micrograph of multicomponent  $Co_{25}Fe_{25}Ni_{25}Ti_{20}V_5$ HEA.

### Phase equilibria in multicomponent $Co_{25}Fe_{25}Ni_{25}Ti_{20}V_5$ HEA

It is important to note from microstructural characterization that there are one peritectic reaction i.e.  $Ni_3Ti + L \rightarrow FCC\_1(\alpha_1)$  and two eutectics reactions i.e. coarse eutectic:  $L \rightarrow$  disorder  $FCC\_1(\alpha_1) +$  order  $FCC\_2(\alpha_2)$  and fine eutectic:  $L \rightarrow$  order  $FCC\_2(\alpha_2) + BCC(\beta)$  features in the microstructure of studied HEA.

The solidification pathways for the investigated multicomponent EHEA has been described in the following;

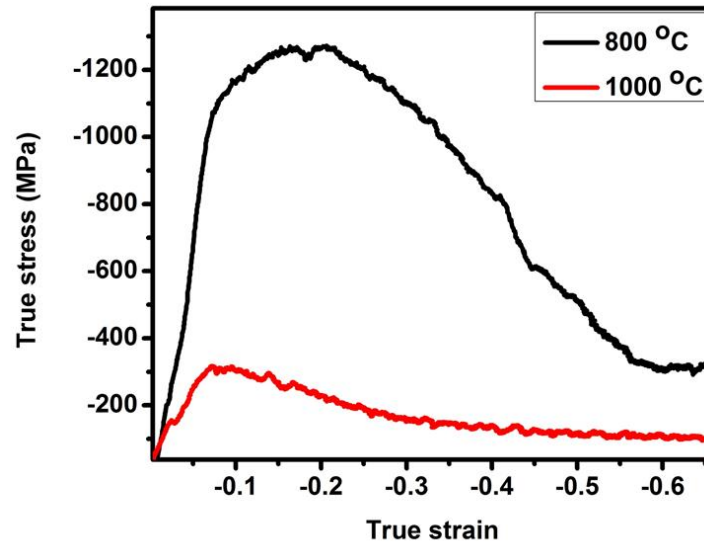
- (i) at first  $Ni_3Ti$  primary dendritic phase is evolved from the liquid during solidification, followed by
- (ii) the peritectic reaction to form disorder  $FCC\_1$  solid solution phase  $FCC\_1(\alpha_1)$  i.e.  $Ni_3Ti + L \rightarrow FCC\_1(\alpha_1)$  and then
- (iii) the remaining liquid undergoes eutectic reaction to form disorder  $FCC\_1(\alpha_1)$  and order  $FCC\_2(\alpha_2)$  phases (i.e. coarse eutectic:  $L \rightarrow FCC\_1(\alpha_1) + FCC\_2(\alpha_2)$ ) and
- (iv) finally, the remaining liquid undergoes eutectic reaction to form order  $FCC\_2(\alpha_2)$  and  $BCC(\beta)$  (i.e. fine eutectic:  $L \rightarrow FCC\_2(\alpha_2) + BCC(\beta)$ )

Based upon the microstructural features observed in the studied multicomponent EHEA, the two different types of four phases reactions i.e.  $L + Ni_3Ti \rightarrow FCC\_1(\alpha_1) + FCC\_2(\alpha_2)$  and  $L + FCC\_1(\alpha_1) \rightarrow FCC\_2(\alpha_2) + BCC(\beta)$  have been proposed for the investigated HEA. These four phase reactions are known as pseudo-quasiperitectic reactions. The first four phases reaction at point P1 is cooperated by two reactions i.e.  $Ni_3Ti + L \rightarrow FCC\_1(\alpha_1)$  and  $L \rightarrow FCC\_1(\alpha_1) + FCC\_2(\alpha_2)$  above and below point P1 respectively. Similarly, the second four phases reaction at point P2 is

cooperated by two eutectic reactions i.e.  $L \rightarrow \text{FCC}_1 (\alpha_1) + \text{FCC}_2 (\alpha_2)$  and  $L \rightarrow \text{FCC}_2 (\alpha_2) + \text{BCC} (\beta)$  above and below point P2 respectively.

### Mechanical properties of $\text{Co}_{25}\text{Fe}_{25}\text{Ni}_{25}\text{Ti}_{20}\text{V}_5\text{HEA}$

The true stress-strain curves of the multicomponent EHEA at different temperatures (700°C (973 K), 800°C (1073 K), 900°C (1173 K) and 1000°C (1273 K) at a fixed strain rate of  $10^{-1} \text{ s}^{-1}$  were obtained for cylindrical samples (diameter ( $\phi$ ) = 6 mm and aspect ratio of 1.5:1). It is to be noted from Fig. 4 that the flow stress decreases with increase in temperature at a constant strain rate of  $10^{-1} \text{ s}^{-1}$ .



**Figure 4.** (a) True stress vs. strain curve of the multicomponent  $\text{Co}_{25}\text{Fe}_{25}\text{Ni}_{25}\text{Ti}_{20}\text{V}_5\text{HEA}$  at 800°C, 1000°C and strain rate of  $10^{-1} \text{ s}^{-1}$ .

It is also observed that after the reaching the yield stress, the studied alloy deforms plastically up to 65 % of true strain value with no fracture of the specimen. It is important to note that the high strength of the studied HEA at high temperature is attributed to the presence of unique composite microstructure i.e. bimodal eutectics at different length scale and peritectic morphology. One major finding of the present study is the presence of two different eutectics at different length scale in the designed multicomponent HEAs. Therefore, this type of unique microstructural features consisting of peritectic and bimodal eutectics at different length scale observed in the studied multicomponent EHEA can be considered as potential candidate for high temperature structural applications.

### Conclusions

Based on the results and discussion with respect to the present investigated multicomponent  $\text{Co}_{25}\text{Fe}_{25}\text{Ni}_{25}\text{Ti}_{20}\text{V}_5\text{HEA}$ , the following conclusion can be drawn;

- The detailed sequence of phase evolution in the newly designed multicomponent HEA has been understood by adopting experimental and thermodynamic simulation approach.
- The new phase equilibria i.e. Pseudo-quasiperitectic reactions have been proposed in the designed multicomponent HEA
- The high strength at elevated temperature is attributed to the unique microstructural features consisting of one peritectic and two types of eutectics in the microstructure.

## References:

- [1] J.W. Yeh, S.K. Chen, S.J. Lin, J.-Y. Gan, T.S. Chin, T.T. Shun, C.H. Tsau, S.Y. Chang, *Adv. Eng. Mater.* 6 (2004) 299–303.
- [2] B. Cantor, I.T.H. Chang, P. Knight, A.J.B. Vincent, *Mater. Sci. Eng. A.* 375-377 (2004) 213–218.
- [3] S. Mridha, S. Samal, P.Y. Khan, K. Biswas, Govind, *Metall. Mater. Trans. A Phys. Metall. Mater. Sci.* 44 (2013) 4532–4541.
- [4] B.S. Murty, J.W. Yeh, S. Ranganthan, *High Entropy Alloys*, Elsevier, 2014.
- [5] S. Guo, C. Ng, C.T. Liu, *Mater. Res. Lett.* 1 (2013) 228–232.
- [6] Y. Zhang, T.T. Zuo, Z. Tang, M.C. Gao, K. A. Dahmen, P.K. Liaw, et al., *Prog. Mater. Sci.* 61 (2014) 1–93.
- [7] S. Samal, S. Mohanty, A.K. Misra, K. Biswas, B. Govind, *Mater. Sci. Forum.* 790-791 (2014) 503–508.
- [8] S. Mohanty, S. Samal, A. Tazuddin, C.S. Tiwary, N.P. Gurao, K. Biswas, *Mater. Sci. Technol.* 31 (2015) 1214–1222.
- [9] K.Y. Tsai, M.H. Tsai, J.W. Yeh, *Acta Mater.* 61 (2013) 4887–4897.
- [10] D.L. Beke, G. Erdélyi, *Mater. Lett.* 164 (2016) 111–113.
- [11] O.N. Senkov, G.B. Wilks, J.M. Scott, D.B. Miracle, *Intermetallics.* 19 (2011) 698–706.
- [12] A.K. Mishra, S. Samal, K. Biswas, *Trans. Indian Inst. Met.* 65 (2012) 725–730.
- [13] S. Samal, Rahul MR, R. S. Kottada, G. Phanikumar, *Mater. Sci. Eng. A*, 664 (2016) 227–235, 2016.
- [14] Rahul MR, S. Samal, S. Venugopal, G. Phanikumar, *J. Alloys Compd.*, 749 (2018) 1115-1127

# Investigation on the Liquid Flow ahead of the Solidification Front During the Formation of Peritectic Layered Solidification Structures

J.P. MOGERITSCH<sup>1</sup>, T. PEIFER<sup>1</sup>, M. Stefan-Kharicha<sup>1</sup>, A. Ludwig<sup>1</sup>

<sup>1</sup>Department of Metallurgy, Chair for Simulation and Modelling Metallurgical Processes, Montanuniversität Leoben, Austria

\*Corresponding author: J.P. Mogeritsch, [johann.mogeritsch@unileoben.ac.at](mailto:johann.mogeritsch@unileoben.ac.at)

**Keywords:** organic model system, peritectic layered structures, Bridgman-furnace, plumes, thermos-solutal convection

**Abstract:** Several studies have been carried out over the last decades to deepen our understanding of peritectic microstructure formation by using the Bridgman technique. In metals, the formation of layered structures, including bands, island-bands or peritectic coupled growth have been observed post-mortem by analyzing quenched samples. To explain these structures, different theoretical models have been published. Instead of taking metals, organic transparent compounds that show a peritectic region are currently used in this study. This technique provides the advantage of observing in-situ the formation of peritectic morphologies and the dynamics of the solid/liquid interface. Visualizing the flow pattern that occurs during the evolution of the peritectic microstructures represents major progress in this discipline. In order to do so, the organic binary system TRIS-NPG was used as model substance and seeding particles as tracers. It was possible to observe (i) the effect of the mushy zone and its influence on the liquid flow ahead of the solid/liquid interface, for a resting sample, and (ii) the flow pattern during solidification of peritectic layered structures. We found that during the evolution within the mushy zone, an upward movement of liquid through temporarily existing liquid channels into the melt, ahead of the solid/liquid interface takes place. Thus, during solidification, the solutal-buoyancy-driven flow pattern that forms in front of the solid/liquid interface is occasionally interrupted by fine upward flows, called micro-plumes. On the one hand, the formation of banded structures is favorable, since the peritectic phase grows via the existing liquid channels within the initial primary phase. Whereby, the formation of the peritectic layered structures seems to be not influenced by the micro-plumes. On the other hand, the spreading of the primary phase in a lateral direction along the solid/liquid interface of the just-formed peritectic phase is probably hindered by micro-plumes.

## Introduction

Within the peritectic region and close to the limit of constitutional undercooling, the primary phase and the peritectic phase can form layered structures [1] like bands, island bands, and peritectic coupled growth (PCG). Such complex structures were found in metals [2-8], whereby, the author investigated [9-16] the dynamic of formation on layered peritectic microstructures by using the binary transparent organic model system TRIS-NPG [17]. Such model substances display a high-temperature non-faceted phase, called plastic crystal. Which solidify similarly to metals. Additionally, the use of transparent substances enables an in-situ observation of the solid/liquid interface dynamic during the formation of peritectic layered patterns. Therefore, it was possible to observe competing growth in the form of oscillating, non-planar coupled solidification structures of the primary and peritectic phases. It has also been shown that layered structures in form of bands lead to PCG. This is due to varied growth of both phases or by multiple nucleation at the solid/liquid (s/l) interface. Since this morphology is highly influenced by thermo-solutal convection, corresponding micro-gravity ( $\mu g$ ) experiments, organized by ESA, will be done aboard the ISS 2019.

In this paper, the influence of thermo-solutal convection on the formation and growth of peritectic layered structures on earth was studied.



## Experimental Set-up

Directional solidification was carried out by using the Bridgman technique. The cooling and heating zone consisted of brass plates, with a guide for a glass sample, encased by a ceramic cover. The temperature in both zones was selected in such a way that the s/l interface is visible within the adiabatic zone. Rectangular glass samples were pulled vertically with a constant velocity PC-controlled through the temperature gradient of  $G_T = 5.6$  K/mm within the adiabatic zone. The sample was illuminated through the adiabatic zone to observe the forming solidification morphology with a light transmission microscope and every 30 seconds pictures were recorded by a CCD camera for a subsequent evaluation.

For visualization of the flow pattern seeding particles were used, in the form of hollow glass spheres HGS [18] with an average distribution size of 2–20  $\mu\text{m}$ . The material density was similar but a little bit larger compare to the melt density; this ensures that the seeding particles approximately follows the flow.

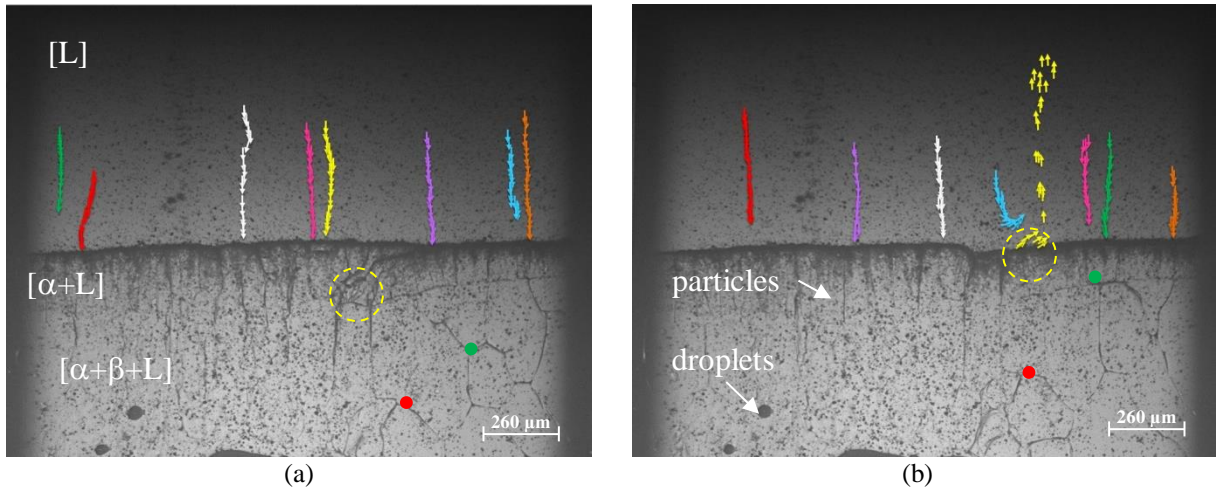
The peritectic model system consists of the two organic substances TRIS and NPG which were obtained as a powder. NPG has the lower melting point and about 20% lower density than TRIS. NPG, with a purity of 99%, and TRIS with 99.9% were used as delivered and alloys within the peritectic concentration ( $0.47 \leq x \leq 0.54$  mol fraction NPG) were prepared within a glove box under an argon atmosphere. The preparation was carried out by mixing in the solid state and homogenization by melting and cooling, respectively. Finally, the alloy was ground to a powder and mixed with HGS particles. The rectangular quartz tubes (100 x 2000  $\mu\text{m}^2$  cross sectional area, 100  $\mu\text{m}$  glass wall thickness) were filled with the organic alloy by capillary force and sealed with an UV-hardening glue. More details of the preparation are given in detail in [16]. The glass sample was placed into the furnace and pulled up at 2000  $\mu\text{m/s}$  in order to homogenize the alloy concentration within the sample. After remaining stationary for 1 h to reach a state of thermal equilibrium, the sample was pulled down at a constant rate of  $0.12 \leq V_p \leq 0.21$   $\mu\text{m/s}$ .

## Results and Discussion

**Micro plumes:** The evolution of the solid and liquid phase within the mushy zone was investigated for a concentration of  $x = 0.54$ . After one hour at rest within the temperature gradient, thermal stability was reached and the s/l interface showed a planar front. The seeding particles' motion in the melt and the dynamics of liquid droplets, channels and grain boundaries within the mushy zone, where the phases  $\alpha$ ,  $\beta$  and liquid coexist, was observed for 27030 s (7.5 h). During this time, the particles sediment due to their slightly higher density following the gravitational force with  $v = 0.66 \pm 0.11$   $\mu\text{m/s}$ . The motion of a few selected individual particles ahead of the s/l interface is visualized by arrows (Fig. 1a), whereby, each arrow represents the alteration of the position within 30 seconds. Once the particles have reached the interface, they accumulate and in particular, they remain unmoved, which highlights the structure of the solidification front, channels, and cracks.

In contrast to the precipitation of the particles, a temporary localized upward movement was observed, as highlighted in Fig. 1b, marked with yellow arrows. Particles were detected, indicating which stream flows upwards from the s/l interface into the liquid in form of a micro-plume. Carefully conducted investigations of the corresponding picture sequences uncover the fact that the particles were initially trapped in a liquid pocket within the solid, shown as a yellow circle in Fig. 1a.

Observations indicate that the upward movement of the particles in the melt causes a local flow noise, recognizable by the change in the direction of the blue arrows, see Fig. 1b. In addition, two grain boundaries (red and green dots) are marked to exhibit the migration by solidification and melting within the three phase region  $\alpha$ ,  $\beta$  and liquid. It can be seen that the migration velocity depends on the position within the mushy zone.

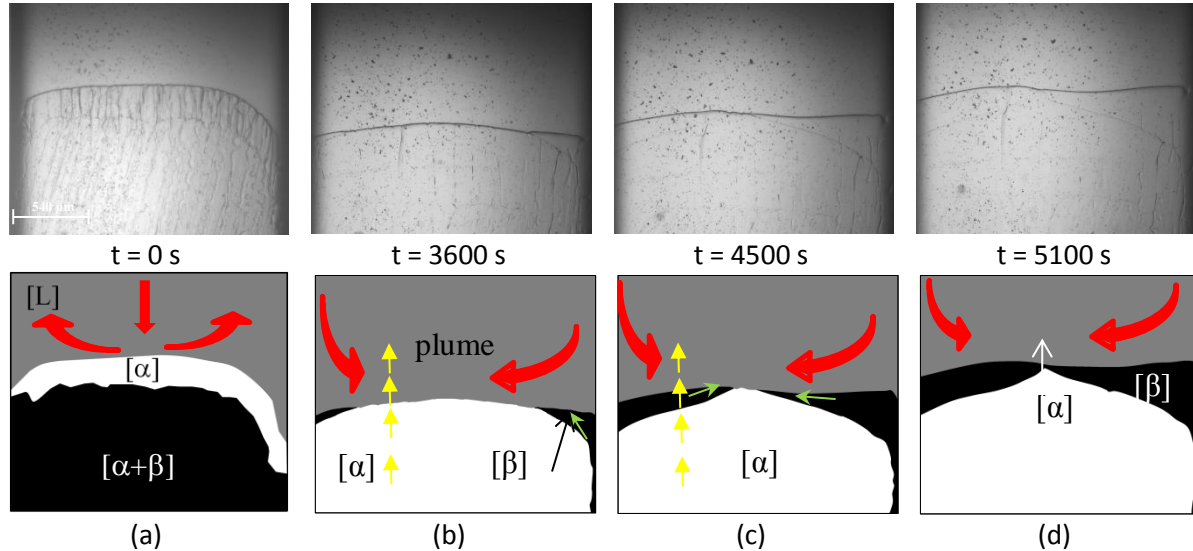


**Figure 1.** Visualization of particle motion in a sample at rest by coloured arrows. The yellow circle marks a liquid pocket and the red and green dots triple points. (a) Time frame is from 810 to 1610 s and (b) from 1650 to 2460 s.

It is important to note that the mushy zone was formed by fast solidification with elongated fine dendrites and corresponding interdendritic liquid. After homogenization a coarse grain structure with traces of the former interdendritic liquid that looked like small channels can be seen. According to the phase diagram the enclosed liquid in the still existing interdendritic liquid is enriched on NPG. Due to the migration of the grain boundaries in the temperature gradient, such high NPG-enriched channels got occasionally connected to the s/l interface. Due to the lower density of NPG-enriched liquid, those ‘open’ channels tends to form micro-plumes with rising flow along the channel towards the melt.

**Layered structures:** The formation of layered structures in the form of bands and the subsequent alteration into a PCG is described in detail for  $x = 0.52$  and pulling velocity  $V_p = 0.174 \mu\text{m/s}$ . In order to better recognize the effects that occur during solidification, an explanatory sketch is attached below the picture (Fig. 2). Initially, there are two solid phases present: the primary  $\alpha$ -phase which forms the planar s/l interface, and at a lower temperature level, the  $\beta$ -phase and eventually remaining  $\alpha$ -phase, (see Fig. 2a). Ahead of the interface, thermosolutal convection showed a downward movement in the center and a corresponding upward motion along the side walls of the sample (red arrows, Fig. 2a). For solidification rates where phases grow in a planar manner, both interfaces try to reach stable growth conditions at the corresponding solidus temperature, and the s/l interface of the  $\alpha$ -phase started to recoil. The interface of the metastable  $\beta$ -phase was frozen and followed the pulling velocity of the sample until the s/l interface of the  $\alpha$ -phase passed the initial temperature level of the  $\beta$ -phase. Here, the  $\beta$ -phase grew through small liquid channels located in the  $\alpha$ -phase close to both glass walls up to the s/l interface. Since the mushy zone is within a temperature gradient, a series of complex processes occur. The microstructural evolution is associated with melting and re-solidification of grain boundaries and migration of liquid pockets. Temporarily, additional liquid channels form by connecting ‘wet’ grain boundaries and/or liquid pockets to the bulk melt. If feeding through a ‘wet’ grain boundary network or a network of liquid pockets is possible, NPG-enriched liquid rises upwards through the liquid channels towards the melt forming micro-plumes, like the one shown in Fig. 2b. This plume originated in a liquid channel in the length of approx.  $1500 \mu\text{m}$  deep into the solid phase. At this temperature level only concentrations close to pure NPG are liquid. Although, a slight fluctuation of the new formed  $\beta$ /l interface was observed, no direct influence on the peritectic band could be detected. However, both effects induced a new convection pattern in the melt, with an upward movement slightly offset from the center and a downward movement along the sidewall of the glass tube.

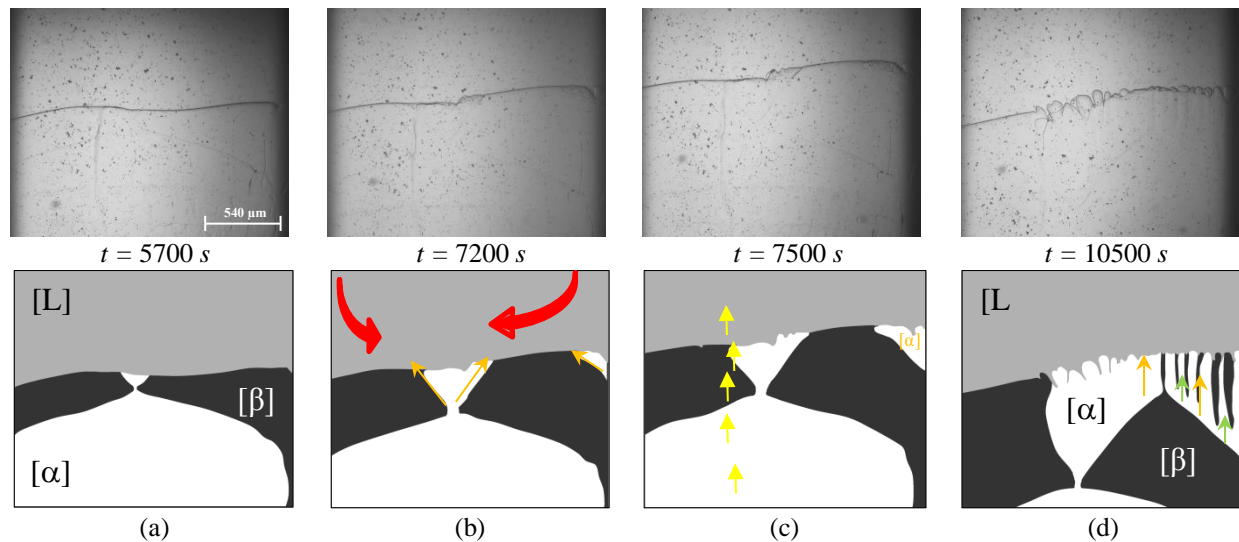
While  $\beta$  is the preferred solidifying phase it spreads out from the side glass wall along s/l interface of the  $\alpha$  phase toward the center. During the growth of the peritectic phase on both side, the micro-plume on the left part is still active (Fig.2c). Shortly before the two  $\beta$ -phase bands were combined in the center, the primary  $\alpha$ -phase became the preferred phase again (Fig. 2d). This can be seen by the fact that the  $\alpha$ -phase expands in a lateral direction, forming the growing triangle shown in Fig. 3a.



**Figure 2.** Formation of two  $\beta$  island bands unaffected by the liquid flow of a NPG enriched plume (yellow arrows). The black dots in the pictures are the seeding particles and the red arrows shows the thermosolutal convection in front of the s/l interface.

Additionally, Fig. 3b shows a newly occurring  $\alpha$ -phase on the right side of the sample. The phase seems to have originated by nucleation at the  $\beta$ /l interface close to the wall. However, a precise determination is not possible. As the primary phase grew along the s/l interface in all directions, two events that initiate the transition to PCG were observed: the micro-plume to the left of the center of the sample and the transition of the new  $\alpha$  interface from planar to cellular growth on the right side of the image (Fig. 3c). The growth of the primary phase from the center to the left edge was stopped as the  $\alpha$ -phase came into contact with the micro-plume. Unlike the spread of the peritectic phase, here, the flow prevented the lateral growth of the  $\alpha$ -phase. This is attributed to the influence of the NPG enriched liquid.

Different to the previously described formation of the two  $\beta$ -island bands, the following can be observed here: (i) At the right side of the sample, the growth in the lateral direction initially did not take place in the full depth of the sample. Rather, a growth of the band near the front and rear glass walls was seen. Furthermore, it seems that this was followed by a partial phase transformation from the existing  $\beta$  phase to the  $\alpha$  phase. (ii) The newly formed  $\alpha$ /l interface changed from planar to cellular growth. At the same time, the preferred phase changed from the primary to the peritectic one, also shortly before both  $\alpha$  island bands linked up. This led to a PCG (Fig. 3d), which finally developed into stable dendritic growth of the  $\alpha$ -phase. (iii) On the left side of the sample, the micro-plume halted the growth of the  $\alpha$ -phase, and  $\beta$  remained the preferred phase. The solidification structure remained planar on the left side and on the right  $\alpha$  and  $\beta$  grew in a PCG manner. As soon as the  $\alpha$ -phase became the ultimately preferred phase on the right side, the entire solidification morphology was dendritic (not shown here).



**Figure 3.** Transformation from banded layered structures to peritectic coupled growth. (a) Shortly before both  $\square$ -island bands are joining together the  $\square$ -phase is the new preferred phase. (b) Additionally, the  $\alpha$ -phase forms a new band coming from the right side. The new band solidifies in a planner manner before the s/l interface becomes unstable and cellular growth occurs (c). The lateral growth of the  $\square$ -phase growing at the center is stopped on the left side by a liquid channel/micro plume. (d) Within the intercellular liquid of the cellular  $\square$ -phase the  $\square$ -phase grows and peritectic coupled growth is formed.

## Conclusions

Peritectic systems show a multitude of layered solidification morphologies at the limit of constitutional undercooling. Such structures are strongly influenced by thermosolutal convection, which is always present on Earth due to the influence of gravity. Solidification experiments were carried out with the transparent peritectic model system TRIS-NPG under 1g conditions. Further experiments are planned under  $\mu g$  one aboard the ISS in 2019. In order to visualize the thermosolutal convection flow for experiments under 1g conditions, seeding particles were added to the organic substances as tracers.

The investigations show a visible influence on the layered structures by the formation of a micro-plumes which has its origin in the former mushy zone of the primary and peritectic phase. The solid is interspersed with melt of lesser density in form of droplets and channels which has it origin in the former interdendritic liquid. Migration movements in the solid form small liquid channels, which leads to the development of micro-plumes. Interestingly, the formation of two  $\beta$ -island bands in combination with the existing micro-plume changed the flow pattern of the thermosolutal convection in the melt ahead of the s/l interface. Despite of the convection occurring in the bulk melt, the formation of peritectic coupled growth was observed.

## Acknowledgement

This research has been supported by the Austrian Research promotion Agency (FFG) in the frame of the METTRANS projects and by the European Space Agency (ESA) in the frame of the METCOMP project.

## References

- [1] R. Trivedi, Theory of layered-structure formation in peritectic systems, *Metal Mater. Trans.* 26 (6) (1995) 1583-90.
- [2] J.H. Lee, J.D. Verhoeven, Peritectic formation in the Ni-Al system, *J. Cryst. Growth* 144 (3-4) (1994) 353-66.
- [3] M. Vandyoussefi, H.W. Kerr, W. Kurz, Two-phase growth in peritectic Fe-Ni alloys, *Acta Mater.* 48 (9) (2000) 2297-306.
- [4] M. Sumida, Evolution of two phase microstructure in peritectic Fe-Ni alloy, *J Alloy Compd* 349 (1-2) (2003) 302-10.
- [5] S. Dobler, T.S. Lo, M. Plapp, A. Karma, W. Kurz, Peritectic coupled growth, *Acta Mater.* 52 (9) (2004) 2795-808.
- [6] Y.Q. Su, C. Liu, X.Z. Li, J.J. Guo, B.S. Li, et al., Microstructure selection during the directionally peritectic solidification of Ti-Al binary system, *Intermetallics* 13 (3-4) (2005) 267-74.
- [7] L.S. Luo, Y.Q. Su, J.J. Guo, X.Z. Li, H.Z. Fu, A simple model for lamellar peritectic coupled growth with peritectic reaction, *Sci. China Phys. Mech. Astron.* 50 (2007) 442-50.
- [8] Z.R. Feng, J. Shen, Z.X. Min, L.S. Wang, H.Z. Fu, Two phases separate growth in directionally solidified Fe-4.2Ni alloy, *Mater Lett.* 64 (16) (2010) 1813-15.
- [9] A. Ludwig, J. Mogeritsch, In-situ observation of coupled peritectic growth, *Solidif. Sci. Technol. Proc. John Hunt Int. Symp.* (2011) 233-42.
- [10] J. Mogeritsch, A. Ludwig, In-situ observation of coupled growth morphologies in organic peritectics, *IOP Conf. Ser. Mater Sci. Eng.* 7 (2011) 12028.
- [11] J. Mogeritsch, A. Ludwig, Microstructure formation in the two phase region of the binary peritectic organic system TRIS-NPG, *TMS Annual Meeting Symposium, Materials Res Microgravity, Orlando, Florida, USA* (2012) 48-56.
- [12] A. Ludwig, J. Mogeritsch, Recurring instability of cellular growth in a near peritectic transparent NPG-TRIS alloy system, *Mater Sci. Forum* (2014) 317-22.
- [13] J. Mogeritsch, A. Ludwig, In-situ observation of the dynamic of peritectic coupled growth using the binary organic system TRIS-NPG, *IOP Conf. Ser. Mater Sci. Eng.* 84 (2015) 12055.
- [14] A. Ludwig, J. Mogeritsch, Compact seaweed growth of peritectic phase on confined, flat pro-peritectic dendrites, *Journal of Crystal Growth* 455 (2016) 99-104.
- [15] J.P. Mogeritsch, A. Ludwig, Investigation on Peritectic Layered Structures by using the Binary Organic Components TRIS-NPG as Model Substances for Metal-Like Solidification, *Crimson Publishers, Res. Dev. Mater. Sci.* 4(1) (2018) 1-3.
- [16] J.P. Mogeritsch, PhD thesis, Leoben, 2012 (available at <http://smmp.unileoben.ac.at>)
- [17] M. Barrio, D.O. Lopez, J.L. Tamarit, P. Negrier and Y. Haget, Degree of miscibility between non-isomorphous plastic phases: Binary system NPG(Neopentylglycol)-TRIS[Tris(hydroxymethyl)aminomethane], *J. Mater. Chem.* 5 (1995) 431-39.
- [18] Information on <https://www.dantecdynamics.com>

# Liquid phase separation and rapid solidification of $\text{Ti}_{60}\text{Y}_{40}$ alloys

Dandan ZHAO<sup>1,2</sup>, Jianrong GAO<sup>1,\*</sup>, Dirk Holland-Moritz<sup>2</sup> and Matthias Kolbe<sup>2</sup>

<sup>1</sup>Key Laboratory of Electromagnetic Processing of Materials (Ministry of Education), Northeastern University, 3-11 Wenhua Road, Shenyang, China

<sup>2</sup>Institut für Materialphysik im Weltraum, Deutsches Zentrum für Luft- und Raumfahrt (DLR), 51170, Köln, Germany

Corresponding author. E-mail: jgao@mail.neu.edu.cn (J. Gao)

**Keywords:** Ti–Y alloys, electrostatic levitation, liquid phase separation, solidification

**Abstract:** A millimetre-sized  $\text{Ti}_{60}\text{Y}_{40}$  sample was electrostatically levitated and melted using infrared lasers. The sample was undercooled far below the monotectic temperature due to containerless melting under high vacuum. The undercooled sample showed two distinct recalescence events during metastable solidification. The formation of a core-shell structure in the solidified samples suggested the occurrence of liquid phase separation prior to solidification. The results are discussed by comparing with those occurring in undercooled Cu–Co alloys.

## Introduction

Liquid phase separation has been observed in many metallic alloys [1–3]. It can be thermodynamically stable or metastable depending on alloy system or composition [4]. The metastable liquid phase separation has attracted much attention because it allows rapid freezing of a dispersed structure by undercooling-induced rapid solidification [5]. One of typical examples is the metastable phase separation in undercooled Cu–Co alloys, which has been investigated using electromagnetic levitation, glass fluxing and drop-tube processing over the past years [6–9]. It was shown that the liquid phase separation kinetics is sensitive to melt convection, which can be damped by electromagnetic levitation under reduced gravity [7] or in static magnetic fields [8]. On the other hand, it was found that liquid phase separation can improve the glass forming ability of Y–Ti alloys [10]. For such reasons, it is of fundamental and technical interest to study liquid phase separation in metallic systems.

The equilibrium phase diagram of the Ti–Y system exhibits a stable miscibility gap in the composition range 30–80 at.% Y [11]. The two elements of it show similar melting temperatures and similar mass densities. Because of these characteristics, the Ti–Y system is regarded as an ideal one for investigating liquid phase separation under normal gravity conditions. However, Ti–Y alloys are susceptible to oxidation because of their high chemical reactivity. Then, containerless processing is the only possible way for access to large undercoolings [12]. While electromagnetic levitation is more often used for containerless undercooling of a bulk melt, it involves strong melt convection due to electromagnetic stirring [13]. Experimental observations [14] and numerical simulation [15] revealed that melt convection in an electrostatically levitated droplet is much weaker than in an electromagnetically levitated one. In addition, cooling of an electrostatically levitated droplet does not require a flow of gas over the sample surface [16]. For such advantages over electromagnetic levitation, electrostatic levitation was chosen to undercool bulk  $\text{Ti}_{60}\text{Y}_{40}$  composition aiming at an understanding of liquid phase separation and subsequent metastable solidification.

## Experimental details

A master alloy of  $\text{Ti}_{60}\text{Y}_{40}$  composition was prepared by arc-melting elemental Ti of 99.995% purity and elemental Y of 99.99% purity under an Ar-atmosphere of 99.9999% purity. The arc-melted ingot was suction cast into a rod-like ingot with a diameter of 3 mm. The suction-cast ingot was sectioned into pieces with a length of about 3 mm and a mass of about 100 mg. Those pieces were remelted into spherical samples in the arc-melting furnace and were stored in a glove box under an Ar-atmosphere with concentrations of  $\text{H}_2\text{O}$  and  $\text{O}_2$  less than 0.1 ppm. A single sample was placed onto a sample holder and positioned in the vacuum chamber of an ESL facility installed at German

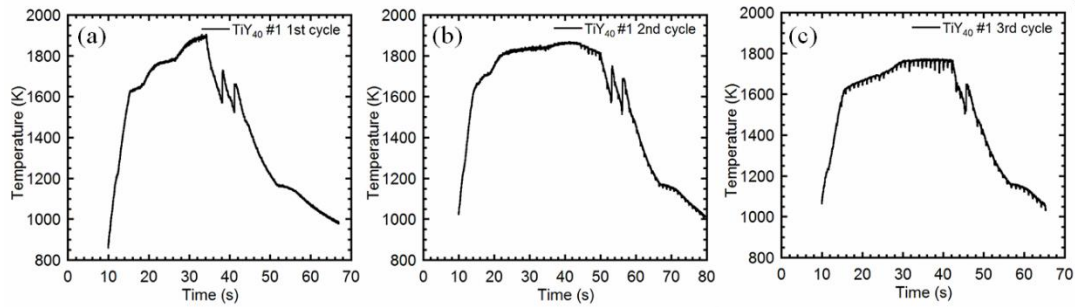
Aerospace Center (DLR), Cologne [16]. The chamber was evacuated to a vacuum of  $10^{-8}$  mbar. The sample was electrostatically levitated in the UHV chamber. Once the levitation was realized and stabilized, the sample was heated and melted using two infrared heating lasers with a maximum power of 75 W and a wavelength of 808 nm. The temperature of the sample surface was measured using a fiber-coupled pyrometer with a sampling rate of 1 kHz and an accuracy of  $\pm 5$  K. The position of the levitated sample was monitored by a video camera, which is integrated in the laser unit. After the power of the heating laser was switched off, the sample cooled by radiating to the vacuum chamber and solidified containerlessly. Due to rapid release of latent heat in solidification, the sample temperature increased, which is known as recalescence. The advancing of the recalescence front on the sample surface were in-situ monitored using an Ultima-APX 755k high-speed camera at a frame rate of 5,000 or 10,000 fps. The sample was remelted and solidified three times to investigate their solidification behavior at different melt undercoolings. The solidified samples were mounted in an epoxy resin. The microstructure of their cross-sections was examined using a LEO 1530 VP scanning electron microscope (SEM).

## Results

### Temperature-time profiles

Fig. 1 shows temperature-time profiles of the levitated  $\text{Ti}_{60}\text{Y}_{40}$  sample in three sequential heating-cooling cycles. The measured temperature signals were calibrated by reference to the eutectic temperature during heating. The eutectic temperature is a well defined temperature that marks the onset of the melting of the sample and that can be easily identified in the temperature-time profiles. Due to a higher emissivity of Ti than that of the Y [17], changes of the distribution of Ti-rich and Y-rich phases in the sample due to phase separation may affect the emissivity of the sample in the liquid or partly liquid state in a way that is difficult to predict. This may result in significant deviations of the measured temperatures from the real temperatures. The sample experienced three thermal events in the first heating cycle (see Fig. 3a). A first event is indicated by a slight and short reduction of the heating rate of the sample. According to the phase diagram of the Ti–Y system [11], this low-temperature event corresponds to a solid-state transition of  $\alpha$ -Ti into  $\beta$ -Ti. A second thermal event brings about a thermal arrest at a temperature of slightly above 1600 K. It corresponds to eutectic melting of  $\beta$ -Ti and  $\alpha$ -Y. A third thermal event is also indicated by a thermal plateau. It corresponds to monotectic melting of  $\beta$ -Ti, but it is higher than it should be, most likely due to an increase of the emissivity of the sample. No clear thermal signal was observed for the mixing of Ti-rich and Y-rich liquids at the binodal temperature because the heat of mixing of the two elements in the liquid state is small. During cooling, the sample showed three thermal events as well. Unlike those observed in heating, two events observed in the high temperature region show a rapid rise of temperature and thus, represent two recalescence events. The second event set in at a slightly lower temperature and shows a slightly smaller rise of temperature. The third event occurring at a much lower temperature produced a plateau, which can be ascribed to the  $\beta \rightarrow \alpha$  transformation. The temperature-time profile of the sample in the second heating-cooling cycle looks similar (see Fig. 1b). However, the second thermal event showed a higher temperature rise during heating than that of the first thermal event. It is unclear if this higher rise is due to changes of the emissivity of the sample associated with liquid phase separation or if it indicates a change of the solidification behavior. The sample was even not heated to the monotectic temperature in the third heating-cooling cycle (see Fig. 1c), but its temperature-time profile showed a recalescence event in cooling. This recalescence event may correspond to solidification of Y-rich liquid. Ti-rich phase is supposed to grow from the liquid on the unmelted Ti-rich core(s) prior to this recalescence.





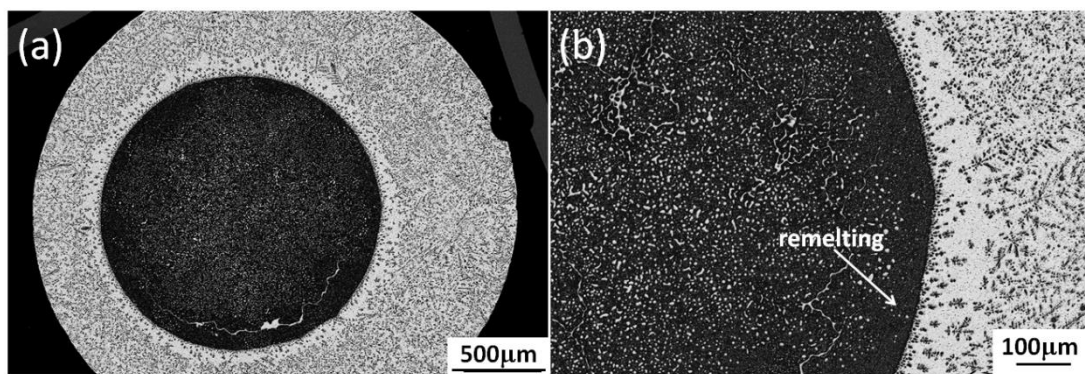
**Figure 1.** Temperature-time profiles of a levitated sample in three heating-cooling cycles.  
(a) 1st cycle (b) 2nd cycle (c) 3rd cycle.

### Solidification microstructure

As shown in Fig. 2a, the sample solidified into a core-shell microstructure during cycle 3. The core is Ti-rich whereas the shell is Y-rich. This core-shell microstructure provided evidence for liquid phase separation. The liquid phase separation may be inherited from the second heating-cooling cycle, because the sample was not heated to the monotectic temperature (see Fig. 1c). Examination of the cross-section of the sample under high magnification provided evidence for secondary phase separation-like features. As shown in Fig. 2b, the Ti-rich core has a dispersion of Y-rich particles in its matrix. The Y-rich shell has a dispersion of fine Ti-rich particles in its matrix. Both Ti-rich and Y-rich particles are supposed to be droplets, which solidified by independent nucleation events during continuous cooling of the sample. Because of relatively high cooling rates, they did not have sufficient time to diffuse out of the matrix and merge with the same species of larger sizes. The micrograph of Fig. 2b also shows a remelting region, suggesting incomplete melting of the sample.

### Thermal imaging of recalescence process

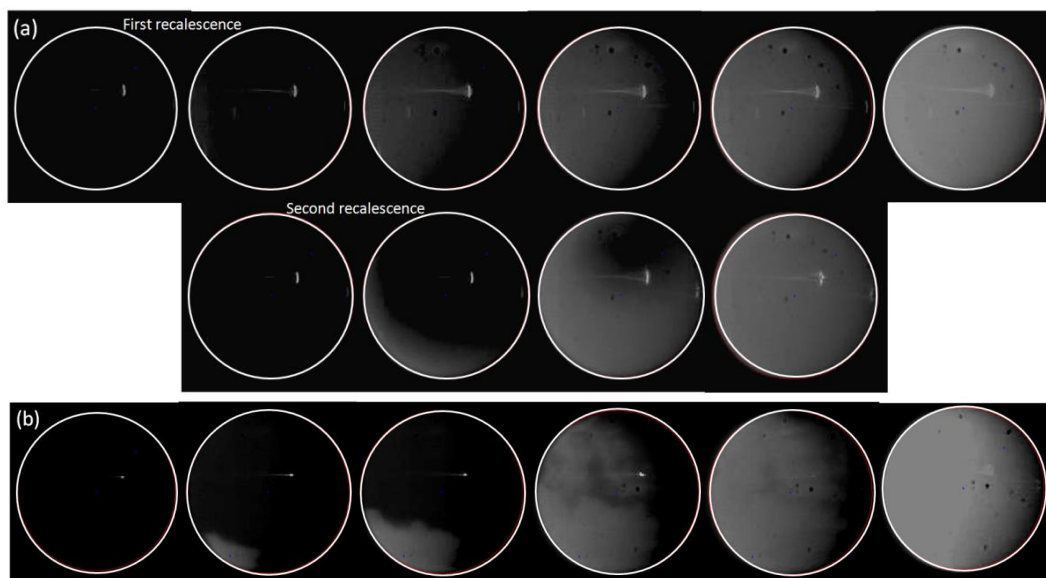
The sample surface during solidification was in-situ monitored using the high-speed video camera. Fig. 3 shows surface images of the sample during recalescence. Their temperature-time profiles are shown in Fig. 1a and Fig. 1c, respectively. Fig. 3a shows the images taken during the first heating-cooling cycle of the sample. The images show the advancing of a smooth thermal front from one side of the sample surface towards the other side of the sample surface in the first recalescence and the advancing of a zig-zagged thermal front in the second recalescence. The images of Fig. 3b also show the advancing of a zig-zagged thermal front from one side towards



**Figure 2.** SEM back-scattering micrographs illustrating the microstructure of the levitated sample.  
(a) overall view (b) remelted zone

the other side of the sample surface. Those images correspond to the recalescence shown in Fig. 1c. While a solidified part of the sample surface appears bright due to release of heat of fusion during crystallization, an unsolidified part appears dark [18]. The recalescence time in all recalescence events was determined by counting the frames of the images. This time amounts to few milliseconds generally. It is one order of magnitude longer than that typically observed for deeply undercooled melts of pure metals, indicating sluggish growth during the solidification event [18]. On the other hand, it is clear that the growth in the second recalescence is faster than the first recalescence in Fig.

3a. The advancing of the thermal front in Fig. 3b showed only one thermal event, which is supposed to be of same origin as the second recalescence of Fig. 3a.



**Figure 3.** High-speed camera video images of the recalescing surface of a levitated sample. The dark and bright parts of the circled area are the undercooled liquid and the solidified part, respectively.

## Discussion

The present results showed that despite high affinity of Ti and Y to oxygen, millimetre-sized droplets of bulk  $\text{Ti}_{60}\text{Y}_{40}$  composition can be significantly undercooled below the equilibrium monotectic temperature. The high melt undercooling inversely can promote liquid phase separation and induce sequential crystallization of two solid solutions from the two separated liquids, respectively. Such an undercooling effect on the solidification of the phase-separated sample is similar to that observed in the binary Cu–Co system [6–8]. However, there are differences between the metastable solidification behaviour of the two systems. The nucleation temperatures of Y-rich and Ti-rich solid solutions are close to each other. Thus, the crystallization sequence of the two solid solutions can be reversed. Because of this possibility, it is difficult to judge the species of primary crystals formed during solidification in terms of the temperature rises of two cascading recalescence events only (see Figs. 1a and 1b). There are two ways to overcome this difficulty. One way is to perform undercooling experiments on Y-richer or Ti-richer bulk compositions to alter the volume fraction ratio of the two separated liquids. Then, the primary solid with a higher volume fraction should show a stronger recalescence and vice versa. The other way is to directly identify the primary crystals by performing in-situ XRD experiments [19]. This second method is quite plausible because the time intervals between the two recalescence events are by a factor of 3 to 10 larger than the temporal resolution, typically 1 s, of the synchrotron radiation XRD experiments. Such experiments are foreseen in future studies.

## Conclusions

A  $\text{Ti}_{60}\text{Y}_{40}$  sample composition has been undercooled by means of electrostatic levitation processing. Large undercoolings have promoted liquid phase separation leading to metastable solidification of two separated liquids with large time intervals. A core-shell microstructure has been frozen in with a Y-rich shell and a Ti-rich core. However, the phase formation sequence in solidification of undercooled and phase-separated Ti–Y melts remains to be determined.

## Acknowledgements

The authors thank F. Yang, B. Nowak and R. Kobold for assistance in the experiments. JG and DDZ are grateful to financial support by the National Science Foundation of China (51271055). DDZ is indebted to the China Scholarship Council for a visiting PhD student fellowship.

## References

- [1] L. Ratke, S. Diefenbach, Liquid immiscible alloys, *Mater. Sci. Eng. Rep.* 15 (1995) 263–347.
- [2] G. Wilde, J. H. Perepezko, Critical-point wetting at the metastable chemical binodal in undercooled Fe–Cu alloys, *Acta Mater.* 47 (1999) 3009–3021.
- [3] P. L. Schaffer, R. H. Mathiesen, L. Arnberg,  $L_2$  droplet interaction with  $\alpha$ -Al during solidification of hypermonotectic Al–8 wt.% Bi alloys, *Acta Mater.* 57 (2009) 2887–2895.
- [4] M. Palumbo, S. Curiotto, L. Battezzati, Thermodynamic analysis of the stable and metastable Co–Cu and Co–Cu–Fe phase diagrams CALPHAD 30 (2006) 171–178.
- [5] X. Song, S. W. Mahon, R. F. Cochrane, B.J. Hickey, M. A. Howson, Liquid phase separation in melt-spun Cu<sub>70</sub>Co<sub>30</sub> ribbon, *Mater. Lett.* 31 (1997) 261–266.
- [6] C. D. Cao, G. P. Görler, D. M. Herlach, B. Wei, Liquid-liquid phase separation in undercooled Co–Cu alloys, *Mater. Sci. Eng. A* 325 (2002) 503–510.
- [7] M. Kolbe, J. R. Gao, Liquid phase separation of Co–Cu alloys in the metastable miscibility gap, *Mater. Sci. Eng. A* 413–414 (2005) 509–513.
- [8] Y. K. Zhang, J. Gao, D. Nagamatsu, T. Fukuda, H. Yasuda, M. Kolbe, J. C. He, Reduced droplet coarsening in electromagnetically levitated and phase-separated Cu–Co alloys by imposition of a static magnetic field, *Scrip. Mater.* 59 (2008) 1002–1005.
- [9] L. Battezzati, S. Curiotto, E. Johnson, N. H. Pryds, Undercooling and demixing in rapidly solidified Cu–Co alloys, *Mater. Sci. Eng. A* 449–451 (2007) 7–11.
- [10] B. J. Park, H. J. Chang, D. H. Kim, In situ formation of two amorphous phases by liquid phase separation in Y–Ti–Al–Co alloy, *Appl. Phys. Lett.* 85 (2004) 6353–6355.
- [11] D. H. Kim, W. T. Kim, E. S. Park, N. Mattern, J. Eckert, Phase separation in metallic glasses, *Prog. Mater. Sci.* 58 (2013) 1103–1172.
- [12] D. M. Herlach, R. F. Cochrane, I. Egry, H. J. Fecht, and A. L. Greer, Containerless processing in the study of metallic melts and their solidification, *Inter. Mater. Rev.* 38 (1993) 273–347.
- [13] J. H. Lee, D. M. Matson, S. Binder, M. Kolbe, D. Herlach, R. W. Hyers, Magneto-hydrodynamic modeling and experimental validation of convection inside electromagnetically levitated Co–Cu droplets, *Metall. Mater. Trans. B* 45 (2014) 1018–1023.
- [14] P.-F. Paradis, T. Ishikawa, G.-W. Lee, D. Holland-Moritz, J. Brillo, W.-K. Rhim, J. T. Okada, Materials properties measurements and particle beam interactions studies using electrostatic levitation, *Mater. Sci. Eng. Rep.* 76 (2014) 1–53.
- [15] R. W. Hyers, Fluid flow effects in levitated droplets, *Meas. Sci. Technol.* 16 (2005) 391–401.
- [16] T. Kordel, D. Holland-Moritz, F. Yang, J. Peters, T. Unruh, T. Hansen, A. Meyer, Neutron scattering experiments on liquid droplets using electrostatic levitation, *Phys. Rev. B* 83 (2011) 104205.
- [17] G. K. Burgess, R. G. Waltenberg, The emissivity of metals and oxides. II. Measurements with the micro pyrometer, *Bulletin of the Bureau of Standards.* 11 (1914) 591–605.
- [18] J. W. Lum, D. M. Matson, M. C. Flemings, High-speed imaging and analysis of the solidification of undercooled nickel melts, *Metall. Mater. Trans. B* 27 (1996) 865–870.
- [19] O. Shuleshova, D. Holland-Moritz, W. Löser, G. Reinhart, G. N. Iles, B. Büchner, Metastable formation of decagonal quasicrystals during solidification of undercooled Al–Ni melts: in situ observations by synchrotron radiation, *EPL* 85 (2009) 36002.

# Investigation on the Binary Organic Components TRIS-NPG as Suitable Model Substances for Metal-Like Solidification

J.P. Mogeritsch<sup>1</sup>, A. Ludwig<sup>1</sup>

<sup>1</sup>Department of Metallurgy, Chair for Simulation and Modelling Metallurgical Processes, Montanuniversitaet Leoben, Austria

\* johann.mogeritsch@unileoben.ac.at

**Keywords:** organic model system, thermal conductivity, vapor pressure, viscosity, peritectic layered structure;

**Abstract.** Metallic solidification structures show a huge variation of patterns, which may be observed in many solidification processes such as casting and welding. To improve our understanding of the formation of these patterns, directional solidification experiments are carried out by using the Bridgman-technique. Hereby, not only metal alloys are investigated, model substances are also considered for this purpose. Such model substances consist of transparent organic components with a non-faceted high temperature (simply called plastic) phase. These organic components solidify like metals, which have the advantage of being able to observe the formation as well as the dynamics of solidification patterns with a standard light microscope. Studies on the formation of layered peritectic solidification structures have been carried out by using the model system TRIS-NPG. So far only very few binary organic systems reveal a peritectic region which is suitable for such experiments. For these rare systems, and especially for the TRIS-NPG system, there is insufficient knowledge of corresponding physical and chemical properties. As further studies on peritectic layered structures are planned on board of the ISS for 2019, it is of utmost importance to discover more about the specific properties of this type of material. Therefore, partial complimentary studies on thermal conductivity, vapor pressure, and viscosity for peritectic concentrations were conducted. The corresponding values are needed for the correct interpretation of the dynamics of peritectic pattern formation, within a temperature gradient in a Bridgman furnace using this model system.

## Introduction

Only organic components that display the formation of a non-faceted (nf) high-temperature (plastic) phase [1], as opposed to the faceted low-temperature phase, are suitable as model systems for metal-like solidification behavior. Such organic substances are optically isotropic and consist of molecules with a globular shape, which act as stacked spherical objects with weak interactions; usually by hydrogen bonds. In the plastic phase, the molecules are more or less free to rotate around their center [2, 3, 4]. Therefore, organic compounds which show a plastic phase are quite attractive to study metal-like solidification morphologies by means of in-situ observation techniques. Investigations on peritectic solidification morphologies require model systems, which show a peritectic reaction within a suitable concentration and temperature range. Currently, only few systems are known which meet the necessary requirements [5]. One of them, the model system NPG (Neopentylglycol)-TRIS (Tris[hydroxymethyl]aminomethane) has been selected by the authors for investigation on peritectic layered structures [6-14]. This system was thermodynamically studied by [5, 15, 16] and the pure substances NPG and/or TRIS investigated by [17-22]. In contrast to metals, organic compounds consist of molecules, therefore, they may have properties in the solidification temperature range which do not occur in metals. Since NPG and TRIS are commercial used at room temperature, their properties at higher temperatures are not well-studied. From publications and material data sheets, it is well-established that NPG is hygroscopic and has the tendency to sublime [23], whereas, the plastic phase stability of TRIS correlates with the selected annealing temperature [26] and is relatively sensitive to impurities [3, 24, 25]. Investigations on peritectic layered structures with a concentration of  $x = 0.5$  mol fraction NPG are to be conducted aboard the International Space

Station (ISS) for 2019. To carry out the in-situ observations under  $\mu\text{g}$  conditions with the model system TRIS-NPG European Space Agency (ESA) designed a Bridgman furnace. One prerequisite for the construction of the device was to design a glass sample which would withstand the mechanical stress of the experiments. Therefore, extensive literature studies on the two pure substances were performed and selected properties of the molecular alloy in the melting range were determined; namely the thermal conductivity, the vapor pressure and the viscosity in the area of the peritectic plateau ( $0.46 \leq x \leq 0.53$  mol fraction NPG). The findings of this research are published in this article.

## Experimental

The experimental setups are described here only briefly. A detailed description of the different scientific investigations is provided in [27].

**Alloy Preparation:** NPG and TRIS, as delivered from Aldrich [28], have a purity of 99 % and 99.9+ %, respectively. An additional treatment process for NPG was applied to reduce the water content by dehydration, as shown in [5]. Since TRIS, as delivered, already has a purity of 99.9+ %, and is thermally sensitive [3, 24, 25], it was used as delivered. The alloys were prepared in an inert atmosphere by mixing the powders of both organic substances and heated up shortly above the melting point [26]. Since NPG has a tendency to sublime, the alloys were prepared in closed glass containers to avoid a shift of concentration by vaporization. The alloy was cooled down to room temperature and subsequently stored in an inert atmosphere until use for further studies.

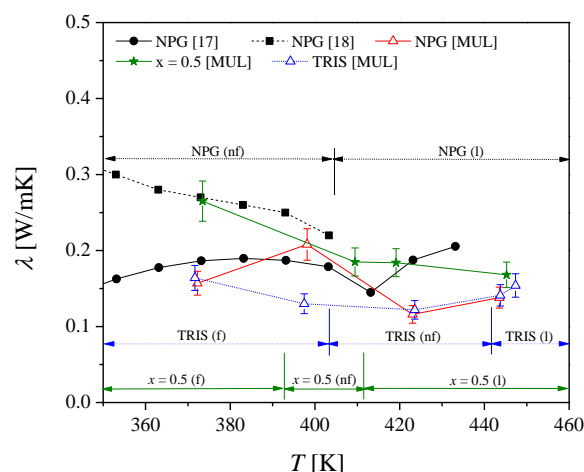
**Thermal Conductivity:** The measurement of the thermal conductivity was performed with the heat conductivity measuring device: type K-system II, according to ASTM D5930-97 standard at normal atmospheric pressure. Further details are in [27]. The measurements were carried out within a temperature range from 373 K to 443 K, for both pure substances and  $x = 0.5$  mol fraction NPG.

**Vapor Pressure:** The experimental equipment consists of an autoclave, the heating system, a thermal Fe-Cu-Ni sensor, a pump, and a digital pressure gauge. For measurements 50 g of the substance was filled into the autoclave and the inner pressure was reduced to -80 kPa. Afterwards, the temperature was raised in incremental steps from room temperature up to 500 K. Three independent experiments were carried out for TRIS, NPG,  $x = 0.3$ ,  $x = 0.5$ , and  $x = 0.7$ .

**Dynamic Viscosity.** The measurement of the dynamic viscosity was conducted by using a Brookfield programmable rheometer DV-III Ultra [29]. The prepared alloy (TRIS, NPG,  $x = 0.4$ ,  $x = 0.5$ , or  $x = 0.6$ ) is placed in a 250 ml beakers and heated until the sample had completely liquefied. To avoid vaporization during the melting process, the beakers were sealed with a foil until the measurements of the viscosity with the rheometer had taken place under normal atmospheric conditions.

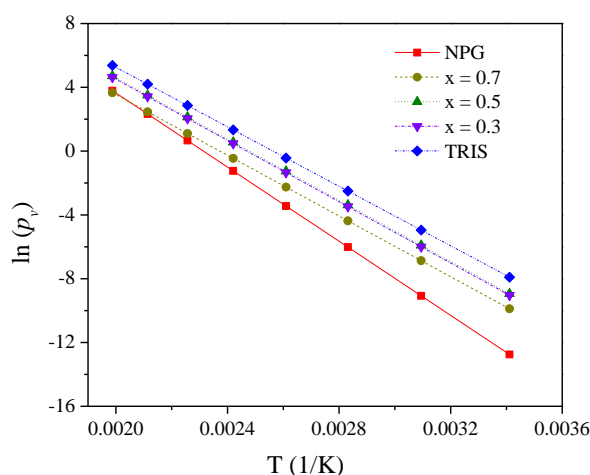
## Results and Discussion

**Thermal Conductivity.** In general, the thermal conductivity,  $\lambda$ , as a function of temperature shows a non-linear correlation. In fact, it depends on the corresponding phase, namely melt, faceted- or plastic phase. To compare the accuracy of the measurement the obtained experimental results and the published values [18, 19] are shown in Fig. 1. The values measured at Montanuniversitaet Leoben (MUL) for the temperature range of the melting point of NPG ( $401.3 \pm 1.0$  K), are within the range of the published results [18, 19]. For the plastic phase, the trend towards thermal conductivity diverges between [18] and [19]. Whereby, the results of MUL correlates with the trend presented in [18], which shows a drop in thermal conductivity at lower temperatures. For TRIS, the experimental data indicate a nearly constant thermal conductivity over the entire investigated temperature range. However, in this case the conductivity slightly increases in the faceted phase with a drop in temperature, and in the melt once the temperature rises. The alloy  $x = 0.5$  shows a correlation between an increasing thermal conductivity and a falling temperature.



**Figure 1.** The graph shows the experimentally obtained values for the thermal conductivity of NPG, TRIS and the alloy of  $x = 0.5$  (observed at MUL), compared to the results published by [18,19].

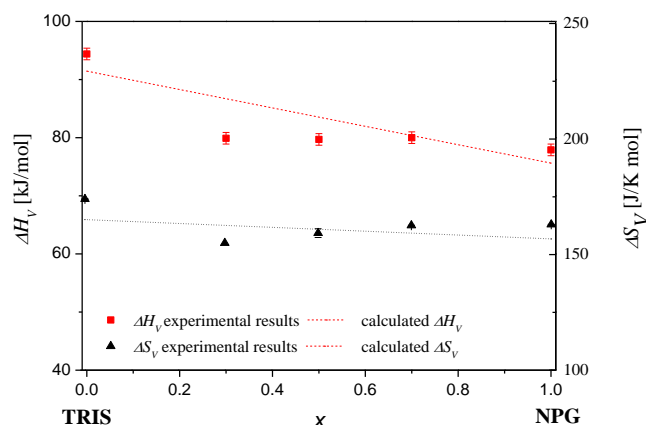
**Vapor Pressure.** With the determination of the vapor pressure,  $p_v$ , the enthalpy,  $\Delta H_v$ , and the entropy,  $\Delta S_v$ , were determined by using the Clausius-Clapeyron relation [30]. This equation can be derived to a simpler first order equation, where the slope multiplied by the gas constant  $R$  is equal to the enthalpy  $\Delta H_v$ . The relation between the logarithm of the vapor pressure and the reciprocal of the temperature, taken from the experimental results, is shown in Fig. 2.



**Figure 2.** Natural logarithm of the vapor pressure at 293 K to 503 K in  $\Delta T = 30$  K steps (dots). The lines are the regression analysis for the vapor pressure.

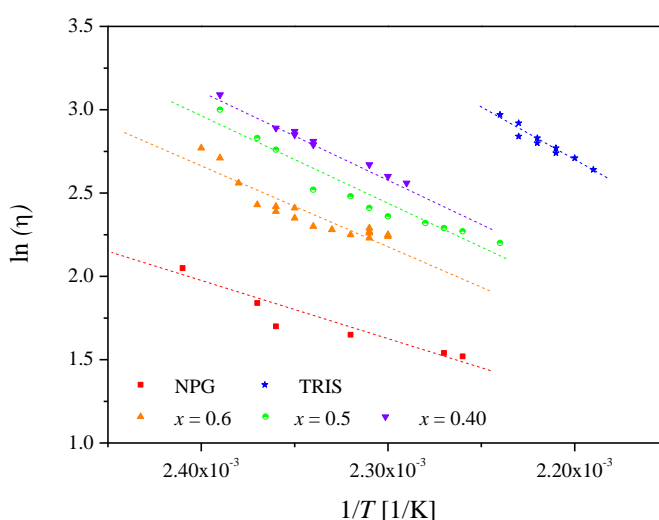
The expected vapor pressure for the entire concentration range is calculated according to Raoult's law [30] and compared with the experimental results (Fig. 3). As a comparison, the study of [13] was used, where  $\Delta H_v$  for NPG is given with 74.7 kJ/mol. The results do not confirm the expected values, but show nearly constant values for NPG and all other alloys with  $\Delta H_v = 78.4 \pm 1.6$  kJ/mol. An exception is TRIS which has a significantly higher  $\Delta H_v$  of  $96.4 \pm 2.3$  kJ/mol.  $\Delta S_v$  has been calculated from  $\Delta H_v$ , divided by the corresponding boiling temperature  $T_b$ . According to Trouton's rule, all alloys and both organic compounds TRIS and NPG show a vaporization entropy value  $\Delta S_v$  above 88 J/K mol, which proves that the organic compounds are associated in the liquid state by hydrogen bonds, irrespective of the specific molecular structure [30].





**Figure 3.** The graph shows the experimental results enthalpy (squares) and entropy (triangles) of vaporization in comparison with the calculated results (broken lines).

**Dynamic Viscosity:** Viscous flow in a homogeneous temperature field is described by the Arrhenius-Andrade equation [30]. A logarithmic application of viscosity,  $\eta$ , and temperature result in a linear correlation, which is depicted in Fig. 4.



**Figure 4.** The figure displays the linear correlation between the logarithms of the measured dynamic viscosity of selective concentrations from organic compounds TRIS and NPG and the reciprocal of temperature. The left end of the regression line is equal to the freezing point.

Based on the experimental viscosity data, the activation energy  $E_a$  can be roughly estimated by applying the Arrhenius-Andrade equation. The energy is in the order of  $E_a = 58.6 \pm 0.2$  kJ/mol for TRIS constantly decreasing to  $27 \pm 0.3$  kJ/mol for NPG.

## Conclusions

It is essential to consider two peculiarities if the TRIS-NPG binary organic system is to be selected as a model substance; the tendency for NPG to sublime and the limited thermal stability of TRIS near the melting point. The thermal stability of TRIS has already been investigated and published by the authors [26]. The sublimation tendency for NPG was taken into account in the sample preparation insofar as the smallest possible gas volume was available above the liquid level.



Concerning thermal conductivity, a decreasing thermal conductivity was measured for the peritectic alloy ( $x = 0.5$ ), with an increasing temperature. It should be noted that this trend does not apply to the two pure substances. Both exhibit an increasing thermal conductivity with increasing temperature in the respective liquid phase(s). By comparing the obtained measured values with the published ones, the thermal conductivity of the liquid phase for the model system TRIS-NPG can be assumed as being in the range of  $\lambda = 0.15 \pm 0.5 \text{ W/m K}$ .

The determination of the vaporization-enthalpy and entropy for the selected alloys follows Raoult's law, exhibiting  $\Delta H_V \sim 80 \text{ J/mol}$  for pure NPG and the investigated alloys. Pure TRIS turns out to be an exception in that it exhibits a vaporization enthalpy of  $94.4 \text{ KJ/mol}$ . The study confirms that the molecules are also connected in the liquid phase via hydrogen bonds, since  $\Delta S_V > 90 \text{ J/K mol}$ .

The viscosity of the liquid is in the magnitude of  $1.0 \pm 0.5 \text{ mPa}\cdot\text{s}$ , comparable with salad vinegar. The investigations facilitate an estimation for the activation energy potential, which is one third of the vaporization enthalpy for NPG; up to one and a half times that value for TRIS. This is a well-established empirical indication and proved to be true for the NPG values. In summary, it can be stated that the different, independent methods of investigation have been able to determine a general tendency of the alloy to behave as both the experimental and simulation data have managed to indicate, and confirm each other in their order of magnitude. For exact determination of the values, it will be necessary to conduct further extensive investigations under both experimental (in-situ) and simulation conditions.

## Acknowledgement

This research has been supported by the Austrian Research promotion Agency (FFG) in the frame of the METTRANS projects and by the European Space Agency (ESA) in the frame of the METCOMP project.

## References

- [1] R. Rudman, Structural relationships between the orientationally disordered (plastic) and ordered phases of tetrahedral molecules, *Solid State Commun.* 29 (1979) 785-7.
- [2] M. Barrio, D.O. Lopez, J.L. Tamarit, P. Negrier and Y. Haget, Degree of miscibility between non-isomorphous plastic phases: Binary system NPG(Neopentyl glycol)\_TRIS[Tris(hydroxymethyl)aminomethane], *J. Mater. Chem.* 5 (1995) 431-9.
- [3] D. Eilerman and R. Rudman, Polymorphism of crystalline poly(hydroxymethyl) compounds. III. The structures of crystalline and plastic tris(hydroxymethyl)-aminomethane, *J.Chem.Phys.* 72 (1980) 5656-66.
- [4] A. Ludwig, K. Greven, Solidification of Metallic Melts in Research and Technology, in: A. Ludwig, *Transparent Model Systems*, Wiley-VCH Verlag, (1999) pp. 61-6.
- [5] M. Barrio, D.O. Lopez, J.L. Tamarit, P. Negrier and Y. Haget, *J. Solid State Chem.* 124 (1996) 29-38.
- [6] A. Ludwig, J. Mogeritsch and M. Grasser, In-situ observation of unsteady peritectic coupled growth, *Trans. Ind. Inst. Metals* 62 (2009) 433-6.
- [7] J.P. Mogeritsch, S. Eck, M. Grasser and A. Ludwig, In situ observation of solidification in an organic peritectic alloy system, *Mater. Sci. Forum* 649 (2010) 159-64.
- [8] A. Ludwig, J. Mogeritsch, In-situ observation of coupled peritectic growth, in: *Solidif. Sci. Technol. Proc. John Hunt Int. Symp.* (2011) 233-42.
- [9] J. Mogeritsch, A. Ludwig, In-situ observation of coupled growth morphologies in organic peritectics, *IOP Conf. Ser. Mater. Sci. Eng.* (2011) 27 12028.
- [10] J. Mogeritsch, A. Ludwig, Microstructure formation in the two phase region of the binary peritectic organic system TRIS-NPG, TMS Annual Meeting Symposium "Materials Res. Microgravity," Orlando, Florida (2012) 48-56.
- [11] A. Ludwig, J. Mogeritsch, Recurring instability of cellular growth in a near peritectic transparent NPG-TRIS alloy system, *Mater. Sci. Forum* 790-791 (2014) 317-22.

- [12] J. Mogeritsch, A. Ludwig In-situ observation of the dynamic of peritectic coupled growth using the binary organic system TRIS-NPG, IOP Conf. Ser. Mater. Sci. Eng. 84 (2015) 12055.
- [13] A. Ludwig, J. Mogeritsch, Compact seaweed growth of peritectic phase on confined, flat pro-peritectic dendrites, J. Crystal Growth 455 (2016) 99–104.
- [14] J.P. Mogeritsch, A. Ludwig, Investigation on Peritectic Layered Structures by using the Binary Organic Components TRIS-NPG as Model Substances for Metal-Like Solidification, Crimson Publishers, Res. Dev. Mater. Sci. 4(1) (2018) 1-3.
- [15] D.O. Lopez, J. Van Braak, J.L. Tamarit and H.A.J. Oonk, Molecular mixed crystals of neopentane derivatives. A comparative analysis of three binary systems showing crossed isodimorphism, Calphad 19 (1995) 37-47.
- [16] J.L. Tamarit, Thermodynamic study of some neopentane derivated by thermobarometric analysis, Mol. Cryst. Liq. Cryst. 250 (1994) 347-58.
- [17] Information on [http:// www.merck.de](http://www.merck.de)
- [18] Z. Zhang, Y. Xu and M. Yang, Measurement of the thermal conductivities of neopentylglycol, 1,1,1 Trishydroxymethylpropane, and their mixture in the temperature range from 20°C to their supermelting temperatures, J. Chem. Data 45 (2000) 1060-3.
- [19] S. Akbulut, Y. Ocak, K. Keslioglu and N. Marasli, Thermal conductivities of solid and liquid phases for neopentylglycol, aminomethylpropanediol and their binary alloy, J. Phy. Chem. Solid 70 (2009) 72-8.
- [20] S. Divi, R. Chellapa and D. Chandra, Heat capacity measurement of organic thermal energy storage materials, J. Chem. Thermodyn. 38 (2006) 1312-26.
- [21] Z.Z. Ying and Y.M. Lin, Heat capacity and phase transitions of 2-amino-2-hydroxymethylpropan-1,3-diol from 290 K to 455 K, J. Chem. Thermodyn. 22 (1990) 617-22.
- [22] J. Font and J. Muntasell, Pressure-Temperature equilibrium Curves in Plastic Crystals Derived From Neopentane, Mat. Res. Bull. 30 (1995) 479-89.
- [23] Information on <https://de.wikipedia.org/wiki/Neopentylglycol>
- [24] R.E. Wasylishen, P.F. Barron and D.M. Doddrell, Molecular reorientation in the plastic crystalline phase of Tris, Aust. J. Chem. 32 (1979) 905 -9.
- [25] Information on <http://www.dow.com>
- [26] J.P. Mogeritsch, A. Ludwig, S. Eck, M. Grasser and B.J. McKay, Thermal stability of a binary non-faceted/non-faceted peritectic organic alloy at elevated temperatures, Scripta Mater. 60 (2009) 882-5.
- [27] J.P. Mogeritsch, PhD thesis, Leoben, 2012 (available at <http://smmp.unileoben.ac.at>)
- [28] Information on <http://www.sigmaaldrich.com>
- [29] Information on <http://www.brookfieldengineering.com/>
- [30] G.M. Barrow, Physical Chemistry, McGraw-Hill Inc., (1973) [ISBN 3-528-23806-2].

## Overview of the $\mu$ g-Foam ESA MAP project

F. Garcia-Moreno, T. Neu, P. Kamm, F. Bülk, S. Hutzler and J. Banhart

### Abstract

Metal foams are already found in commercial applications, but beside costs there are still other aspects hindering their breakthrough in the market. The main one is the sometimes unsatisfactory quality of the foam structure represented by the pore size distribution and density homogeneity. It is hard to cope with this due to the lack in understanding basic phenomena ruling foaming and in the availability of data for simulations. To overcome these problems there is a need to understand bubble nucleation, foam growth and evolution and cell wall stabilization in the liquid state, as they determine the cellular structure after solidification. For this purpose, non-destructive methods and different gravity levels are required to measure liquid foam properties in-situ.

X-ray radioscopy is known to be a powerful tool for qualitative and quantitative in-situ analyses in materials science in general and especially for metal foams. The method was used under microgravity in the ESA MAP project ' $\mu$ g-Foam' for the first time and enabled studies of liquid foam evolution, drainage, bubble coarsening, diffusion of alloy constituents, liquid metal imbibition and foam solidification. We will review the highlights of the 46th and 51st ESA Parabolic Flight Campaigns and of the ESA Sounding Rocket Maser 11, but concentrate on recent results obtained during the 65th and 67th ESA Parabolic Flight Campaigns.

On Earth, gravitational flow induces changes of foam structure such as liquid metal drainage during and after the growth process and make fabrication of foams with homogeneously distributed liquid fractions difficult. The latter influences liquid film thickness and consequently the bubble rupture rate, bubble size distribution and gas interdiffusion. Liquid drainage under 1 g and 1.8 g followed by liquid metal imbibition of a foam during  $\mu$ g is evaluated. The imbibition ability of evolving liquid metal foams is demonstrated at 1.8 g and explained by a balance of capillary and gravitational forces. The role of liquid foam viscosity of aluminium-based metal foams prepared by the Formgrip method with 5, 10 and 20 vol% of SiC particles is presented. The resulted density profiles of the foams during gravity transitions were used to obtain non-destructively quantitative data about properties of liquid metal foams such as their effective viscosity and surface tension by solving the foam drainage equation. The foam coalescence rate was analysed during parabolic flights but also for more than 6 minutes microgravity. The unexpected conclusion was that not only gravity but also the external blowing agent contribute to liquid film rupture. This encouraged the MAP team to develop an external blowing agent free alloy which gives rise to an improved cellular structure and a reduced coalescence rate as demonstrated recently in a parabolic flight.

# **The effect of forced melt flow induced by rotating magnetic field on the structure of Al-Si eutectic**

Zsolt Veres, Arnold Rónaföldi, Kassab Al-Omari, András Roósz

**Keywords:** eutectic, melt flow, unidirectional solidification, UMC, electromagnetic stirring

## **Abstract**

Al-Si alloys, which contains eutectic, are used in large quantities. Those are used not only like cast alloys but for base material of brazing technology as well. It is well known that too long Si lamellae can reduce the joining force of brazing, therefore it is necessary to produce finer eutectic structure. During manufacturing of brazing materials, the use of modifying agent (Na, Sr) is not always permitted. In these cases, we can perform to stir the melt.

Eutectic and hypoeutectic Al-Si samples were solidified unidirectionally in a rotating magnetic field of different intensity and the developing structure was investigated. The regular investigation method for these irregular eutectics is the measure of the average distance of eutectic Si lamellae. But this technique is not saying anything about the size of lamellae and about the direction of growing them. Because that we worked out a measuring method by use of mosaic pictures.

During our research work it was found that stirring of melt can change the microstructure of the sample radically: primary silicon and primary aluminum appear near each other and the structure of eutectic is very different around the primary phases. The size and the direction of eutectic lamellae were modified by stirring as well.

Our study shows interesting effects of magnetic stirring and generate some question about the causes.



## **Phase transformation and morphology evolution of $\text{Ti}_{50}\text{Cu}_{25}\text{Ni}_{20}\text{Sn}_5$ during mechanical milling at room temperature and $-78\text{ }^{\circ}\text{C}$**

D. Janovszky<sup>a</sup>, F. Kristaly<sup>b</sup>, T. Miko<sup>c</sup>, A. Racz<sup>d</sup>, M. Sveda<sup>a</sup>, A. Sycheva<sup>a</sup>, T. Koziel<sup>e</sup>

\*corresponding author: [fejd@uni-miskolc.hu](mailto:fejd@uni-miskolc.hu)

<sup>a</sup>MTA-ME Materials Science Research Group, Miskolc, Hungary

<sup>b</sup>Institute of Mineralogy and Geology, University of Miskolc, Hungary

<sup>c</sup>Institute of Physical Metallurgy, Metalforming and Nanotechnology, University of Miskolc, Hungary

<sup>d</sup>Institute of Raw Material Preparation and Environmental Processing, University of Miskolc, Hungary

<sup>e</sup>Faculty of Metals Engineering and Industrial Computer Science, AGH University of Science and Technology, Krakow, Poland

Nanocrystalline/amorphous powder was produced by ball milling of  $\text{Ti}_{50}\text{Cu}_{25}\text{Ni}_{20}\text{Sn}_5$  (at.%) master alloy at room temperature and using dry ice cooling around of grinding bowl. Scanning electron microscope (SEM) and X-ray analysis (XRD) was used to observe the changes in the phases/amorphous content and in the shape of particles as function of milling time and temperature. During both milling process the deformation-induced hardening and phase transformation caused the hardness value to increase from 506 to 780  $\text{HV}_{0.01}$ . During ball milling, the average particle size decreased with milling time to  $\sim 25\text{ }\mu\text{m}$  and  $\sim 38\text{ }\mu\text{m}$  after 180 min of milling. The amount of amorphous fraction increased continuously and independently of temperature until 120 min milling (36 wt% and 33 wt% amorphous content). The interval of crystallite size is below than 12 nm after 180 min of milling. Cubic  $\text{Cu}(\text{Ni},\text{Cu})\text{Ti}_2$  structure was transformed into the orthorhombic structure owing to the shear/stress, dislocations and Cu substitution during milling process. The weight fraction of  $(\text{Cu},\text{Sn})\text{Ti}_3$  phase continuously changes during milling process.

## **Compositional templating for heterogeneous nucleation of intermetallic compounds**

**Z.P. Que, Y. Wang and Z. Fan**

BCAST, Brunel University London, Uxbridge, Middlesex, UB8 3PH, UK

The understanding of heterogeneous nucleation of intermetallic compounds (IMCs) during solidification of engineering alloys is of both scientific and technological importance, and is particularly relevant to recycling. However, effective refinement of IMCs is currently hampered by our poor understanding of their heterogeneous nucleation. In this contribution, we present our latest understanding of heterogeneous nucleation of Fe-containing IMCs in Al-alloys. First we demonstrate that heterogeneous nucleation of IMCs is difficult and therefore requires large nucleation undercooling. Our differential scanning calorimetry (DSC) measurements show that under normal solidification conditions the undercooling required for heterogeneous nucleation of IMCs is in the order of tens of Kelvin, and that the undercooling increases with increasing complexity of the stoichiometry of the IMCs. This is because nucleation of IMCs needs to create not only the correct crystal structure but also the correct elemental compositions. We then present our new approach to enhancing heterogeneous nucleation of IMCs by both structural templating and compositional templating. We show that chemical segregation of selected elements at the liquid/TiB<sub>2</sub> interface can lead to significant reduction of nucleation undercooling and hence refinement of IMCs in Al-alloys.

## **Segregation of Y at the Mg/MgO interface and its effect on grain refinement**

**Shihao Wang<sup>1</sup>, Yun Wang<sup>1</sup>, Quentin Ramasse<sup>2</sup>, Zhongyun Fan<sup>1</sup>**

1, BCAST, Brunel University London, Uxbridge, Middlesex, UB8 3PH, UK

2, SuperSTEM Laboratory, SciTech Daresbury Campus, Daresbury, WA4 4AD, U.K

Grain refinement of Mg alloys is usually achieved through enhanced heterogeneous nucleation by chemical inoculation. However, there is no universal grain refiner for Mg alloys. For example, Mg-Zr master alloy works only for Al-free Mg alloys. Recently, our research demonstrated that high shear can induce significant grain refinement in Mg-alloys, which is mainly attributed to the enhanced heterogeneous nucleation on native oxide particles. Despite this, some of the details of the mechanisms are still unclear. One major question is how the alloying elements in the Mg-alloys affect the nucleation potency of native oxide particles and hence effectiveness of grain refinement. Therefore, there is a need to understand the surface condition of oxides in Mg-alloy melts, especially at atomic level. In this work, heterogeneous nucleation and grain refinement have been studied in Mg-Y alloys. Advanced electron microscopy was used to investigate the effect of Y addition on the nature of the oxide particles in the Mg-0.5Y alloys. The mechanism underlying the heterogeneous nucleation of  $\alpha$ -Mg on the native MgO particles is discussed in terms of the Y segregation and crystallographic match at the Mg/MgO interface.



## **Effect of positive lattice misfit on prenucleation**

H. Men and Z. Fan

BCAST, Brunel University London, Uxbridge, Middlesex, UB8 3PH, UK

The liquid adjacent to the substrate can exhibit pronounced atomic ordering, which is referred to as prenucleation. Prenucleation has significant implication on subsequent heterogeneous nucleation process. In this work, we investigated the effect of structure of the substrate on the prenucleation using molecular dynamics (MD) simulation. For simplification, the substrates are set to have {111} surface orientation and varying lattice misfit with the corresponding solid phase. This study revealed that the in-plane atomic ordering of the liquid at the interface degrades with increasing the lattice misfit although the layering is nearly irrelevant to the lattice misfit. Furthermore, we found that there exists 2-dimensional (2D) ordered structure within a few atomic layers at the interface through structural templating. The atoms in the 1<sup>st</sup> layer continue the lattice of the surface layer of the substrate, rendering a perfect matching between the 1<sup>st</sup> layer and the surface layer of the substrate. It is noted that the 2D ordered structure at the interface in the systems with positive misfit is distinct from that in the system with negative misfit, where Shockley partial dislocations with predominant edge component are generated in the 1<sup>st</sup> layer. This implies that positive or negative misfits could produce different effects on atomistic mechanism of the heterogeneous nucleation.

## **Effect of high shear on the grain refinement of Al-alloys**

Feng Wang, Hu-tian Li, Zhongyun Fan

BCAST, Brunel University London, Uxbridge, Middlesex, UB8 3PH, UK

Grain refinement of aluminium alloys has always been desirable because it benefits the casting process, ensuring consistent properties and facilitates the subsequent processing. However, the efficiency of the common grain refiners is extremely low as only approximately 1% of the particles do initiate aluminium grains while the rest remain inactive and often form agglomerates, becoming inclusions in the final castings. This effect further accumulates with repeated recycling. Therefore, searching for a more sustainable alternative to achieving grain refinement has attracted increasing interest from both academia and industry. In this work, we present our recent investigation on the effect of high shear on grain refinement of a series of Al-alloys including commercial-purity, Al-Mg and modified wrought alloys. In general, the alloy melts were subjected to high shear prior to casting in a TP-1 mould for grain size measurement. The grain size results show that, without any addition of exogenous grain refiners, effective grain refinement has been achieved in all the investigated alloys. Although the detailed mechanisms need further investigation, these direct grain refinement results demonstrate that high shear is a promising technology for grain refinement without the necessity of adding exogenous grain refiners.

## **Grain initiation behaviour and its effect on grain refinement**

F. Gao and Z. Fan

BCAST, Brunel University London, Uxbridge, Middlesex, UB8 3PH, UK

Effective grain refinement strongly depends on the interplay between nucleation potency of nucleant particles, grain initiation behaviour and solidification conditions. Recently, we have made good progress in understanding grain initiation behaviour, and developed the concepts of progressive grain initiation and explosive grain initiation. We found that the most effective grain refinement can be achieved by impeding nucleation using nucleant particles of least potency, which is in direct contrast to the traditional approach to grain refinement, in which the most potent nucleant particles are used to enhance heterogeneous nucleation. In this contribution we present our latest understanding of effective grain refinement through analytical and numerical modelling of solidification processes. We will show the grain initiation behaviour can be best presented by a grain initiation map, which can be used as a practical guide for effective grain refinement.

## **An *ab initio* study of the potency of MgO particles for heterogeneous nucleation of light metals**

C. M. Fang and Z. Fan

BCAST, Brunel University London, Uxbridge, Middlesex, UB8 3PH, United Kingdom

Potency of a substrate surface is crucial in the heterogeneous nucleation of light metal alloys. This can be reflected in the atomic ordering of the liquid atoms adjacent to the substrate at temperatures above the liquidus, which is defined as prenucleation. We investigated the prenucleation of liquid metals adjacent to the MgO surfaces using an *ab initio* molecular dynamics simulation (AIMD) technique. Our study reveals that MgO surfaces in contact with liquid metals exhibit a variety of two dimensional (2D) structures which may contain atomic vacancies and displacements. We observed the formation of atomically rough MgO{111} surfaces in both Mg and Al liquid during the AIMD simulations. This atomic roughness eliminates not only the in-plane ordering, but also largely the atomic layering in the liquid adjacent to the liquid/substrate interfaces. Another interesting result is that, although MgO{001} is flat, the 1<sup>st</sup> Mg layer templated by the MgO{001} surface is atomically rough, making it impotent to heterogeneous nucleation in liquid Mg. This study improves our understanding of both prenucleation and heterogeneous nucleation processes. Moreover, roughening substrate surfaces may be used as a practical means to manipulate heterogeneous nucleation and hence to achieve more effective grain refinement.

---